
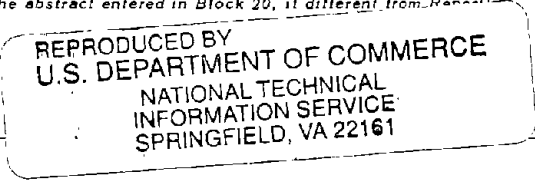


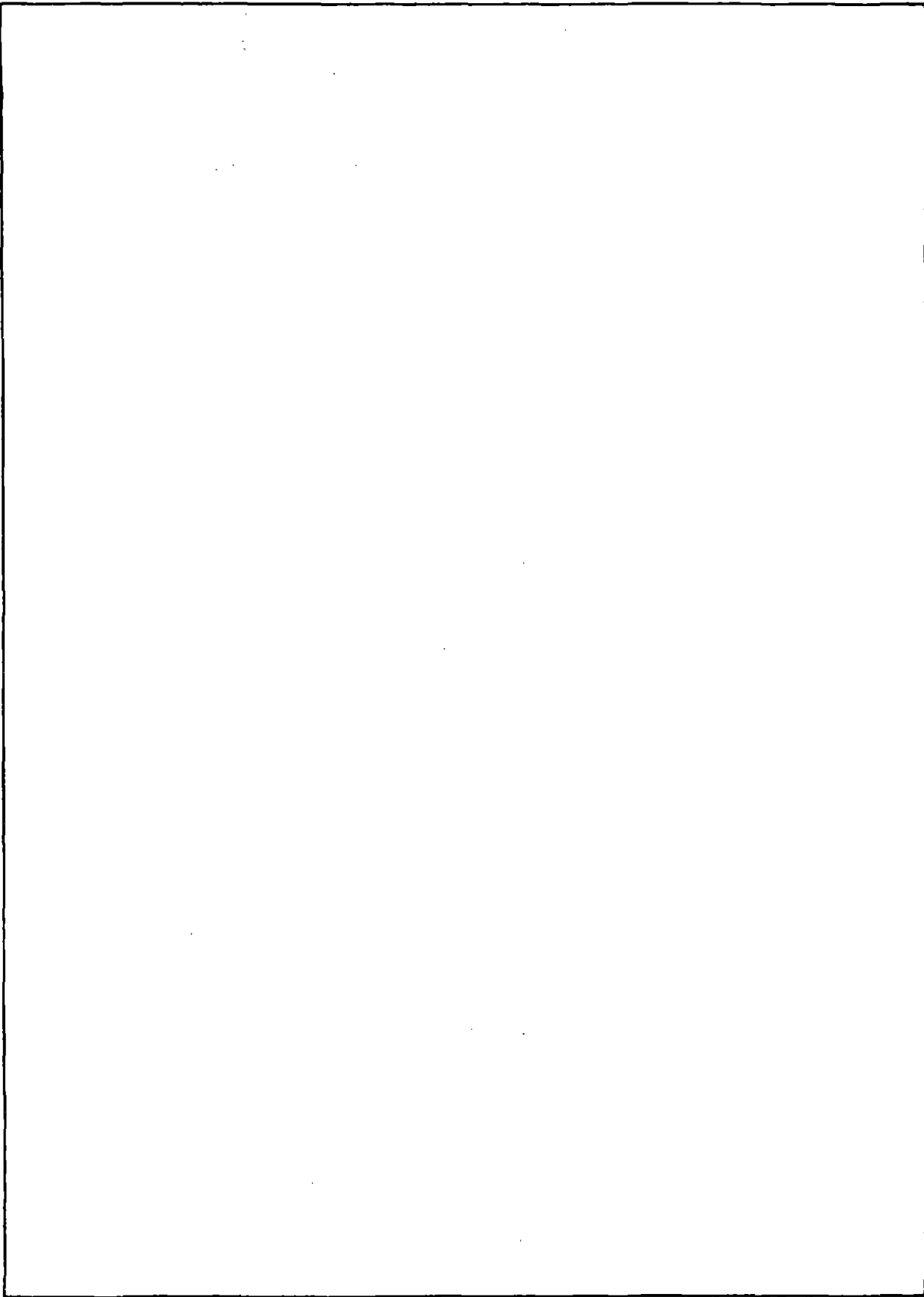
UNCLASSIFIED

SECURITY CLASSIFICATION OF THIS PAGE (When Data Entered)

REPORT DOCUMENTATION PAGE		ADA073765
1. REPORT NUMBER DNA 4797P-1	2. GOVT ACCESSION NUMBER	
4. TITLE (and Subtitle) PROCEEDINGS OF THE NUCLEAR BLAST AND SHOCK SIMULATION SYMPOSIUM 28-30 November 1978, Volume I	5. TYPE OF REPORT & PERIOD COVERED Proceedings	
	6. PERFORMING ORG. REPORT NUMBER	
7. AUTHOR(s) See individual presentations.	8. CONTRACT OR GRANT NUMBER(s) DNA 001-79-C-0081	
9. PERFORMING ORGANIZATION NAME AND ADDRESS General Electric Company--TEMPO DASIAC, 816 State Street Santa Barbara, California 93102	10. PROGRAM ELEMENT, PROJECT, TASK AREA & WORK UNIT NUMBERS Subtask P99QAXDC008-09	
11. CONTROLLING OFFICE NAME AND ADDRESS Director Defense Nuclear Agency Washington, D.C. 20305	12. REPORT DATE December 1978	
	13. NUMBER OF PAGES 430	
14. MONITORING AGENCY NAME & ADDRESS (if different from Controlling Office)	15. SECURITY CLASS (of this report) UNCLASSIFIED	
	15a. DECLASSIFICATION/DOWNGRADING SCHEDULE	
16. DISTRIBUTION STATEMENT (of this Report) Approved for public release; distribution unlimited.		
17. DISTRIBUTION STATEMENT (of the abstract entered in Block 20, if different from Report)		
		
18. SUPPLEMENTARY NOTES This work sponsored by the Defense Nuclear Agency under RDT&E RMSS Code B337079464 P99QAXDC00809 H2590D.		
19. KEY WORDS (Continue on reverse side if necessary and identify by block number)		
Airblast	DABS	Simulation
Ammonium Nitrate Fuel Oil	DIHEST	Simulators
BLEST	Environmental Impact	Site Selection
Cratering	Ground Shock	Thermal
HEST	Proceedings	Underwater Shock
20. ABSTRACT (Continue on reverse side if necessary and identify by block number)		
<p>→ This report contains the papers presented at the Proceedings of the Nuclear Blast and Shock Simulation Symposium held 28-30 November 1978 at the Naval Ocean Systems Center, San Diego, California, under the sponsorship of the Shock Physics Strategic Structures Division (SPSS) of the Defense Nuclear Agency. The Symposium provided a forum for the exchange of information on technical approaches and recent accomplishments in the development of nuclear blast and shock simulators. ★ (cont on p. 1)</p>		

UNCLASSIFIED

SECURITY CLASSIFICATION OF THIS PAGE(When Data Entered)



UNCLASSIFIED

SECURITY CLASSIFICATION OF THIS PAGE(When Data Entered)

GENERAL DISCLAIMER

This document may be affected by one or more of the following statements

- **This document has been reproduced from the best copy furnished by the sponsoring agency. It is being released in the interest of making available as much information as possible.**
- **This document may contain data which exceeds the sheet parameters. It was furnished in this condition by the sponsoring agency and is the best copy available.**
- **This document may contain tone-on-tone or color graphs, charts and/or pictures which have been reproduced in black and white.**
- **This document is paginated as submitted by the original source.**
- **Portions of this document are not fully legible due to the historical nature of some of the material. However, it is the best reproduction available from the original submission.**

(cont R p 1473A)

*Volume I contains papers on the following topics:

CONTENTS

VOLUME 1

Accession For	4
NTIS Grant	
DDC TAB	
Unannounced	
Justification	
By	
Dist	Dist special
Availability Codes	
Availand/or	

SITE SELECTION AND ENVIRONMENTAL CONSIDERATIONS

TEST SITE SELECTION FOR NUCLEAR BLAST AND SHOCK SIMULATION –
LTC J.T. Neal, Air Force Systems Command

ENVIRONMENTAL CONSIDERATIONS FOR BLAST AND SHOCK SIMULATION –
R.H. Rowland, K.E. Gould, General Electric Company-DASIAC

7
17

AIRBLAST/THERMAL EFFECTS SIMULATION SESSION

A STATUS AND CAPABILITY REPORT ON NUCLEAR AIRBLAST SIMULATION
USING HEST – H.W. Wampler, G.G. Leigh, Civil Engineering Research Facility;
Capt. M.E. Furbee, F.E. Seusy, Air Force Weapons Laboratory

27

NUCLEAR AIRBLAST SIMULATION WITH EMPHASIS ON DYNAMIC PRESSURE –
Capt. D.P. Martens, DNA Field Command

95

SOME CONSIDERATIONS IN THE DESIGN OF A DYNAMIC AIRBLAST
SIMULATOR – J.D. Renick, Air Force Weapons Laboratory

125

NUMERICAL COMPUTATIONS OF SIMULATION TESTS – G.G. Leigh, Civil
Engineering Research Facility; C.E. Needham, Air Force Weapons Laboratory

159

FEASIBILITY INVESTIGATION OF A PERMANENT FUEL-AIR EXPLOSIVE BLAST
SIMULATOR – R.T. Sedgwick, H.B. Kratz, R.G. Herrmann, T.H. Pierce, Systems, Science
and Software

205

THERMAL LAYER SIMULATION BY SOLAR FURNACE RADIATION – T.M. Knasel,
M.D. McDonnell, R. Sievers, A. Houghton, Science Applications, Incorporated

253

THE THERMAL RADIATION SIMULATOR DEVELOPMENT PROGRAM –
J.F. Dishon III, Science Applications, Incorporated

281

THERMAL/BLAST SIMULATION FACILITIES AT THE U.S. ARMY BALLISTIC
RESEARCH LABORATORY – G.Teel, Ballistic Research Laboratory

311

SIMULATION OF TRANSIENT SURFACE LOADS USING PLANE, CYLINDRICAL,
AND SPHERICAL BLAST WAVES – H.E. Lindberg, SRI International

327

EFFECTS OF RIBS ON SHOCK WAVE PROPAGATION IN TUBES – T.H. Schiffman,
H.F. Korman, TRW Defense and Space Systems Group

365

Sand → UNDERWATER SHOCK SIMULATION SESSION

SIMULATION OF THE PULSE FROM AN UNDERWATER NUCLEAR
EXPLOSION WITH A PLANAR ARRAY OF EXPLOSIVE SOURCES –
A.L. Florence, C.M. Romander, SRI International

387

LOCAL SPHERICITY OF THE ACOUSTIC FIELD GENERATED BY A LINE
CHARGE – T.L. Geers, Lockheed Palo Alto Research Laboratory

417

VOLUME 2

UNDERGROUND SHOCK SIMULATION SESSION

A REVIEW OF PRESENT ESTIMATES OF NEAR SURFACE GROUND MOTIONS FROM NUCLEAR DETONATIONS AT OR NEAR THE EARTH'S SURFACE – Capt. G.W. Ullrich, VELA Seismological Center	7
THE HIGH EXPLOSIVE STANDARD NUCLEAR SOURCE – C.T. Vincent, J.M. Thomsen, Physics International Company	31
GRAVITY-SCALING METHODS APPLIED TO CRATER-INDUCED GROUND MOTIONS AND EFFECTS – K.A. Holsapple, R.M. Schmidt, R.L. Dyrdaahl, Boeing Aerospace Company	55
MULTIPLE BURST HE GROUND MOTION GENERATION TECHNIQUES – Capt. R.G. DeRaad, DNA Field Command	93
BLEST – A GROUND SHOCK SIMULATOR – F.E. Seusy, Air Force Weapons Laboratory; H.E. Auld, Civil Engineering Research Facility	123
GROUND SHOCK SIMULATION USING DIHEST – K.B. Simmons, C. J. Higgins, Civil Engineering Research Facility	151
SIMULATION VERSUS STIMULATION – R.J. Port, R&D Associates	177

INSTRUMENTATION SESSION

HE BLAST PRESSURE MEASUREMENTS – Capt. D.J. Ray, Air Force Weapons Laboratory	203
---	-----

HIGH-ENERGY SIMULATION SESSION

MACH 130 AIR SHOCK ATTENUATION STUDIES – H.D. Glenn, H.R. Kratz, D.D. Keough, R.P. Swift, Lawrence Livermore Laboratory	223
HE SIMULATION OF GROUND SHOCK-INDUCED MX TRENCH COLLAPSE – J.C. Baker, H.R. Kratz, F.I. Peterson, K.D. Pyatt, Jr., L.E. Bailey, J.L. Waddell, Systems, Science and Software	241
COMPUTATIONAL STUDIES OF A VOITENKO COMPRESSOR – P.S. Brown, M.L. Lohman, Lawrence Livermore Laboratory	261
ANFO FOR NUCLEAR WEAPONS EFFECTS SIMULATION – J. Petes, Naval Surface Weapons Center	289
CONVENTIONAL HIGH EXPLOSIVES FOR NUCLEAR SIMULATION – Capt. G.F. Lederman, Jr., Air Force Weapons Laboratory	311

ATTENDEES

Allen, R.T.	PAC Tech	Edwards, T.Y.	SAMSO
Armstrong, W.L.	CEL	Ernst, C.	MMC
Auld, H.E.	CERF	Ethridge, N.	BRL
Baker, J.C.	SSS	Fletcher, R.	LB&ERI Inc.
Balachandra, M.	Aghabian	Florence, A.	SRI
Baron, M.	PWA	Flory, R.	HQ/DNA
Barron, N.	DA/DAMA	Freiberg, R.	NWEF
Barthel, J.	SSS	Furbee, M.	AFWL
Bell, K.	CERF		
Bertrand, B.	BRL	Gantick, N.	FC/DNA
Bestgen, R.	FC/DNA	Gauthey, R.	NSEC
Beyatte, W.	LLL	Geers, T.	LMSC
Bloodgood, V.	NSRDC	Giltrud, M.	NSWC
Bratton, J.	C/NSC	Glenn, H.	LLL
Brode, H.	RDA	Gordon, J.	NSRDC
Brown, P.	LLL	Grine, D.	SSS
Bultmann, E.	C/NSC		
		Hanagud, S.	GIT
Calhoun, D.	CERF	Heyman, R.	MMC
Carpenter, H.	RDA	Holland, J.	FC/DNA
Coleman, P.	SSS	Holsapple, K.	Boeing
Colton, J.	SRI	Homes, D.	Aerospace Corp.
Conley, W.	NSRDC	Hove, D.	SAI
Conrad, E.	HQ/DNA	Huffington, N.	BRL
Cooper, H.	RDA	Hulcher, G.	TRW
Craig, B.	LASL	Huntington, J.	Acurex
Craig, J.	SAI		
Crenshaw, W.	NARADCOM	Jaramillo, E.	EG&G
Dai, P.	TRW	Keefer, J.	BRL
Davis, H.	MC	Keller, C.	FC/DNA
Davis, R.	FC/DNA	Kennedy, L.	GE-TEMPO
Deevy, T.	HQ/DNA	Kennedy, T.	HQ/DNA
Delaar, R.	FC/DNA	Kitchens, C.	BRL
Demaris, E.	SSS	Knasel, T.	SAI
Dishon, J.	SAI	Kramer, G.	LLL
Dudash, M.J.	GE-TEMPO	Kratz, H.	SSS
Dyrdahl, R.	Boeing	Kuhl, A.	RDA

ATTENDEES (Continued)

Lai, J.	TRW	Quigley, E.	BRL
Laupa, A.	Rand		
Lederman, G.	AFWL	Radkowski, P.	Radkowski Assoc.
Leigh, G.	CERF	Ranlett, D.	PWA
Lewis, J.	RDA	Ravotto, M.	ARRADCOM
Lindberg, H.	SRI	Ray, D.	AFWL
Linnerud, H.	JAYCOR	Renick, J.	AFWL
Lipner, N.	TRW	Richmond, D.	LB&ERI Inc.
		Rowland, R.	GE-TEMPO
Mackey, J.	EG&G		
Malthan, J.	Agbabian	Sachs, D.	Kaman
Marlitt, M.	FC/DNA	Safford, F.	Agbabian
Martens, D.	FC/DNA	Sauer, F.	PI
Matalucci, R.	AFWL	Schalug, R.	SAI
McCall, G.	USANACA	Schiffman, T.	TRW
McDonnell, M.	SAI	Schmidt, R.	Boeing
McKay, M.	SAI	Schuster, S.	CRT
McMullan, F.	FC/DNA	Sedgwick, R.	SSS
Melzer, L.	C/NSC	Senseny, P.	SRI
Merritt, J.	Merritt CASES	Sevin, E.	HQ/DNA
Meyer, G.	NOSC	Shievell, D.	FC/DNA
Mills, T.	LLL	Shunk, R.	ESI
Moore, E.	PI	Stefani, L.	FC/DNA
Mortensen, R.	Aerospace Corp.	Strange, J.	WES
		Strode, J.	FC/DNA
Nakayama, P.	JAYCOR	Sullivan, J.	NAVSEC
Neal, J.	AFSC	Summerfield, M.	PCRL
Nicholson	NSWC		
Noh, W.	LLL	Teel, G.	BRL
		Thomas, J.	FC/DNA
Orphal, D.	CRT	Thomson, J.	PI
		Tillery, R.	NWEF
Petersen, C.	SSS	Triebes, K.	Acurex
Petes, J.	NSWC	Tyler, W.	FC/DNA
Phillips, J.	CNSC		
Pierce, T.	SSS	Ullrich, G.	HQ/DNA
Pittman, J.	NSWC	Ullrich, G.	VELA
Port, R.	RDA		
Pusey, H.	NRL	Vincent, C.	PI
Pyatt, K.	SSS		

ATTENDEES (Continued)

Walker, P.E.	LLL	Whitener, J.	RDA
Walker, R.	NSRDC	Williams, J.	AFWL
Wampler, H.	CERF	Wilson, H.	SAI
Waxler, D.	ARRADCOM	Wolf, C.	Acurex
Whang, B.	NSRDC		

INTRODUCTION

All of the services are involved in the simulation of nuclear blast and shock effects, usually with support of the Defense Nuclear Agency. Air Force and Army programs are similar with respect to obtaining and using field sites, even though the simulation methods vary. On the other hand, underwater simulation required by the Navy has little in common with land-based efforts, especially concerning environmental effects.

In every recent case where a field site has been chosen for the simulation of nuclear blast and shock effects, difficulties of one kind or another were encountered. Delays and chagrin resulted, causing management discomfort at all levels. The procedures need examining and that is the purpose of this paper. The selection of a site is a subjective decision, but the process must be as objective as possible.

Order

Site selection requires a sequence of events, frequently under duress. Program finalization and funds availability seldom materialize quickly, so site selection frequently becomes a pacing activity. Site selection is a multi-faceted activity having multiple, concurrent tradeoffs. The sequence of activity involves:

Program Requirement → Site Criteria → Site Investigation and Evaluation

PROGRAM REQUIREMENT

The requirement prompting the simulation effort usually supports a specific system or is technology development, but a combination is also common. The distinction needs to be recognized because the simulation effort will reflect different attributes of each. DOD system acquisition management policy calls for more realistic testing environments as programs near the production stage. Consequently, testing scale, site representation, and instrumentation amount and accuracy must increase. On the other hand, technology development efforts tend to be more "laboratory-like," cost less, and generally show less need for those qualities stated for systems oriented programs. These aspects are reflected in the criteria for site selection.

Testing Objectives

Overall program objectives are better understood at the outset than are the individual tests, so flexibility must be maintained and also included in the site selection. A range in site conditions is thus generally desirable, so that when a need for introducing variations arises, those conditions will be available. A range of depths to water table, bedrock, and material property interfaces is most often required. Some variations in site geology are not always recognized early in a site selection effort, and may become evident later in the detailed characterization phase. Detailed characterization is required for material modeling and analysis.

SITE CRITERIA

Site criteria tend to be idealistic at the start, and then become negotiable when they can't be satisfied. Nonetheless, the specifying of mandatory, desirable,

and negotiable criteria into clearly delineated categories (a difficult task) will help in the site decision process. To specify these criteria categories, it is necessary that test requirements and objectives be well defined. It is desirable to specify acceptable ranges in values of material properties and geology because tradeoffs may become necessary. Criteria used for the HAVE HOST and MISERS BLUFF sites were generally achieved, yet both are difficult operating locations because of the harsh desert environment (Fig. 1, ref. 1).

Testing Realism

The program requirement dictates in large part the degree of realism demanded in the testing; consequently, scale and geographic location requirements may narrow the field. Credibility derived from the proximity of a test site to a strategic system is difficult to argue when perceptions of national security issues are involved. Safety and support concerns may further restrict the possibilities for siting.

Scaling

Scaling a test site, or a portion of it, to match a scaled nuclear yield presents difficulty for the simple reason that nature usually doesn't cooperate as one might hope for. For example, water tables result from many natural influences; a shallow water table may not be a scaled form of the full-scale (deeper) condition. The same difficulties are experienced with sedimentary rock sequences. Density/depth interfaces that affect outrunning ground motion can usually be scaled, provided the criteria are not too stringent.

When we identified the Pre-DICE THROW 100-ton sites, we relaxed our material size criteria, going to a finer grain size than was desired. It was the only solution if we were to have a shallow water table. Fortunately, it turned out to be a fruitful site for ground motion and cratering research.

Safety/Distance

Safe operating distances for blast overpressure have been generally set at about the 0.1 psi range, and for ground acceleration at 0.1 g; conservatism is contained in these values (2). During the criteria development phase, the largest event should be considered, and some 30 percent yield added to that. Surface equivalent yields must be calculated for buried events; empirical data exists to provide confidence in predicting attenuation ratios due to overburden (3).

Focussing and amplification of blast waves by factors of five to ten are possible when low altitude atmospheric inversions or wind shear interfaces exist (4, 5). Testing can usually circumvent these conditions through judicious timing of the event, but ground shock focussing is geology dependent and doesn't vary much.

Operational Factors

The operational appraisal of site suitability requires a thorough analysis of support and logistics requirements as these criteria will be constrained by budgetary factors. Basic logistic costs are hard to change, so efforts to economize should be started early. Operating costs invariably expand and projects don't often shrink. No good reason exists why the logisticians shouldn't suggest operating locations early in the process, assuming that technical acceptability is more or less equal. A variety of considerations (Fig. 2) are subject to numerous tradeoffs, so every

FIG.1 MX Tests - Site Criteria

- PREMISE**
- Trench and Shelter tests co-located
 - 500-ton same unless W.T. needed
 - L-Y/Nellis Suitable (MX environment)
 - Full-scale site

FACTOR	500-Ton <small>(MILES BLUFF)</small>	Trench & Shelter <small>(HAVE HCST)</small>
• Material	- Dry Sand / B.R. to 50' - Dry Sand / W.T. 35-45'	Dry sand to 50'
• Bedrock	100-150'	50-100' (desired)
• Slope	< 2%	Same
• Area	≥ 50 acres	≥ 640 acres
• Safe distance	- 2.5 mi. dwlg. - 8.0 mi. town - 20 mi / 5000 pop.	- 1.5 mi. dwelling - 5 mi. town - 15 mi. / 5000 pop.
• Owner	Gov't.	Same

- DESIRABLE**
- Location
 - Logistics
 - Activity
- L-Y/Nellis
 ≤ 100 mi. pop. ctr.
 no interference
- Same
 Same
 minimal int.

Fig. 2 Support / Logistics* (tradeoffs = \$\$\$)

- TDY Costs
 - Daily travel
 - Billeting
 - Contractor/Unions
 - Transhipment point
 - Support: supply/vehicles/
equipment/maintenance
 - Utilities: power/water/comm
 - Access roads
-
- Security < Physical information
 - Safety < Personal environmental

* (military vs. BLM vs private lands
have different attributes)

candidate site must be evaluated in toto with respect to cost, schedule, and technical suitability. Fig. 3 identifies natural factors that are usually considered.

SITE EVALUATION AND SELECTION

The process of finding and choosing the best site requires the integration of much data of many different kinds and sources. It's hard to say exactly how to do it, because of the many subjective factors involved. Warm feelings begin developing early; as supporting data are obtained and evaluated relative to the criteria, candidate standings will rise and fall relatively. When all data are assembled, a choice can be made that considers technical acceptability, cost, and schedule.

Every site selection effort will be different, and so the activity leading to the final choice will vary. A hypothetical event sequence (from experience) shows that some 120 days are needed if all activities mesh on schedule (Fig. 4).

The ideal site probably doesn't exist, so the task then is to increase the degree of acceptability as much as possible within the time available, and in the most cost-effective manner.

Screening

The initial screening serves to narrow the field of possible sites as rapidly as possible, which in turn will help subsequent tasks of access, reconnaissance, and environmental appraisal. Nearly every state has long-established ground-water and geological specialists who have the background to quickly provide this screening advice. They will also have access to maps, well data, and other sources of information. Identifying that person(s) early and laying out the exploration plan will save time and money later on.

Field reconnaissance is enhanced by using a light aircraft or helicopter. Safe operating distances and other environmental factors are often more easily seen from the air. Faults are usually more visible from the air, and should be avoided, whether they exhibit evidence of recent movement or not. The discontinuity along a fault line can only complicate the interpretation of ground motion and cratering data. A capable fault nearby a test site might also present a potential condition for litigation, in the event movement occurs during the test program.

Field Investigations

Promising locations are perhaps best examined first by geophysical methods, especially in areas of sparse data. Refraction profiling has been the principal seismic method used in previous investigations, but shallow reflection methods are now being used for mapping near-surface bedrock depth, sometimes in conjunction with electrical resistivity (6-9). Care must be exercised in overrelying on seismic data as two recent examples of erroneous interpretation resulted from velocity reversals and incomplete saturation levels (10).

Once promising areas are identified, drilling will verify the subsurface conditions. Trenching will establish the continuity of near-surface conditions, and make discontinuities easily visible. Drilling can also begin without geophysics if reasonable knowledge of the subsurface exists. Rotary drilling or auguring are economical ways of obtaining material and water table data rapidly. Experienced drillers can tell a lot about materials just from drilling rates and the sounds

Fig. 3 NATURAL FACTORS

- **Critical Nuclear Weapon Effects**
 - physical and engineering properties of soil and rock
 - anisotropy
 - water table depth
 - layering and bedrock depth
- **Construction Factors**
 - slope; topography
 - ground-water quality
 - CBR (California Bearing Ratio)
 - preconsolidation and compaction
- **Engineering Construction Materials**
 - rip rap ; fill
 - aggregate suitability
 - clays (binders , liners)
- **Geologic Hazards**
 - flooding ; mud flow areas
 - landslide susceptibility
 - Swelling clays; active dunes
 - faults

and vibrations of their rig. The drill cuttings provide impure samples, but are useful for gross discrimination of strata. There is no substitute for a borehole!

Core samples can be taken periodically if material properties are needed. Borehole geophysical methods can also provide useful material property data (11). Cores are taken continuously when the preferred site is identified. Undisturbed samples are waxed and shipped to testing labs to obtain quantitative values of strength and stiffness. This is really the beginning of the detailed characterization phase and can continue for several months (Fig. 4).

Site Acquisition

Sites leased from private owners create fewer problems when the owner is adequately compensated. He may in fact become a defender of the program and serve to mitigate local concerns over safety, environmental protection, and workforce presence. On the other hand, unsuccessful negotiation with private owners over property values has led to acquiring sites by legal means, and resulted in litigation that was costly in time and dollars.

Environmental Protection Considerations

Compliance with the intent and letter of the National Environmental Protection Act and associated DOD regulations is an integral and pervasive part of the site selection process. The decision to prepare an Environmental Impact Assessment (EIA) rather than a Statement (EIS) can spell a difference of six months in program starting time. However, to not be able to satisfy requirements of an EIS, if needed, can cause serious delays. A safe solution is to produce an essentially complete document if there is any possibility that an EIA is not sufficient, or if unresolved questions exist. A great help in this regard is to engage someone who can clearly identify with local environmental sensitivities, and who has experience with acceptable levels of detail. Siting on Federal land has major advantages, as EISs may already exist and usually include a large variety of activities within the scope of a particular mission. For example, several of the National Ranges and Test Centers will allow high explosive testing.

Public Notification

Experience shows that state Governors need to be informed of major projects, even when operating on Federal land. The notification of plans to site in a particular state should be made as early as possible, followed by an active public information program.

EPILOGUE

Alternatives

Murphy's law applies to site selection and therefore backup choices are desirable; other fallback positions can be achieved by relaxing the criteria. A nonideal location may be a reasonable compromise for either technical or operational reasons, or testing at reduced scale may also be possible.

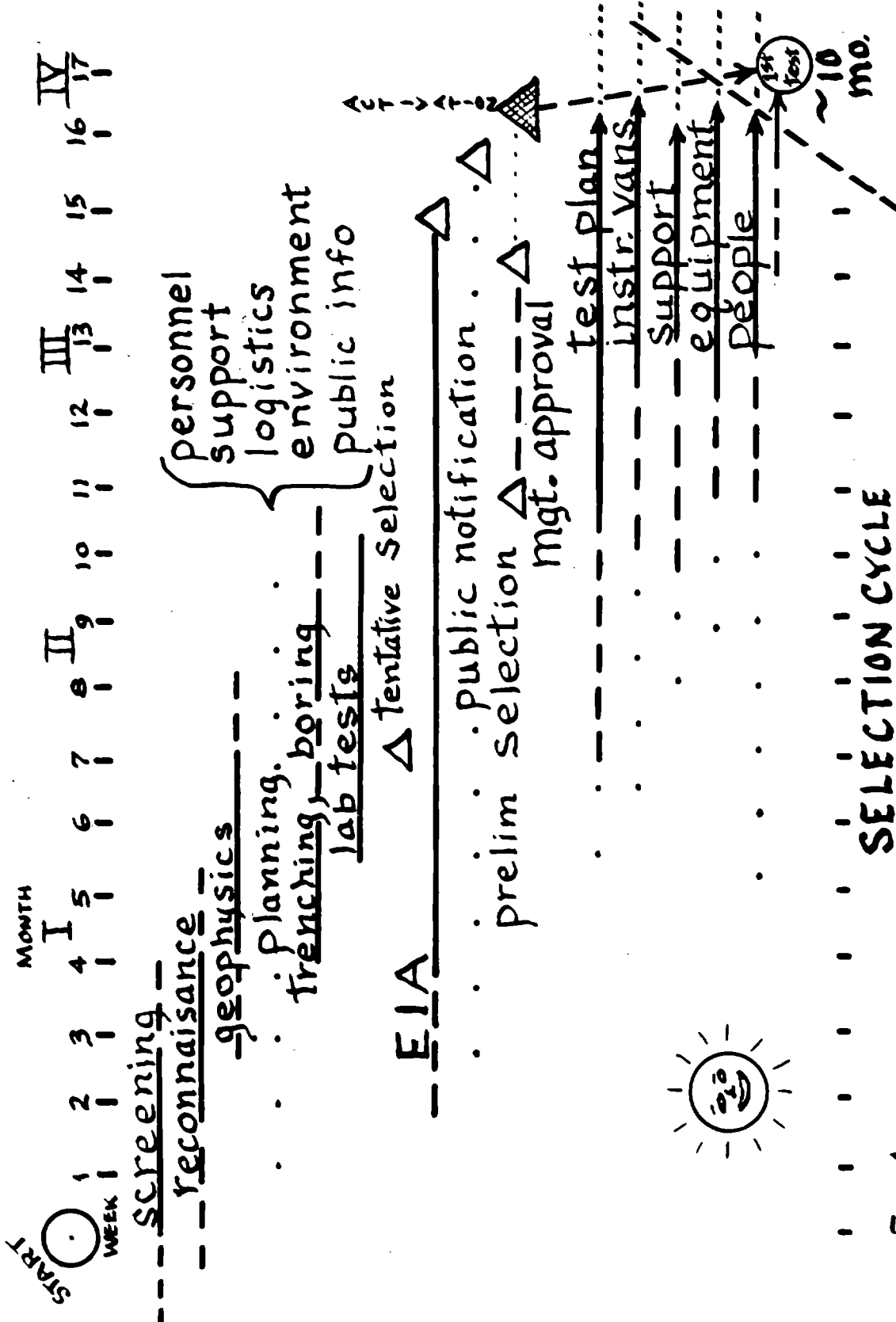


Fig. 4

Lessons Learned

Corporate memory is an essential ingredient in the site selection process. The memory of individuals (or their residency) fades all too quickly, so that if "lessons learned" are not documented almost immediately, corporate memory is compromised. A number of organizations have established handbooks to systematically incorporate their lessons learned. I believe this is an essential element in every testing program. In fact, it should include every aspect of test programs, not just the site selection (12).

Outlook

Those individuals tasked with the site selection process have learned the following lessons:

- a. Federal lands are favored, especially National Ranges, for a variety of reasons involving operations and support.
- b. Every site requirement is different, and yet a similar site selection process can be tailored to that requirement.
- c. Attention to an ordered sequence of events will help make management's decision task less painful and more timely.
- d. Precedents establish confidence.

REFERENCES AND NOTES

1. Melzer, L. S. (1976) Unpublished notes, Air Force Weapons Laboratory, Albuquerque, NM.
2. Ristvet, B. L. (1978) Personal communication; data from several sources. Defense Nuclear Agency Field Command, Albuquerque, NM.
3. Furbee, M. E. (1978) Personal communication; cavity energy and venting pressures are extrapolated to equal surface equivalence of TNT. Air Force Weapons Laboratory, Albuquerque, NM.
4. Perkins, B., Jr., P. H. Lorrain, and W. H. Townsend (1960) Forecasting the Focus of Airblast Due to Meteorological Conditions in the Lower Atmosphere, U. S. Army Ballistic Research Laboratory Report No. 1118.
5. Rasmussen, R. A., and J. Kahler (1971) Prediction Method for Blast Focussing, U. S. Air Force Environmental Technical Applications Center Tech Note 71-8.
6. Neal, J. T. et al (1976) Site Investigation Methodology for Multiple Aim Point Missile Systems, Air Force Weapons Laboratory TR-76-145, 231 pp.
7. Rinehart, J. S. (1976) Chapter 7 in reference 6 (Neal et al) describes seismic methods.
8. Ritchey, J. E. (1964) Elements of Engineering Geology, Pitman Pub Co., N.Y. 157 pp.
9. Shepard, E. R. (1949) Subsurface Exploration by Geophysical Methods, Proc. Am. Soc. Testing Materials, pp. 993-1015.
10. Bratton, J. L. (1978) Personal communication, Civilian Nuclear Systems Corporation, Albuquerque, NM.
11. Ristvet, B. L. (1976) Chapter 9 in reference 6 (Neal et al) describes borehole geophysical methods.
12. Peterson, F. H. (1978) Personal communication; the Civil Engineering Research Division has started documenting lessons learned on their HAVE HOST Program. Air Force Weapons Laboratory, Albuquerque, NM.

ENVIRONMENTAL CONSIDERATIONS FOR BLAST AND SHOCK SIMULATION

by

R.H. Rowland and K.E. Gould

INTRODUCTION

A growing number of local and Federal laws require that Federal activities in field simulation of nuclear effects or the construction and operation of simulation devices and facilities thoroughly consider and evaluate the environmental consequences of their operations. This paper, based on DASIAC* experience in preparing environmental analyses for DNA experimental programs, discusses the effect of this environmental legislation on simulation and field test planning. A thorough understanding of these requirements will assist individual experimenters as well as decision makers in avoiding costly delays and possible litigation. A brief synopsis of the major environmental laws affecting simulation tests is given along with some examples of the process as required by DoD and DNA. The presentation describes how environmental considerations can be easily accommodated early in simulation test planning without undue cost or delay.

With all the publicity given to the phrase *environmental impact statement* (EIS), it may come as a surprise that this procedural task is neither the touchstone of legal requirements nor even the principal requirement of DoD-mandated compliance with the law, but rather a formalized record of the alternatives considered in test planning.

REQUIREMENTS

Environmental impact analysis is a prime candidate for the catch phrase of the decade. Its legal status stems from the National Environmental Policy Act of 1970 (PL 91-190, better known as NEPA) which was enacted by Congress to encourage productive and enjoyable harmony between man and his environment and to promote efforts to reduce damage to the environment and biosphere. NEPA established a broad statement of national policy and requirements for Federal agencies to implement the policy. The Act also established the Council on Environmental Quality (CEQ) under the Office of the President whose responsibilities include coordinating implementation of NEPA's requirements. The basic NEPA requirement was to include environmental

*DASIAC is the DoD Nuclear Information and Analysis Center, operated by the General Electric Company for the Defense Nuclear Agency.

considerations in planning all Federal actions. One particular section of that act, Section 102(C), specifies a procedural requirement to assist in implementing the act. This section requires, in some cases, a formal EIS, but it is important to realize that the EIS was envisioned as a documentation of the planning process. It is specifically not to be used as a justification of some particular course of action.

The basic requirements of NEPA that are particularly applicable to simulation tests are really quite simple.

1. Evaluate all reasonable project alternatives
2. Consider the environmental consequences of the anticipated activity along with the usual operational, technical, and budgetary factors
3. Do not begin the project until that evaluation is completed.

The basic idea of meaningful evaluation of alternatives—and for blast and shock simulation this must include alternative methods of developing the required data as well as alternative yields and test locations—was reemphasized by the original guidelines for impact assessment issued by the President's Council on Environmental Quality,* by DoD Instruction 6050.1, and by the complementary DNA Instruction 6050.1A, *Environmental Considerations in DNA Actions*, which gives the basic guidance consistent with the CEQ guidelines.

The intent of NEPA is that impact analysis be treated as an integral part of planning analysis, aimed at developing information to clarify tradeoffs among alternative actions rather than documenting the possible effects of a chosen course of action. The DoD and DNA directives are very clear in their interpretation of this intent. DoD Instruction 6050.1 states, "[The environmental analysis shall] be a complete and objective appraisal of the beneficial and adverse environmental effects of available alternatives, rather than a justification for the proposal. DoD components shall insure that a decision is not made until the environmental consequences of the decision have been assessed."

The CEQ has recently proposed new regulations designed to make the environmental assessment process more useful.† The regulations were developed in compliance with a presidential mandate issued in 1977 to develop binding regulations for NEPA that would replace the present nonbinding guidelines. The new regulations, when enacted, will supplement and modify DNA Instruction 6050.1. The proposed regulations are designed to reduce both paper work and procedural delays

*39 *Federal Register* 20550-20562, 1 August 1973.

†43 *Federal Register* 25230-25247, 9 June 1978.

by streamlining the NEPA process. A theme of the new regulations is to focus major emphasis on a consideration of project alternatives and their effects. CEQ considers evaluation of the alternatives "the heart of the environmental analysis." CEQ expects that the environmental analysis and subsequent EIA or EIS prepared under the proposed rules will represent a "decision document" rather than a justification of an agency decision. The analysis must be clear, concise, and to the point; analytic rather than encyclopedic. CEQ will require that agencies integrate the NEPA process with other planning at the earliest possible time to insure that all "decisions reflect environmental values." Establishing a clear record of this early planning and decision-making process is obviously one method to forestall possible litigation.

It is important to recognize that NEPA does not forbid projects that may have significant environmental impact (other laws are available to do that), but rather it requires that environmental factors be given appropriate consideration along with technical and economic factors.

In the first 7 years that NEPA was in force, the DoD (excluding the Corps of Engineers) was challenged in court about 60 times. In about half of those cases, the Services had neglected to file an EIS; in about 60 percent of the remainder of the cases, the EIS was felt to be a justification document for an action in which the EIS played no part in the action planning. In most of the rest, the main objection was to the lack of adequate consideration of alternatives. Thus, the major challenge to DoD actions from NEPA in the courts comes from not following procedures, rather than from possible environmental degradation.

PROCEDURE

The environmental impact review (EIR) is an important part of the planning process. It must be a fair and complete evaluation of the environmental consequences of an action and its alternatives. It is shown in Figure 1 as an iterative process, exchanging data between project planning and site selection. Based on the information gathered in the EIR, an environmental impact assessment (EIA) is usually prepared. The EIA is a formal record of the environmental considerations made during the planning process. It is usually cost effective to prepare the EIA in the same format as an EIS. It is possible at this point for the lead agency to determine that the project has no significant environmental effect and file a *negative declaration* (however, it is doubtful if any simulation experiment would qualify). Even if a negative declaration is ultimately filed, 2 to 6 months may elapse before the lead agency review has been completed, as indicated by the figure.

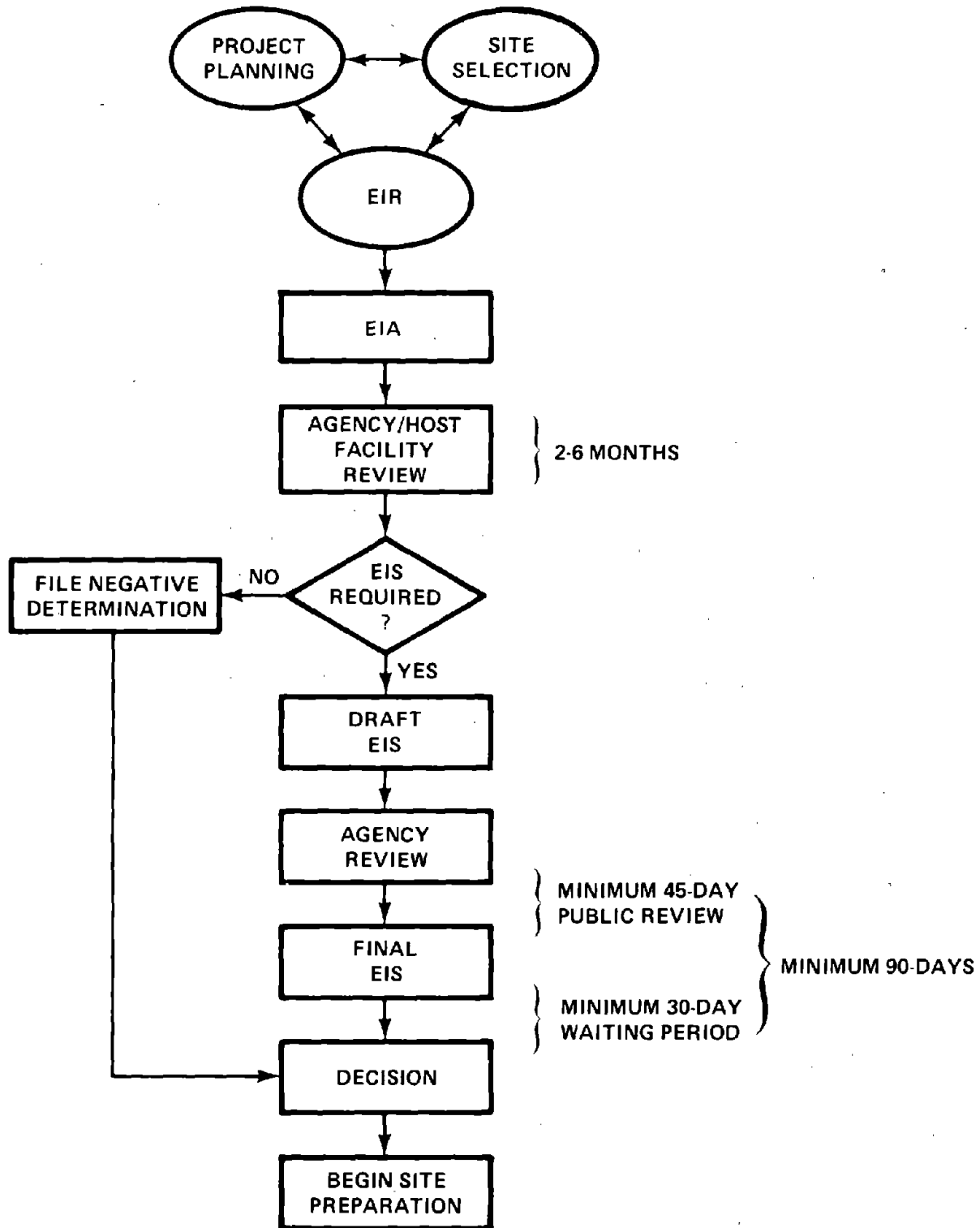


Figure 1. The environmental assessment process.

If an EIS is required, there are mandatory time constraints which are explained in detail later. The important point is to realize that until the entire process is completed, absolutely nothing can be started that indicates a decision on a particular course of action.

Any of three tests will determine if a formal EIS is required (actually, many more tests are listed in DoD 6050.1, but these three are particularly applicable to blast and shock simulation):

1. Is significant environmental damage done?
2. Is the action controversial?
3. Does the action require justification in program budget review procedures?

By these criteria, virtually all DNA field tests or simulation development programs seem to qualify. It is important to recognize that environmental damage is not limited to the physical and biological environments, but includes the social and economic environments as well.

The EIR and EIA requirements are not lessened if the program is on a military range or other Federal property. In fact, in these cases, the decision makers may have a false sense of security, believing they are exempted from environmental assessments, but although most test ranges have environmental impact reviews for their normal continuing operations, these typically do not include DNA test actions.

If the environmental analysis is begun while the program is in the early planning stages, potentially significant environmental impacts can often be alleviated by modifying the program sufficiently to avoid significant environmental impacts or environmental controversies. In this case, an EIA is sufficient and a negative determination is filed with CEQ.* However, if the EIA indicates that significant impact on the physical, biological, or socioeconomic environments is likely to occur, or that the program may be environmentally controversial, an EIS is required.

It is important to understand that the decision to require an EIS is a judgmental one that may be imposed during the review of an EIA. The lead times for preparing and processing EISs often conflict with DNA project schedules, and the requirement that the EIA or EIS procedure be complete before the decision to conduct the test imposes a severe (and often ignored) constraint on planning. The EIR and EIA usually require some details on the project before the pertinent program decisions have been made. This dilemma is best handled when environmental impact analysts are part of the program planning team

*The negative determination may become public record.

and are consulted and kept informed of program plans as they are evolving. A series of EIAs may be required, each one incorporating more information as program decisions become firm. Project changes can also be accommodated by addendums to a previously approved EIA. (The EIA is usually written as broadly as possible to allow for program changes, but some changes may be outside the scope of the EIA. In this case, an addendum or another EIA is required.)

Public information on the project can be a delicate issue, particularly for high-explosive field tests which a layman might automatically assume causes significant environmental damage. It is the natural inclination of the project officer not to want to inform local and State officials of the project until project plans are firm, but this poses the possibility that *local* environmental concerns are not recognized in time to influence project decisions. It is certainly undesirable to have State or local officials object to a project when it is in the advanced planning stage. Also, it is more difficult to obtain the necessary environmental information if the project cannot be openly discussed. If the project is on the land of a Federal facility, the facility's public information office usually handles the public information for the project; otherwise, the Public Affairs Office, Headquarters, Defense Nuclear Agency, has cognizance.

DASIAC strongly recommends that open and frank information contacts be made with State and local environmental offices as soon as possible to make them aware of the project at an early stage so that project planning can take any public concern into account in the EIA, thus reducing the chance of delaying the project.

After the EIA is prepared, DNA Headquarters sends copies to the cognizant DoD component or other Federal agency for review. Usually, field tests are on land under government control and therefore must be reviewed by the host facility. The host facility's review time period varies considerably, but typically 2 to 3 months are required to obtain and incorporate the review comments unless the process is expedited in some manner. An effective way to do this is to maintain contact with the Logistics Directorate at DNA Headquarters.

When the Service (or other agency) and DNA review comments have been incorporated and the revised EIA has been accepted by the review process, field work can begin *if it has been determined by both DNA and the host agency* that an EIA is sufficient. Otherwise, additional processing of the EIA as an EIS is required. To save time, DASIAC recommends that an EIA be prepared to EIS specifications. Usually, an additional month of preparation time is needed for the more thorough and rigorous analysis necessary for a Draft EIS.

An EIS is subject to public review and has mandatory review time periods established by Federal law. *After* the DoD review, the Draft

EIS is forwarded to the CEQ and to pertinent government agencies that announce the EIS availability for public review.* From the date of its forwarding to the CEQ, 45 days are required for a comment period by government agencies and the public. All review comments must be evaluated and the EIS revised as necessary. Approximately 1 month should be allowed for evaluation of such comments and the preparation of the Final EIS. When the Final EIS is forwarded to the CEQ and announced, an additional 30-day waiting period is required before proceeding with field work on the project. In no case can the time period from submission of the Draft EIS to the CEQ to starting the field work on the project be less than 90 days.

TEST IMPACTS

The level of sophistication for environmental analysis depends on the scale and type of a project. Projects that are expected to impact significantly on air quality, water quality, noise levels, and the ecology require analytical personnel trained and experienced in these areas, as well as the capacity to monitor baseline conditions and quantify impacts.

The impacts to be considered include:

1. Construction—magnitude of activity, number of workers, and socioeconomic impacts
2. Actual test—physical parameters that might affect the environment: blast, ground shock, dust, possible harmful explosive products, and the expected results of these physical manifestations
3. Cleanup and restoration of the area.

The socioeconomic impacts are often not treated in detail for field tests. However, they may be a major consideration for a simulator facility development. In some cases, major impacts can be overlooked by not analyzing socioeconomic aspects, thereby resulting in poor project site location. For example, employment projection models are available for projects that might stimulate economic activity and sociological models can be used for projects that impact on residential areas; these variables might be significant at some locations.

During planning, the environmental emphasis must be shared among evaluation of the effects of different types of tests, of different yields, and of alternative sites.

*There is a special provision in the CEQ guidelines for classified EISs, if necessary.

For the various sites, most of the environmental factors are considered in the normal site screening process:

1. Demography and site accessibility
2. Geology
3. Meteorology
4. Land use, including the proximity of gas lines, dams, tunnels, mines, etc.

About the only factor not usually considered explicitly in site selection is ecology. DASIAC uses analyses of four factors for ecological site screening. These usually require a site visit and a little research at a local collegè biology department and are used to determine whether:

1. The site possesses a unique habitat not available elsewhere nearby
2. Endangered species are known to be in the area or nearby
3. A similar habitat is utilized by endangered species
4. The probability of archaeological artifacts being found on the site is significant.

Answers to these simple questions can usually be found easily and quickly, and can be used to eliminate sites which probably would be found unacceptable, or to alert the planners of potential problems.

The usual cause for NEPA challenge is procedural, but other laws can stop programs also. Two of these of particular importance to field test simulation are the Endangered Species Act, which prohibits modification of the habitat of any endangered species, and the Antiquities Act, which requires an evaluation of the scientific usefulness of possible archaeological remains at a proposed test location. A field survey and evaluation of possible sites may be required for compliance with these two laws before undertaking any test planning.

TYPICAL ISSUES

The best possible project selection, the best site selection, and comprehensive documentation of planning to minimize the project's conflict with the environment will not necessarily mean that the analysis will be unopposed or not taken to court. Controversial projects can be (and have been) substantially delayed by litigation. The usual base cause for litigation is *not* environmental issues—although they are used as the excuse—but rather when some social issue arises. Social issues usually cannot be resolved by technical means. That is, changing the technical parameters of a test will not be adequate to solve the social issue raised.

As examples: The Pacific Atoll Cratering Experiment (PACE) had a number of problems—not the least of which was the fact that test bed preparation began before the EIS was prepared*—but the fundamental issue that ultimately stopped PACE revolved around the social issue of the resettlement of the native population. The HARD-PAN HEST/BLEST test in Kansas almost was stopped by a social issue. Here again, the cause was not helped by the failure of Systems Command to release the Draft EIA before beginning to construct the test bed. The people of Kansas had experienced a situation with the AEC at Lyons that led them to believe that statements made by any government agency were incorrect, if not dishonest. However, in this case an adequate paper trail had been laid; the Governor of Kansas and his environmental committee were assured of the Air Force's sincerity in considering environmental matters, and the project did not end up in court. In a very recent example, the MISERS BLUFF test, an injunction was sought by a group which was possibly objecting to the MX program rather than the test. The basis of the complaint was that NEPA procedures had not been followed. The injunction was not granted. The EIA (no EIS was felt to be necessary for this test) was judged as evidence of environmental considerations in planning. DNA/FC had taken the added precaution of circulating the EIA to various state agencies and had acted on comments from the agencies to mitigate possible environmental harm. The MISERS BLUFF experience had another related social problem. The original owner of the test site had planned a land development project for second homes and had attempted to arrange a land swap with BLM. An EIS was required for the land swap. BLM received much criticism during the EIS review, and the project was abandoned. When attempting to locate some test instruments on BLM land, DNA was informed that BLM would first have to prepare its own EIS that would require a minimum of 18 months time and would cost \$250,000.

In reviewing various problems with blast and shock related EIAs, five general areas were found where additional planning and analytic work is often needed:

1. The law is not followed because it is unfamiliar to the project planners—e.g., PACE.
2. Often, facile problems must be evaluated in detail—e.g., what is the probability that Parker Dam would be hurt by MISERS BLUFF? These problems may be scientifically and technically trivial, but the analysis is often difficult and they form the basis for many possible social issues.
3. A lack of scientific knowledge—e.g., the unverified possibility that an area in the North Pacific could

*This project began soon after NEPA and it was not clear if an EIS was required for an overseas project.

be the summer home for Pacific Salmon helped cancel the NOISE deep water explosive test.

4. Ignoring environmental analysis—e.g., the superboom from FLAME which broke windows as predicted—fortunately at the Air Base administration building rather than at the nearby town.
5. Recognizing differences between an experimental program and, say, construction of a road, and structuring the EIR and EIA to accommodate possible changes in the experimental program.

SUMMARY

Experimental analysis is being given more emphasis by government agencies. Those agencies that prepare statements on a regular, continuous basis do not view impact analysis as a delay but rather as a step in planning that must be carried out. The problem with DNA experiments is that the normal tour of duty for a project officer usually encompasses a single test. The result is a constant learning problem as to if and when an EIS is required. In cases where a decision is made to prepare an EIS well into the planning or design stage, delay may be experienced. But if undertaken early enough, the EIS process can be used as an important phase of project planning.

CONTENTS

Section

- I INTRODUCTION
- II NUCLEAR ENVIRONMENTS
- III BACKGROUND
- IV HEST CAPABILITIES AND APPLICATIONS
- V HEST DESIGNING
- VI ANALYSIS OF DATA
- VII HEST, FUTURE DEVELOPMENT AND APPLICATION

REFERENCES

- APPENDIX A: HEST TEST BED SIZE DETERMINATION
- APPENDIX B: HEST DESIGN LOCKUP CODE DESCRIPTION
- APPENDIX C: BRODE IDEALIZED NUCLEAR AIRBLAST EQUATIONS

ILLUSTRATIONS

Figure

- 1 Nuclear Airblast and Ground-Shock Effects
- 2 Gas Bag Experiment I - Simulation of Airblast-Induced Ground Motion Using Detonation Wave
- 3 Simulation of Airblast-Induced Ground Motion High Explosives
- 4 Rebar Cage for Launch Equipment Room of Structural Model
- 5 Three-Dimensional Detonating Cord Weave Installation (Typical)
- 6 Completed Explosives Installation (Typical)
- 7 Placing Event 3 Detonating Cord Weave
- 8 Placing Overburden on Event 3 Box Beam Roof
- 9 High Explosive Simulation Technique (HEST)
- 10 HEST Simulation Capabilities
- 11 Typical Foam HEST Cavity - 75 Percent Foam
- 12 Incident and Reflected Pressures on Aboveground Structures
- 13 Simulated Reflected Pressure Waveform Using Initial Spike
- 14 Typical Waveform from Simultaneously Initiated Low Yield HEST
- 15 Detonating Cord External Driver for Reliable HEST Velocities

ILLUSTRATIONS (Concl'd)

Figure

- 16 Peak Simulation Pressure Versus Charge Density
- 17 FOAM HEST 2 MEA 10 Early History Showing Spikes
- 18 FOAM HEST 2 MEA 10 Full History Showing Baseline Shift
- 19 FOAM HEST 2 Gage Impulse Comparisons
- 20 FOAM HEST 2 MEA 10 Photopole and Impulse Comparisons
- 21 FOAM HEST 2 MEA 10 BLC-.140 Photopole and Impulse Comparison
- 22 FOAM HEST 2 MEA 10 BLC-.140 and Brode Nuclear Design Curve, 35 ms
- 23 FOAM HEST 2 MEA 10 BLC-.140 and Design Using Lockup Model
- 24 FOAM HEST 2 MEA 10 BLC-.140 Best Fit Using Lockup Model
- 25 FOAM HEST 2 MEA 10 BLC-.140 Brode Nuclear Best Fit, 35 ms
- 26 FOAM HEST 2 MEA 10 BLC-.140 Brode Nuclear Best Fit, 57 ms
- 27 FOAM HEST 2 MEA 10 BLC-.140 Brode Nuclear Best Fit, 100 ms
- 28 FOAM HEST 2 MEA 10 BLC-.140 Double-Exp. Peak Pressure, 100 ms
- 29 FOAM HEST 2 MEA 10 BLC-.140 Double-Exp. Peak Pressure, 200 ms
- 30 FOAM HEST 2 MEA 10 BLC-.140 Double-Exp. Peak Pressure, 100 ms, BLC-.140 Back Corrected to Original Data
- 31 Typical Nuclear Airblast Forms
- 32 Shaped HEST Over Target Structure

I. INTRODUCTION

Requirements for the simulation of nuclear weapon effects were recognized soon after the first nuclear devices were exploded. Interest in simulation techniques continued to grow with the requirements for designing and testing hardened structures to withstand severe nuclear environments. The first Nuclear Test Ban Treaty (1958) brought forth a need for ways of simulating nuclear airblast and ground-shock loadings on military systems. This led to further studies and the first development of simulator concepts. The second (limited) Nuclear Test Ban Treaty, signed in the fall of 1963, increased the urgency for development of valid simulation techniques which could be used for testing full-sized or large-scale defense structures. The president's scientific advisory board, meeting shortly after the signing of the second treaty, placed the development of nuclear simulation testing methods high on the list of national priorities. The Air Force Weapons Laboratory (AFWL) immediately started a program to satisfy this need which led to the development of the High Explosive Simulation Technique (HEST).

II. NUCLEAR ENVIRONMENT

To fully understand the problems encountered in the development of simulation techniques, a brief description of the nuclear airblast and ground-shock environment is warranted. Extensive discussions of nuclear weapon effects are provided in References 1 and 2.

Energy from a near-surface nuclear explosion is transmitted to a structural target along two paths--through the air and through the ground (Figure 1). A hemispherical air shock propagates radially outward from the explosion source decreasing in peak pressure and in velocity of propagation as it advances. This airblast wave is a source of direct pressure loading on surface-flush, imbedded structures and causes reflected-pressure loadings on above-ground structures which are many times greater than the incident-airblast pressures.

As the airblast propagates outward it loads the ground over which it passes and causes an airblast-induced ground shock which moves through the ground and encompasses buried structures. The angle of propagation of this airblast-induced ground shock relative to the structure is dependent upon the velocity of airblast propagation and the shock-propagating properties of the soil.

Near the point of the explosion, portions of the ground are vaporized and a crater is formed. Substantial energy is coupled directly into the ground causing a direct-induced ground-shock wave which travels through the ground and loads buried structures. The rate of propagation of this direct-induced ground shock is dependent upon the energy level introduced and upon the soil properties. Subsurface layers of hard rock may cause the direct-induced shock to run out ahead of the airblast-induced ground shock at certain ranges.

The HEST discussed in this paper is used primarily for the simulation of direct airblast loading on surface flush structures and surrounding free field and to produce airblast-induced ground motion for buried structures. Additionally recent work has established the feasibility of the HEST for the simulation of reflected pressure on aboveground structures.

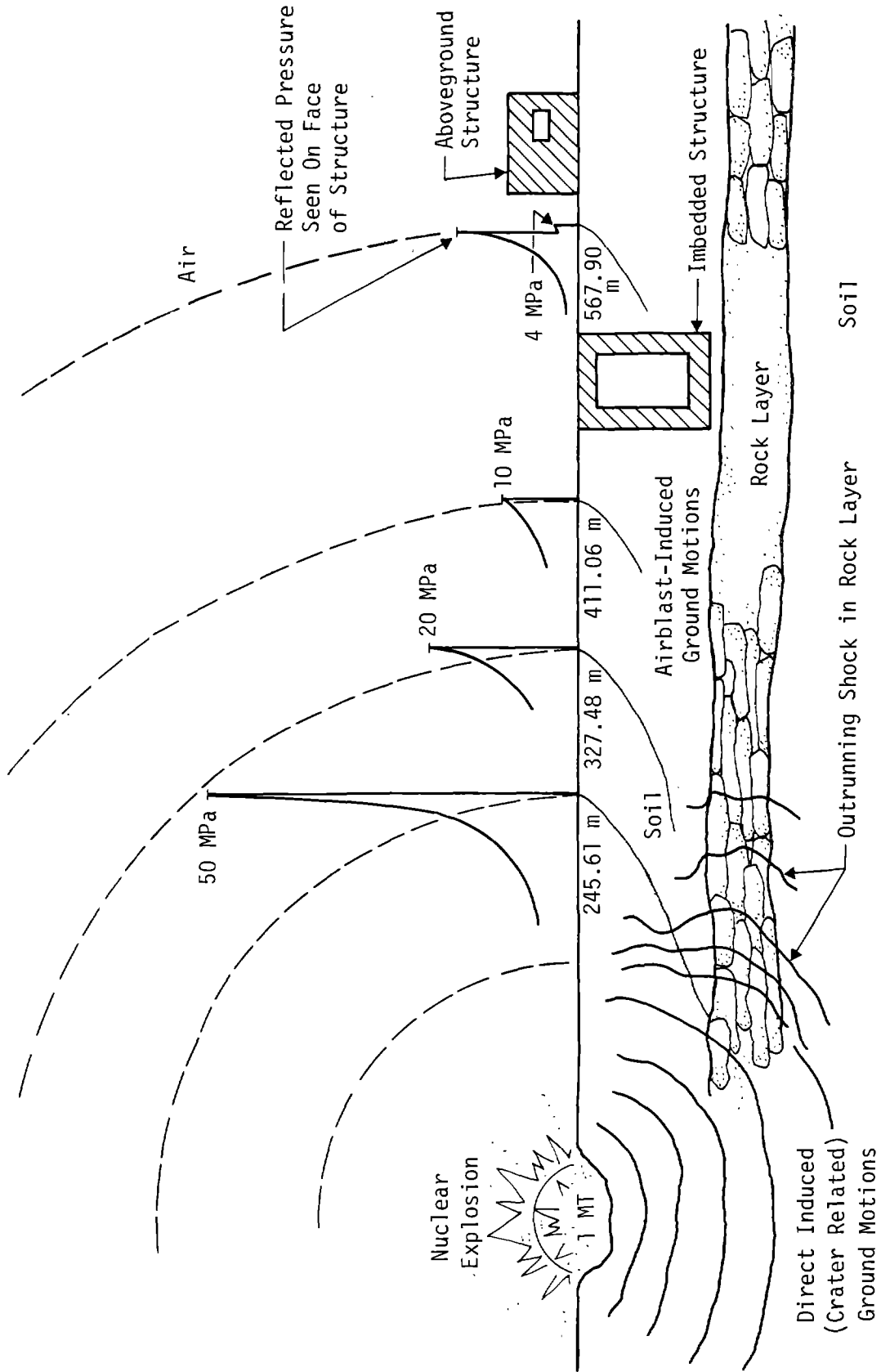


Figure 1. Nuclear Airblast and Ground-Shock Effects

III. BACKGROUND

Development of the HEST was started late in 1963 following the signing of the Limited Nuclear Test Ban Treaty. A series of small experiments conducted earlier by the Stanford Research Institute had shown the possibility of using confined volumes of detonable gas to obtain the long duration pressure pulses necessary for nuclear simulation. The first efforts in the development of the HEST used mixtures of hydrogen and oxygen (Reference 3) confined with a water overburden (Reference 4). An 18-m (60-ft)-long by 12-m (40-ft)-wide "swimming pool" was used for the first HEST test bed. The rise of a 540-m³ (19,200-ft³) block of water from the explosion of the first HEST test in February 1964 is shown in Figure 2. Difficulties were encountered in achieving the required simulation properties (detonation rate, peak pressure, and so on) from the detonable gas mixture. In addition the use of hydrogen/oxygen mixtures posed serious operational and safety problems. Hence a search for a more practical solid explosive source and a simpler overburden arrangement was initiated.

A multisource solicitation resulted in the award of a small contract to Mechanics Research Division (MRD), now renamed General American Research Division (GARD) of the General American Transportation Corporation (GATX) of Niles, Illinois, based on their proposal to use a weave of detonating cord confined in an air cavity by an earthen overburden to simulate the nuclear airblast overpressure. This contract led to the development of the HEST as it was known until 1974. Further testing was accomplished throughout the summer of 1964 by both GARD and AFWL to determine design parameters and airblast-induced ground motion effects produced by the HEST (Figure 3).

The first large-sized HEST [46 m (151 ft) by 30 m (97 ft)], performed in the fall of 1964, was used to load a large structural model (Figure 4) with airblast and airblast-induced ground motions (Reference 5).

In the winter of 1965 the HEST was first used to provide a simulated nuclear airblast environment and ground motion environment for the testing of a full-scale military system. In project HEST I an operational Minuteman Launch Control Facility near Cheyenne, Wyoming, was tested using the HEST. A number of other tests of operational systems soon followed.

In the following years substantial development of the HEST was accomplished (References 6 through 8). Results of these efforts included:

1. Realistic simulation capability;
2. The option of matching nuclear peak pressure and shock-front velocities over the length of the HEST cavity which represented some scaled nuclear field; and
3. Improved methods for installing detonating cord in the HEST cavity.

Many of these improvements were incorporated in Event 3 of the HARD PAN test series conducted in December of 1975 (Reference 9). This test was the last large-scale test employing the traditional HEST, and it marked the end of development efforts for the air-cavity HEST.



Figure 2. Gas Bag Experiment I - Simulation of Airblast-Induced Ground Motion
Using Detonation Wave (Kirtland Air Force Base, New Mexico, March 1964)



Figure 3. Simulation of Airblast-Induced Ground Motion with High Explosives
(Kirtland Air Force Base, New Mexico, August 1964)

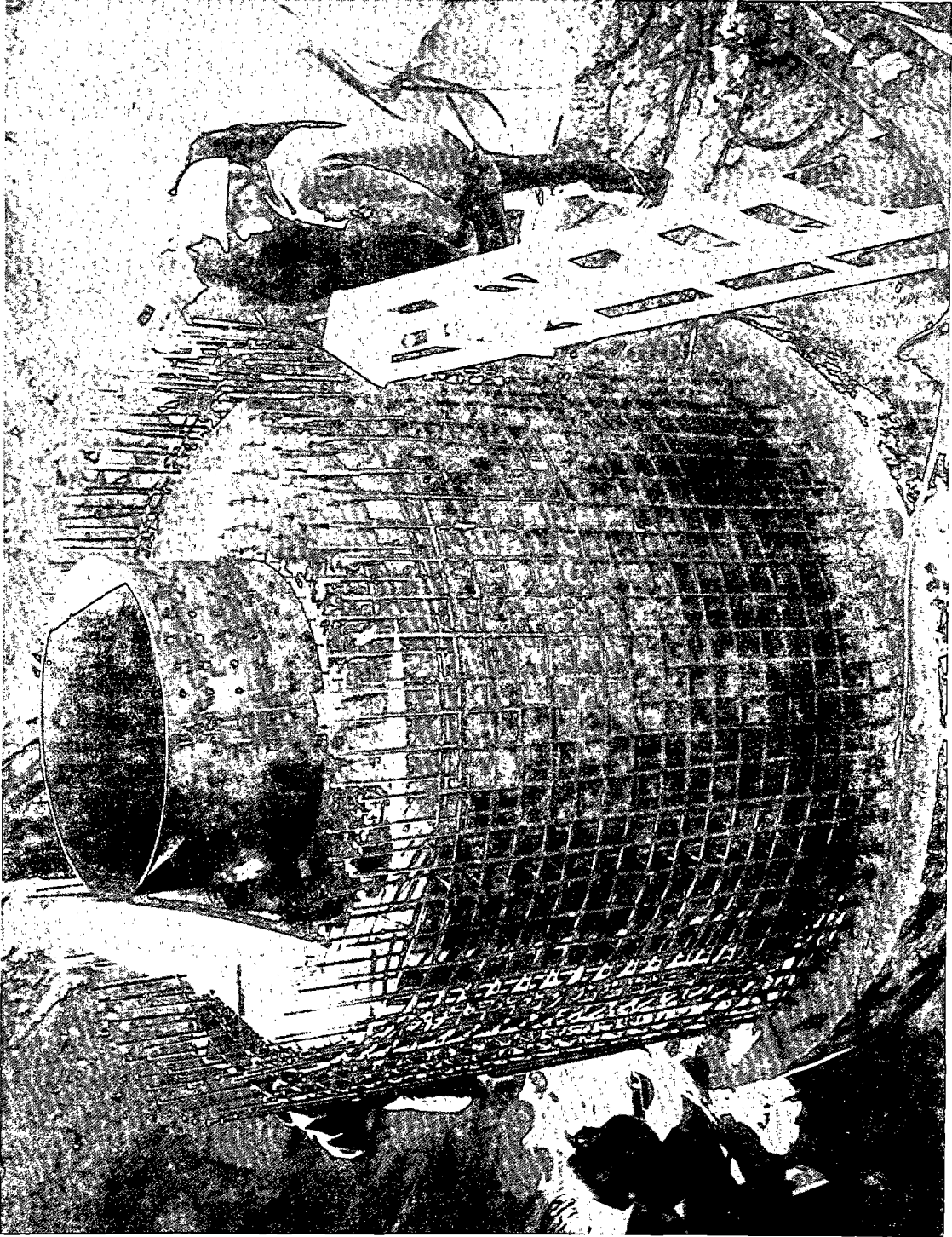


Figure 4. Rebar Cage for Launch Equipment Room of Structural Research Model
(Tested December 1964, Kirtland Air Force Base, New Mexico)

This test consisted of a 36.6- by 61-m (120- by 200-ft) HEST cavity with 85 g/m (400 gr/ft) PETN detonating cord assembled in a three-dimensional "weave." The test was designed to match the peak pressure and velocity decay of a 125-kt weapon over a range from 16.5 to 6.9 MPa (2400 to 1000 lb/in²). The cavity depth varied from 0.26 to 1.21 m (0.85 to 4 ft), and an earth overburden with a loading of 23.9 kpa (500 lb/ft²) was used to provide the required 30 ms simulation time. Details of this test are illustrated in Figures 5 through 8.

Development efforts since December 1975 have been directed toward improving design procedures, further increasing peak pressure, and yield simulation capability, improving the quality of the HEST waveform, and reducing costs through the introduction of new explosives and construction materials (expanded polystyrene bead board). These will be discussed in more detail in the following sections.



Figure 5. Three-Dimensional Detonating Cord Weave Installation (Typical)

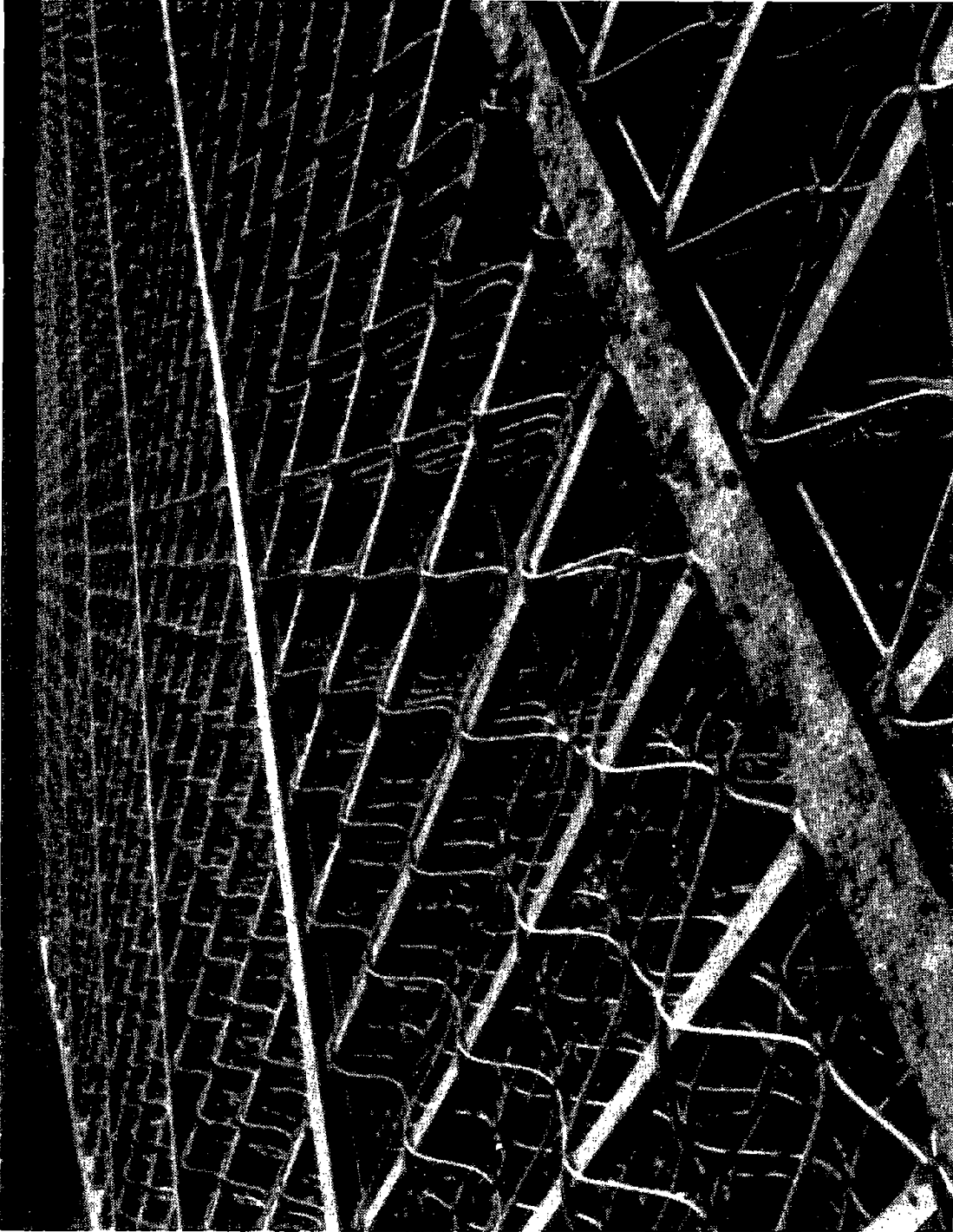


Figure 6. Completed Explosives Installation (Typical)



Note heavy supports for overburden over air cavity and unexpanded detonating cord lying in floor of bay on right.

Figure 7. Placing Event 3 Detonating Cord Weave



Figure 8. Placing Overburden on Event 3 Box Beam Roof

IV. HEST CAPABILITIES AND APPLICATIONS

The objective of the HEST is to accurately reproduce over large areas peak overpressure, rate of pressure decay, overpressure duration or simulation time, and shock front velocity for a given nuclear yield and range or ranges. Figure 9 depicts the most common HEST configuration and the simulation parameters. Figure 10 depicts HEST capability in terms of peak overpressure and yield. It should be noted, however, that these simulations are generally carried out for limited times which are much shorter than the nuclear positive phase durations. Shock-front velocity match is, in varying degrees, attainable over the entire range of HEST pressures and yields through the use of various explosive charge designs and firing systems. That is, for large test beds it is possible to tailor the explosives and the cavity height to vary the pressure and propagation velocity and waveform as desired.

Within the areas of simulation capability described above, HEST possesses a very distinct cost advantage over other nuclear airblast simulation techniques such as free airblast conventional explosives or the Dynamic Airblast Simulator (DABS). HEST is at least an order of magnitude cheaper than these other methods, but one must be willing to accept several undesirable side effects. First, HEST is designed to generate nuclear shock-front overpressures without the dynamic winds normally associated with shock propagation. Therefore it is not possible to use the HEST in examining the phenomenology of shock interactions with aboveground structures. If, however, through previous tests or calculations, the dynamic airblast loading can be specified, then the HEST may be used to simulate this loading just as though it was an incident overpressure.

Controlling the shock-front velocity in a HEST can be a problem, however. The explosive charge in the HEST is normally constructed as a two-dimensional weave with the angle between the various strands of explosive specified to provide the correct shock-front velocity. Data have suggested that shock-front velocity is not totally a function of the weave angle. Attempts to correct this problem through modification of the weave angle or changing the nature of self-propagation have been largely unsuccessful; however, to date this has not appeared to cause a significant problem since its effect is to cause only a slight change in the orientation of the airblast-induced ground motion. When shock-front velocity is critical to a given test it is possible to use an external detonating cord timing system as described later under HEST Designs.

Another potential problem with the HEST is that of overburden fallback. The effect of this problem can be greatly reduced through the employment of various overburden dispersal techniques. Since overburden fallback occurs very late in time relative to the time required for structural responses, its effect is not usually observed on the data recorded electronically. However, it does cause a certain amount of confusion in the posttest visual structural analysis and is best minimized. The simplest corrective technique available is to build the HEST on a slight incline so that the overburden is cast to the side which minimizes the effect on the structure.

Simulation Parameters

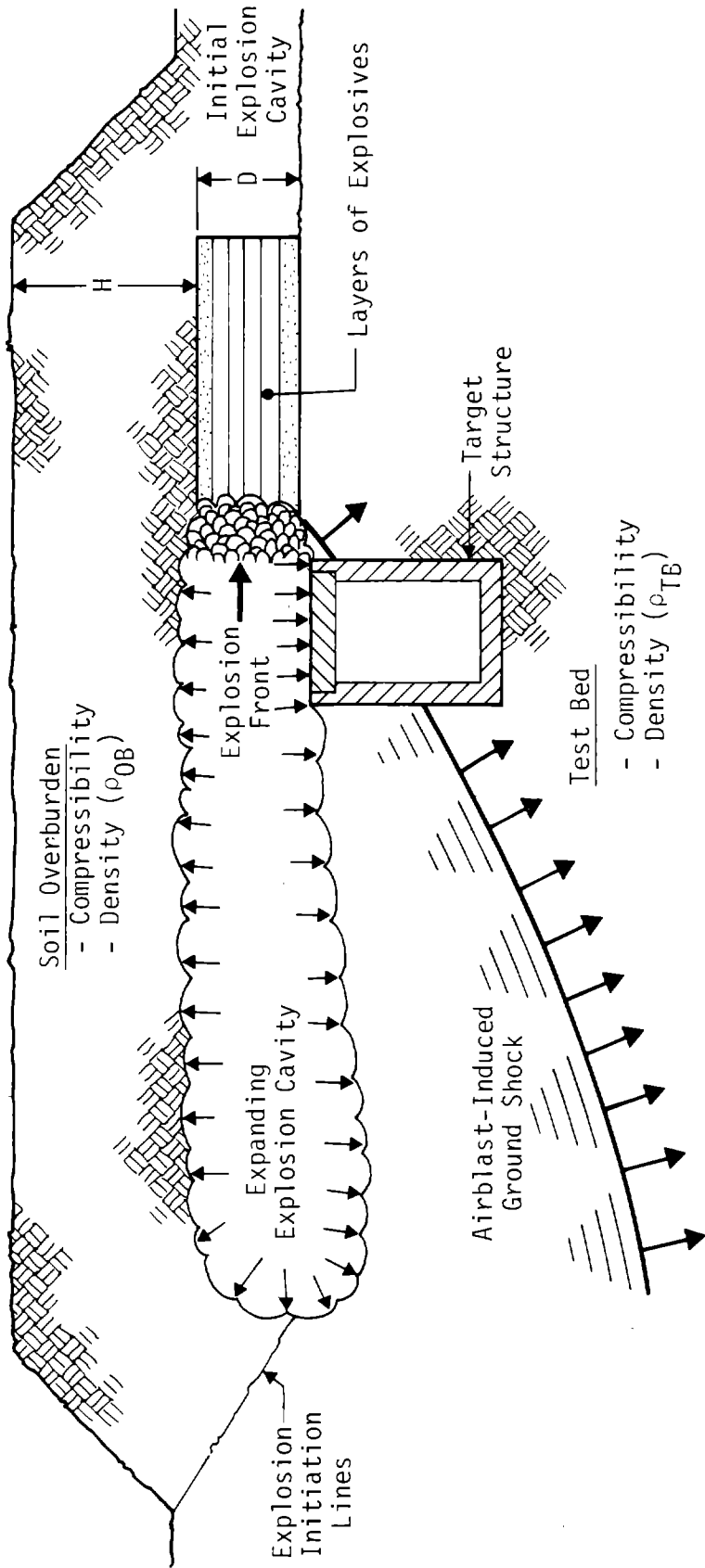
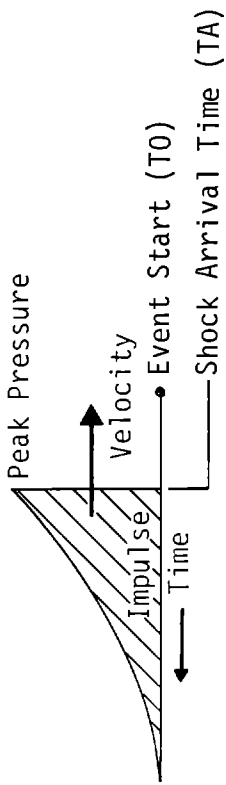


Figure 9 High Explosive Simulation Technique (HEST)

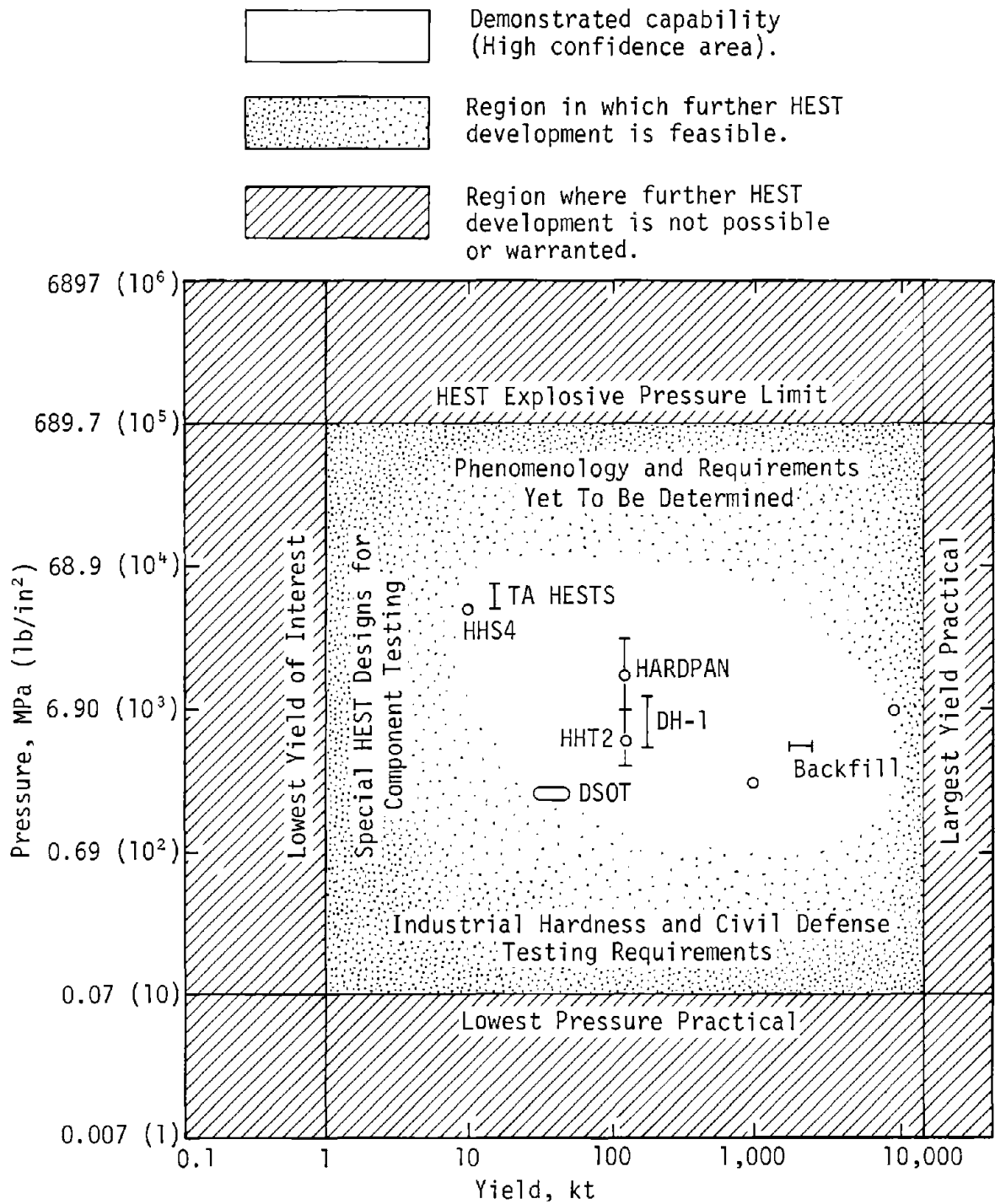


Figure 10. HEST Simulation Capabilities

Lastly, the HEST pressure waveforms are characterized by high-frequency (> 2000 Hz) pressure oscillations. These oscillations are created initially by shock fronts from individual explosive strands interacting at the transducer and later by HEST boundary reflections which cause the shocks to "bounce" throughout the cavity until they damp out. These oscillations are generally of little importance for large-scale strategic structure testing due to their low energy content and high frequency, but they do cause significant difficulties with transducer survivability/linearity. In addition they are a source of considerable confusion since they effectively mask the peak simulation pressure and cause significant effort to be expended in data analysis. These problems are discussed later in the analysis of HEST testing.

V. HEST DESIGNING

Two significant improvements have been made in the last three years in HEST design. First was the replacement of the air HEST in which the overburden is supported by heavy posts and beams with the FOAM HEST in which expanded polystyrene bead board foam totally supports the overburden and explosives (Reference 13). This has resulted in significant cost reductions. Secondly, the availability of ammonium nitrate-based slurry-sausage explosive such as Iremite by Ireco Chemical Corporation, which is consistent, reliable and cheap, has further reduced HEST costs without degradation to the simulation. While it may be necessary to return to the air-detonating cord HEST for extremely high nuclear yield simulations where the overburden weight exceeds 62 kPa (9 lb/in²), the vast majority of future HEST's will undoubtedly use the FOAM HEST, probably with a cheap sausage explosive. Arriving at the cheapest HEST which will adequately perform a particular simulation is a somewhat lengthy process, but those familiar with the process have no trouble working through it quickly, exploring all options.

The FOAM HEST structure uses layers of either foam boards or alternate layers of foam boards and foam beams layered with detonating cord weaves. The number of foam layers may be selected to provide the desired explosives distribution. Usually a layer thickness of 3 to 4 in is satisfactory for cavity depths greater than 11 in. The foam used in these tests is expanded polystyrene beadboard (white), which has a density of about 0.03 kg/m³ (1 lb/ft³). This material is easy to shape and handle, yet can support earthen berms and earth-moving equipment without crushing. A typical 75 percent FOAM HEST configuration will use both solid foam boards and foam beams between the layers of detonating cord weave, as shown in Figure 11. The foam is held together with large "U" pins, or staples, and the weave is tacked down to the foam with these staples. The cavity is then 25 percent air and 75 percent foam (excluding the explosives).

The HEST design is carried out in somewhat separate steps although, due to unexpected outcomes in one area or another (such as cost estimates), it may be necessary to iterate the procedure somewhat. It may be summarized as follows:

1. Define the environment to be simulated.
 - a. Type of waveform - normal overpressure or reflected.
 - b. Load application - simultaneous or sweeping wave.
If sweeping wave, then single or multiple pressures;
determine criticality of shock time of arrival.
 - c. Peak simulation pressure(s).
 - d. Nuclear yield or impulse histories.
 - e. Minimum acceptable simulation time.
2. Using 1a and 1b, select the HEST initiation system; if sweeping, define the propagation velocity(ies).
 - a. Planewave generator.
 - b. Self-timing weave.
 - c. External driver.
3. Select the explosive (detonating cord or Iremite) and using the selection in Step 2, find the explosive charge density(ies).
4. Using 1e, and 2, determine the required test bed size.

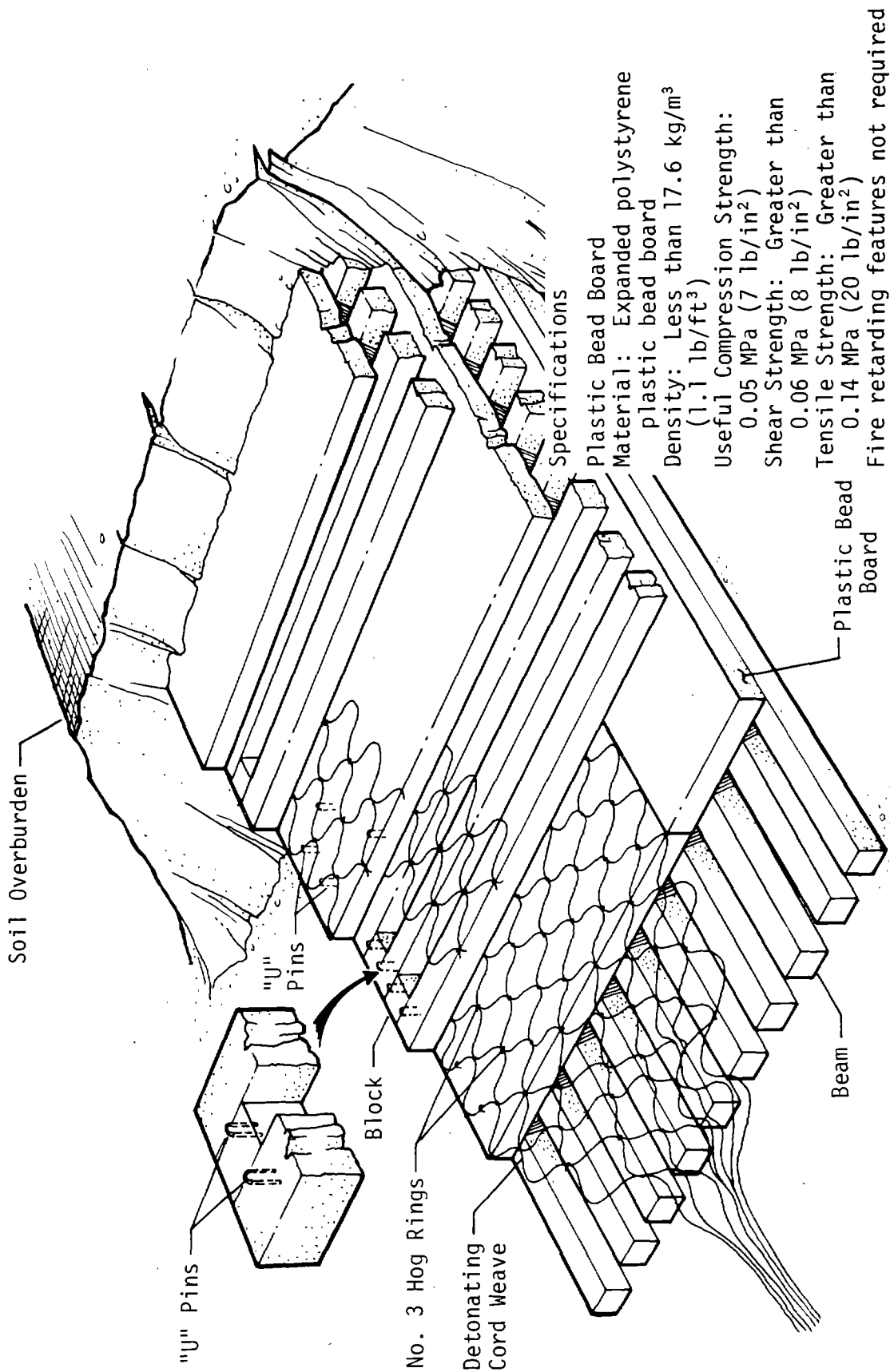


Figure 11. Typical FOAM-HEST Cavity - 75 Percent Foam

5. Using 1c, 1d, 1e, and Step 4 as inputs to the HEST DESIGN LOCKUP CODE, calculate the required cavity depth and overburden characteristics (material, density, and height).
6. Estimate HEST cost.
7. Design HEST.
 - a. Foam or air cavity.
 - b. Explosives layout.
 - c. Instrumentation layout.

DEFINING THE ENVIRONMENT

The FOAM HEST may be used (Reference 11): (1) with lengths of detonating cord or sausage explosive that are initiated simultaneously to produce an instantaneous loading over some given test area as in the HORS* tests, or (2) with two-dimensional weave design to produce a loading that sweeps across the test bed with a given velocity. In the second case the two-dimensional weave can be fixed to produce a propagation and pressure loading that is the same over the test bed to create one nuclear range simulation, as in V-HEST I; it can be varied to produce a decaying pressure loading and a changing propagation velocity to simulate the loading between two nuclear ranges, as in DH-1.

As mentioned earlier, HEST has the capability to simulate normal overpressure waveforms or, if the loading is known, to simulate reflected waveforms which would have resulted from airblast interaction with aboveground structures. The relationship between the two types of waveforms is shown in Figure 12. It can be seen that the reflected pressure returns to the value of the overpressure after a time which is determined by the yield of the incident pressure. For yields below 50 kt, this time is of the order of a few milliseconds and advantage can be taken of the sweeping foam HEST front-end spike below 20 MPa (3000 lb/in²) to simulate the reflected pressure. The peak reflected pressure appears to be controlled by the explosives charge density while the next few milliseconds appear influenced by the percentage of foam in the cavity--the higher the foam density, the more narrow the reflected waveform. An example can be seen in Figure 13. Above 20 MPa (3000 lb/in²) or so, there is little front-end spike in the sweeping foam HEST, but the same effect can be achieved by initiating the HEST from the top (or bottom) simultaneously over a large area. The reaction of the wavefront striking the floor head-on is to produce a significant front-end spike of about double the sweeping wave peak (Figure 14). Considerable effort could be expended in this area to investigate and improve this technique.

For normal overpressure simulations, the nuclear airblast impulse may be matched for a period of time which is determined essentially by the height of the overburden. For practical HEST design it is, therefore, necessary to specify a time beyond which the simulation will not be considered so that inordinate costs can be avoided. This is called the effective simulation time.

* HEST Over Rectangular Slabs

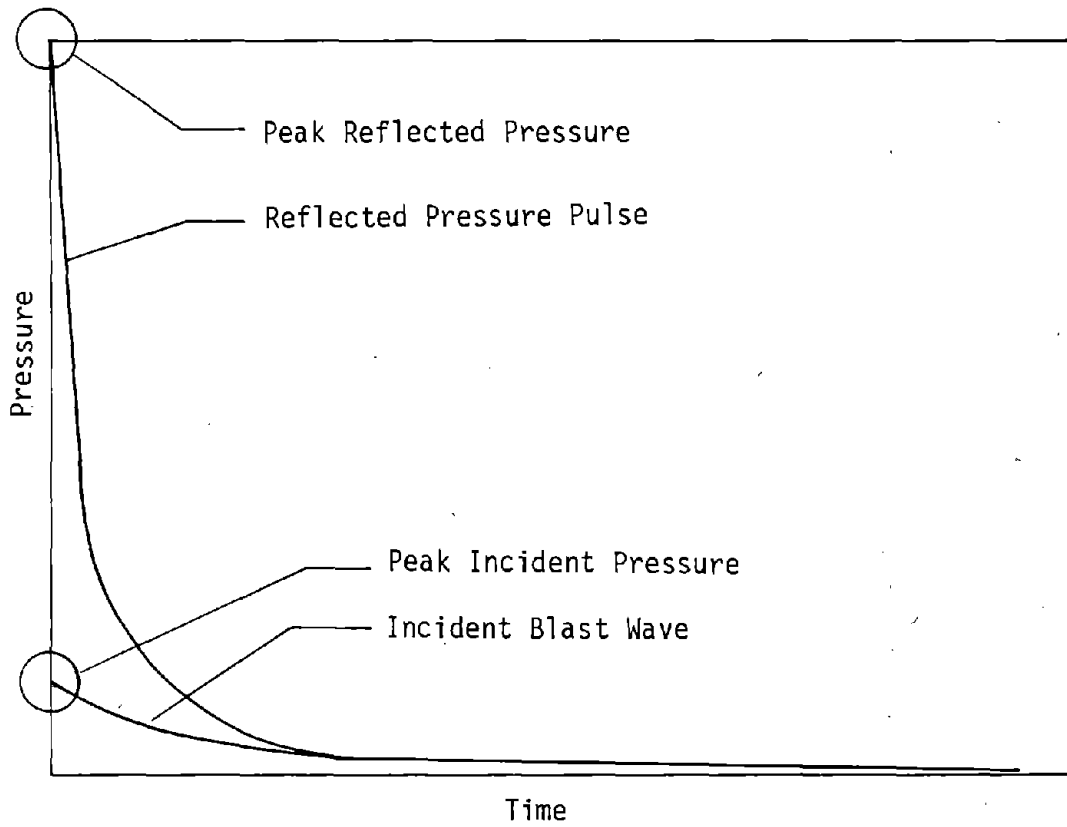


Figure 12. Incident and Reflected Pressures on Aboveground Structures

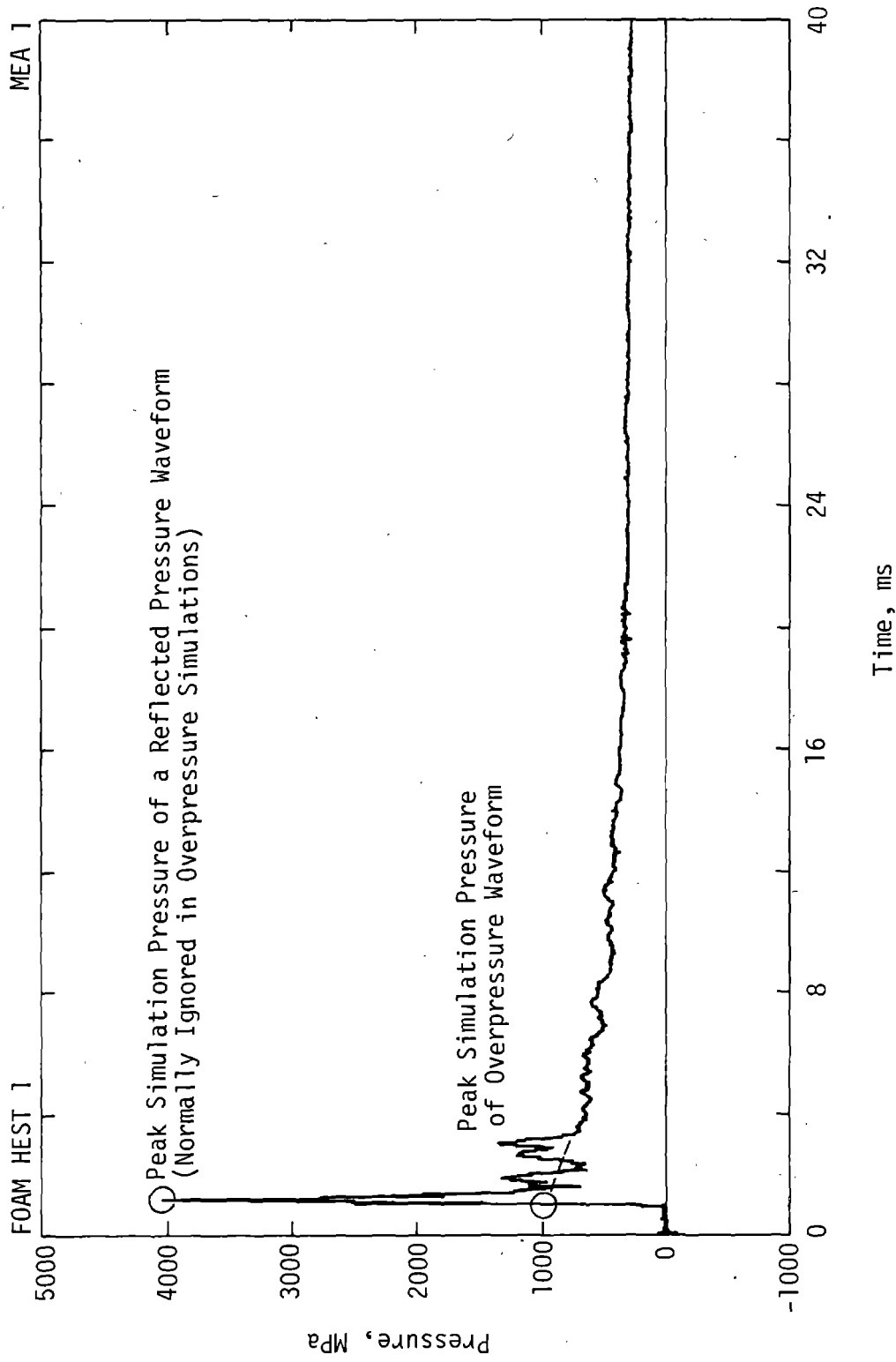


Figure 13. Simulated Reflected Pressure Waveform Using Initial Spike

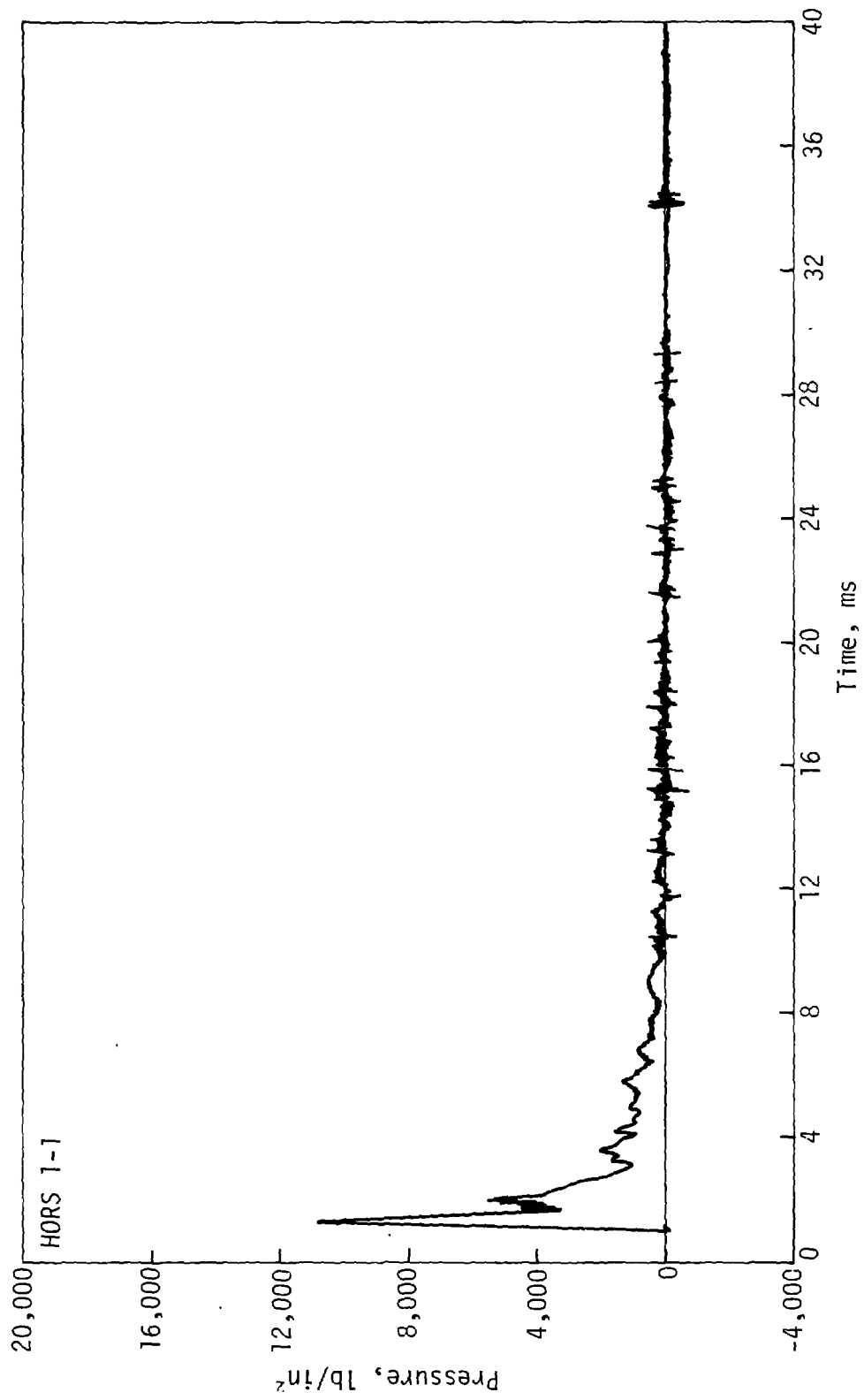


Figure 14. Typical Waveform from Simultaneously Initiated Low Yield HEST

HEST INITIATION

To initiate a HEST simultaneously, a planewave generator of some sort is required. In most cases this is easily accomplished by tying equal-length detonating cord lead-ins together at one end to small sections of the HEST at the other and initiating each bundle of lead-ins by other equal-length cords which are in turn tied to one detonator. This causes a delay between the times the detonator and the HEST are initiated but this is no problem as long as time of arrival gages are installed in the HEST to note when it is initiated.

Most HEST designs are of the sweeping wave variety and the detonating cord or sausage explosive itself can be used to propagate the detonation down the cavity at the proper rate. Since the detonating cord normally burns at nominally 6700 m/s (22,000 ft/s), HESTs simulating normal overpressures below 43.5 MPa (6300 lb/in²) must have detonating cord canted at an angle to the direction of propagation. (Airblast waves of 43.5 MPa propagate through standard air at 6700 m/s.) This can be accomplished most practically by weaving the detonating cord into a mat which during installation will be expanded to form a bed of two-dimensional diamonds with cords at the proper angle to achieve the proper propagation rate. Since it is also necessary to specify the amount of detonating cord per unit volume of foam to achieve the proper peak simulation pressure, the dimensions of the diamonds become fixed as soon as the number of explosive layers is specified. A rigorous treatment of the HEST weave design is given in Reference 11, copies of which are available from the authors upon request.

The Iremite sausage explosive, used by UNM/CERF to date propagates at a nominal velocity of 3800 m/s (12,500 ft/s)* and hence normal overpressure simulations below 14 MPa (2080 lb/in²) will require that the Iremite be canted relative to the propagation direction. Iremite has a minimum diameter of about 2.5 cm (1 in) and does not lend itself to weaving. Normally then the explosive is oriented at the proper angle and initiated at the ends. Continuing the propagation to the end of the cavity can be achieved by tying the ends of the Iremite together with loops of detonating cord down the edge of the cavity.

As mentioned earlier, both the detonating cord weaves and the Iremite propagation schemes suffer from a velocity speed-up problem which appears to be associated with the detonation cutting acute corners short. Attempts to compensate by making the angles more acute merely cause the corners to be cut shorter. If the propagation velocity is particularly critical, then it is possible to use an external timing driver explosive as shown in Figure 15. Virtually any nuclear airblast propagation velocity is available using the technique including those which exceed the propagation rate of the high explosives. For this reason this is the technique required anytime normal airblast overpressure simulations in excess of 43.5 MPa (6300 lb/in²) are made using the sweeping wave HEST. If the HEST width is substantial, a planewave generating system is also required to ignite the entire width at one time (not shown in Figure 15).

* In cases where a greater velocity is required, sausage explosive with a detonating cord core and PETN propagation velocity is available.

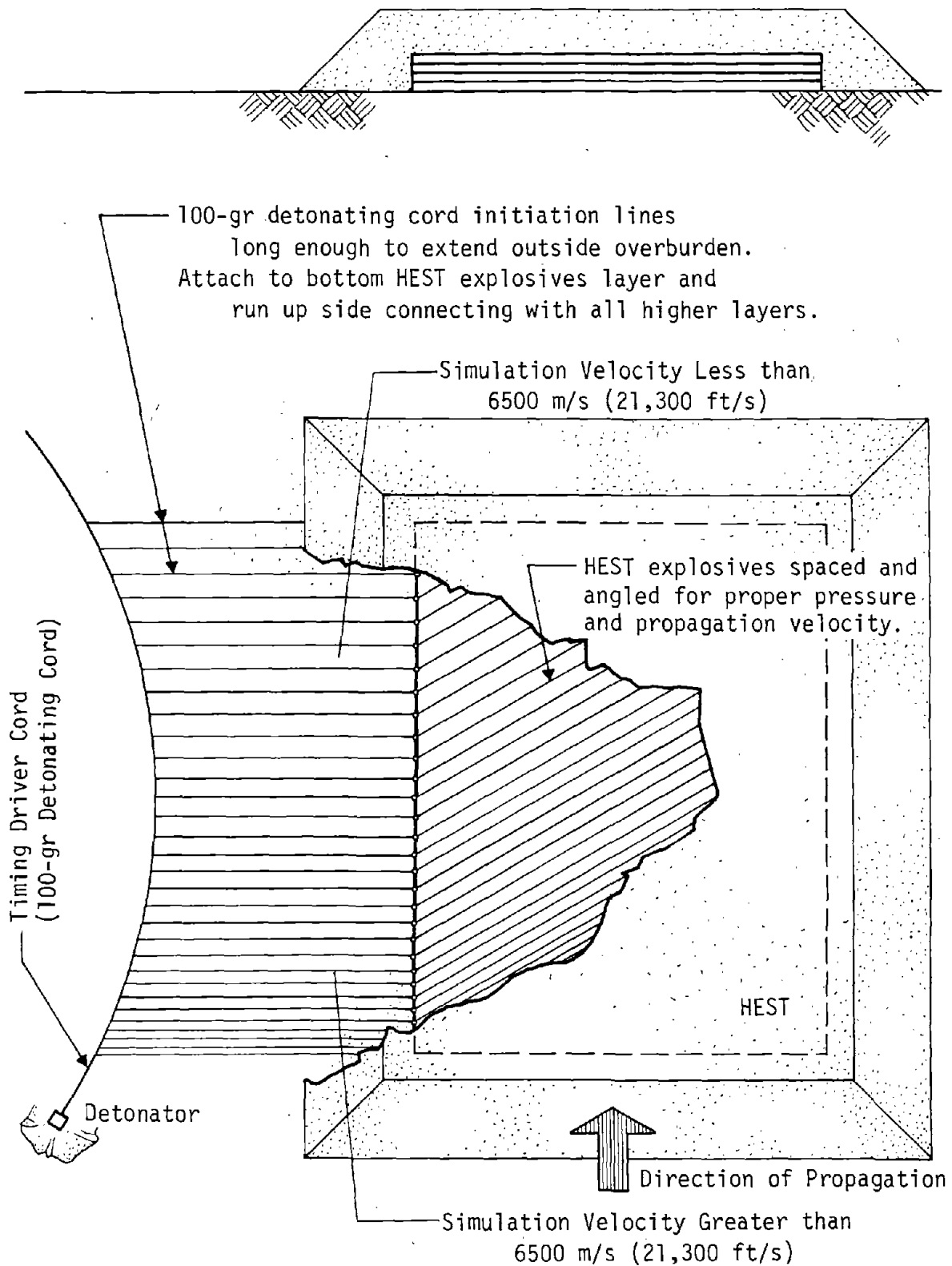


Figure 15. Detonating Cord External Driver For Reliable HEST Propagation Velocities

EXPLOSIVES SELECTION - CHARGE DENSITY DETERMINATION

The charge density required to produce a given peak simulation overpressure is shown in Figure 16. These relationships have been under consideration for many years and much work remains to be done before a full understanding is achieved. A discussion of the techniques used to derive these curves is given later in HEST analyses.

DETERMINING TEST BED SIZE

The size of the test bed to be used in the HEST simulation test is determined by the size and the depth of burial of the target structure, by the subsurface geology of the test bed, and by the blast wave propagation velocity. If only the surface-exposed portion of the target structure is to be loaded (airblast only), the HEST test bed need be only slightly larger than the target structure. When buried structures are required to be loaded with airblast-induced ground motions, much larger HEST beds are required to prevent relief waves traveling from the unloaded ground from reaching the target structure during the simulation time. A method for test bed size estimation is given in Appendix A. It should be emphasized that the calculation of the minimum test bed size is complex and that this method provides only an approximation.

DESIGN OF HEST USING THE LOCKUP MODEL CODE

The design of a HEST to provide the required blast pressure and impulse history is accomplished using the HEST DESIGN LOCKUP CODE. The code, developed at AFWL by Mr. Edward Seusy for the HP 9820 calculator, was rewritten and modified by UNM/CERF to run on the Tektronix 4051 Minicomputer. A plot routine was written to provide in graphical form the calculated outputs of pressure, impulse, displacement, velocity, acceleration and shock radius histories.

The code calculates a three-dimensional expansion of a given HEST cavity by treating the mixture of detonation products in the cavity as a gamma law gas. The compressions of the test bed and the soil overburden are calculated one-dimensionally from polynomial relationships relating the particle velocity to the average stress. These curves were developed from soil stress measurements made at CERF. The code iteratively calculates test bed and overburden stresses, accelerations, velocities, displacements, cavity volume expansions, and pressure drops. When the shock radius in the overburden has traveled to the top of the overburden, the overburden is considered to be fully compressed and locked up. The overburden is then considered to move as a rigid body until the bottom of the overburden has cleared the original overburden height at which time venting is presumed to have started and the problem is terminated. The HEST design is done iteratively, changing the cavity depth and overburden height until an acceptable match to the desired impulse history for the effective simulation time is found. A full mathematical description as originally written can be found in Appendix B. The UNM/CERF expanded version is available from the authors.

The calculated results from the HEST DESIGN LOCKUP CODE have been compared with experimental data from several large HEST tests. The correlations have, in general, been quite good. A problem is encountered when this code is used to predict the performance of small-sized HEST tests (less than 40 ft² of test bed area) where the edge and corner volumes become a significant fraction of

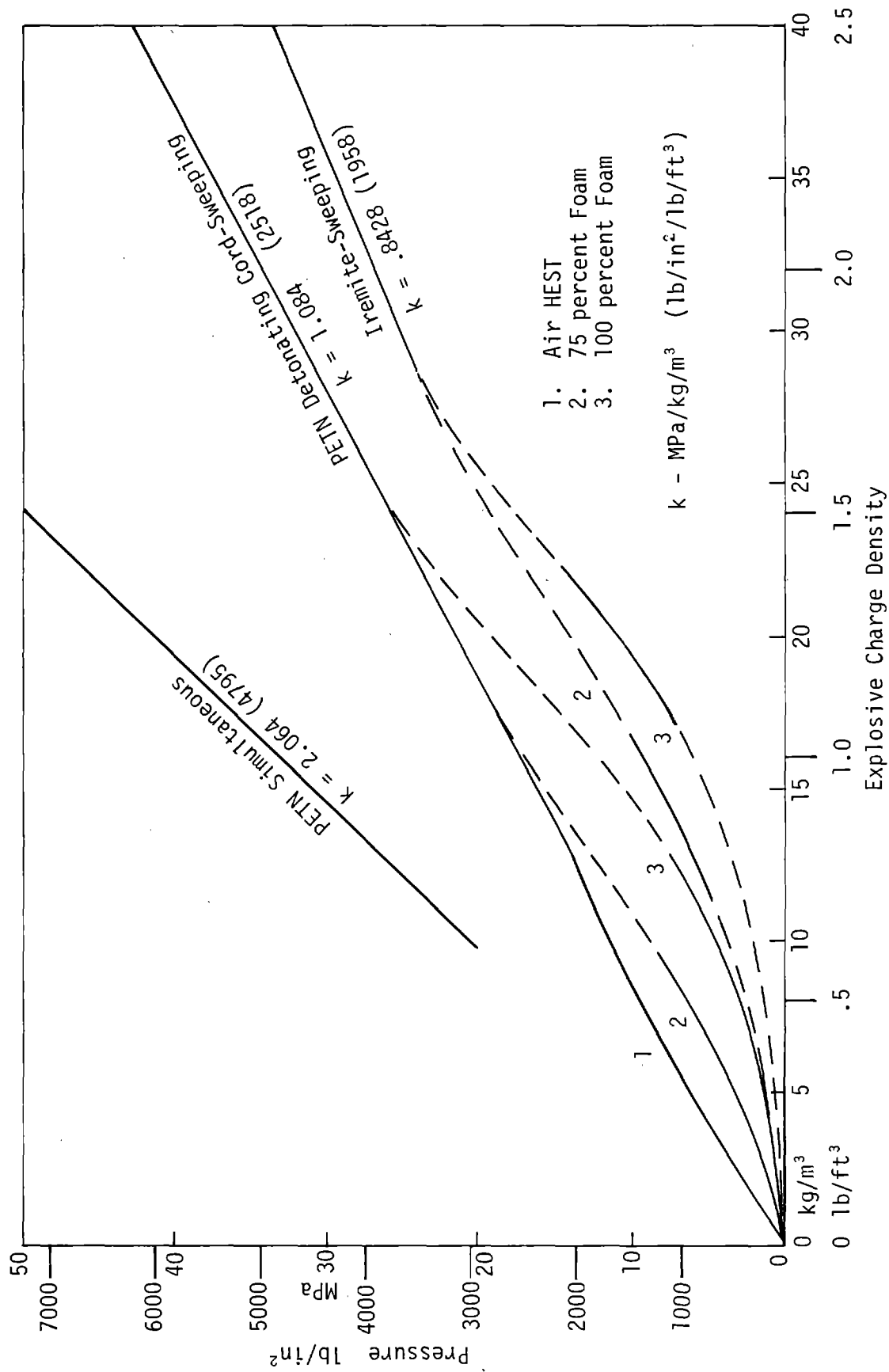


Figure 16. Peak Simulation Pressure versus Charge Density

the total cavity volume. A corner routine has been developed and incorporated which empirically relates small cavity expansions to observed results, at least in some cases.

ESTIMATING HEST COSTS

Cost estimations can be made using the procedure described in Reference 10. The inputs required are peak simulation pressure, nuclear yield, simulation time, and test bed size with an output of 1978 dollars per square meter of test bed.

HEST CONSTRUCTION DESIGN

The actual HEST construction design chosen depends on the overburden load calculated in the design code and on the explosives design selected. Thereafter the application of good engineering principles will result in an appropriate construction design. There are many explosives design pitfalls which can cause anomalies in the HEST performance. The det cord weave and Iremite designs mentioned previously possess few such problems. Other designs are available but should be implemented only after review by experienced HEST designers. Further information on these techniques as well as alternatives is available in Reference 11, which is available from the authors upon request.

Because of the severe environment in a HEST, instrumentation gages should be installed with many redundancies and dual recordings. Very small 1.3 m x 1.3 m (4 ft x 4 ft) HESTS, for instance, were monitored with 6 pressure gages, each recorded at two sensitivity levels. The gage numbers in large tests have numbered in the hundreds.

VI. ANALYSIS OF DATA

The performance of a HEST can be evaluated:

1. Relative to the design nuclear waveform,
2. Relative to the design lockup model, or
3. Relative to some other model.

It would be most desirable to be able to specify some single indicator of deviation of the achieved waveform from the design nuclear waveform. In practice this is difficult to accomplish since there are at least two measures of merit:

1. Peak pressure.
2. Impulse delivered from shock arrival time to end of simulation time.

The relative importance of these two measures varies with the HEST application. Obviously some test structures are sensitive to the peak applied load (diaphragms, for instance), while others are relatively insensitive to the peak but very dependent on the total applied load (i.e., block masses). In most cases, however, both the peak overpressure and the total impulse are of about equal significance, yet the determination of either is not as straightforward as it might seem. Figure 17 is an actual data trace taken from FOAM HEST 2, a test designed to simulate a 1-Mt, 16.89 MPa (1000 lb/in²) peak overpressure for a simulation time of 32 ms and reaching a total delivered impulse of 0.172 MPa-s (25 lb/in²-s) at 200 ms. In this view of the early pressure history, there is no apparent singular peak pressure due to the high frequency oscillations just after shock arrival. The absolute maximum peak of 19.5 MPa could not be a reasonable selection. Its very narrow width at the top suggests that it is limited by the frequency response of the recording system (20 kHz). There is little justification for using the first peak (12 MPa) since the second peak is much wider at that level. In fact the oscillatory nature of the waveform suggests that the peak effective or simulated pressure is some mean value.

Further difficulty may be encountered in evaluating the impulse. It is not clear from Figure 17, for instance, if the pressure is actually holding at 0.8 MPa or whether the transducer has taken a baseline shift wherein zero pressure registers some positive output (a rather common occurrence). Looking at Figure 18, which looks at the entire pressure history, far beyond the simulation end of about 200 ms, it is clear that there has been some baseline shift, but its absolute magnitude is in question because the pressure after 180 ms fluctuates up and down slightly. Such differences appear small until the integration of the pressure is undertaken. Then a small shift of perhaps 0.2 MPa will have caused a 25 percent change in impulse of 0.04 MPa-s in the 200 m-s under consideration. Fortunately there are some compensations which can be made. First the impulse history of this gage can be compared with the histories of other gages located in the same environment and some average deduced. For instance Figure 19 is a histogram showing the impulse developed on the other gages in the test at 35 ms after shock arrival. An average of all the data gives a total impulse of 0.0938 with a standard deviation (sigma) of 0.018 MPa-s. Dropping those data points which exceed one sigma from the average results in an average of 0.094 and sigma = 0.004. This appears to be the best impulse value at 35 ms after shock arrival and baseline corrections can then be made to the data so that this is the achieved value.

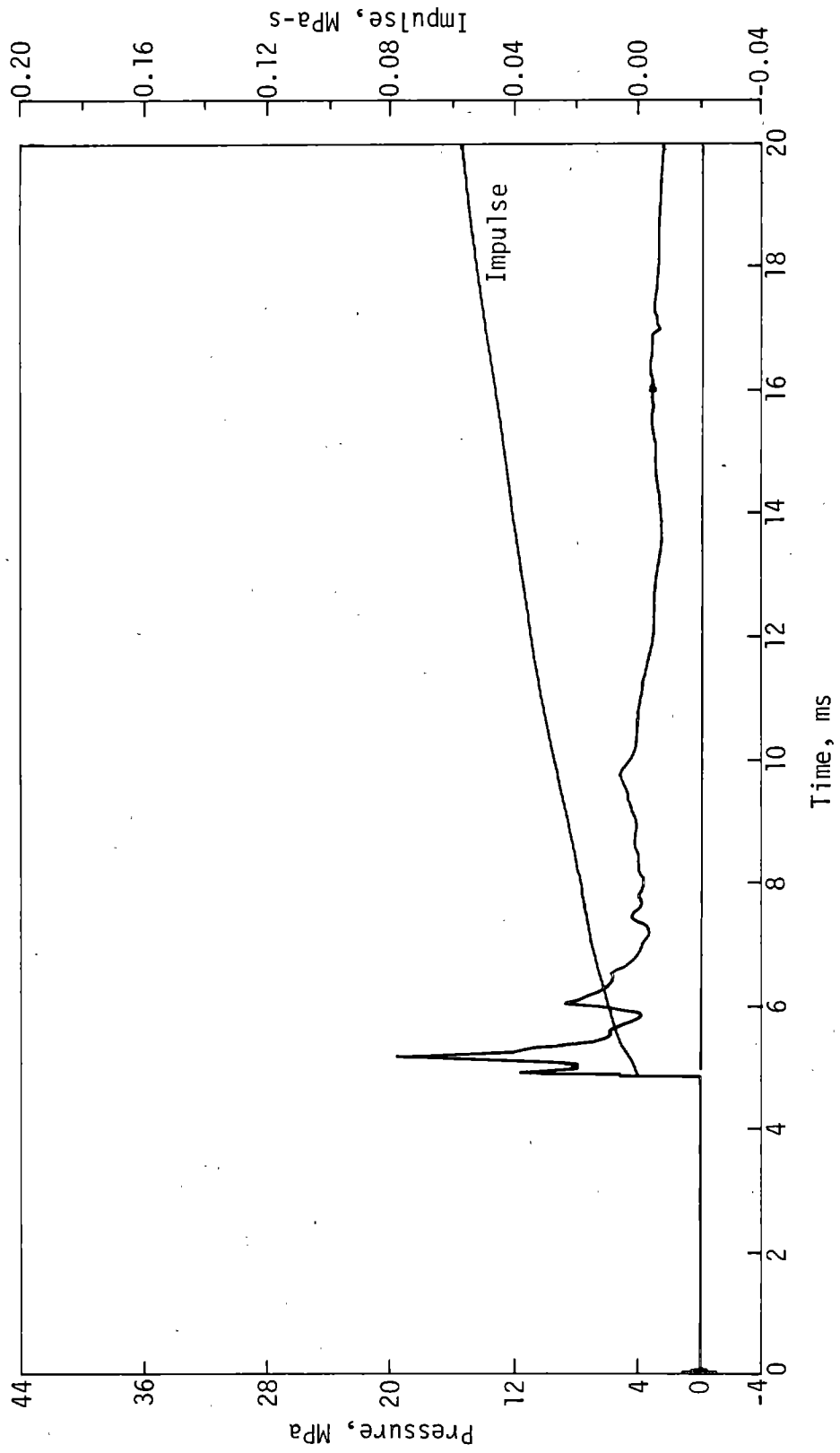


Figure 17. FOAM HEST 2 MEA 10 Early History Showing Spikes

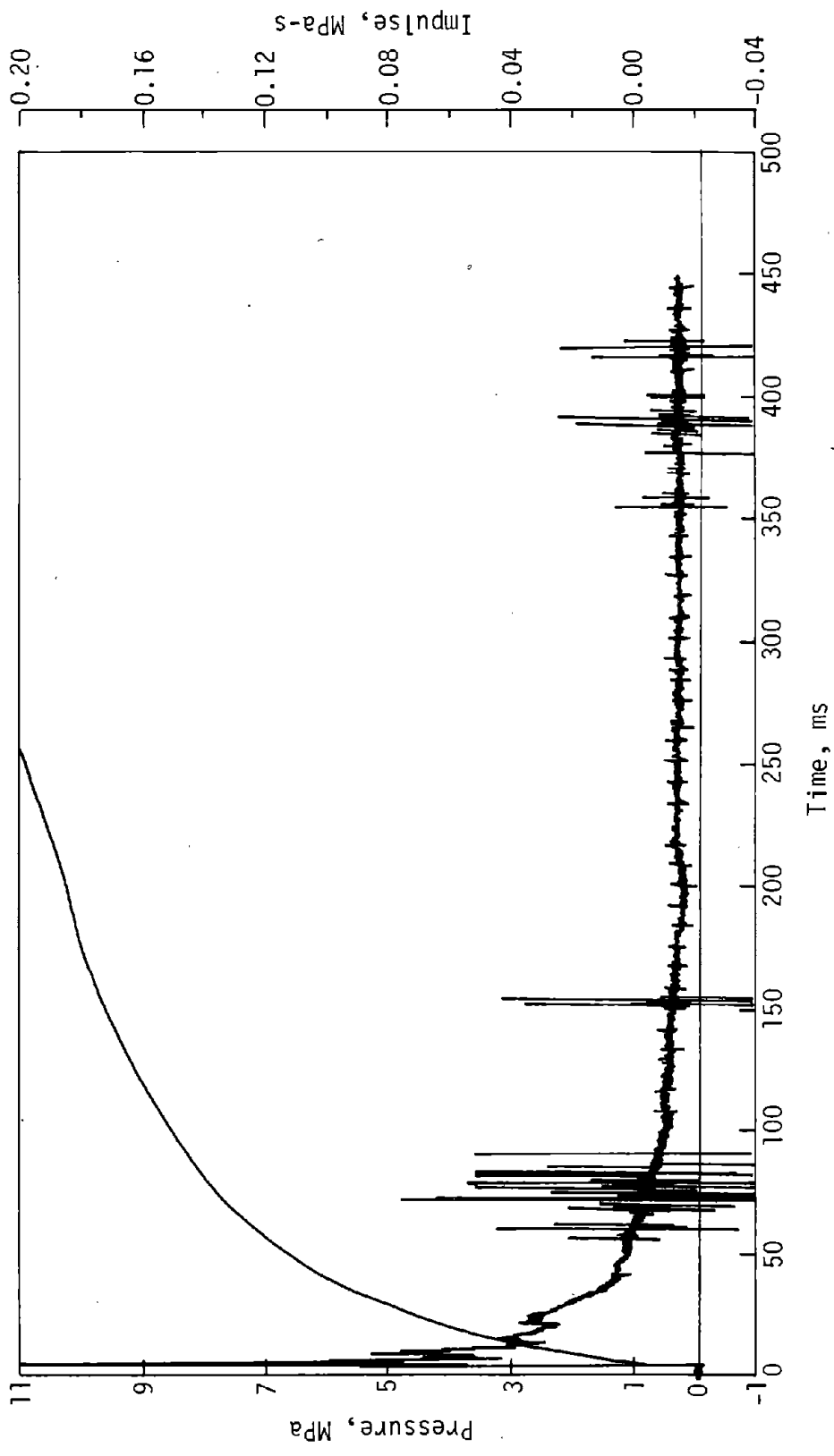
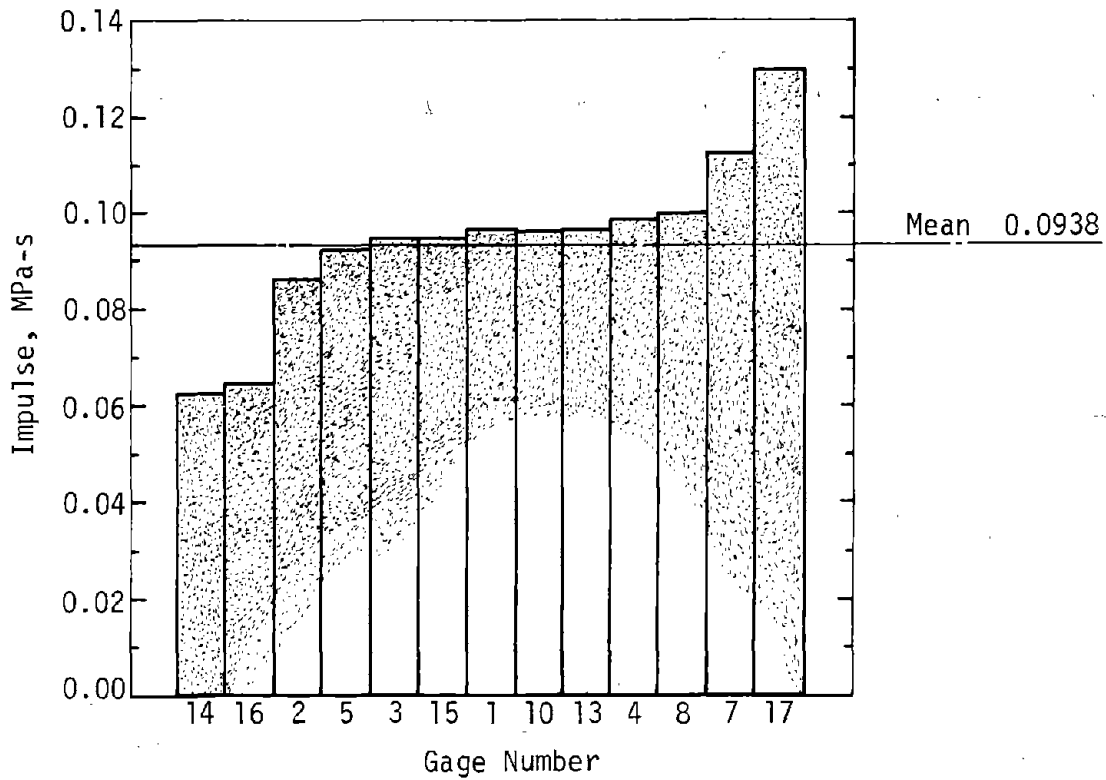
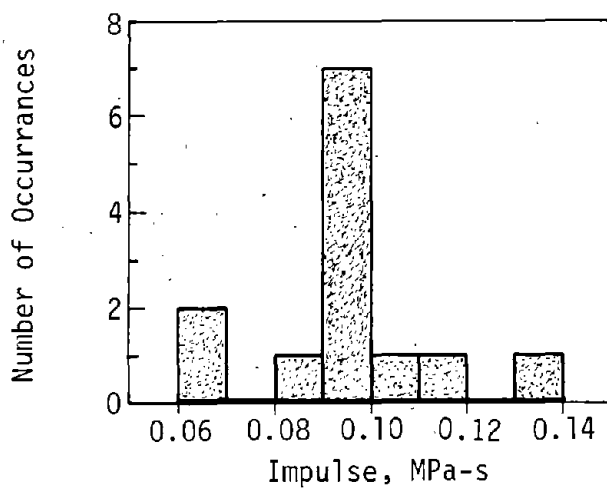


Figure 18. FOAM HEST 2 MEA 10 Full History Showing Baseline Shift



(a) FOAM HEST 2 Gage Histogram
Impulse at 35 ms After Shock Arrival



(b) Frequency Distribution of Gage Impulses
Figure 19. FOAM HEST 2 Gage Impulse Comparisons

Naturally, if the HEST environment is uniform throughout the test bed, an even better technique would be to compare the total impulses developed, in this case at some time near 200 ms. Gages which did not return to zero pressure, i.e., exhibited an impulse which was not horizontal, would normally be rejected. Unfortunately in this test all but one of the gage leads were cut by the expanding overburden before 60 ms. It should also be noted that this averaging technique, while appearing attractive, ignores systematic errors. If the baseline shifts are occurring due to a consistent transducer abnormality, then all gages could have a positive shift which would not average out.

Another technique is also available in which overburden tracking photopoles are used for independent measurements of impulse. In FOAM HEST 2, for instance, 6 poles which rested on the top of the explosive cavity were visible to high-speed motion picture cameras which captured the poles' displacement histories. Analysis using a film reader/computer combination at CERF yields displacement, velocity, and impulse histories, the latter shown in Figure 20. By setting them on large [1 m by 1 m (0.25-in)] steel plates, the photopoles are effectively coupled to the inside of the expanding HEST cavity, and once full overburden compression has been achieved, they possess a velocity which is directly proportional to the force-time product (impulse) which has been applied (less the 1 g deceleration of gravity).

Analysis of the FOAM HEST 2 photopole data indicates that the impulse delivered at 35 and 52 ms after shock arrival was 0.094, and 0.117 MPa-s respectively. A comparison of this to the gage 10 impulse history suggests that a baseline shift of 0.14 MPa is required to correct the pressure history. It should be noted at the 35 ms impulse figure of 0.094 agrees well with the 0.0938 MPa-s average derived earlier from the average of all gages. A baseline correction of -0.140 MPa has been overlaid on the photopole impulse plots in Figure 21, and this impulse history will be used for all further analyses.*

Having decided on a composite impulse history, it is now possible to return to the problem of assessing the HEST performance according to some selected model. The design nuclear waveform and the design lockup model waveform (adjusted for the as-built dimensions and material properties) are overlaid on the baseline corrected measurement 10 identified hereafter as MEA 10 BLC-.140 (Figures 22 and 23 respectively). As mentioned earlier, the HEST DESIGN LOCKUP CODE terminates when the overburden displacement exceeds the original overburden height and venting is presumed to have occurred. This problem terminated at 77 ms but a prediction of the delivered impulse at 200 ms was required. To accomplish this the code was modified to allow infinite expansion of the cavity as though the walls were joined to the roof by more overburden and the result is included in Figure 23.

PEAK SIMULATION PRESSURE DETERMINATION

There are three methods currently in use for determining the peak simulation pressure. All use the best fit of a model to the impulse history.

* This analysis of the baseline correction assumes that the shift occurred at shock arrival. There is some evidence that the shift may have occurred between 16 and 20 ms on most gages, but lacking a postulate to explain this phenomenon, further analysis proceeds on the shock arrival assumption.

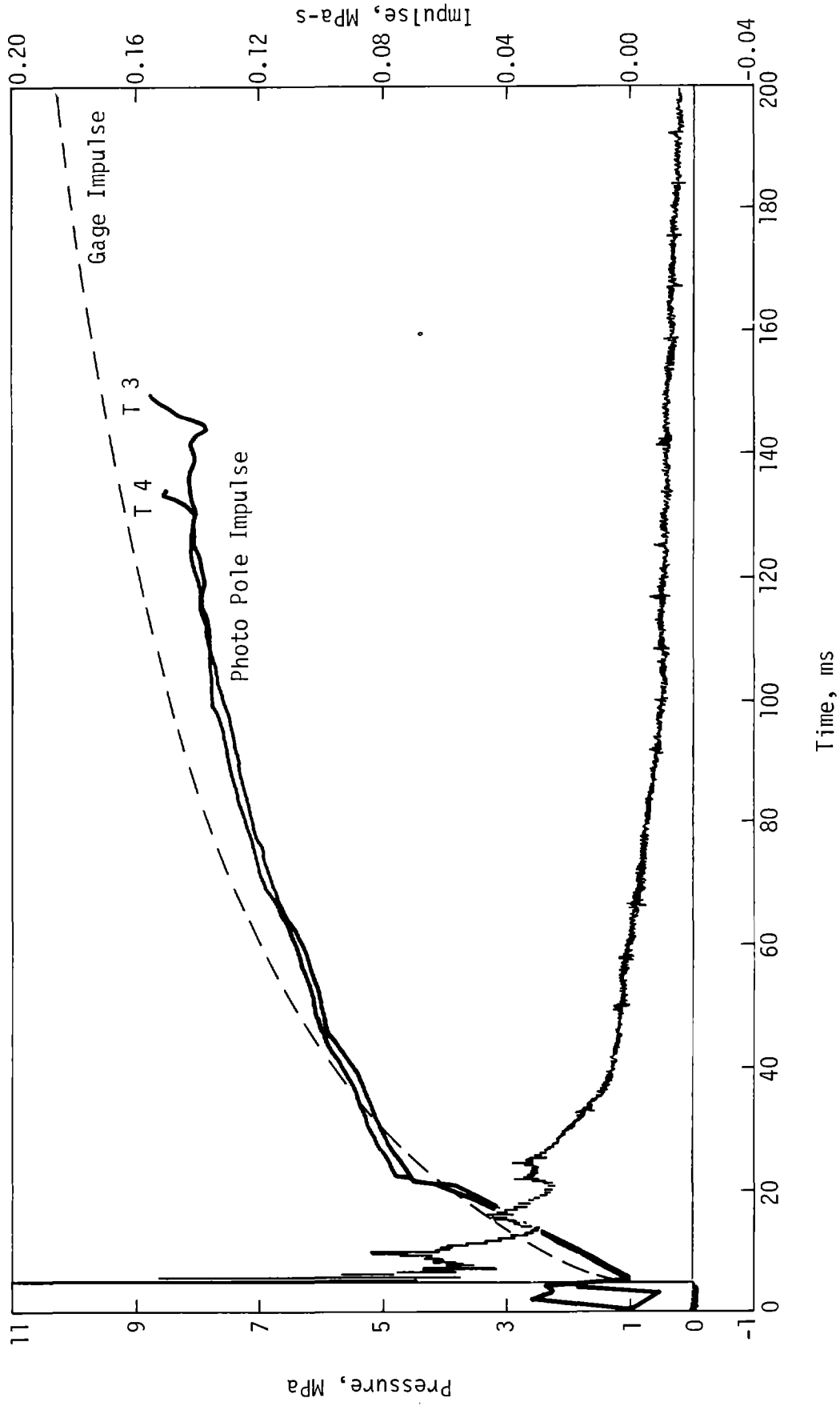


Figure 20. FOAM HEST 2 MEA 10 and Photopole Impulse Comparison

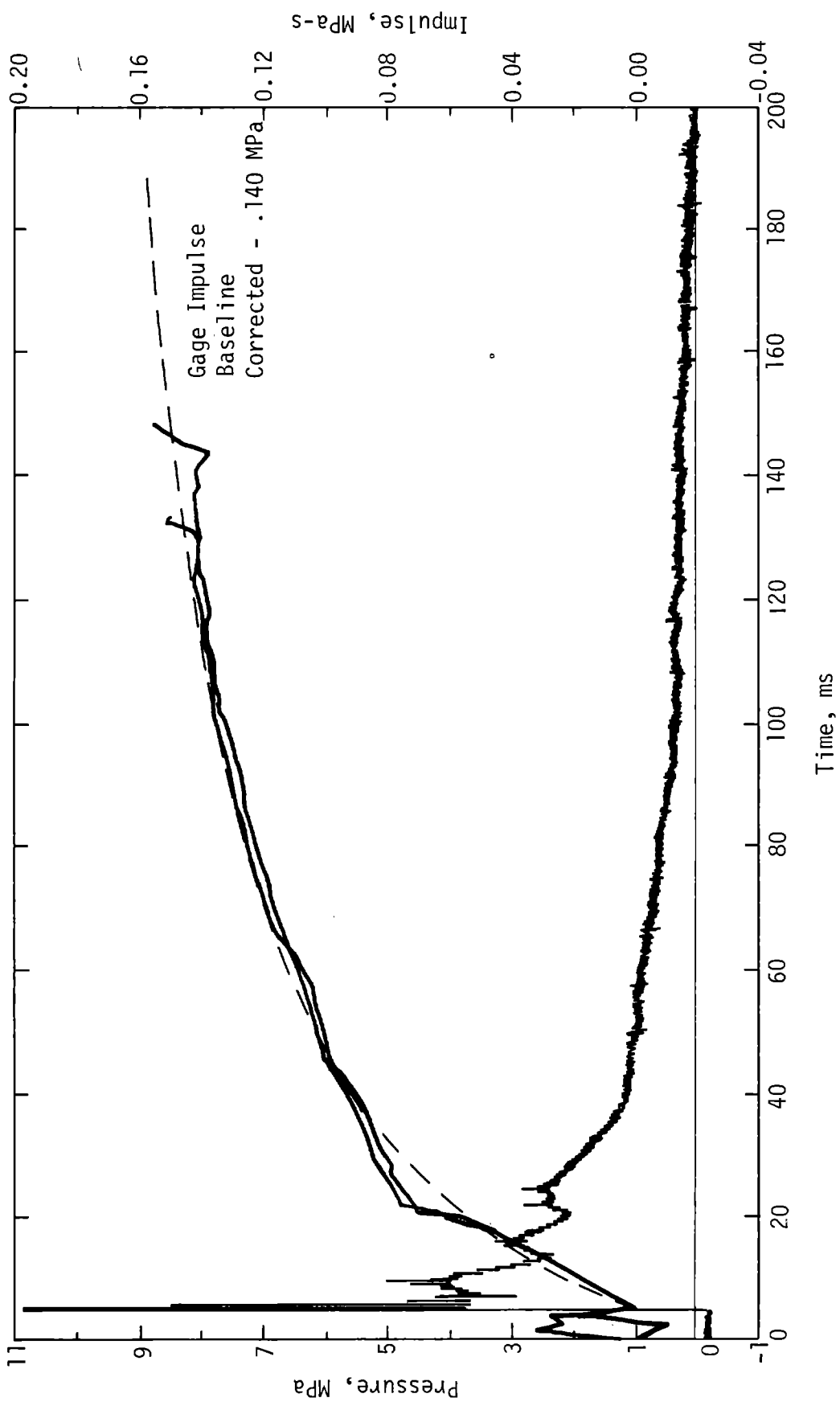


Figure 21. FOAM HEST 2 MEA 10 BLC-.140 and Photopole Impulse Comparison

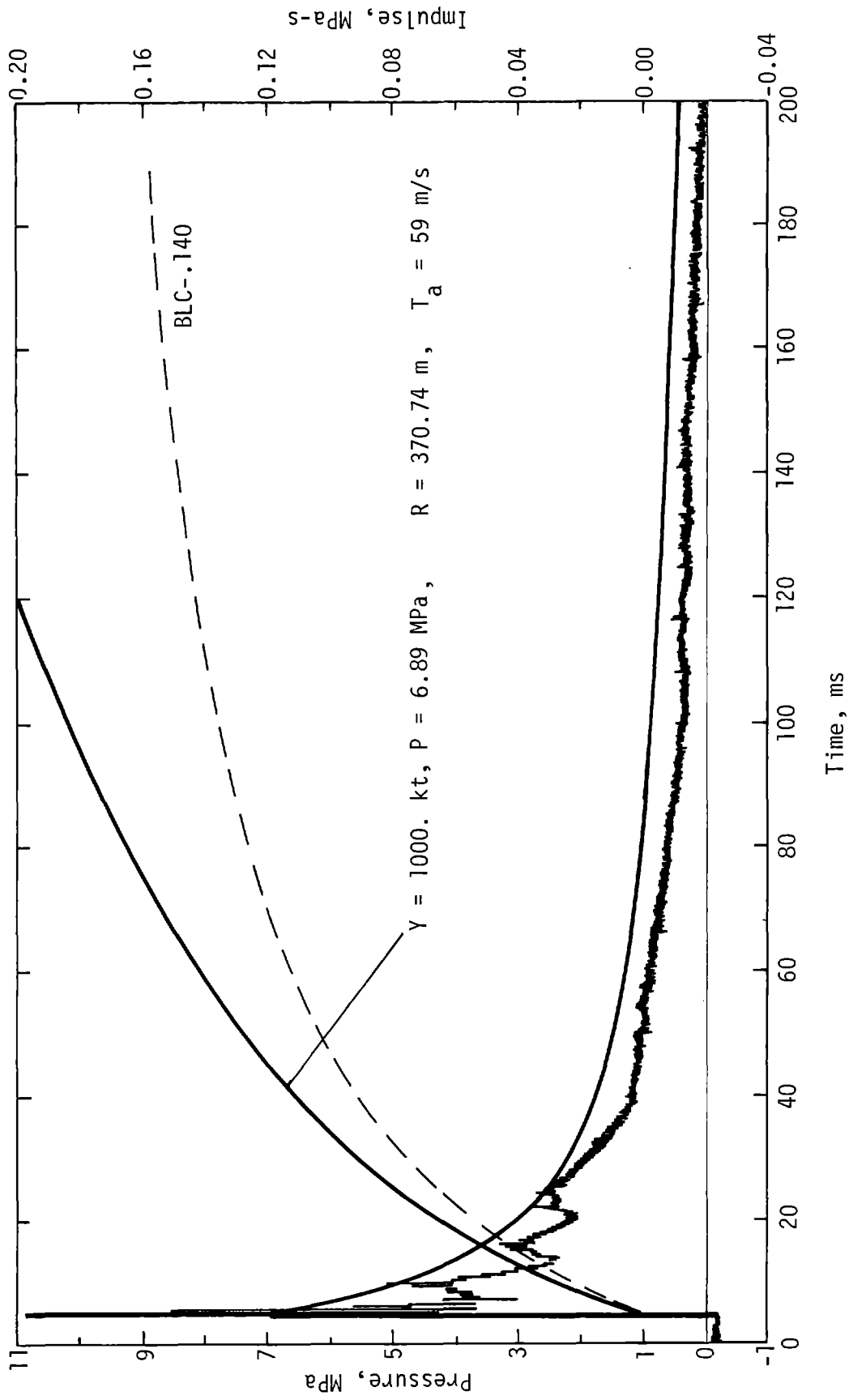


Figure 22. FOAM HEST 2 MEA 10 BLC-.140 and Brode Nuclear Design Curve, 35 ms

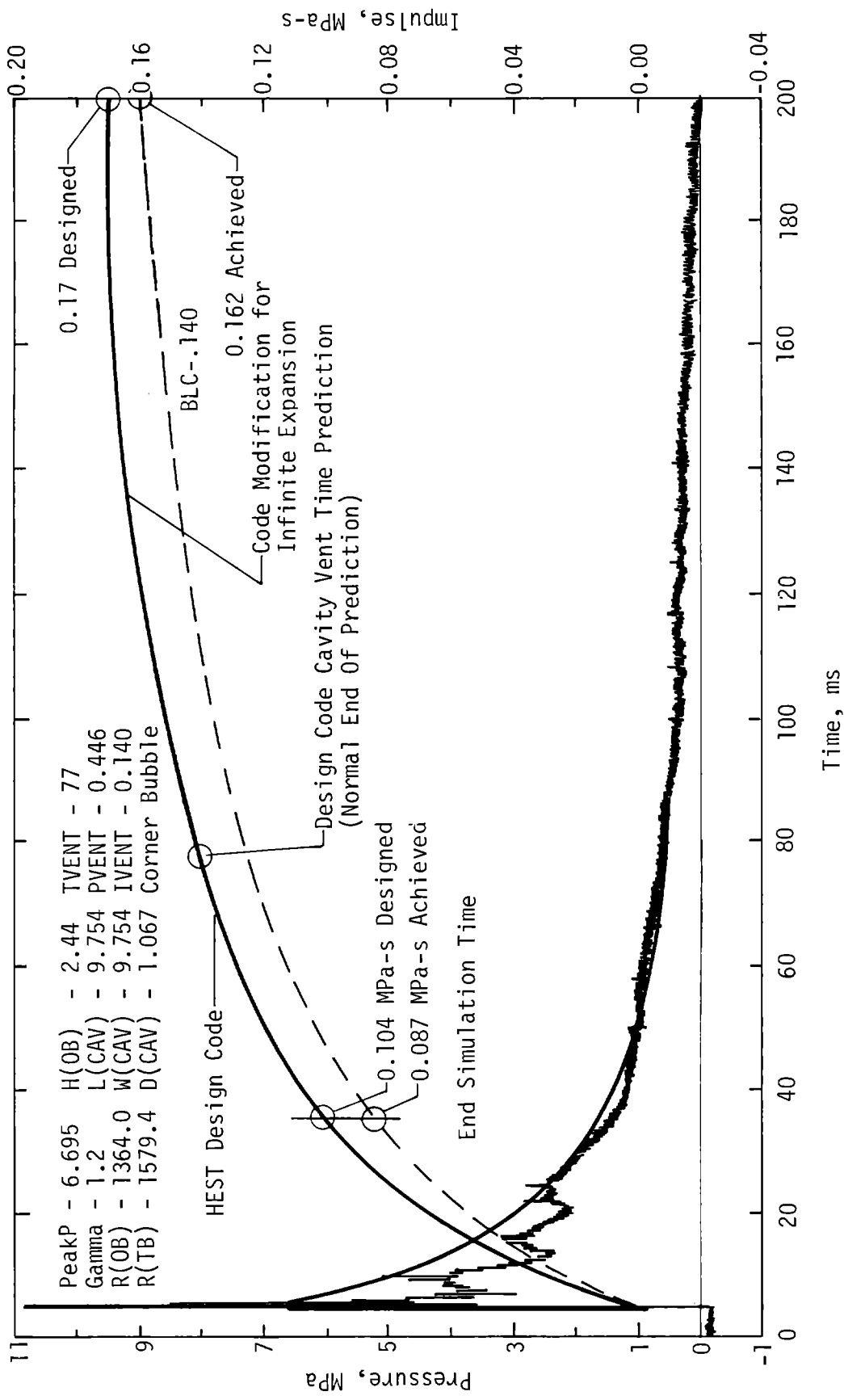


Figure 23. FOAM HEST 2 MEA 10 BLC-.140 and Design Using Lockup Model

The first and most tightly constrained model uses the HEST DESIGN LOCKUP CODE and assumes that all model parameters except the peak pressure are fixed at the as-built values. Iterations of the code with different peak pressures are then made until a best "eyeball" fit to the impulse is achieved. The fit is compared to the data all the way to the calculated vent time, after which the lockup model normally makes no further prediction. Such a comparison to the FOAM HEST 2, MEA 10 BLC-.140 data is shown in Figure 24. The peak simulation pressure found is 5.52 MPa (800 lb/in²).

The second method uses the Brode nuclear airblast model with two degrees of freedom (yield and peak pressure). The equations for this model are contained in Appendix C. Computer iterations are made until the best least-squares-fit to the impulse is achieved. The fit to the data is made only to some arbitrary time, usually the simulation time predicted by the lockup model. The best Brode fit to FOAM HEST 2 MEA 10 BLC-.140 data at four times gave peak simulation pressures and yields as shown:

Fit Time, ms	Peak Pressure MPa lb/in ²	Free Air Yield, kt
35	6.70 972	305
57	6.72 975	295
100	6.70 972	272
200	7.95 1153	138

The first three fits are shown in Figures 25 through 27. Since the design simulation time was 32 ms after shock arrival (35 ms actual time for the gage) the first value of 305 kt and 6.7 MPa (972 lb/in²) are best representations. It can be seen, however, that as the fit time is increased, lower yields and higher peak pressures are found.

The third method for peak pressure determination assumes a pressure wave-form model of the form

$$P = A1 \times B1 e^{B1 \times t} + A2 \times B2 e^{B2 \times t}$$

where

P = pressure

A1, B1, A2, B2 = constants

t = elapsed time past given shock arrival time

The integral then is of the form

$$I = A0 + A1 e^{B1 \times t} + A2 e^{B2 \times t}$$

where

I = impulse

A0 = constant = asymptote of total impulse

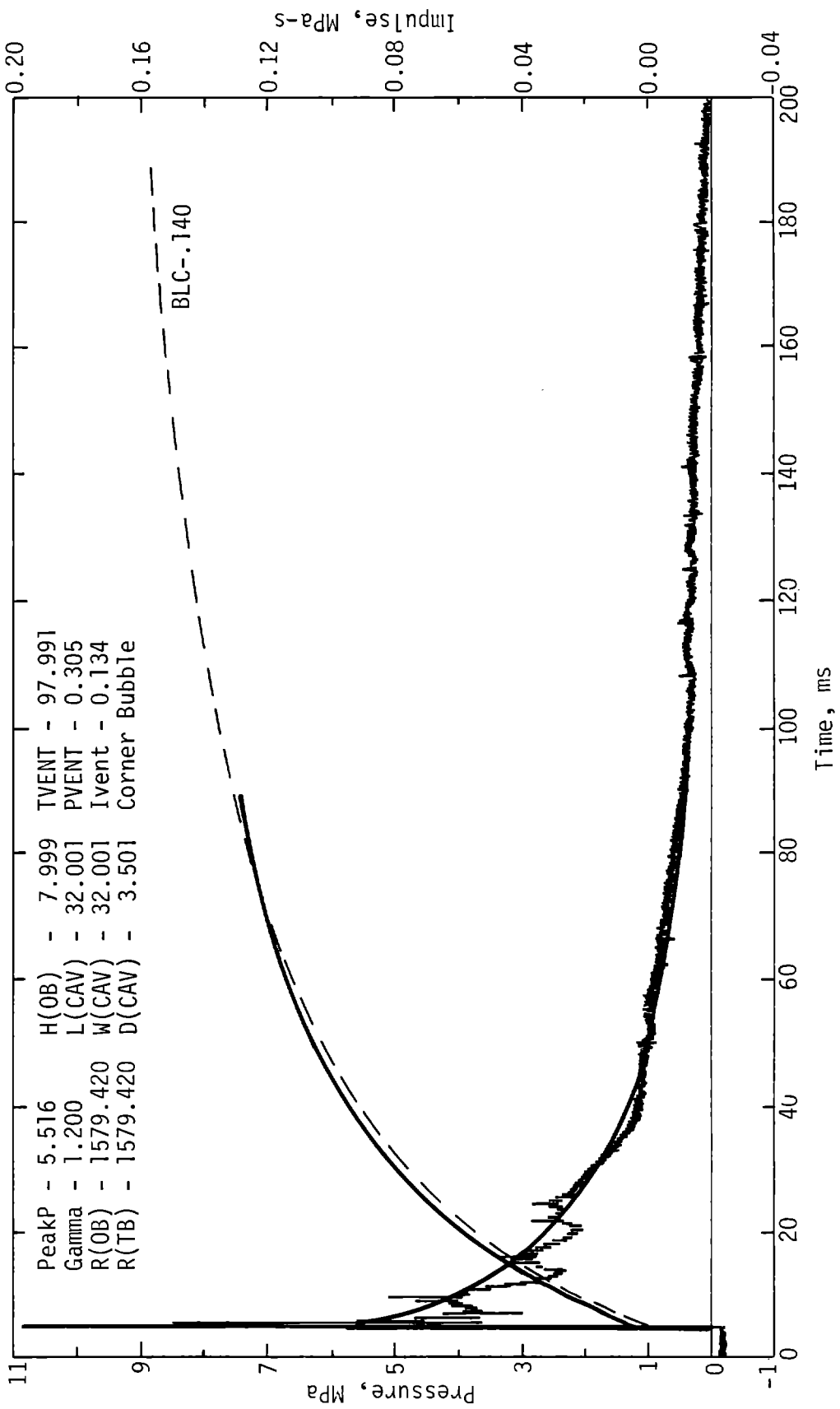


Figure 24. FOAM HEST 2 MEA 10 BLC-.140 Best Fit Using Lockup Model

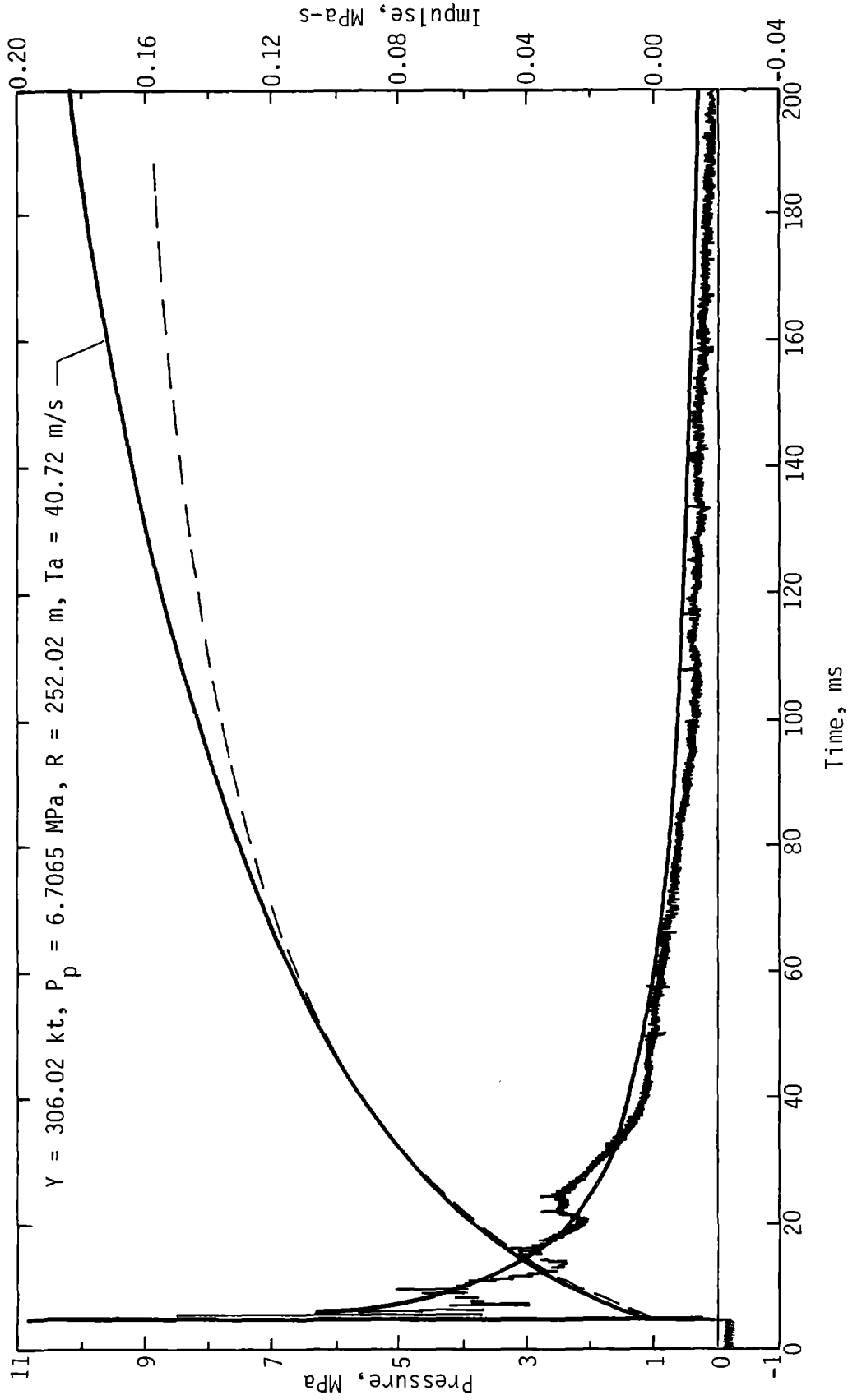


Figure 25. FOAM HEST 2 MEA 10 BLC-.140 Brode Nuclear Best Fit, 35 ms

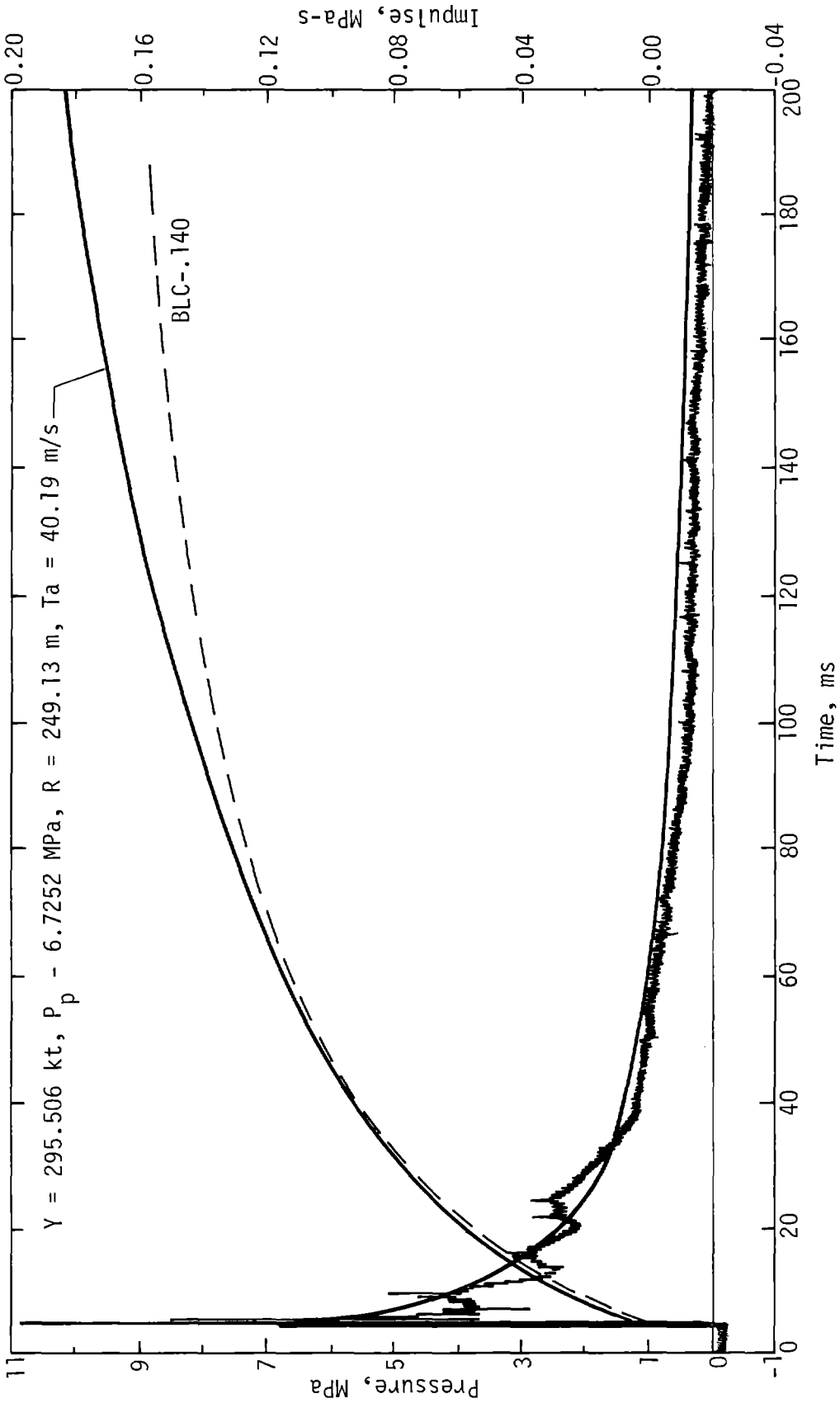


Figure 26. FOAM HEST 2 MEA 10 BLC-.140 Brode Nuclear Best Fit, 57 ms

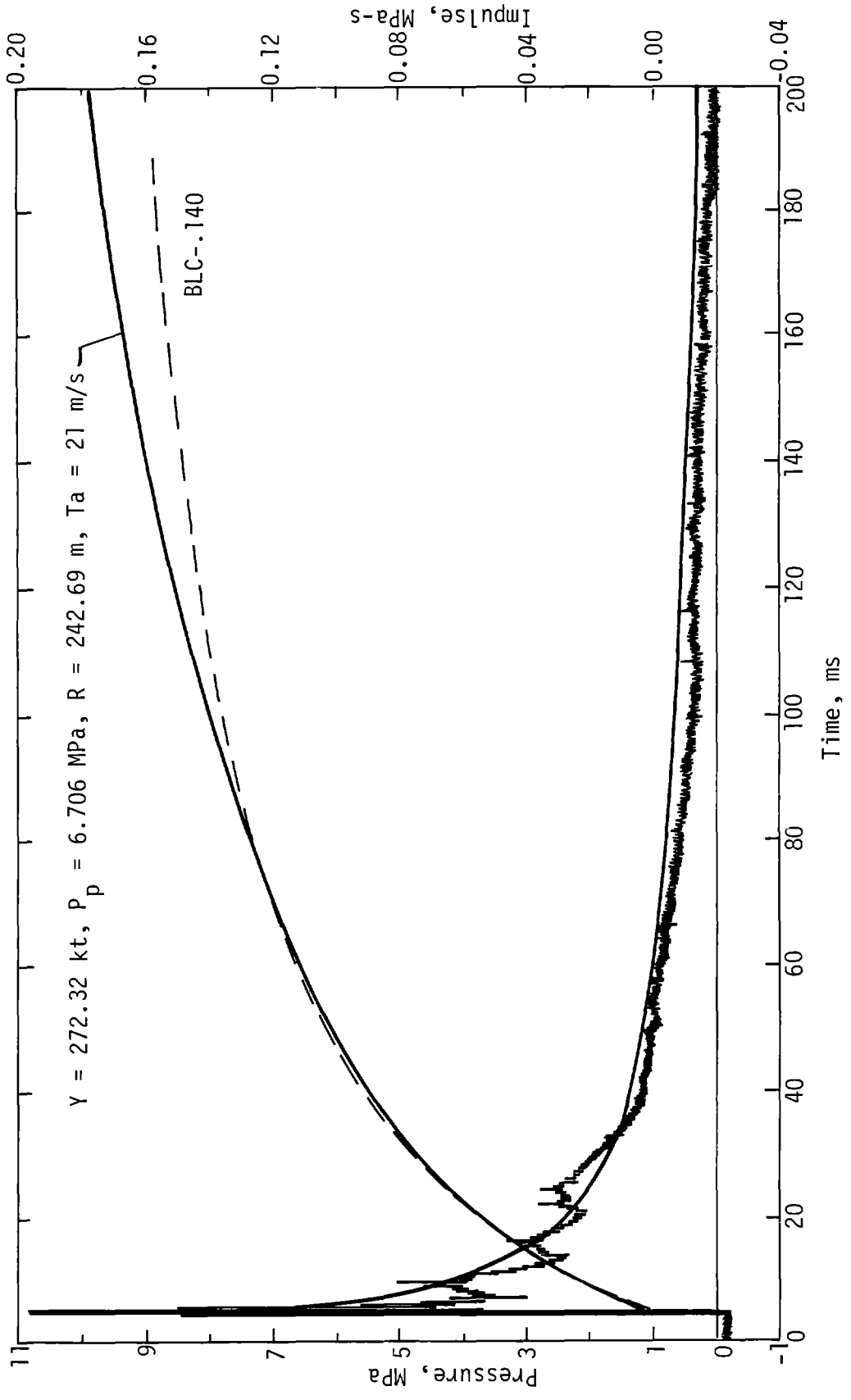


Figure 27. FOAM HEST 2 MEA 10 BLC-.140 Brode Nuclear Best Fit, 100 ms

A computer routine determines the values for the five constants and provides a best least-squares-fit to the impulse data. This model has the advantage of not requiring a value for the positive phase duration, as is required, for instance, in classical waveform descriptions by Friedlander or Brode (Reference 12). This model will fit a wide variety of monotonically decaying pressure waveforms, but a judicious selection of the time over which the data is to be fit is required, just as with the Brode description. The purpose of the model is to smooth through high and low frequency oscillations to provide an ideal monotonically decaying waveform and while the use of data which has late-time humps can be fit quite well, it usually has significant effect on the computed peak pressure. This model was applied to the example data FOAM HEST 2 MEA 10 BLC-.140 using the data up to 100 ms and also the data up to 195 ms. The hump which occurs just after 100 ms causes a reduction in the computed peak pressure from 7.0 MPa (1015 lb/in²) (Figure 28) to 4.75 MPa (689 lb/in²) (Figure 29). The routine also has a correction plot which allows the baseline correction to be removed so that the fit can be compared to the original data. This has been done in Figure 30.

The use of these analysis techniques has been applied to a large amount of HEST data. The major objective of this effort has been to define a peak simulation pressure versus explosives charge density relationship for each candidate HEST explosive. In fact it has been found that the presence of expanded polystyrene foam in the HEST cavity affects the pressure waveform at the peak simulation pressures of about 20 MPa (3000 lb/in²) and below. In addition the method of HEST initiation also has a significant effect on the relationship.

Figure 16 depicts the relationship as it is currently envisioned. The AIR HEST propagating across the test bed possesses a curve which is linear for peak simulation pressures above 14 MPa (2000 lb/in²) with a slope of 1.084 MPa/kg/m³ (2518 lb/in²/lb/ft³) for PETN explosive* and 0.8428 MPa/kg/m³ (1958 lb/in²/lb/ft³) for Iremite. The FOAM HEST and the AIR HEST are essentially the same above 25 MPa (3600 lb/in²). Moving down the FOAM HEST curve, however, the polystyrene foam appears to require a larger and larger proportion of the available energy for vaporization/dissociation, and the achieved peak simulation pressures fall more and more below the AIR HEST curve depending on the percentage of foam in the cavity. It should be noted, however, that the pressures depicted here were determined using method 1, the HEST DESIGN LOCKUP CODE iteration. A close examination of the waveforms and the best fit using method 1 shows that very little energy absorption has taken place during the first 0.5 to 1 ms and the absolute peak pressures are several times greater than the peak simulation pressure. The use of method 3, the double-exponential decay fit with its five degrees of freedom, will generally fit the first millisecond with a fast decaying waveform and will yield peak simulation pressures which lie on the AIR HEST curve. In most cases these first high pressure oscillations have been ignored since they contain very little impulse, and the model 1 pressures have been used in the HEST analyses. While normally considered undesirable, there is some potential for using these higher pressures in HEST designs to simulate reflected pressure waveforms which possess very fast pressure decays at first with slower decays in later elapsed times.

* Above 14 MPa, the specific heat ratio--which determines the pressure decay given a particular volumetric cavity expansion--is assumed to be fixed at 1.2 in most calculations for explosives/air mixes. As the explosives charge density approaches zero, the ratio must approach the ideal gas value of 1.4, resulting in a boost in the peak pressure causing the curve to be convex.

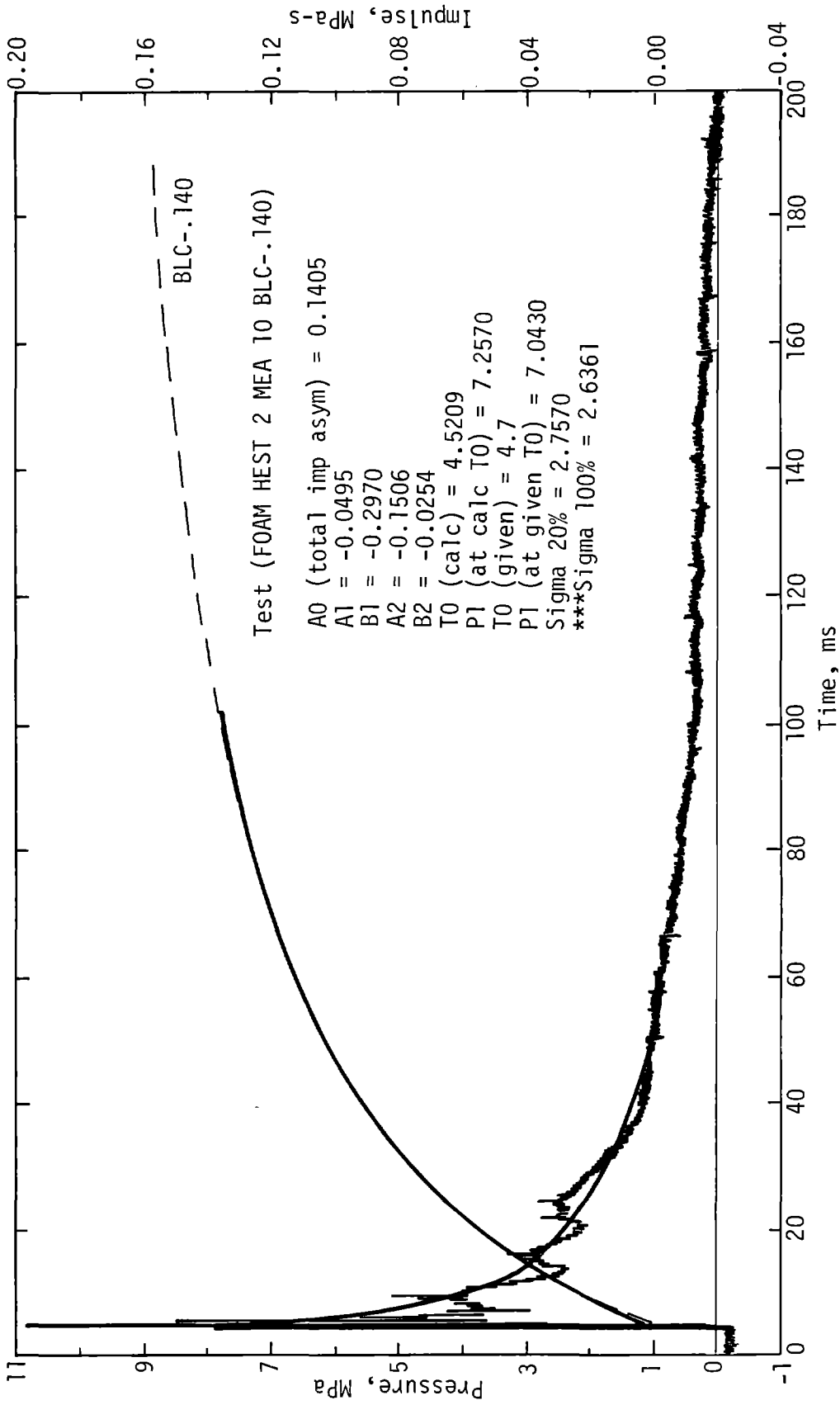


Figure 28. FOAM HEST 2 MEA 10 BLC-.140 Double-Exp. Peak Pressure, 100 ms

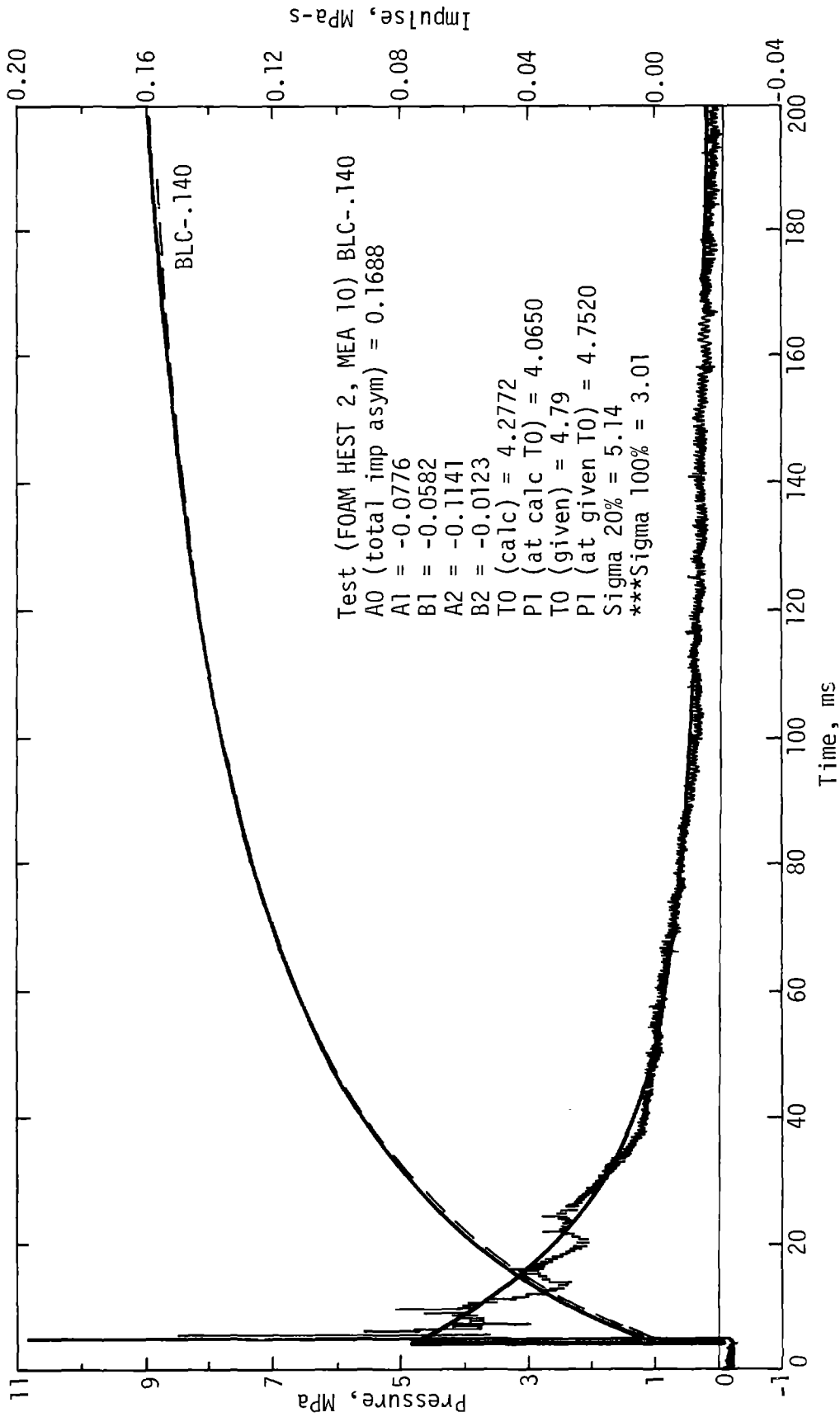


Figure 29. FOAM HEST 2 MEA 10 BLC-.140 Double-Exp. Peak Pressure, 200 ms

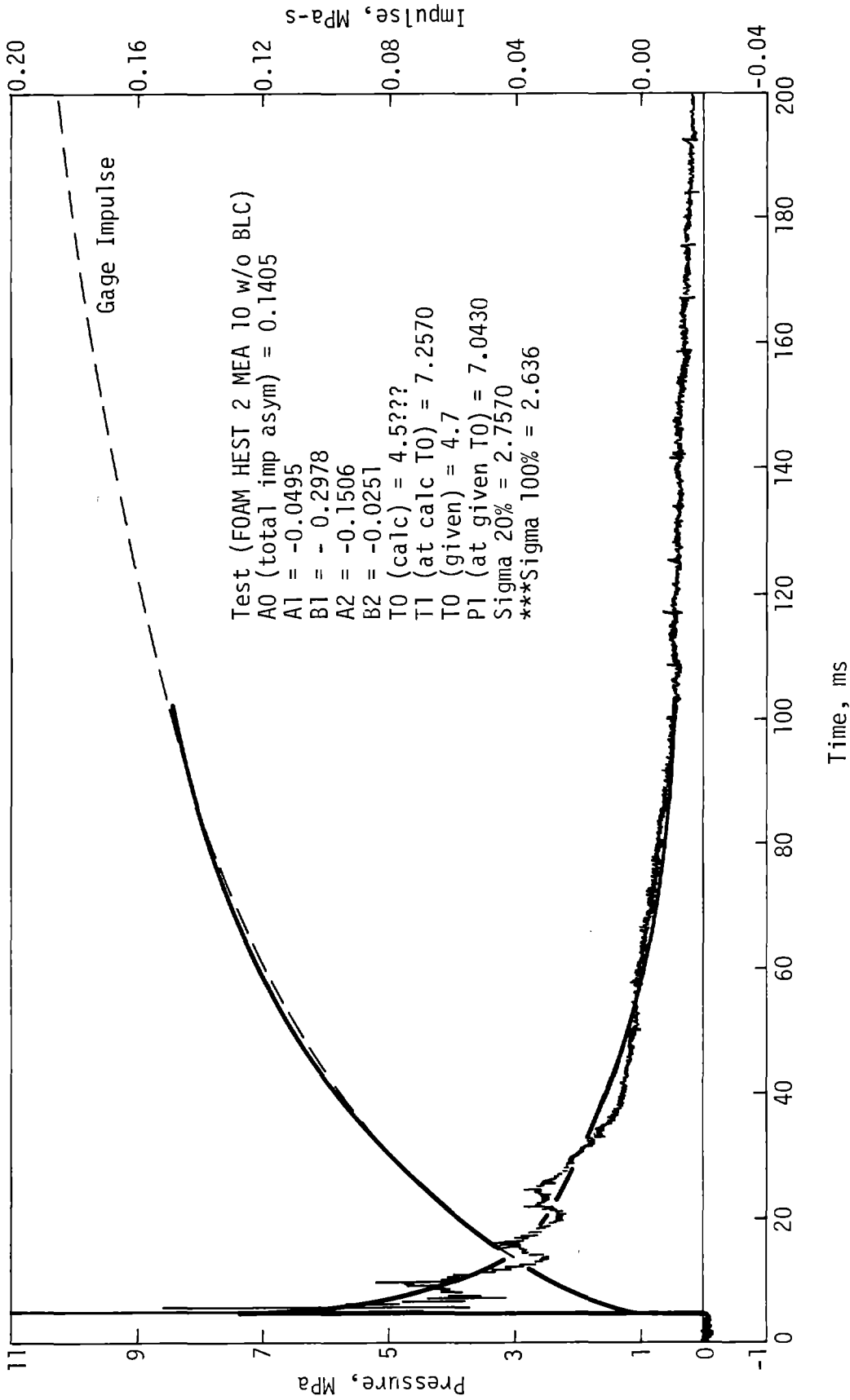


Figure 30. FOAM HEST 2 MEA 10 Double-Exp. Peak Pressure, 100 ms, BLC-.140, Back Corrected to Original Data

The effect just described (high-pressure front-end spikes) has been observed at pressures above 20 MPa (3000 lb/in²) when the method of HEST initiation is changed from sweeping the detonation across the test bed to simultaneously igniting the explosives at the top or bottom and letting the detonation progress vertically. The peak simulation pressures obtained using method 3 are approximately double the sweeping wave values, but again are of short duration. Advantage has been taken of this effect in simulating reflected pressure waveforms on concrete doors at pressure levels of approximately 35 MPa (5000 lb/in²).

The presence of these high-frequency, high-pressure oscillations has caused some concern since they appear as significant departures from the idealized nuclear waveforms. Fourier transforms on the data allow examination of the power spectral density. These have shown that usually there is very little energy contained in the spikes relative to the rest of the waveform. It would still be conceivable for some excessive loading to occur if the pressure oscillations occurred very close to the natural structural frequency, but very few test articles respond to frequencies above 2000 Hz where the oscillations are prevalent. Also, while it has been useful to compare HEST data to idealized nuclear waveforms for analysis purposes, it is also constructive to review the raw nuclear data in a similar fashion. Unfortunately the state of transducer art at the end of aboveground nuclear testing was apparently limited to 500-Hz frequency response systems, although a few 2500-Hz gages were fielded experimentally. Figure 31 shows the only high pressure nuclear data traces which could be found in the published literature. It is assumed that much better quality presentations are available from BRL and others involved in the recovery of such data. Since the recording data tapes were not available, spectral density plots were not possible. A visual comparison suggests that the true nuclear waveforms contain as many departures from the idealized nuclear as do the HEST waveforms.

Nevertheless, attempts have been made to smooth the HEST waveforms through a number of techniques. They have all been either unsuccessful or possess other more undesirable characteristics. Among these attempts have been ultra-fine explosives distributions, baffles and soil filters. Maximized consolidated explosives distributions have little or no effect. Baffles do smooth the oscillations but seem to distort the waveform. A decimeter or more of soil between the HEST and a test article works remarkably well in smoothing the waveforms without degrading the rise time, but the effects of the earthen mass on a test article which is not supposed to be buried are probably disagreeable. Structures which are buried as a part of their design naturally possess their own filter and are unbothered by the oscillations in the HEST. However, the difficulty of assessing the HEST pressure input remains the same.

In summary the analysis of a HEST's performance can be divided into three parts:

1. Determination of the waveform(s) which best represents the actual pressure history (and its integral) in the HEST cavity:
 - a. By comparison of multiple gage recordings made in close proximity to each other.
 - b. By comparison of pressure integrals (impulse) with photopoles which match the overburden velocity.

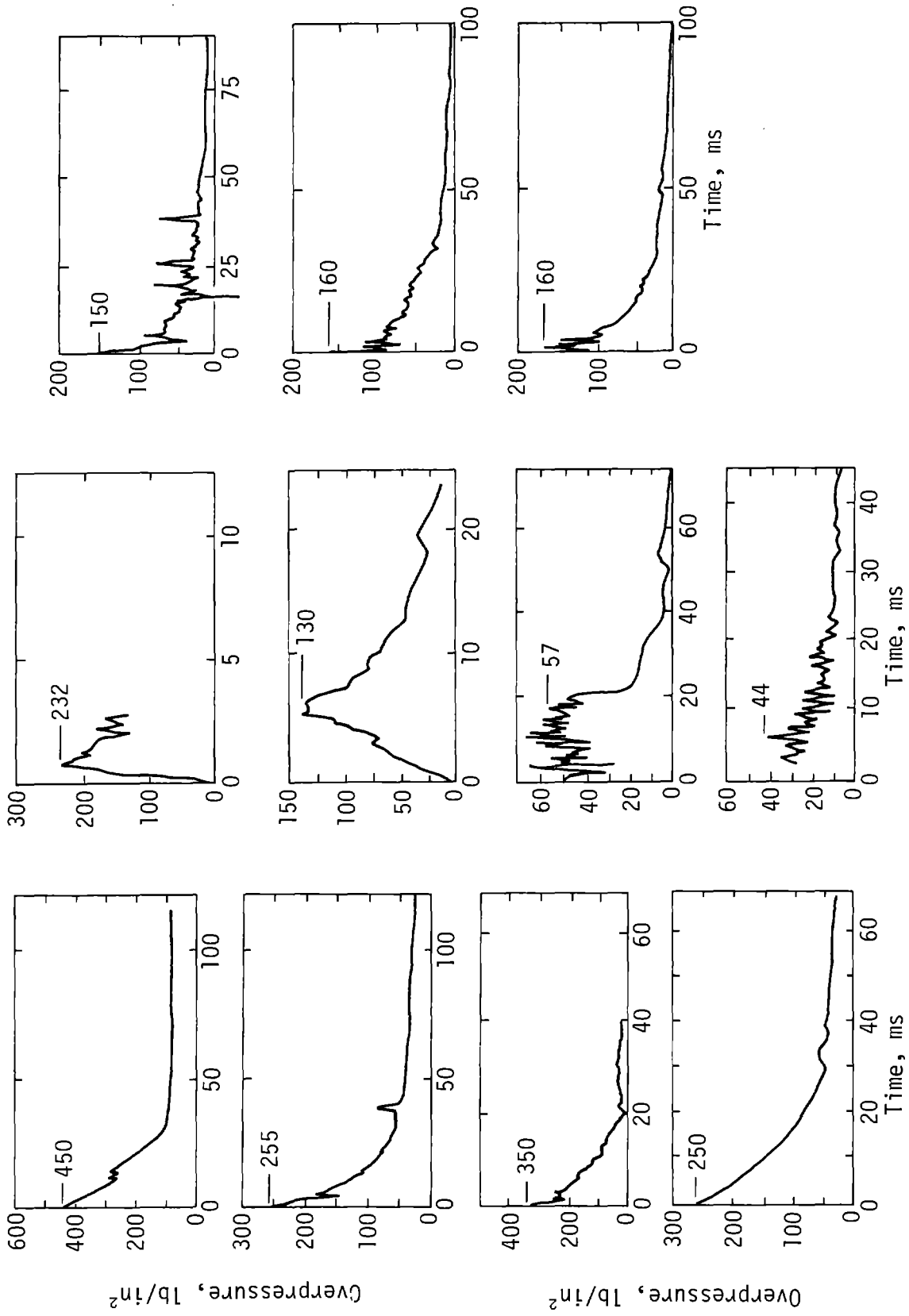


Figure 31. Typical Nuclear Airblast Forms

2. Determinations of the peak simulation pressure from the selected (or corrected) waveforms using up to three models listed below and comparison of this peak and the impulse at selected times with the HEST design values. (The Brode fit outputs simulated nuclear yield instead of impulse.)
 - a. HEST Design Lockup Model
 - b. Brode Nuclear Airblast Model
 - c. Double-Exponential Peak Pressure Model
3. Determination of the HEST wavefront propagation velocity from time of arrival gages or pressure gages and comparison of this with the design velocity.

The test, FOAM HEST 2, was selected for this paper as an example on which most of the HEST analysis techniques could be demonstrated. It should be emphasized that most HEST's require little raw data manipulation and an analysis yields fairly good agreement on the peak pressure using the three methods except as previously noted. Other tests have defied the use of any standard analysis and have required more in-depth investigation for explanation. It is unusual for actual HEST results to deviate more than 20 percent from the design peak simulation pressures or more than 15 percent from the impulse history up to the simulation time. In fact, FOAM HEST 2 with its obvious deviations from the design was in many respects quite satisfactory. Below are the tabulated results with the percentage deviations from the design values.

<u>Measurement</u>	<u>Method of Determination</u>	<u>Measured Value</u>	<u>Design Value</u>	<u>% Difference</u>
Peak Simulation Pressure	Design Lockup Code	5.52 MPa	6.9 MPa	20
	Brode Fit	6.7 MPa	6.9 MPa	2.8
	Double-Exp. Peak	7.0 MPa	6.9 MPa	1.5
Impulse @ +32 ms	Baseline Corrected	0.087 MPa-s	0.104 MPa-s	16
Impulse @ 200 ms	Baseline Corrected	0.162 MPa-s	0.170 MPa-s	4.7
Yield @ +32 ms	Brode	305 kt	1000 kt	*

The peak simulation pressure found by the DESIGN LOCKUP CODE and the impulse delivered at +32 ms are possibly in error due to the soil model in use in the DESIGN LOCKUP CODE and future analysis will be directed into this area.

* A percentage difference in YIELD is meaningless since the yield effects are not linear.

VII. HEST, FUTURE DEVELOPMENT AND APPLICATION

The HEST has been the most useful high-explosive simulator developed for three reasons.

1. It simulates nuclear overpressure, a major weapon effect.
2. It is adequate for testing of surface flush or buried structures which are most frequently used where hardness is important.
3. It is relatively inexpensive and easy to construct.

The HEST has been used in pressure ranges from approximately 1.4 to 70 MPa (200 to 10,000 lb/in²) and at yields from 15 kt to more than 1 Mt. There are some inherent limitations in the design of a HEST with current techniques.

At very low yields the cavity depth becomes very small, and in turn impractical to build using normal construction tolerances, and it becomes increasingly difficult to achieve a reasonable distribution of explosives. It has been shown by calculations that a lower density overburden, which might be achieved with a soil-polystyrene foam mix, allows use of a deeper cavity. Conversely, at very high yields, cavities become very deep, and there could be cost advantages with a less compressible, higher density overburden. In both extremes of yield, the quality of waveform fit to ideal waveforms is not optimum, and could be improved by tailoring the overburden properties. Very little work has been done in this area. The MX program may generate a requirement for modified overburden properties at high yields. Lower yield simulation would be needed for small-scale model testing, which is not currently being pursued.

Overburden fallback is a nonsimulation effect associated with HEST. At large scales, long simulation times, and with large area test beds, the overburden fallback problem can become serious. Cohesive soils are avoided to that extent possible to provide a maximum dispersion of the overburden. Various techniques for overburden dispersal have been used including explosive charges, sloped cavities, and plastic separator sheets. While most techniques have apparently performed in an acceptable fashion, little data has been collected to evaluate the various methods or to quantify the environment resulting from the overburden fallback. There are plans for an effort in conjunction with the MX simulation development program to expand the data base in this area for the purpose of developing a design approach to minimize and/or characterize fallback effects.

For a considerable period of time HEST cavities contained air and racks or hanging weaves of detonating cord. This configuration gave a single calibration curve for peak pressure versus charge density. With the advent of FOAM HEST, new variables were added to the problem of charge density calibration. The foam variables are type, density, and physical configuration. The use of foam provides the option of utilizing many types of explosives other than detonating cord in a variety of physical configurations. The use of soil-bounded HEST cavities for calibration of the large number of variables is expensive and time consuming. A development effort has been recently started to develop a reusable facility for calibration of explosives and foams. In addition to obtaining peak pressure-charge density data, the current objective is to obtain pressure-volume data as the explosive product-foam mixture is allowed to expand.

Historically the scatter in pressure data in HEST cavities has been considerable. Some measurement deviation such as baseline shift can be clearly attributed to gages. Other deviations cannot be clearly assigned to the environment or to the instrumentation. As a part of the FY 79 instrumentation development program a large sample of pressure gages will be tested in a common environment to assess deviations that are due to the gage and instrumentation system. The environment in most HEST cavities is severe, and the problem of designing survivable, repeatable gages is not trivial. Major progress has been made in the last year on the gage survivability problem, and it is hoped that equivalent progress can be made on the repeatability question.

Where the dynamic pressure and overpressure loads on a nonsurface flush structure are known, they can be approximated with a specially designed HEST. This technique has been limited to essentially single planar surfaces. It appears feasible to extend this technique to encompass more complex surfaces and provide an effective dynamic pressure loading over an entire structure. Such a technique would require a rather complex shaping of the HEST cavity, the explosive weave, and the overburden above the target structure. A "shaped HEST" concept is depicted in Figure 32.

Recent interest in ground motions caused by multiple-burst explosions indicates the possibility for even another variation of the HEST simulator, the multiburst simulator. If the pressure waveforms from an actual multiburst explosion over a large test bed are known, either from experiment or calculations, then it appears feasible to design a specially tailored sweeping-wave HEST to be constructed over the test bed to produce these same pressure-loading histories at each point of the test bed. Difficulty may be encountered in trying to simulate both the incident blast wave and the reflected blast wave reflecting from implosion centers which occur in the multiburst case. Dual explosion cavities for HEST or the combination of two or more simulation methods [HEST, Berm Loaded Explosive Simulation Technique (BLEST)] may possibly provide the needed simulation.

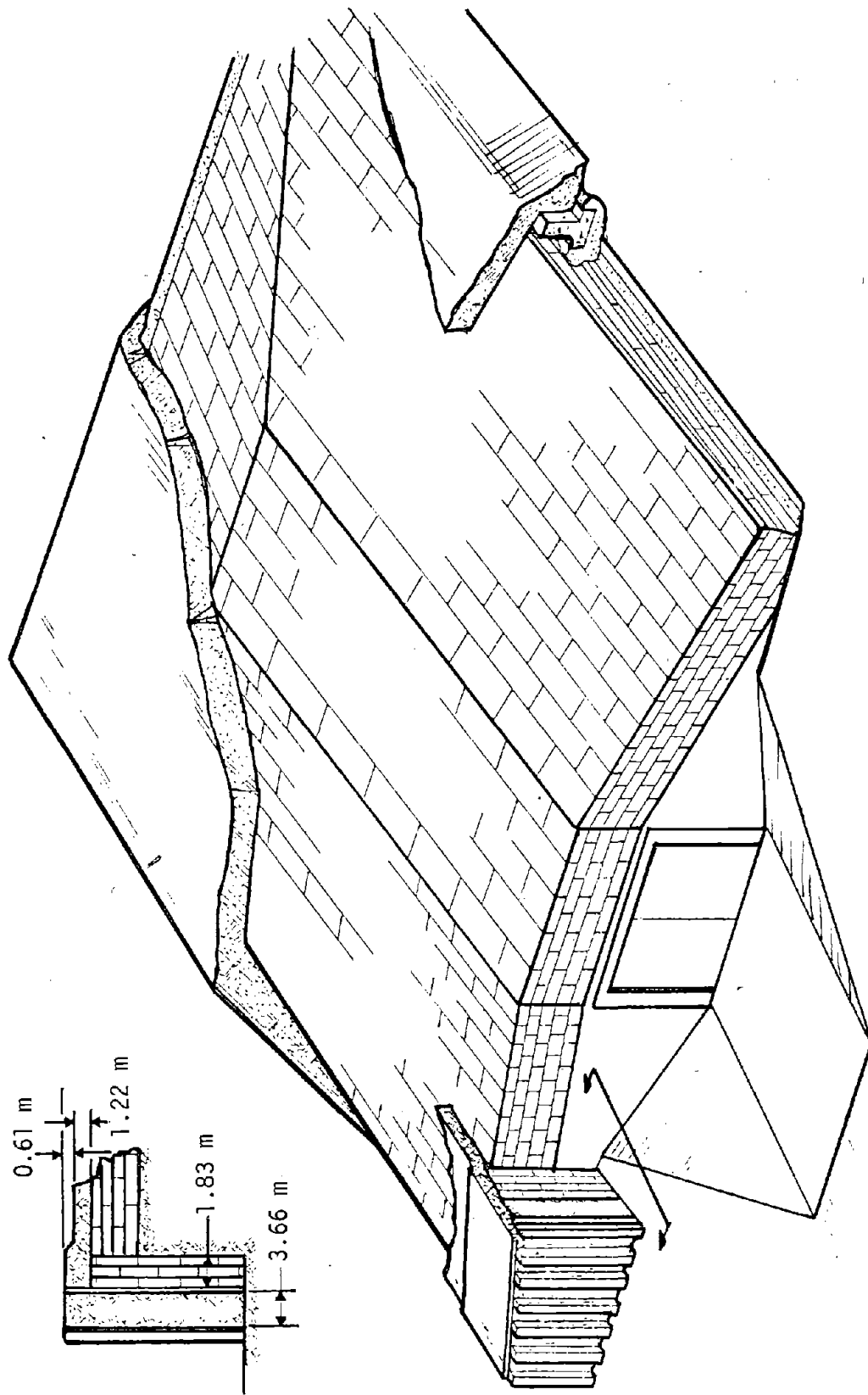


Figure 32. Shaped HEST Over Target Structure

REFERENCES

1. Brode, H. L., *Review of Nuclear Weapons Effects*, The Rand Corporation, Santa Monica, 1968.
2. Cooper, H. F., Brode, H. L., and Leigh, G. G., *Some Fundamental Aspects of Nuclear Weapons*, AFWL-TR-72-19, Air Force Weapons Laboratory, Kirtland Air Force Base, New Mexico, March 1972.
3. D'Arcy, G. P., and Clark, R. O., *Simulation of Air Shocks with Detonation Waves*, AFWL-TR-65-9, Air Force Weapons Laboratory, Kirtland Air Force Base, New Mexico, February 1966.
4. Auld, H. E., D'Arcy, G. P., and Leigh, G. G., *Simulation of Airblast-Induced Ground Motion, Phase I*, AFWL-TR-65-11, Vol. I, Air Force Weapons Laboratory, Kirtland Air Force Base, New Mexico, April 1965.
5. Auld, H. E., D'Arcy, G. P., and Leigh, G. G., *Simulation of Airblast-Induced Ground Motions (Phase II)*, AFWL-TR-65-26, Vols. I and II, Air Force Weapons Laboratory, Kirtland Air Force Base, New Mexico, April 1965.
6. Brattton, J. L., and Pratt, H. R., *Simulation of Airblast-Induced Ground Motions*, AFWL-TR-66-85, Air Force Weapons Laboratory, Kirtland Air Force Base, New Mexico, October 1967.
7. Triandafilidis, G. E., and Zwoyer, E. M., *Parameters Influencing the Airblast Environment Induced by High Explosives*, AFWL-TR-67-126, Vols. I and II, Air Force Weapons Laboratory, Kirtland Air Force Base, New Mexico, July 1968.
8. Kurz, F. R., and Balczak, M. J., *A Theoretical Investigation of Gas-Augmented High Explosive Simulation Techniques*, unpublished report to the Air Force Weapons Laboratory, General American Research Division of General American Transportation Corporation (GATX).
9. Boltman, Pozega, *HARD PAN I Test Series - Design and Construction of Test Facilities*, AFWL-TR-76-60, Air Force Weapons Laboratory, Kirtland Air Force Base, New Mexico, June 1976.
10. Leigh, G. G., Simmons, K. B., Wampler, H. W., and Scheuch, K., *A Report on Simulator Status and Capabilities*, CERF Report AFWL-TR- (Draft), Civil Engineering Research Facility, University of New Mexico, August 1978.
11. Wampler, H. W., and Earickson, J., *Foam HEST Design and High Pressure HEST Analysis*, CERF Report AFWL-TR- (Draft), Civil Engineering Research Facility, University of New Mexico, February 1978.
12. Baker, Wilfred, *Explosions in Air*, Austin, Texas, University of Texas Press, 1973.
13. Systems, Science and Software, *Experimental Program to Demonstrate Feasibility of FOAM HEST*, DNA Report 3526F, 26 March 1975.

APPENDIX A
HEST TEST BED SIZE DETERMINATION

Find:

$$L = R + X$$

$$W = 2Y + L_S$$

Given:

D = depth of simulation

L_S = length of structure

C = test bed seismic velocity

U = shock velocity in HEST cavity

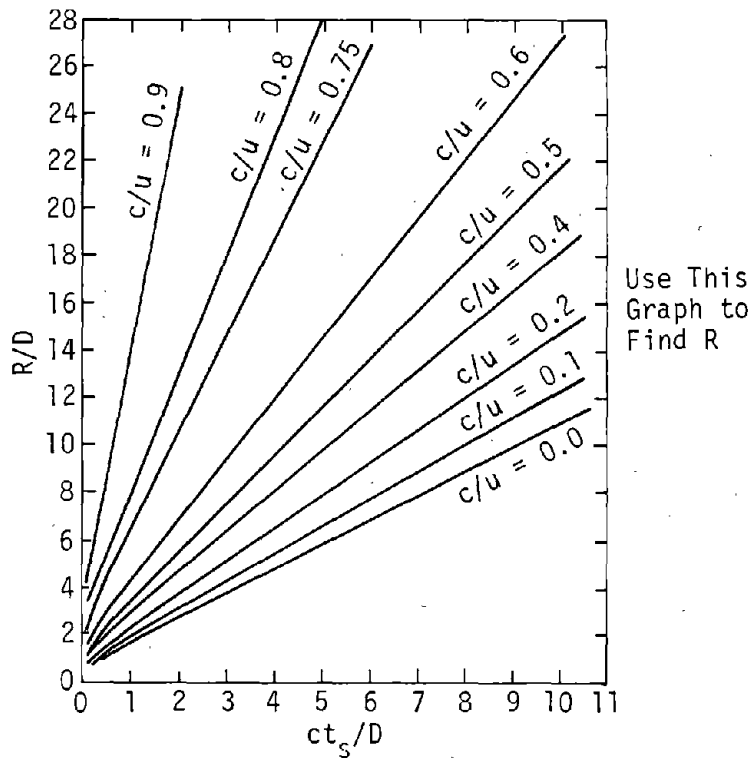
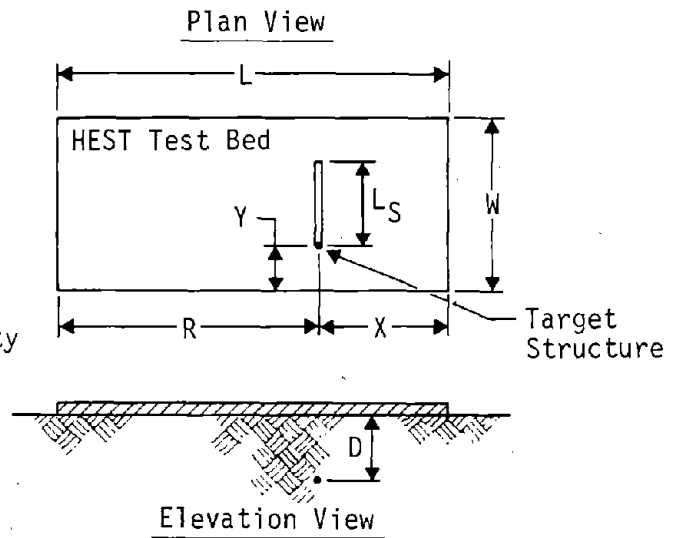
t_s = simulation time = $t_r - t_a$

where:

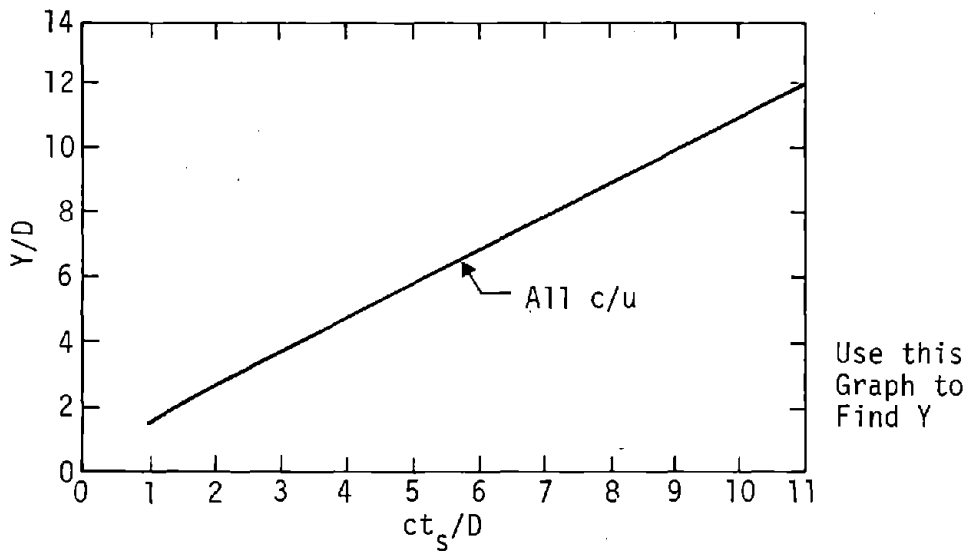
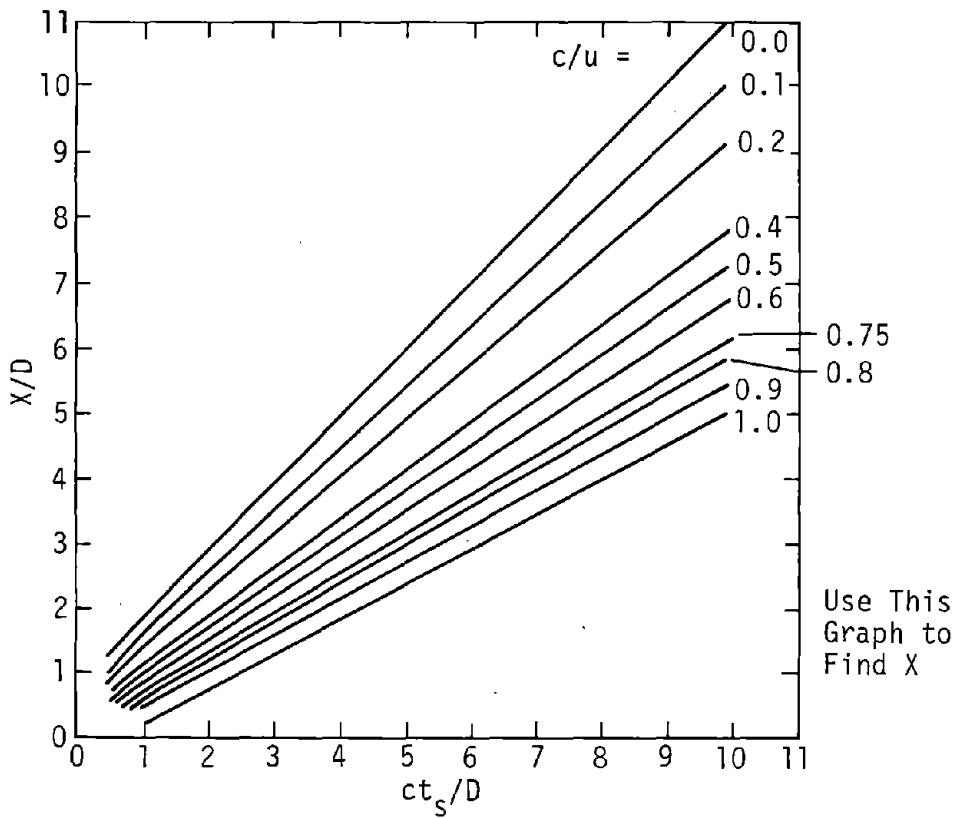
t_a = time of first shock arrival
(front, rear, side)

t_r = time of arrival of relief wave

t_s = simulation time = $t_r - t_a$



Method for Estimating Required HEST Test Bed Size



Method for Estimating Required HEST Test Bed Size

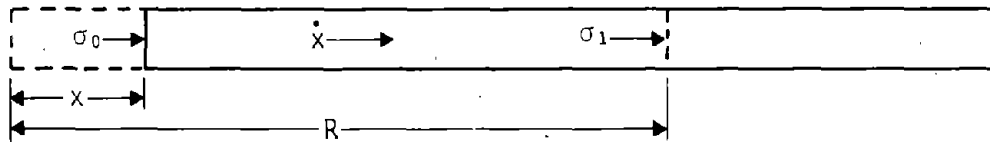
APPENDIX B
HEST DESIGN LOCKUP CODE DESCRIPTION

TECHNICAL MEMORANDUM (DED)/Ed Suesy
SUBJECT: HEST DESIGN LOCKUP CODE Description

5 November 1976

The HEST DESIGN LOCKUP CODE was developed for the HP9820 programmable calculator to calculate HEST pressure and impulse time histories for given initial pressure, cavity and overburden dimensions, soil properties and the ratio of the specific heats (γ) of the detonation products. There is no provision for handling layers; the overburden and the test bed materials are assumed uniform and homogeneous. The use of a lockup soil model makes the problem easily handled with a small programmable calculator. The calculations are one-dimensional and the three-dimensional properties of a HEST calculation are approximated. The detonation product/air mix in the cavity is assumed to have a uniform pressure distribution, and dynamic properties are neglected. The detonation product/air mix is assumed to be a "gamma law" gas with gamma held constant.

The following is a description of a one-dimensional "lockup" model. The figure below shows a column of material which is loaded with a stress σ_0 , has a total strain of x , through which the shock has traveled a distance R , is traveling at a velocity of R , and all of the material behind the shock has a uniform velocity of \dot{x} . The stress at the shock front is σ_1 .



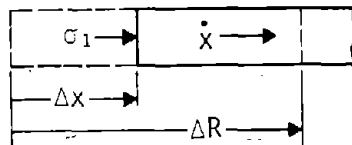
For momentum to be conserved:

$$\int_0^t \sigma_0 dt = \rho R \dot{x} \quad (1)$$

Differentiating (1):

$$\sigma_0 = \rho R \ddot{x} + \rho \dot{R} \dot{x} \quad (2)$$

The increment of material loaded in a time step Δt is shown below.



For momentum to be conserved:

$$\sigma_1 \Delta t = \rho \Delta R \dot{x} \quad (3)$$

$$\sigma_1 = \rho \dot{R} \dot{x} \quad (4)$$

Substituting (4) into (2):

$$\sigma_0 - \sigma_1 = \rho R \ddot{x} \quad (5)$$

And from (4):

$$\dot{R} = \frac{\sigma_1}{\rho \dot{x}} \quad (6)$$

$$\dot{R}^2 = \frac{\sigma_1 \dot{R}}{\rho \dot{x}} \quad (7)$$

$$\epsilon = \frac{\dot{x}}{\dot{R}} \quad (\epsilon = \text{strain})$$

$$\dot{R} = \sqrt{\frac{\sigma_1}{\rho \epsilon}} \quad (8)$$

$$\dot{x} = \epsilon \dot{R} = \sqrt{\frac{\epsilon \sigma_1}{\rho}} \quad (9)$$

If density ratios are used instead of strain:

$$\epsilon = 1 - \frac{\rho_0}{\rho_1} \quad (10)$$

The next part of the problem is to define a soil model, and for the high pressure HEST, a model that is reasonable in the high pressure regions. Some tests were conducted at UNM/CERF on samples of soil and sand taken from McCormick Ranch using the Riehle 100,000-lb machine as a loader and fixtures designed and fabricated at UNM/CERF to hold and load the soil sample. The results discussed here have not been published and are considered preliminary. A measured weight of soil was placed in a 6-in-diameter fixture and loaded with a piston. As load was applied to compress the sample the load and the displacement of the piston were measured and recorded continuously. The soil sample was disturbed and therefore the measured strain properties do not represent the in situ soil properties. The data scatter was quite large and an average curve was used. The data in Table B1 was adjusted to different initial densities by finding the stress level associated with the assumed density and subtracting that stress from the measured numbers. Stress versus the new density ratio or strain using (10) was listed. For a given initial density, the data in Table B1 can be used to calculate particle velocity, x , versus stress, σ , from (10) and (9).

Since we are interested occasionally in higher pressures than the 80 MPa (11,000 lb/in²) available from test data, a means of extrapolating to higher pressures was needed. The specific gravity of soil solids is typically about 2.7, or about 2700 kg/m³ (170 lb/ft³), about the same density as basalt. Basalt has a bulk modulus between 2.76E4 and 6.90E4 MPa (4E6 and 10E6 lb/in²). At a confining pressure of 6.90E3 MPa (1 x 10⁶ lb/in²), and assuming elastic

compression, basalt would have a density between 3028 kg/m³ (189 lb/ft³) and 3637 kg/m³ (227 lb/ft³). If we assume the soil would be at similar densities at 6.90E3 MPa (1 x 10⁶ lb/in²), \dot{x} would be between 1432 and 1554 m/s (4700 and 5100 ft/s) for an initial density of 1602 kg/m³ (100 lb/ft³). For purposes of defining the high pressure end of the σ versus \dot{x} curve, at $\rho_0 = 1602$ kg/m³ (100 lb/ft³) and $\sigma = 6.90E3$ MPa (1 x 10⁶ lb/in²), \dot{x} was assumed to be 1524 m/s (5000 ft/s). This data point and the average test data were used to calculate \dot{x} , and a polynomial of the following form was fit to the data.

$$\sigma = A_4 \dot{x}^2 + A_3 \dot{x}^{3/2} + A_2 \dot{x} + A_1 \dot{x}^{1/2} + A_0 \quad (11)$$

Values of the coefficients are given in Table B2 for sand and soil at various densities. (Updated test data were used, rather than the Table B1 data.) The force versus displacement data show a very nearly vertical unload line which tends to justify the locking solid model for the materials tested.

The calculational process of the impulse code is illustrated in Figure B1. The register assignments are given in Table B3, and the program is listed in Table B4.

The code calculates displacements at the HEST cavity boundary in subroutines P1, P2, and P3. Subroutine P1 calculates \dot{x} , \dot{y} for an input stress; P2 calculates a stress given a particle velocity \dot{x} , \dot{y} . Subroutine P3 calculates the rigid body motion of the overburden after lock up. P1 and P2 also return a \ddot{x} , \ddot{y} , and x , y . Subroutine VP, given initial cavity dimensions, x and y displacements and initial cavity pressure, calculates a new cavity volume, pressure, and total impulse. Figure B2 contains equations for a corner routine for small HESTs which is included in subroutine VP.

The code as written could no doubt be improved. It was written and exercised to demonstrate the feasibility of the approach to calculation of HEST cavity pressures, and little effort was expended to improve it from the demonstration level.

There is an obvious need for better input data and further comparison with experimental data. Soil equations based on dynamic tests and a better representation for γ are the most needed data improvements.

TABLE B-1. STRESS/DENSITY DATA

Sand* (1.62 lb sample)		Soil (.84 lb sample)	
σ (lb/in ²)	ρ_g (lb/ft ³)	σ (lb/in ²)	ρ_g (lb/ft ³)
0	101.5	198.6	79.1
334	106.8	397.3	89.1
1112	111.4	595.9	96.1
2225	115.3	794.5	101.5
4449	119.3	1192.0	108.7
6674	121.6	1589.0	113.8
8899	123.3	1986.0	118.0
11123	124.6	2384.0	121.5
		2781.0	125.5
		3178.0	128.4
		3973.0	131.9
		4767.0	135.9
		5562.0	138.0
		6356.0	141.3
		7151.0	143.1
		7945.0	145.9
		8740.0	147.5
		9534.0	149.1
		10329.0	151.6
		10925.0	153.2

*Raw Test Data Corrected to 0 Stress
At $\rho_{0g} = 101.5 \text{ lb/ft}^3$

TABLE B-2. COEFFICIENTS FOR EQUATION 11
(Stress Calculated from Velocity)

McCormick Ranch Soil 7 Mar 78

	85 lb/ft ³	90 lb/ft ³	95 lb/ft ³	100 lb/ft ³	105 lb/ft ³	110 lb/ft ³
a ₀	9.4850E1	9.3606E1	9.3137E1	9.3769E1	9.5894E1	9.6922E1
a ₁	-1.7045E1	-5.1496E0	2.7106E0	5.7895E0	2.0554E0	-8.3258E-1
a ₂	6.6644E0	5.9059E0	4.7786E0	4.1585E0	5.3398E0	6.5505E0
a ₃	-1.5234E-1	-8.9280E-2	6.9711E-2	2.4166E-1	2.9987E-1	4.0117E-1
a ₄	3.5118E-2	3.7763E-2	3.7607E-2	3.6808E-2	3.8898E-2	3.9487E-2
Vmin	0	0	0	0	0	0

McCormick Ranch Sand 7 Mar 78

a ₀	1.0014E2	1.0218E2	1.0020E2	9.9493E1	9.9188E1	9.9108E1
a ₁	3.7100E1	-3.7630E0	-5.2194E0	-1.9973E0	-3.6159E0	-6.8616E0
a ₂	-9.7622E0	-1.8143E0	-3.7314E-1	5.6561E-1	3.0580E0	8.5034E0
a ₃	-1.0538E0	6.8796E-1	7.3281E-1	8.6771E-1	1.0202E0	1.0298E0
a ₄	2.0833E-2	3.3710E-2	3.9642E-2	4.4640E-2	4.9037E-2	5.9019E-2
Vmin	0	0	0	0	0	0

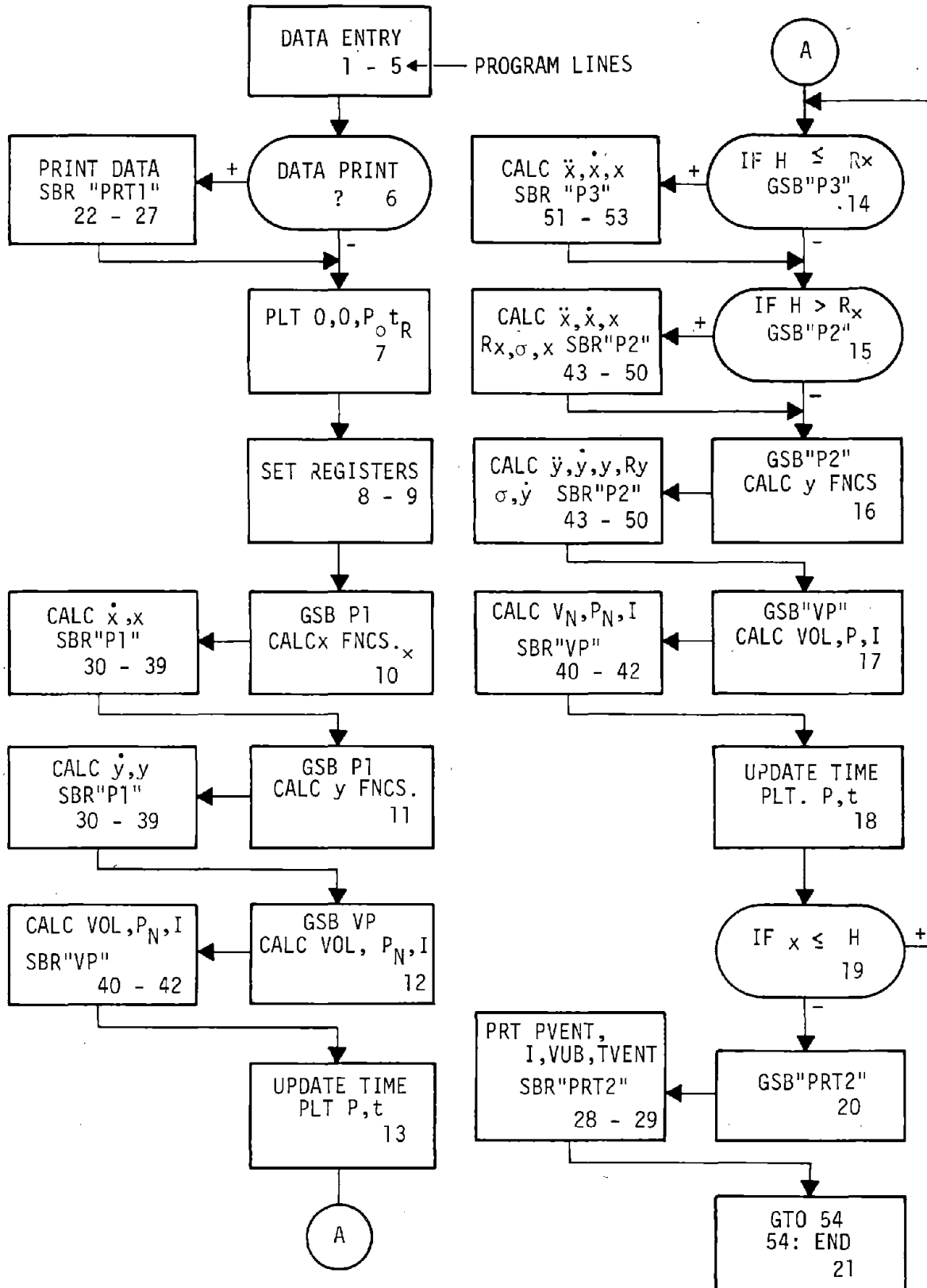


Figure B1. Lockup Impulse Code Flow Diagram HP9820

TABLE B3. REGISTER ASSIGNMENTS (1 of 2)

Register Number	Parameter	Register Number	Parameter
0	Po, Initial Cavity Pressure (lb/in ²)	22	B2, Test Bed Polynomial Coefficient
1	G, Ratio of Specific Heats	23	B3, Test Bed Polynomial Coefficient
2	D, Cavity Depth (ft)	24	B4, Test Bed Polynomial Coefficient
3	H, Overburden Height (ft)	25	B5, Test Bed Polynomial Coefficient
4	L, Cavity Length (ft)	26	B6, Test Bed Polynomial Coefficient
5	W, Cavity Width (ft)	27	Vmin, Min \dot{x} that B0-BN are Correct
6	DT, Intial ΔT (s)	28	TB, Test Bed Mass Density
7	DTN, Δt at the Nth Step (s)	29	N, Order of Test Bed Polynomial
8	T, Current Time (s)	*30	C0, Trench Cover Polynomial Coefficient
9	TA, Arrival Time (s)	*31	C1, Trench Cover Polynomial Coefficient
10	A0, Overburden Polynomial Coefficient	*32	C2, Trench Cover Polynomial Coefficient
11	A1, Overburden Polynomial Coefficient	*33	C3, Trench Cover Polynomial Coefficient
12	A2, Overburden Polynomial Coefficient	*34	C4, Trench Cover Polynomial Coefficient
13	A3, Overburden Polynomial Coefficient	*35	C5, Trench Cover Polynomial Coefficient
14	A4, Overburden Polynomial Coefficient	*36	C6, Trench Cover Polynomial Coefficient
15	A5, Overburden Polynomial Coefficient	*37	Vmin, Min \dot{z} that C0-CN are Correct
16	A6, Overburden Polynomial Coefficient	*38	TC, Trench Cover Mass Density
17	Vmin, Min \dot{x} that A ₀ - A _n are Correct	*39	N, Order of Trench Cover Polynomial
18	OB, Overburden Mass Density	40	σ , x Stress at Overburden Shock Front
19	N, Order of Overburden Polynomial	41	\ddot{x}_n , Acceleration of O.B. Rigid Body, N Step
20	B0, Test Bed Polynomial Coefficient	42	\ddot{x}_{n+1} , Acceleration of O.B. Rigid Body, N + 1 Step
21	B1, Test Bed Polynomial Coefficient	43	\dot{x}_n , Velocity of O.B. Rigid Body, N Step

* Indicates registers not used in current version but reserved for incorporation of trench collapse problem.

TABLE B3. REGISTER ASSIGNMENTS (2 of 2)

Register Number	Parameter	Register Number	Parameter
44	\dot{x}_{n+1} , Velocity of O.B. Rigid Body, N + L Step	*60	$\sigma_1 Z$
45	x, Displacement at O.B. Boundary	*61	\ddot{z}_n
46	Not Used	*62	\ddot{z}_{n+1}
47	Rx, Distance to Shock Front	*63	\dot{z}_n
48	Not Used	*64	Same as 40 Through 49 Except Related to Trench Cover
49	Not Used	*65	
50	$\sigma_1 y$	*66	
51	\ddot{y}_n	*67	
52	\ddot{y}_{n+1}	*68	
53	\dot{y}_n	*69	
54	\dot{y}_{n+1}	70	P_N , Cavity Pressure (lb/in ²) at Step N
55	y	71	P_{N+1} , Cavity Pressure (lb/in ²) at Step N + 1
56		72	I, Impulse (lb/in ² -s)
57	Ry	73	V_0 , Initial Cavity Volume
58		74	V_N , Current Cavity Volume
59		75-190	Not Used
		X, Y, Z, A, B, C	Used for Transient Calculated Storage

* Indicates registers not used in current version but reserved for incorporation of trench collapse problem.

TABLE B4. PROGRAM LISTING (1 of 2)

MAIN PROGRAM	SBR "PRT1"	SBR "PRT2"
0: ENT "P0",R0,"G", P1,"D",R2,"H",R3 ,"L",R4,"M",R5," DT",R6,"TA",R9F	22: "PRT1";SPC 2; PRT "P0,G,D,H,L, M,DT";PRT "TA,R 00,RTB=";R0,R1,R 2,R3,R4,R5F	28: "PRT2";SPC 1; PRT "PVENT,I,V08 ";PRT "TVENT="; R71,R72,R44,R8F
1: 10+R10+R1;CFG 13F	23: PRT R6,R9,R13,R2 8;PRT "A0,AH=";11 0+R10+R1F	29: RET F
2: ENT "AH",R10+R1; IF FL6 13=8;IF 6 >R1:1+D+R1;GTO +0F	24: PRT R10+R1;IF 9> R11+R10;GTO +0F	
3: B+R10+R1;ENT "V MIN",R17;"R0B",R 18;0+R1;20+R1;CFG 13F	25: PRT "R0,BH=";120+ R10+R1F	
4: ENT "BM",R10+R1; IF FL6 13=0;IF 6 >R1:1+D+R1;GTO +0F	26: PRT R10+R1;IF 9> R11+R10;GTO +0F	
5: B+R10+R1;ENT "V MIN",R27;"RTB",R 28;CFG 13F	27: RET F	
6: ENT "ENT 1 FOR P RHT";Z;IF Z=1; GSE "PRT1" F		
7: 40+0F		
8: 0+R0;IF 0<R0;1+R 0+R1;GTO +0F		
9: R0+R20+R71+R40+R 50;R6+R7;R2R4R5+ R79;0+R61		

TABLE B4. PROGRAM LISTING (2 of 2)

SBR "P1"	SBR "VP"	SBR "P2"	SBR "P3"
30:	40:	47:	55:
"P1":R71+Y;1E2+X.	"VP":IF R57<R3;R.	"P2":R(A+32)+R(A	"P3":R(A+32)+R(A
+C;0+Z+	R57+2(R4+R5)/2+2	+31);144(R71-R(A	+31);144R71/R(A+
31:	R57+3/3+R74+	+30)))/R(A+8)R(A+	8)R3+R(A+32)F
R(A+B)X+B+Z+Z;I+	41:	37)+R(A+32)F	56:
B+B;IF R(A+9)>B;	IF R57>R3;R3F(R	R(A+34)+R(A+33);	R(A+32)+R(A+33);
GT0 +0F	57+2-R3+2)+R57+	(R(A+32)+R(A+31)	(R(A+32)+R(A+31)
32:	2ASH (R3/R57)/18	R7/2+R(A+34)+R(A	R7/2+R(A+34)+R(A
IF Z>1.0001Y;IF	0)(R4+R5)+R74+	+34)F	+34)F
X>R(A+7);X-C/2+	42:	57:	57:
X;C/2+C;0+Z+B;	IF R57>R3;R74+0	(R(A+34)+R(A+33)	(R(A+34)+R(A+33)
JMP -1F	R3R57+2-R3+3)+	R7/2+R(A+35)+R(A	R7/2+R(A+35)+R(A
33:	R74+	+35)F	+35)F;RET F
IF .9999Y>Z;IF X	43:	49:	58:
>R(A+7);X+C/2+X	R57+2(R4+R5+2R2	(R(A+33)+R(A+34)	END F
;C/2+C;B+Z+B;)/2+2+R57+3/3+R7	R7/2+R(A+35)+R(A	R150
JMP -2+	4+R74;.5R55R74/R	A+35)F	
34:	57+R74+	50:	
IF X>R(A+7);	44:	R(A+34)+X;0+Z;	
JMP 4+	R73+R+5R4R5+R55(IF X+2<R(A+7);R	
35:	R4R5+2R2(R4+R5))	(A+7)+X+	
0+B+Z;R(A+7)+X+	+R74+R74+	51:	
36:	45:	R(A+B)X+B+Z+Z;I+	
R(A+B)X+B+Z+Z;	R71+R70;R0(R73/R	B+B;IF R(A+9)>B;	
IF R(A+9)>B;I+B+	74)R1+R71F	GT0 +0F	
B;GT0 +0F	46:	52:	
37:	R71+R70)R7/2+R7	IF X=FR(A+7);ZR(
R71X+2/2+X;R X+X+	2+R72;RET F	A+34)/X+2+Z+	
38:		53:	
X+2+R(A+34);R(A+		2+R(A+30);R(A+32	
34)R7+R(A+35)F)>R(A+31);144(R7	
39:		1-R(A+30))/R(A+8	
144R(A+30)R7/R(A		R(A+37)+R(A+32)	
+8)R(A+34)+R(A+3		F	
7)+R(A+37);RET F		54:	
		144R(A+30)R7/R(A	
		+8)R(A+34)+R(A+3	
		7)+R(A+37);RET F	

THIS PAGE IS BEST QUALITY FRAGMENT
FROM COPY FURNISHED TO DDC

Cavity Volumes: (overburden on surface)(current code configuration)

(1) Planar Volume:

$$V_p = LWD + LW(x + y) + 2 LDy + 2 WDy$$

(2) Cylindrical Volume:

$$V_c = \frac{y}{R_y} K V_{sc} \quad (V_{sc} = \text{cylindrical soil volume})$$

$$V_{sc} = \frac{\pi R_y^2}{4} (4L + 4W + 4D)$$

$$= \pi R_y^2 (L + W + D)$$

$$V_c = K y \pi R_y (L + W + D)$$

(3) Spherical Volume:

$$V_s = \frac{K y}{R_y} V_{ss} \quad (V_{ss} = \text{spherical soil volume})$$

$$V_{ss} = \frac{4}{3} \pi R_y^3$$

$$V_s = \frac{4}{3} K y \pi R_y^2$$

(4) $V_c = V_p + V_c + V_s$

$$V_c = LWD + LWx + y(LW + 2LD + 2WD)$$

$$+ K \phi D^3 P_1 S(3) [L1 + W1 + D1 + 4 S(3)/3]$$

$$+ K y \pi R_y (L + W + D + 4 R_y/3)$$

Figure B2. Corner Model for Small HEST Tests

APPENDIX C
 BRODE IDEALIZED NUCLEAR AIRBLAST EQUATIONS (REF. 1)
 (Free Air)

Parameters:

$$r(\text{k ft}), w(\text{kt}), t(\text{ms})$$

Peak Overpressure:

$$P(r, w) \approx \frac{1.58 w}{r^3} + \frac{5.4}{r} \sqrt{\frac{w}{r}} + 0.0215, \text{ lb/in}^2$$

Time of Arrival:

$$t_a(r, w) = \frac{0.5429 w - 21.185 r w^{2/3} + 361.8 r^2 w^{1/3} + 2383 r^3}{w^{2/3} + 2.048 r w^{1/3} + 2.687 r^2}, \text{ ms}$$

Positive Phase Duration:

$$D = \frac{820350 w + 15515 w^{2/3} t_a + 330.3 w^{1/3} t_a^2}{6854 w^{2/3} + 491.9 w^{1/3} t_a + t_a^2}, \text{ ms}$$

Overpressure Versus Time:

$$\Delta P(t, t_a, w) = \frac{13493 w^{1/3}}{(t + 0.0135 w^{1/3})} \left[0.4587 + 0.6413 \left(\frac{t_a}{t} \right)^6 \right] \left(1 - \frac{t - t_a}{D} \right)^v, \text{ lb/in}^2$$

$$v = \frac{w^{2/3} + 0.6715 w^{1/3} t + 0.004813 t^2}{w^{2/3} + 1.8836 w^{1/3} t + 0.02161 t^2}$$

NUCLEAR AIRBLAST SIMULATION
WITH EMPHASIS ON DYNAMIC PRESSURE

I. BACKGROUND

The United States Military Services have a continuing requirement to test their systems for survivability against nuclear attack. Many (if not most) of these systems are sensitive to nuclear induced airblast and especially the dynamic winds. Required levels of survivability span the spectrum of pressures from many Mega Pascals (MPa) to less than 10 Kilo Pascals (KPa) and durations associated with yields of several Megatons (MT) to Kilotons (KT). Many of these systems and facilities are very large, and nonlinear or nonscalable responses require testing at large scales. Therefore, required test facilities are necessarily very large. The moratorium on nuclear testing above ground, imposed by the Test Ban Treaty of 1963, has ruled out the possibility of testing operational facilities in an actual nuclear environment. Therefore, non-nuclear capabilities for testing these facilities are required. Many methods have been used in the past but each has had certain limitations. This paper reviews the previous test capabilities, traces the evolution of simulation, and presents the initial development of a new method for Dynamic Airblast Simulation.

II. THE NUCLEAR ENVIRONMENT

Any discussion of simulation must be preceded by a review of the environment to be simulated. Several attempts have been made to develop simple models to predict the Nuclear Airblast Environment. The most prominent of these are the Brode fit to measure nuclear environments (Ref 1), the AFWL 1 KT standard (Ref 2) which is an analytic fit to detailed calculations, and self similar flow approximations by Von Nueman (Ref 3) and Sedov (Ref 4). Each of these has its limitations and advantages, as do the other approximations, and no attempt will be made to evaluate them. Suffice it to say that each of the models does a credible job of matching recorded data over the pressure range of interest. For the purpose of this paper the Brode analytic fit was picked as the standard.

The analytic expressions from Reference 1 were used to develop the relationships for peak pressure versus range (both static and dynamic) shown in figure 1 and impulse vs range shown in figure 2. For use in later analysis these expressions were programmed on an HP 9820 Programable Desk Top Calculator in a way to allow generation of pressure and impulse histories for various ranges and yields. Some selected waveforms in the range of interest are shown in figure 3.

Since the Brode and other models are analytic approximations to strictly spherical flow results, they can not be utilized to extrapolate to cylindrical and planar flow geometries which are of interest to simulation approaches. Only the self similar flow approximation is in a form which can be developed for any of the one-dimensional geometries. However, because of the approximations made in developing the self similar

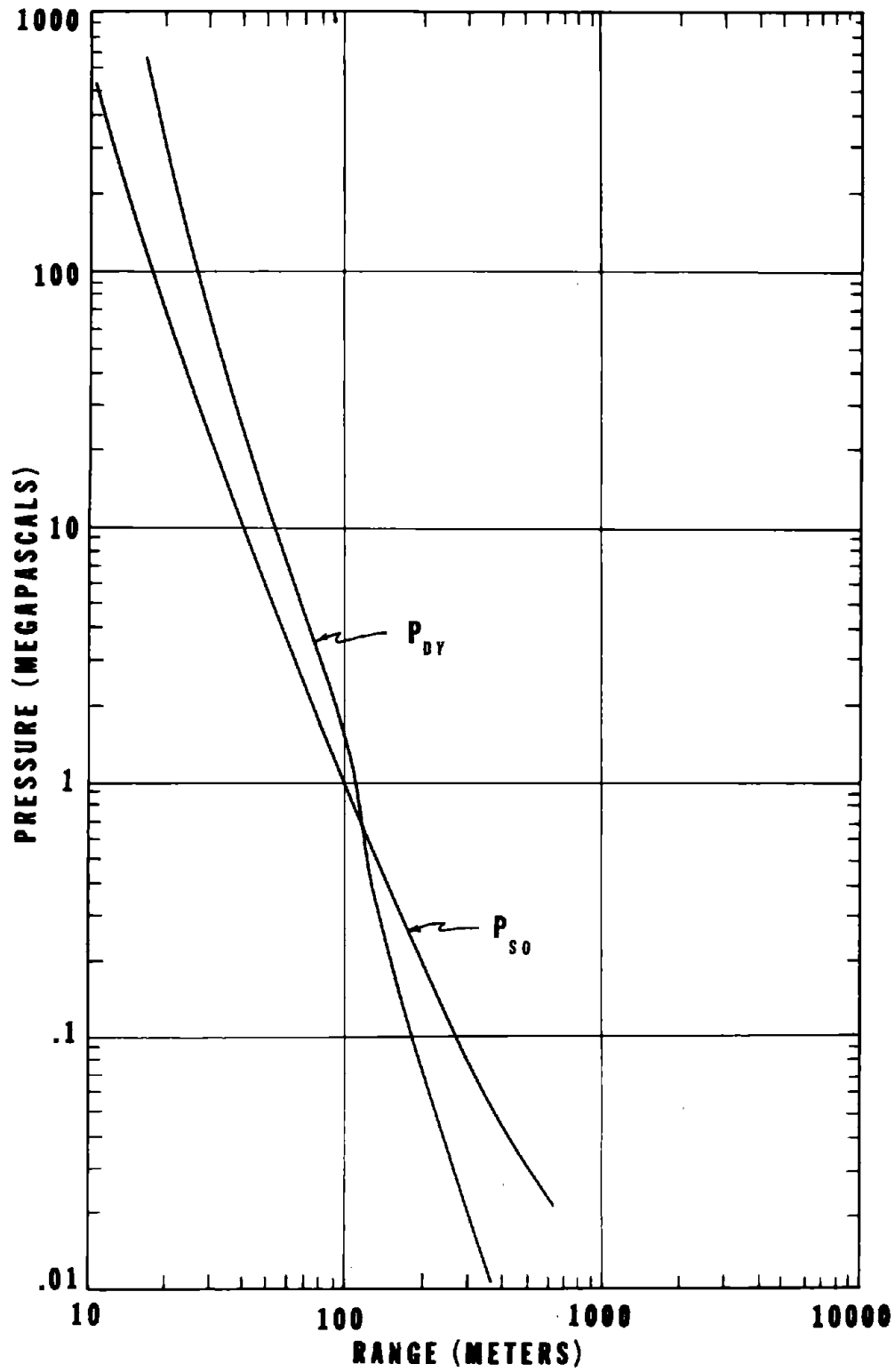


FIGURE 1. PEAK PRESSURES VERSUS RANGE FROM BRODE FIT FOR 1KT

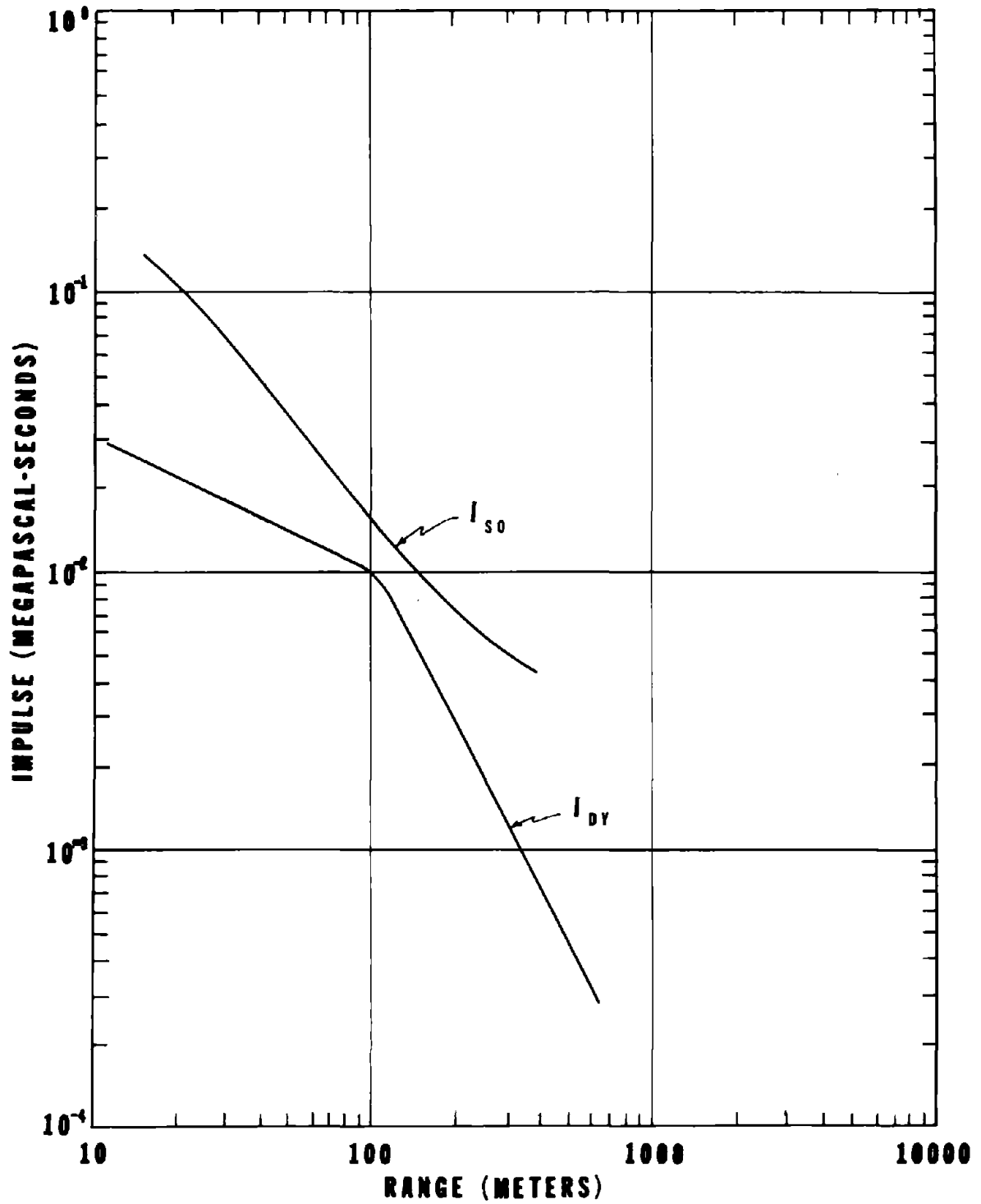


FIGURE 2. IMPULSE VERSUS RANGE FROM BRODE FIT FOR 1KT

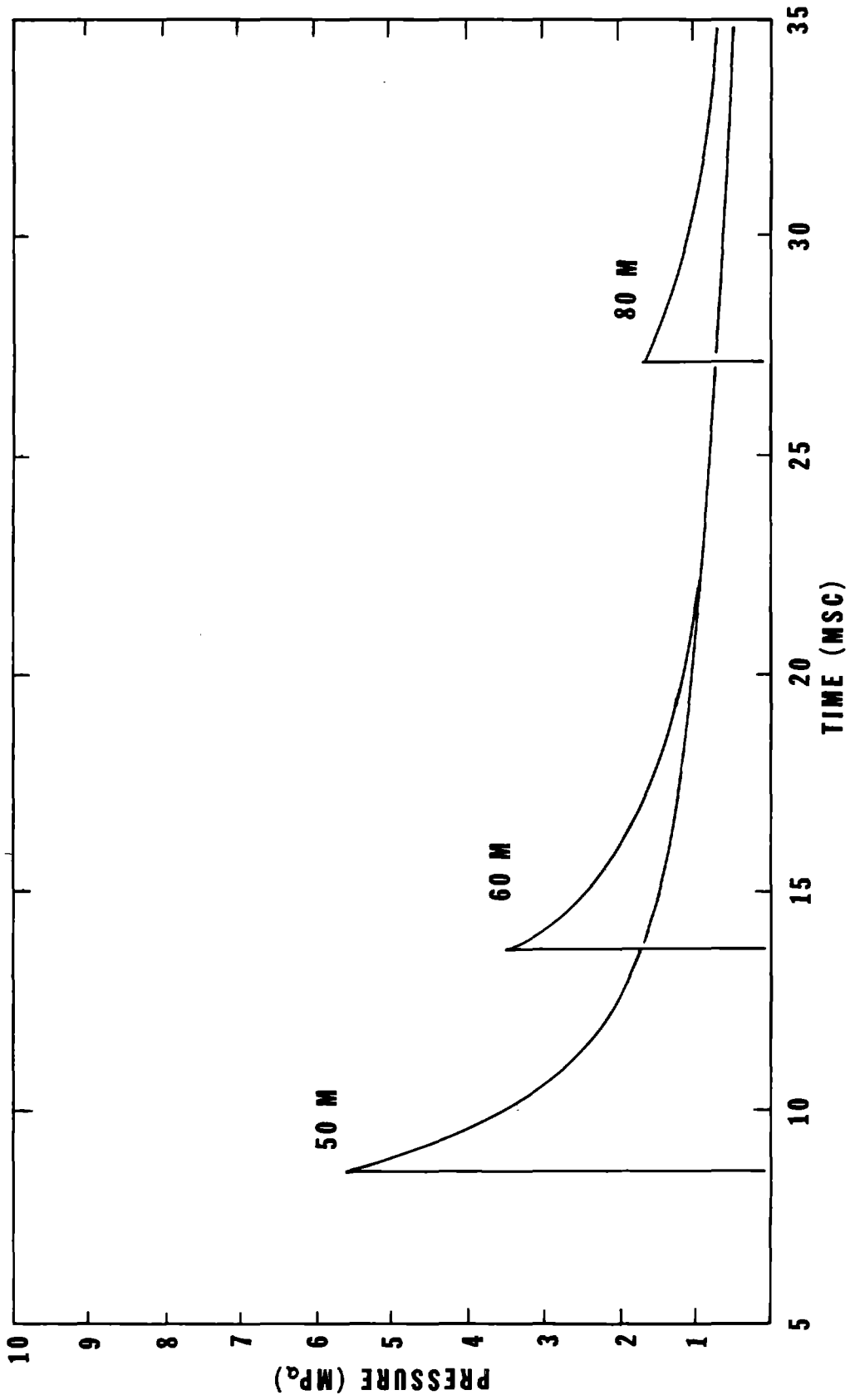


FIGURE 3. REPRESENTATIVE PRESSURE HISTORIES FROM BRODE FIT FOR 1KT

flow model and the fact that it has its roots in theory rather than actual data, this model must be evaluated before being applied. The most direct method of evaluation was to use the spherical self similar flow model and compare it with the chosen standard nuclear approximation.

To perform this comparison the general one-dimensional flow model from Sedov was programmed on the HP9820 calculator in the same manner as the Brode fit. The general one-dimensional flow model is discussed in Appendix A. This program was used to generate relationships for peak pressure and impulse vs range for comparison with those from the Brode fit. One variable which comes into question is the energy equivalence of a kiloton of nuclear yield. The value chosen for this study was $4.69E 12$ joules per KT nuclear. Figures 4 and 5 present the similarity model results for peak pressure and impulse versus range overlayed on the Brode fit results presented in figures 1 and 2. Figures 6 and 7 present an example of the pressure and impulse comparison for a selected value in the range of interest.

This comparison shows that the one-dimensional self similar flow model is a reasonable approximation of the spherically symmetric nuclear airblast environment over a considerable range of pressures. Therefore, this model should generate reasonable predictions for tests in the cylindrical and planar geometries. The importance of this conclusion will become evident in the following sections. At pressures below approximately 1 MPa the overpressure and dynamic pressure start deviating significantly from the nuclear. This is a result of assuming that the pressure in front of the shock is negligible relative to the shock. Corrections can be made by either incorporating a weak shock solution or by some empirical adjustment. Sedov attempts to quantify the error when he makes the assumption. For example, where the peak overpressure is predicted to be 0.1 MPa Sedov estimates that peak dynamic pressure will be only 17% of the predicted value. Figure 4 shows this as a much better approximation.

III. SIMULATION

A. Spherical Simulation - TNT spheres (and approximations thereto). The nearest approximation of the spherical nuclear airblast environment is that produced by a sphere of non-nuclear explosives. A perfect sphere of high-explosive is the ideal; however, capped cylinders of blasting agents have been used with satisfactory results. This approach is a direct attempt to duplicate the spherical airblast (and other mechanical effects) created by a nuclear detonation by using a spherical non-nuclear energy source. Some of the most notable limitations of this approach include the lower energy density of conventional explosives and increased time for total energy release. In spite of these limitations, the high explosive charge does a very credible job of simulating the nuclear induced airblast over a very large range. Figure 8 presents a comparison of the pressure versus range results of a series of 500 ton HE detonations compared with the Brode approximation and similarity model predictions for an equivalent nuclear event. Note that for pressures above approximately 1 MPa, the high explosive results fall below nuclear and for lower pressures the HE data exceeds nuclear at a given range. The higher density detonation products tend to overdrive the airshock at larger ranges.

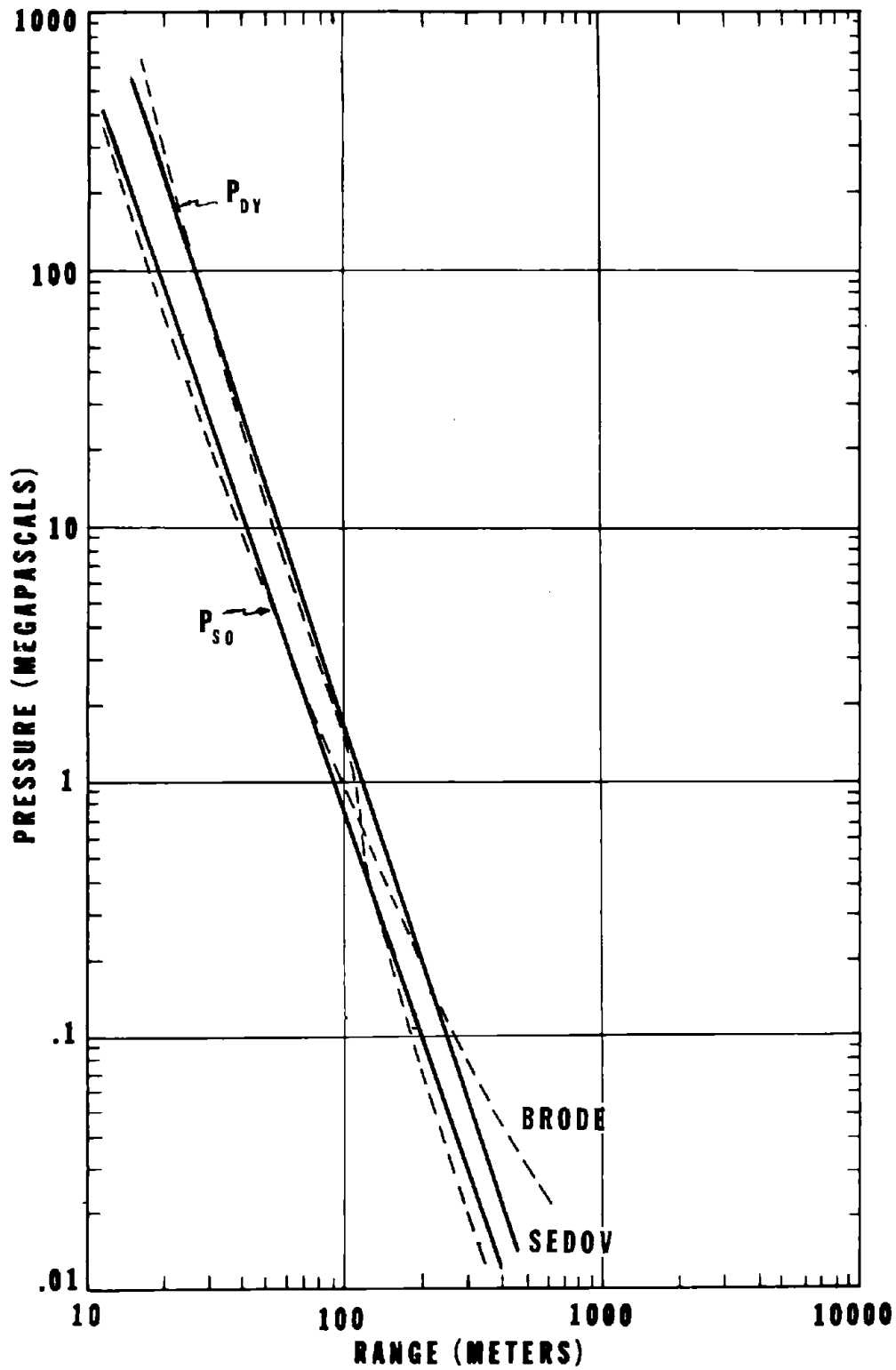


FIGURE 4. PEAK PRESSURE VERSUS RANGE COMPARISON FOR BRODE FIT AND SEDOV SIMILARITY SOLUTION

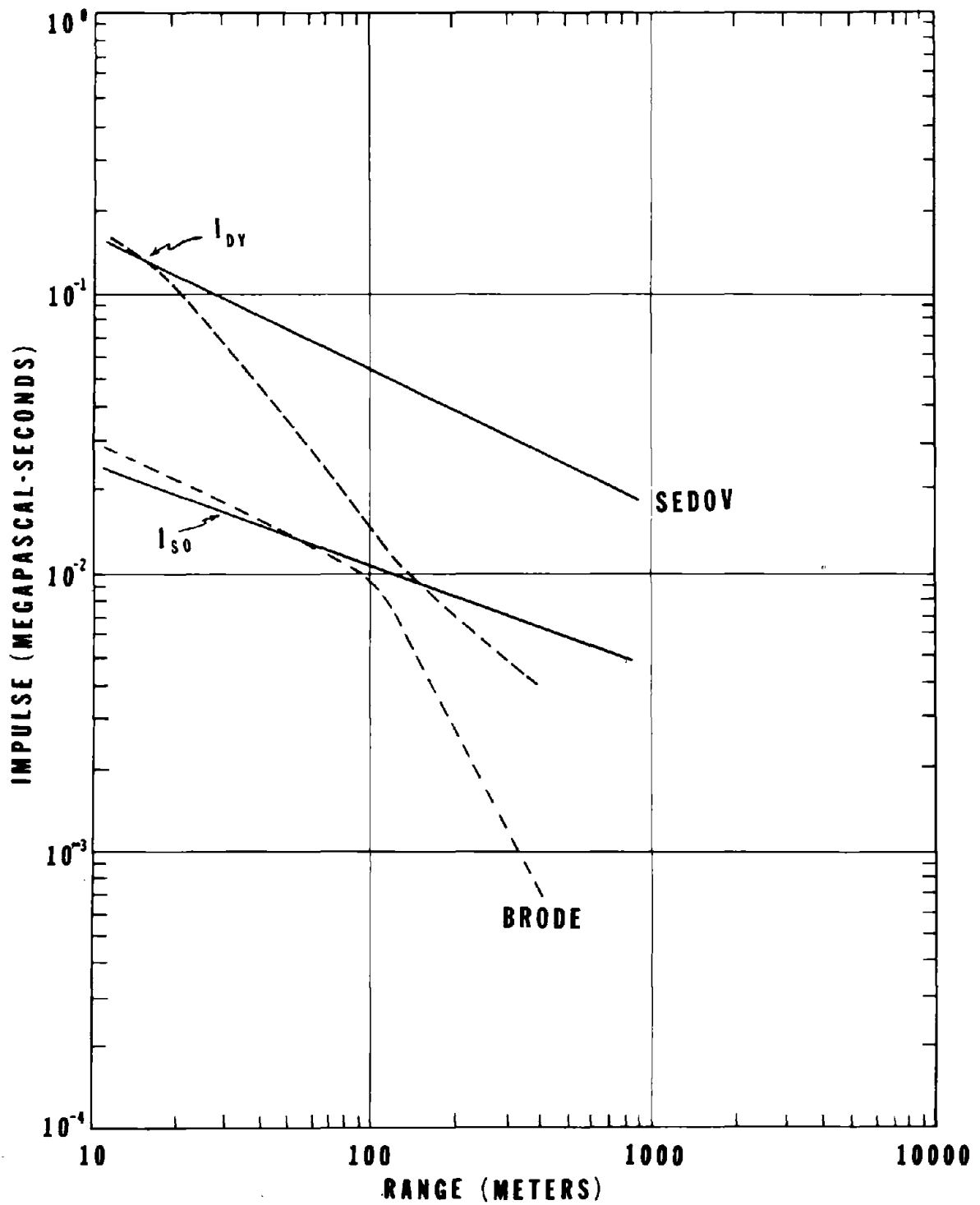


FIGURE 5. IMPULSE VERSUS RANGE COMPARISON FOR BRODE FIT AND SEDOV SIMILARITY SOLUTION

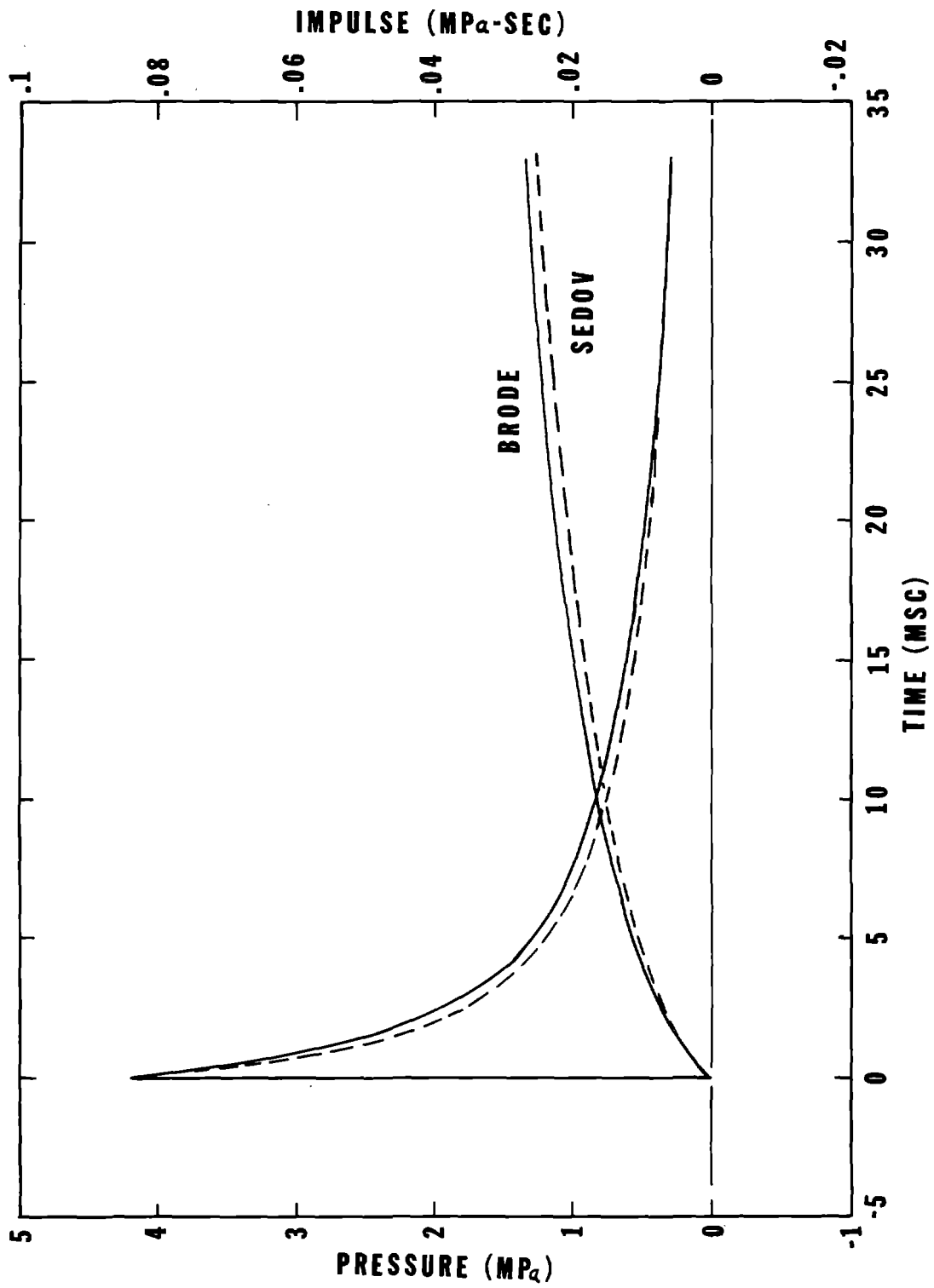
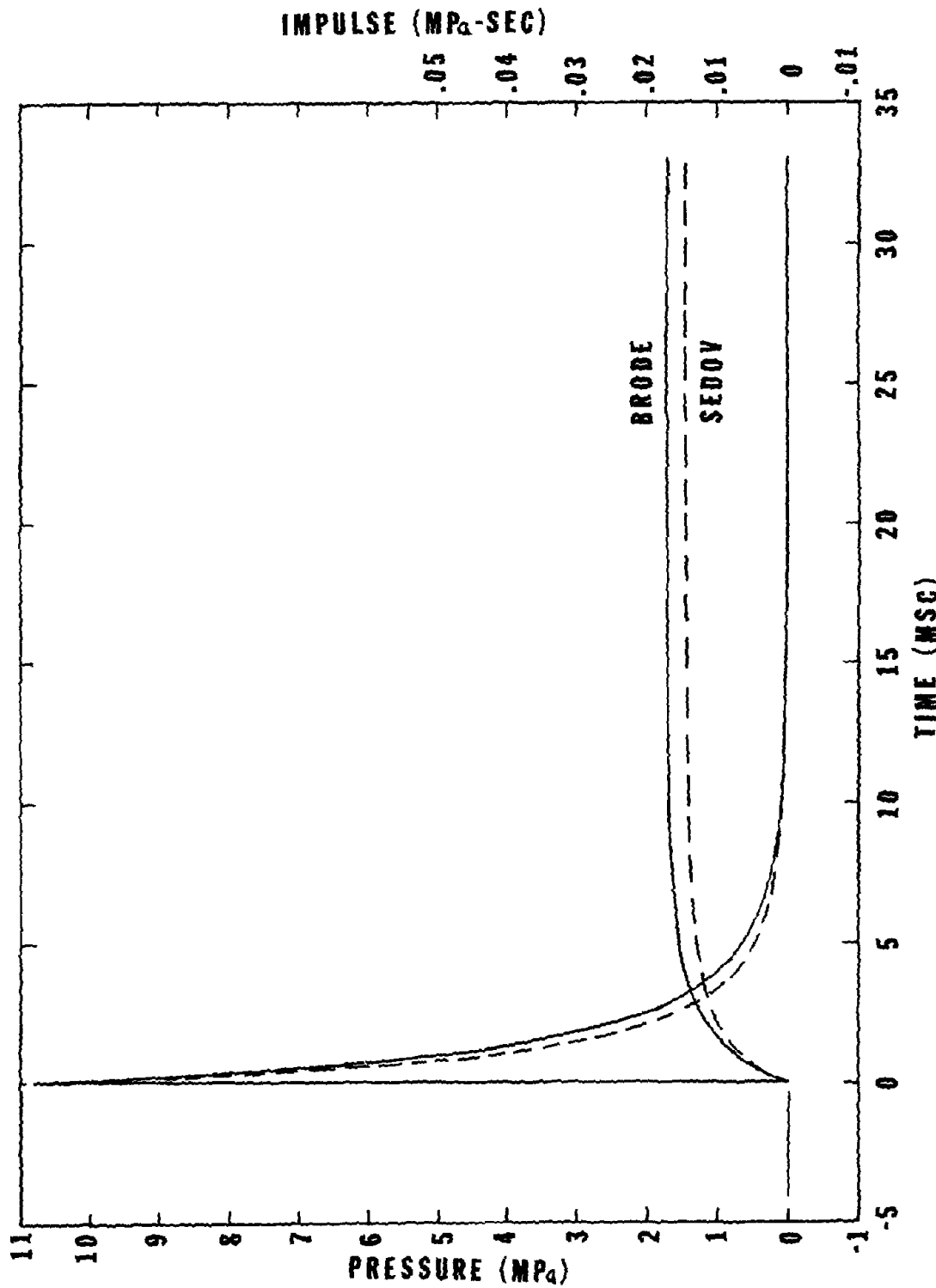


FIGURE 6. EXAMPLE PRESSURE AND IMPULSE HISTORY COMPARISON FOR BRODE FIT AND SEDOV SIMILARITY SOLUTION



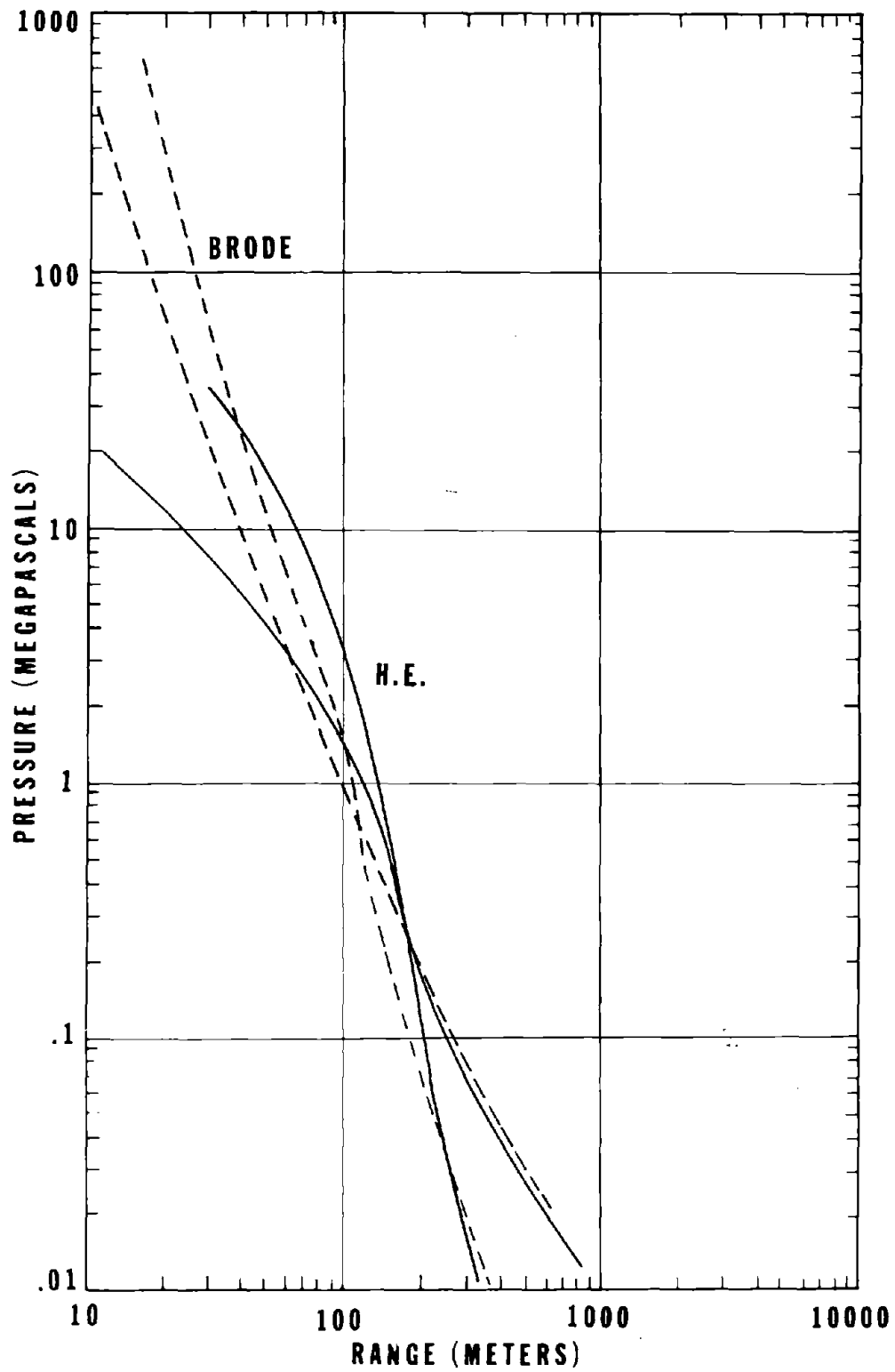


FIGURE 8. PEAK PRESSURE VERSUS RANGE COMPARISON FOR BRODE FIT AND TNT SPHERE DATA

A comparison of nuclear and HE overpressure waveforms is shown in figures 9,10 and 11 for peak pressures above, at, and below 1 MPa respectively. Note that ranges have been adjusted to match peak pressures. We can see that the degree of correlation is best for 1 MPa peak pressure and degrades both above and below that value. Also note the differences in range between the nuclear and HE. A more complete comparison of impulse versus range for both overpressure and dynamic pressures is presented in figure 12.

Perhaps the most severe limitation of the high explosive sphere is the practical limitation on size. Although one could theoretically continue to add more and more explosive to achieve greater yields, the cost and construction problems rapidly overwhelm the experiment. Generally, the test requirements for such an experiment do not require the total exposed area and, thus, much of the energy in the charge is wasted. Therefore, if by changing the geometry one can achieve a significant reduction in both total explosive charge and test area, the effective yield of the test can be substantially increased.

B. Spherical Simulation-conical shock tube. The first and most straight forward step to reduce total charge and test volume is to utilize only a conical section of the spherical geometry. This is accomplished by using a cone shaped facility to contain a segment of the HE and resulting environment. Theoretically, this could result in a very large increase in simulated yield for the same total charge. The required charge to simulated yield ratio is related to the fraction of the spherical charge volume contained within the tube.

The principal example of this technique is the conical shock tube at Dahlgren, VA. (Ref 6). Physical problems of containing the detonation and blast wave limit the peak pressures and blast durations which can be achieved in a permanent facility of this type. Additionally, construction difficulties limit the size of a permanent facility of this type. For example the facility at Dahlgren is limited to pressures less than 1 MPa and test articles of 1 M dimensions.

Construction of a large disposable facility of this geometry would require use of a continuously changing cross section. In a large construction project as would be required for a full size test this would be exceedingly expensive and perhaps totally impractical. Therefore, a geometry which is easier to construct should be investigated. The next step in simplifying construction would be a cylindrically symmetric approximation where the height of the facility is held constant and the width is continuously varied from zero to the width of the test section.

C. Cylindrical Simulation - A facility of this type would result in an environment approximating cylindrical self similar flow. To the best of my knowledge no facility has ever been constructed or tested in this configuration. Additionally, since construction of a constant area tube would be more straight forward, this is not the optimum geometry to investigate. However, as the intermediate step between spherical and planar self similar flow, it

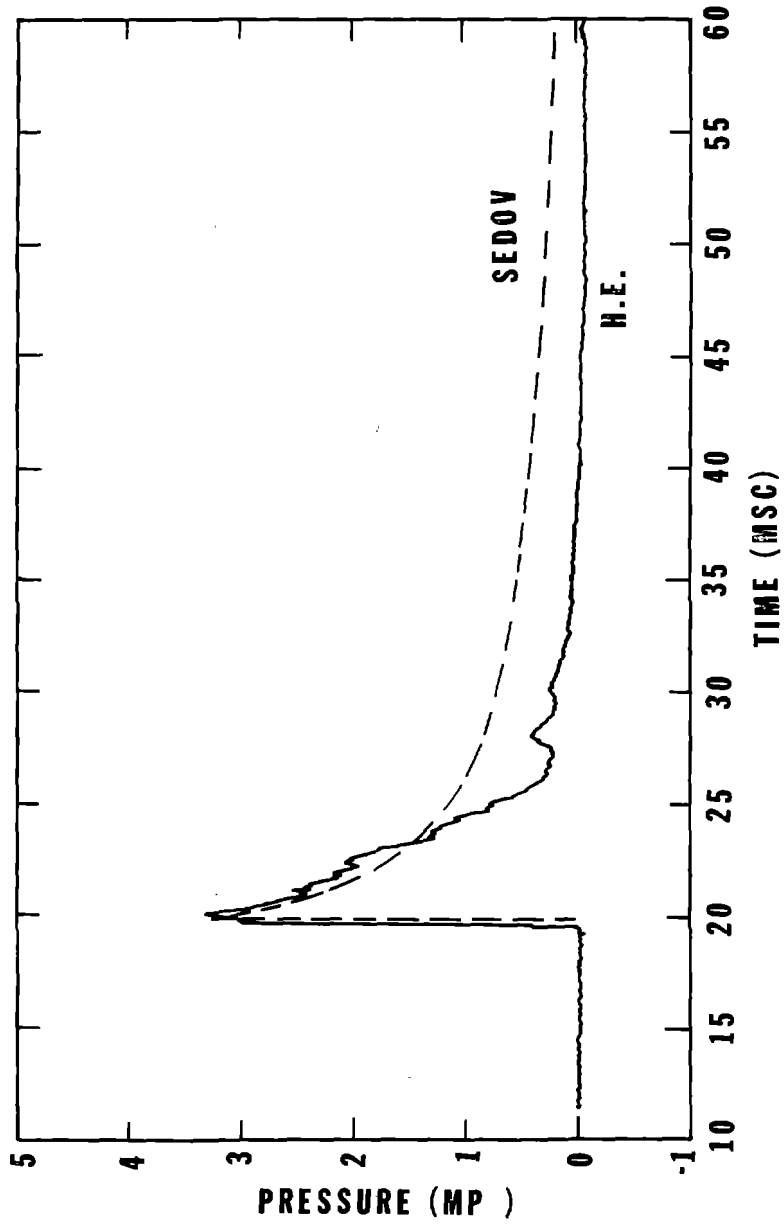


FIGURE 9. PRESSURE HISTORY COMPARISON FOR DICE THROW DATA AT 63 M AND SIMILARITY SOLUTION FOR 1KT. PEAK PRESSURE MATCHED.

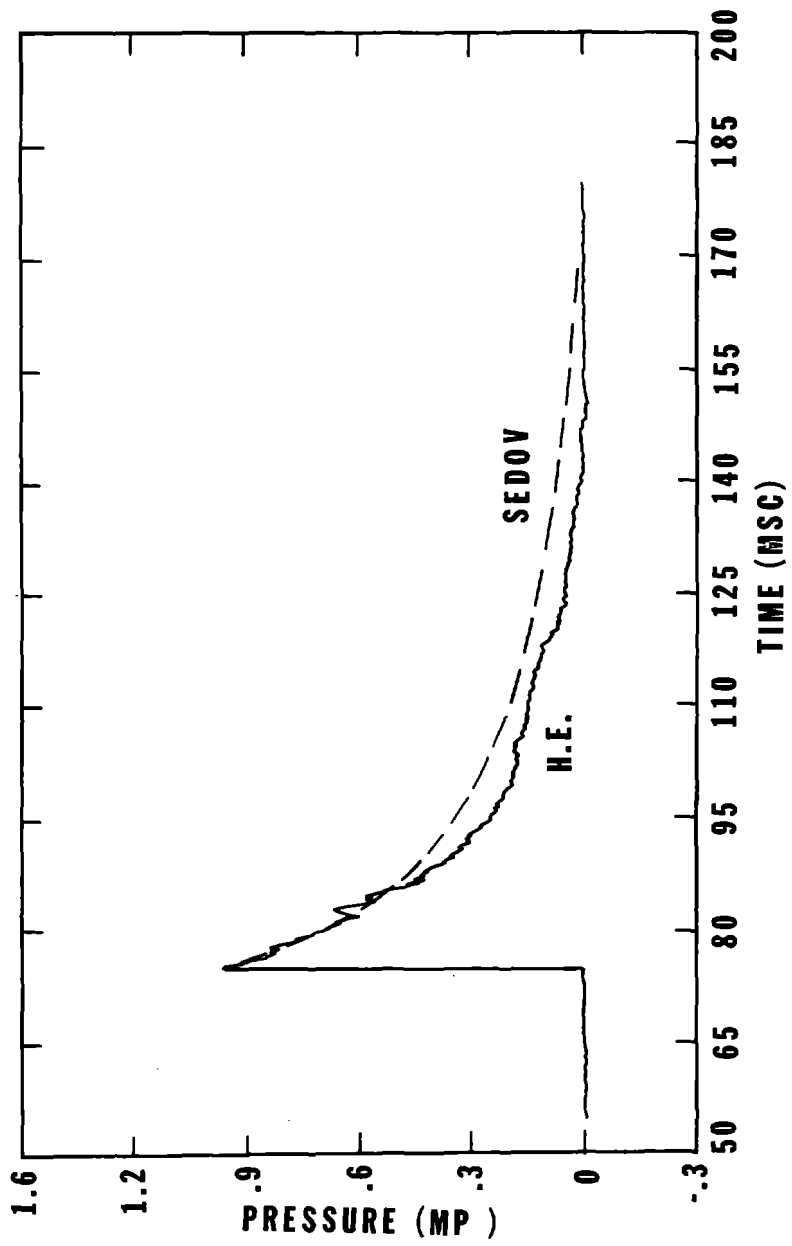


FIGURE 10. PRESSURE HISTORY COMPARISON FOR DICE THROW DATA AT 150 M AND SIMILARITY SOLUTION FOR 1KT. PEAK PRESSURE MATCHED.

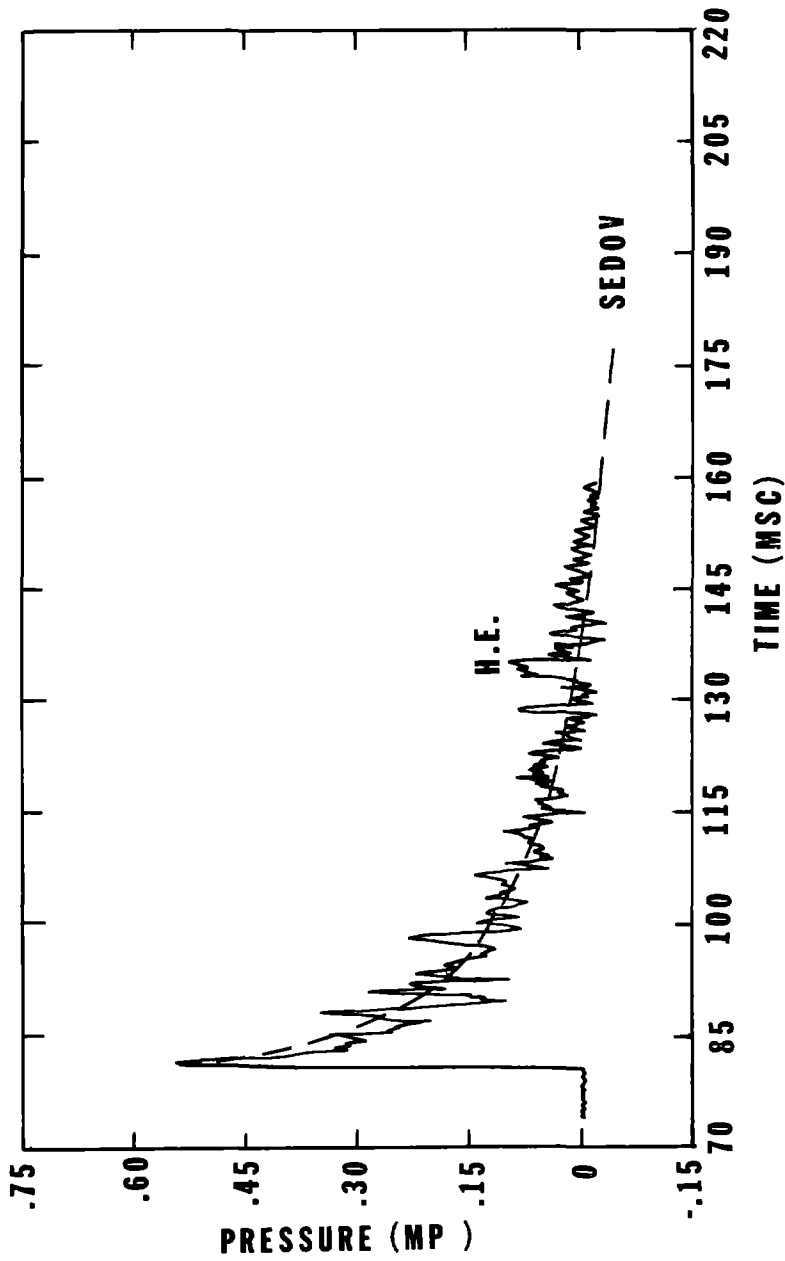


FIGURE 11. PRESSURE HISTORY COMPARISON FOR DICE THROW DATA AT 116 M AND SIMILARITY SOLUTION FOR 1KT. PEAK PRESSURE MATCHED.

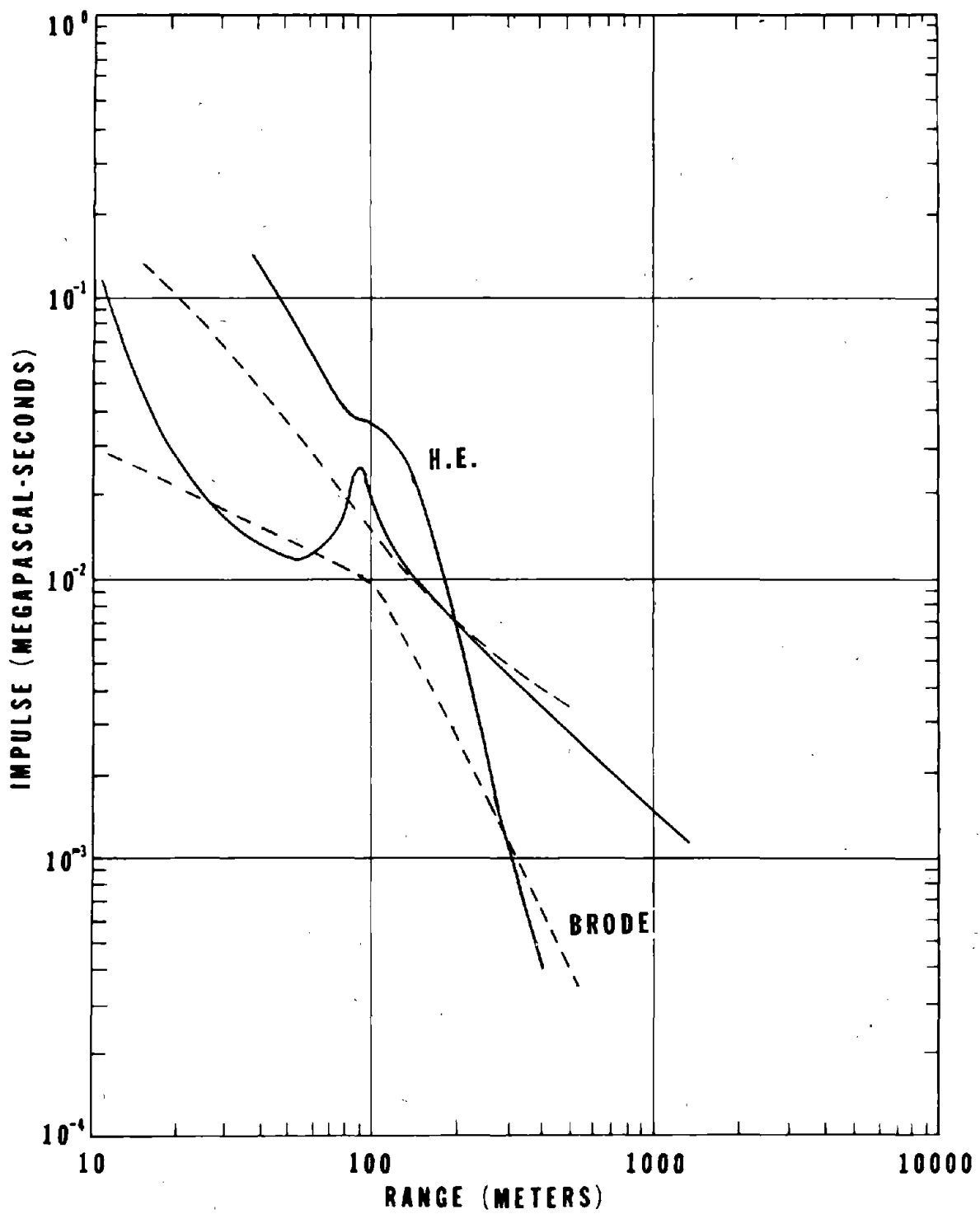


FIGURE 12. IMPULSE VERSUS RANGE COMPARISON FOR BRODE FIT AND TNT SPHERE DATA

was worth some study. To make a meaningful comparison between spherical and cylindrical self similar flow models, a specific peak pressure and yield must be chosen as a point of reference.

For this study a peak pressure of 4 MPa and yield of 1 KT was selected. Additionally, since the pressure decay functions are different, some measure of goodness of fit must be selected. A match of pressure decay to time of 20 percent of peak was selected. A comparison of peak pressures versus range for the spherical and cylindrical flow models is shown in figure 13. Note that the cylindrical curve has been shifted in range to match the spherical pressure curve at 4 MPa. Figure 14 presents a comparison of the overpressure and impulse histories and figure 15 presents a similar comparison for dynamic pressures.

From figure 13 we see that a test facility using cylindrical similarity results in a test facility length reduction of one third over a test facility using spherical symmetry. A significant reduction in total charge energy over a spherical charge is also achieved. However, a comparison of a test facility using cylindrical symmetry with an equivalent conical shock tube would show that the cylindrical case utilized more energy.

D. Planar Simulation. As was mentioned earlier, the primary motivation for investigating a simulator concept using plane one-dimensional flow was its overall simplicity and ease of construction on large scales. However, that is but one attraction of this approach. This section will outline the development of the theoretical basis for this type of simulation and identify some of the other attractive features. The final product will be a method of transitioning from spherical nuclear environments thru spherical similarity models to a plane of one-dimensional representation of an airblast simulator and the resulting scaling relationships.

The simulator concept is basically that of an infinitesimally thick plane of explosives either infinite in span or with some boundary to direct the flow in one direction. Practical constraints may restrict consideration to concepts with physical boundaries to direct the flow. The flow in such a facility would be plane one-dimensional in nature, and if the explosive charge were indeed infinitesimal in thickness with infinite energy density, the flow would be truly self similar. Finite charge thickness will result in lower initial shock pressures which, with increasing range, will tend to approach those of self similar flow approximations. Previous facilities of this type have included shock tubes of both the bursting diaphragm and volume detonation type (Ref 7) and various blast directing techniques (Ref 8). All of these techniques either utilize fixed facilities of limited size and pressures or were only developed at small size and yield.

To investigate the advantages and disadvantages of a simulation technique using plane one-dimensional flow we can compare the self similar flow models for plane and spherical similarity. Since we have already compared the spherical flow model with nuclear, we then obtain a qualitative evaluation of the plane one-dimensional flow model with nuclear. The expressions discussed

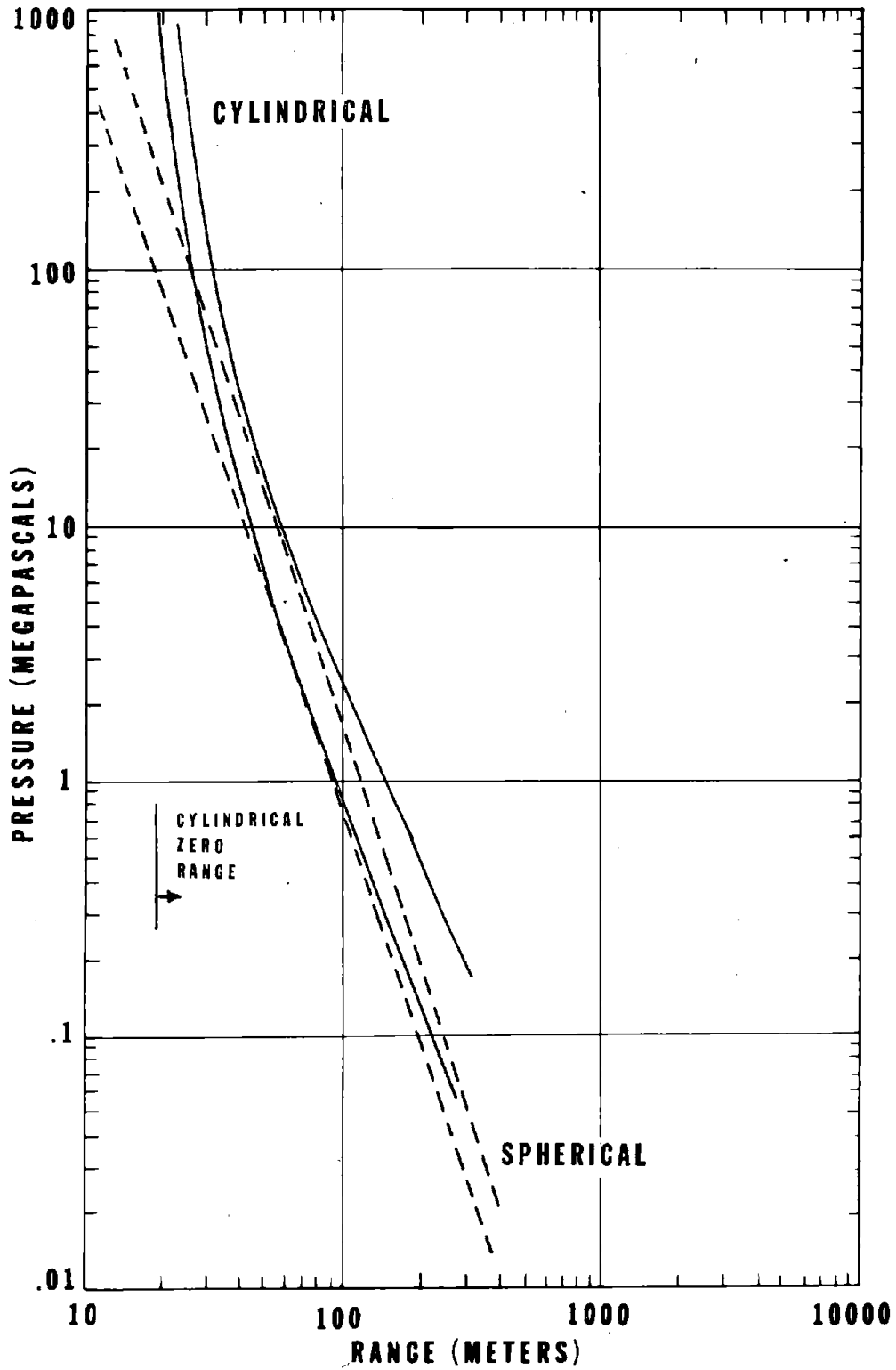


FIGURE 13. PEAK PRESSURE VERSUS RANGE COMPARISON FOR CYLINDRICAL AND SPHERICAL SIMILARITY SOLUTIONS. CYLINDRICAL RANGE SHIFTED TO MATCH SPHERICAL AT 4 MPa PRESSURE

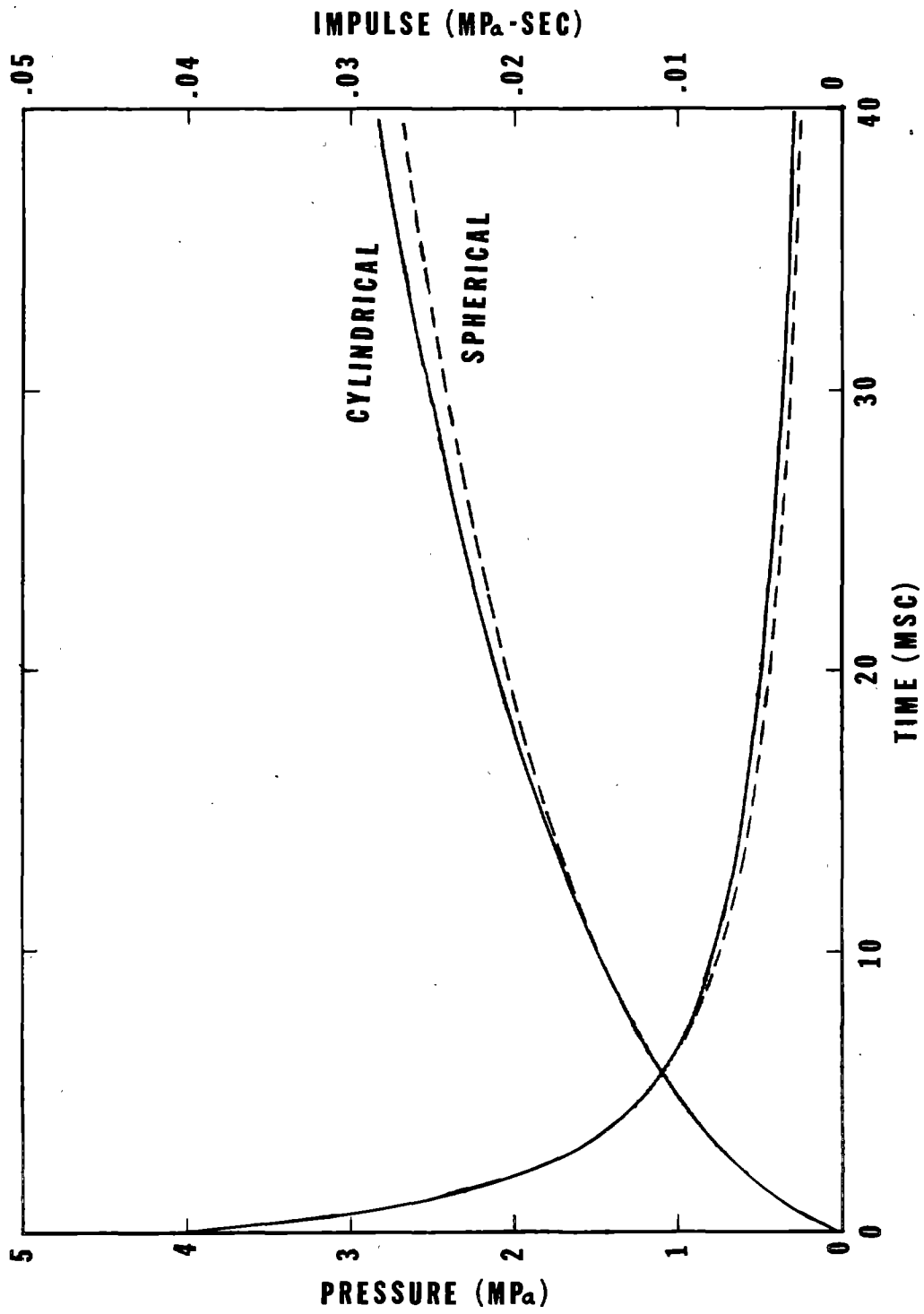


FIGURE 14. OVERPRESSURE AND IMPULSE HISTORY COMPARISON FOR CYLINDRICAL AND SPHERICAL SIMILARITY SOLUTION AT 4 MPa PRESSURE.

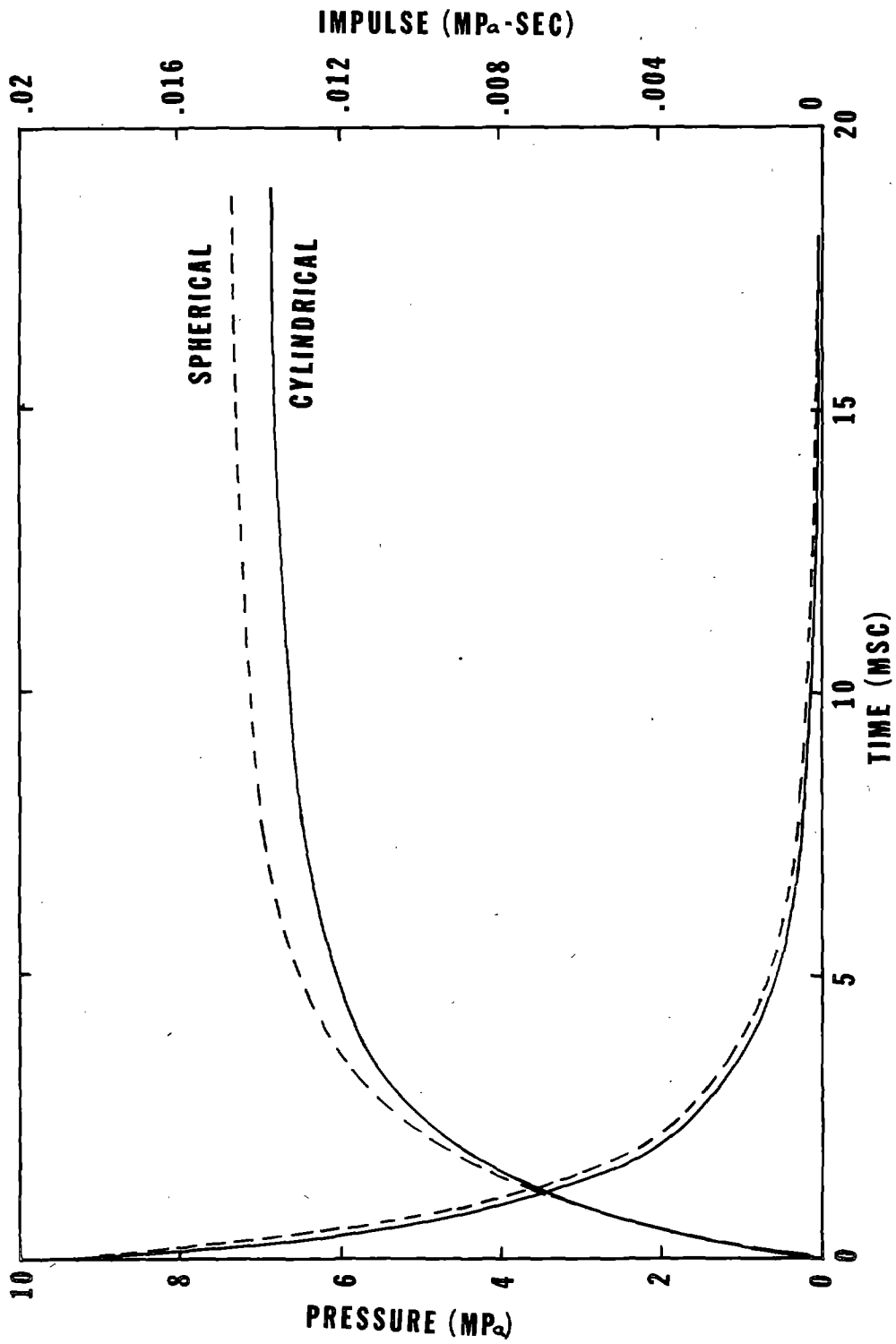


FIGURE 15 DYNAMIC PRESSURE AND IMPULSE HISTORY COMPARISON FOR CYLINDRICAL AND SPHERICAL SIMILARITY SOLUTION AT 4 MPa OVERPRESSURE RANGE

in appendix A were used to develop peak pressure versus range comparisons for plane and spherical similarity (figure 16), overpressure impulse versus range comparisons (figure 17), and pressure/impulse history comparisons for selected peak pressures (figure 18). As in the cylindrical case discussed earlier, the pressure versus range curves have been shifted to match at the range of 4 MPa peak pressure. Also, the criteria selected for evaluating waveform comparisons was again matching impulse at time of decay to 20% of peak overpressure.

We can see from figure 16 that a plane one dimensional simulator results in a test facility considerably shorter than a spherical one dimensional facility. The figure also would tend to indicate that at ranges shorter or greater than that of the test location, where peak pressures are matched, the peak pressures would exceed the spherical case. However, when we recognize that real explosives generate finite strength air shocks, the peak pressures at ranges shorter than the test range will actually be closer to the spherical case. This then will tend to result in a reasonable match of peak pressures approaching the target and a good match of pressure histories at the range of the target. However, the impulse on the target and the pressure behind the target will still exceed the spherical case.

One other factor can still be used to improve the degree of simulation. Since most other simulator concepts in this category use permanent facilities they require high cost construction and force the environment toward the plane one dimensional case. However, if cheaper construction techniques are used and the facility is allowed to disassemble, the late time pressure will be relieved and the peak pressure at large distances will also be reduced. We can see that both of these effects will tend to improve the degree of correlation with the spherical case.

The equation from appendix A for peak pressure as a function of range and source energy can be reduced to a very simple relationship for each case for any selected ratio of specific heats. For $\gamma=1.4$ the expression reduces to the following:

$$P=0.345 W_a/x \text{ for Planer,}$$

$$P=0.208 W_1/r^2 \text{ for Cylindrical,}$$

and $P=.157 Y/R^3 \text{ for Spherical.}$

A series of investigations of waveform matches using the previously established criteria of matching pressure and impulse to time of 20% of peak pressure resulted in an empirical relationship between x, r and R and thus W_a, W_1 and Y . This relationship reduced to:

$$3x = 1.5r = R$$

for constant pressure. Using this we can write an expression for transitioning from spherical to planer geometries. Assuming we wish to match peak pressures

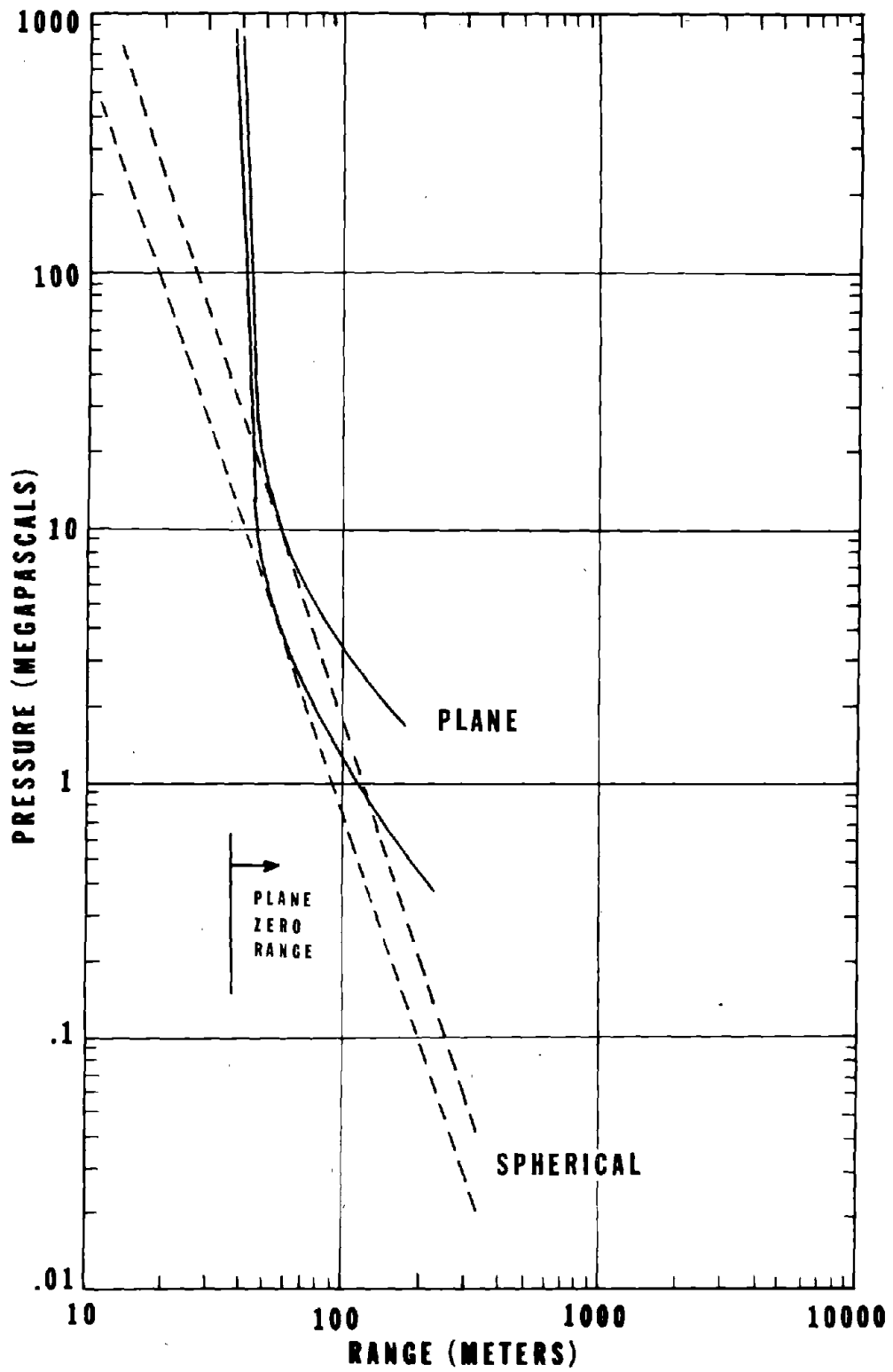


FIGURE 16. PEAK PRESSURE VERSUS RANGE COMPARISON FOR PLANE AND SPHERICAL SIMILARITY SOLUTIONS. PLANE RANGE SHIFTED TO MATCH SPHERICAL AT 4 MPa PRESSURE

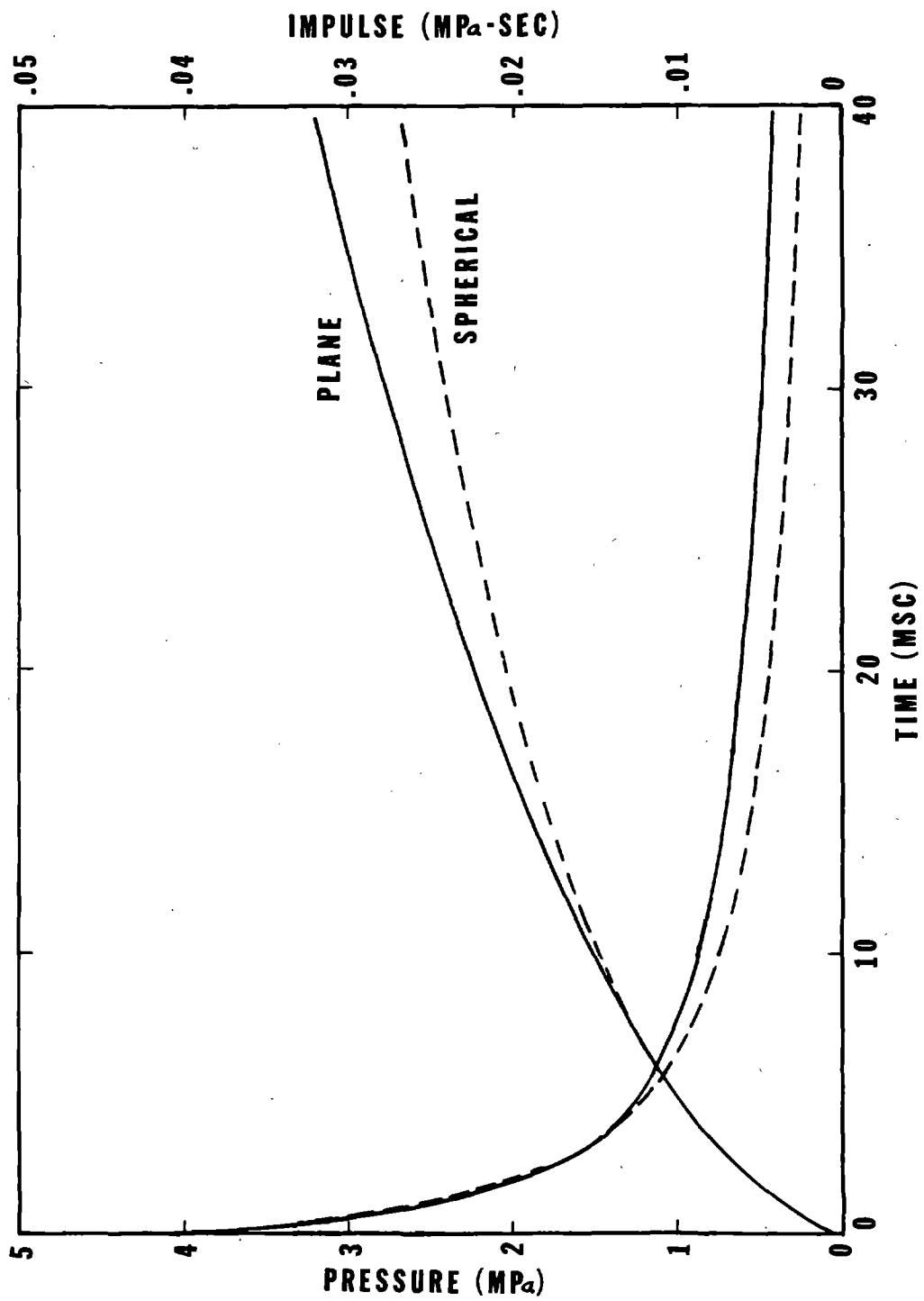


FIGURE 17. OVERPRESSURE AND IMPULSE HISTORY COMPARISON FOR PLANE AND SPHERICAL SIMILARITY SOLUTIONS AT 4 MPa PRESSURE RANGE.

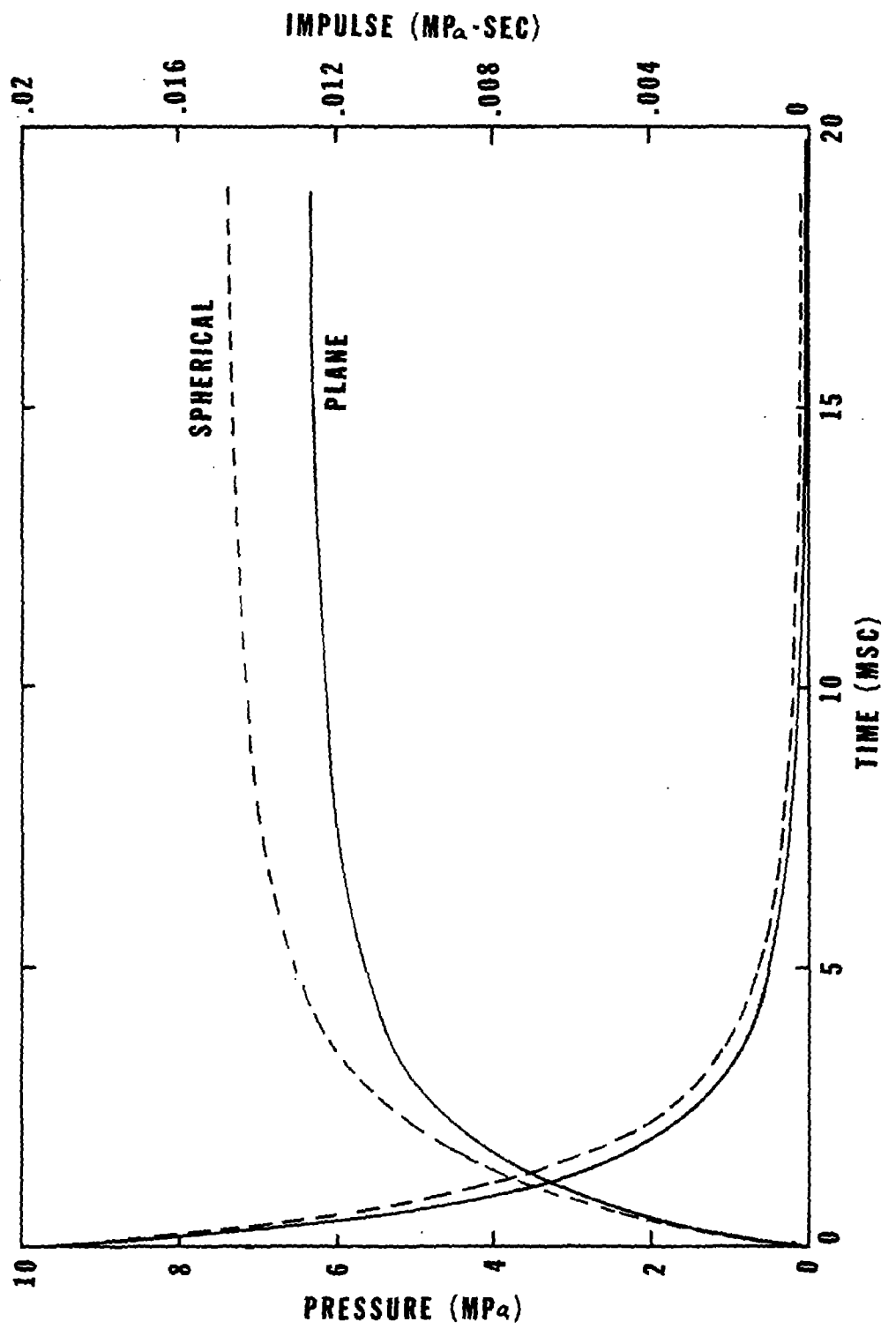


FIGURE 18. DYNAMIC PRESSURE AND IMPULSE HISTORY COMPARISON FOR PLANE AND SPHERICAL SIMILARITY SOLUTIONS AT 4 MPa OVERPRESSURE RANGE

and know the yield of interest in the spherical case we find:

$$\frac{W_a}{x} = .455 \frac{Y}{R^3}$$

and

$$3x = R.$$

When we select a yield (Y) and range (R), and hence a peak pressure, we have two equations and two unknowns. Thus we can solve for the energy required in the plane one-dimensional simulator and the length of the simulator required to match peak pressure and satisfy the impulse criteria previously established

Also using the set of equations for peak pressure from the previous paragraph we can develop an expression for scaling from one yield to another for a given peak pressure. It can be shown that:

$$\frac{W_a}{W_{a1}} = \left(\frac{Y}{Y_1}\right)$$

for $P = P_1$. We now have the basis for a design procedure. We must however recognize that the "Real" simulator does not exactly match the plane one-dimensional case and that the spherical case does not exactly match the nuclear. Therefore the design procedure must be empirically adjusted to allow a direct transition from nuclear environments to the simulator design.

Finally, some consideration must be given to the characteristics of the physical facility used for the simulator. As previously discussed, there are several advantages to be realized from a minimal construction disposable facility. This approach results in reduced cost, ability to go to larger test facilities and also provides an altered environment which should be a better match to the nuclear. A complete study of facility design concepts was made to evaluate cost and constructability as well as their effect on the environment. A complete report on this study can be found in reference (9). No attempt will be made to summarize the findings in this paper other than to say that metal arch buildings with minimum earth cover are most attractive for test facilities that can use commercially available materials. This type of facility was used in the HAVE HOST test series (Ref (10)). The primary facility strength requirement is that it stand up pre-test and the earth overburden is primarily to hold up the late time pressures. Physical dimensions of the facility are primarily controlled by the time required for reflections to reach the wall and return to the target. This is a parameter individually determined for each test.

IV. THE DYNAMIC AIRBLAST SIMULATOR

In the preceding section we discussed the theoretical basis of a plane one dimensional dynamic airblast simulator and presented the design equations. A requirement for empirically calibrating the design equations to account for

differences between the self similar flow model and the nuclear environment, as well as real effects such as explosive energy density. A proposed simulator concept facility configuration is shown in figure 19. The test series should vary over a significant yield and peak pressure range and be aimed at supporting design of both large and small size tests.

The design procedure is to select a nuclear yield and range of interest and determine the peak pressure. These values are then used to enter the design curves to determine the energy, W_a , for the simulator and the range to the test station. The design equations used to generate the design curves may be expressed as:

$$R = 3x$$

$$\text{and} \quad W_a = 0.455 \frac{xY}{R^3}$$

where

Y is nuclear yield in Joules

R is nuclear range in Meters

X is simulator range in Meters

W_a is simulator energy in Joules/(Meters)².

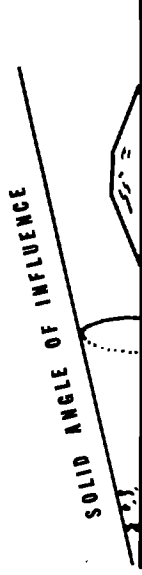
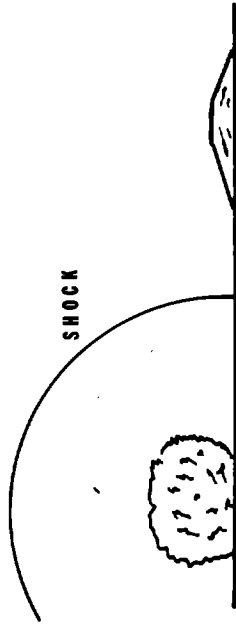
To account for deviations from the theoretical models the constant must be adjusted by the test results. The basic form of the equation should hold however. Results of the feasibility and development tests may be found in references 11 and 12. The present status of the dynamic airblast simulator is discussed in another paper in these proceedings, reference 13.

V. SUMMARY

In this paper we have developed the theoretical basis for transitioning from a given nuclear environment to a simulator configuration using theoretical models. An evaluation of the models was made at critical transition points and the limitations noted. A set of simulator design relationships were developed to relate nuclear yield and range to simulator energy and length requirements. The requirement for empirically adjusting the design relationships to account for non-ideal effects such as explosive energy density and facility expansion was identified. A facility design study was referenced and a configuration recommended.

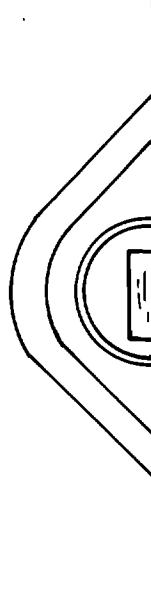
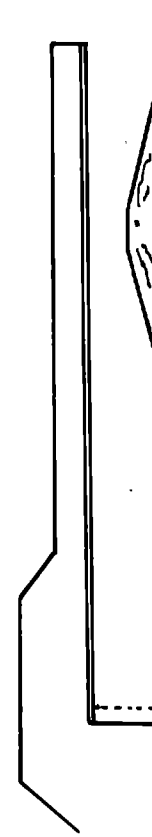
Additional refinements appear feasible and perhaps even attractive. Since the facility walls are only to direct the flow and prevent relief waves from effecting the pressures, and since the pressures presently decay slower than nuclear, perhaps the walls could be eliminated. Significant

DYNAMIC AIRBLAST SIMULATION



THE PROBLEM

THE APPROACH



EXPENDABLE SHOCK TUBE

FIGURE 19. SIMULATOR REQUIREMENT AND FACILITY CONCEPT

facility cost savings may have to be offset by additional explosive costs but the concept should be investigated. Other refinements may be identified and should be investigated if they show possibilities for reducing test cost or improving the simulation.

REFERENCES:

1. Brode, H.L., "Height of Burst Effects at High Overpressures", DASA 2506, The Rand Corporation, Santa Monica, CA, July 1970.
2. Needham, C.E., et al, "Nuclear Airblast Standard (1 KT)", AFWL-TR-73-55, Air Force Weapons Laboratory, Kirtland AFB, NM, April 1975.
3. Bethe, fuchs, VonNeumann, et al, "Blast Wave", LA-2000, Los Alamos Scientific Laboratory, Los Alamos, NM, March 1958.
4. Sedov, L.I., Similarity and Dimensional Methods in Mechanics, Academic Press, New Yor, N.Y., 1959.
5. Kingery, C.N., Killner, R.C., "Airblast Overpressure Versus Time Histories (Nuclear and TNT Surface Bursts)", BRL-R-1638, USA Ballistic Research Laboratories, Aberdeen Proving Grounds, MD, March 1973.
6. Miller, G.W., et al, "An...in the (DASACON) Conical Shock Tube", Paper G-3, Proceedings of the Fourth International Symposium on Military Application of Blast Simulators, Sept 1974.
7. Vigil, M.G., "Performance Characteristics of Sandia Laboratories 5.8 Meter Explosive Driven Blast Simulator", Paper B7, Proceedings Fourth International Symposium on Military Applications of Blast Simulators, Sept 1974.
8. Lucole, S.W., and Balcerzak, M.J., "Blast and Shock Simulation Blast Directing Technique", DASA 2150, Defense Atomic Support Agency, Washington, D.C., Feb 1968.
9. Civil Nuclear Systems Corporation, "Airblast Simulator Design", AFWL-TR-77-106, Air Force Weapons Laboratory, Kirtland AFB, NM, July 1978.
10. Martens, D.P., "Dynamic Airblast Simulator Feasibility Test (DABS 1-A), Quick Look Report", DE-TN-75-027, Air Force Weapons Laboratory, Kirtland AFB, NM, Jan 1976.
11. Martens, D.P., "Dynamic Airblast Simulator Parametric Test Series, Events 1-A; 1-B, 1-C, 1-D, and 1-E Data Report", DE-TN-76-018, Air Force Weapons Laboratory, Kirtland AFB, NM, Nov 1976.
12. "Have-Host Data Report", AFWL-TR-78-17, Air Force Weapons Laboratory, Kirtland AFB, NM, June 1978.
13. Renick, J.D., "Some Considerations in the Design of a Dynamic Airblast Simulator", This Proceedings.

APPENDIX A

SELF SIMILAR MOTION OF WAVES IN A GAS

This appendix presents a brief summary of the one-dimensional self similar flow model for the problem of an intense explosion according to Sedov (Ref 4). Sedov first assumes that the gas is perfect, inviscid and non-heat-conducting. The equations of motion take the form

$$\begin{aligned}\frac{\partial v}{\partial t} + v \frac{\partial v}{\partial r} + \frac{1}{\rho} \frac{\partial p}{\partial r} &= 0, \\ \frac{\partial \rho}{\partial t} + \frac{\partial \rho v}{\partial r} + (\nu - 1) \frac{\rho v}{r} &= 0, \\ \frac{\partial}{\partial t} \left(\frac{p}{\rho^\gamma} \right) + v \frac{\partial}{\partial r} \left(\frac{p}{\rho^\gamma} \right) &= 0,\end{aligned}$$

where γ is the adiabatic index; $\nu=1$ for plane flow, $\nu=2$ for cylindrical flow and $\nu=3$ for flow with spherical symmetry. In the flow field associated with an intense explosion the disturbed region is separated from the undisturbed region by a shock wave and from the definition of intense explosion the pressure ahead of the shock wave can be neglected.

To estimate the error resulting from this assumption we start with the shock conditions for propagation into a gas at rest. They are:

$$\begin{aligned}v_2 &= \frac{2}{\gamma+1} c \left[1 - \frac{a_1^2}{c^2} \right] = \frac{2c}{\gamma+1} f_1, \\ \rho_2 &= \frac{\gamma+1}{\gamma-1} \rho_1 \left[1 + \frac{2}{\gamma-1} \frac{a_1^2}{c^2} \right]^{-1} = \frac{\gamma+1}{\gamma-1} \rho_1 f_2, \\ p_2 &= \frac{2}{\gamma+1} \rho_1 c^2 \left[1 - \frac{\gamma-1}{2\gamma} \frac{a_1^2}{c^2} \right] = \frac{2}{\gamma+1} \rho_1 c^2 f_3\end{aligned}$$

where C is the shock propagation velocity and a is the ambient sound speed. Figure A-1 shows f_1 , f_2 , and f_3 as functions of a/c for $\gamma=1.4$. We observe that for values of $a/c < 0.1$ the three functions differ from unity by less than 5 per cent and that for all values of a/c , f_3 differs from unity by less than 15 percent.

Sedov then proceeds to develop an expression for shock front position as a function of energy released. The expression is:

$$r_2 = \left(\frac{E_0}{\rho_1} \right)^{1/(2+\nu)} t^{2/(2+\nu)}$$

Where $E_0 = \alpha E$ and E_0 is the energy released. This equation defines shock front position as a function of time. Using the shock conditions and the adiabatic condition behind the shock wave Sedov derives the following system of equations to describe the complete flow field.

$$\frac{r}{r_2} = \left[\frac{(\nu+2)(\gamma+1)}{4} V \right]^{-2/(2+\nu)} \left[\frac{\gamma+1}{\gamma-1} \left(\frac{\nu+2}{2} V - 1 \right) \right]^{-\alpha_1} \\ \times \left[\frac{(\nu+2)(\gamma+1)}{(\nu+2)(\gamma+1) - 2[2+\nu(\gamma-1)]} \left(1 - \frac{2+\nu(\gamma-1)}{2} V \right) \right]^{-\alpha_2},$$

$$\frac{r_0}{r_2} = \left[\frac{(\nu+2)(\gamma+1)}{4} V \right]^{-2/(2+\nu)} \left[\frac{\gamma+1}{\gamma-1} \left(\frac{\nu+2}{2} V - 1 \right) \right]^{\alpha_3} \\ \times \left[\frac{(\nu+2)(\gamma+1)}{(\nu+2)(\gamma+1) - 2[2+\nu(\gamma-1)]} \left(1 - \frac{2+\nu(\gamma-1)}{2} V \right) \right]^{\alpha_4} \\ \times \left[\frac{\gamma+1}{\gamma-1} \left(1 - \frac{\nu+2}{2} V \right) \right]^{-[\alpha_5 + \alpha_6] \frac{1}{2} [2/(2+\nu)]},$$

$$\frac{v}{v_2} = f = \frac{(\nu+2)(\gamma+1)}{4} V \frac{r}{r_2},$$

$$\frac{\rho}{\rho_2} = g = \left[\frac{\gamma+1}{\gamma-1} \left(\frac{\nu+2}{2} V - 1 \right) \right]^{\alpha_3} \left[\frac{\gamma+1}{\gamma-1} \left(1 - \frac{\nu+2}{2} V \right) \right]^{\alpha_5} \\ \times \left[\frac{(\nu+2)(\gamma+1)}{(\nu+2)(\gamma+1) - 2[2+\nu(\gamma-1)]} \left(1 - \frac{2+\nu(\gamma-1)}{2} V \right) \right]^{\alpha_4},$$

$$\frac{p}{p_2} = h = \left[\frac{(\nu+2)(\gamma+1)}{4} V \right]^{2\nu/(2+\nu)} \left[\frac{\gamma+1}{\gamma-1} \left(1 - \frac{\nu+2}{2} V \right) \right]^{\alpha_3+1} \\ \times \left[\frac{(\nu+2)(\gamma+1)}{(\nu+2)(\gamma+1) - 2[2+\nu(\gamma-1)]} \left(1 - \frac{2+\nu(\gamma-1)}{2} V \right) \right]^{\alpha_4-2\alpha_1},$$

$$\frac{T}{T_2} = \frac{p}{p_2} \frac{\rho_2}{\rho},$$

where

$$\alpha_1 = \frac{(\nu+2)\gamma}{2+\nu(\gamma-1)} \left[\frac{2\nu(2-\gamma)}{\gamma(\nu+2)^2} - \alpha_2 \right], \quad \alpha_2 = \frac{1-\gamma}{2(\gamma-1)+\nu},$$

$$\alpha_3 = \frac{\nu}{2(\gamma-1)+\nu}, \quad \alpha_4 = \frac{\alpha_1(\nu+2)}{2-\gamma},$$

$$\alpha_5 = \frac{2}{\gamma-2}, \quad \alpha_6 = \frac{\gamma}{2(\gamma-1)+\nu},$$

$$\alpha_7 = \frac{[2+\nu(\gamma-1)]\alpha_1}{\nu(2-\gamma)}.$$

The variable V is the non-dimensional variable define by:

$$\frac{2}{(\nu+2)\gamma} \leq V \leq \frac{4}{(\nu+2)(\gamma+1)}$$

The system of equations discussed above can then be used to develop complete descriptions of the flow. They were programmed on an HP 9820 desk top calculator and used to generate the similarity solution curves presented in this paper. The only remaining constant to be defined is the porportionality constant α . Sedov determines that $\alpha = 1.075$ for planer flow, $\alpha = 1.0$ for cylindrical flow and $\alpha = 0.85$ for spherical flow.

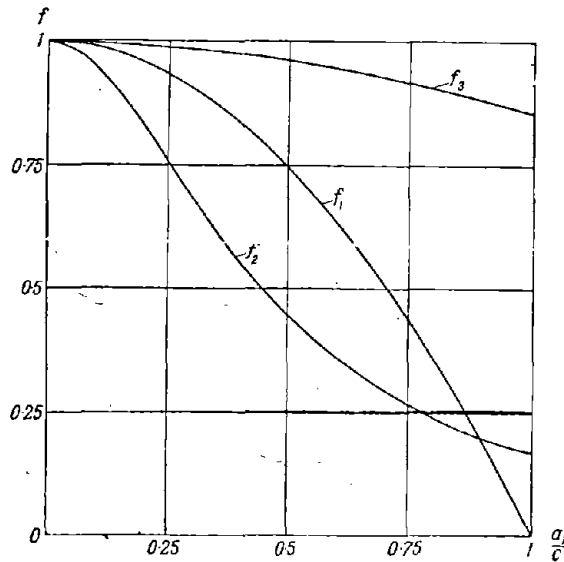


FIGURE A1. ERROR FUNCTIONS FOR DENSITY, VELOCITY AND PRESSURE

Some Considerations in the Design
of a Dynamic Airblast Simulator

by

Joseph D. Renick
Air Force Weapons Laboratory
Kirtland AFB NM 87117

INTRODUCTION

The Air Force Weapons Laboratory (AFWL) has been developing an explosively driven shock tube, called DABS (Dynamic Airblast Simulator), to simulate the dynamic and overpressure environment associated with a nuclear detonation. The requirement for a simulator of this type is in testing the response of structures where the dynamic flow properties of the environment are important in determining the structural loads. Examples are for testing of above-ground or partially buried structures, or for simulating the enhanced environment over a buried structure produced by the shock interaction of airblast environments from multiple bursts. A capability to simulated nuclear yields of from 1 kT to 3 MT in a pressure range of .5 to 10 MPa peak overpressure is required. This paper discusses some important considerations in the development of a design procedure for DABS.

APPROACH

The approach to the development of the DABS design procedure was to empirically relate overpressure environments generated in DABS experiments to the nuclear overpressure environment. Scaling laws were then applied to generate data at environment scales which differ from that of the experimental data. Effects of simulator facility size on the simulated airblast environment were characterized which led to the formulation of charge-size-overburden relationships which could then be incorporated into the design procedure.

ANALYTIC AND CALCULATIONAL METHODS

Three "tools" were developed in support of the design procedure. A code called BRNUFT (BRode NUclear FiT) was developed to find the Brode waveform which best matches experimental data; relationships between planar and spherical blast parameters were developed to determine how to scale the experimental data for yield and a 1-D Lagrangian hydrocode was modified to account for radial motion effects on the DABS environment. These "tools" and their application to the DABS design procedure will be described in subsequent paragraphs. The design procedure itself will not be presented here but will be included in a design manual (ref. 1) to be published.

BRNUFT

BRNUFT is a code which uses the analytic formulation of the Brode overpressure waveform (ref. 2) in an iterative scheme to converge on the Brode nuclear yield and peak pressure (or range) which gives a "best" fit to input impulse-time data. Good results have been observed in the use of this program when the input waveform is classical in nature. The ability of the program to converge to the proper yield and range has been demonstrated using actual Brode waveforms as the input data. The results are shown in table 1.

At this time, BRNUFT does not contain a scheme for selectively weighting the fit toward either the early- or late-time portions of the data. There is some sensitivity of the results as to how the data time intervals are selected, especially for non-ideal waveforms. The AFWL has had good results with a scheme which increases the increment in time between each impulse sample by a factor of 1.10. The distribution of points is such that the early-time portion of the waveform is weighted and good matches to peak pressure are obtained.

BRNUFT is in its infancy at this time and understanding of its behavior and limitations is incomplete. There is clearly a need

Table 1

COMPARISON OF BRNUFT OUTPUT WITH BRODE INPUT

<u>Input</u>		<u>Output</u>		Δ
Yield (kT)	Range (m)	Yield (kT)	Range (m)	
1	56.23	1.008	56.40	.0029
1	21.06	.986	21.06	.0011
75	1953.04	74.80	1950.48	.0046
75	237.09	74.92	236.82	.0004
75	88.82	75.85	89.26	.0010
800	4299.19	816.08	4340.17	.0025
800	521.91	801.96	522.12	.0003
800	195.51	796.48	195.13	.0002

for further analyses such as that performed recently by Mlaker (ref. 3) at Waterways Experiment Station.

The iterative scheme utilized in BRNUFT is described in figures 1 and 2. The underlying assumption is that, for any given set of impulse-time data points, a single nuclear waveform, described in terms of peak pressure and yield, may be found which will minimize the parameter δ which is defined as the sum of the absolute values of the differences in impulse at each time between the input data and nuclear. The procedure is as shown in the flow diagram in figure 1. Five values of peak pressure and yield are selected in such a way as to ensure that δ_{\min} for the function $\delta = \delta(P, Y)$ lies in the region bounded by $P(1), P(5), Y(1), Y(5)$. The first four $I(t)$ points are fit with a polynomial and differentiated to provide an estimate of peak pressure, P_0 , at $t = 0$. The range of pressures is chosen according to

$$P(1) = .5 P_0$$

$$P(2) = .75 P_0$$

$$P(3) = 1.0 P_0$$

$$P(4) = 1.25 P_0$$

$$P(5) = 1.5 P_0$$

There is no convenient, general way to initialize yield values over a small range, so a wide range of initial values is chosen.

$$Y(1) = .02 \text{ kT}$$

$$Y(2) = .2 \text{ kT}$$

$$Y(3) = 2 \text{ kT}$$

$$Y(4) = 20 \text{ kT}$$

$$Y(5) = 8000 \text{ kT}$$

For each value of $P(J)$, $\delta(K)$ is calculated for each value of $Y(K)$. As shown in figure 2 (which illustrates only one case) the

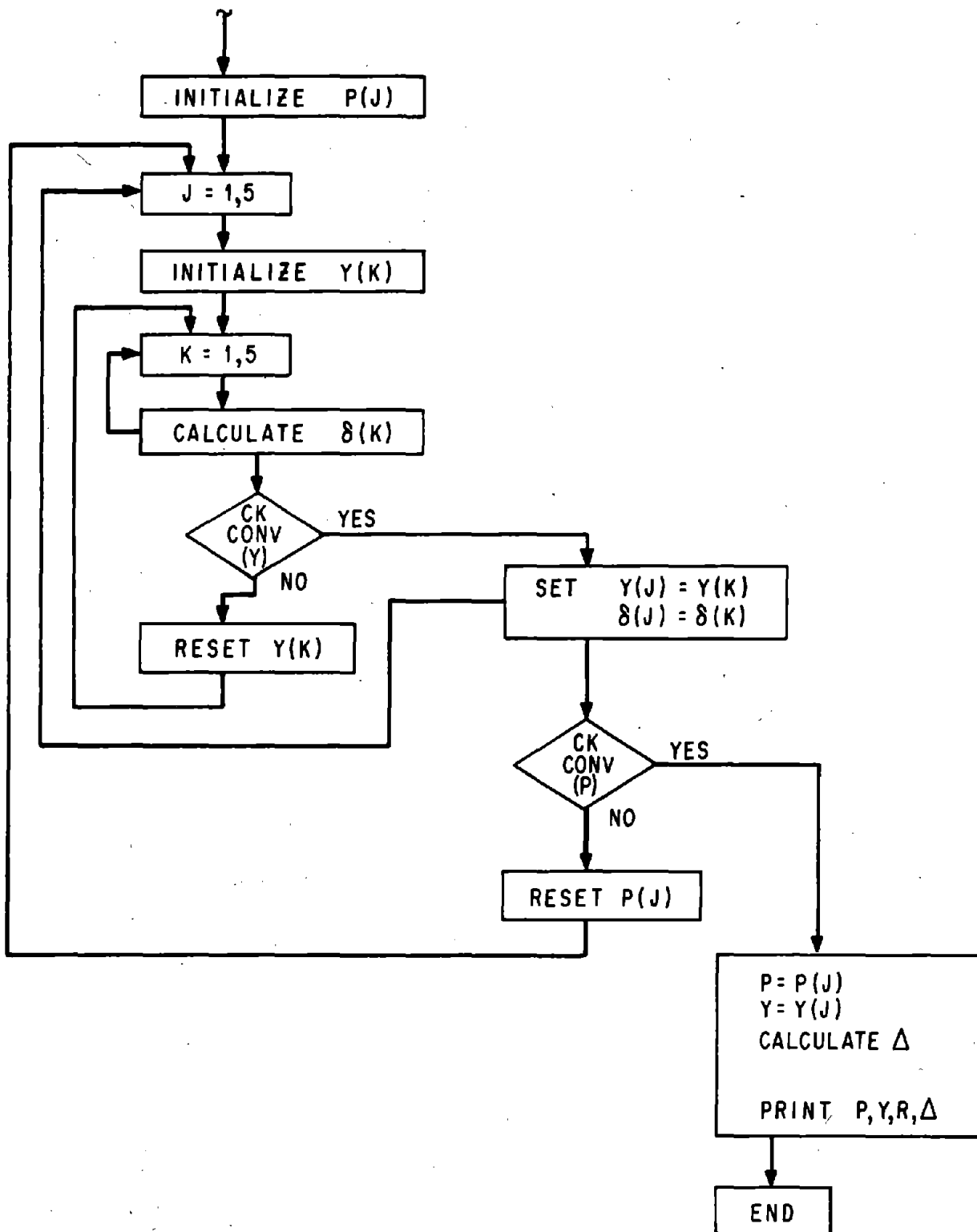


Figure 1. Iterative Scheme Utilized in BRNUFT

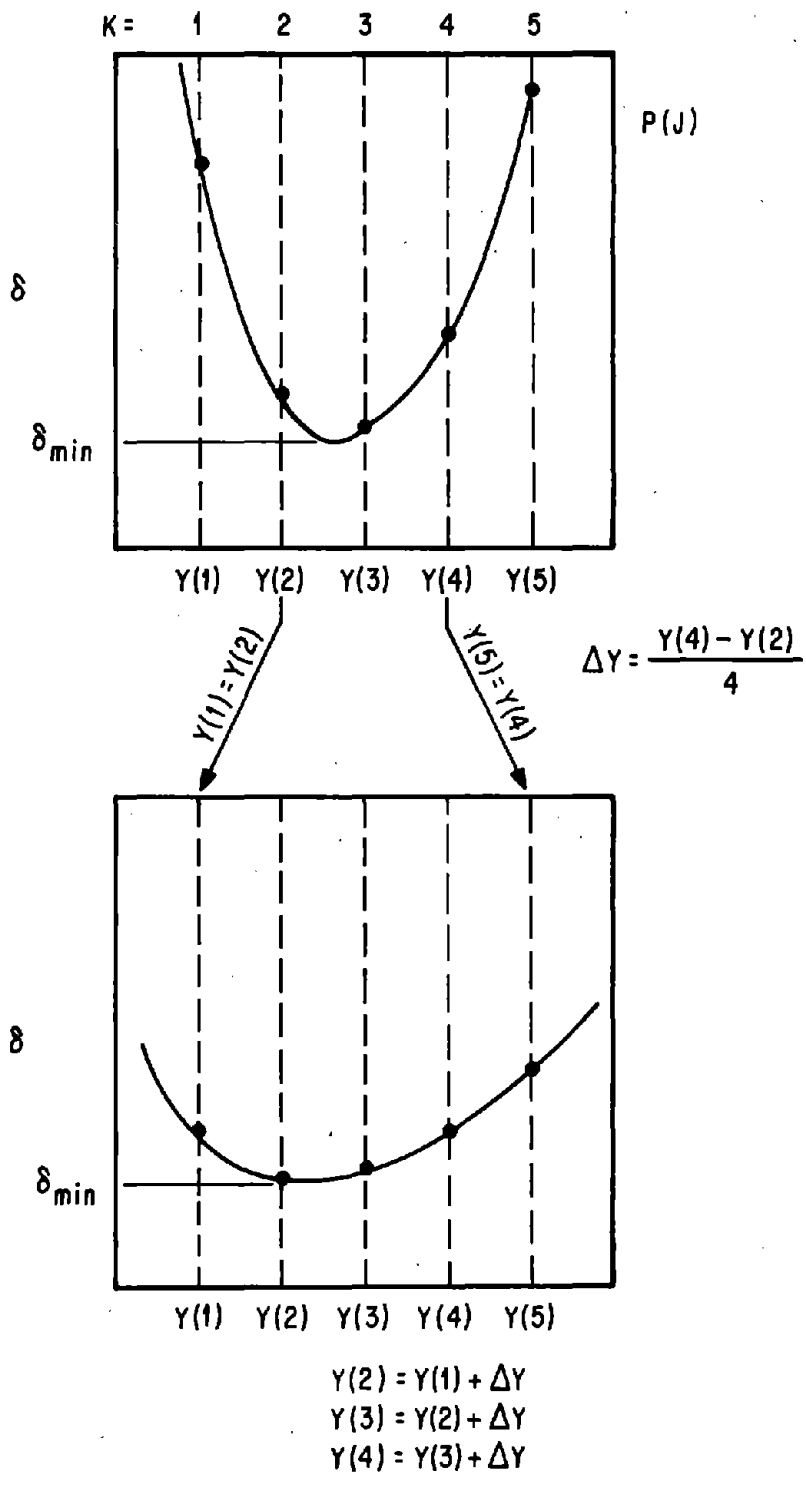


Figure 2. Convergence Technique Utilized in BRNUFT

location of δ_{\min} is refined from between Y(1) and Y(5) to between Y(2) and Y(3). A convergence check is performed such that convergence occurs for

$$\frac{2[Y(5) - Y(1)]}{Y(5) + Y(1)} < \epsilon$$

where $\epsilon = .001$. For non-convergence, the values of yield are redistributed such that

$$\begin{aligned} Y(1) &= Y(2) \\ Y(5) &= Y(4) \\ Y(2) &= Y(1) + \Delta Y \\ Y(3) &= Y(2) + \Delta Y \\ Y(4) &= Y(3) + \Delta Y \end{aligned}$$

where $\Delta Y = \frac{Y(5) - Y(1)}{4}$

Note that δ_{\min} could also occur between Y(1) and Y(2), Y(1) and Y(3), Y(3) and Y(5) or Y(4) and Y(5) which would result in different redistribution schemes.

The procedure continues until convergence. At convergence, the yield is labeled Y(J) and the error δ is labeled $\delta(J)$ which correspond to P(J). After $\delta(J)$ and Y(J) values are determined for each P(J), a similar convergence routine is entered where the search for δ_{\min} is now on pressure. After the new values of P(J) are determined (according to the same redistribution scheme described in figure 2 where δ is a function of pressure instead of yield) the program returns to a search on yield, as before. The scheme iterates between searches on yield and pressure until convergence on pressure occurs and the problem is complete. A "quality of fit" parameter, Δ , is then defined as

$$\Delta = \frac{1}{N} \sum_{M=1}^N \left| \frac{\Delta I(M)}{I(M)} \right|$$

where N is the number of impulse-time samples, I(M) is the data impulse of sample M, and $\Delta I(M)$ is the difference in data and Brode nuclear impulse of sample M. Thus, Δ is defined as the absolute value of the average fractional difference between the Brode nuclear impulse and data impulse over the time $t = 0$ to $t = t(N)$. In general, very good quality fits are obtained for $\Delta \leq .01$ which corresponds to an average impulse variation over the duration of the data of $\leq 1\%$. An example of the results of applying BRNUFT to DABS data is shown in figure 3. Input I(t) data was terminated at 32 msec when arrival of a signal reflected from a test structure occurred.

BRNUFT provides a purely empirical method of accurately describing experimental pressure data in terms of nuclear yield and peak overpressure. As will be shown, this capability is the key to the development of the DABS design procedure. Applications to the general area of airblast simulation technology are obvious.

Scaling Laws

From Sedov (ref. 4), equation 11.11, the general shock pressure vs. range law for strong blast waves is

$$P_2 = \frac{8E}{(\nu+2)^2 (\gamma+1) r_2^\nu} \quad (1)$$

$$E_0 = \alpha E \quad (2)$$

where

- P_2 is shock front pressure,
- E_0 is source energy,
- r_2 is range from source, and
- γ is specific heat ratio, 1.4.

Table 2 describes the relationships between ν , E_0 and α and labels the range and source energy parameters for each blast geometry. From (1) and (2) and table 2, the pressure-range laws for planar and spherical geometries become

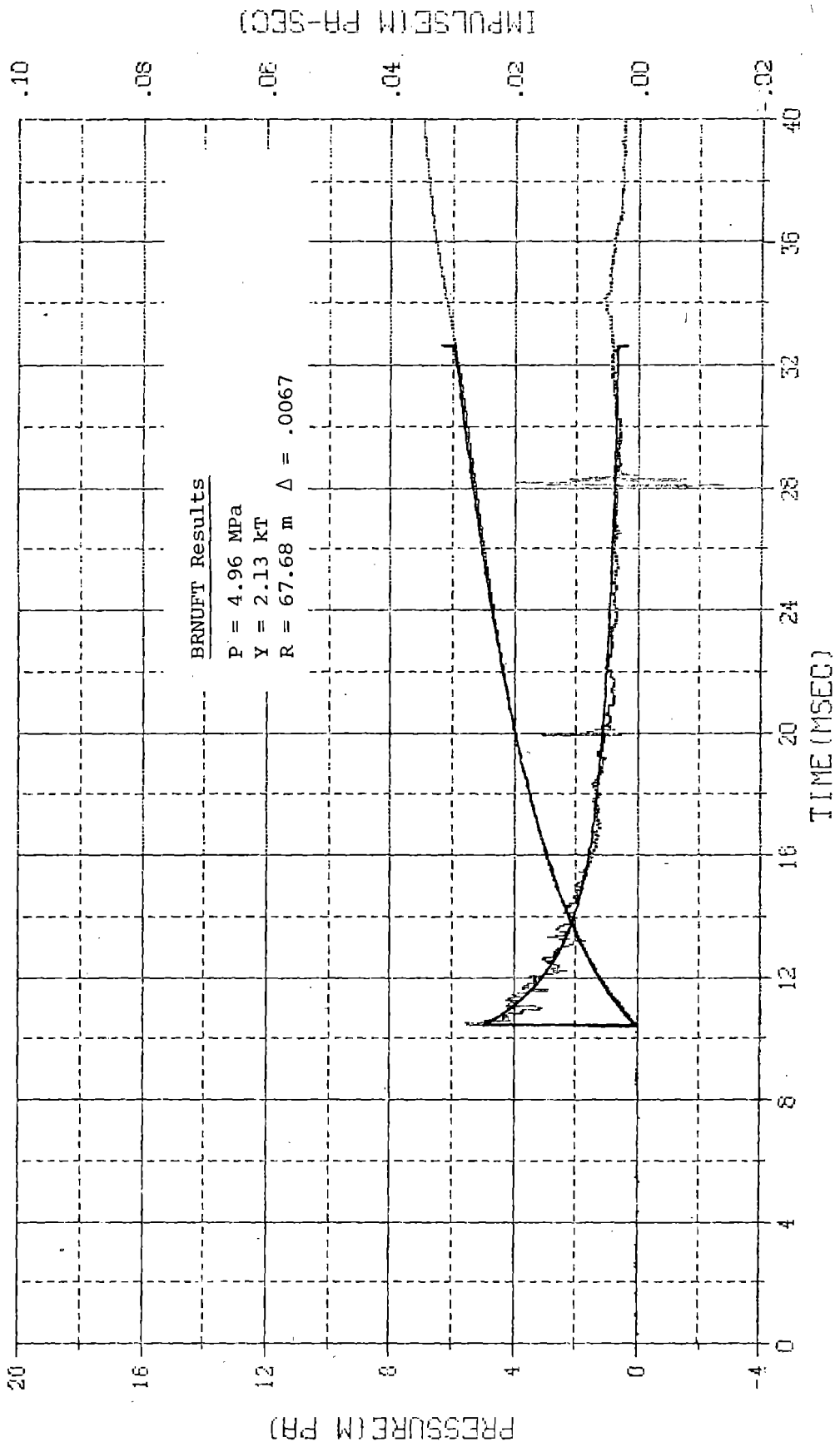


Figure 3. Fit of Brode Nuclear to Pressure Data from HAVE HOST S-3, MN 0031, 24 Meters

Table 2

DEFINITIONS AND VALUES OF SEDOV PARAMETERS AS A FUNCTION OF BLAST GEOMETRY

<u>Geometry</u>	<u>ν</u>	<u>α</u>	<u>E_0</u>	<u>E_0 (Units)</u>	<u>r_2</u>
Plane	1	1.075	W_A	Energy/Area	x
Cylindrical	2	1.000	W_L	Energy/Length	r
Spherical	3	.850	Y	Energy	R

$$P = .345 W_A/x \quad v = 1 \quad (3)$$

$$P = .157 Y/R^3 \quad v = 3 \quad (4)$$

where the subscript on pressure has been dropped.

From equation (3) for constant P

$$x/x_1 = W_A/W_{A_1} \quad (5)$$

and from equation (4) for constant P

$$R/R_1 = (Y/Y_1)^{1/3} \quad (6)$$

Equation (6) is well known as Hopkinson's scaling law and equation (5) is the planar version of that law.

We now make the assumption that

$$W_A/W_{A_1} = (Y/Y_1)^{1/3} \quad (7)$$

for $P = P_1$, where subscript 1 denotes a reference condition where values of W_{A_1} , Y_1 , P_1 , x_1 , and R_1 are known. Equation (7) holds if

$$x/x_1 = R/R_1 \quad (8)$$

If equations (7) and (8) satisfy (3) and (4) for constant P, then (7) and (8) are validated for Sedov's solution for blast waves. We now equate (3) and (4)

$$.345 W_A/x = .157 Y/R^3$$

and form ratios to obtain

$$\frac{W_A}{W_{A_1}} \frac{x_1}{x} = \frac{Y}{Y_1} \frac{R_1^3}{R^3}$$

if $x/x_1 = R/R_1$, then

$$\frac{W_A}{W_{A_1}} = \frac{Y}{Y_1} \frac{R_1^2}{R^2} \quad (9)$$

Substituting R/R_1 from (6) in (9), we obtain

$$W_A/W_{A_1} = (Y/Y_1)^{1/3}$$

and we have an analytic proof of equation (7) for $P = P_1$.

During investigations of the ability to fit spherical waves with planar waves, a "1 - 2 - 3" relationship was noted between planar, cylindrical and spherical ranges such that

$$r = 2x, \text{ and}$$

$$R = 3x$$

when peak pressures were equal and when impulse waveforms matched to times corresponding to approximately 20% of peak pressure. A typical example is shown in figure 4. The relationship

$$R = 3x \tag{10}$$

is equivalent to equation (8) in proving equation (7) but also permits a complete analytic solution to the problem of matching planar and spherical waves independent of any reference conditions. Equations (3), (4) and (10) may now be used to construct idealized design charts based on the Sedov similarity solution for strong blast waves. The design chart approach is to specify Y and P and determine W_A and x . Equations (3), (4) and (10) may be combined to provide the desired parametric relationships

$$P = 2.657 (W_A^3/Y)^{1/2} \tag{11}$$

$$x = .1798 (Y/P)^{1/3} \tag{12}$$

$$W_A = .5212 (P^2 Y)^{1/3} \tag{13}$$

Figures 5 and 6 show the parameters $\log P$ vs. $\log Y$ from equation (11) and $\log W_A$ vs. $\log Y$ from equation (13). On the log-log plots, P varies linearly with Y for constant W_A at a slope of $-1/2$ and

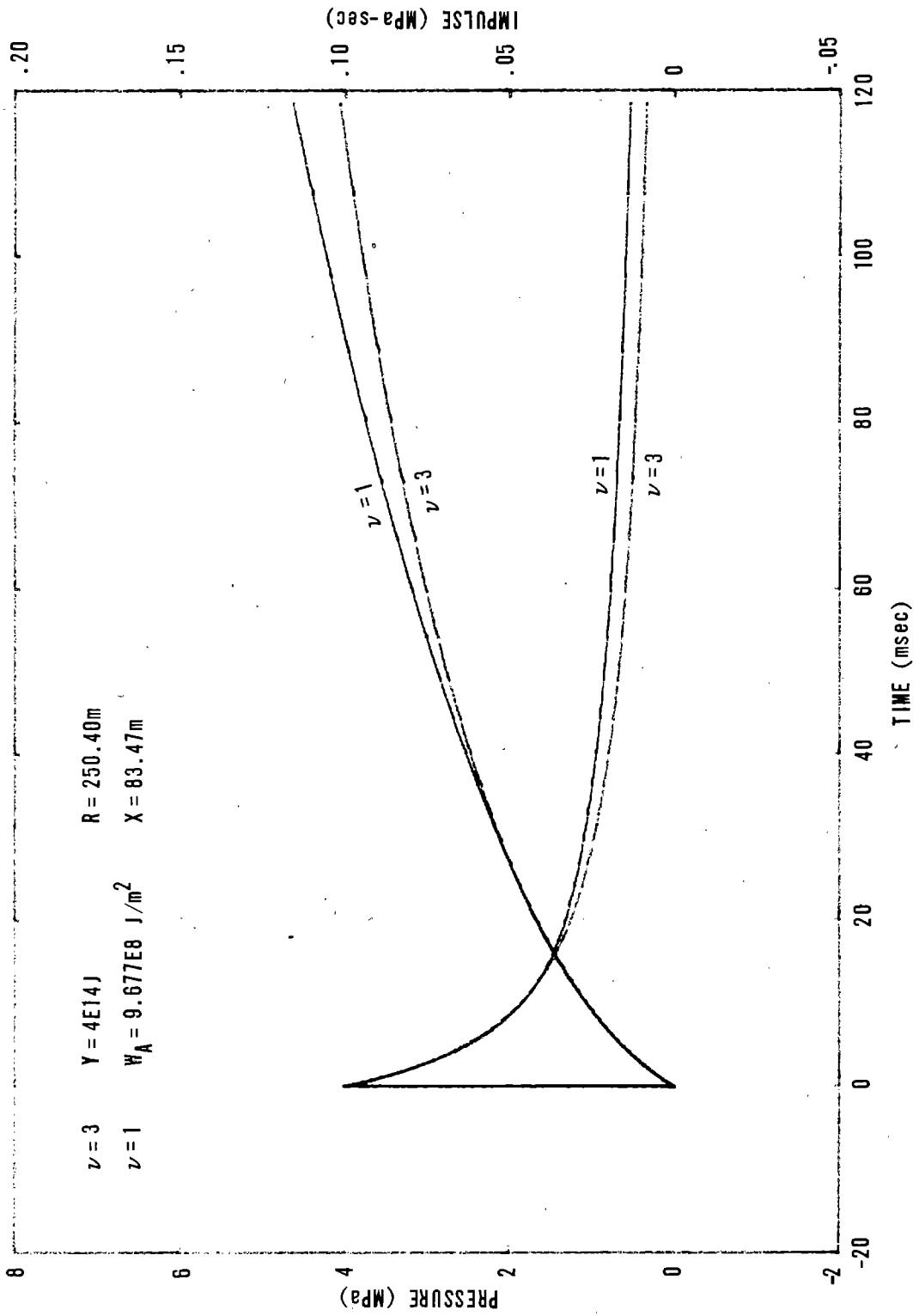


Figure 4. Comparison of Planar and Spherical Blast Waves for Equal Peak Pressures and $R = 3x$

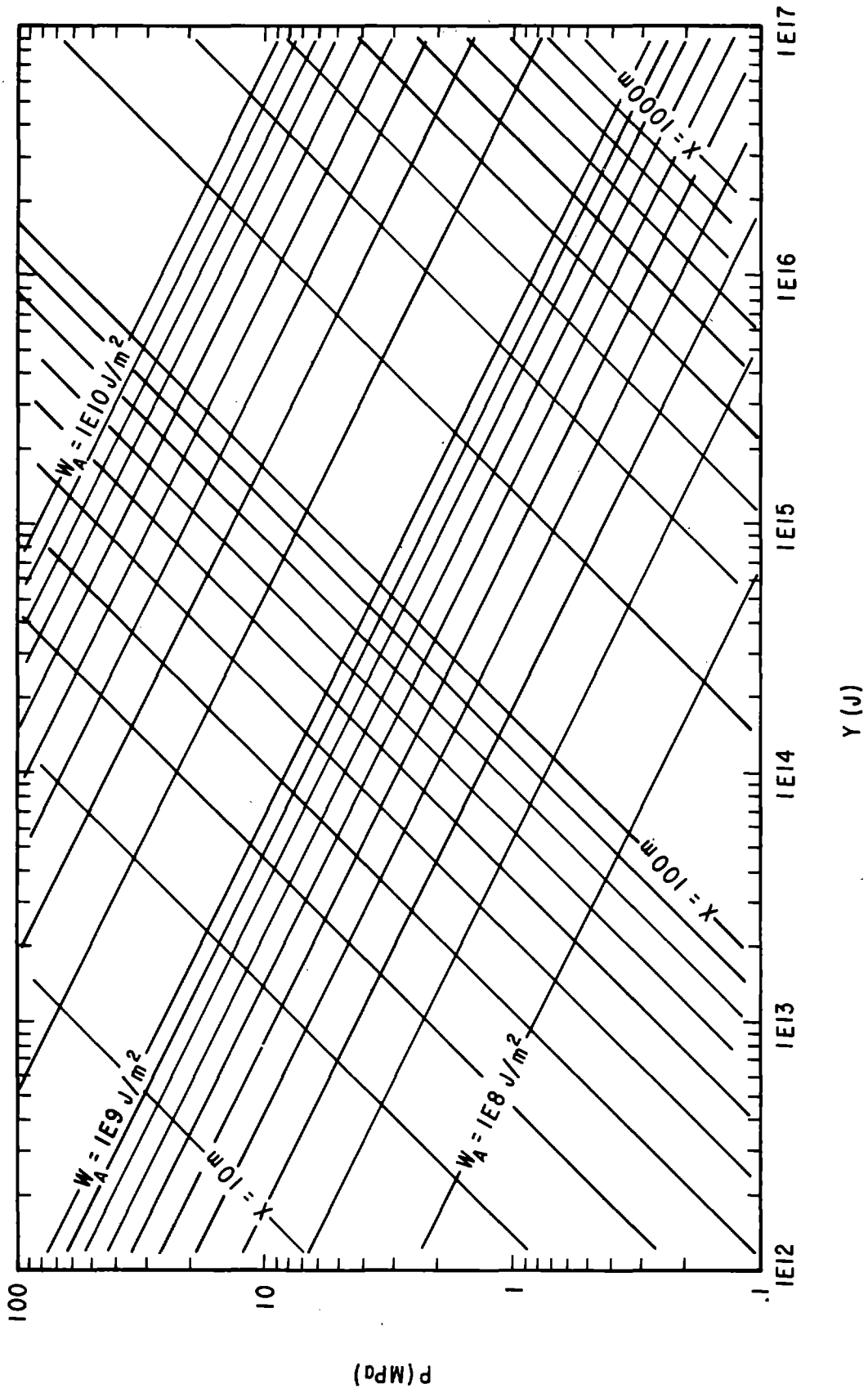


Figure 5. Design Chart for Relating Planar W_A and x to Spherical Y and P (or R) for Sedov Similarity Solution Where $R = 3x$

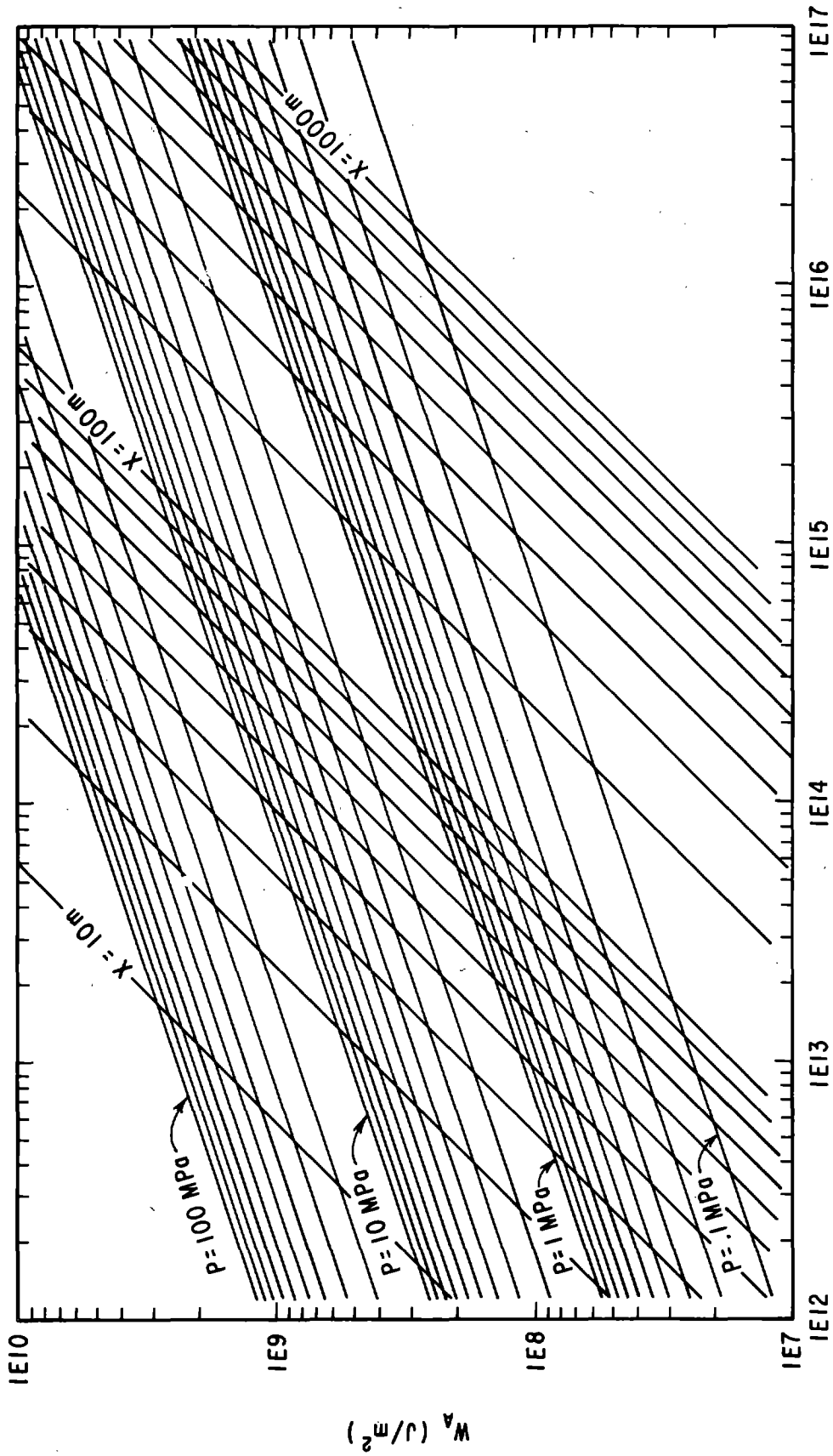


Figure 6. Design Chart for Relating Planar W_A and x to Spherical Y and P (or R) for Sedov Similarity Solution Where $R = 3x$

W_A varies linearly with Y for constant P at a slope of $+ 1/3$. Either of the figures may be used to determine W_A and x from Y and P . A plot of $\log x$ vs. $\log Y$ could also be constructed from equation (12); however, lines of constant W_A have a slope of $+ 1/2$ and lines of constant P have a slope of $+ 1/3$ which visually makes the figure difficult to interpret. Figures 5 and 6 are presented in a linear-linear plot in figure 7 and 8 where yield, Y , has been replaced by a scale factor, S , such that

$$S = (Y/Y_0)^{1/3}$$

where Y_0 is the reference yield. For the results here we have chosen the energy equivalent of 1 MT of TNT, $Y_0 = 4.2 \text{ E}15\text{J}$, which is equivalent to a 1 MT nuclear surface burst or 2 MT airburst.

In applying the theoretical design procedure to calculational or experimental data, it might be expected that the difficulties encountered, if any, would be related to the assumptions involved in the theory. The two major assumptions in the Sedov analysis make themselves known in the same way in that they both affect the pressure-range law. The assumptions are that the source is infinitesimal in size (no length or mass), while finite in energy and the pressure in the driven gas is negligible when compared to the shock pressure. The source assumption results in much higher pressures close to the source than actually encountered with HE. The zero pressure assumption for the driven gas results in a more rapid attenuation of the pressure with range at long ranges and low pressures than actually encountered in a real atmosphere. Therefore, the Sedov pressure-range law only approximates the behavior of HE in air.

Two 1-D hydrodynamic calculations were performed to further verify equation (7) and to investigate the effects of a real HE driver model in the design procedure. The calculations are identified by

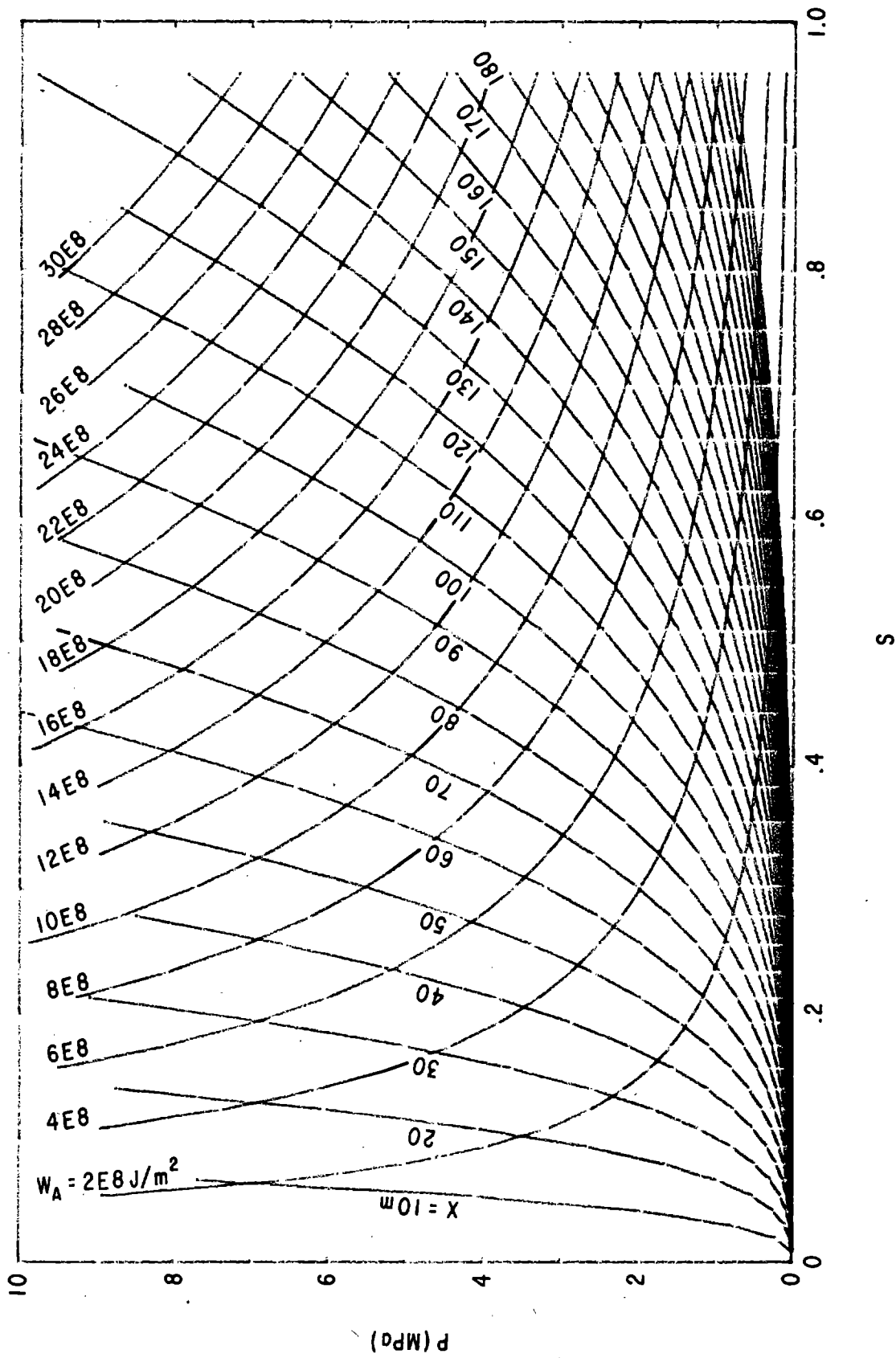


Figure 7. Design Chart for Relating Planar W_A and x to Spherical S and P (or R) for Sedov Similarity Solution Where $R = 3x$, $S = (Y/Y_0)^{1/3}$ and $Y_0 = 4.2E15 \text{ J}$

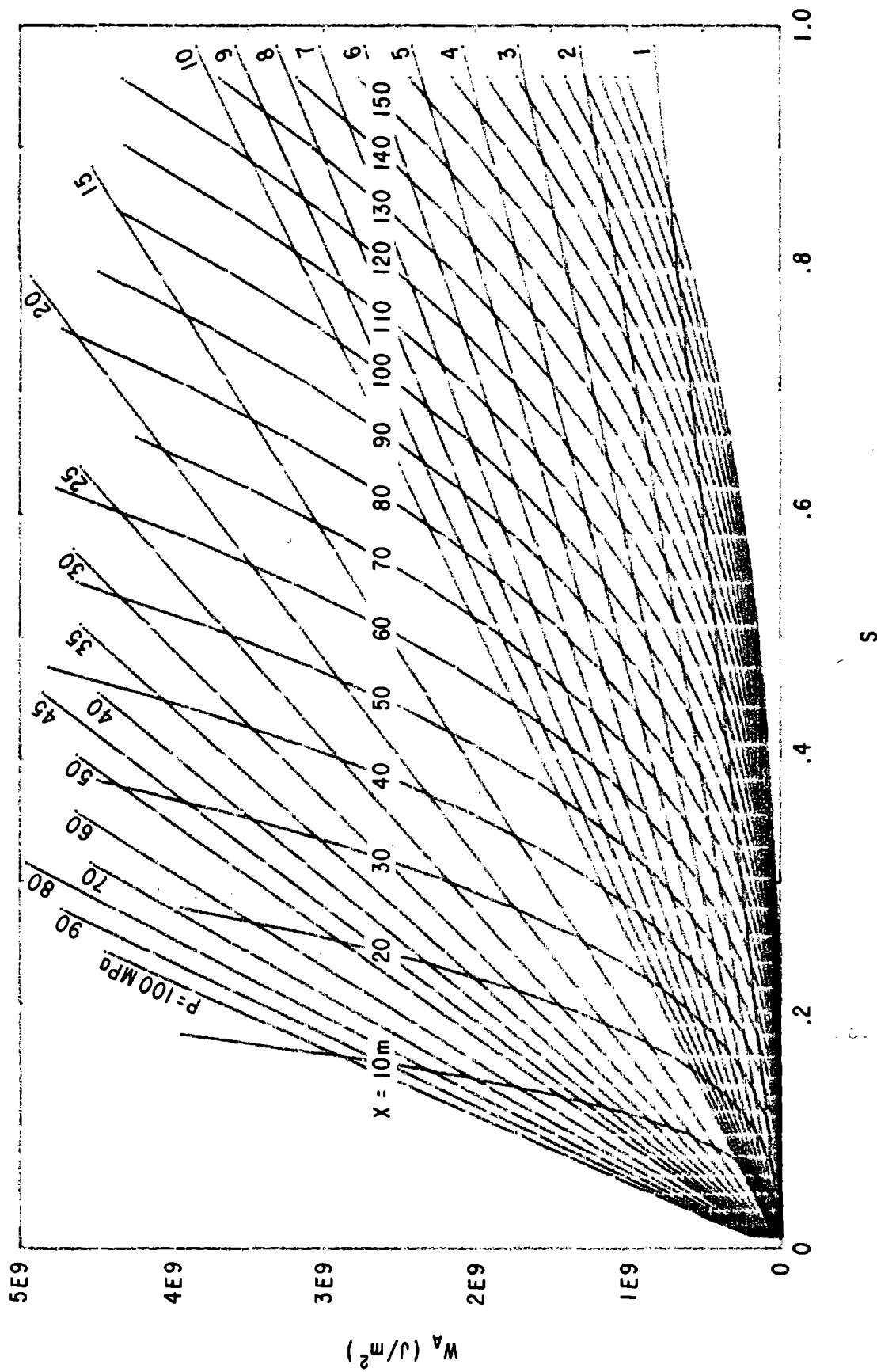


Figure 8. Design Chart for Relating Planar W_A and x to Spherical S and P
 Where $R = 3x$, $S = (Y/Y_0)^{1/3}$ and $Y_0 = 4.2E15J$

subscripts 1 and 2 with $W_{A_2} = 2W_{A_1}$ and $x_2 = 2x_1$. The resulting waveforms at each station were fit by BRNUFT up to arrival time of the contact surface to produce values for Y and R. In verifying equation (8), R_2 was plotted against $2R_1$, and Y_2 was plotted against $8Y_1$ to verify equation (7). The results are shown in figures 9 and 10. Note that good correlation is demonstrated in both cases. Note also that the $R = 3x$ law does not hold as for the Sedov similarity solution.

The calculational results are also plotted in figures 11 and 12 to observe the effects of a HE driver model. In figure 11 for lines of constant W_A , we see that as the DABS pressure decreases, the results tend toward the ideal solution with a slope of $-1/2$. In figure 12 lines of constant pressure have a slope of $+1/3$ which also agrees with the ideal solution. The implication is that the scaling laws given in equations (7) and (8) are obeyed and that DABS experimental pressure-range data may be used with the theoretical scaling laws to provide an approach to the design procedure which is identical to that for the Sedov strong shock similarity solution.

So far we have defined design charts based on a theoretical blast wave solution where planar W_A and x are related to spherical Y and P (or R). With the BRNUFT program experimental data corresponding to a given W_A and x may be fit to obtain nuclear Y and P and the results applied in a manner similar to that demonstrated with the theoretical solution. The next step is to investigate the effects of non-rigid boundaries such as encountered in actual DABS tests. These effects were characterized by means of a 1-1/2-D hydrodynamics code to be described in the next section.

1-1/2-D Hydrocode

During the early part of the DABS development program, a 1-D Lagrangian hydrocode, APOD (a gas dynamics version of IMPACT, ref. 5), was adapted for DABS parametric studies. An important concern was in characterizing different HE driver designs. It soon became apparent in comparing calculations with experiments that a substantial portion of the

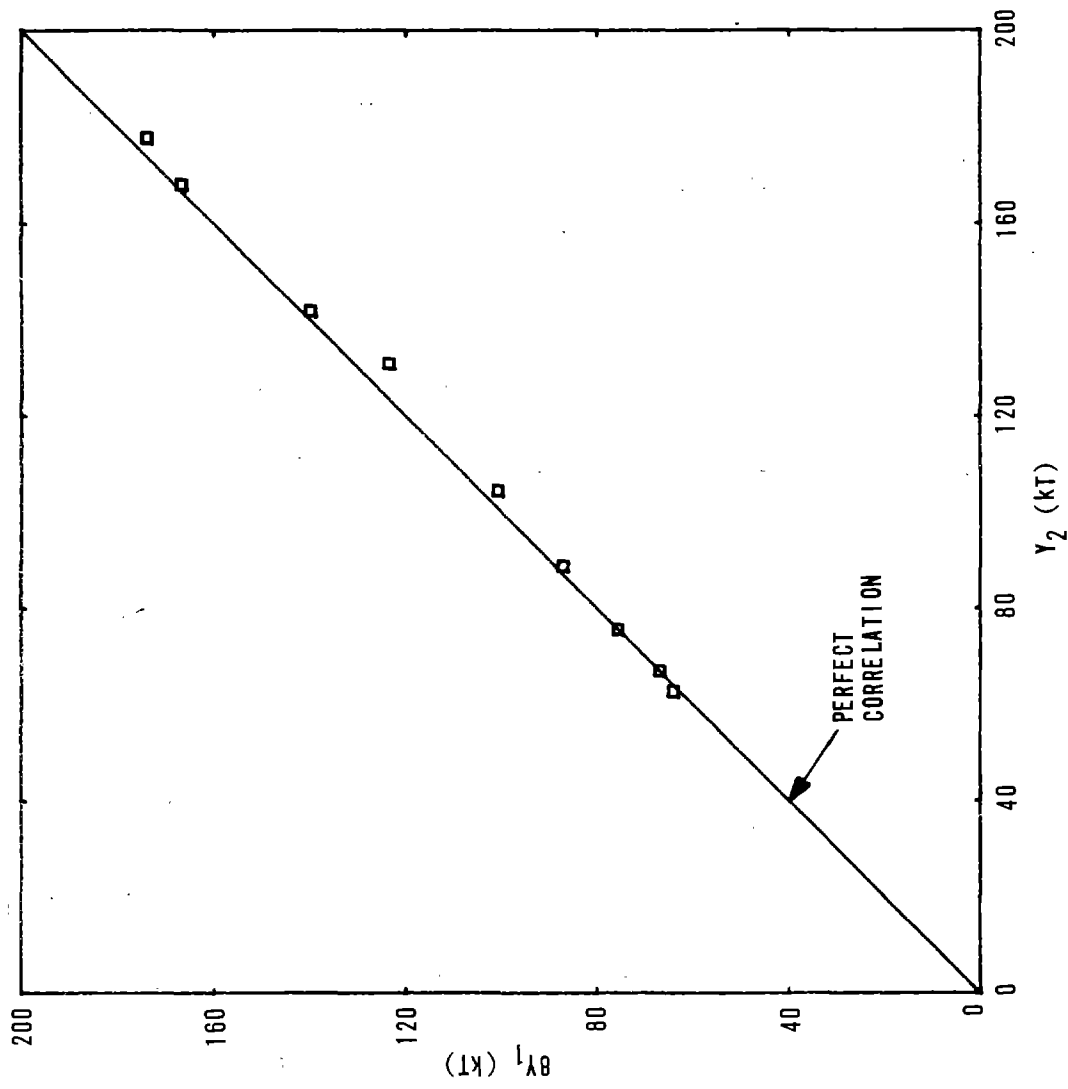


Figure 9. Verification of Equation (7) With
 1-D Calculations for $x_2 = 2x_1$ and
 $W_{A_2} = 2 W_{A_1}$

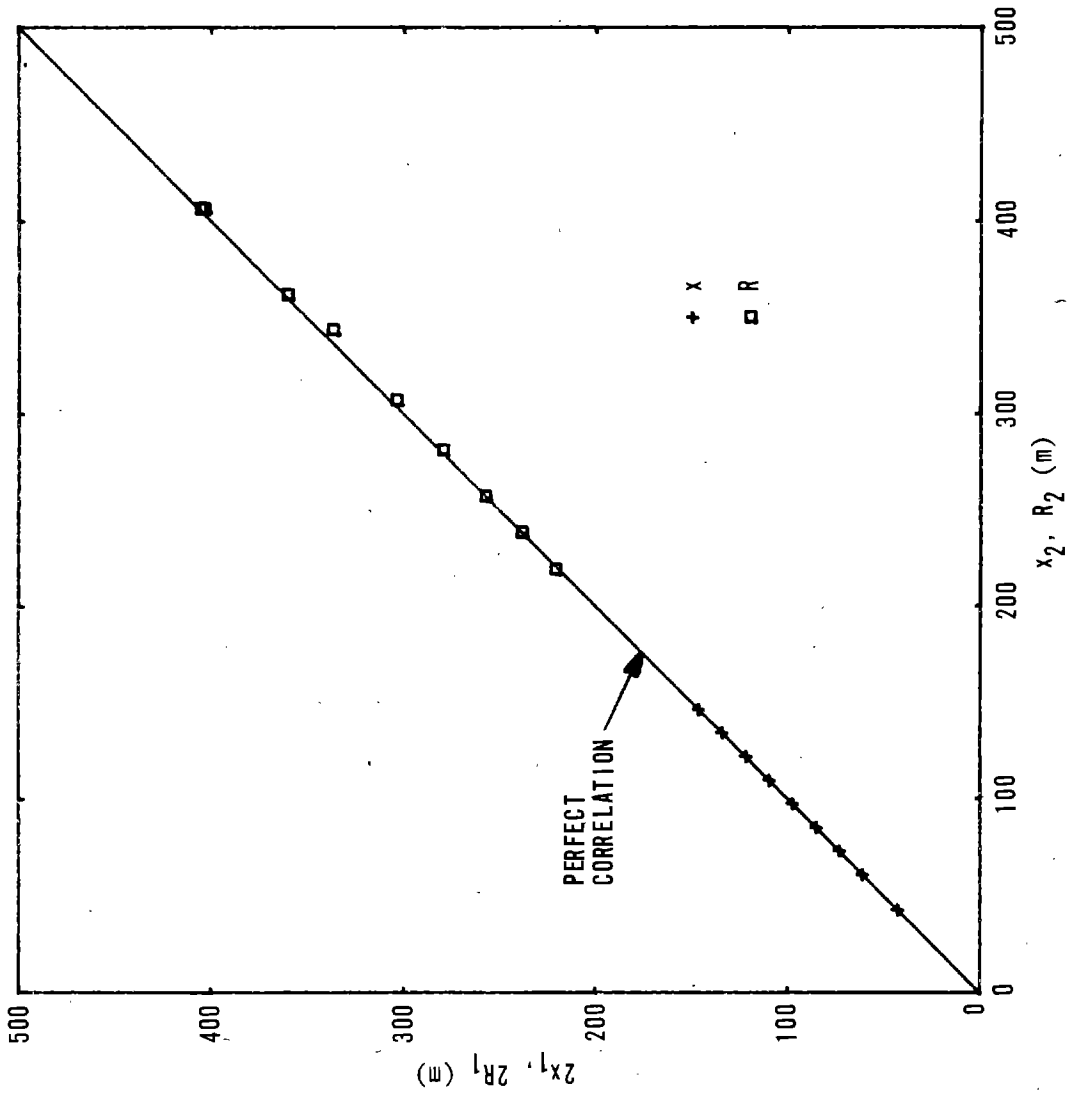


Figure 10. Verification of Equation (8) With 1-D Calculations for $x_2 = 2x_1$ and $W_{A_2} = 2W_{A_1}$

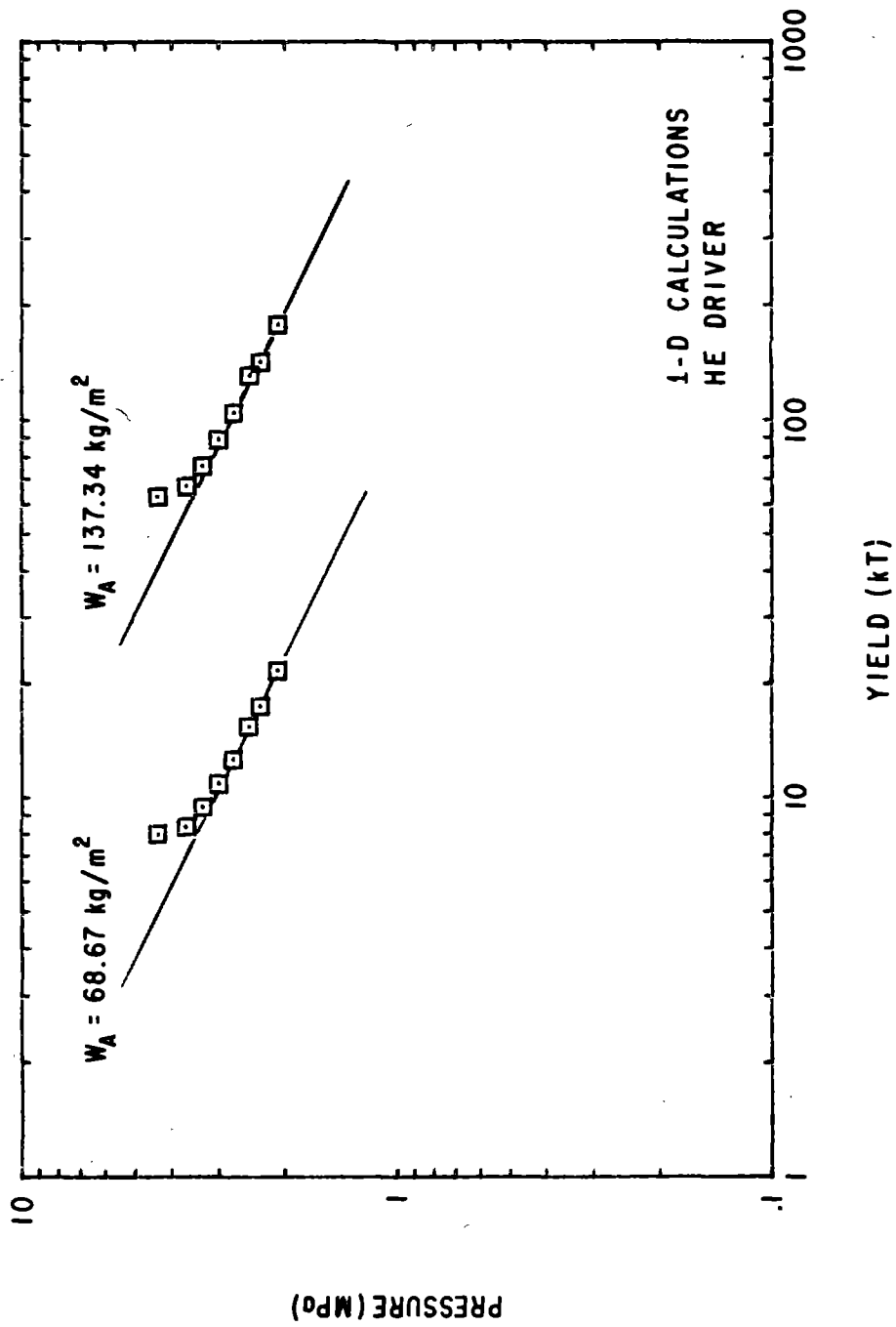


Figure 11. Results of 1-D Calculations and Comparison with Theoretical Solution

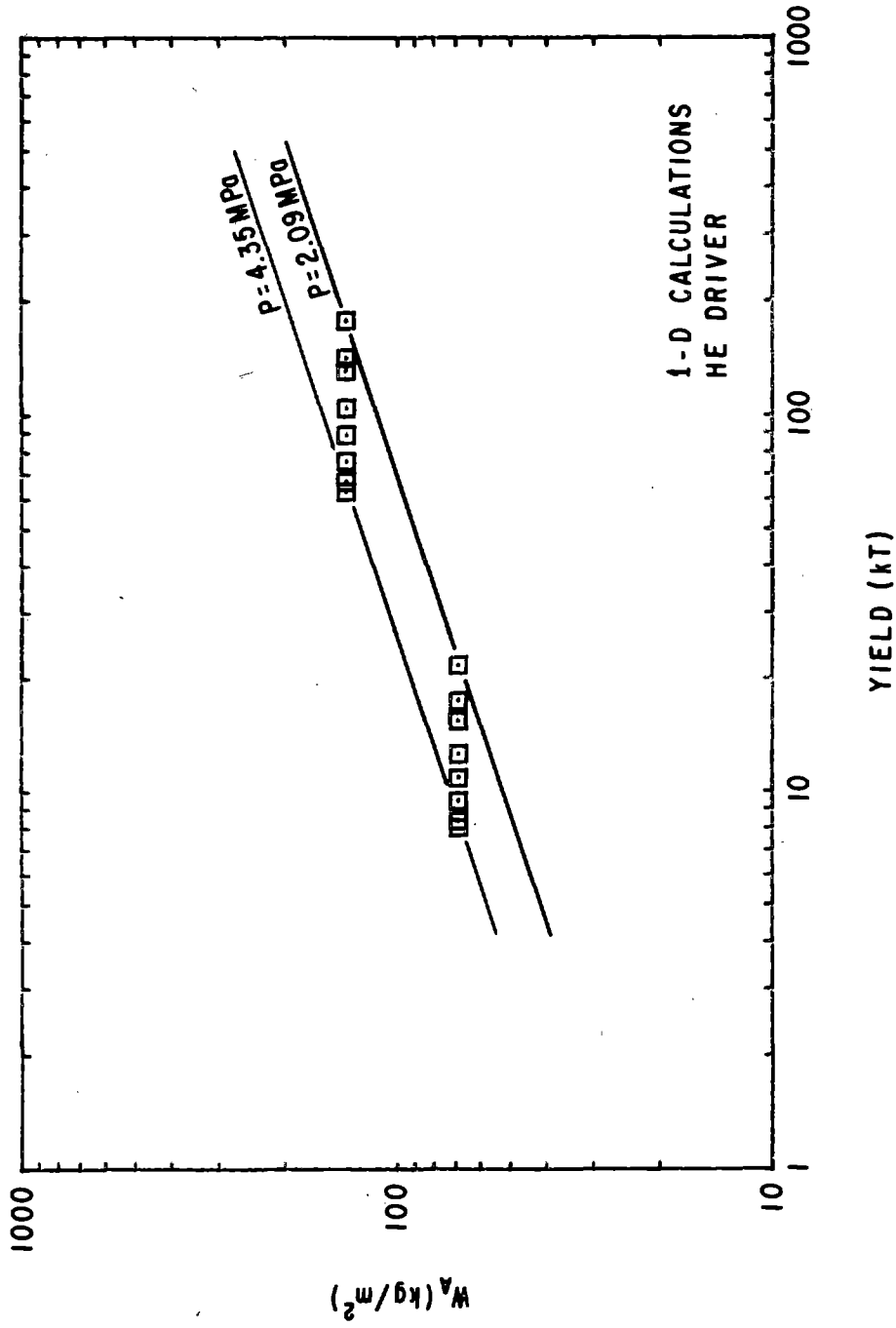


Figure 12. Results of 1-D Calculations and Comparison with Theoretical Solution

energy released by the explosives was being coupled into wall and overburden motion and that it would probably be inadequate to account for this energy loss in the calculations merely by reducing the initial energy released in the driver model. Therefore, APOD was modified to account for radial motion of the boundaries. The main features of the code will be described and some typical calculational results presented.

The wall and overburden motions were introduced by allowing the pressure in the zones to act on the wall zones to produce motion over a time period of Δt according to a lock-up or rigid body motion model. The lock-up model (ref. 6) relates soil stress to particle velocity through a polynomial which has been fit to experimental data obtained in soil compression tests. As shown in figure 13, both planar and cylindrical motion, single- and two-material models are available. In the two-material model, the shock which is propagated through the wall and soil is positioned initially at the concrete-soil interface so that the concrete is treated as being in rigid body motion only. Figure 14 shows a typical modeling of a DABS cross section where the boundary motion is calculated in three different regions. The total cross-sectional area change is then used to adjust the gas zone properties at each time step. Figure 15 shows how the driver and air zones interface with the overburden and wall zones. Note that variations in overburden depth and wall thickness with range may be modeled. Figure 16 is a flow diagram showing how the "1/2-D" portions of the problem fit into the calculational sequence. The actual effects of the radial motion on the gas flow are introduced in the update of the driver and air zone properties. The mass, momentum and energy equations are applied in calculating density, velocity and energy in each zone as follows:

$$\rho_2 = \rho_0 \left(\frac{z_0}{z_2}\right)^{\frac{1}{n}}$$

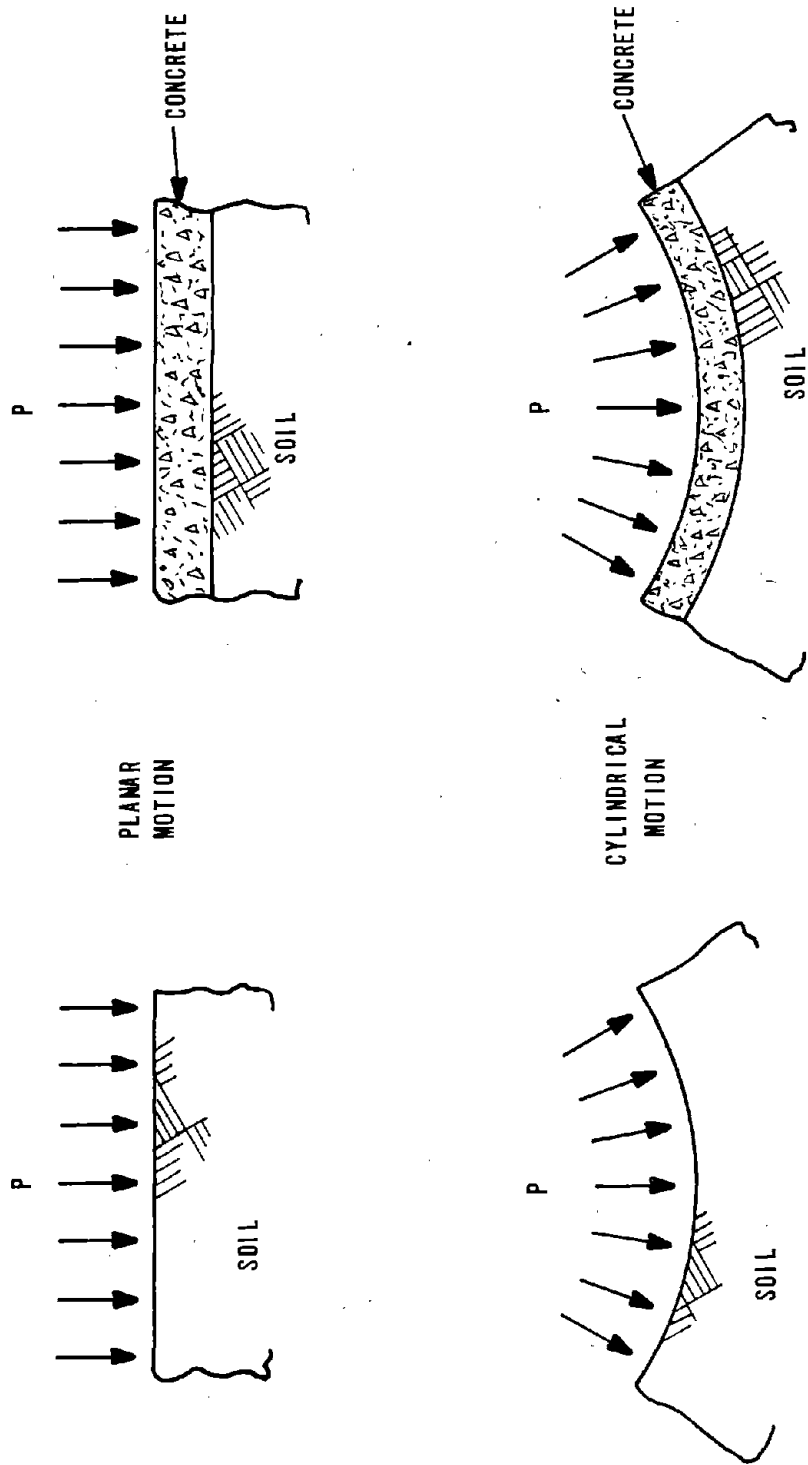


Figure 13. Boundary Motion Models Available in the APOD 1-1/2-D Hydrocode

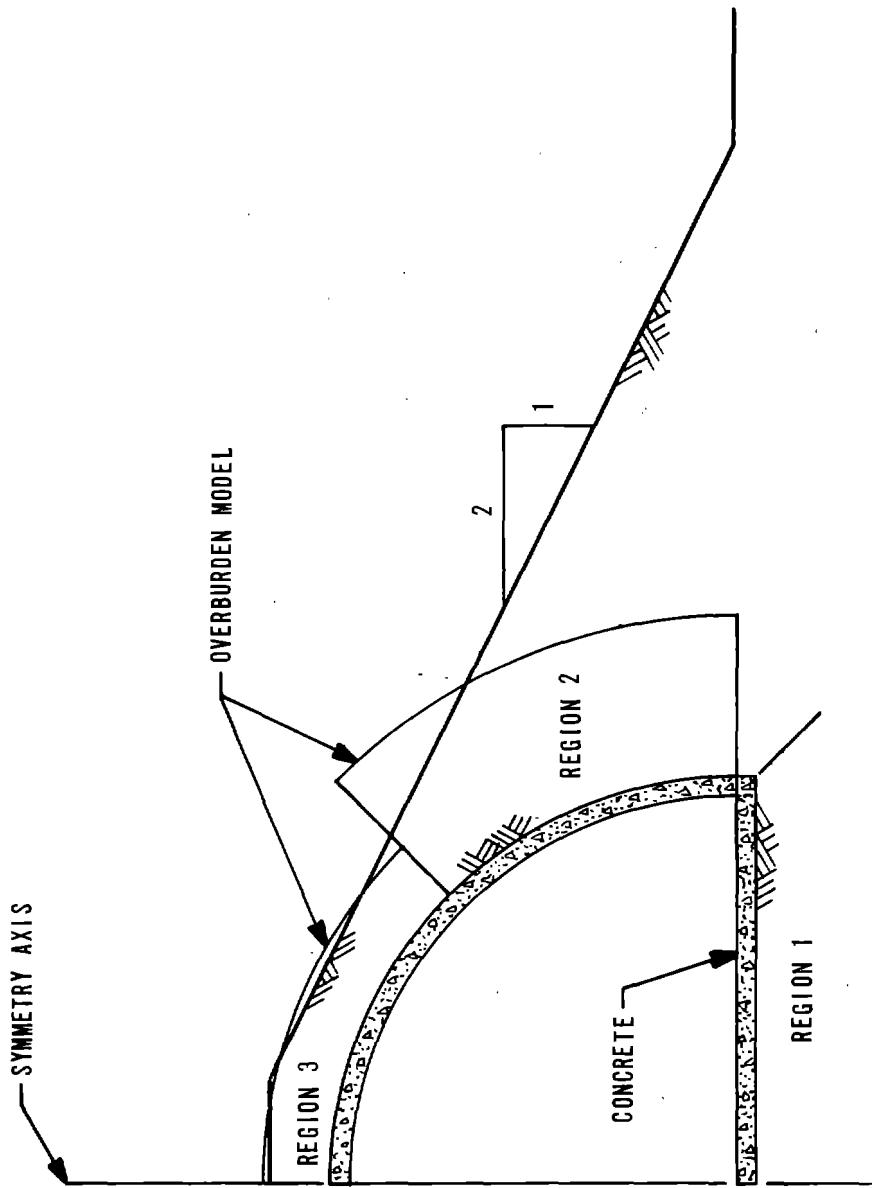


Figure 14. Typical Model of DABS Cross-section in the APOD 1-1/2-D Hydrocode

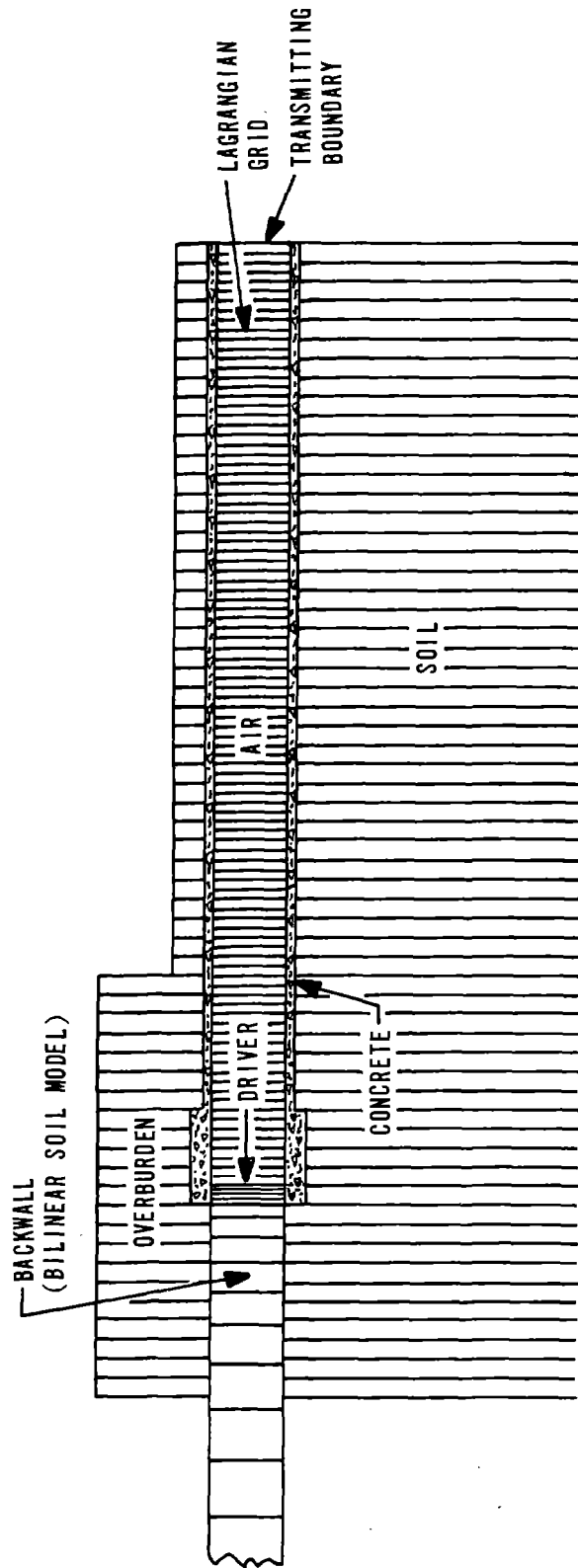


Figure 15. APOD 1-1/2-D Zone Layout for DABS Calculations

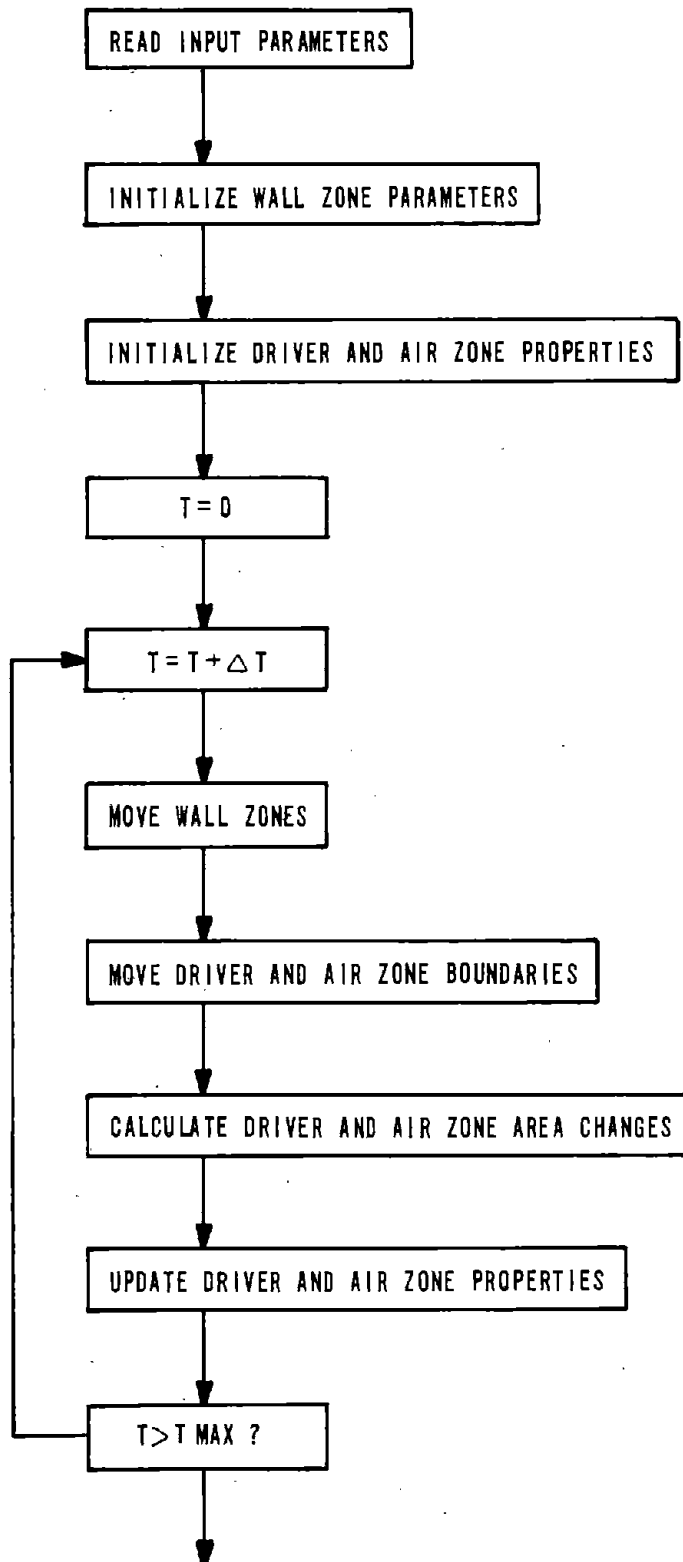


Figure 16. Flow Diagram for APOD 1-1/2-D Code

$$v_2 = v_1 + \left[\frac{P_a - P_b}{\rho_2 z_2} \right] \Delta t$$

$$E_2 = E_1 - \frac{P_1}{\rho_1} \left[\frac{\rho_1}{\rho_2} - 1 \right]$$

$$\eta = A_2/A_0$$

where

ρ is density

z is zone length

η is zone cross-sectional area ratio

v is zone boundary velocity

$P_{a,b}$ are pressures acting at left and right zone boundaries

Δt is time step

E is energy per unit mass

P is zone pressure

A is cross-sectional area

and subscripts 0, 1 and 2 refer to times $t = 0$, $t = t_1$ and $t = t_2$, respectively, where $t_2 = t_1 + \Delta t$.

With the 1-1/2-D capability, it is possible to make a matrix of calculations in which facility diameter, overburden load and charge load are all varied to identify their effects on the simulation environment. These calculations were performed and typical results are shown in figure 17 where comparisons are made with the previous 1-D calculations.

The results shown in figure 17 demonstrate that the radial motion effects for certain combinations of charge loading, size and overburden loading are quite significant in affecting the yield. The only difference between the two 1-1/2-D calculations is that the charge loading has been doubled. The size and overburden loading are identical. Note

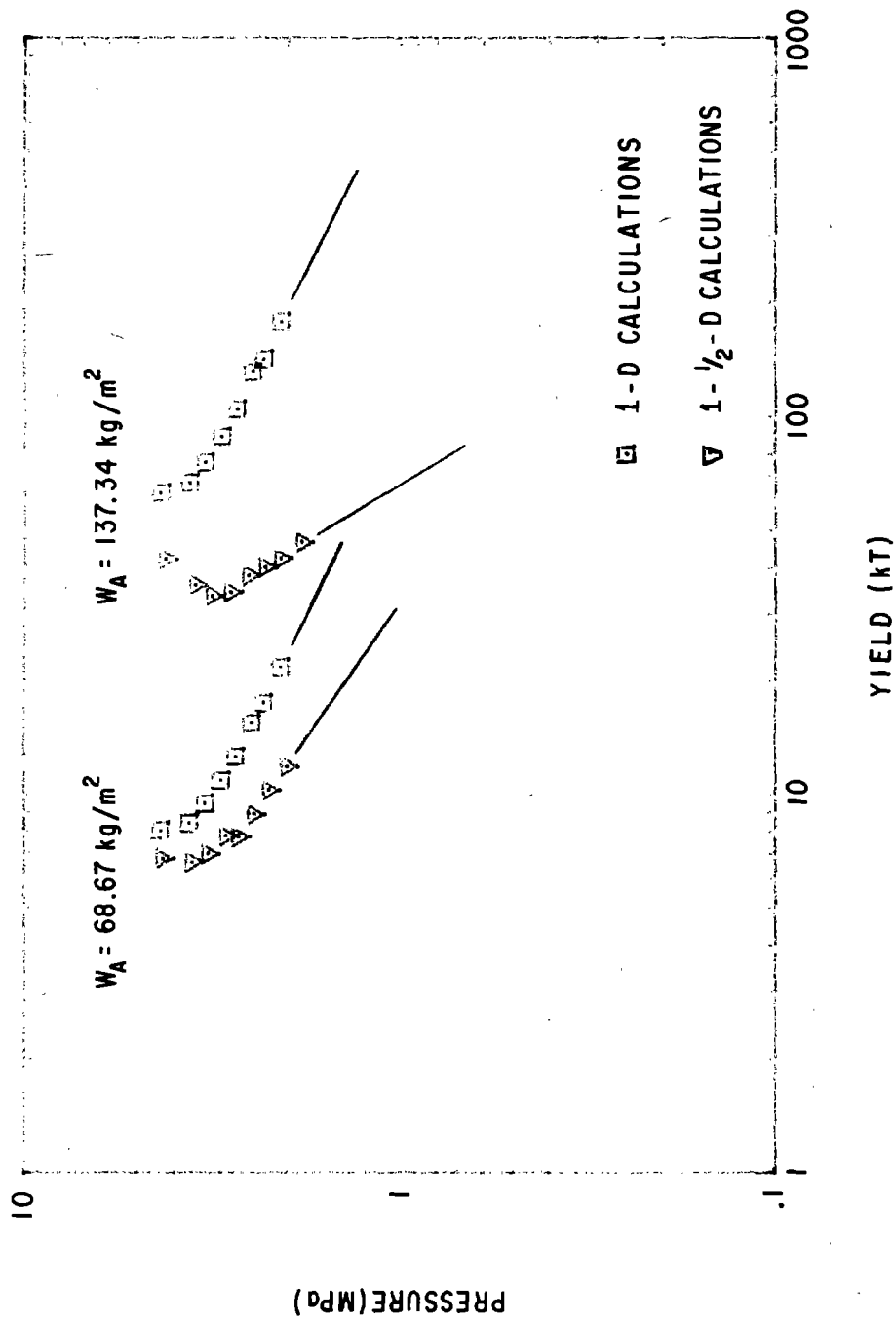


Figure 17. Comparison of 1-D and 1-1/2-D Hydrocode Calculations

that for these two calculations, equation (7) no longer holds.

The APOD 1-1/2-D code may be used in the design procedure according to two different approaches. The first approach is to fully characterize the effects of all combinations of charge, size and overburden load with no consideration for equation (7). The consequence of this approach is that the scaling law described by equation (7) no longer holds. The preferred approach is to use the calculations to identify the combinations of charge, size and overburden load that provide good quality simulations with the minimum overburden load for a given W_A and size while being constrained by equation (7). This provides a straightforward design procedure because the scaling law, equation (7), applies. This is the approach used in the design manual.

SUMMARY

Three "tools" important to the development of the DABS design procedure have been described. While each "tool" has been discussed from the perspective of its application to DABS, clearly there are broad applications in the general area of airblast simulation technology. BRNUFT is operational and has been utilized by AFWL and others in data analysis. The Sedov analysis is complete for relating planar and spherical overpressure waveforms. Extensions may be made to include the cylindrical geometry, and for dynamic airblast problems the dynamic pressure waveforms must be considered. For low pressure the Sedov strong shock assumption becomes less valid and incorporation of a weak shock approximation such as developed by Korobeinikov (ref. 7) becomes important. The 1-1/2-D hydrocode has been very useful in studying DABS problems. However, considerable work is required to develop the code to the desired level of sophistication. AFWL/CERF will incorporate the 1/2-D coding into SAP (ref. 8) and improvements in the radial and backwall motion models will be investigated.

There are other technical issues which have not been discussed but are important to the DABS development. The major issues are: the general area of explosives selection and characterization, interaction of the DABS facility with the test structure through reflected shocks, condensation shocks, interaction of the contact surface and detonation products with instrumentation and the test structure, scaling for ambient pressure and temperature, data analysis techniques for environment assessment, and instrumentation design, evaluation and performance. All of these issues have been investigated and the results considered in the design manual.

ACKNOWLEDGEMENTS

Lester Bowers (AFWL) was of great assistance in the BRNUFT and APOD 1-1/2-D programming. Ed Seusy (AFWL) suggested that the fitting of Brode waveforms to pressure data was a worthwhile problem to work (he was right). W. E. Baker (Southwest Research Institute) was very helpful in working out the scaling laws. And Bob Port (Research and Development Associates) provided some key criticisms which led to the development of the sound theoretical basis for the DABS design procedure. The contribution of each of these individuals is appreciated.

REFERENCES

1. Renick, J. D., "Dynamic Airblast Simulator Design Manual," Draft Technical Report, Air Force Weapons Laboratory, Kirtland AFB, NM, Nov 78.
2. Brode, H. L., "Height of Burst Effects at High Overpressures," DASA 2506, The Rand Corporation, Santa Monica, Calif., July 1970.
3. Mlakar, P., "Statistical Estimation of Simulated Yield and Overpressure," Working Papers, U.S. Army Engineer Waterways Experiment Station, Vicksburg, Miss., Sep 78.
4. Sedov, L. I., Similarity and Dimensional Methods in Mechanics, Academic Press, New York, N.Y., 1959.
5. Port, R. J. and Asano, W., "Users' Instructions for Program Impact," RDA-TR-107006-015, R&D Associates, Marina del Rey, Calif., Aug 78.

6. Seusy, F., "Lock-up Impulse Code Description," DED-A Technical Memorandum, Air Force Weapons Laboratory, Kirtland AFB, NM, 5 Nov 76.
7. Korobeinikov, V. P., "Approximate Formulas for Calculation of the Characteristics of a Shock Wave Front in the Case of a Point Explosion in a Gas," Dokl. Akad, Nauk SSSR, 3, 3, 1956, pp. 557-559, Translated Associated Tech. Services, Inc., Glen Ridge, N.J.
8. Whitaker, W. A., et al., "Theoretical Calculations of the Phenomenology of HE Detonations," AFWL-TR-66-141, Vol. 1, Air Force Weapons Laboratory, Kirtland AFB, NM, Nov 66.

ABSTRACT

The paper describes recent efforts involving computational modeling of two types of nuclear airblast and ground shock simulators, the High Explosive Simulation Technique (HEST) and the Dynamic Airblast Simulator (DABS), using the HULL and SAP hydrodynamic computer codes (hydrocodes).

Recent development efforts directed towards improving the performance of these nuclear simulators have revealed a need for a better understanding of the basic physics and explosion mechanics of the simulators. Results obtained in some developmental tests have been difficult to explain without first-principle theoretical computations.

The paper briefly describes the calculational tools now in use which include: 1) a computerized version of the one-dimensional similarity solution, 2) the one-dimensional SAP hydrocode, and 3) the two-dimensional HULL hydrocode. High-explosive burn routines and/or energy deposition schemes used with these hydrocodes are also described.

Several computations dealing with the HEST are presented and discussed. These include: 1) the effects of several explosive distribution arrangements within the HEST explosion cavity, 2) the effects of different test geometries, and 3) the predicted influence on measuring systems.

Several calculations of the DABS simulator are presented to show the relationship between explosive energy in the driver-chamber and downstream shock profiles, the effect of ribs and obstructions on the airblast wave, shock interactions with target structures, etc.

The summary includes a brief discussion of current calculational capabilities and a prognosis of where computational efforts are expected to progress in the near future.

ACKNOWLEDGEMENT

The authors wish to acknowledge the contributions of Ms. Susan E. Check, of the Air Force Weapons Laboratory, and Mr. William B. Chown and Mr. Billy D. Harrison, of the University of New Mexico Civil Engineering Research Facility, who performed a number of the calculations reported in this paper.

CONTENTS

Section

- I INTRODUCTION
- II CALCULATIONAL TOOLS
 - Similarity Solution
 - SAP Hydrocode
 - HULL Hydrocode
- III HEST SIMULATOR CALCULATIONS
 - ID Similarity Solution
 - HULL Calculations
- IV DABS SIMULATOR CALCULATIONS
- V CONCLUSIONS
- REFERENCES

ILLUSTRATIONS

Figure

- 1 Typical HEST Airblast Pressure Trace
- 2 HORS I-3 Experiment Configuration
- 3 1D Approximation of HEST Explosion Cavity
- 4 1D Similarity Solution (Planar Blast Wave)
- 5 HULL Calculation Grid (1D Planar Blast Wave)
- 6 HULL Calculation (1D Planar Blast Wave at 2 and 12 μ s)
- 7 HULL Calculation (1D Planar Blast Wave at 16 and 21 μ s)
- 8 HULL Calculation (1D Planar Blast Wave - Pressure Time Histories)
- 9 HULL Calculational Grid (Distributed Explosive Array)
- 10 HULL Calculation (Distributed Explosive Array at 12 and 500 ns)
- 11 HULL Calculation (Distributed Explosive Array at 1000 ns and 4.5 μ s)

ILLUSTRATIONS (Concl'd)

Figure

- 12 HULL Calculation (Distributed Explosive Array at 5 and 6.5 μ s)
- 13 HULL Calculation (Distributed Explosive Array - Pressure Time Histories)
- 14 HULL Calculation (Distributed Explosive Array - Pressure versus Range)
- 15 HULL Calculational Grid (Modified Distributed Explosive Array)
- 16 HULL Calculation (Modified Distributed Explosive Array at 15 and 1000 ns)
- 17 HULL Calculation (Modified Distributed Explosive Array at 2.5 and 4.5 μ s)
- 18 HULL Calculation (Modified Distributed Explosive Array at 6.5 and 9 μ s)
- 19 HULL Calculation (Modified Distributed Explosive Array - Pressure Time History)
- 20 Overpressure Versus Range (DABS 1E)
- 21 Arrival Time Versus Range (DABS 1E)
- 22 Overpressure Versus Range (DABS 2A and 2B)
- 23 Arrival Time Versus Range (DABS 2A and 2B)
- 24 Overpressure Versus Range (Iretol Detonation, DABS 2C)
- 25 Overpressure Versus Range (S1 Event)
- 26 Overpressure Versus Range (T1 Event)
- 27 Arrival Time Versus Range (T1 Event)
- 28 Effects of DABS Roof and Shelter Model on Shock Position
- 29 HULL Calculation of 1 Megaton in Corrugated Tube at 6.9 MPa (100 lb/in²)

I. INTRODUCTION

The signing of the Limited Nuclear Test Ban Treaty in 1963 made necessary the development of methods for simulating nuclear airblast and ground-shock effects. The High Explosive Simulation Technique (HEST) was developed during the mid 1960's to simulate airblast overpressure and the airblast-induced ground-shock loadings (on near-surface buried structures) (Ref. 1 and 2). The HEST, as originally devised, did not simulate the dynamic airblast effects (reflected pressures, etc), which would be experienced by above-ground structural targets. The Dynamic Airblast Simulator (DABS) was developed during the mid 1970's to provide this simulation capability for testing above-ground missile shelter concepts (Ref. 3).

The development of these and other nuclear airblast and ground-shock simulation methods over the past fifteen years was accomplished by primarily experimental methods. Empirically derived expressions, based on previous experimental data, were used for the design and sizing of future tests (Ref.4).

As the requirements for more accurate simulation of a wider range of nuclear environments continued to grow, these experimental and empirical design methods became less adequate. Certain problems continued to plague each of these simulations. Not only did variation of the experimentally derived design parameters fail to provide solutions, but certain phenomena observed in the data defied explanation by purely empirical means.

Over the past fifteen years, substantial progress has been made in the area of first-principle hydrodynamic calculations. Several large hydrodynamic computer codes (hydrocodes) have evolved with which the simulation methods could be examined in greater detail. A program of hydrocode calculations of the HEST and DABS simulators was undertaken by the Air Force Weapons Laboratory (AFWL) and the University of New Mexico Civil Engineering Research Facility (UNM/CERF).

1. Auld, H. E., D'Arcy, G. P., Leigh, G. G., *Simulation of Airblast-Induced Ground Motions (Phase I)*, AFWL-TR-65-11, Air Force Weapons Laboratory, Kirtland AFB, New Mexico, April 1965.
2. Auld, H. E., D'Arcy, G. P., Leigh, G. G., *Simulation of Airblast-Induced Ground Motions (Phase II)*, AFWL-TR-65-26, Vol. I, Air Force Weapons Laboratory, Kirtland AFB, New Mexico, April 1965.
3. Martens, Daniel P., and Bradshaw, Joel C., *Dynamic Airblast Simulator Parametric Test Series, Events I-A, I-B, I-C, I-D, and I-E Data Report*, AFWL-TN-76-018, Air Force Weapons Laboratory, Kirtland AFB, New Mexico, November 1976.
4. Bratton, J. L., and Pratt, H. R., *Simulation of Airblast-Induced Ground Motions (Phase IIA)*, AFWL-TR-66-85, Air Force Weapons Laboratory, Kirtland AFB, New Mexico, October 1967.

Some difficulties have been encountered with both the HEST and the DABS simulators that were not resolvable through experimental or empirical techniques. In the HEST, high pressure spikes and severe oscillations were often encountered near the beginning of the pressure pulse (Fig. 1). Whether these were caused by the positioning of individual strands of detonating cord near the pressure gages or by larger shock oscillations within the HEST explosion cavity was not known. Tests conducted in which all the explosives in the cavity were initiated nearly simultaneously resulted in greater peak overpressures for a given charge density than tests in which the detonation was caused to propagate through the explosion cavity at some specified rate (sweeping wave). Finally, the relation between the charge density of explosives in the cavity and the peak overpressure thus obtained was not well defined for a wide range of pressures and for different explosive materials.

The DABS technique must provide waveforms of overpressure, as in HEST, at the desired magnitude and yield. In addition, DABS must provide the dynamic pressure waveform consistent with this overpressure waveform. These conditions alone place severe restrictions on the design of DABS. Coupled with the requirement for large-scale testing capability, DABS presents a unique challenge for numerical design calculations.

Difficulties encountered with the DABS included uncertainties about explosive charge density in the driver section versus peak pressures and impulse at locations down range, shock interaction from ribs in the trench sections, shock reflections and other dynamic effects from the detonation product contact surface, and modification of the flow field by the test structure.

These and other design considerations led to the need for hydrocode calculations in support of these simulation methods.

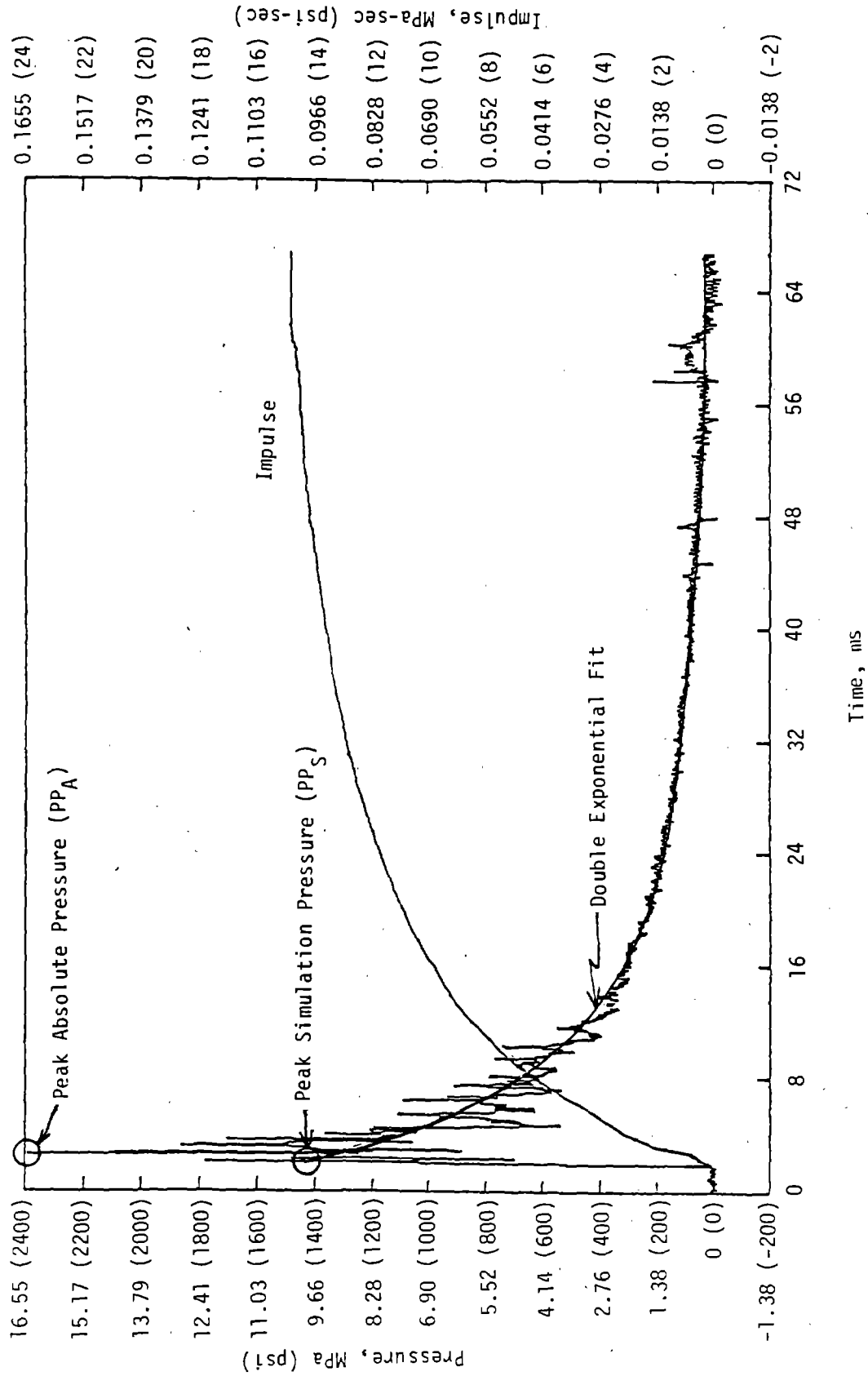


Figure 1. Typical HEST Airblast Pressure Trace

II. CALCULATIONAL TOOLS

The calculational tools used during this technical effort included the one-dimensional (1D) similarity solution, the SAP 1D hydrocode (both Eulerian and Lagrangian versions), and the HULL two-dimensional hydrocode. Each is briefly described below.

SIMILARITY SOLUTION

The 1D similarity solution followed the method of Sakurai (Ref. 5), which provides similarity solutions for blast waves in planar, cylindrical, and spherical geometries. A small code was written to computerize this method in order to ease the solution of a variety of problems. Idealized blast wave problems, using a pure energy source in an ideal gas, can be calculated out to the point of encounter with a reflecting surface. The similarity solution, however, will not handle shock reflections and thus can only be used to estimate the very early portion of most explosion problems.

SAP HYDROCODE

SAP is a one-dimensional hydrocode developed at the AFWL in 1966 by Whitaker, et al (Ref. 6). In 1975, SAP was integrated into the HULL system which used the SAIL updating management system (Ref. 7). The SAIL system provides numerous variations in coding by the proper selection of several options. This allows a high degree of versatility in customizing any given calculation.

Two finite differencing options are provided, and the code is adaptable with a minimum of effort to any differencing scheme desired. The first method is a Lagrangian method described in detail in AFWL-TR-66-141 (Ref. 6). The second method is an adaption of the HULL differencing scheme which offers either Eulerian or Lagrangian methods and is described further in AFWL-TR-76-183 (Ref. 8).

-
5. Sakurai, A., "On the Propagation and Structure of the Blast Wave, I," *Journal of the Physical Society of Japan*, Vol. 8, No. 5, Sep-Oct 1953.
 6. Whitaker, W. A., et al, *Theoretical Calculations of the Phenomenology of HE Detonations*, AFWL-TR-66-141, Vol. 1, Air Force Weapons Laboratory, Kirtland AFB, New Mexico, November 1966.
 7. Graham, D. C., Gaby, L. P. II, and Rhoades, C. E., Jr., *SAIL, An Automated Approach to Software Development and Management*, AFWL-TR-(Pre-publication), Air Force Weapons Laboratory, Kirtland AFB, New Mexico, October, 1976.
 8. Fry, M. A., et al, *The HULL Hydrodynamics Computer Code*, AFWL-TR-76-183, Air Force Weapons Laboratory, Kirtland AFB, New Mexico, September 1976.

Cartesian, cylindrical, or spherical coordinates systems may be elected. SAP may be run on smaller calculations with or without tapes. Because SAP offers a restart capability, a longer calculation may be continued should the calculation abort before completion. The code will compute flows at any angle to the horizontal. The mesh may be rezoned periodically so that the shock is always located interior to the mesh.

SAP uses a real atmosphere that is stable under a R^{-2} gravity field and an air equation of state that is an empirical fit to Hilsenrath's data (Refs. 9 and 10). Six additional formulations provide equations of state for TNT, PBX-9404, Pentolite, methane and ammonium nitrate/fuel oil with provisions for including others if desired.

A continuous-burn routine based on Chapman-Jouget theory is present in the code. Any material may be used if its equation of state for the burned and unburned material is known. This routine provides the conditions existing in the gaseous explosive products at the instant the detonation wave reaches the surface of the exploding charge. The routines work for a forward burn only. In other words, the process must be initiated by starting with at least one cell of burned material at the left-most perimeter of the section of the mesh containing any materials other than air.

Some other features of SAP are as follows. First, boundary conditions may be specified by card input as transmissive, reflective, or a specified function of time. Secondly, one of the tapes used with SAP is a station tape which records the time histories of hydrodynamic variables at particular (fixed) locations. Next, plotting options for SAP allow graphs of overpressure, overdensity, and velocity versus radius to be generated at specified times during the calculation. After the calculation is completed, a station plotter provides for plots of time histories of overpressure, overpressure impulse, density, velocity, dynamic pressure and dynamic pressure impulse.

Further, a provision for energy loss due to radiation is provided with three different techniques. And, finally, to provide a sharply defined stable shock front, there are three viscosity options: 1) no artificial viscosity terms used, 2) additions of a constant viscosity term, and 3) the addition of a pseudoviscous pressure (Ref. 11).

-
9. Hilsenrath, J., Green, M. S., and Beckett, C. W., *Thermodynamic Properties of Highly Ionized Air*, SWC-TR-56-35, National Bureau of Standards, Washington, D.C., April, 1957.
 10. Doan, L. R., and Nickel, G. H., *A Subroutine for the Equation of State of Air*, RTD (WLR) TM-63-2, Air Force Weapons Laboratory, Kirtland AFB, New Mexico, May 1963.
 11. Needham, C. E., *Development of an Artificial Viscosity Function*, AFWL-TR-77-53, Air Force Weapons Laboratory, Kirtland AFB, New Mexico, August 1977.

HULL HYDROCODE

HULL is a two-dimensional hydrocode written for either Cartesian or cylindrical coordinates (Ref. 8). It is an outgrowth of the SHELL-OIL code developed by Johnson in the early 1960's. Matuska and Durrett made the code second order in time and space and developed the SAIL system in 1971 (Ref. 7), thus providing accuracy and flexibility not possible previously.

The HULL code was originally designed to model fluid behavior in a multi-dimensional Eulerian continuum. As a result of an extensive and ongoing development program by the AFWL, this code has evolved into a sophisticated and versatile computational tool. Among its capabilities are the simulation of high-explosive detonations, nuclear weapons effects (including radiation and airblast precursors), diffusion limitation for multi-material environments, elastic-plastic strength of solids, etc. HULL is used in conjunction with the SAIL preprocessor program which efficiently tailors the calculational coding to the model specifications.

The basic HULL code solves finite-difference analogs for a set of partial differential equations which govern the behavior of a compressible, nonconducting, inviscid fluid. The local state variables are updated in two phases. First, the velocity and energy state of the fluid are advanced in time by a Lagrangian calculation. Then, instead of the Lagrangian phase's being completed by reconfiguring the calculational mesh, final fluid properties are defined in an Eulerian reference system by taking into account the flux of mass, momentum, and energy. In the absence of mesh gradients, this method is fully second-order accurate.

Two features of HULL are of particular importance when considering HEST and/or DABS experiments. Detonation phenomena can be simulated by routines which both model the burning of an explosive and limit diffusion when treating several material species in the Eulerian framework. An algorithm controls the burning process so that the detonation propagates sequentially through the mesh at the local sound speed and in the direction of the local pressure gradient. Equations of state for both the unburned explosive and the products of combustion are used to update the relative masses and the internal energy as the detonation progresses. The HULL code diffusion limiter plays a significant role in such a multi-material environment. It tends to restrict the mixing of species in the direction of flow and thereby preserves contact discontinuities which are characteristic of explosively generated planar blast waves. Diffusion is constrained by an algorithm which arbitrarily adjusts the flux of mass by giving preference to those species already downstream.

Some of the options used for the following calculations were multiple materials, high-explosive burn, immovable islands, stations, and special input boundary conditions. The islands permit calculation of shock interactions with structures. The boundary conditions permit input from previous SAP or HULL calculations. The stations allow description of time histories of all hydrovariables as a function of time at any point in space.

III. HEST SIMULATOR CALCULATIONS.

The pressures and shock oscillations produced during the explosion of a HEST cavity are of substantial interest to the community of research in simulation development. A number of complex hydrocode calculations have been performed to further understand and define these HEST characteristics. To achieve a crude approximation of HEST cavity pressures, a 1D similarity solution was generated for comparison with a recently performed HEST experiment. The HORS I-3 experiment produced good pressure data and was selected for comparison between experimental data and an 1D approximation of similarity. The HORS I-3 HEST configuration depicted in Figure 2 contained five planes of explosive materials in a 35.56-cm (14-in) cavity. A first approximation for this experiment is achieved by considering the five explosive planes in the experiment to be consolidated into a single plane located along the midplane of the cavity (Fig. 3). The charge density of 0.02 g/cm^3 (1.3 lb/ft^3) used in the experiment then becomes a planar loading of $4.297 \times 10^{10} \text{ ergs/cm}^2$. The foam filled cavity used in HORS I-3 is considered to be filled with an ideal gas ($\gamma = 1.4$). Upon initiation, shock waves emerge from both sides of the explosive plane and propagate through the ideal gas until they reach the cavity boundaries. Since the problem is symmetrical about the explosive plane, only one side of the problem is calculated.

1D SIMILARITY SOLUTION

The results from the similarity solution are shown in Figure 4. To carry the solution beyond the point of arrival of shock at the boundary is not valid because the similarity solution does not hold for reflected shocks.

The solution shows the shock arrival at the cavity edge [17.78 cm (7 in)] at 11.87 ms with a peak pressure of 83.5 MPa ($12,108 \text{ lb/in}^2$) which would cause reflected shocks in the neighborhood of 517 MPa ($75,000 \text{ lb/in}^2$). The cavity equilibrium pressure near the center of the cavity at this time is approximately 32 MPa (4640 lb/in^2). The data from the experiment showed the cavity equilibrium pressure (peak simulation pressure) to be approximately 34.65 MPa (5024 lb/in^2) and the absolute peak pressure spikes in excess of 207 MPa ($30,000 \text{ lb/in}^2$). There is some question as to whether the instrumentation system was able to respond to reflected shocks of higher pressure (and higher frequency). Hence, reflected shocks with magnitudes in the range of 517 MPa ($75,000 \text{ lb/in}^2$) may have occurred but were not recorded. The foam material in the cavity may also have attenuated the peak pressures somewhat over those expected in an ideal gas.

The 1D similarity solution has provided a first-order approximation for the initial blast wave produced in the HORS I-3 experiment and thus a basis for comparison for the hydrocode calculations.

HULL CALCULATIONS

A HULL calculation was performed for comparison with the 1D similarity problem discussed previously (Figure 3). A 6-cell by 72-cell Cartesian grid was used with the left boundary considered to be the center line of the HEST cavity (Fig. 5). The right boundary was set to be reflective in order to

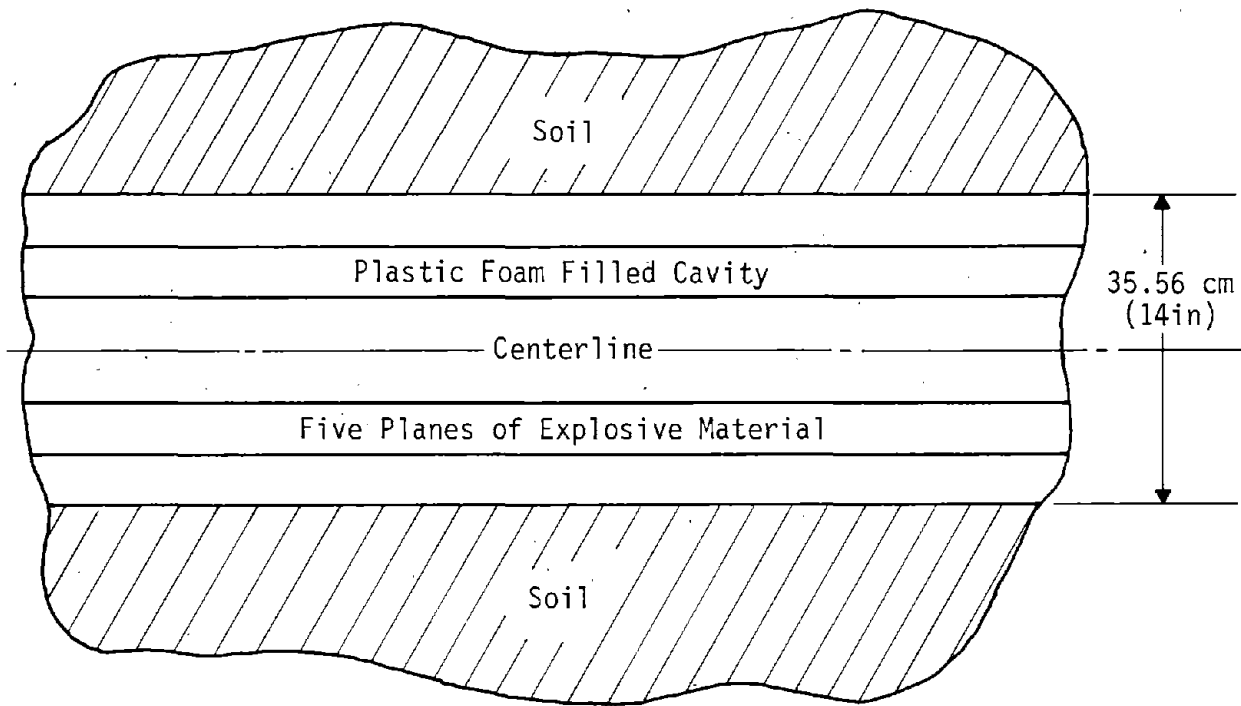


Figure 2. HORS I-3 Experiment Configuration

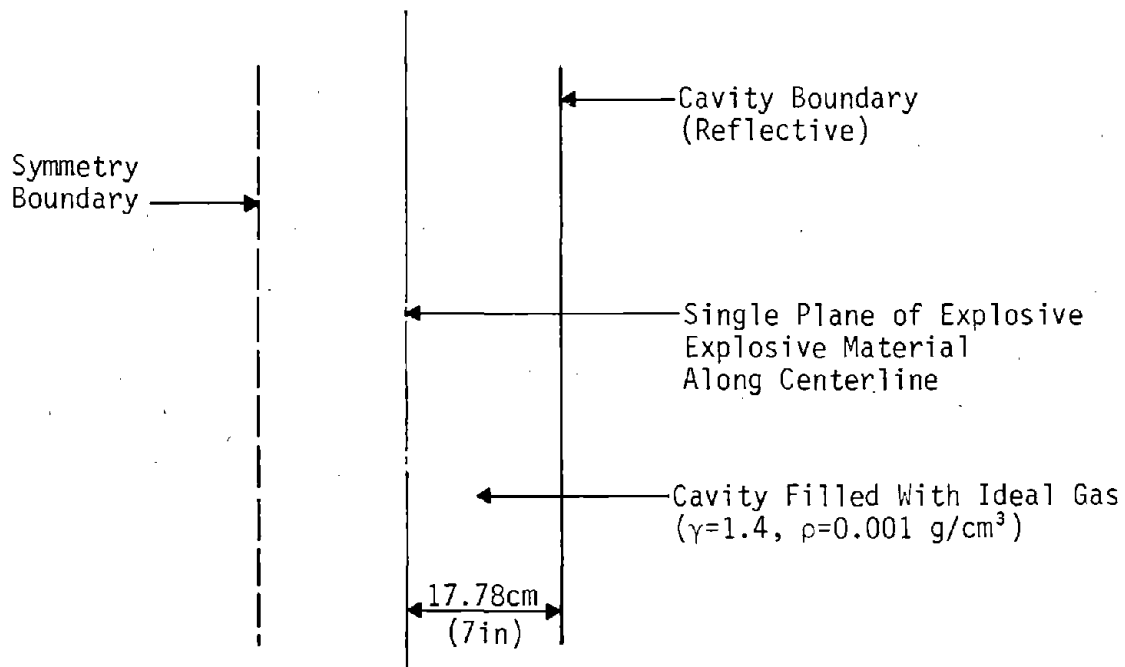


Figure 3. 1D Approximation of HEST Explosion Cavity

Planar Blast Wave Problem
 1 Dimensional Similarity Solution
 Energy=4.297E+010 Ergs Per cc, J0=1.70
 Init Dns=0.001 Gm Per cc, Ratio of sp Ht=1.40

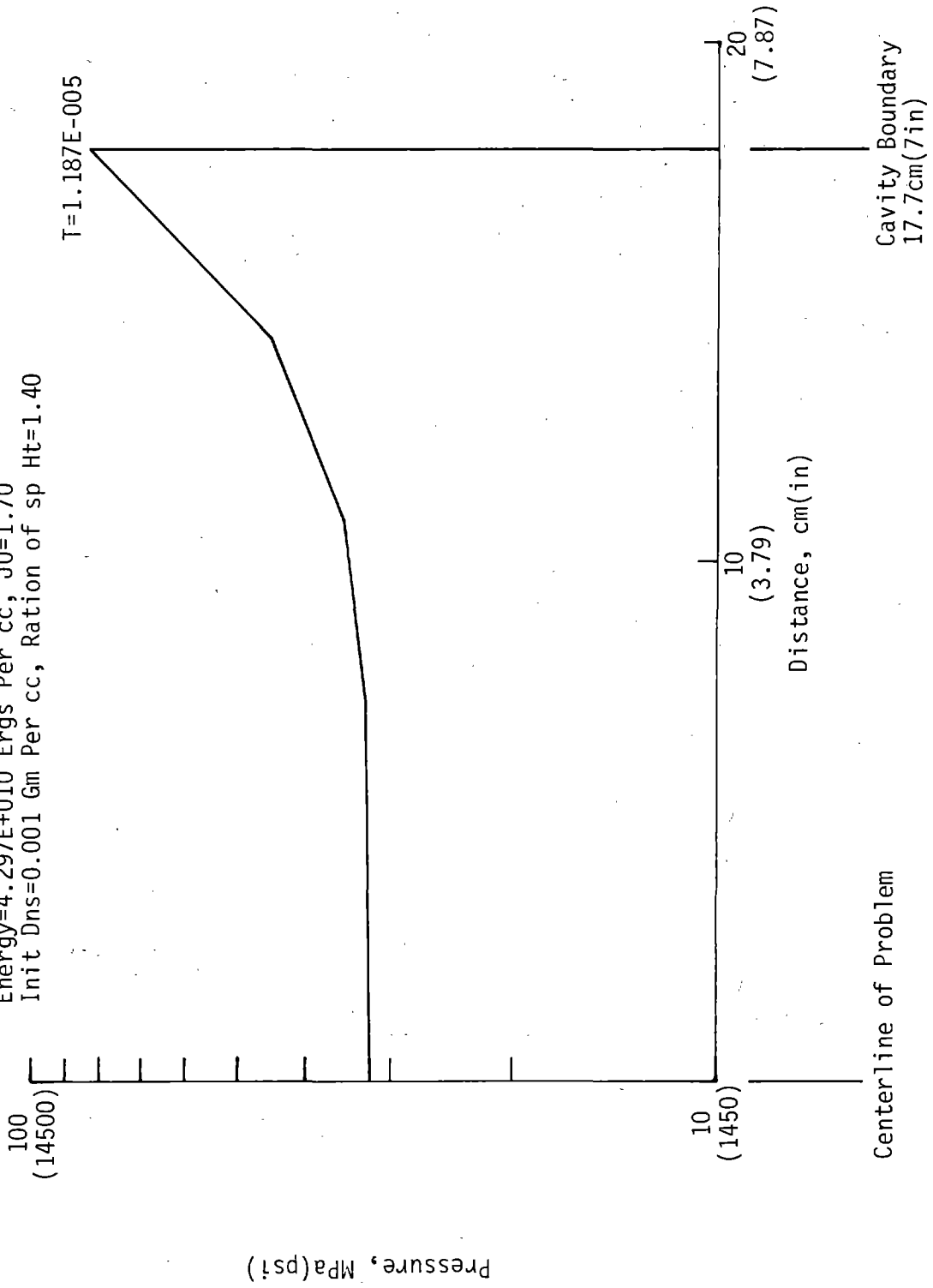


Figure 4. 1D Similarity Solution (Planar Blast Wave)

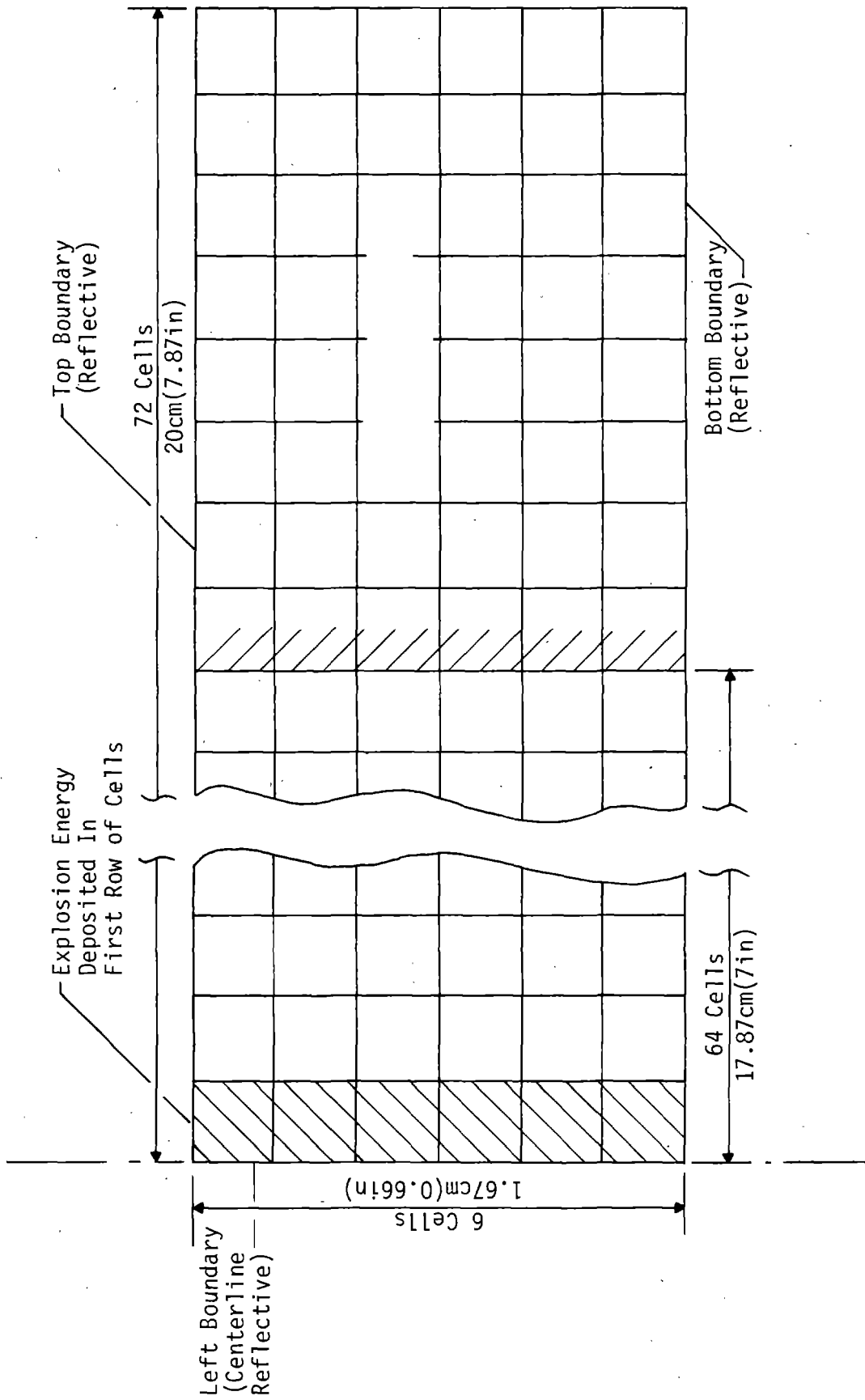


Figure 5. HULL Calculation Grid (1D Planar Blast Wave)

simulate the edge of the HEST explosion cavity. Top and bottom boundaries were also set to be reflective. The grid was loaded initially with an ideal gas having a gamma of 1.4 and a density of 0.0001 g/cm^3 ($.06 \text{ lb/ft}^3$). A quantity of energy equivalent to $4.358 \times 10^{10} \text{ ergs/cm}^2$ was introduced into each of the cells along the left boundary at time zero to begin the explosion process.

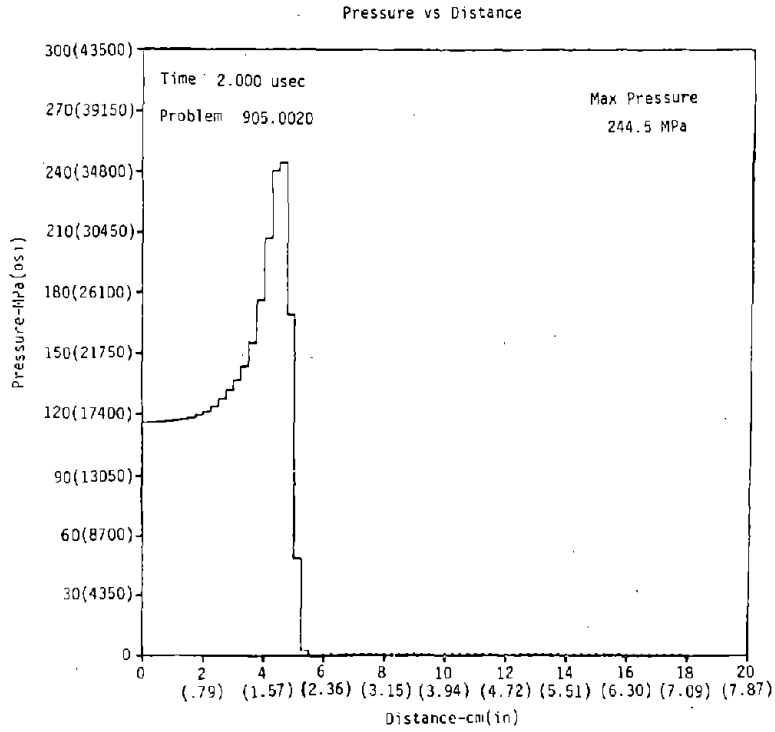
The results of this HULL calculation are shown in Figures 6 through 8. Figure 6a shows the calculated shock wave at $2 \mu\text{s}$ moving from the centerline (left boundary) towards the right boundary [which is located at 17.78 cm (7 in)]. Figure 6b shows the shock immediately before arrival at the reflecting boundary. The time is $12 \mu\text{s}$ and the peak overpressure is 81.31 MPa ($11,790 \text{ lb/in}^2$) which agrees well with the $11.87 \mu\text{s}$ and 83.87 MPa ($12,161 \text{ lb/in}^2$) obtained from the similarity solution.

Shock reflections from rigid surfaces can be calculated with the HULL code. Figure 7a shows the calculated wave at $16 \mu\text{s}$, a short time after reflecting off of the right boundary. It is now moving back toward the centerline and has a peak pressure of 389 MPa ($56,405 \text{ lb/in}^2$). Figure 7b shows the reflected wave at $21 \mu\text{s}$ continuing to move towards the left with the peak pressure now down to 114 MPa ($16,530 \text{ lb/in}^2$).

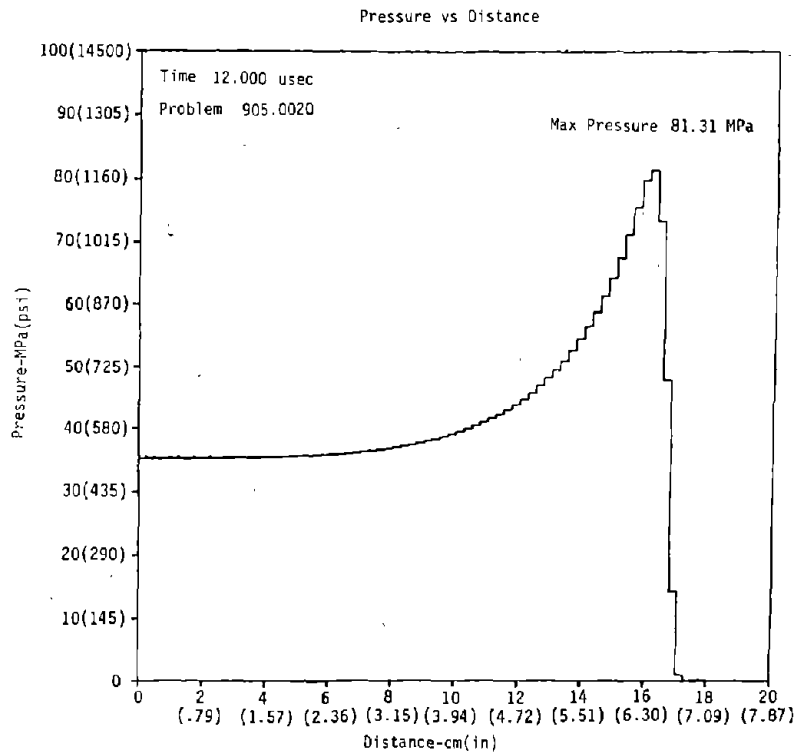
Figures 8a and 8b are calculated pressure time history plots for two gage stations, one at the right reflecting boundary [Figure 8a at 17.78 cm (7 in)] and the other midway between the centerline and the right boundary [Figure 8b at 8.89 cm (3.5 in)]. The peak reflected pressure at the right boundary is 589 MPa ($85,405 \text{ lb/in}^2$), occurring at $14.57 \mu\text{s}$. This is in reasonable agreement with the estimate of 517 MPa ($74,965 \text{ lb/in}^2$) based on the similarity solution. The arrival and reflection of the shock from the right boundary a second time can also be seen in Figure 8a. The peak reflected pressure is substantially lower the second time [140 MPa ($20,300 \text{ lb/in}^2$)], due primarily to viscous effects in the HULL code. Figure 8a shows four distinct shock arrivals which are identified as: 1) the first arrival of the incident wave traveling from the centerline toward the right boundary, 2) the arrival of the reflected wave from the right boundary, 3) the arrival of the reflecting wave from the centerline due to symmetry about the centerline, and 4) the arrival of the second reflection from the right boundary. The small oscillations in the waveform following the third and fourth peaks are caused by instabilities in the calculation.

From these results, it can be seen that in a HEST experiment where a single plane of explosive is placed at the midplane of the explosion cavity, a very large pressure spike, many times the magnitude of the cavity equilibrium pressure, would be expected at the edge of the cavity along with numerous shock oscillations throughout the cavity during the first few milliseconds of the experiment. Later calculations have confirmed that a greater distribution (multiple planes) of explosives greatly reduced both the initial pressure spike at the boundary and the magnitude of the shock oscillations.

The explosive charge used with the HEST simulator has generally been fabricated from individual strands of detonating cord. The distance that pressure measurement gages should be located away from these individual strands of detonating cord has been a matter of concern to HEST designers. To help understand and resolve this issue, a series of HULL calculations were

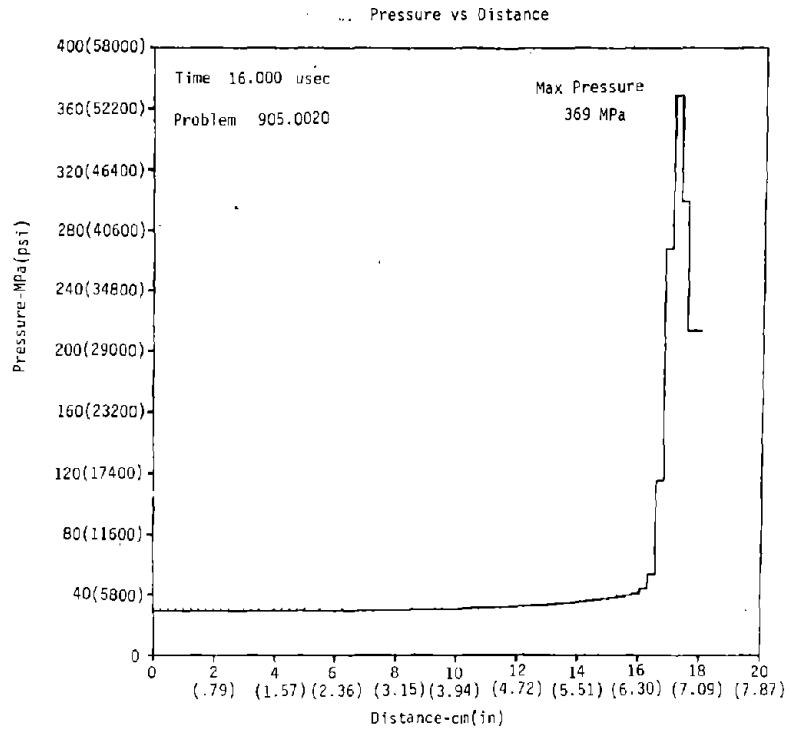


(a)

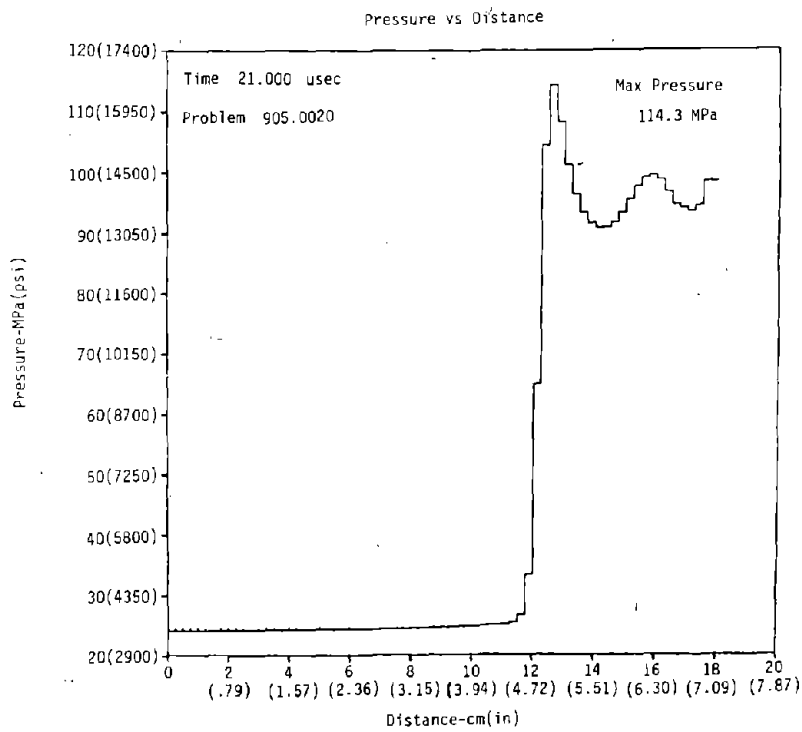


(b)

Figure 6. HULL Calculation (1D Planar Blast Wave at 2 and 12 μ s)

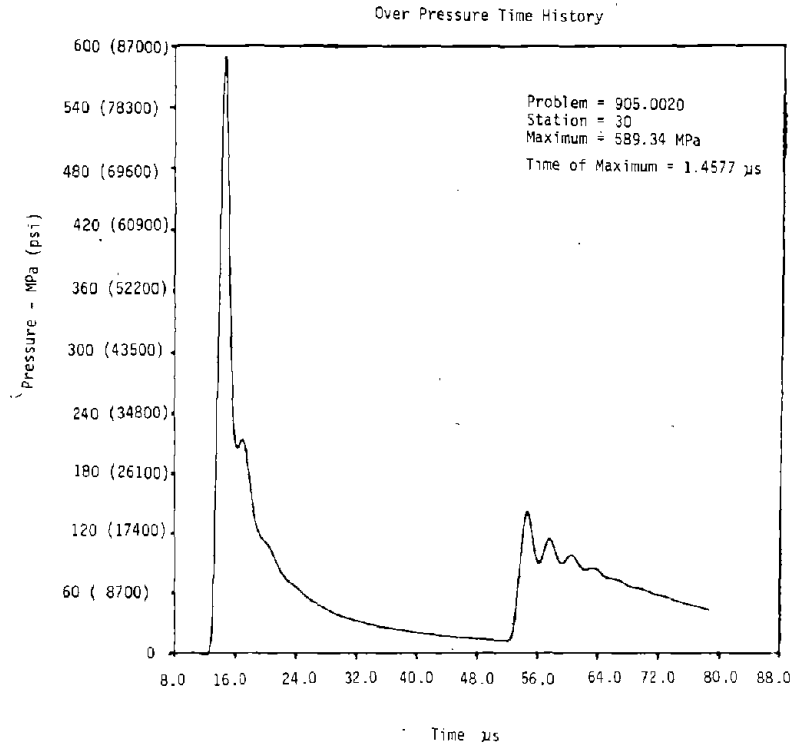


(a)

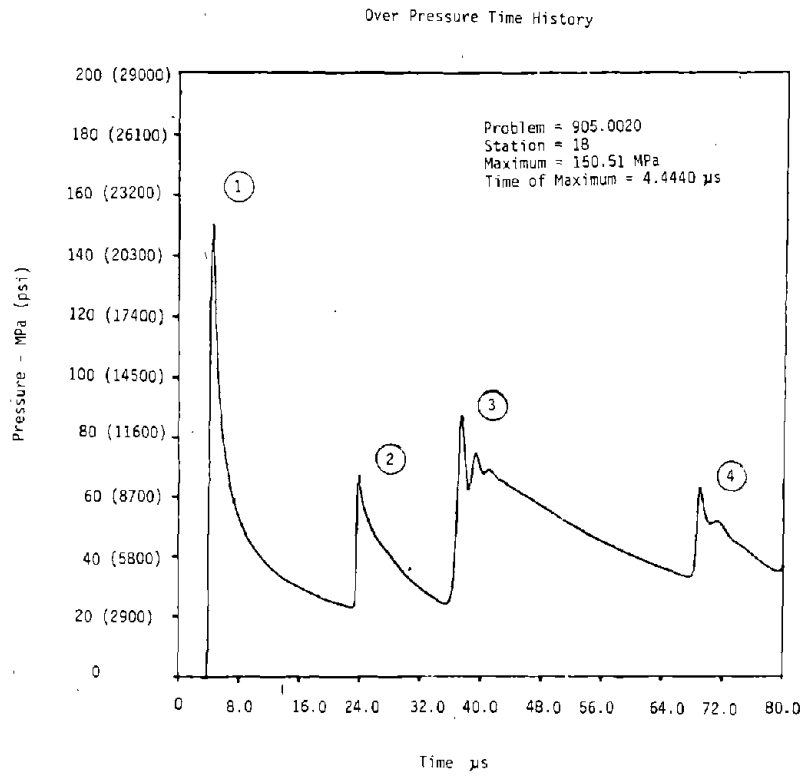


(b)

Figure 7. HULL Calculation (1D Planar Blast Wave at 16 and 21 μ s)



(a)



(b)

Figure 8. HULL Calculation (1D Planar Blast Wave - Pressure Time Histories)

performed in which individual strands of detonating cord were coarsely modeled. The calculational model (Figure 9) consisted of a 70-by-70 grid of cells, each 0.254 cm (2.1 in) square, initially filled with an ideal gas [$\gamma = 1.4$; $\rho = 0.001 \text{ g/cm}^3$ (0.614 lb/ft³)]. Square energy deposition zones were established representing the cross sections of individual strands of (hypothetical) square detonating cords. The appropriate amount of energy was dumped into each of the zones at time zero to begin the explosion problem.

The results of this calculation are seen in pressure contour plots in Figures 10 through 12. The expanding shock waves from individual cords converge to form high pressure spikes in the regions between the cords. These in turn re-expand to compress the original detonation zones. While these shock oscillations between strands of detonating cord and the spaces in between them are occurring, a shock front is moving steadily towards the right boundary (cavity edge). Because of the convergence of shocks from the individual strands of detonating cord, small shock jets are superimposed on this main front (Figure 12a). When this front reflects off of the right boundary (Figure 12b), localized peak pressures are obtained ranging from 157 MPa (22,765 lb/in²) at locations directly beneath the detonating cord (Station 10 - Figure 13a) to 227 MPa (32,915 lb/in²) at locations between the cords (Station 7 - Figure 13b). The pressure distribution across the half of the HEST cavity at 12 μs is shown in Figure 14. The high and low pressure zones at that instant can be clearly seen. The result shows that gages placed in a HEST test bed directly beneath individual strands of detonating cords register lower peak pressures than those placed midway between those locations.

Concern for the close proximity of pressure gages to the detonating cord in a HEST cavity led past experimenters to remove strands of detonating cord in the vicinity of the gage, thus creating an explosive free hemisphere above the gage. Yet gages protected in this manner were more often destroyed than ones not so protected. The next calculation modeled this situation and provided the explanation. The same grid geometry and explosive loading arrangement as for the previous calculation was used except that one explosive zone immediately adjacent to Gage Station 10 was deleted, modeling the deletion of one strand of detonating cord (Figure 15).

The results of this calculation are shown in Figures 16 through 19. The pressure contours clearly show the formation of a strong jet which impinges on the boundary precisely at the location of Gage Station 10 and which produces peak reflected pressures of 633 MPa (91,785 lb/in²) at 12 μs (Figure 17b). This is a factor-of-four increase in the peak reflected pressure loading on this gage location and explains the loss of many gages during HEST experiments.

Simulation of HEST/HORS I-3 Det Cord Array

Geometry - 2-D Cartesian
 Boundary Conditions - Reflective
 Initial Conditions - Standard Atmosphere MSL
 EOS - Fixed Gamma Law

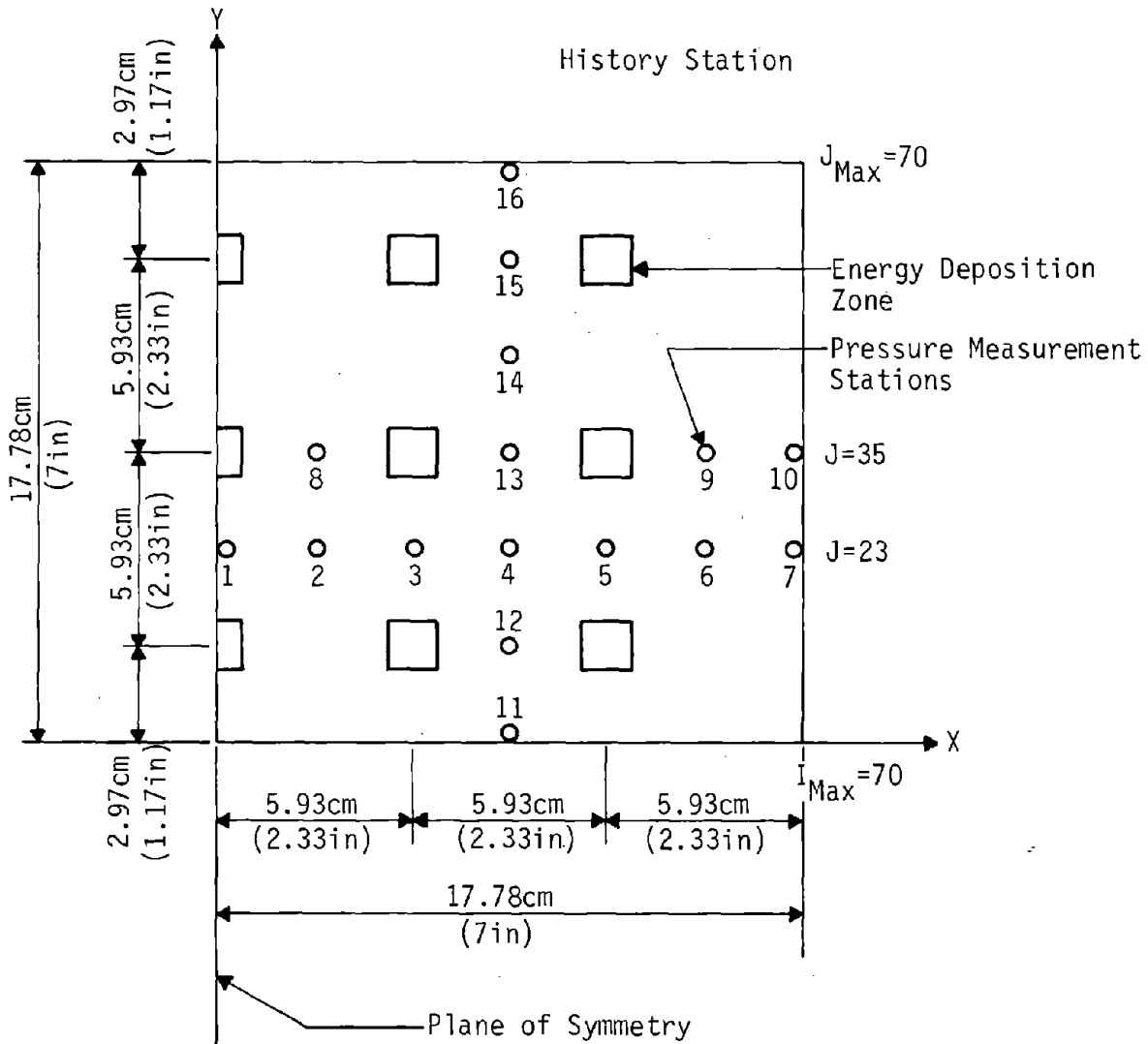
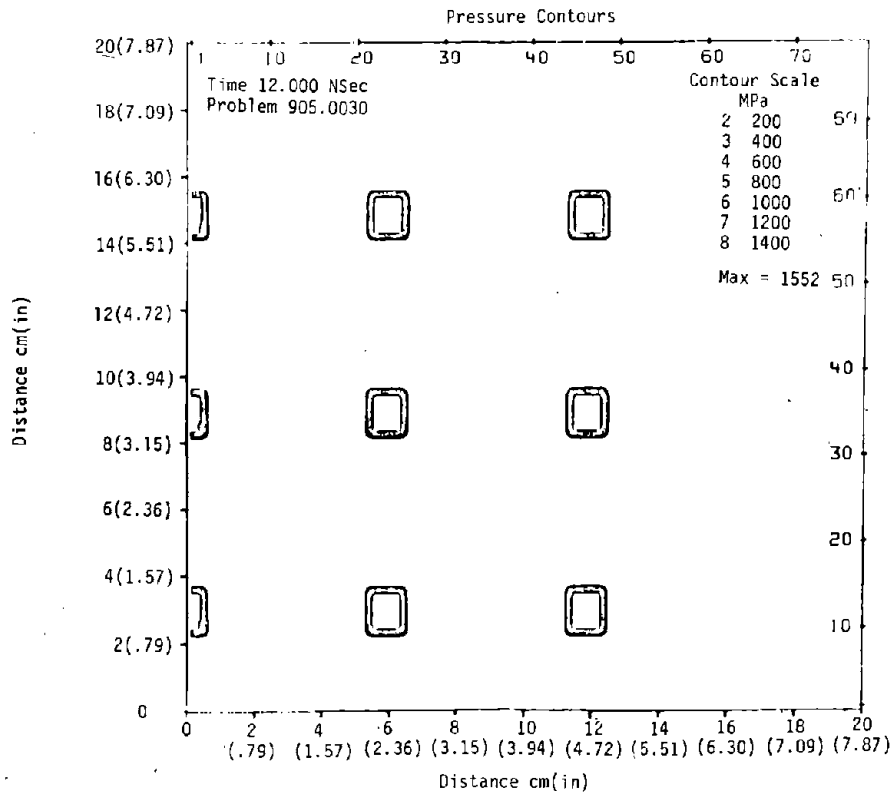
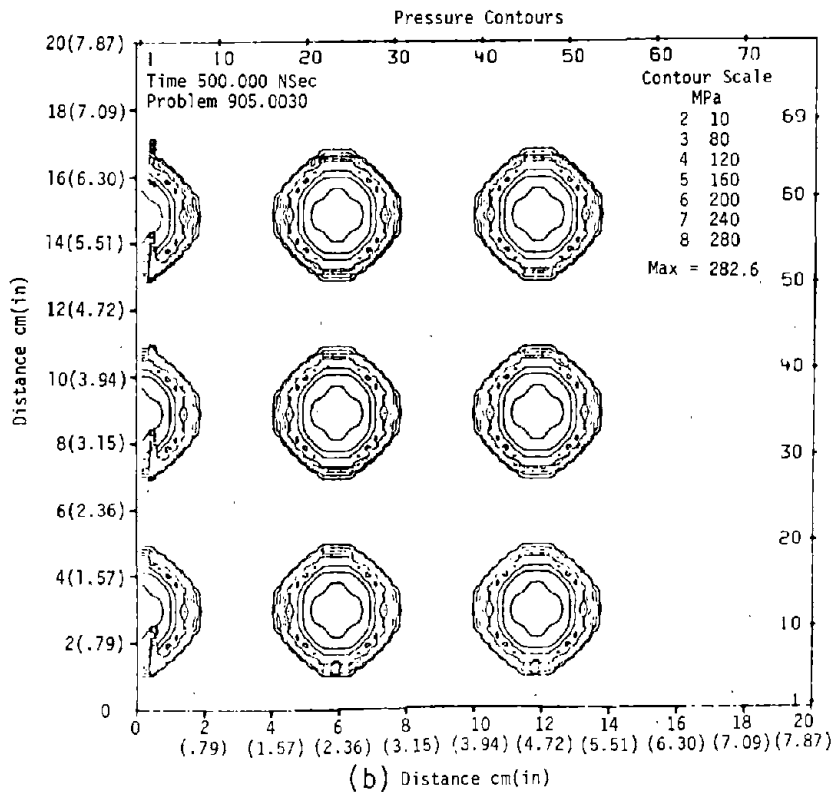


Figure 9. HULL Computational Grid (Distributed Explosive Array)



(a)



(b) Distance cm(in)

Figure 10. HULL Calculation (Distributed Explosive Array at 12 and 500 ns)

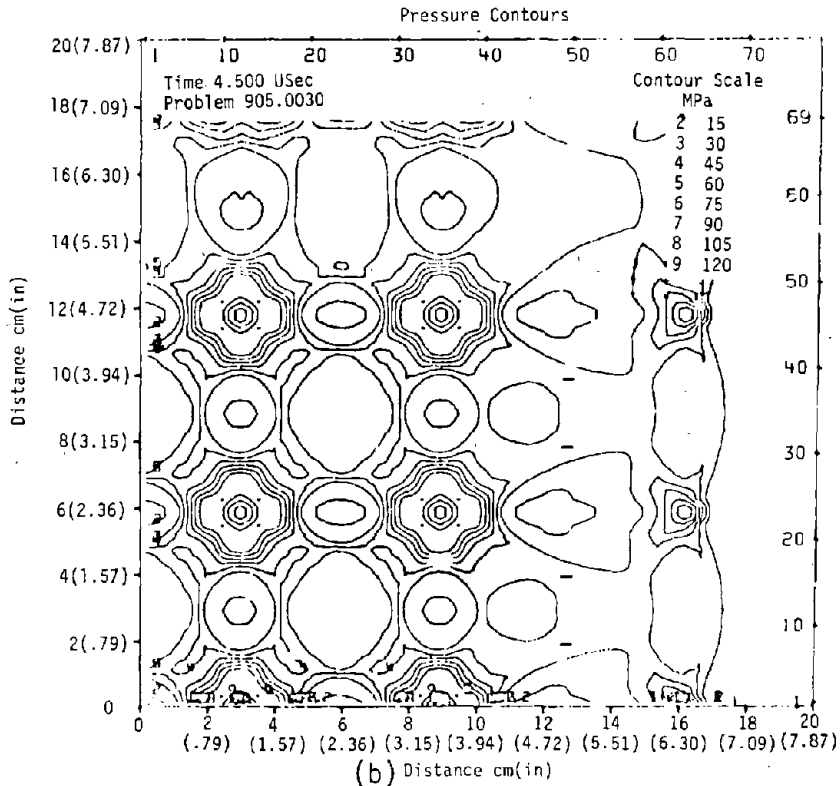
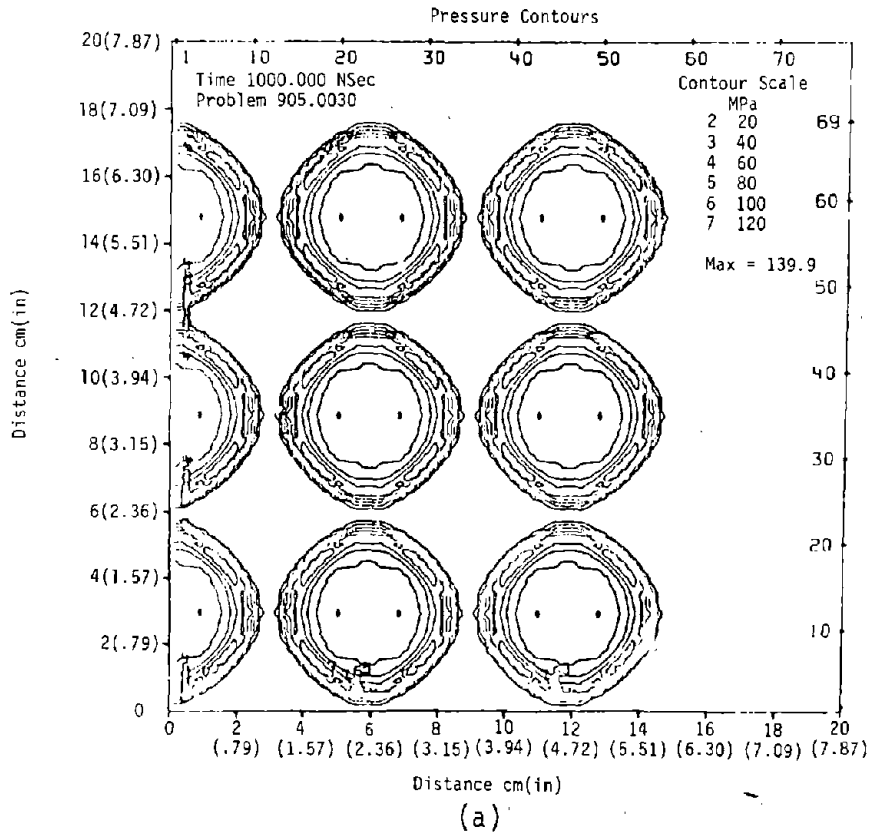


Figure 11 HULL Calculation (Distributed Explosive Array at 1000 ns and 4.5 μ s)

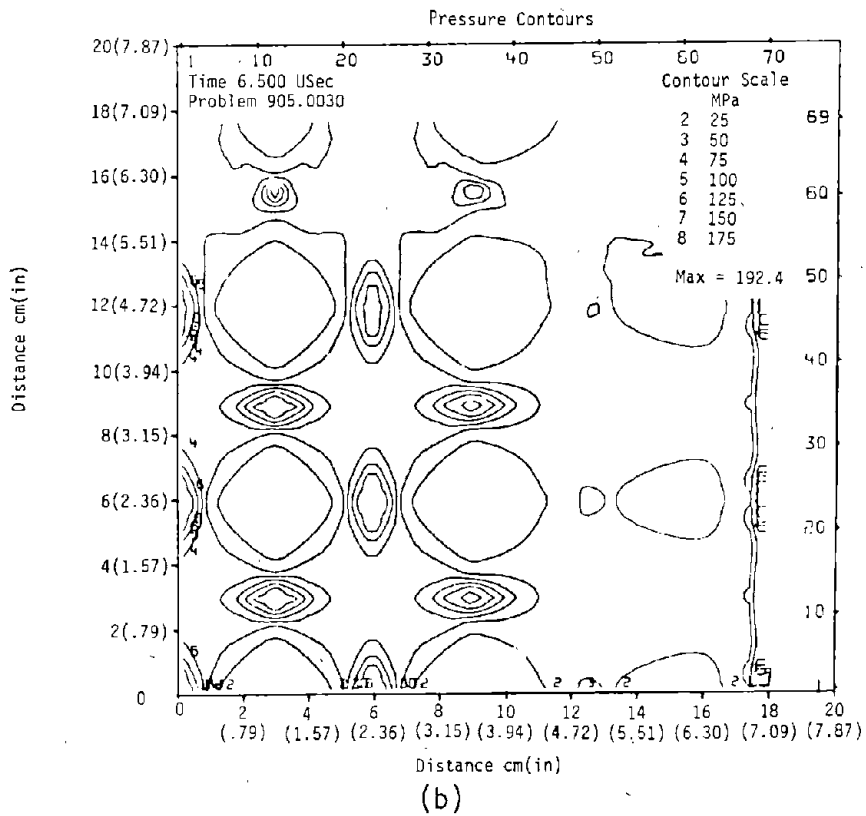
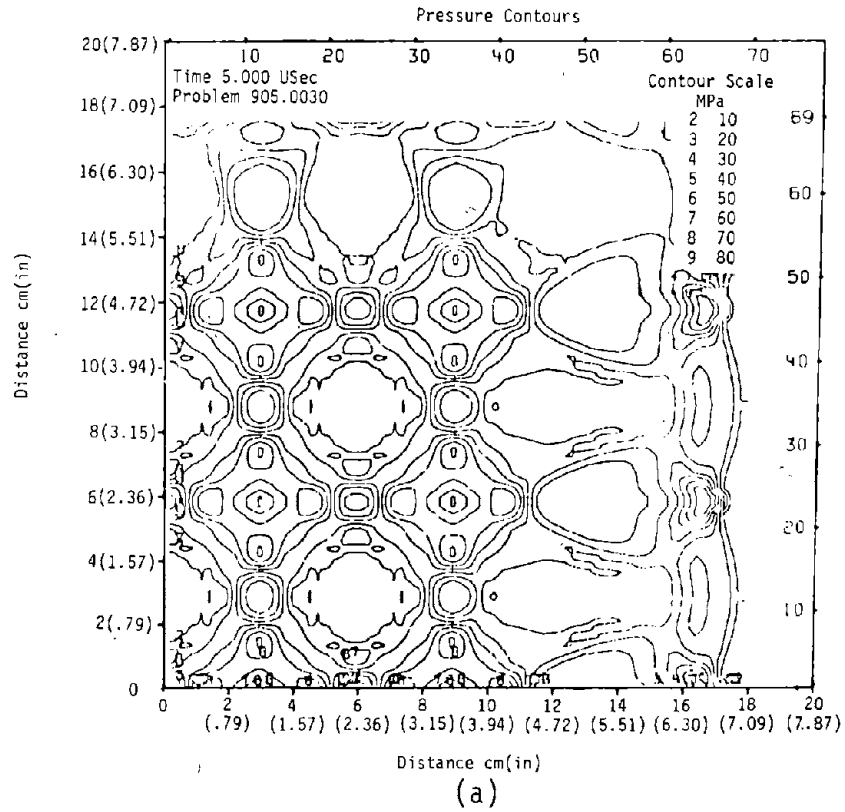
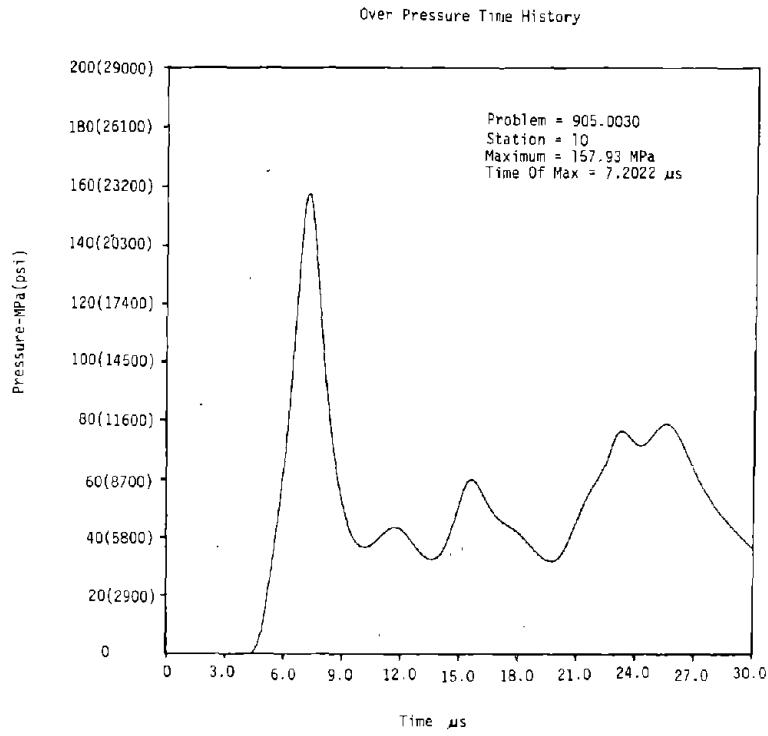
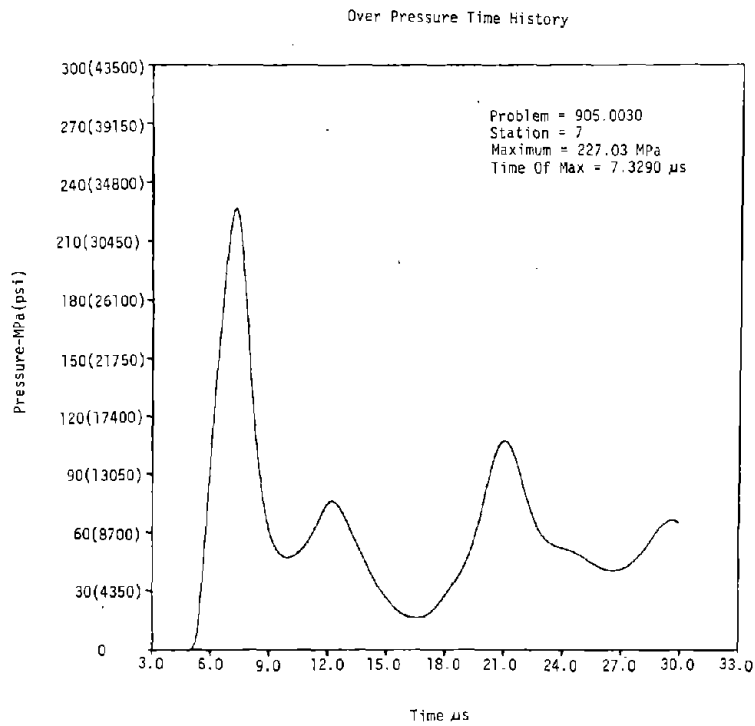


Figure 12. HULL Calculation (Distributed Explosive Array at 5 and 6.5 μ s)



(a)



(b)

Figure 13. HULL Calculation (Distributed Explosive Array - Pressure Time Histories)

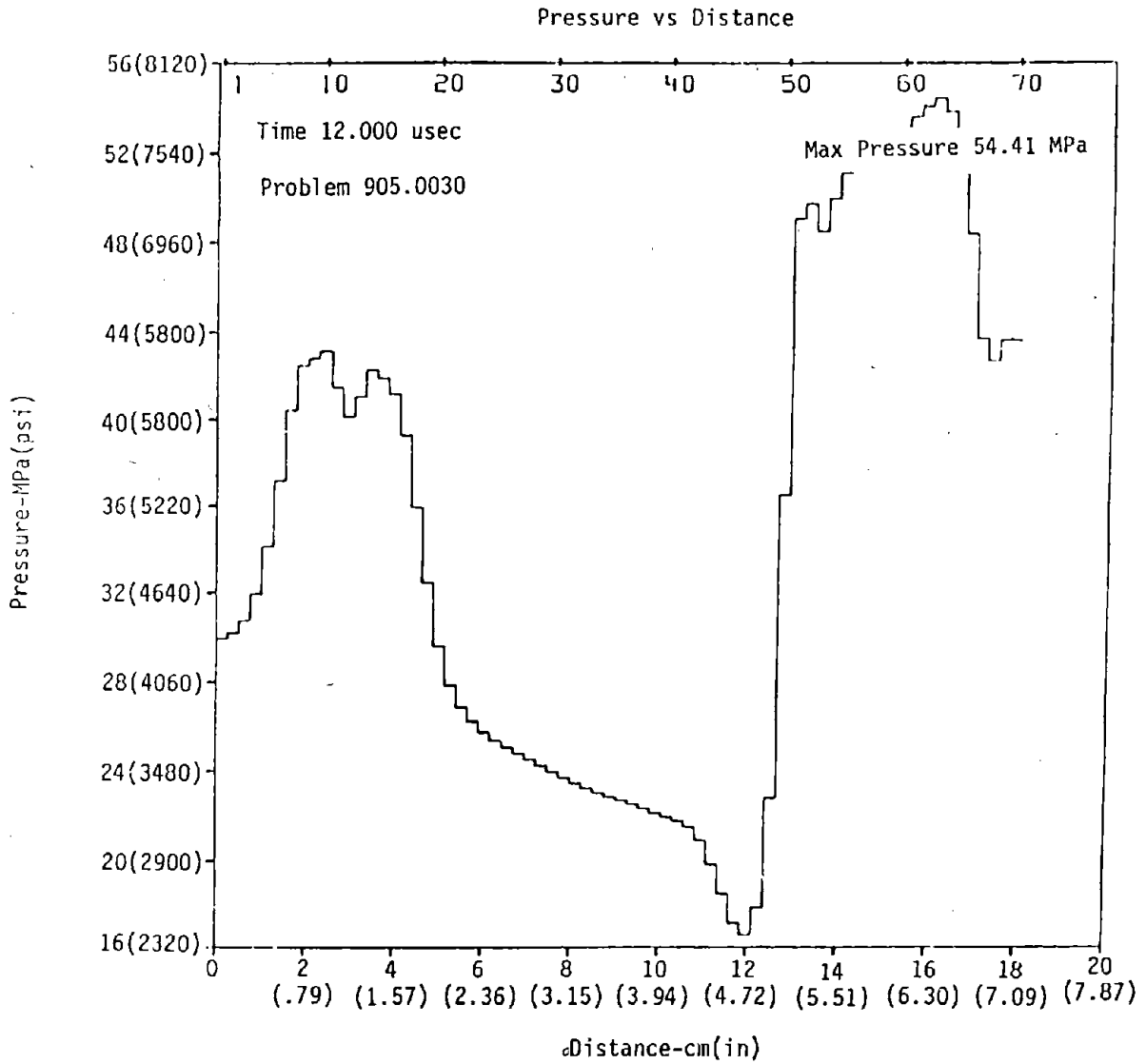


Figure 14

Figure 14. HULL Calculation (Distributed Explosive Array - Pressure Versus Range)

Simulation of HEST/H0rs I-3 Det Cord Array

Geometry - 2-D Cartesian

Boundary Conditions - Reflective

Initial Conditions - Standard Atmosphere MSL

EOS - Fixed Gamma Law

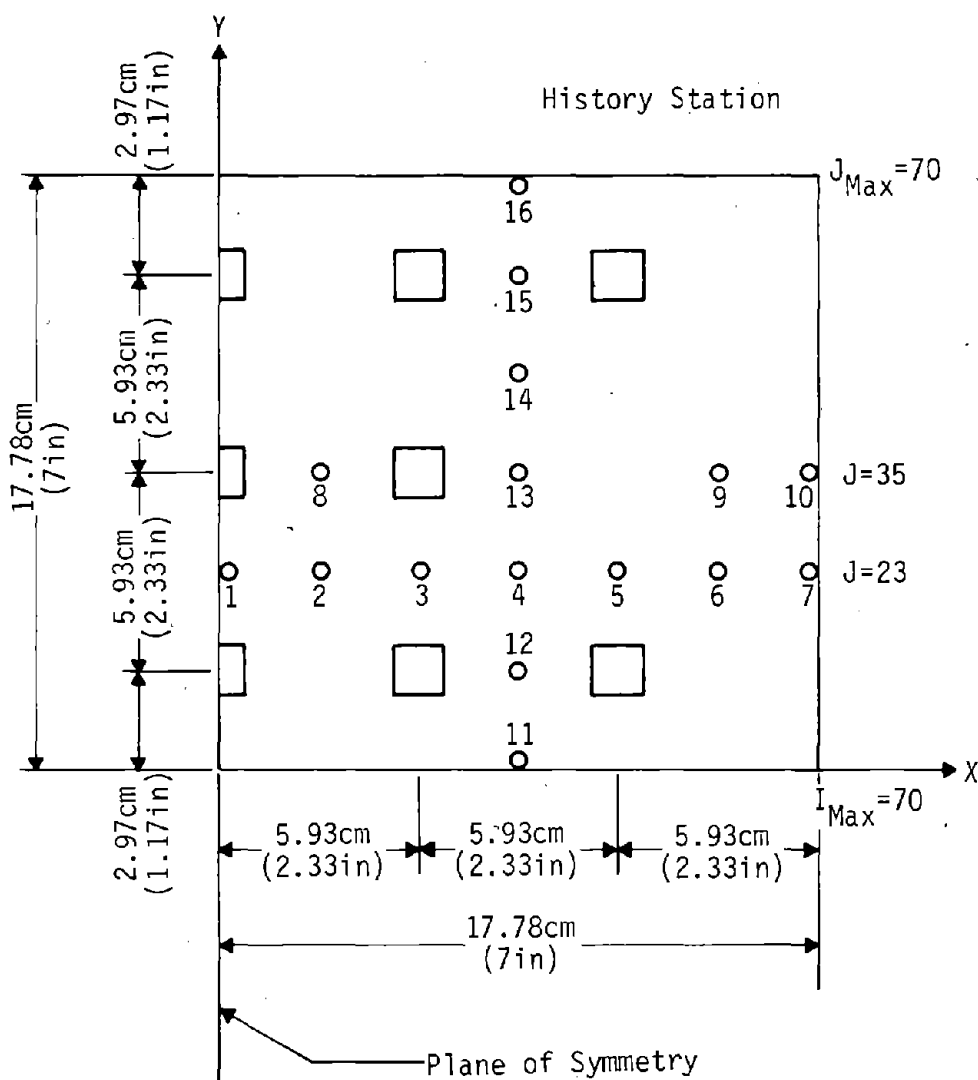
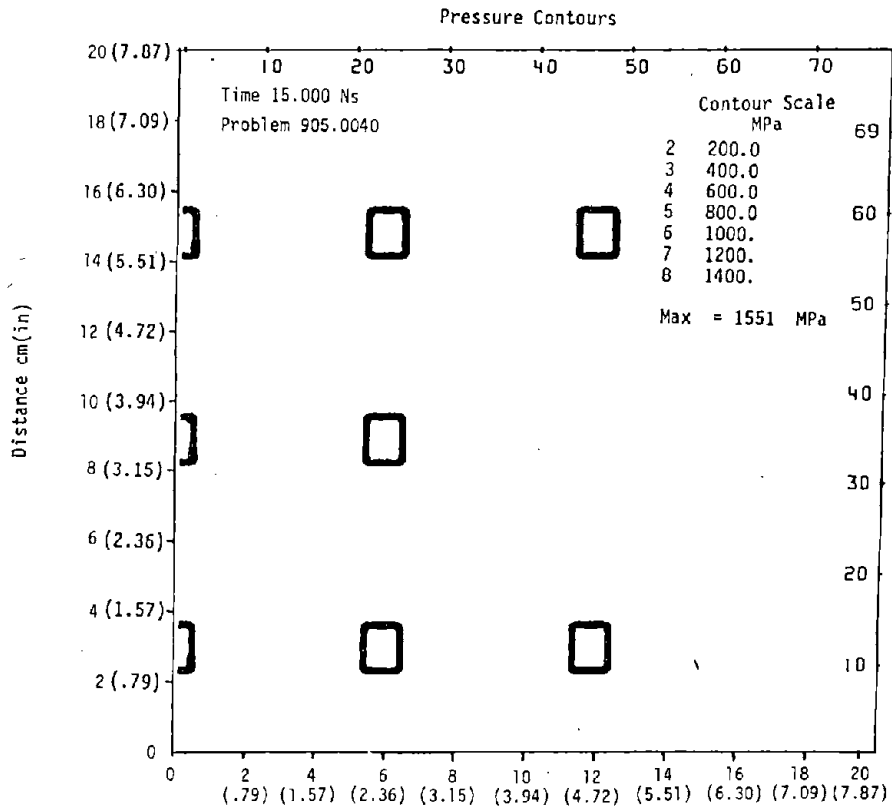
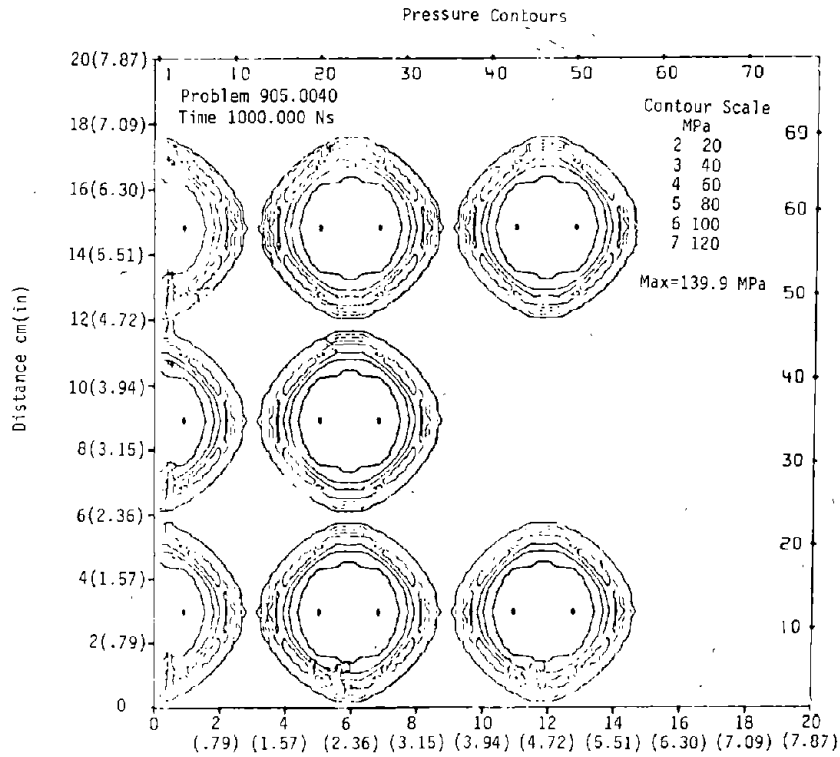


Figure 15. HULL Calculational Grid (Modified Distributed Explosive Array)



(a) Distance cm(in)



(b) Distance cm(in)

Figure 16. HULL Calculation (Modified Distributed Explosive Array at 15 and 1000 ns)

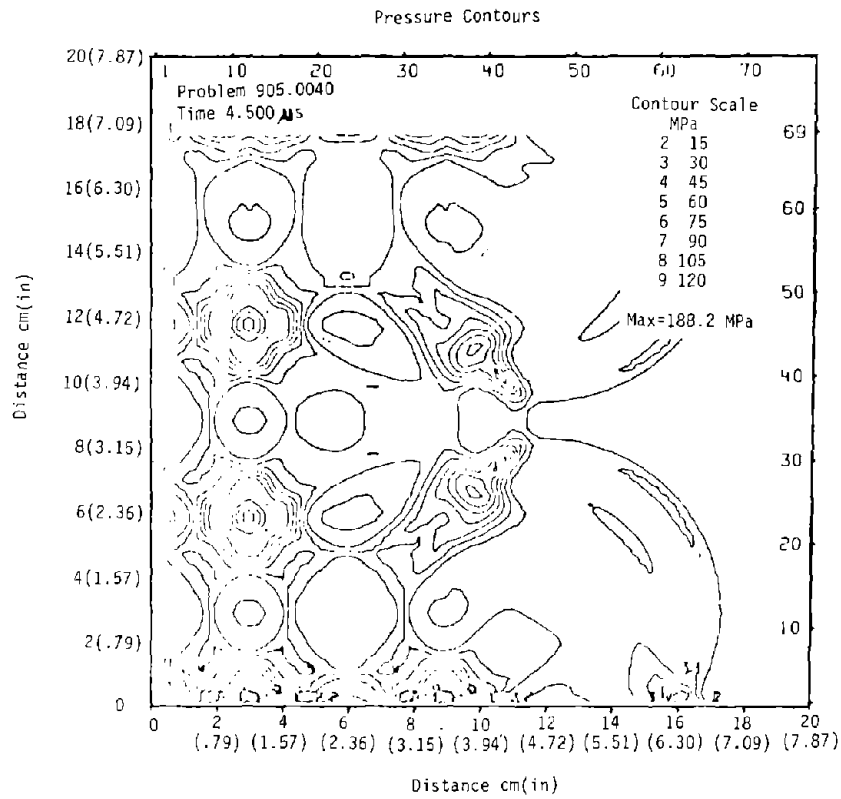
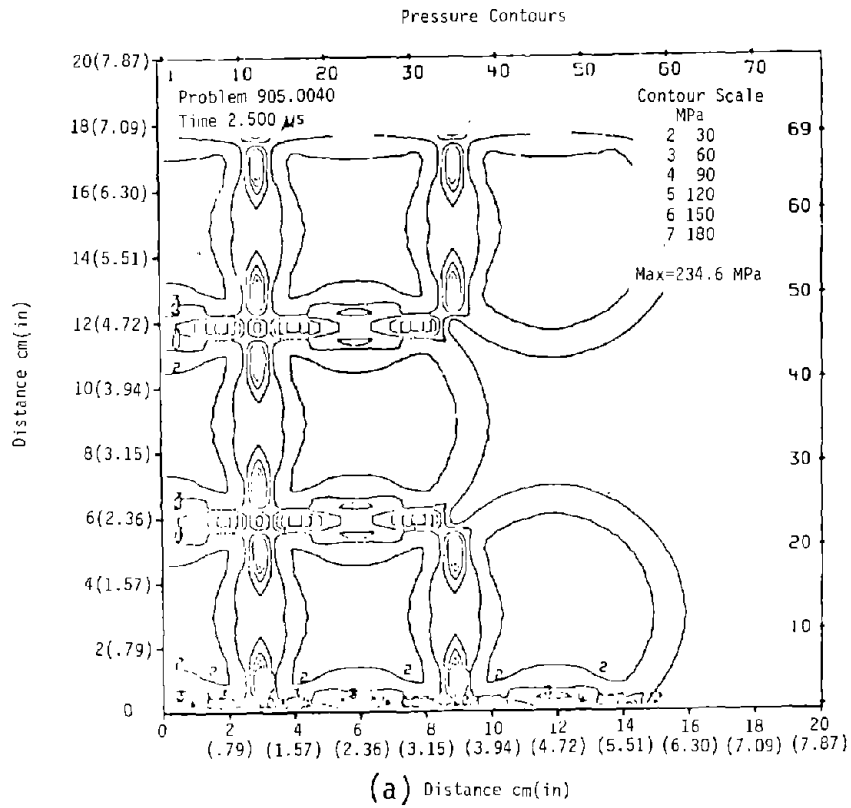
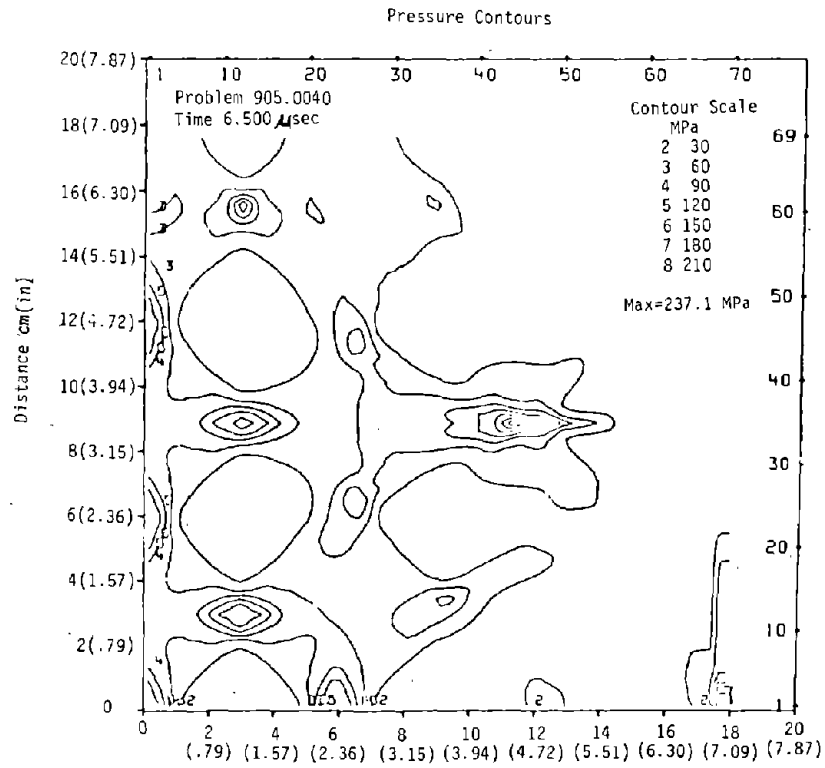
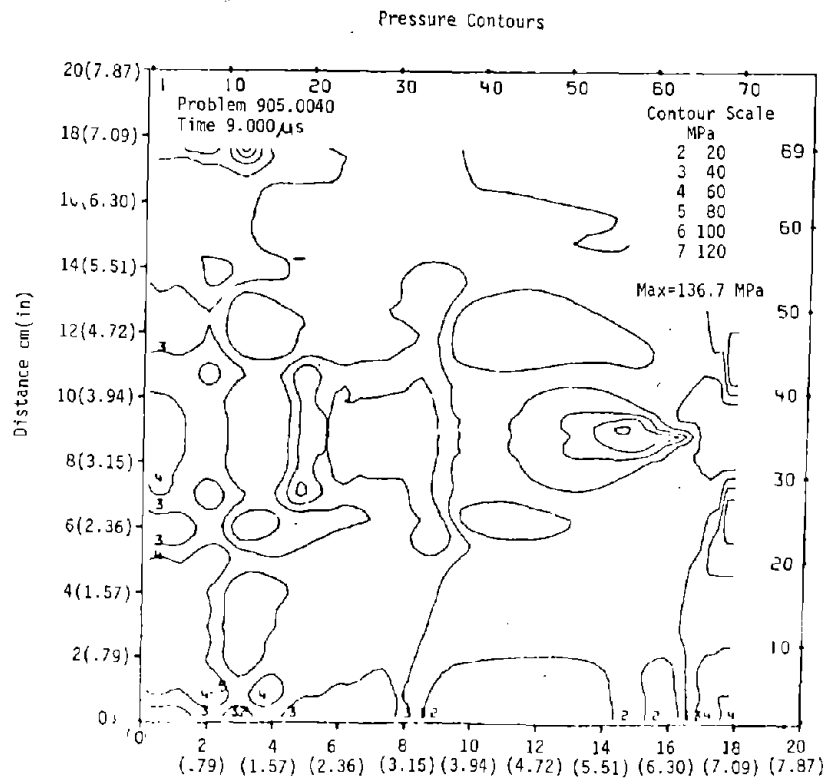


Figure 17. HULL Calculation (Modified Distributed Explosive Array at 2.5 and 4.5 μ s)



(a) Distance cm(in)



(b) Distance cm(in)

Figure 18. HULL Calculation (Modified Distributed Explosive Array at 6.5 and 9 μ s)

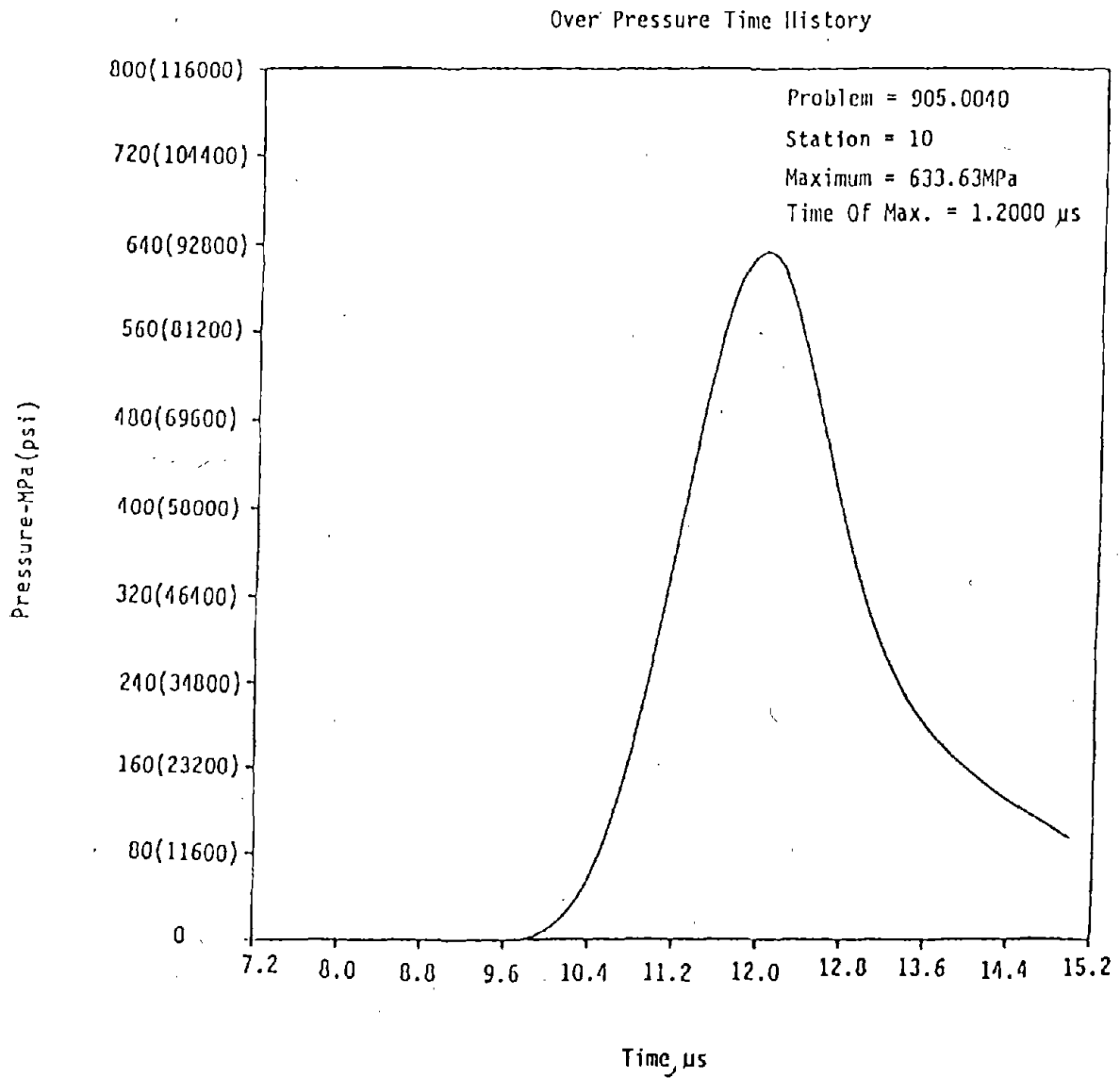


Figure 19. HULL Calculation (Modified Distributed Explosive Array - Pressure Time History)

IV. DABS SIMULATOR CALCULATIONS

In calculating DABS experiments, primary consideration was given to calculation of the propagated blast wave. The first assumptions made were that the boundaries of the DABS simulator facility were perfectly reflecting and non-expanding. Because the presence of test structures was ignored, one-dimensional SAP calculations would be sufficient.

The first series of calculations were made to model the DABS I-E event and used detonating cord as the driver explosive. The calculation modeled the detonating cord by averaging its mass over the volume in which it was placed. The resulting charge density was 0.12 g/cm^3 (7.49 lb/ft^3).

Three calculations were made while varying only the energy density of the explosive driver. The uncertainties in the energy density were introduced by the mixture of air, explosive, plastic wrapping material and other mass present in the driver section. Runs were made with energy densities of 2×10^{10} and 3×10^{10} ergs/g. Results were compared with DABS I-E experimental data and an energy density interpolated. The third calculation used an energy density of 2.2×10^{10} ergs/g. Agreement between this calculation and experimental data was excellent (Figs. 20 and 21).

These calculations served several purposes. The agreement between calculation and experiment shows that expansion and venting played essentially no role in the experiment for pressures between 13.79 and 3.45 MPa (2000 and 500 lb/in^2). The initial conditions, although simple, are sufficient to define the blast for detonating cord drivers. All three calculations, including plots, used less than \$100 of computer time and thus established the availability of a powerful yet very economical tool for definition and prediction of detonating cord-driven DABS experiments.

Because of the expense of detonating cord, a low-cost explosive was used for the DABS-2A and 2B experiments. The explosive chosen was Iregel 475-C. This choice presented severe problems for theoretical computer predictions since the explosive was not well characterized. As a matter of fact, for all practical purposes, the detonation characteristics of the explosive were unknown. Using the data provided by the manufacturer, an approximate equation of state was developed and a series of calculations made.

The first calculation used an isothermal region similar to that used in the DABS-1E calculation. Results were not in good agreement with data in that the calculated decay of the propagated pressure was significantly greater than observed in the experiment. Simply adjusting the energy density did not rectify the differences.

A detailed one-dimensional burn calculation was undertaken. The resulting pressure exceeded that measured by more than a factor of two, but the decay paralleled the measured data. A second-burn calculation was made using 40 percent of the detonation energy (Figs. 22 and 23). The pressure decay was in good agreement with the experimental data, but peak pressures fell generally above the experimental data. An additional 10-percent reduction in energy would have better matched the experiment.

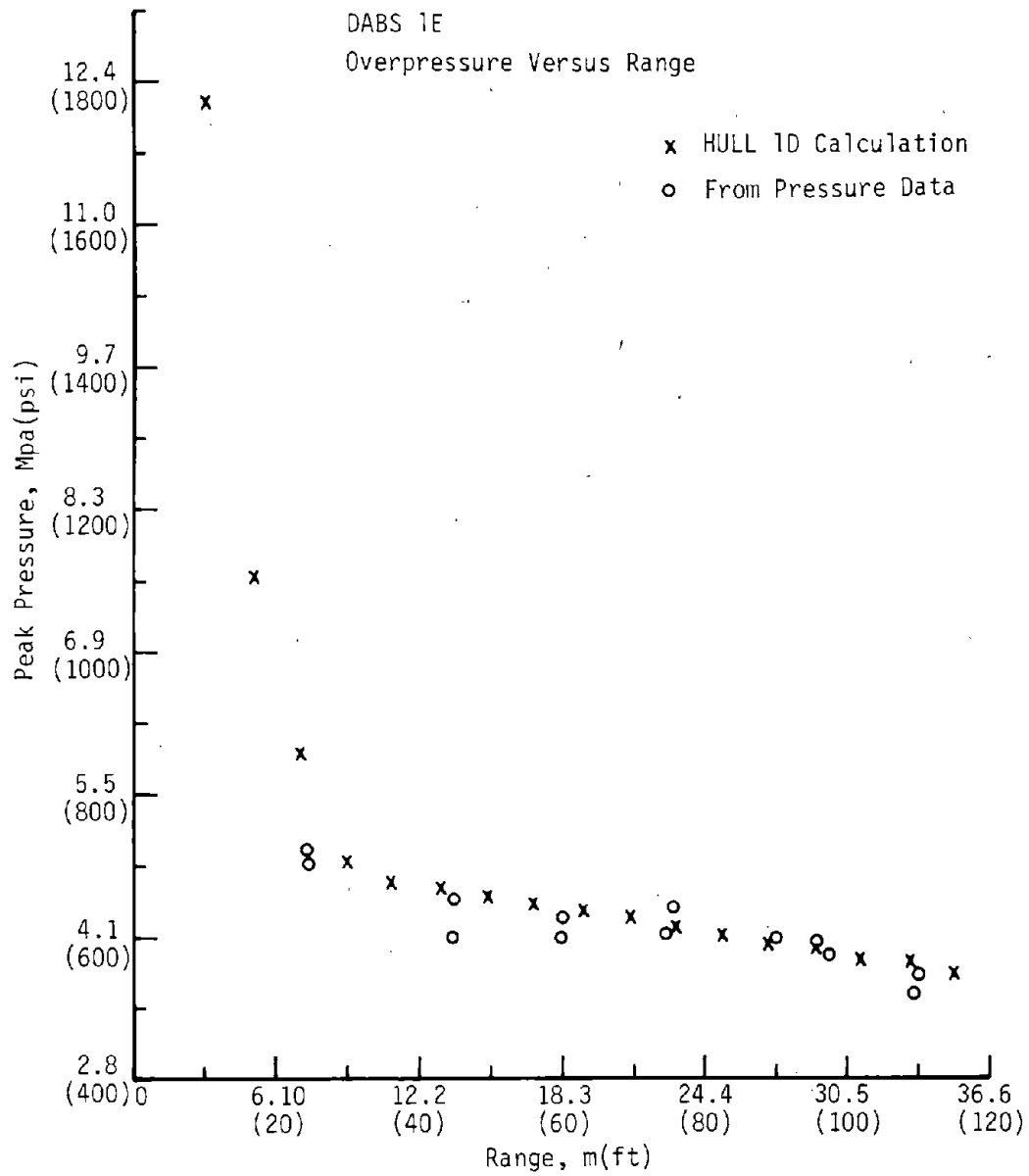


Figure 20. Overpressure Versus Range (DABS 1E)

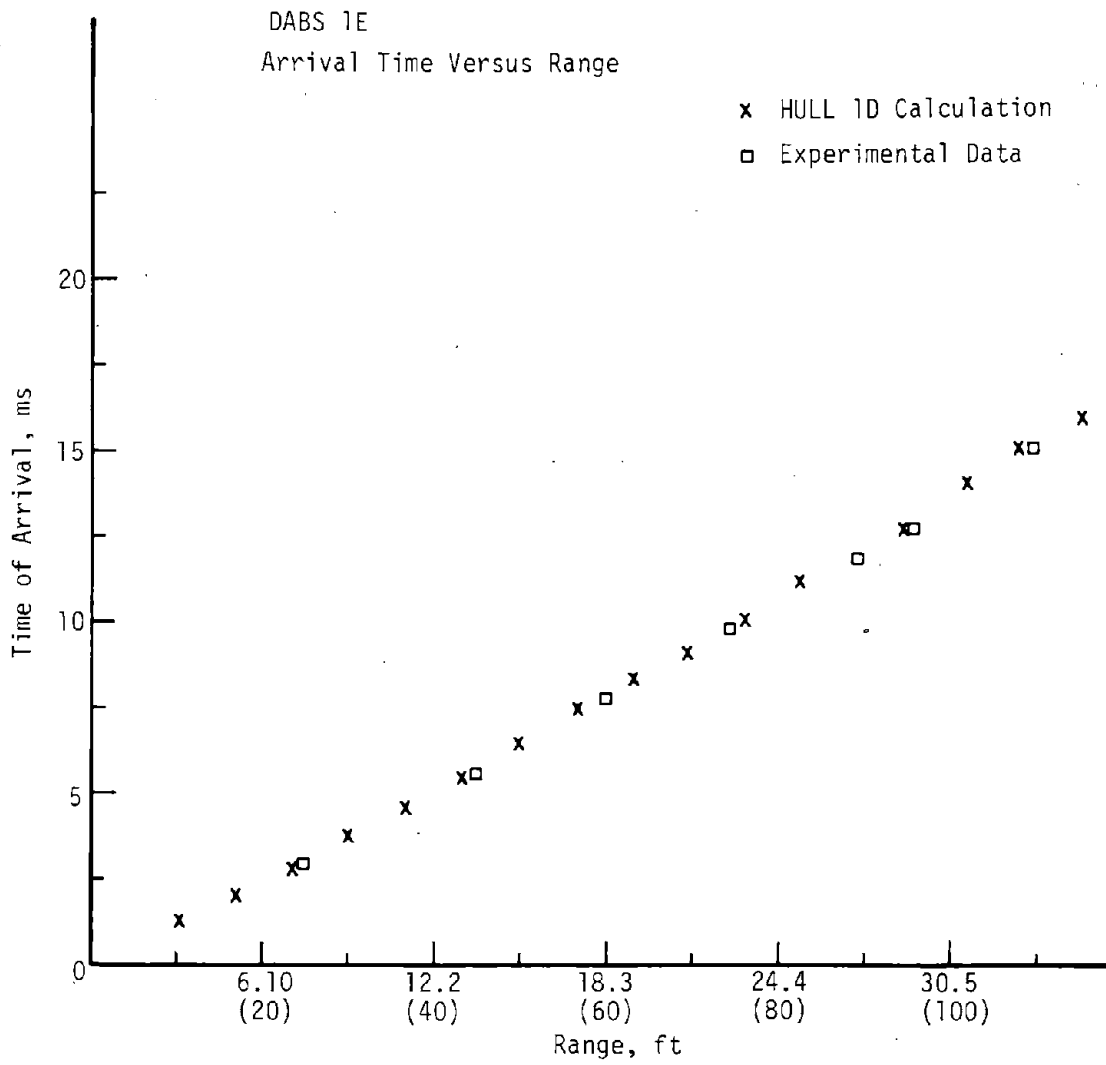


Figure 21. Arrival Time Versus Range (DABS 1E)

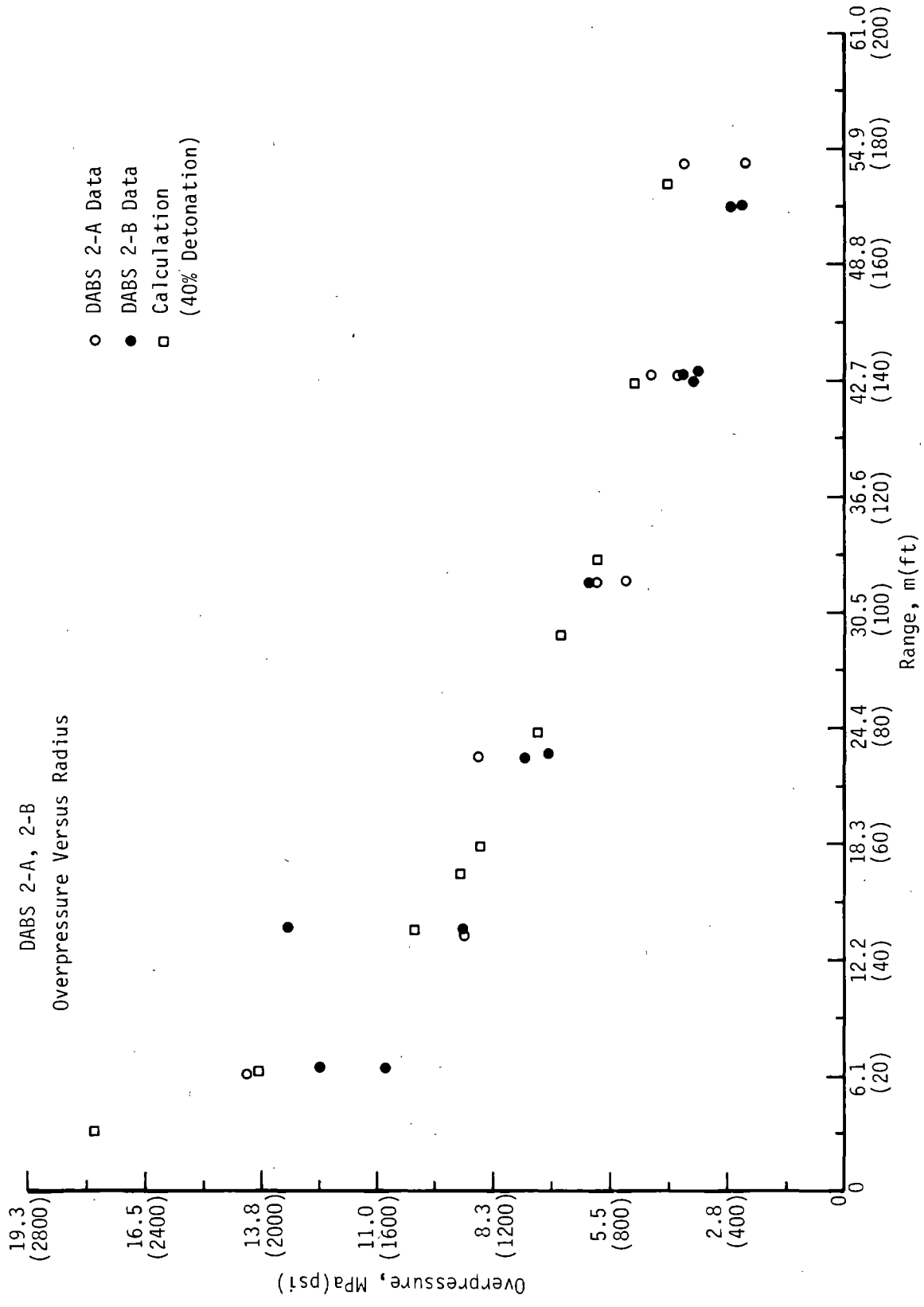


Figure 22. Overpressure Versus Range (DABS 2A and 2B)

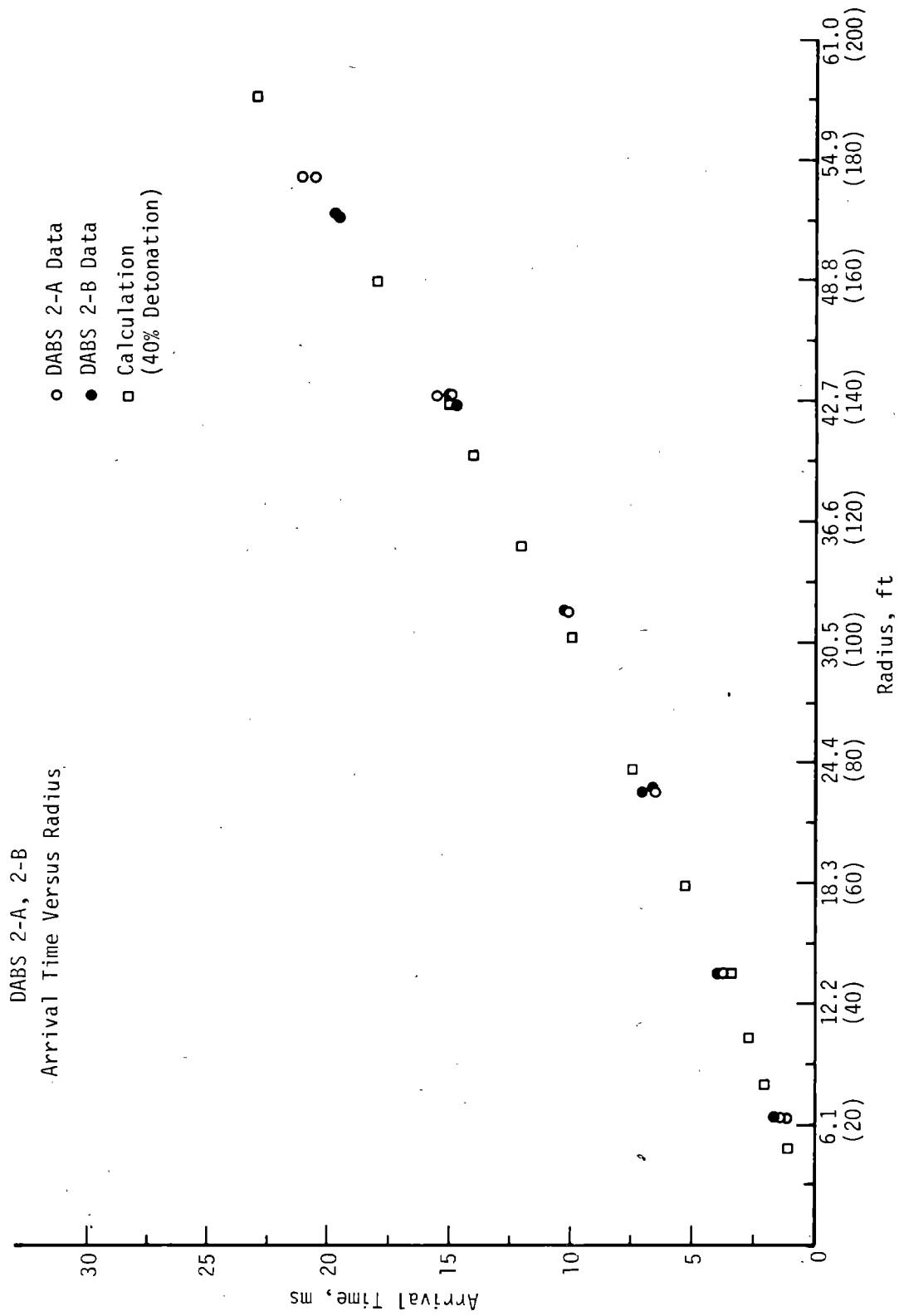


Figure 23. Arrival Time Versus Range (DABS 2A and 2B)

The results of these calculations indicated that the simple isothermal region which worked so successfully for detonating cord did not work for solid explosives. The momentum and kinetic energy distribution close to the charge are important to the propagation of the shock and must be properly modeled. The necessity for reducing the detonation energy of the explosive indicated either poor detonation or improper description of the detonation properties.

The DABS-2C event used an explosive called Iretol which suffered the same shortcomings as the Iregel. Iretol was found to be somewhat more energetic than Iregel but had inconsistent detonation properties. By adjusting the detonation energy used in the calculation, the experimental data were reasonably well matched (Fig. 24).

The DABS series of experiments, coupled with calculations, permitted resolution of several questions regarding blast propagation in the facilities. The fact that simple one-dimensional calculations matched the data over the entire range meant that boundary layers, expansion, and venting played an insignificant role in shock propagation. The amount of explosive is not the only important parameter. The placement and detonation of solid explosives in the driver section are also important considerations.

The DABS development tests provided the basis for the large-scale HAVE HOST S and T tests as well as other experiments including plug-in-trench tests. Supporting calculations were accomplished for a number of these tests. Some of the more interesting aspects of the more complex geometry calculations and experiments have been compared.

The S-1 test used detonating cord in the driver section. The experience with DABS-1E indicated that an isothermal region approximation would be sufficient to define the blast propagation for the S-1 experiment (Fig. 25). The results indicate that boundary layers, expansion, and venting were not important in the S-1 test. The presence of the structure made significant changes to the propagated shock.

All other S and T tests used Iretol for the driver explosive. In all cases it was found that calculations using 50 to 60 percent of the ideal detonation energy predicted the blast propagation in a satisfactory manner. This was consistent with the DABS-2C experience.

The T-1 test included several meters of ribbed trench section between the driver and the plug being tested. The effects of the ribs for the flow conditions present were minor, of the order of 10 percent in overpressure and arrival time. The ribs delayed the arrival time and slightly decreased the peak pressures (Figs. 26 and 27).

For more complete modeling of the phenomenology of the S and T tests, it was necessary to make two-dimensional calculations using the HULL code. The inclusion of the shelter was primarily to define the loads on the shelter. Two-dimensional calculations were made for front, side, and rear incidence. A second shock was observed incident on the shelter and was hypothesized to be a reflected shock from the roof of the DABS facility (Figs. 28 and 29). Close examination of the calculations indicated that this was indeed the case. Two additional calculations defined the effect of the height of the roof of the DABS facility on the timing and magnitude of reflected shock at the shelter.

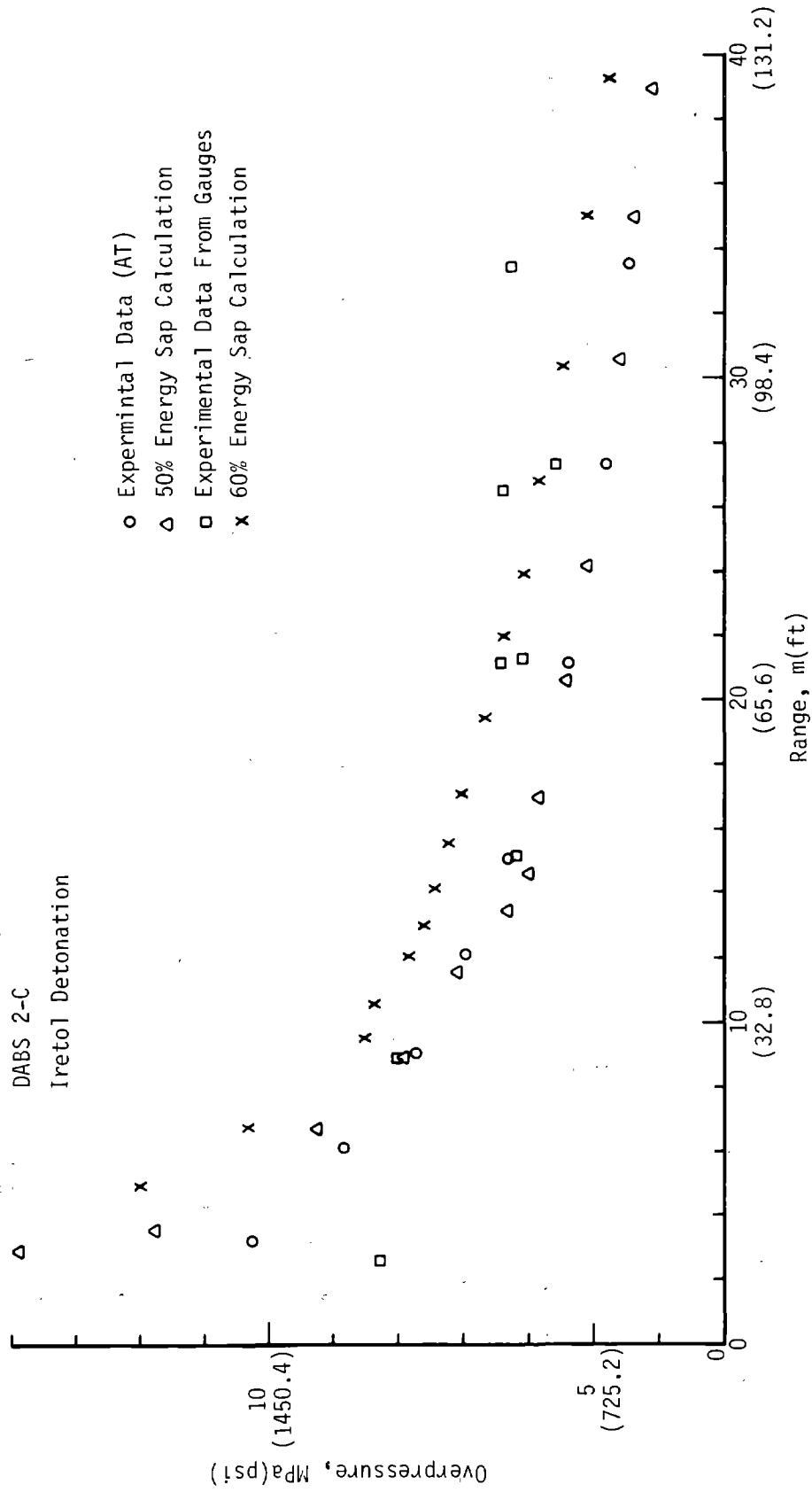


Figure 24. Overpressure Versus Range (Ireto1 Detonation, DABS 2C)

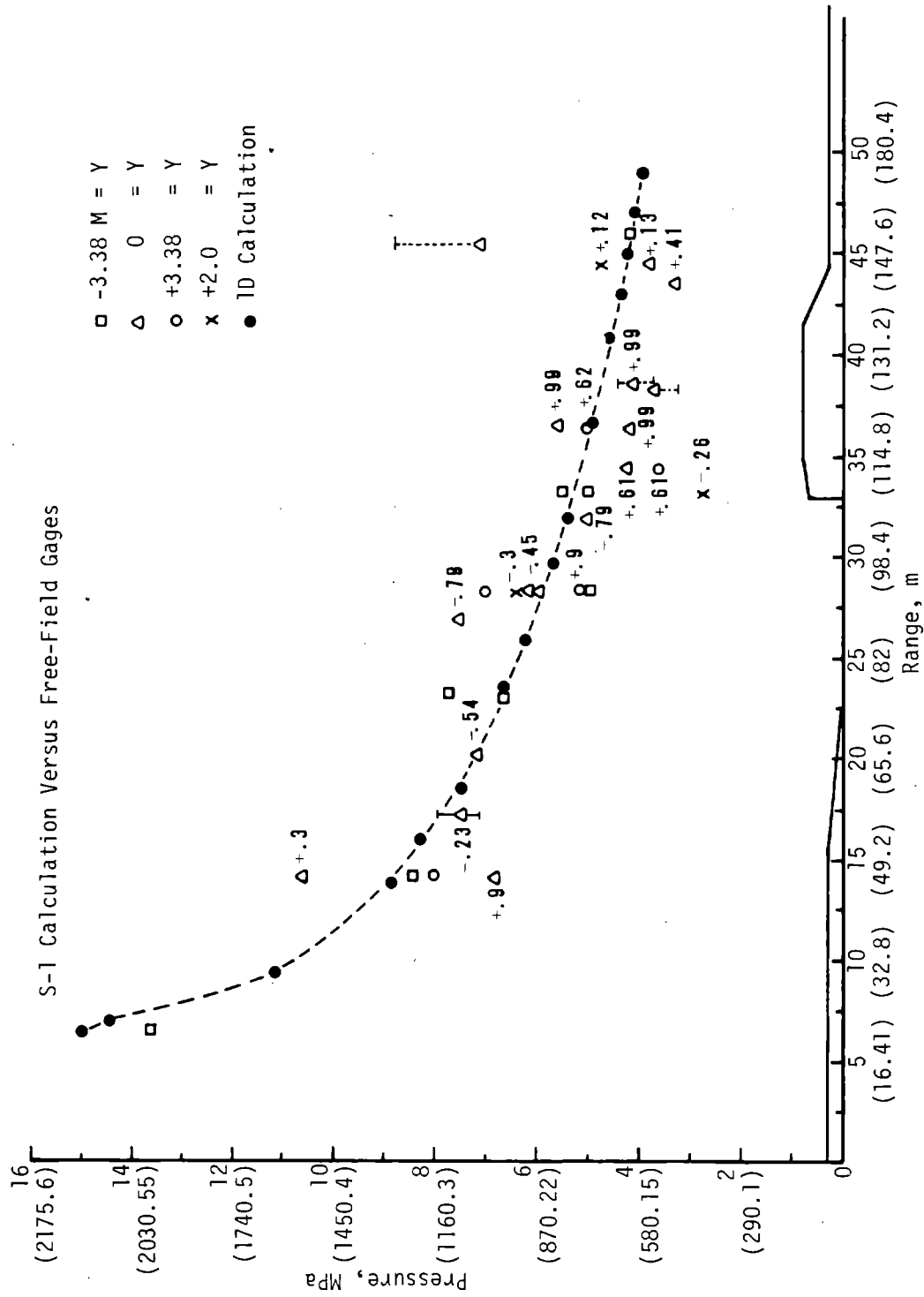


Figure 25. Overpressure Versus Range S1 Event)

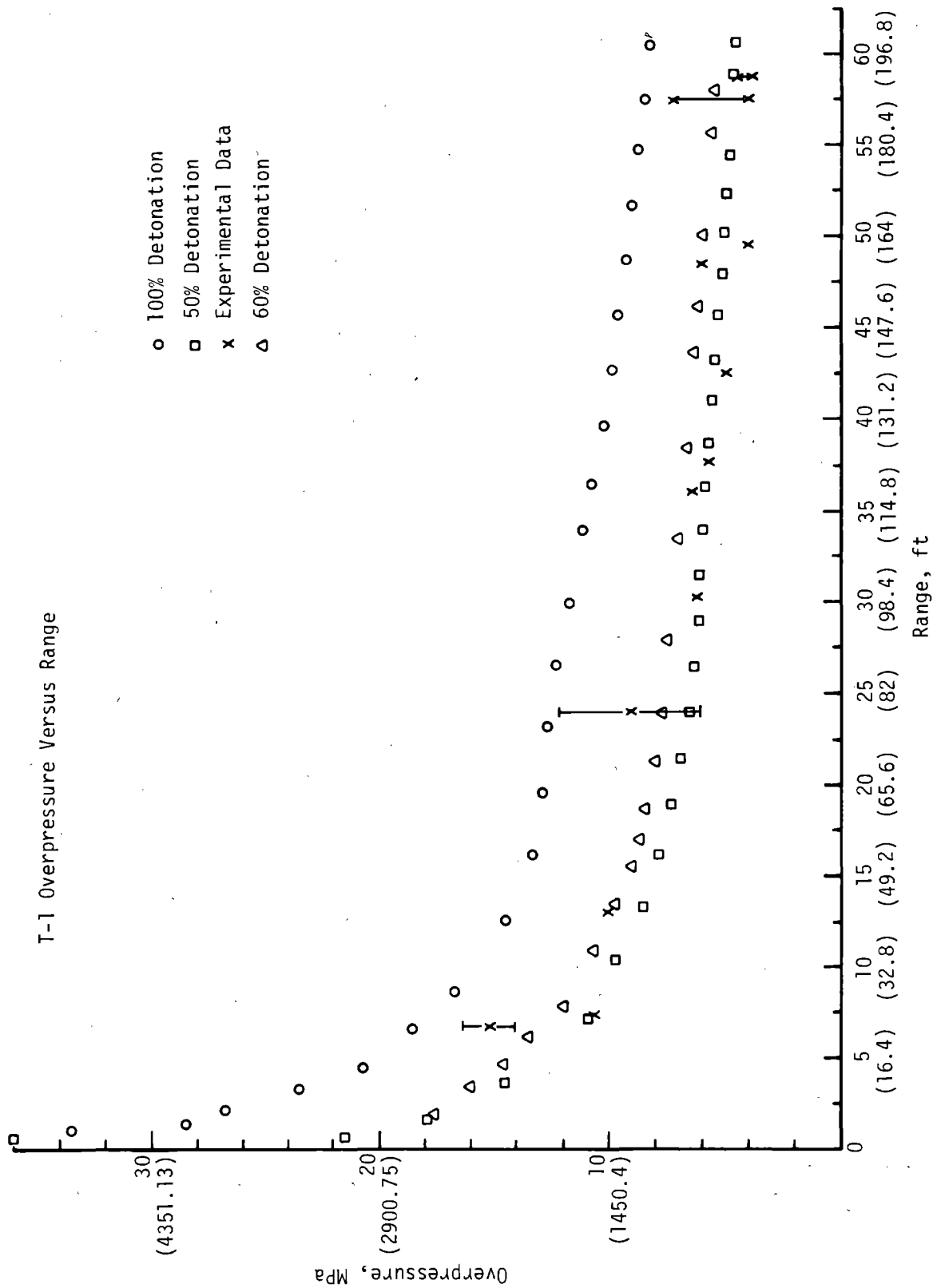


Figure 26. Overpressure Versus Range (T1 Event)

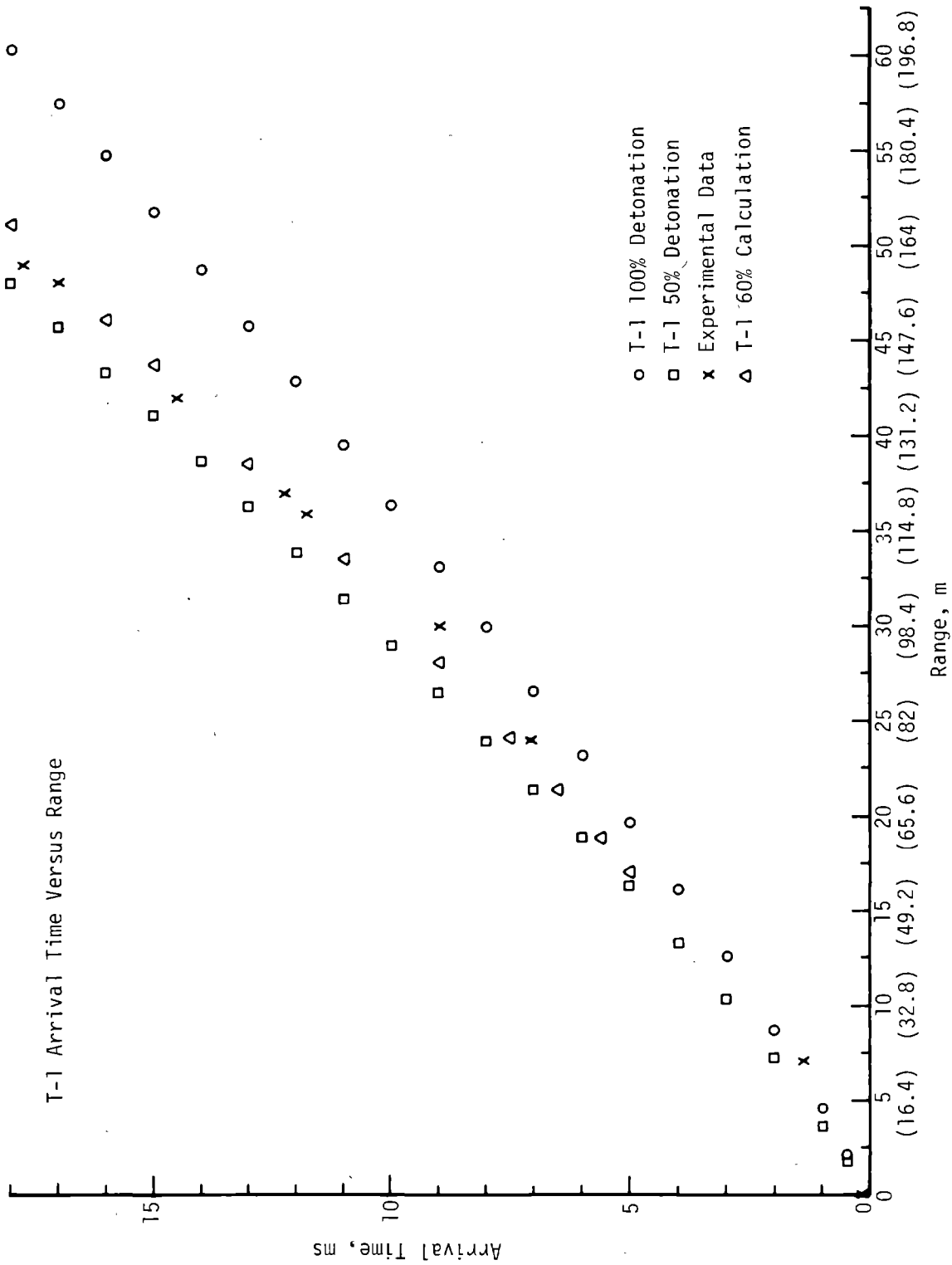


Figure 27. Arrival Time Versus Range (T1 Event)

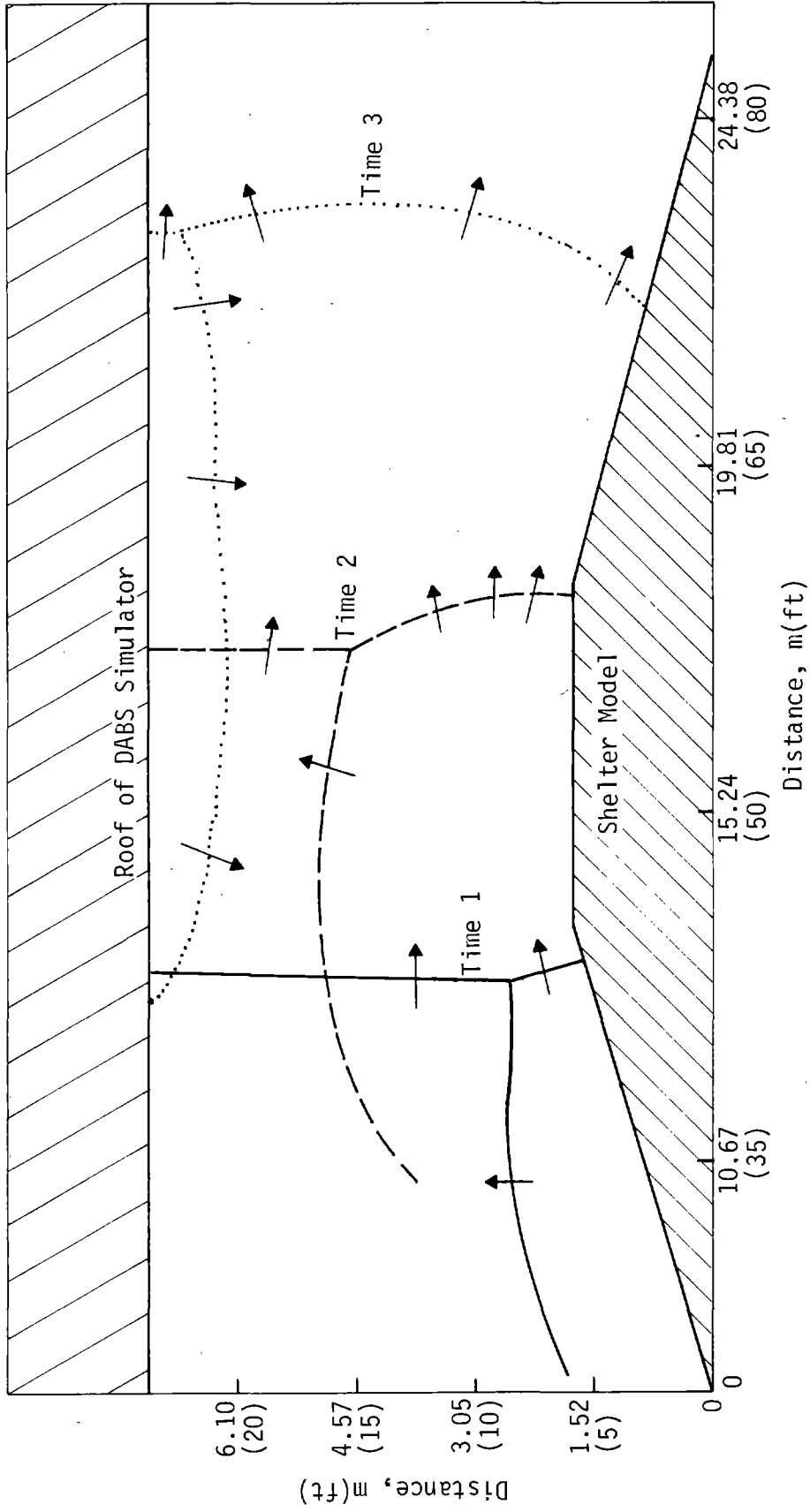


Figure 28. Effect of DABS Roof and Shelter Model on Shock Position.

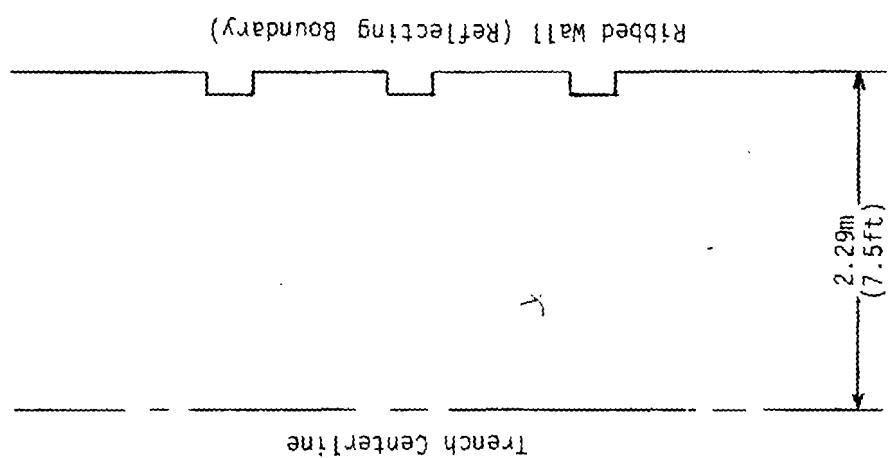
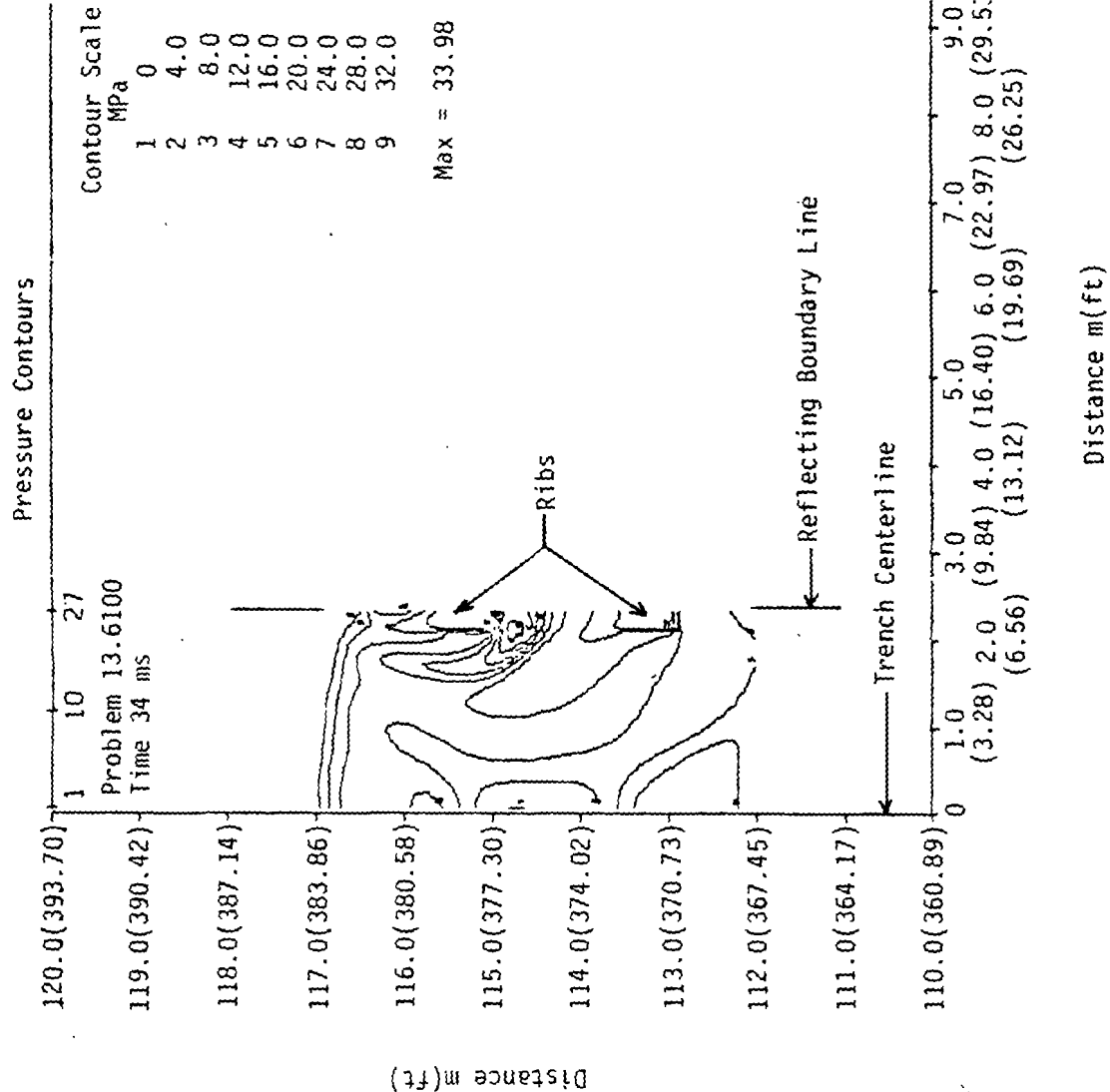


Figure 29. HULL Calculation of 1 Megaton in Corrugated Tube at 6.9 MPa (100 lb/in²)

Two-dimensional calculations were also made to define the effects of ribs in the walls of the trench. These calculations were made in sufficient detail that shock waves and rarefaction regions created by each rib were resolved. The shocks reflected from the concentric ribs converge and reflect on the centerline (Fig. 29). The waveform seen at any point in the ribbed section consists of a number of shocks, the first of which is, in general, not the maximum pressure attained. The relative magnitudes of the peaks and their timing are functions of the shape and size of the ribs, their spacing, and the flow conditions in the pipe as well as the position of the gage relative to the ribs.

The ribs retard the flow and create shocks which redistribute the energy behind the shock front. The shock front becomes a curve in which the center is more advanced than the edges. The arrival time is therefore a function of radial position. Because of the redistribution of energy, the peak pressure may not be derived from the Rankine Hugoniot conditions and the arrival time. Attempts to measure the overpressure directly will not properly represent the overall flow conditions and will result in considerable scatter in the data because of the multiple shock fronts.

One-dimensional calculations, such as described earlier for T-1, are only successful at predicting average behavior. For example, the one dimensional T-1 calculation that used 50-percent energy matched the measured arrival times, while the calculation with 60-percent energy agreed with the peak overpressure. Two-dimensional calculations can provide the additional detail when necessary.

Recent experiments conducted by Science Applications, Incorporated at the National Space Agency Ames demonstrate that no significant (or measurable) boundary layer or viscous effects are present for many pipe diameters behind the shock front.

V. CONCLUSIONS

Since the plastic foam materials used in the construction of HEST experiments was modeled as an ideal gas or as air, the HEST calculations presented in this paper must be considered to be only *qualitative*. They serve, however, to demonstrate the substantial advances which have been achieved in hydrodynamic calculations in recent years. Numerous complex shock interaction problems which were beyond the state of the art can now be satisfactorily modeled. The incorporation into these codes of equations of state for additional materials (such as the plastic foams) and more realistic boundary conditions (such as compressible soil boundaries) will make possible *quantitative* calculations of HEST experiments.

The DABS experiments and similar tests provided data for quantitative comparisons with theoretical calculations. These comparisons provided an understanding of phenomena observed during the experiments which would otherwise have been misinterpreted or ignored. The few examples of recent DABS calculations presented here demonstrate the flexibility and power of state of the art hydrodynamic codes.

The examples of calculation presented here have served to answer a number of questions which have plagued the designers of nuclear airblast simulators and have provided valuable design information for future simulation experiments.

REFERENCES

1. Auld, H. E., D'Arcy, G. P., Leigh, G. G., *Simulation of Airblast-Induced Ground Motions (Phase II)*, AFWL-TR-65-26, Vol. I, Air Force Weapons Laboratory, Kirtland AFB, New Mexico, April 1965.
2. Auld, H. E., D'Arcy, G. P., Leigh, G. G., *Simulation of Airblast-Induced Ground Motions (Phase I)*, AFWL-TR-65-11, Air Force Weapons Laboratory, Kirtland AFB, New Mexico, April 1965.
3. Martens, D. P., Bradshaw, J. C., *Dynamic Airblast Simulator Parametric Series, Events I-A, I-B, I-C, I-D, and I-E Data Report*, AFWL-TN-76-018, Air Force Weapons Laboratory, Kirtland AFB, New Mexico, November 1976.
4. Bratton, J. L., Pratt, H. R., *Simulation of Airblast-Induced Ground Motions (Phase II A)*, AFWL-TR-66-85, Air Force Weapons Laboratory, Kirtland AFB, New Mexico, October 1967.
5. Sakurai, A., "On the Propagation and Structure of the Blast Wave, I," *Journal of the Physical Society of Japan*, Vol. 8, No. 5, September-October 1953.
6. Whitaker, W. A., et al, *Theoretical Calculations of the Phenomenology of HE Detonations*, AFWL-TR-66-141, Vol. 1, Air Force Weapons Laboratory, Kirtland AFB, New Mexico, November 1966.
7. Graham, D. C., Gaby, L. P. II, and Rhoades, C. E., Jr., *SAIL, An Automated Approach to Software Development and Management*, AFWL-TR-(Prepublication), Air Force Weapons Laboratory, Kirtland AFB, New Mexico, October 1976.
8. Fry, M. A., et al, *The HULL Hydrodynamics Computer Code*, AFWL-TR-76-183, Air Force Weapons Laboratory, Kirtland AFB, New Mexico, September 1976.
9. Hilsenrath, J., Green, M. S., and Beckett, C. W., *Thermodynamic Properties of Highly Ionized Air*, SWC-TR-56-35, National Bureau of Standards, Washington, D.C., April, 1957.
10. Doan, L. R., and Nickel, G. H., *A Subroutine for the Equation of State of Air*, RTD (WLR) TM-63-2, Air Force Weapons Laboratory, Kirtland AFB, New Mexico, May 1963.
11. Needham, C. E., *Development of an Artificial Viscosity Function*, AFWL TR-77-53, Air Force Weapons Laboratory, Kirtland AFB, New Mexico, August 1977.

I. INTRODUCTION

The development of a permanent reusable fuel-air-explosive (FAE) blast facility would greatly facilitate the simulation of free-air blast waves from nuclear events for yields as high as 1 KT. The work reported herein was performed for the purpose of investigating the feasibility of such an FAE blast simulator. To accomplish this objective, a test facility was developed for small-scale fuel dissemination and detonation experiments. The facility consisted of a fuel dispenser with a hemispherical nozzle head which was pressurized to force fuel through nozzles to form 9.1 m (30 ft) diameter hemispherical FAE clouds. After sufficient delay for fuel-air mixing, the clouds were detonated. The test pad was instrumented with gauges for measuring both side-on (static) and stagnation pressures. These gauges, together with high-speed photography, provided sufficient data to determine cloud detonability, cloud symmetry, and detonation efficiency. The blast waveforms generated in this manner were scaled and compared with nuclear blast wave data. The agreement between the FAE data and the nuclear data indicated that the use of FAE as a nuclear blast wave simulator is indeed feasible, at least on the small scale.

Results from a scaling investigation indicate that a full-scale facility for simulating 1 KT nuclear blast waves requires the dissemination of 85,400 kg of fuel into hemispherical clouds 142 m in diameter. For such a facility it would, therefore, be required to project fuel a distance of 71 m and do so in such a manner as to form a detonable fuel-air mixture. Initial results from a current investigation involving full-scale single nozzle fuel dissemination are reported. The object of these tests is to determine reach as a function of driving pressure and nozzle parameters as well as to investigate the characteristics of the fuel-air cloud formed in such a manner.

Additional areas that must be addressed before a full-scale FAE blast simulator can be constructed are more engineering oriented and include hardware configuration, fuel dispersal techniques, initiation and cloud detonation, fuel efficiency, repeatability, safety, and construction and life-cycle costs.

The advantages of a full-scale blast simulator include: the absence of cratering, ejecta and significant ground shock; a short turn-around time between blast wave experiments; and relatively lower costs per experiment when compared with other means of blast simulation. These advantages, along with results from the current feasibility study, lead to our

recommendation for continued developmental work towards the construction of a large-scale FAE blast simulator. The existence of such a simulator should greatly enhance the state-of-the-art of blast wave simulation and provide a means for accelerating our knowledge of blast wave-structural interactions.

II. FAE BLAST SIMULATOR CONCEPT

The blast simulator concept under investigation here involves the use of a central fuel dispenser made up of several pressurized dispenser units which will disseminate fuel through nozzle heads into hemispherical clouds 142 m (466 ft) in diameter. A sketch of the proposed simulator is shown in Figure 1. Each dispenser unit must be capable of projecting the fuel out to a 71 m (233 ft) reach and fill a solid angle of the hemispherical cloud. It is envisioned that propellants will be used to pressurize the dispensers and that the pressure will be tailored to fill the desired volume.

It is anticipated that the full-scale facility will consist of a cluster of dispenser units each having a capacity of approximately 2.5 m³ of fuel for a total facility capability of 85,400 kg (188,000 lb) of fuel. These dispenser units will be below ground so that the nozzle heads will be close to the ground surface. The cluster of dispenser units is expected to be approximately 18.3 m (60 ft) in depth and about 4.6 m (15 ft) in radius. The radius of the dispenser is, therefore, small compared to the radius of the FAE cloud and the dispenser can thus be considered a point disseminator.

The full-scale blast simulator facility will be instrumented with pressure gauges located at various ranges both inside and outside the cloud radius. These gauges will measure both side-on and stagnation pressures. In addition, several high-speed cameras will be placed at various locations in order to get a relative measure of detonation efficiency.

To design a blast wave simulation test on an actual structure, the user must first choose the yield of the nuclear blast being simulated and the range from that blast at which he wishes to place the structure. Scaling laws will then dictate to the user the scaled range at which the structure must be placed on the blast simulator pad. A computer program would also be available to provide the user with the expected static overpressure time curve at that scaled range.

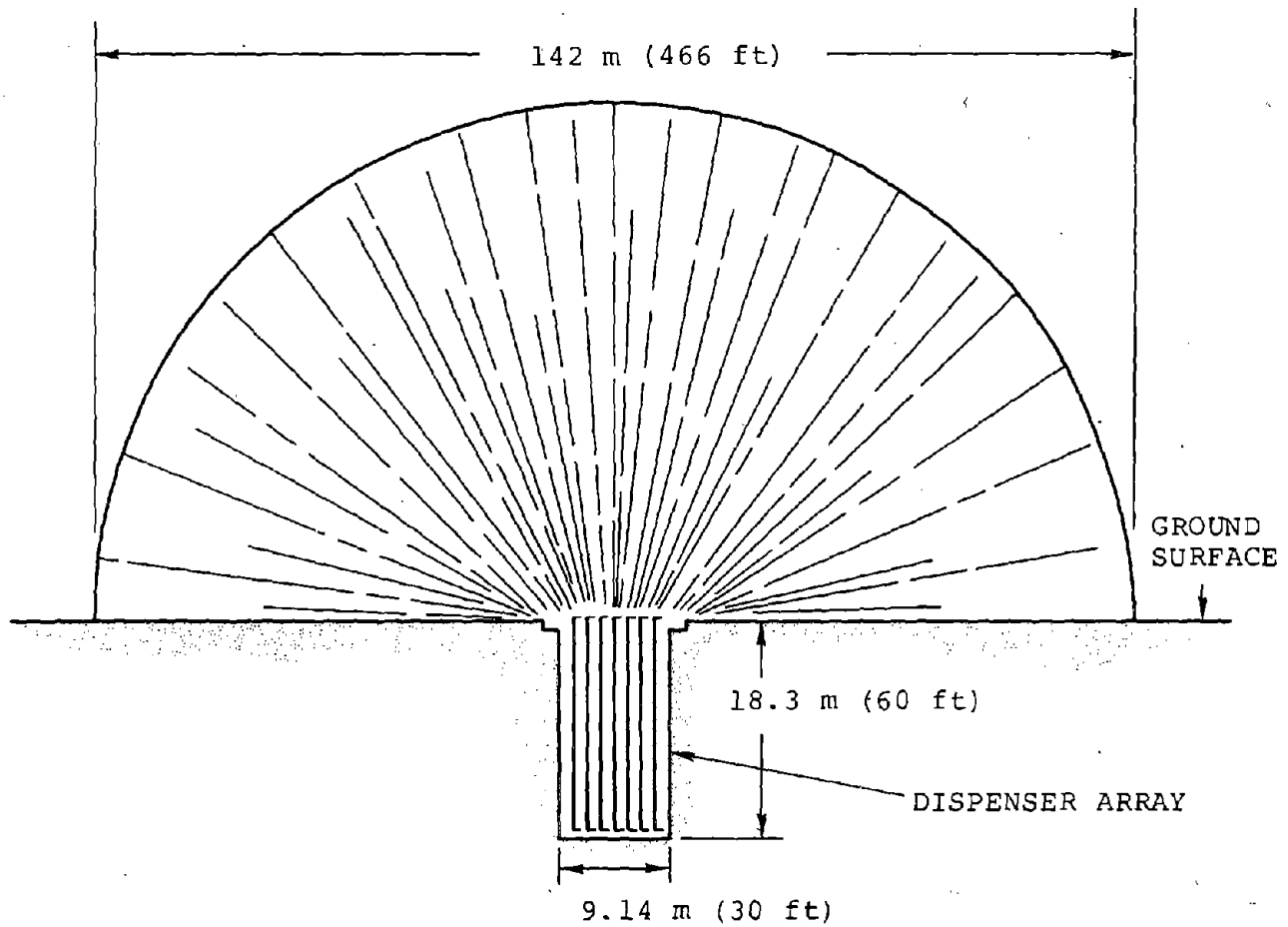


Figure 1. Schematic diagram showing clustered array of fuel dispensers for disseminating a 142 m (466 ft) diameter fuel-air explosive cloud.

III. EXPERIMENTAL INVESTIGATION

3.1 U-TUBE TEST FACILITY

In order to measure the pressure-time histories from FAE blast waves, an experimental test facility was developed for the purpose of disseminating 22.7 kg (50 lb) of propylene oxide fuel into a 9.1 m (30 ft) diameter hemispherical fuel-air cloud. The facility involves a U-tube with a nozzle head on one leg and a pressure supply on the other. As shown in Figure 2, the pressure supply end of the U-tube contains water which when pressurized drives a piston and forces fuel through the nozzle head to form the fuel-air cloud. Figure 3 is a photograph of the facility showing both the nozzle end and pressurized end of the U-tube. A typical nozzle head for disseminating hemispherical fuel-air clouds is shown and is composed of an 8 inch diameter hemispherical shell having a thickness of 7.9 mm (0.31 in). Originally, 605 2.4 mm (3/32 in) diameter holes were drilled in the nozzle head shown. During the course of the investigation, however, it was found that a more nearly hemispherical cloud could be formed if the holes near the center of the nozzle were larger than those near the periphery.

A plan view of the test pad is shown in Figure 4. The location of the nozzle head is shown along with the diameter of an FAE cloud that is formed from 22.7 kg (50 lb) of propylene oxide. Two perpendicular rows of pressure gauges were used in the series of experiments and are shown on the diagram of Figure 4. The short leg, S, has three gauges at 3.0, 9.1 and 18.3 m (10, 30 and 60 ft) from the nozzle head. The long leg, L, has four gauges located at 6.1, 12.2, 24.4 and 48.8 m (20, 40, 80 and 160 ft). So as to be consistent with previously established terminology, these gauge locations are denoted by S10, S30 and S60 on the short leg and L20, L40, L80 and L160 on the long leg. Other gauge placements are similarly designated. The side-on pressure, as a function of time, was measured at these locations. In some of the experiments, additional gauges were included for measuring the stagnation pressure. The dynamic pressure can be determined if both the side-on pressure and the stagnation pressure at a given range are known. The Fastax camera is located in the quadrant between the two perpendicular gauge lines at an angle of 59° from the short-gauge leg and is at a range of 79.2 m (260 ft) from the nozzle head.

The photograph of Figure 5, which was taken from an area near the Fastax camera station, shows the elevation view of the test pad. The U-tube, most of which is buried underground, is shown at the center of the photo. The nozzle

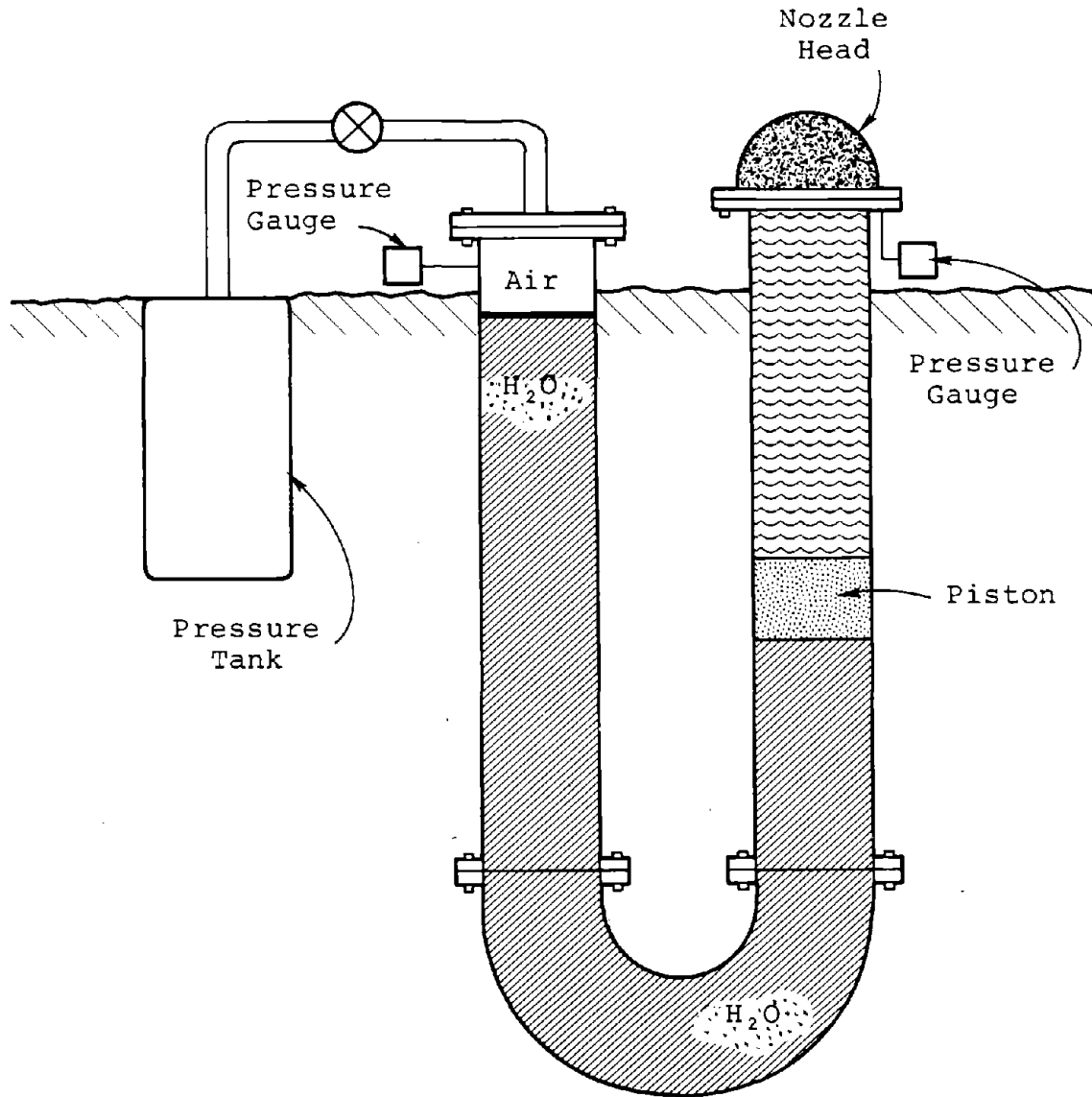


Figure 2. Schematic diagram showing the U-tube used in the experimental investigation for disseminating hemispherical fuel-air explosive clouds. One leg of the U-tube was pressurized in order to force the fuel through a nozzle head attached to the other leg of the U-tube.

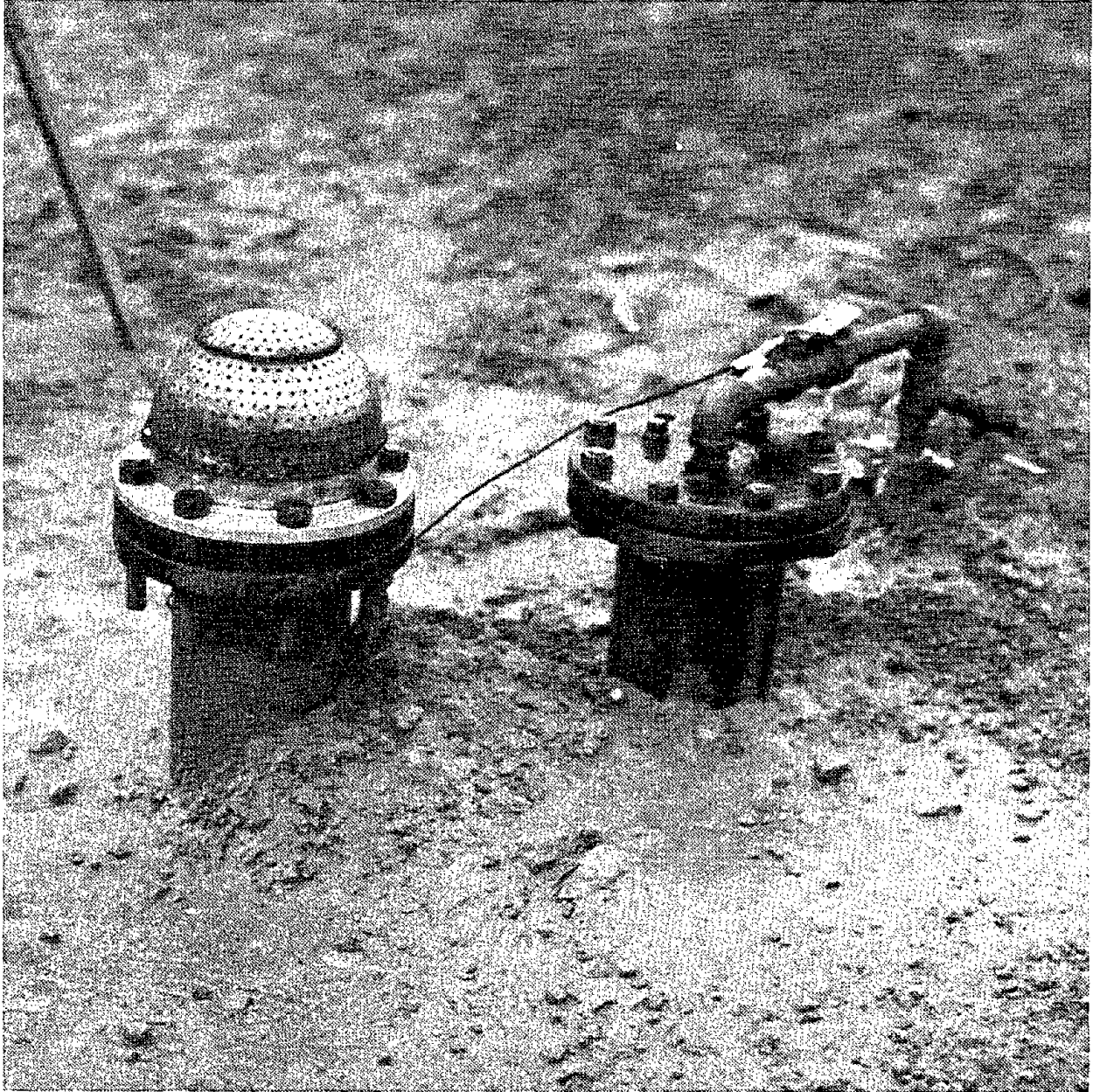


Figure 3. Photograph of the U-tube showing the nozzle head used for disseminating hemispherical FAE clouds.

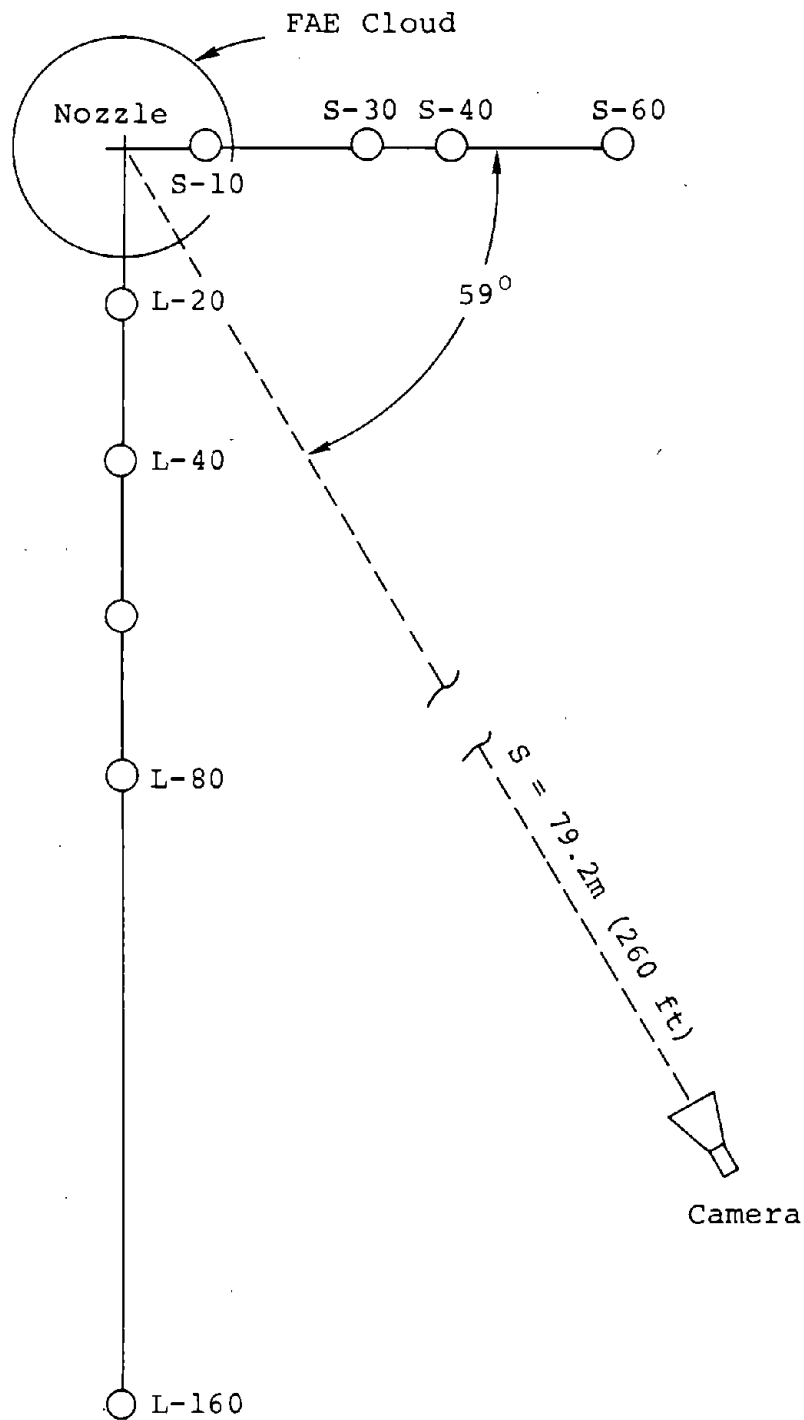


Figure 4. Plan view of the test pad showing the two perpendicular pressure gauge arrays and the line of sight of the Fastax camera.



Figure 5. Photograph showing the elevation view of the test pad. The nozzle head can be seen in the center of the photograph and the graduated uprights are positioned a distance of 4.57 m (15 ft) on either side of the nozzle head. The separation between the graduation marks on the uprights is 1.52 m (5 ft). The numbered sign in the foreground identifies the particular shot. A Cellotex sheet was placed in the background for the purpose of determining the relative transparency of the detonated products, a measure of the detonation efficiency.

head is clearly visible. The two uprights are located 4.6 m (15 ft) from the center of the nozzle head. The graduation marks on the uprights are 1.5 m (5 ft) apart and the uprights themselves are 4.6 m (15 ft) high. The sign in the foreground indicates the date and number of the test and the rectangular sheet in the background provides a means for determining the relative transparency of the detonated products, which is an indication of the efficiency of the detonation process. The actual vantage point of the Fastax camera was such that the sign, the nozzle head, and the rectangular sheet were in line with the camera.

3.2 FAE TEST PROGRAM

The test program was divided into three parts. The first series of tests was oriented toward the design of the U-tube test facility. The second series involved the use of the U-tube facility to disseminate fuel into hemispherical clouds which were subsequently detonated. In this series of tests, static and stagnation pressures were measured at various ranges and Fastax cameras were used to record detonation velocity. The final series of tests involved the dissemination of water and fuel from single nozzles in an attempt to determine the feasibility of scaling to the full-sized test facility.

3.2.1 U-Tube Design Tests

The details of the U-tube design tests will not be presented here since the object of these tests was simply to develop a U-tube facility that would adequately disseminate 22.7 kg (50 lb) of propylene oxide into hemispherical, detonable FAE clouds. The series of design tests that was performed resulted in the achievement of that objective. The various parameters that were investigated during the design test series along with the ranges of those parameters are provided in the following list:

- Driving pressure, 0.27 - 2.04 MPa (40 - 300 psi)
- Fuel weight, 0.91 - 2.27 kg (2 - 50 lb)
- Spray angles, 6° - 180°
- Total nozzle area in head, 1.3 - 45 cm² (0.2 - 7.0 in²)
- Nozzle, L/D (length to diameter) 1 - 5

- Number of nozzles in array, 63 - 1,200
- Delay time, 300 - 1,500 ms
- Detonator mass, 25 - 100 g
- Height of detonator, 0.46 - 4.6 m (1.5 - 15 ft)
- Ambient temperature, 7 - 32°C (45 - 90°F)
- Wind velocity, 0 - 5.1 m/s (0 - 10 knots)

These tests led to the following design decisions. The required U-tube driving pressure for forming a 9.1 m (30 ft) diameter hemispherical propylene oxide cloud was of the order of 0.68 MPa (100 psi). The amount of propylene oxide required to fill this volume in the proper fuel-air mixture is 22.2 kg (49 lb) and the nozzle heads used for fuel dissemination consisted of 20.32 cm (8.0 in) diameter aluminum domes made from either 1.5 mm (0.06 in) or 7.9 mm (0.31 in) thick aluminum with approximately 600 3.2 mm (1/8 in) or 2.9 mm (0.114 in) diameter holes. In one of the designed nozzle heads, the hole size varied from 3.3 mm (0.13 in) in diameter at the center of the nozzle to 2.7 mm (0.106 in) in diameter at the periphery.

3.2.2 F AE Blast Wave Measurements

After the U-tube facility design tests were completed, the facility was used to perform a series of dissemination and detonation tests in which pressure-time histories at various locations were measured. Figure 6 is a series of four frames from a Fastax movie showing cloud growth for a typical propylene oxide dissemination experiment using the final nozzle design. Figure 7, which shows two Fastax movie frames near the end of the detonation of the cloud shown in Figure 6, indicates that the detonable cloud is very nearly hemispherical.

Gauges were installed on the facility to record both side-on and stagnation pressures at various ranges. Figure 8 shows a series of overpressure versus time waveforms that were direct readouts from the eight-channel recorder. The numbers on the left side of the chart are the gauge location designations. As indicated earlier, the letter S denotes the short-gauge leg and the letter L the long-gauge leg. In addition, the notation, LT, indicates stagnation or total pressure. The locations of these gauges are shown in Figure 4 which provides a plan view of the FAE test pad facility.

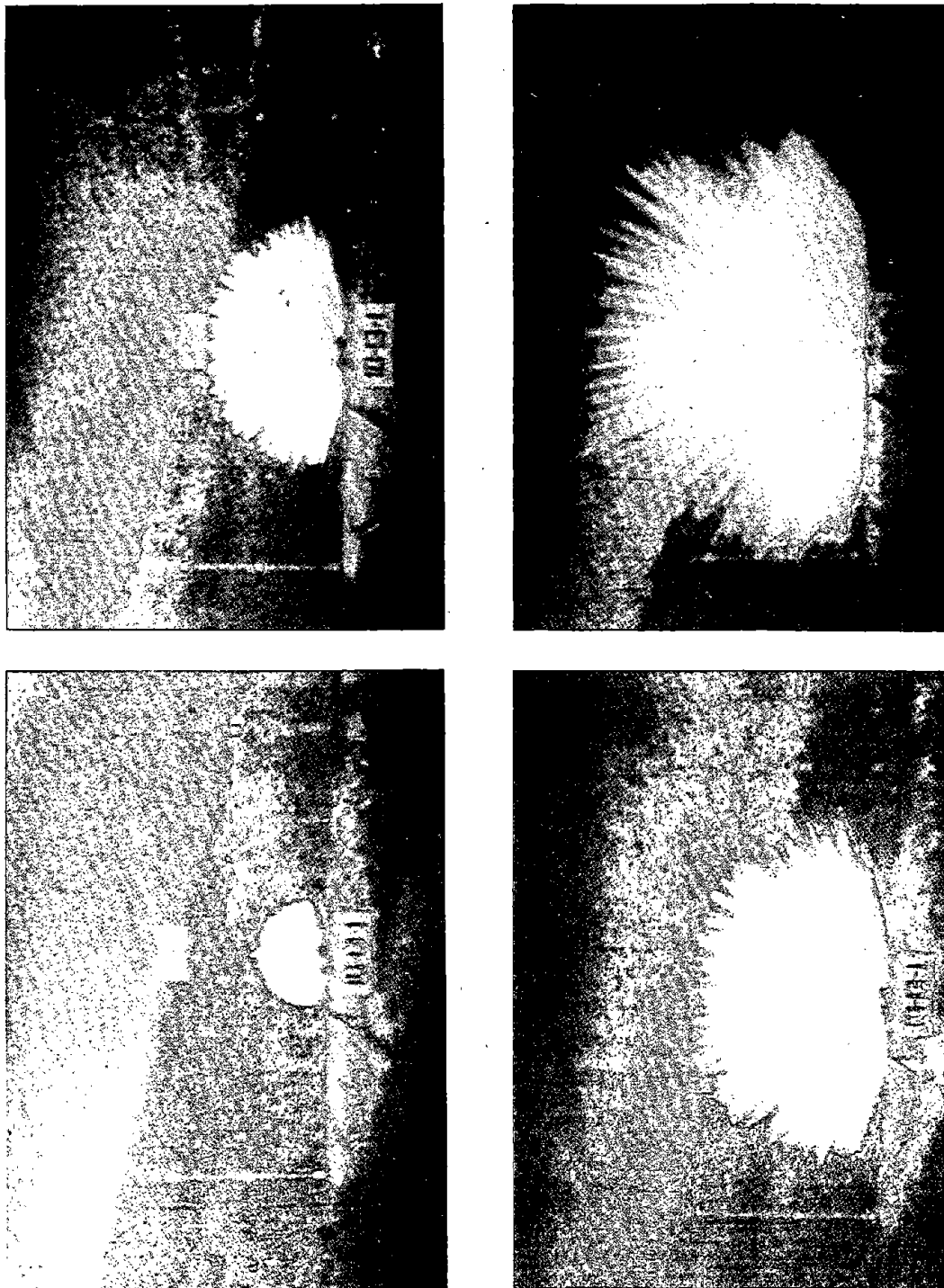


Figure 6. Four frames from a Fastax movie of the dissemination process for the case of propylene oxide being disseminated from the nozzle head of the U-tube facility.

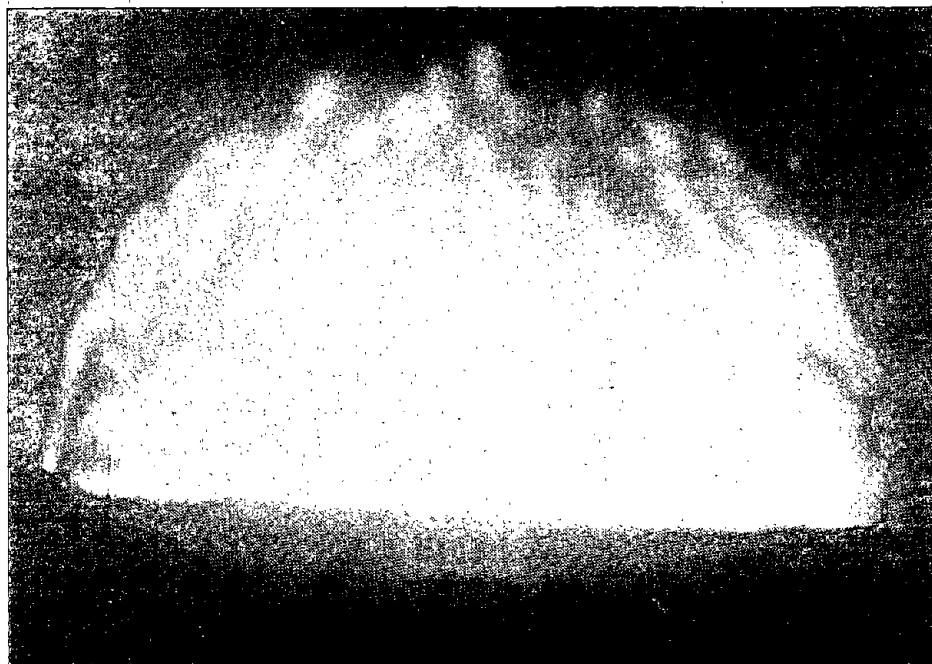
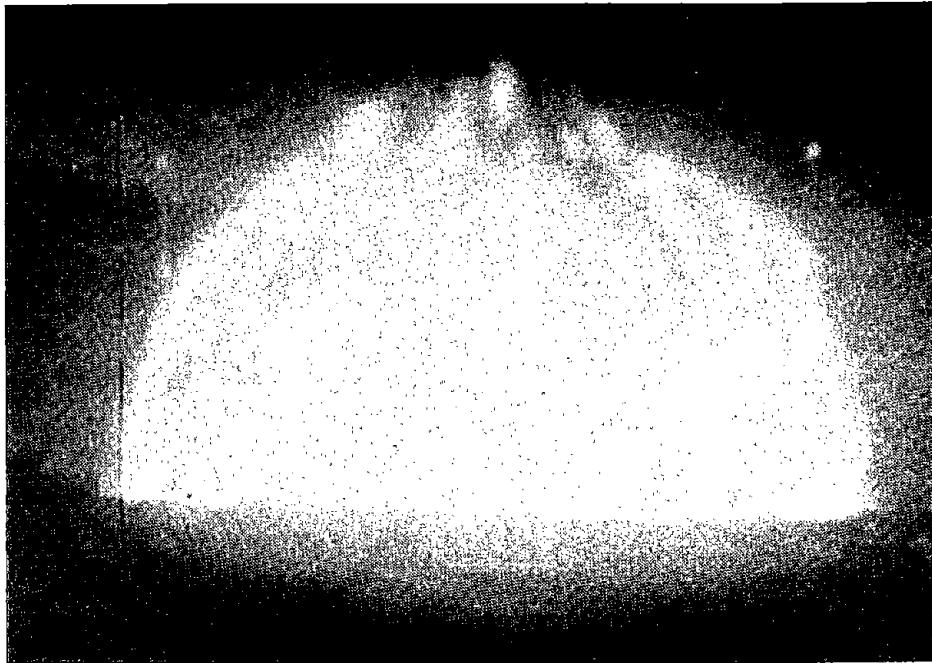


Figure 7. Two frames from a Faxtux movie of the final stages of detonation of a hemispherical FAE cloud. The extent of the detonable portion of the cloud is easily identifiable and is seen to be hemispherical in nature.

In Figure 8, the time (abscissa) has a constant calibration factor: 1.0 cm (vertical line) equals 10 ms. Each overpressure (ordinate) on this recording has its own calibration factor as shown in Table I. It should be noted here that, whereas the recorder operates at a constant speed and therefore the cm-to-time conversion does not change, the cm-to-pressure conversion factors occasionally change between shots as gauges are recalibrated or replaced. The gauge readings shown in Figure 8 are from shot number 1, 0800, Tuesday, 18 October 1977, which involved 22.2 kg (49 lb) of propylene oxide disseminated through a hemispherical nozzle head. The blast waveforms from the gauges in the short leg are shown inverted on the chart.

The overpressure time data in several of the tests were digitized and stored on computer tape so that the data could easily be scaled and plotted for comparison with nuclear blast wave data. Such comparisons are shown in the next section.

It was important in this series of tests to also demonstrate that the blast wave data generated by the facility were both repeatable and symmetric. Figure 9 is a plot of peak static overpressure as a function of range involving measurements from three separate experiments. The letters S and L in the figure represent the short and long gauge legs, respectively. The gauge legs were positioned 90° apart so that cloud symmetry could also be investigated. It is seen that with the exception of one gauge (L20) there is very little scatter in the peak pressures between shots indicating good repeatability in those quantities. Figure 10 is a plot showing total static impulse at each gauge location plotted as a function of range. Again, it is seen that there is very little scatter between shots. Also, since the peak static overpressures and total impulses obtained at the perpendicular gauge locations lie very close to a single curve (with the exception of L20), indications are that good cloud symmetry has been obtained. The following two subsections are devoted to a detailed investigation of the degree of blast wave repeatability and symmetry attainable with the U-tube facility.

3.2.2.1 Blast Wave Repeatability

The curves in Figures 11 through 14 are shown to demonstrate the degree of blast wave repeatability attainable with the U-tube facility. In Figure 11, the measured static overpressure, as a function of time at the 12.2 m (40 ft) station, is shown for three different experiments. Figure 12 is a similar comparison for the measured stagnation overpressure at that range. Figure 13 is a comparison of the measured

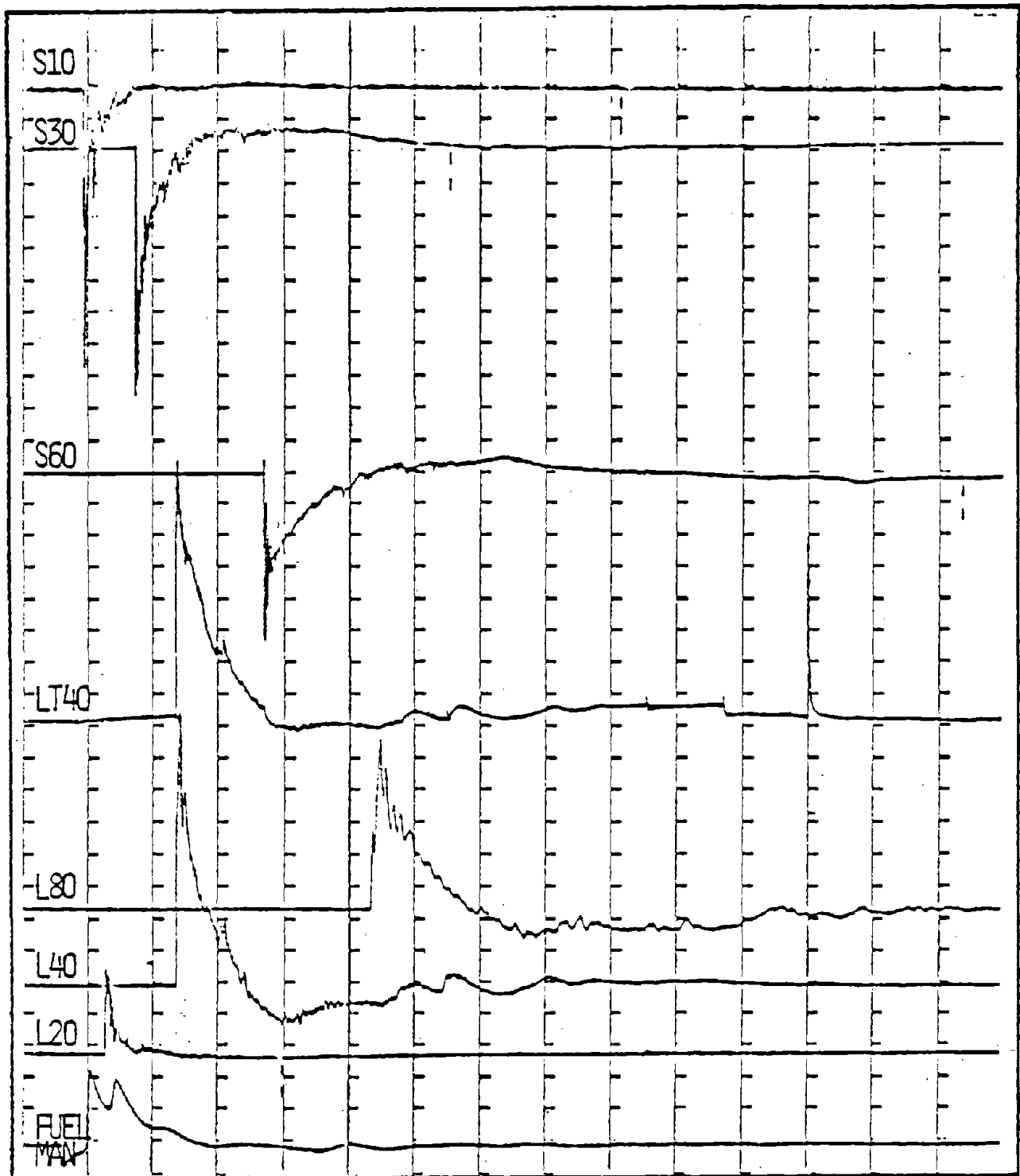


Figure 8. Typical pressure gauge readings from an FAE detonation experiment. The letters S and L refer to the short and long gauge leg respectively. The numbers identify the location of the gauge in feet from the nozzle head. The gauge calibration factors are shown in Table I.

Table I. Gauge Calibration Factors for
Shot No. 1, 0800 Tuesday,
18 October 1977

Gauge	Calibration Factors	
	MPa/cm	psi/in
S10	0.3348	125.00
S30	0.0670	25.00
S60	0.0339	12.67
LT40	0.0497	18.57
L80	0.0160	5.97
L40	0.0287	10.72
L20	0.3501	130.72

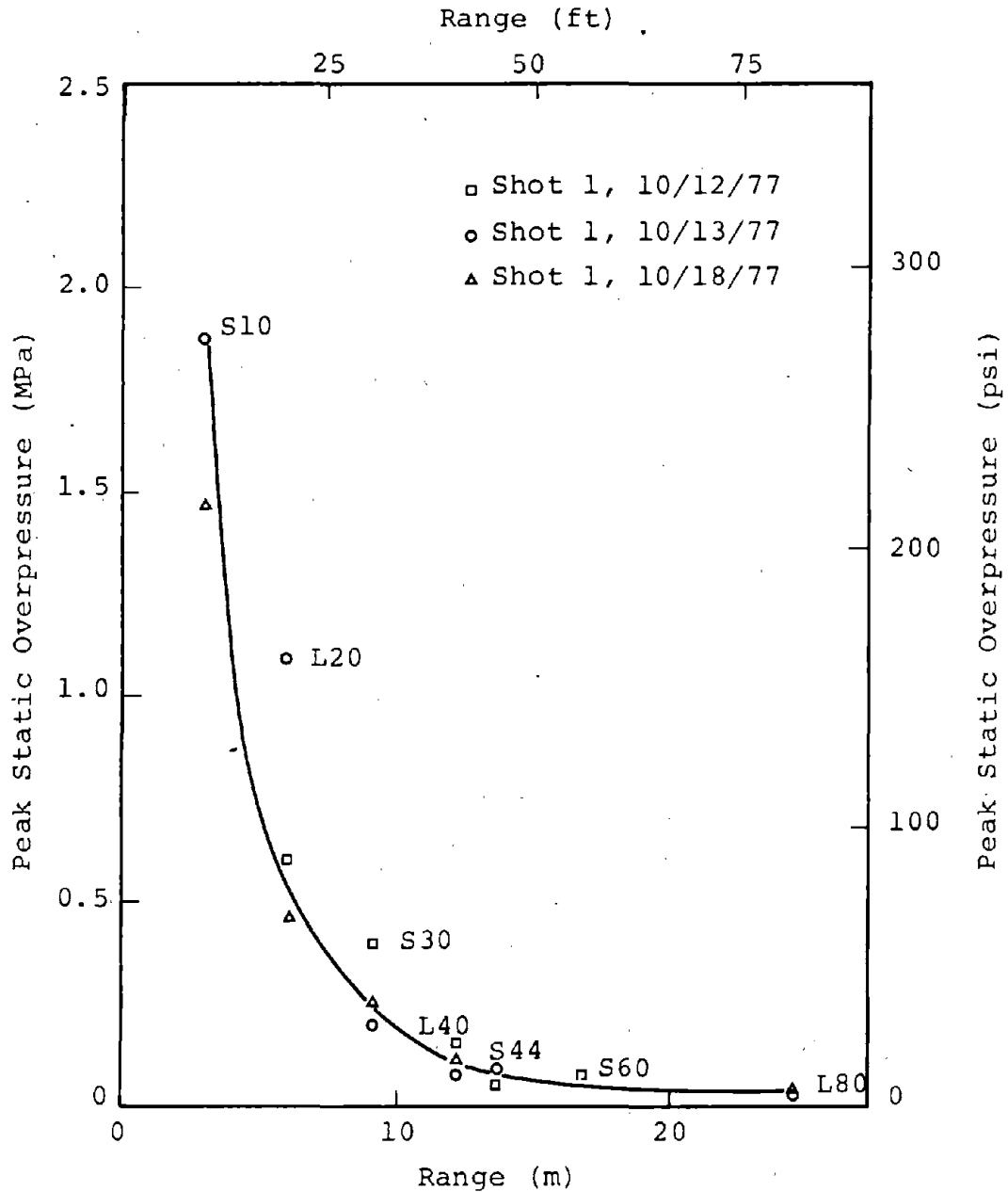


Figure 9. Plot of measured peak overpressure versus range for three different experiments. The fact that most of the pressures lie very close to a smooth curve indicates that repeatability between experiments is good. In addition, since the gauges labeled L and S were separated by 90 degrees the curve indicates that a high degree of symmetry was attained.

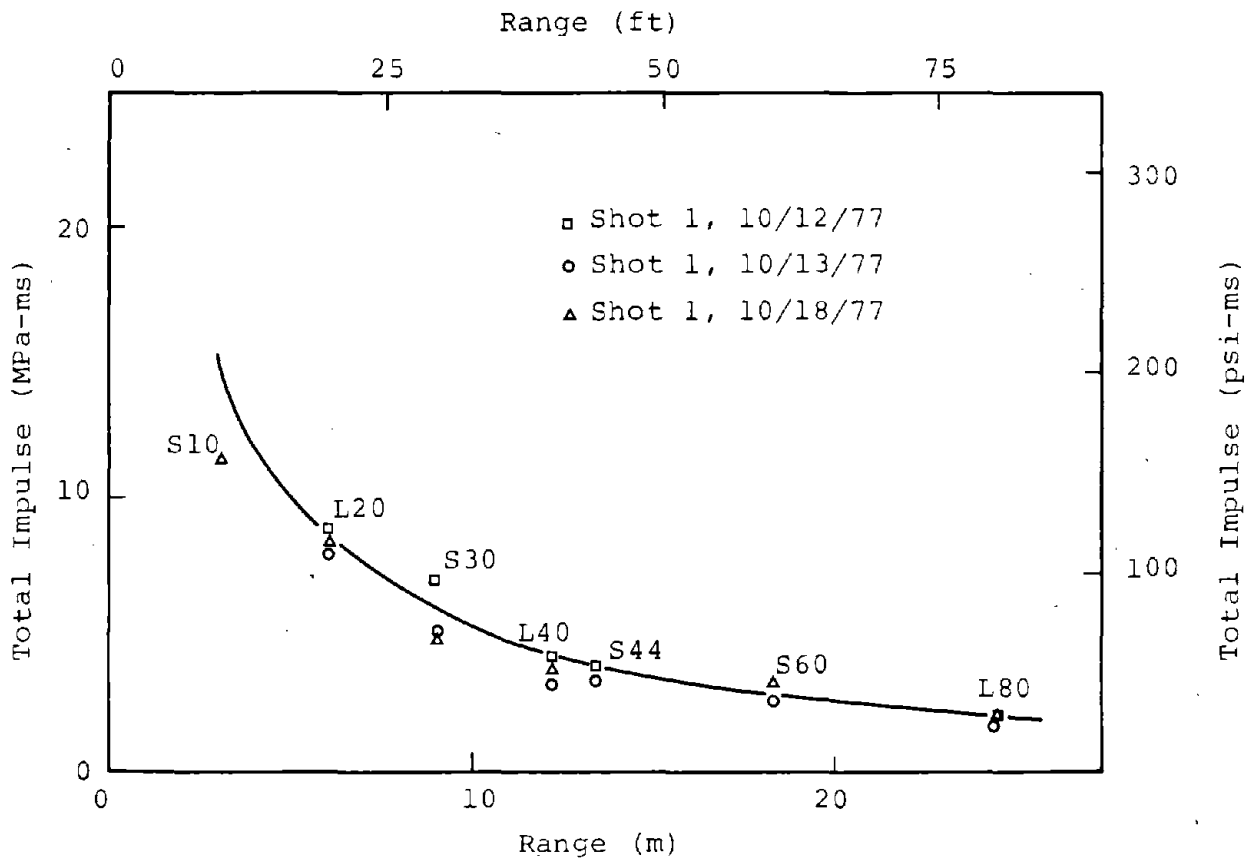


Figure 10. Plot of maximum positive phase impulse versus range for three different experiments. Again it is seen that the points are close to a single curve indicating good repeatability and since the L and S gauge locations were separated by 90 degrees, good cloud symmetry is implied.

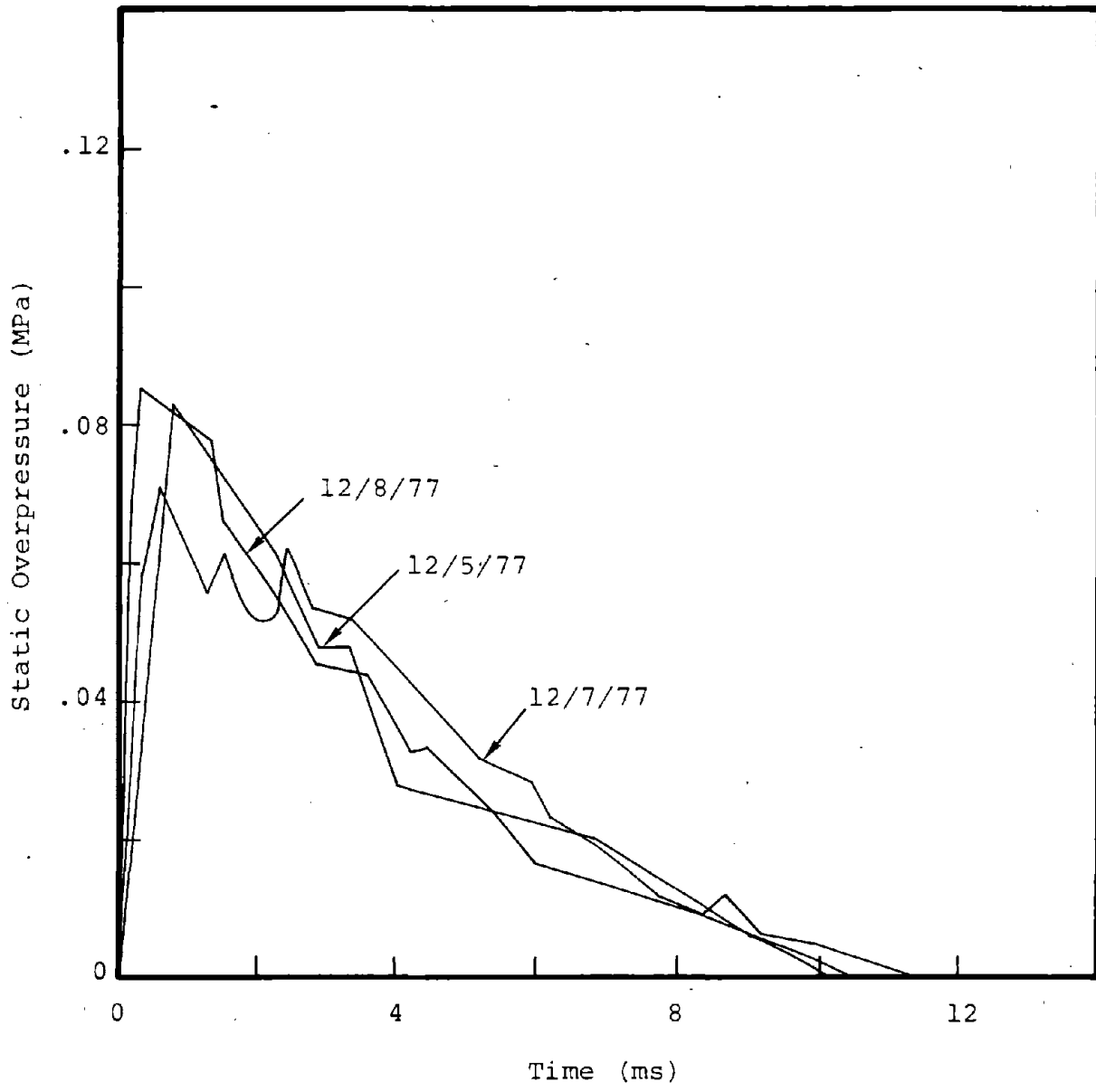


Figure 11. Plot of measured static overpressure as a function of time at the 12.2 m (40 ft) station from three separate experiments.

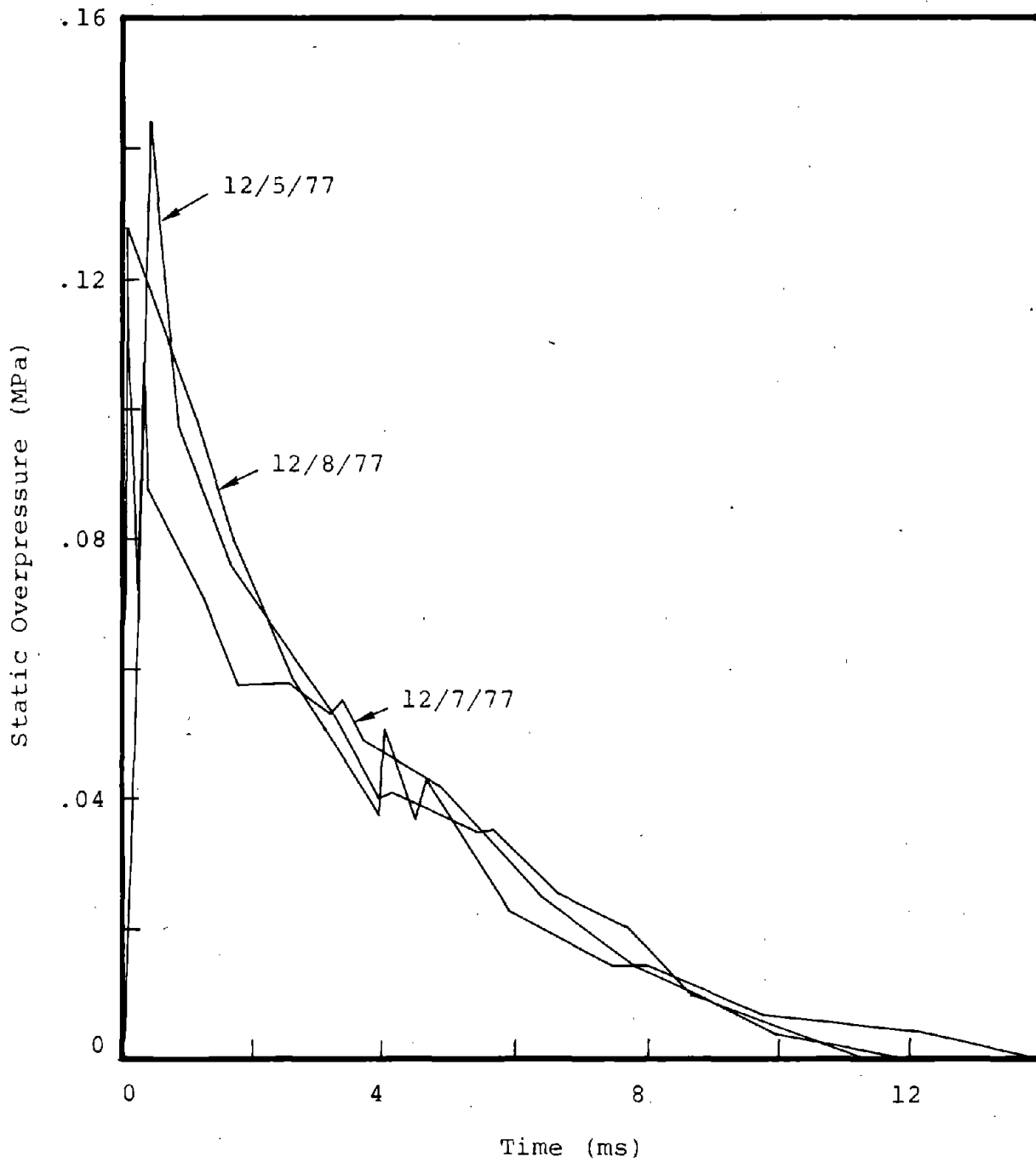


Figure 12. Plot of measured stagnation overpressure as a function of time at the 12.2 m (40 ft) station from three separate experiments.

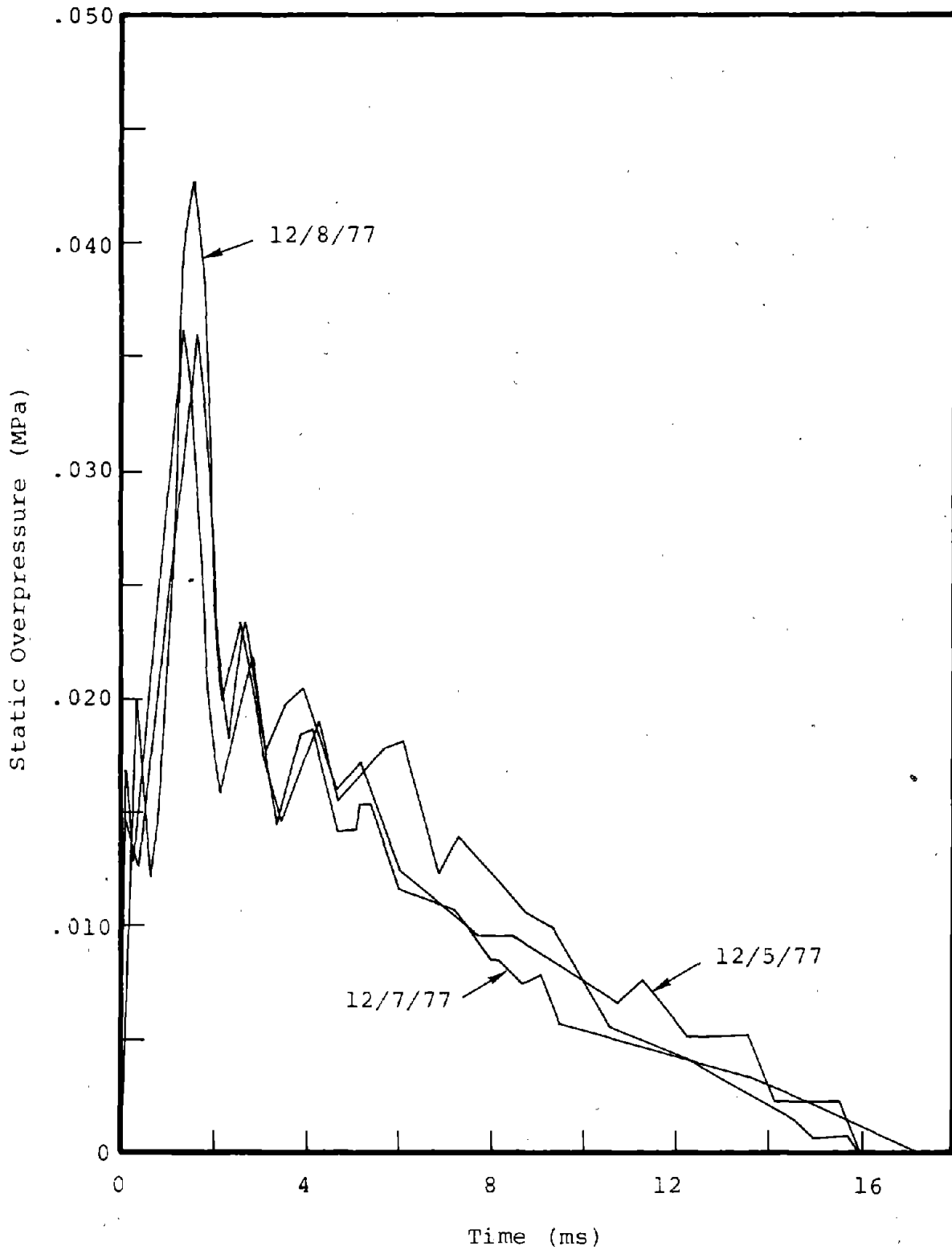


Figure 13. Plot of measured static overpressure as a function of time at the 24.4 m (80 ft) station from three separate experiments.

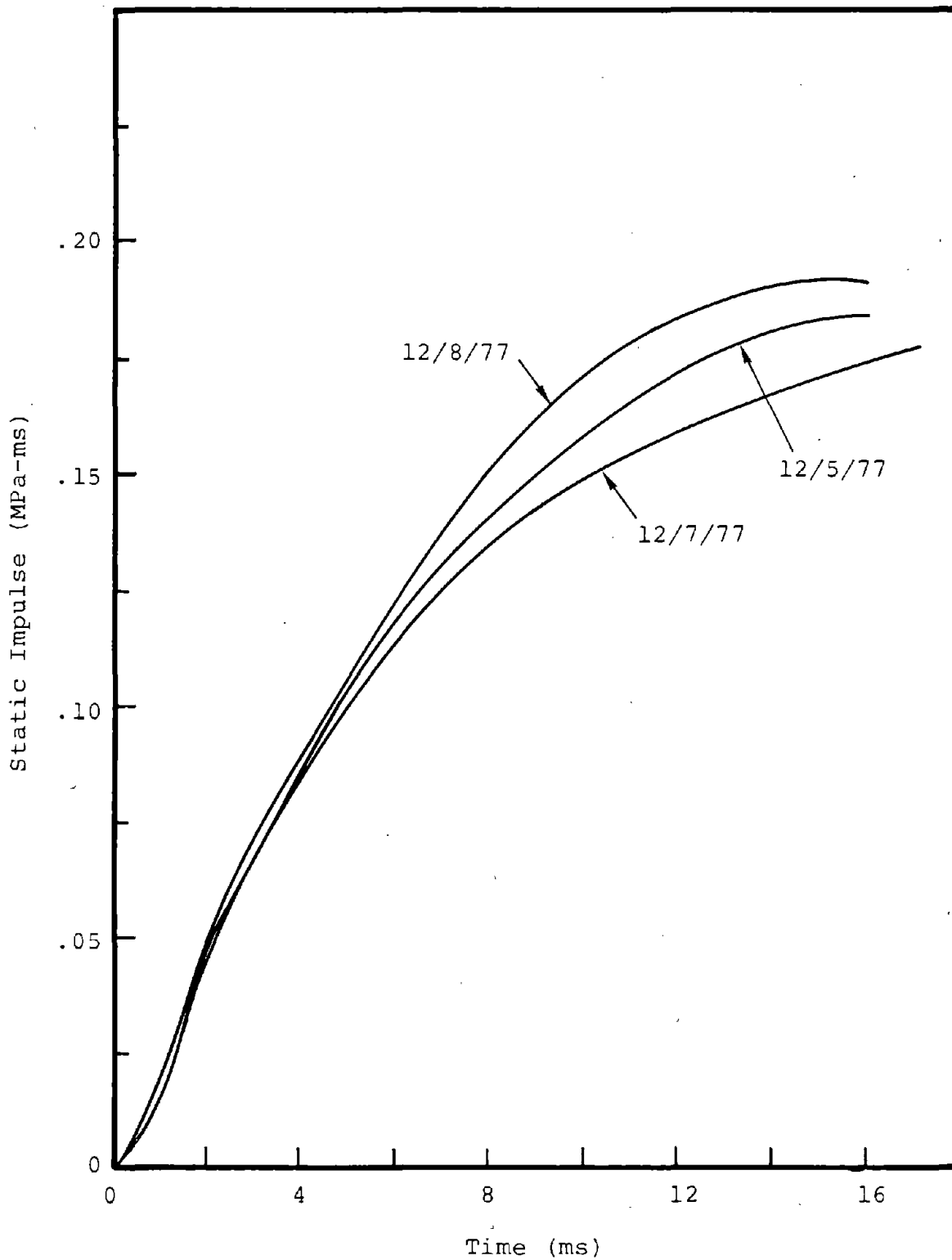


Figure 14. Measured positive phase static impulse as a function of time at the 24.4 m (80 ft) station from three separate experiments.

static overpressure as a function of time at the 24.4 m (80 ft) station from the same three experiments. Figure 14 is a plot of the static impulse as a function of time at the 24.4 m (80 ft) station, again for the same three experiments.

It is seen from the data plotted in Figures 11 through 14 that the degree of repeatability attainable with the U-tube facility is well within acceptable limits.

3.2.2.2 Blast Wave Symmetry

Figures 15 through 17 are provided to demonstrate the degree of symmetry attainable with the U-tube facility. In Figure 15, the measured static overpressure, as a function of time at the 12.2 m (40 ft) station, is plotted for the two stations located 90° apart in a given experiment. Figure 16 provides a similar comparison taken from a different experiment. In Figure 17, static impulse is plotted as a function of time at the same range for two gauges located 90° apart.

It is seen from Figures 15 through 17 that the symmetry attainable with the small-scale U-tube facility is well within acceptable limits.

3.2.3 Single Nozzle Tests

The purpose of the single nozzle tests was to determine if the method of disseminating fuel into hemispherical clouds used in the small-scale test facility could be scaled up to a size that would be practical for the large-scale blast simulator. In the large-scale blast simulator, each nozzle must attain a reach of 71 m (233 ft) in order to form a cloud 142 m (466 ft) in diameter for simulating a 1 KT surface burst. Such a capability can be investigated by using single nozzles and determining reach as a function of driving pressure and nozzle diameter.

A series of single-nozzle reach experiments has been performed for the purpose of determining the parameters required to project fuel to heights that will be necessary in the full-scale blast simulator. Figure 18 shows various stages of a water stream being projected from a 6.35 cm (2.5 in) diameter nozzle. The small upright near the base of the nozzle has markers spaced two meters apart. The perpendicular distance from the nozzle to the horizon is about 55 m (180 ft). The height of the water stream shown in the last photograph of Figure 18 is approximately 61 m (200 ft); however, the contrast against the sky is not good enough for the

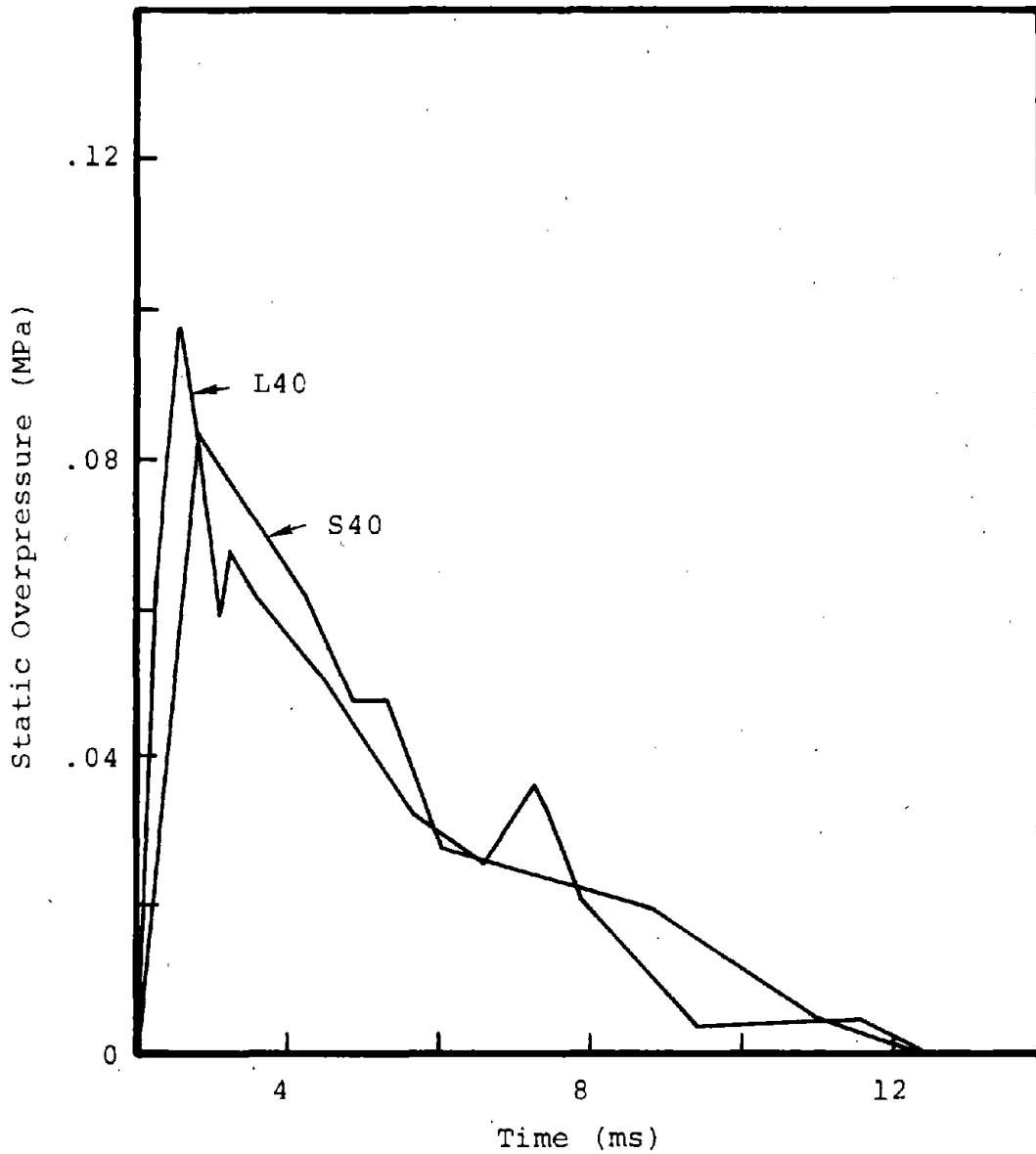


Figure 15. Plot of measured static overpressure as a function of time from a single experiment. The gauges were both located at a range of 12.2 m (40 ft) but were separated by 90 degrees. The experimental data were taken from Shot No. 1, 5 December 1977.

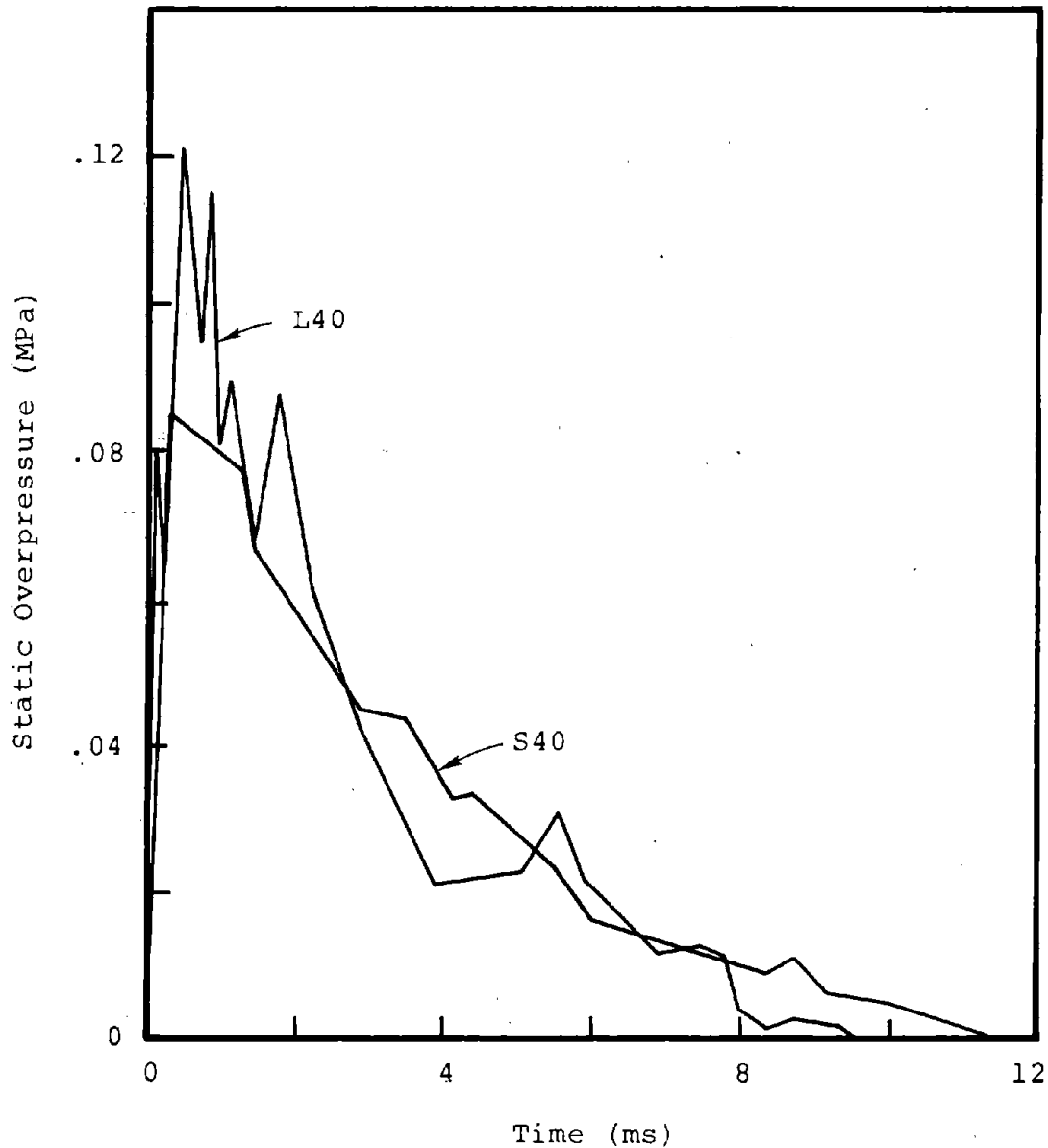


Figure 16. Plot of measured overpressure as a function of time taken from a single experiment. Both gauges were located at a range of 12.2 m (40 ft) but separated by 90 degrees. The comparison is similar to that shown in Figure 15 except that the data plotted are from Shot No. 1, 8 December 1977.

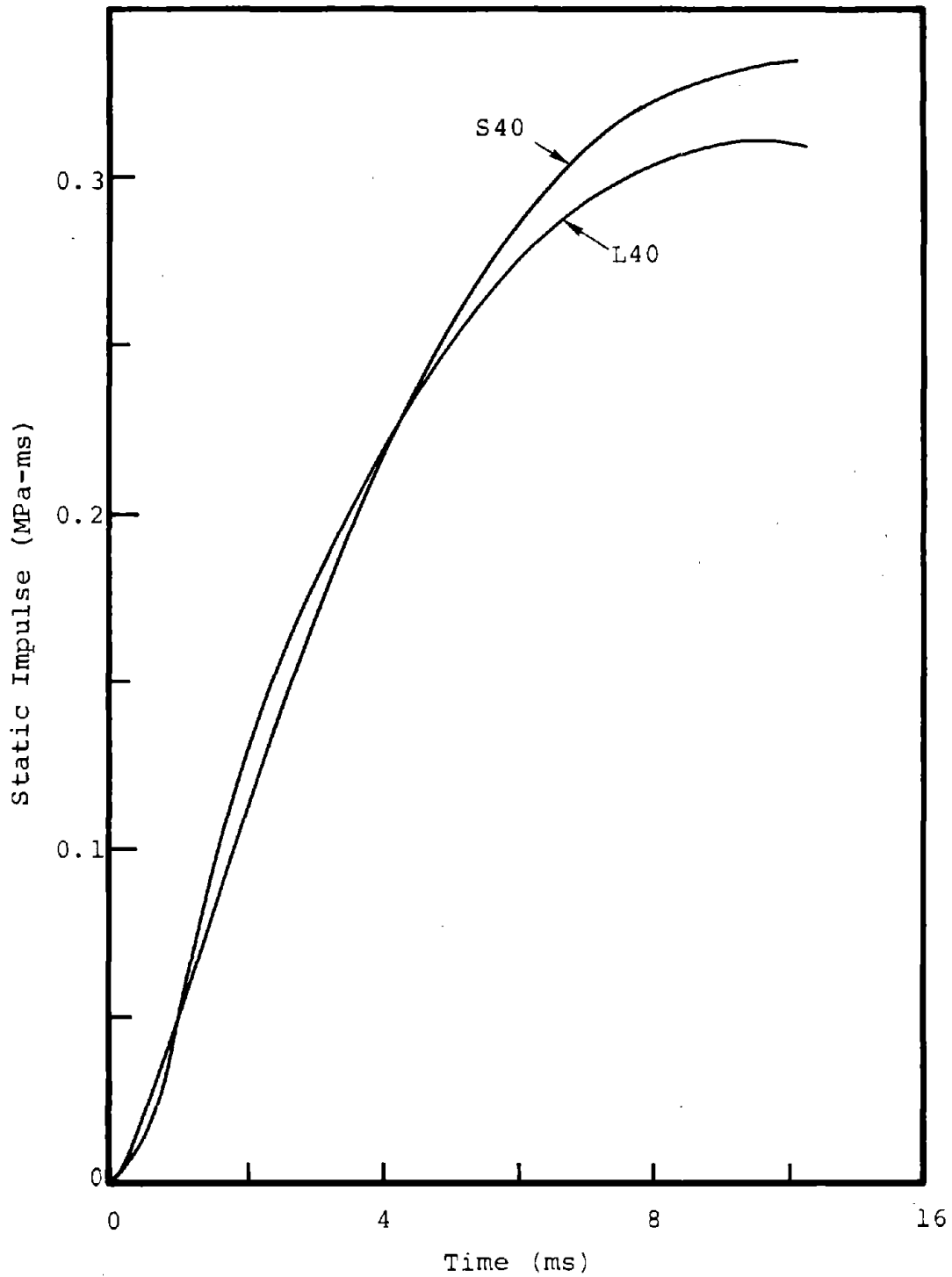


Figure 17. Positive phase static impulse as a function of time from a single experiment. Both gauges were located at a range of 12.2 m (40 ft) but were separated by 90 degrees. The experimental data were taken from Shot No. 1, 8 December 1977.

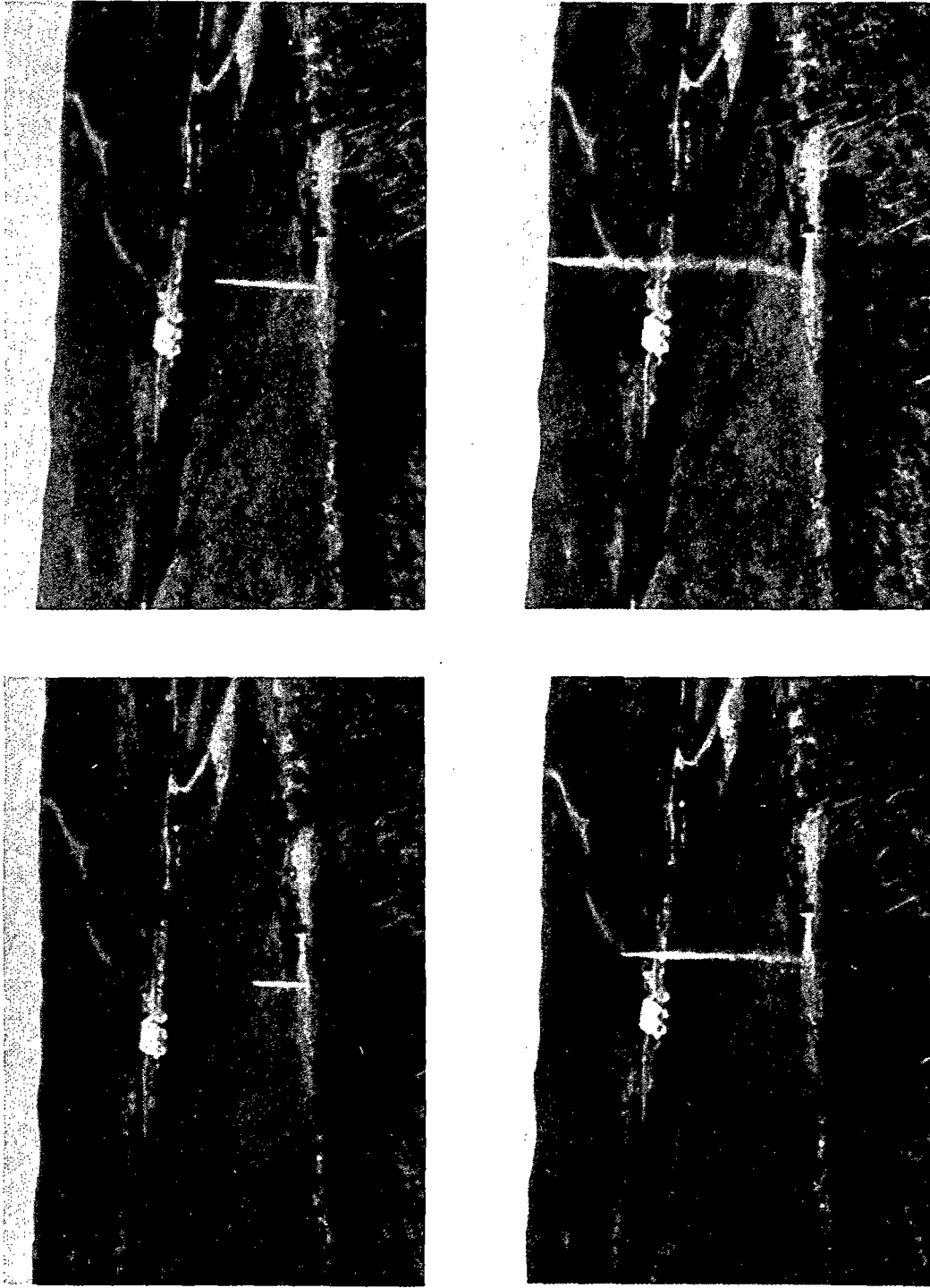


Figure 18. Photographs taken with the Fastax camera showing various stages of a water stream being projected from a 6.35 cm (2.5 in) diameter nozzle.

top of the stream to be seen in the figure. The width of the stream near the top is approximately 5 m (16.4 ft).

The four photographs in Figure 19 show the progress of a propylene oxide stream being projected from a 6.35 cm (2.5 in) diameter nozzle. The final stream height is about 55 m (180 ft). Additional experiments are planned using nozzles of larger diameter in order to obtain streams up to 71 m (233 ft) in height.

The single nozzle reach experiments performed to date are described in Table II. The initial results have been analyzed in an attempt to determine stream height or reach as a function of nozzle diameter and exit velocity, which is related to driving pressure. Results indicate that physical properties of the liquid being projected also affect stream height; however, since only water and propylene oxide have been projected thus far, it is not certain which of the physical properties are important in determining stream characteristics.

If it is assumed that the deceleration of a stream is a result of gravitational forces and drag forces that are proportional to the square of the velocity, the equation of motion of a vertical stream can be written as

$$\ddot{y} = -g - k(\dot{y})^2 \quad (1)$$

where y is vertical distance above the nozzle, g is acceleration due to gravity and k is a drag coefficient. Equation (1) can be solved for stream height to obtain

$$y = \frac{1}{k} \ln \cos (c_1 - \sqrt{kg} \cdot t) + c_2$$

where

$$c_1 = \tan^{-1} \left(\sqrt{\frac{k}{g}} \cdot \dot{y}_0 \right)$$

and

$$c_2 = -\frac{1}{k} \ln \cos c_1.$$

To determine how well Eq. (1) models the stream dynamics, the observed stream height from two different



Figure 19. Photographs taken with the Fastax camera showing various stages of propylene oxide stream being projected from a 6.35 cm (2.5 in) diameter nozzle.

Table II. Single Nozzle Reach Experiments

Experiment Number	Liquid	Nozzle Diameter		Nozzle Exit Velocity	
		(cm)	(in)	(m/s)	(ft/s)
1	H ₂ O	3.81	1.5	50.5	165
2	H ₂ O	3.81	1.5	72.0	236
3	PO	3.81	1.5	51.5	169
4	PO	3.81	1.5	72.0	236
5	H ₂ O	6.35	2.5	42.0	138
6	PO	6.35	2.5	44.5	146

experiments in which water was projected from a 3.81 cm (1.5 in) diameter nozzle are plotted as a function of time in Figure 20, along with the solution of this equation. The initial velocities of the streams were different for the two experiments. It is seen that at early times stream height is modeled well by the equation of motion involving only gravitational forces and drag forces proportional to the square of the velocity (Eq. (1)). However, as the initial velocity is increased, the stream at some point in time decelerates much faster than predicted by the model. A coefficient, k , equal to $8 \times 10^{-5} \text{ m}^{-1}$, gives the best agreement between experiment and theory for the particular case of water being projected from this size nozzle.

In Figure 21, stream height is plotted versus time for two experiments involving the projection of propylene oxide from the same diameter nozzle at two different initial velocities. It is seen that the effect of increasing the initial velocity seems to cause the increase in deceleration to occur at an earlier time. It is also noted from Figure 21 that increasing the initial velocity does not significantly increase the reach.

In Figure 22, water and propylene oxide stream heights are compared for the case of both fluids being projected from the same 3.81 cm (1.5 in) diameter nozzle at initial velocities of 72 m (236 ft) per second. It is seen that the water attained a much greater height and that the propylene oxide began to decelerate faster than that predicted by the model at an earlier time than did the water. This difference in the behavior of the water and propylene streams projected at identical initial velocities from equal diameter nozzles is due to differences in physical properties such as mass density, viscosity, surface tension and vapor pressure. Since only two different fluids have been projected, the dependency of stream height on any of these physical properties cannot be determined here. It can be speculated, however, that the propylene oxide stream decelerates at a greater rate and at an earlier time than does the water stream as a result of increased droplet breakup and stream spreading. Just how droplet breakup and stream spreading are affected by liquid physical properties under the dynamic conditions associated with the high-velocity projection of fuel through a nozzle is not well known at this time.

Stream height is plotted versus time in Figure 23 for the case of water being projected from a 6.35 cm (2.5 in) diameter nozzle. The change in nozzle diameter from 3.81 cm to 6.35 cm required a change in the coefficient, k , of Eq. (1) from $8 \times 10^{-5} \text{ m}^{-1}$ to $1 \times 10^{-5} \text{ m}^{-1}$ in order to obtain the best theoretical-experimental fit. It is interesting to note

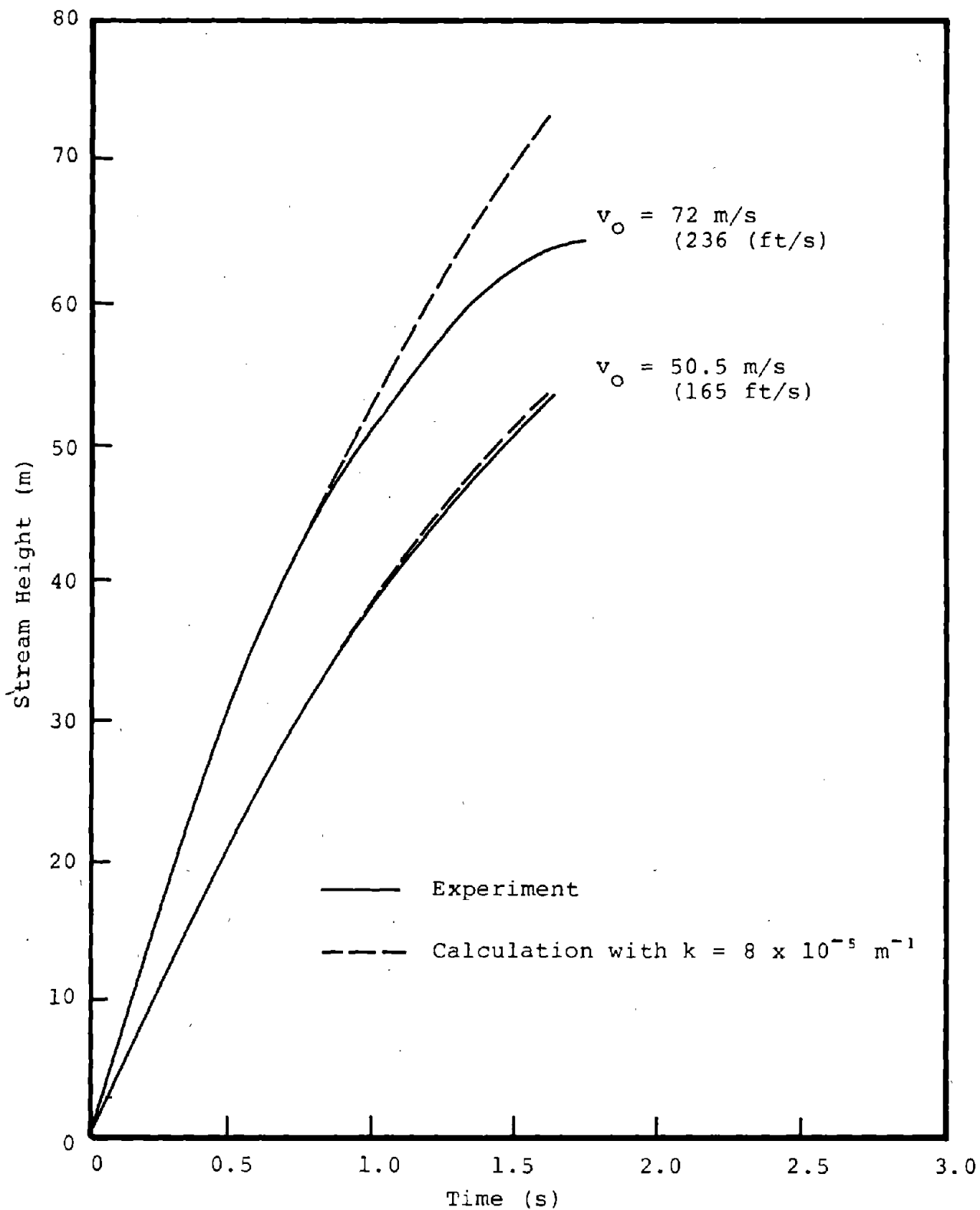


Figure 20. Comparison of stream height as a function of time for two experiments involving the projection of water from a 3.80 cm (1.5 in) diameter nozzle with Eq. (1). The value of the coefficient k used in Eq. (1) was $8 \times 10^{-5} \text{ m}^{-1}$.

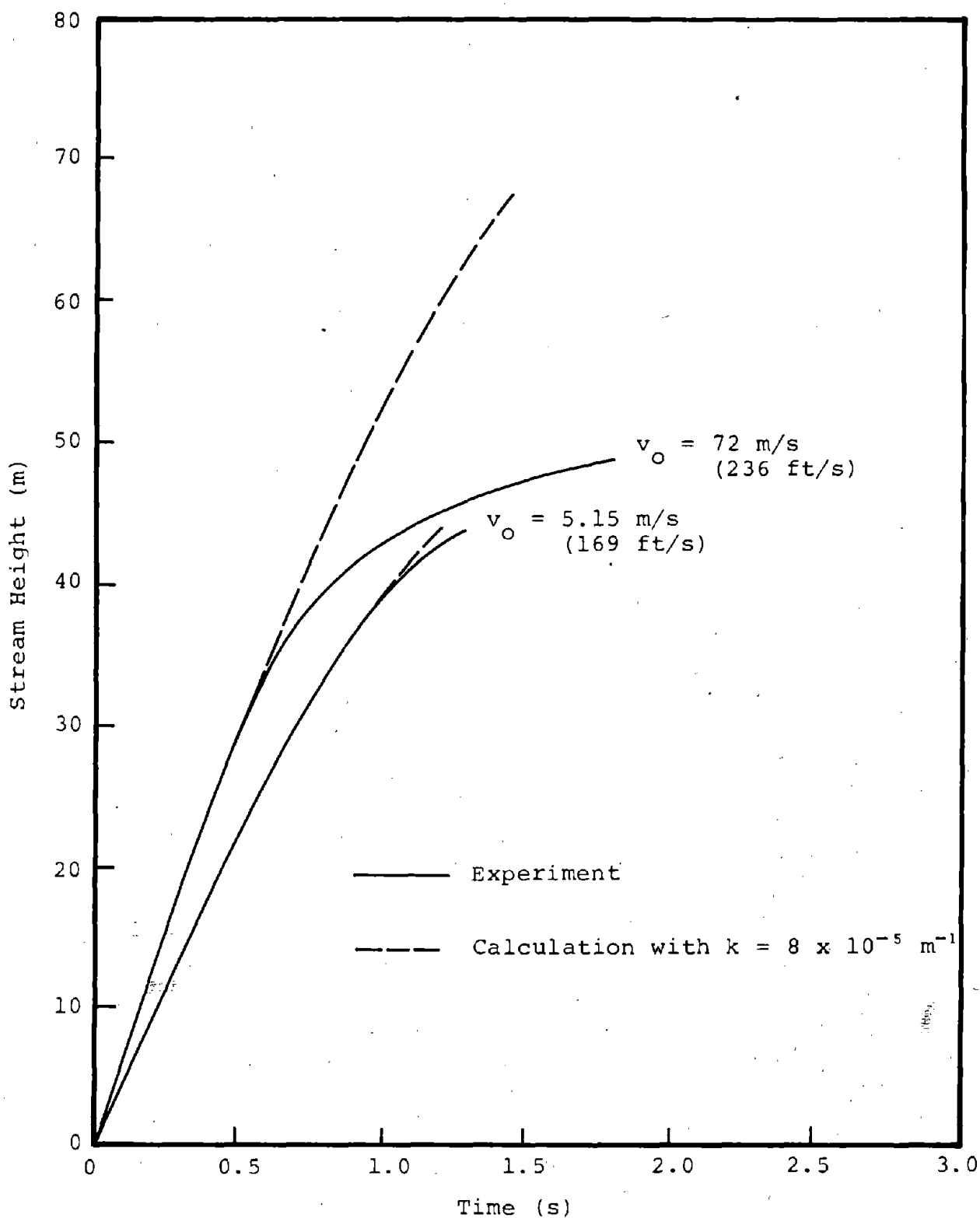


Figure 21. Comparison of stream height as a function of time for two experiments involving the projection of propylene oxide from a 3.81 cm (1.5 in) diameter nozzle with Eq. (1). The value of the coefficient k used in Eq. (1) was $8 \times 10^{-5} \text{ m}^{-1}$.

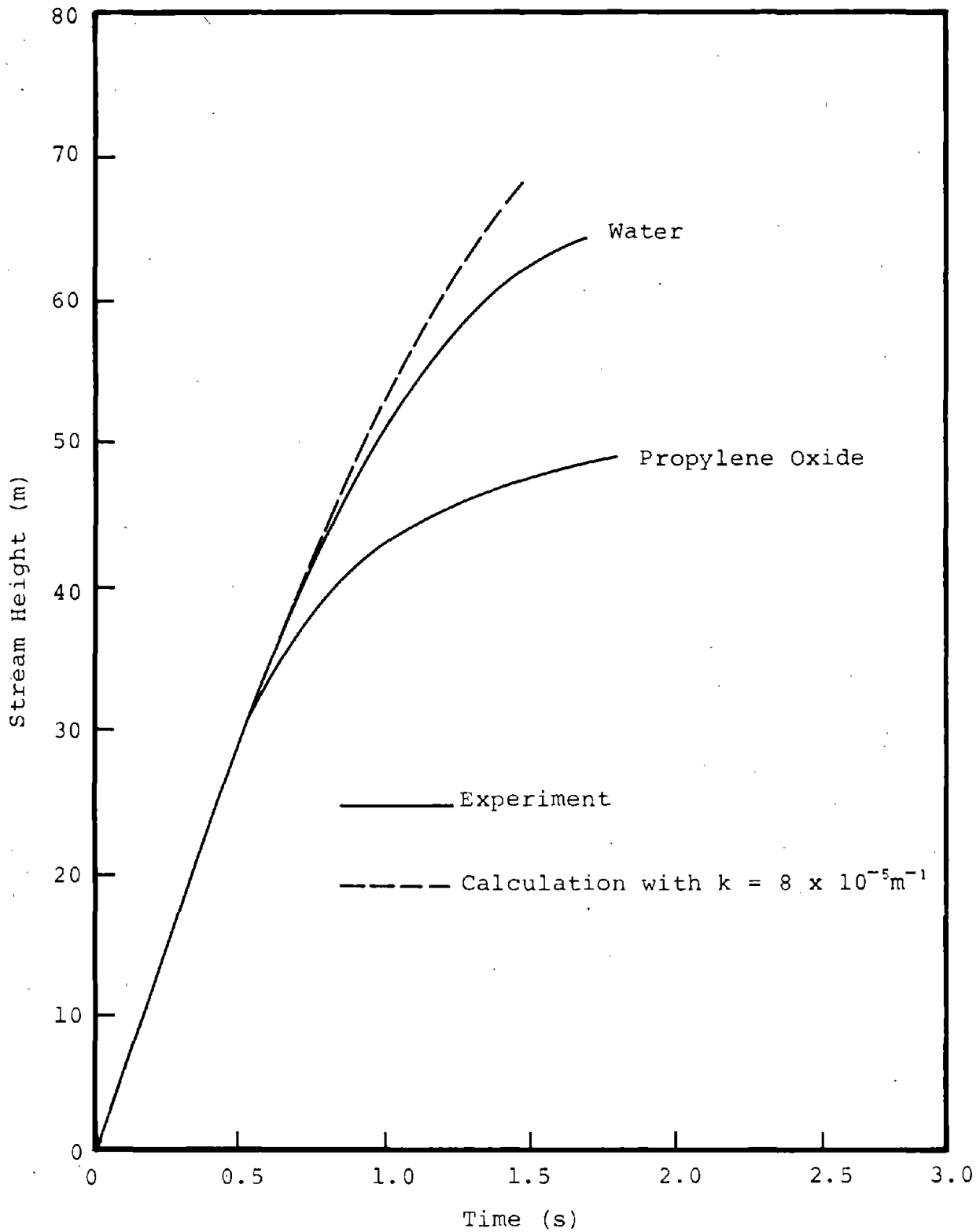


Figure 22. Comparison of water and propylene oxide stream height from two experiments involving projection from a 3.81 cm (1.5 in) diameter nozzle at initial velocities of 72 m/s (236 ft/s).

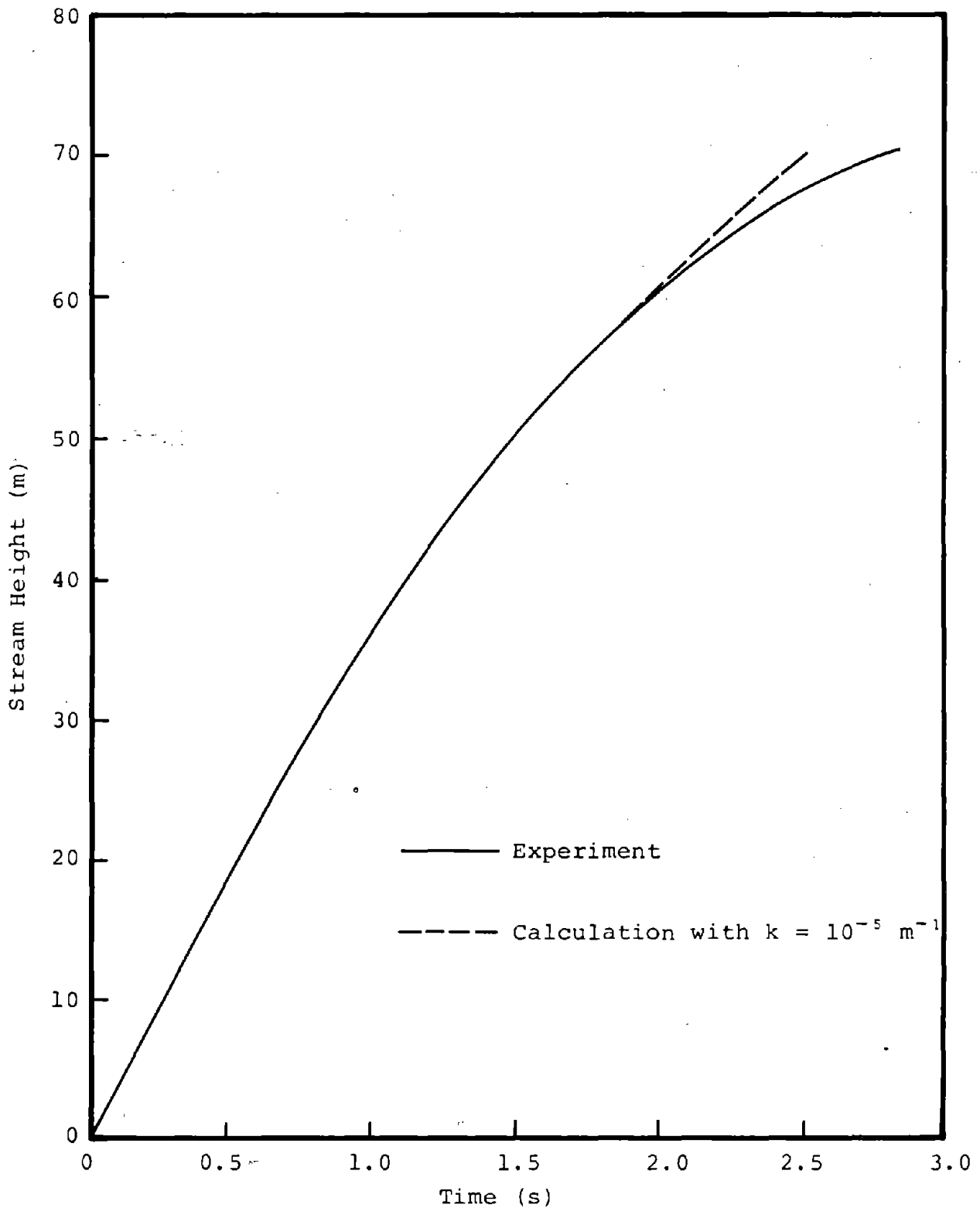


Figure 23. Comparison of stream height as a function of time for the case of water being projected from a 6.35 cm (2.5 in) diameter nozzle with predictions from Eq. (1). The coefficient K used in Eq. (1) was $1 \times 10^{-5} \text{ m}^{-1}$ and the initial velocity was 42 m/s (138 ft/s).

that this coefficient changes with nozzle diameter but is not a function of the physical properties of the fluid being projected. It should be mentioned here that the 3.81 cm and 6.35 cm diameter nozzles employed in the two experiments were not similar, i.e., their length-to-diameter ratios were different. For this reason, no conclusions can be drawn at this time regarding the relationship between the drag coefficient and nozzle diameter.

Figure 24 is a plot of stream height versus time for the case of propylene oxide being projected through a 6.35 cm (2.5 in) diameter nozzle at an initial velocity of 44.5 m/s (146 ft/s). Again, up to the point of rapid increase in deceleration, it appears that the coefficient, k , is more sensitive to changes in nozzle diameter than to changes in fluid properties. The final stream height of the propylene oxide was about 54 m (177 ft), which is about 75 percent of the height required for the full-scale blast simulator. In order to obtain greater stream heights, it probably will be necessary to use nozzles having diameters greater than 6.35 cm (2.5 in).

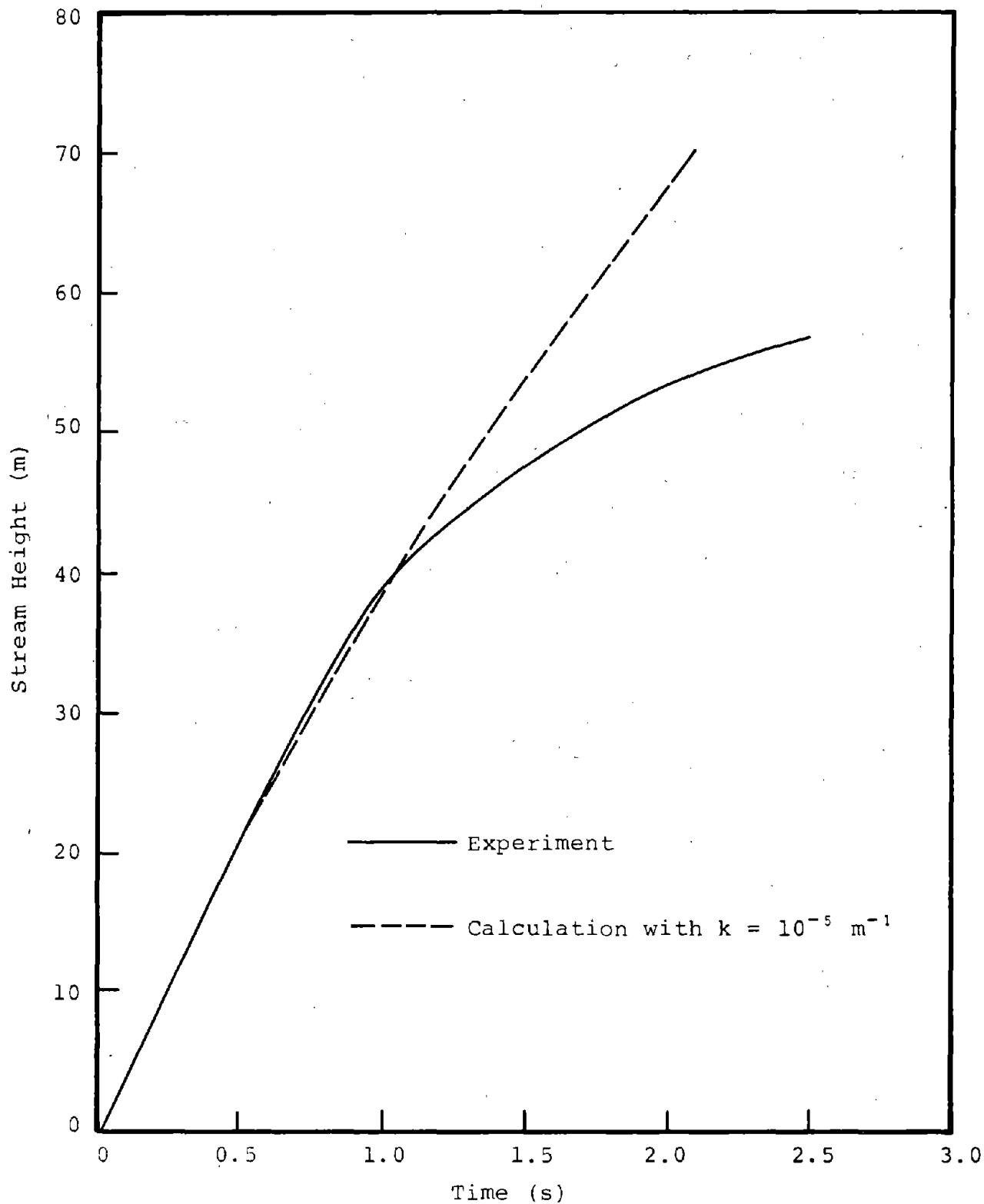


Figure 24. Comparison of stream height as a function of time for the case of propylene oxide being projected from a 6.35 cm (2.5 in) diameter nozzle with predictions from Eq. (1). The initial velocity of the stream was 44.5 m/s (146 ft/s).

IV. SCALED FAE-NUCLEAR BLAST WAVE DATA COMPARISON

The measured overpressure blast waveforms from several of the FAE experiments were digitized and stored in the computer for facilitating both scaling and plotting. Figures 25 through 32 are computer plots of scaled digitized data for several gauge locations for FAE Shot No. 1, 1200 Tuesday, 18 October 1977. Both the experimental ranges and time were scaled linearly, using a scale factor of 16. The scale factor was determined by fitting the measured impulses at various ranges to a 1 KT nuclear impulse versus range curve. Peak impulse rather than peak static pressure was used for determining the scale factor, since the measured peak static overpressures were, in general, low due to finite gauge response times. The solid lines in the plots (Figures 25 through 28) are the scaled experimental blast waveforms and the dashed lines are nuclear blast wave data from a 1 KT yield nuclear event. It is seen that agreement between the scaled FAE data and the nuclear data is acceptable.

Figures 29 through 32 are plots of the positive phase impulse. The data plotted in these figures are from the same gauge locations as those used in the plots of pressure as a function of time. Again, the scaled experimental FAE data are represented by the solid lines and the 1 KT nuclear blast data are represented by the dashed lines. It is seen that agreement is good and in general within 20 percent.

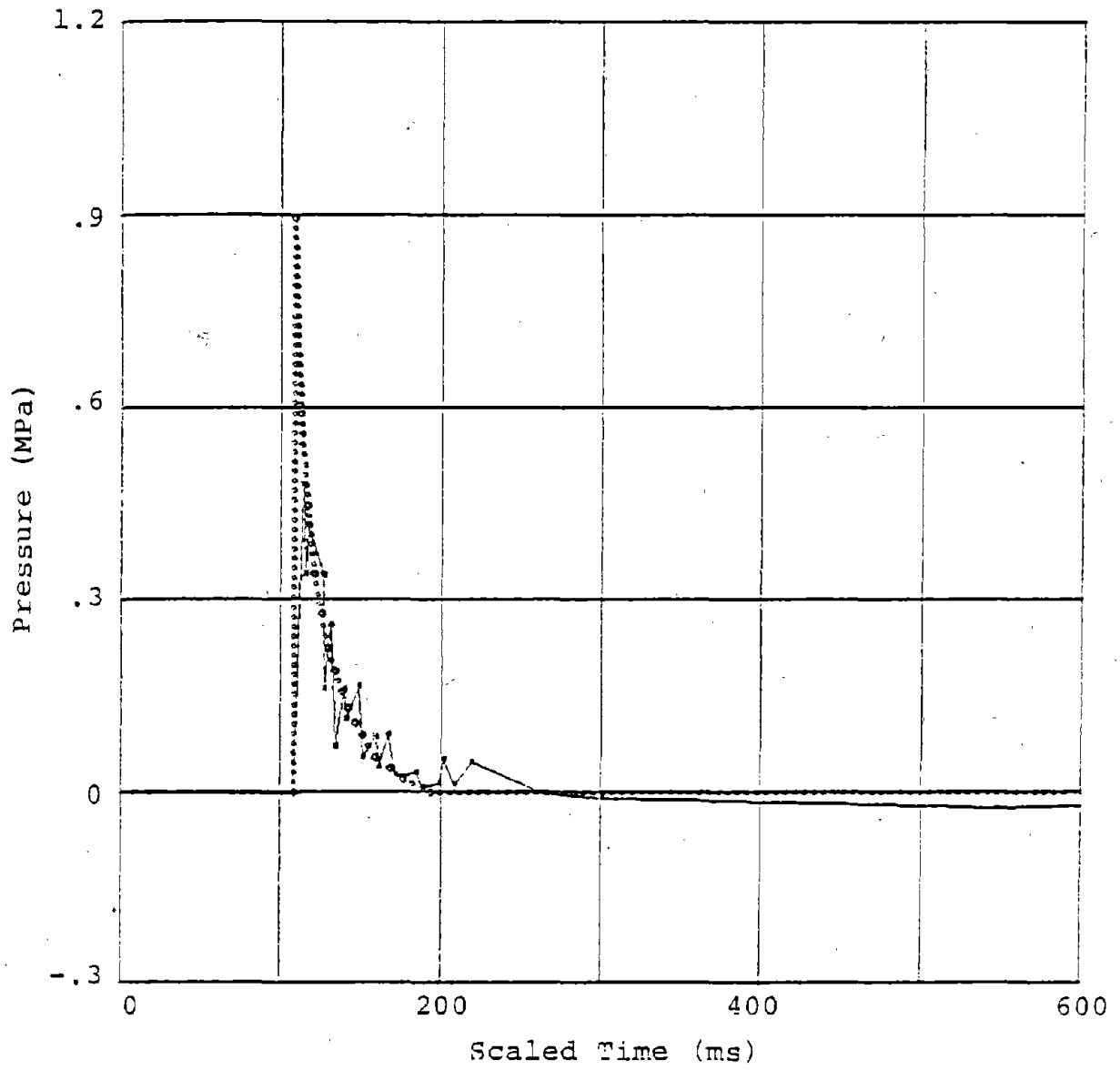


Figure 25. Comparison of scaled measured overpressure as a function of time with a 1 KT nuclear blast waveform. The scaling factor used was 16 and the scaled range was 98 m (320 ft). The experimental data were taken from Shot No. 1, 18 October 1977.

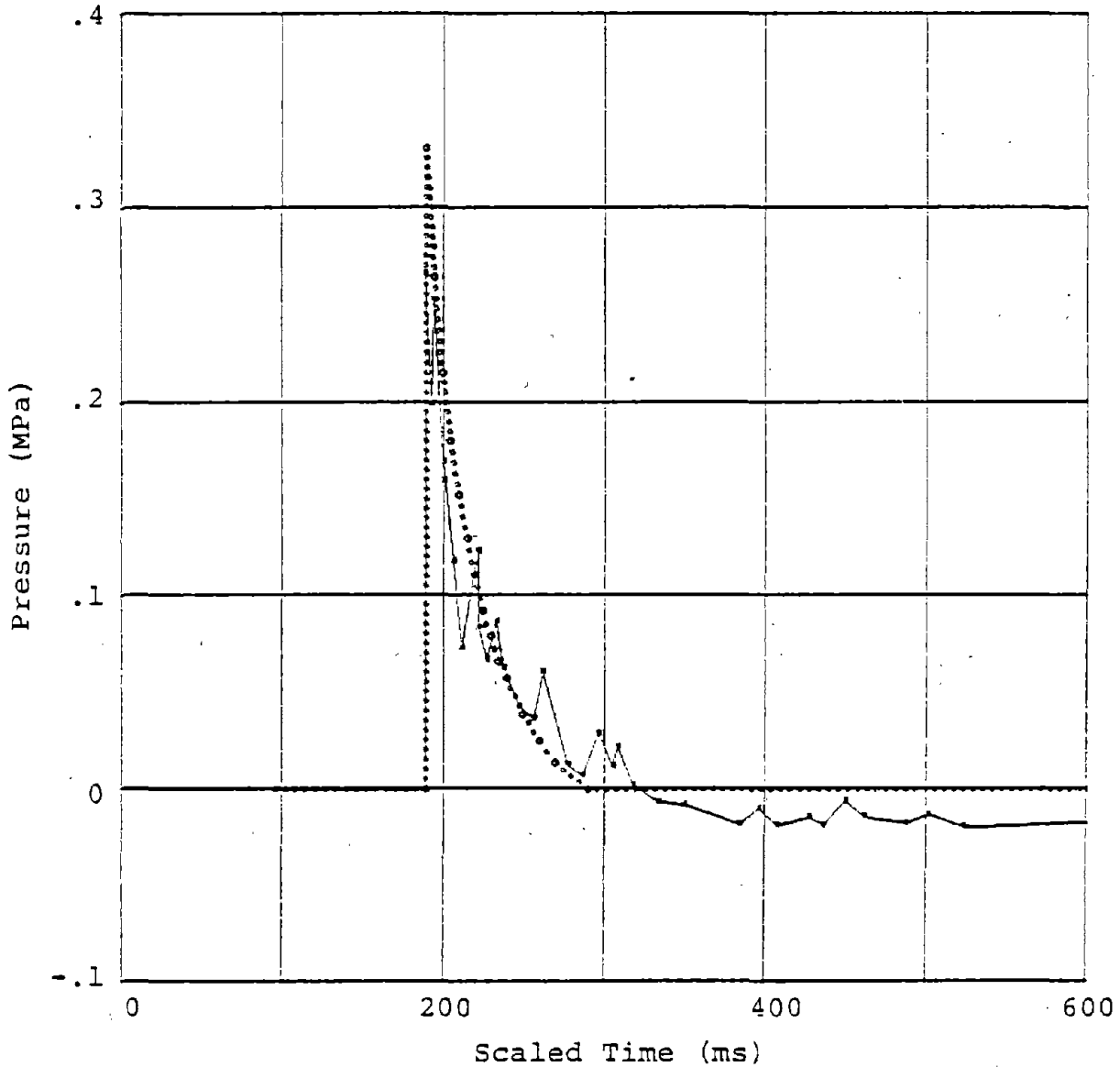


Figure 26. Comparison of scaled measured overpressure as a function of time with a 1 KT nuclear blast waveform. The scaling factor used was 16 and the scaled range was 146 m (479 ft). The experimental data were taken from Shot No. 1, 18 October 1977.

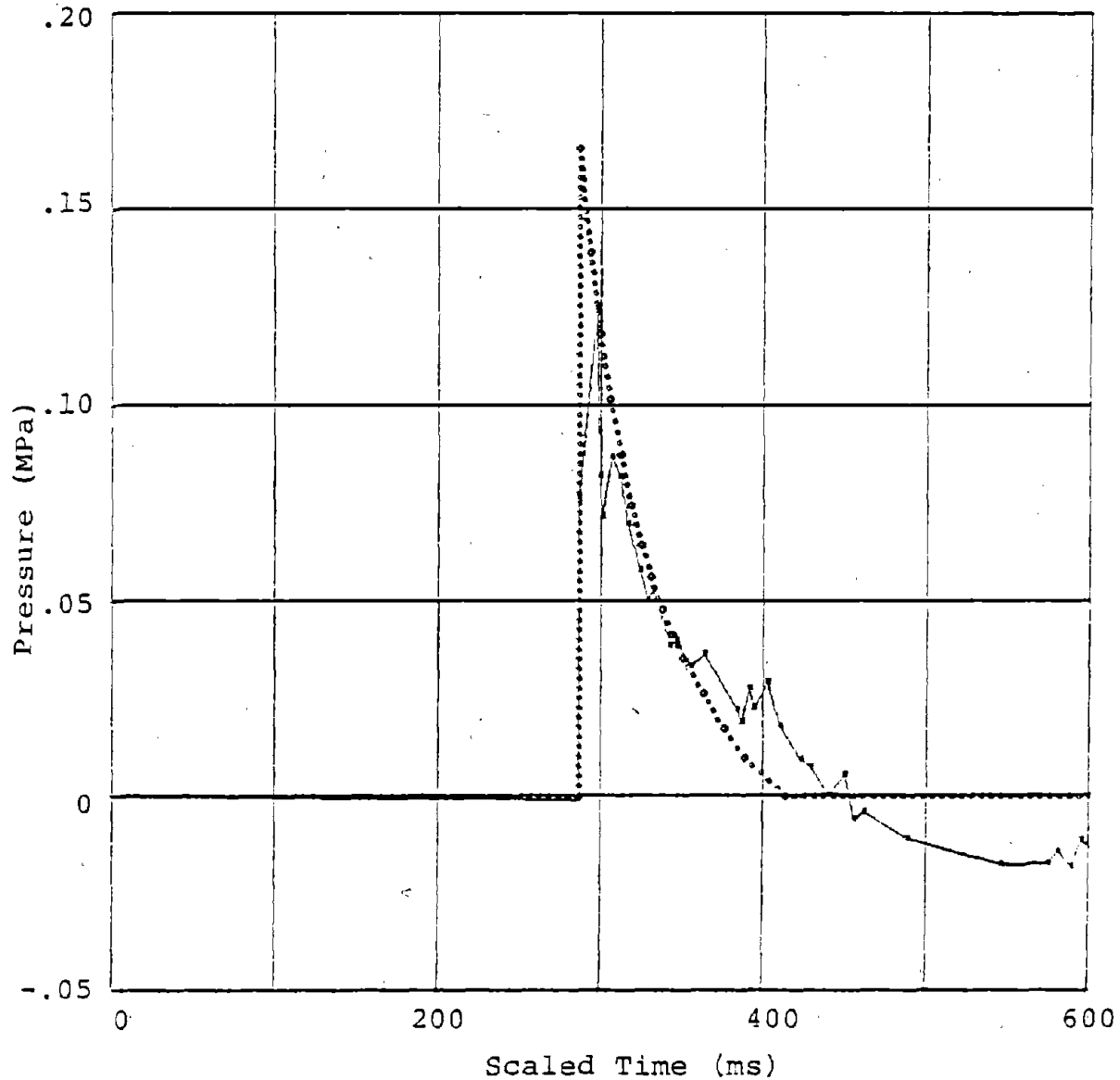


Figure 27. Comparison of scaled measured overpressure as a function of time with a 1 KT nuclear blast waveform. The scaling factor used was 16 and the scaled range was 195 m (640 ft). The experimental data were taken from Shot No. 1, 18 October 1977.

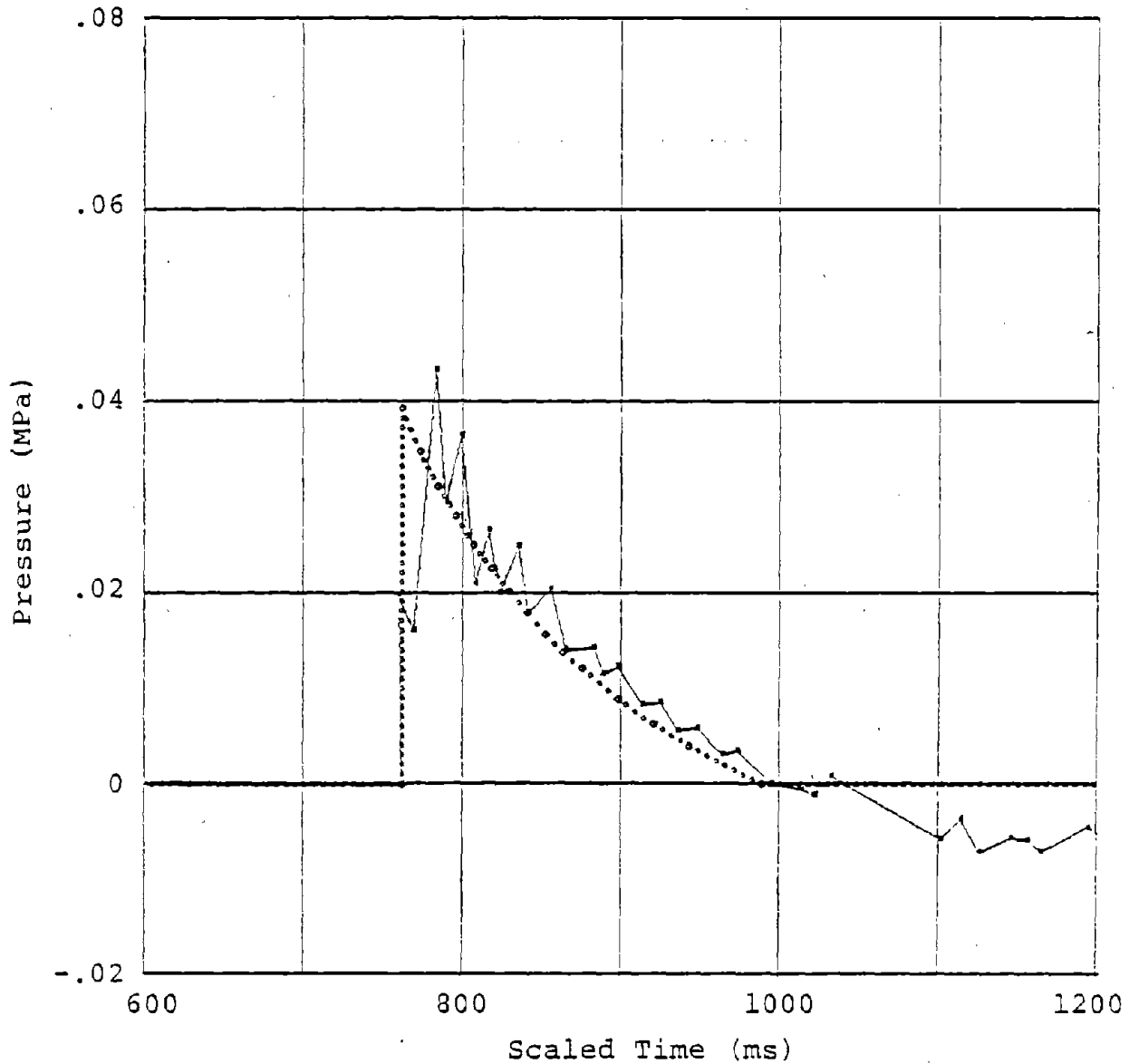


Figure 28. Comparison of scaled measured overpressure as a function of time with a 1 KT nuclear blast waveform. The scaling factor used was 16 and the scaled range was 390 m (1,280 ft). The experimental data were taken from Shot No. 1, 18 October 1977.

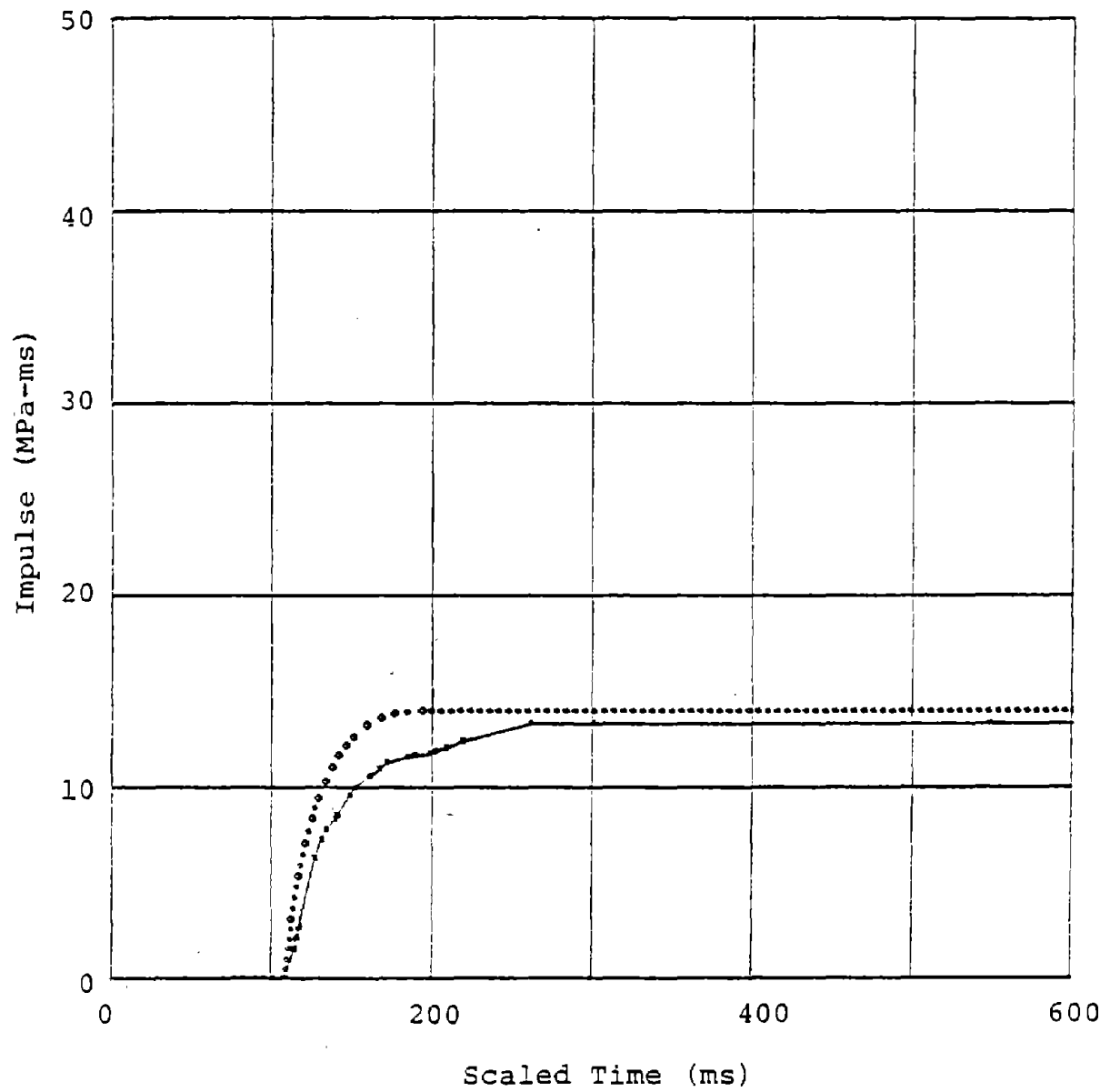


Figure 29. Comparison of scaled measured positive phase impulse with 1 KT nuclear data. The scale factor used was 16 and the scaled range was 98 m (320 ft). The experimental data were taken from Shot No. 1, 18 October 1977.

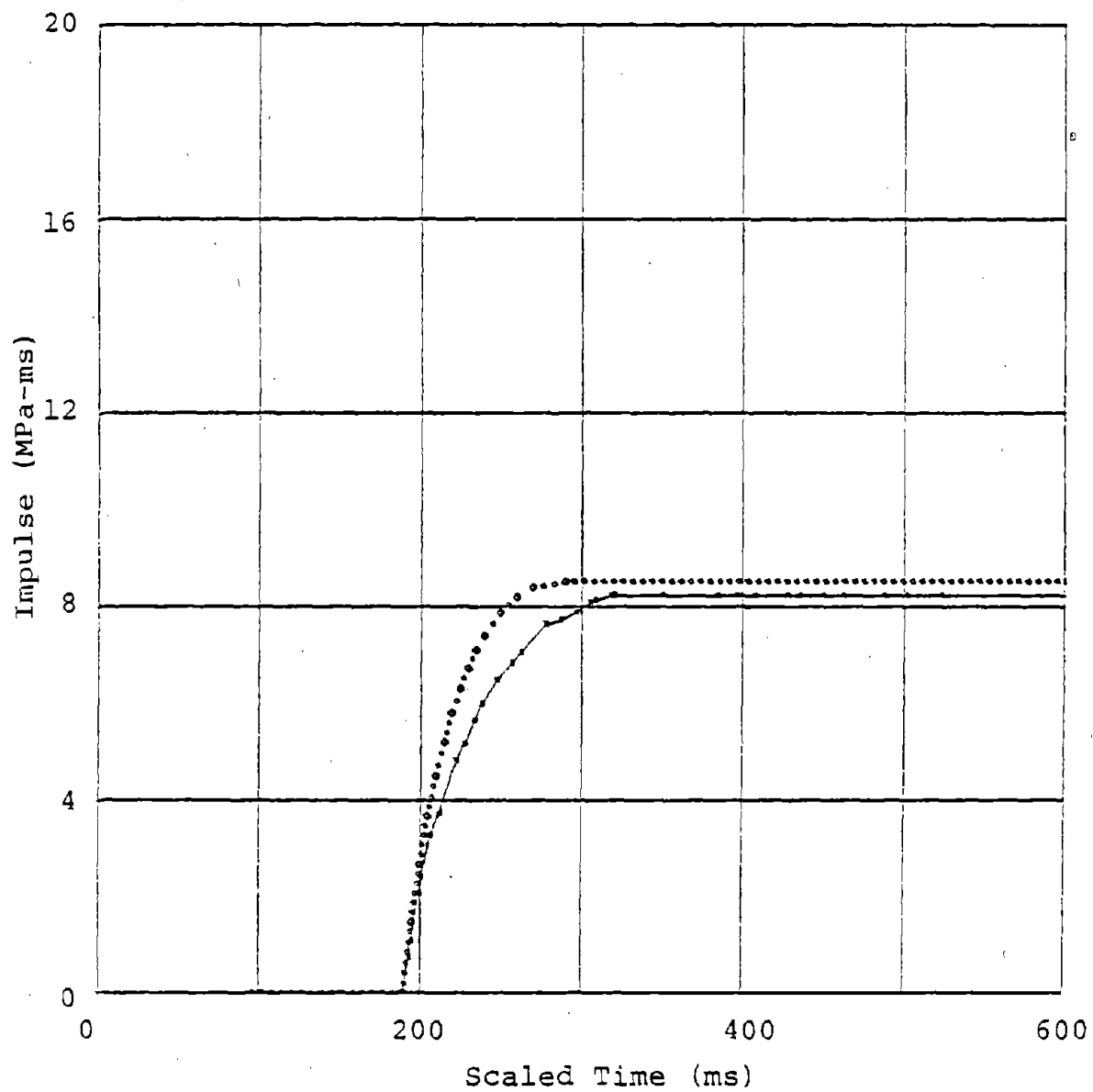


Figure 30. Comparison of scaled measured positive phase impulse with 1 KT nuclear data. The scale factor used was 16 and the scaled range was 146 m (479 ft). The experimental data were taken from Shot No. 1, 18 October 1977.

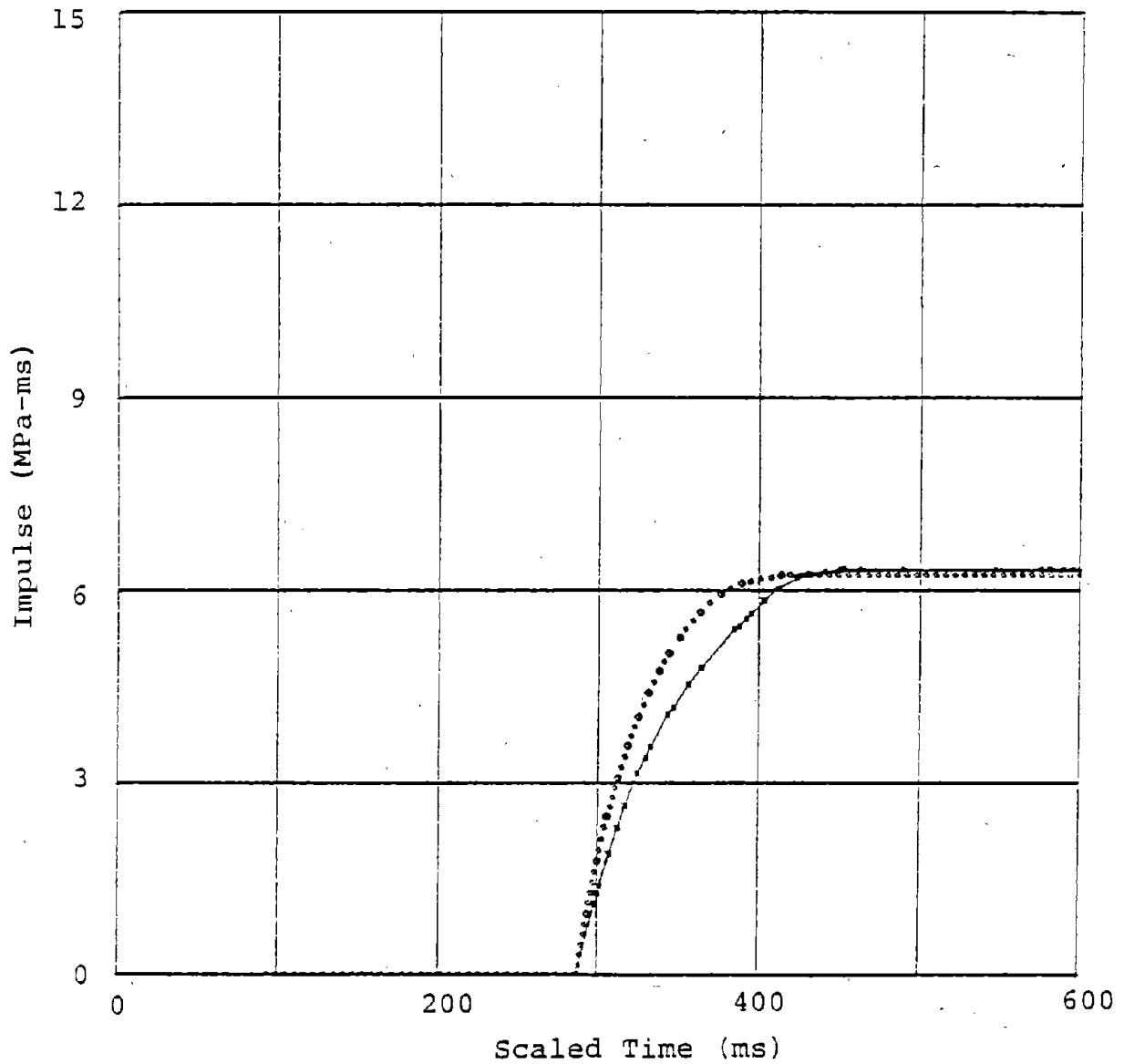


Figure 31. Comparison of scaled measured positive phase impulse with 1 KT nuclear data. The scale factor used was 16 and the scaled range was 195 m (640 ft). The experimental data were taken from Shot No. 1, 18 October 1977.

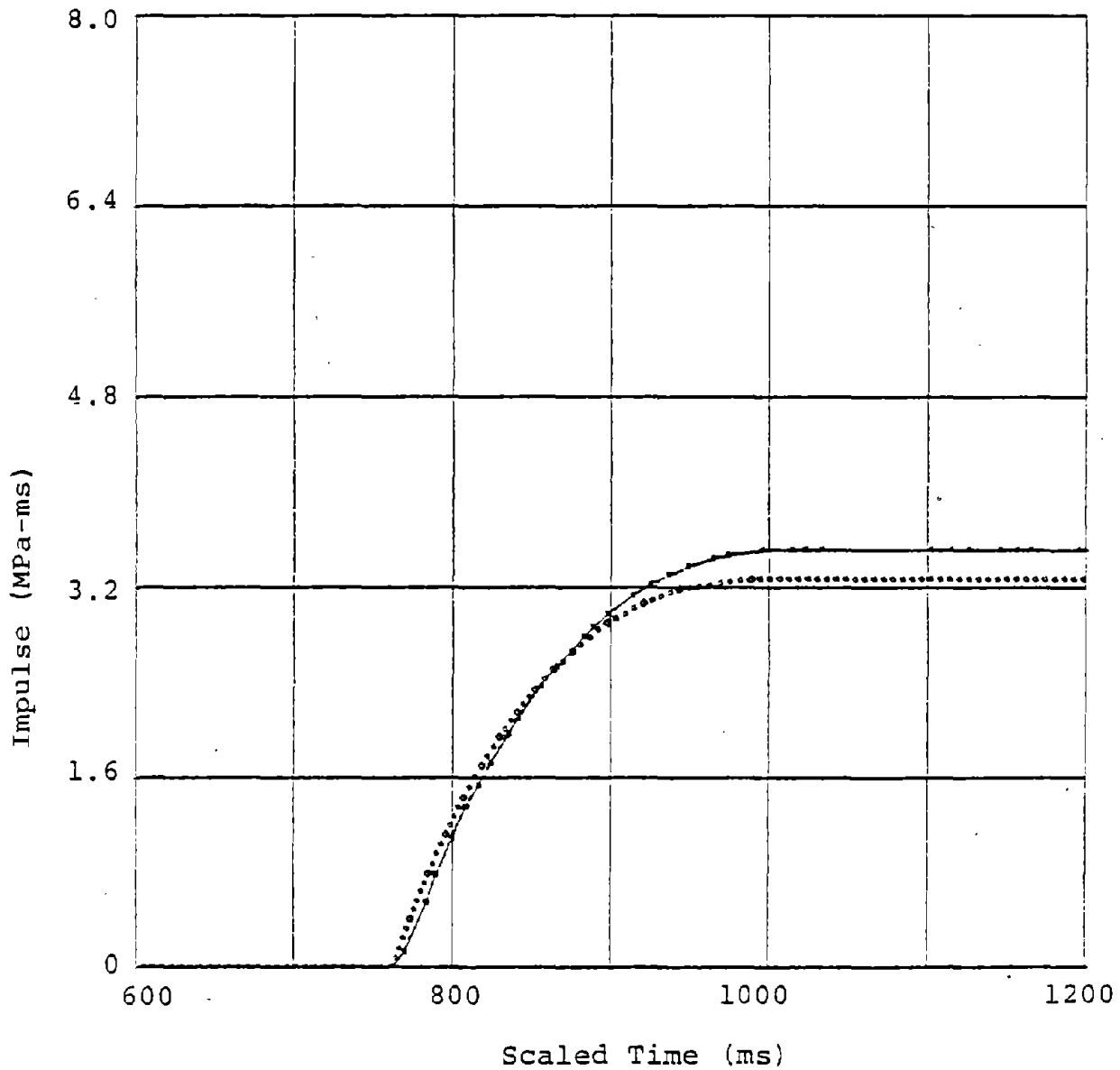


Figure 32. Comparison of scaled measured positive phase impulse with 1 KT nuclear data. The scale factor used was 16 and the scaled range was 390 m (1,280 ft). The experimental data were taken from Shot No. 1, 18 October 1977.

V. CONCLUSIONS AND RECOMMENDATIONS

It can be concluded that the small-scale U-tube facility can be used to disseminate hemispherical FAE clouds, that the clouds can be detonated and that the scaled blast waveforms are in good agreement with 1 KT nuclear waveforms at the scaled ranges. It has also been demonstrated that blast waves generated by the facility are symmetric and repeatable.

Initial data from single nozzle reach experiments indicate that cloud formation time does not scale linearly with cloud diameter. Above a critical nozzle pressure, propylene oxide stream heights are significantly less than those for water. This indicates that nozzles of larger diameter will be required to obtain the heights necessary for the full-scale blast simulator.

Table III lists the remaining problem areas that must be addressed before a full-scale blast simulator can be designed, as well as proposed methods of solution. These problem areas include alternate fuel detonability, fuel property effects, single nozzle stream characteristics, driving pressure requirements, contact surface effects, dispenser design, safety requirements, and construction and life-cycle costs.

While there are still some problem areas remaining that need to be addressed before an intermediate or full-scale FAE blast facility can be constructed, results obtained to date indicate that such a facility is indeed feasible.

Table III. Recommendations for Further Investigations

Remaining Problem Areas	Proposed Methods of Solution
Alternate Fuel Detonability	Hemispherical Cloud Detonation Studies
Fuel Property Effects <ul style="list-style-type: none"> - Viscosity - Vapor Pressure - Surface Tension 	Single Nozzle Experiments Using Various Fuels
Single Nozzle Stream Characteristics <ul style="list-style-type: none"> - Total Height - Breakaway Height - Stripping - Fuel Distribution - Fuel-Air Mixing 	Single Nozzle Experiments
Safety Requirements <ul style="list-style-type: none"> - Test Procedures - Fuel and Propellant Handling 	Hazards Analysis and Required Tests
Construction and Life-Cycle Costs <ul style="list-style-type: none"> - Hardware Configuration and Costs - Fuel Costs - Test Setup Time - Turn-Around Time - Instrumentation - Personnel Requirements 	Cost Analysis
Driving Pressure Requirements <ul style="list-style-type: none"> - Maximum Pressure - Pressure History 	Single Nozzle Experiments
Contact Surface Effects <ul style="list-style-type: none"> - Density Discontinuities - Effect on Close-In Gauge Readings 	Hemispherical Cloud Detonation Studies <ul style="list-style-type: none"> - Drag Measurements - Finely Resolved 1-D Calculation
Dispenser Design Requirements <ul style="list-style-type: none"> - Test Design Concept - Dispenser Unit Requirements - Nozzle Requirements 	Dispenser Tests and Analysis

THERMAL LAYER SIMULATION BY SOLAR FURNACE RADIATION

T.M. Knasel, M.D. McDonnell, R. Sievers, and A. Houghton

1.0 INTRODUCTION AND BACKGROUND

Science Applications, Incorporated (SAI) has been active in the Defense Nuclear Agency Airblast program both with theoretical and experimental studies for many years. The present contract is an extension of a continuing program which has been examining the phenomena associated with soil blow-off and thermal layer development. Almost three hundred soil samples have been subjected to solar furnace radiation at the 35Kwth facility at the White Sands Missile Range to examine the initiation and development of soil blow-off.

The present effort has aimed at the development of an instrumented chamber which would confine blow-off to the vertical direction and allow a simulation of thermal layer development. Identification of sources of thermal radiation suitable for use with such an apparatus was a preliminary design requirement since source geometry plays a significant role in determining useful flux outputs of various sources.

This paper will present some of the preliminary conclusions and designs developed so far in the course of our work. Exhibit 1 outlines the results as they will be presented.

2.0 PROBLEM STATEMENT

When previous experimental efforts had definitely demonstrated that soil blow off could be initiated by the intense light levels created in a solar furnace facility, it was realized that an experimental tool for the investigation of thermal layers and their development was feasible.

BRIEFING OUTLINE

- PROBLEM STATEMENT
- EXPERIMENTAL MODELING
- RADIATION SOURCES
- SAI TEST APPARATUS
- MEASUREMENT OF TOA CONDITIONS
- TEST PLAN
- CONCLUSIONS

EXHIBIT 1

It was suggested that, if the blow off could be confined in a column with a constant cross section and perimeter effects were negligible, containment of the hot air and evolved material might allow simulation of thermal layer development. Instrumentation of the layer to measure properties such as temperature, sound velocity, dust density, etc. would allow comparison with measurements taken on weapons tests when thermal layers were observed. Exhibit 2 indicates some of the major steps required for successful completion of the present program.

3.0 EXPERIMENTAL MODELING

3.1 ASSUMPTIONS

The basic premise behind the experimental program is outlined in Exhibit 3. The initial assumption is that, with proper pulse shaping, solar furnace radiation can be used to simulate the thermal output from a nuclear weapon. If the simulation is accurate then this thermal radiation will interact with the surface of a soil sample in the containment vessel and, if boundary effects are negligible, a thermal layer will develop.

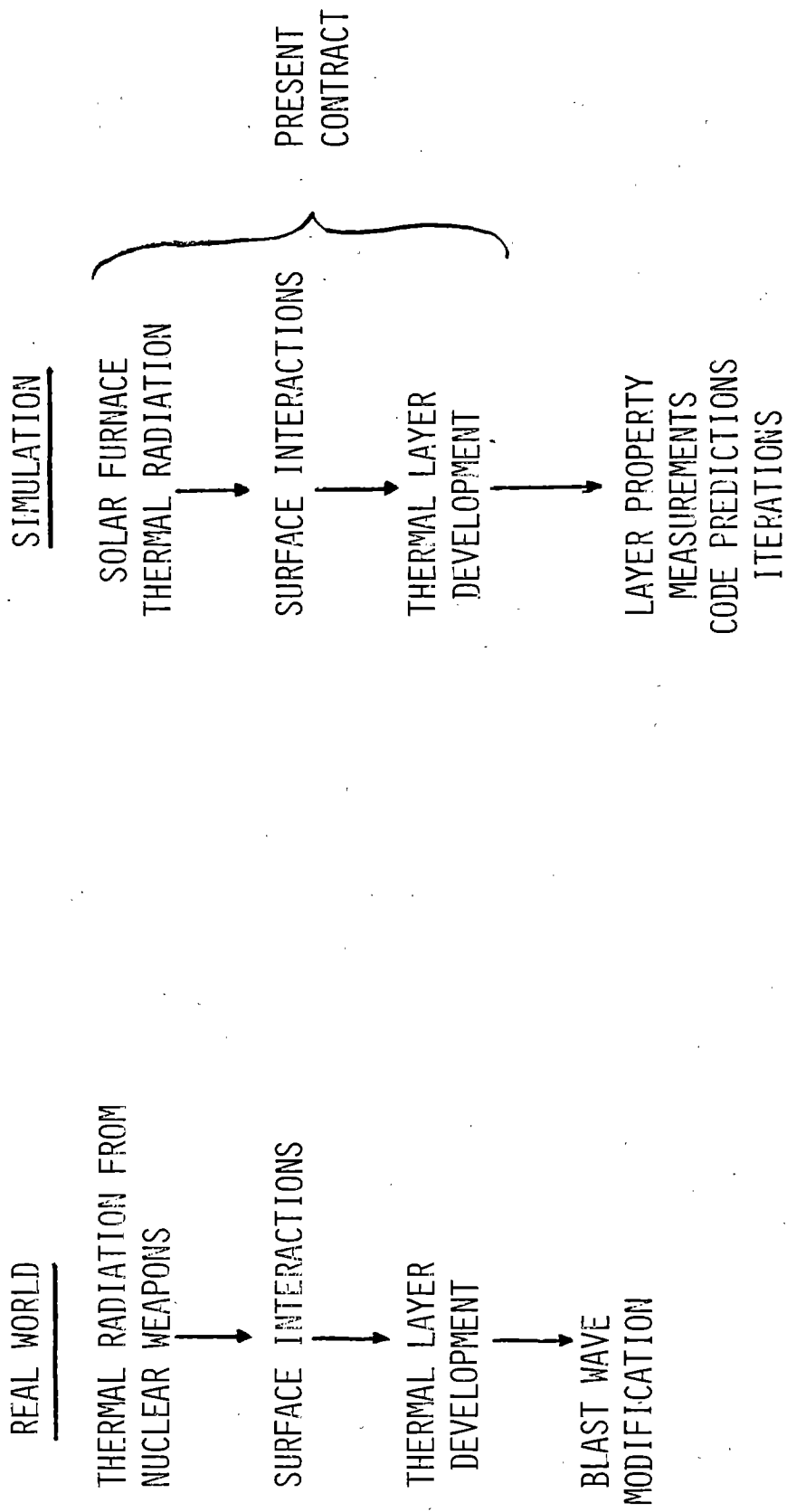
In the real world of an actual above ground nuclear explosion this thermal layer can have a significant effect on the time of arrival and shape of the succeeding blast wave. In the case of the simulation, it has not yet been decided how feasible it would be to study blast wave propagation in the tube but the measurement of thermal layer properties would provide inputs to existing codes which will allow the verification of present predictive techniques.

Exhibit 4 schematically represents the four principle steps in the modification of the nuclear blast wave which is expected to occur when the thermal environment interacts with a non-ideal surface to form a thermal layer and precursor. A more detailed layout of some of the factors effecting thermal layer development specifically is presented in Exhibit 5.

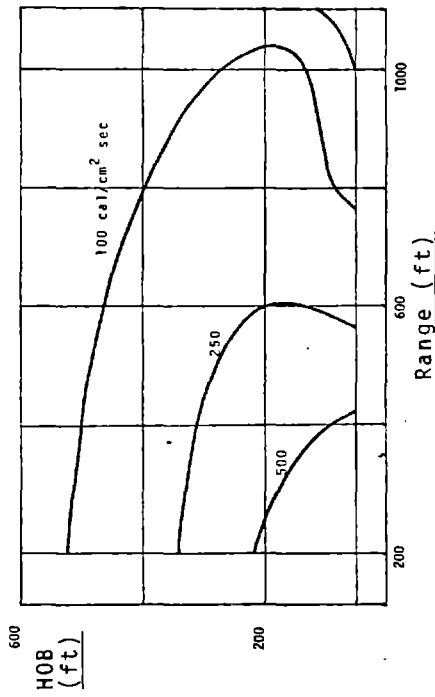
PROBLEM STATEMENT

- DEVELOP AND DEMONSTRATE THERMAL LAYER SIMULATION CAPABILITY
- CALIBRATE INSTRUMENTS TO MEASURE LAYER PROPERTIES
- INTEGRATE AND TEST INSTRUMENTATION
- PERFORM SIMULATION
- INTEGRATE WITH AND SUPPORT
 - PREVIOUS SAI SOLAR FURNACE SOIL TESTS
 - LASL CODE DEVELOPMENTS
 - GEORGIA TECH DIVERTER STUDIES
 - SAI THERMOCHEMICAL REACTION TESTS

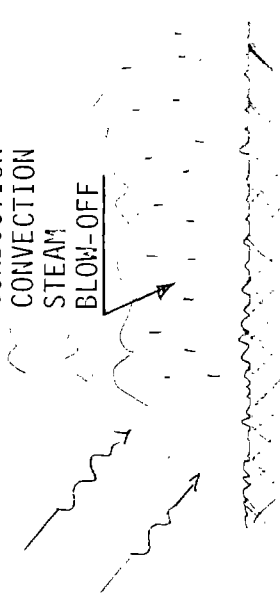
EXPERIMENTAL MODELING



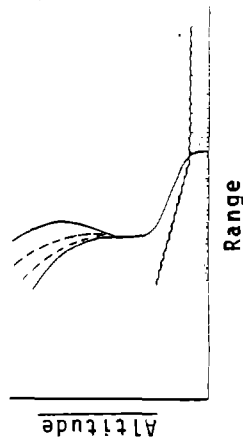
NON-IDEAL BLAST WAVE DEVELOPMENT



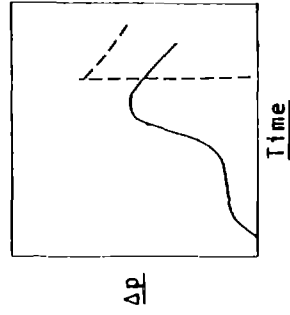
ABSORPTION
CONDUCTION
CONVECTION
STEAM
BLOW-OFF



THERMAL ENVIRONMENT



BLAST WAVE PRECURSOR



OVERPRESSURE MODIFICATIONS

EXHIBIT 4

ILLUSTRATION OF THE THERMAL LAYER DEVELOPMENT

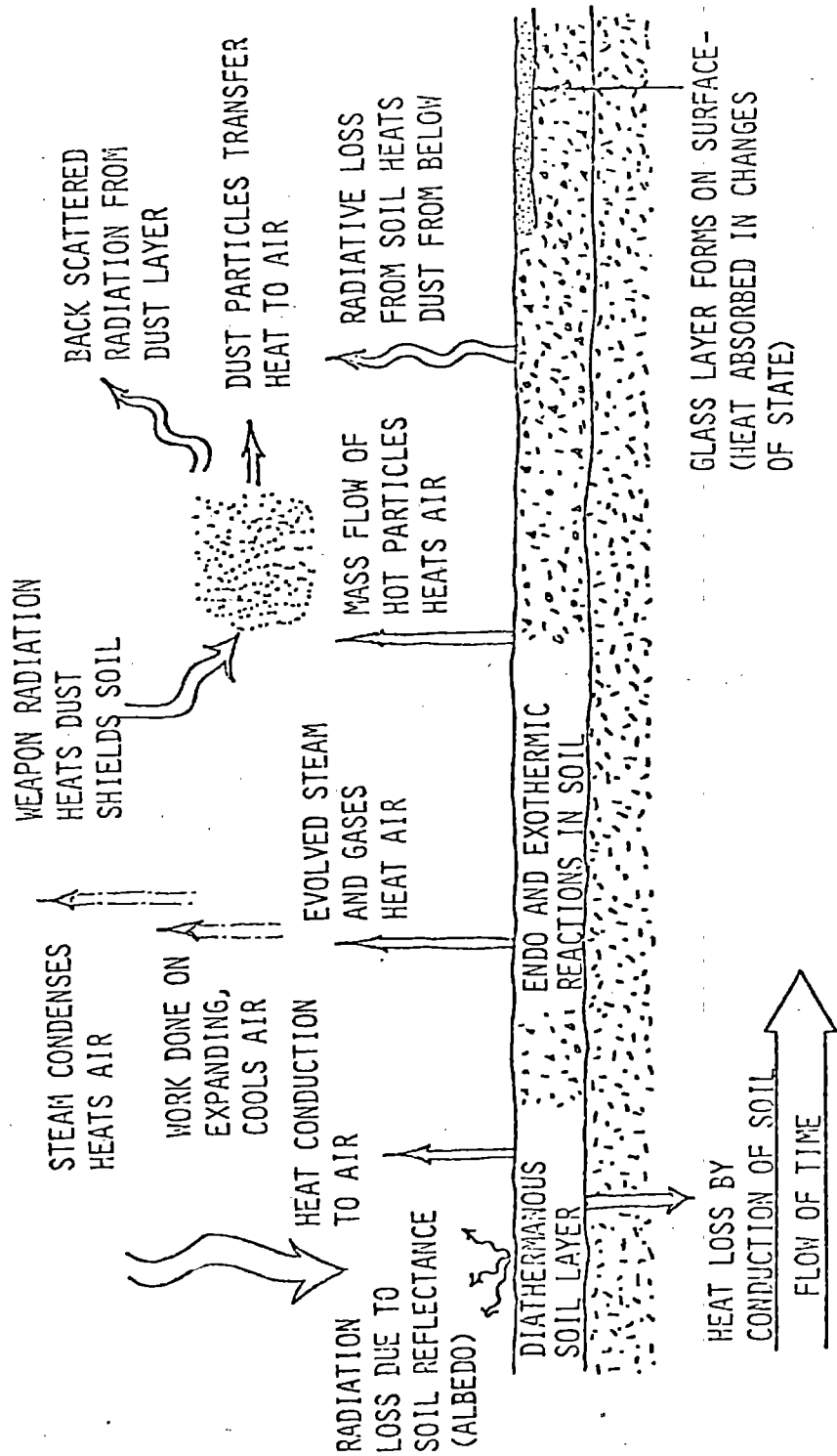


EXHIBIT 5

3.2 PRESENT EXPERIMENTAL APPROACH

3.2.1 Overview

Within the present effort a survey of potential radiation sources has been performed to identify sources suitable to the experimental plan. The apparatus for the experiments has been designed in a modular fashion both for ease of construction and shipping and to allow its employment at various facilities by merely changing the beam diverter section (Exhibit 6).

Construction of the first prototype apparatus and instrumentation has stressed economy since improvements will necessitate design changes. Preliminary tests indicate the equipment will be sufficient for full scale proof of concept tests at existing solar furnaces and will provide useful information on both real time development of thermal layers and conditions at time of arrival (TOA) of the blast pulse. If expectations are fulfilled and thermal layer development is observed work will continue in the subsequent phase to incorporate improvements in the design of the basic apparatus and in the instrumentation.

3.2.2 Source Selection

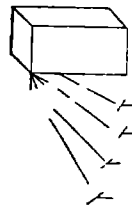
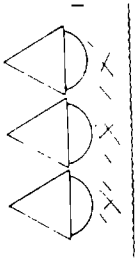
Exhibit 7 presents some of the more pertinent information on the types of radiation sources seriously considered as candidates in the present study. Desirable characteristics would include: high flux, up to $\sim 600 \text{ cal/cm}^2 \text{ sec}$; high fluence, up to $\sim 300 \text{ cal/cm}^2$; large area, a minimum of about $.03 \text{ m}^2$ for the present apparatus; a black body spectrum similar to that of a nuclear weapon, $\sim 5-6000^\circ \text{ K}$; fast response flux control, on off cycling of $\sim .011 \text{ sec}$; rapid recycling of tests; reproducibility; ease of operation and maintenance and; low cost, to mention a few

PURPOSE OF EFFORT

- | | | |
|------------------|---|--|
| THIS PHASE | ● | IDENTIFY POTENTIAL RADIATION SOURCES |
| | ● | DESIGN APPARATUS FOR HIGH FLUX THERMAL LAYER DEVELOPMENT EXPERIMENTS |
| | ● | CONSTRUCT PROTOTYPE APPARATUS |
| | ● | DEVELOP INSTRUMENTATION TO MEASURE TOA* CONDITIONS |
| | ● | DEVELOP TEST PLAN |
| SUBSEQUENT PHASE | ● | TEST AND IMPROVE PROTOTYPE APPARATUS AND TOA INSTRUMENTATION |
| | ● | DEVELOP INSTRUMENTATION TO MEASURE REAL TIME CONDITIONS |
| | ● | INTEGRATE INSTRUMENTATION |
| | ● | CALIBRATE EQUIPMENT |
| | ● | CONDUCT TESTS |
| | ● | ANALYZE DATA |

RADIATION SOURCES

	PEAK FLUX (CAL/CM ² SEC)	AREA (M ²)	BLACK BODY °K	FLUX CONTROL
RADIANT HEAT FACILITIES	20-100	5	2000°	ELECTRICAL
THERMOCHEMICAL REACTIONS	20-200	COST LIMIT	2600°	CONFIGURATION
SOLAR FURNACES	30-360	.03 → 1.0	5600°	MECHANICAL
FLASHLAMPS	TO 4000	COST LIMIT	9000°	ELECTRICAL



Obviously no single source can supply all of the desired characteristics but, on the other hand, no single simulation requires all of the extremes in the parameters. As Exhibit 8 indicates, the majority of the simulations originally planned can be met by the CNRS facility. Limitations are primarily a result of the fact that flux control must be provided by mechanical shutters which cannot open and/or close fast enough to simulate thermal pulses produced by low yield weapons or TOA cutoffs representing short ground ranges. The second major limitation is the practical flux limit of about $200 \text{ cal/cm}^2 \text{ sec}$.

Both of these limits should be improved by a source consisting of a battery of flash lamps. Flash lamps are electrically switched and can produce extremely high flux levels. Their main limitation is cost, especially when large area illumination or high total fluence is required, since energy must be stored in expensive capacitor banks. SAI has developed a concept for a flash lamp source for high flux, low fluence, short to moderate pulse nuclear thermal simulations which would be compatible with the present apparatus.

4.0 TEST APPARATUS

Exhibit 9 shows a schematic diagram of the cross section of the SAI test apparatus. Principal components are the beam shaper, the pulse shaping shutter, the sample chamber, the time of arrival (TOA) shutters, and a soil sample holder at the bottom of the sample chamber.

4.1 BEAM SHAPER

The Beam Shaper shown in Exhibit 10 has been designed specifically for use at the CNRS facility but other designs could be fabricated to allow use of the apparatus with other sources.

SOURCE REVIEW

- CNRS FRENCH FACILITY IS ONLY EXISTING FACILITY THAT CAN FULFILL REQUIREMENTS FOR SIGNIFICANT NUMBER (75-88%) OF TESTS, PRACTICAL FLUX LIMIT IS 200 CAL/CM² SEC
- OTHER FACILITIES (E.G., GEORGIA TECH, STTF) WOULD BE USEFUL FOR PRELIMINARY TESTS AND BACKUP
- FLASH LAMPS HAVE UNIQUE APPLICATIONS FOR REMAINING 12-25% OF TESTS IF DEVELOPMENT PROCEEDS

EXHIBIT 8

SAI TEST APPARATUS - SCHEMATIC CROSS SECTION

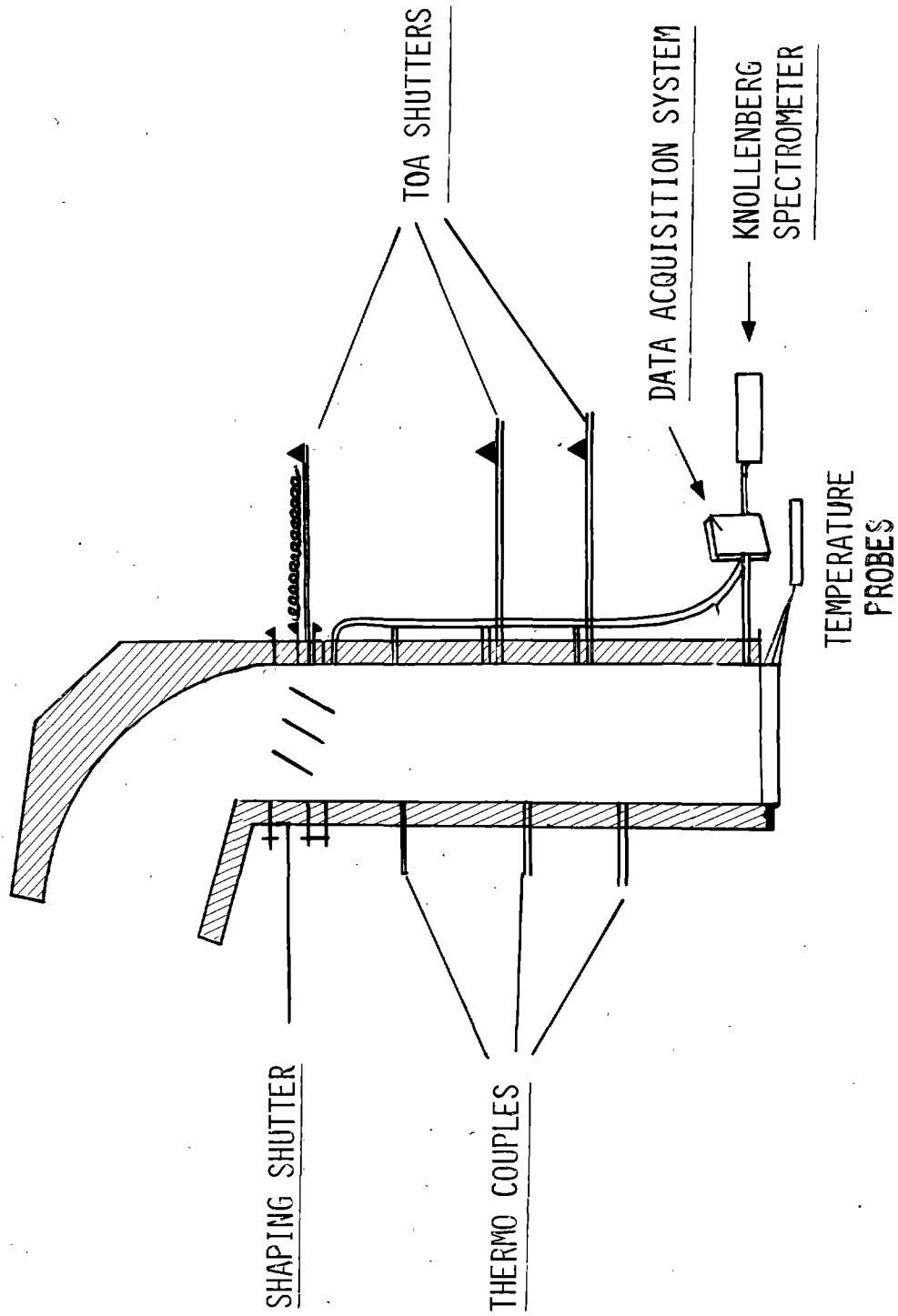
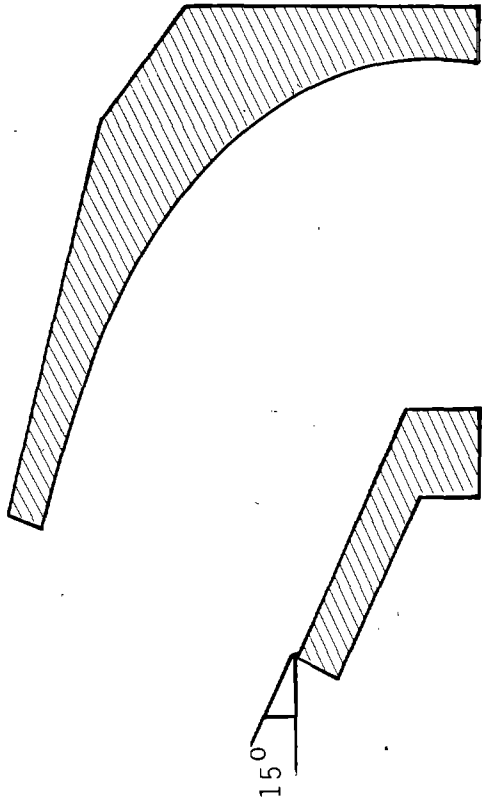


EXHIBIT 9

BEAM SHAPER



- 1 DIMENSION IDEAL LIGHT COLLECTOR 60° FOV
- 8 - 12 GAUGE WELDED STEEL
- 3/4" DIAMETER COOLANT PORTS
- 1" COOLANT JACKET 10 PSI TEST
- REFLECTING SURFACES Ag OVER Ni OVER Cu(R ≈ .85)
- ENTRANCE 7.50" x 6.5"
- EXIT 6.5" x 6.5"

EXHIBIT 10

The 15° angle of orientation for the entrance plane reflects the orientation of the focal zone at the CNRS furnace. The rear reflecting surface is an ideal light collector designed using the principles of non-imaging optics. It has a compound parabolic curvature which reduces the cross section from 7.5" x 6.5" at the entrance to 6.5" x 6.5" at the exit and provides an overall concentration of the flux of about 16 percent.

Construction material is welded steel with a coolant jacket one inch thick, pressure tested for 24 hours at 10 psi to insure against leaks. Internal reflecting surfaces and a reflecting flange around the entrance were electroplated with copper then nickel then silver with hand polishing to improve surface qualities before and after each plating.

Spectral reflectivity of the final silver surface has a theoretical limit averaging about .94 for the visible region. In practice even the smallest amount of tarnish or dust prevents actual attainment of reflectivities greater than .90 to .92. Test coupons of steel polished and electroplated as described above have produced reflectivities ranging from .85 to .89 using an SAI designed reflectometer and a helium neon laser. These lower reflectivity values have been attributed to a non-specular reflectivity component, caused by grain irregularities in the underlying steel substrate, which result in a certain amount of diffuse reflection.

It is felt that the reflectivity can be improved in the next prototype by employing different substrates and/or heavier electroplating. Both of these alternatives would involve added expense, however and field testing will have to be performed to determine whether calculated improvements in performance will justify the expenditure.

4.2 PULSE SHAPING SHUTTER

Exhibit 11 depicts the pulse shaping shutter. This is positioned immediately below the beam shaper and will modify the flux leaving the exit plane so that it simulates the second thermal pulse delivered by a nuclear weapon of any yield ≥ 1.0 KT.

The lower limit of yield simulation is established by the mechanical shuttering problem. Many concepts have been considered in the quest for a shutter which would have the rapid response and variable rise and fall times necessary. Inertia and size problems present the greatest limitations but ease of maintenance, safety and pulse repeatability are not negligible.

The present design employs three butterfly type shutter blades each powered by its own stepping motor. The stepping motors are all controlled by one programmable microcircuit allowing up to 50 steps. Since the limitation is on fast angular acceleration and the rise time of the second thermal pulse from a nuclear weapon is always shorter than the decay time, the limit on yield simulation is established by the minimum shutter opening time of ~ 0.015 sec.

Glasstone quotes the time to the first minimum as

$$T_{\min} = .0025 W^{1/2}$$

and the time to the second maximum as

$$T_{2 \max} = .032 W^{1/2}$$

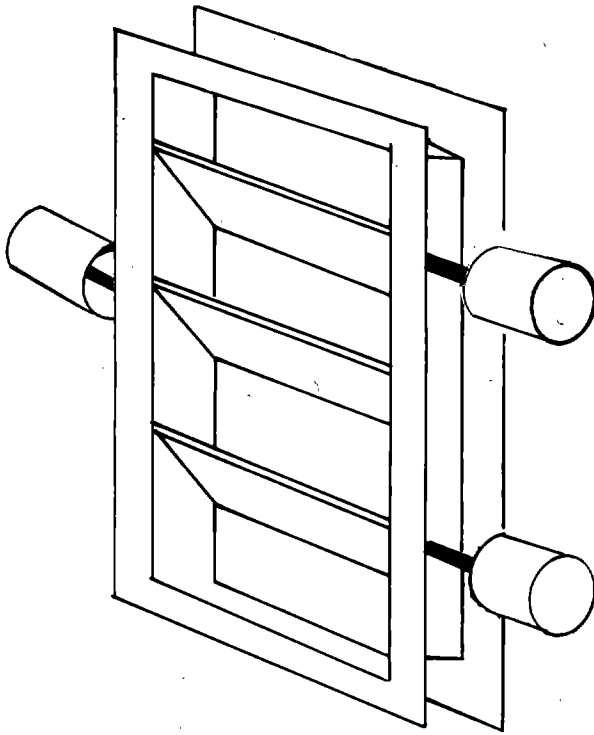
so the rise time of the second pulse is

$$T_{\text{rise}} = T_{2 \max} - T_{1 \min} = (.032 - .0025) W^{1/2}$$

giving, for a $T_{\text{rise}} = 0.015$ sec, a minimum simulatable yield of

$$W \approx 0.7 \text{ KT}$$

PULSE SHAPING SHUTTER



- 3 - 16 GAUGE STEEL ELADES
- 12 GAUGE WELDED STEEL - 2 PIECES
- $\frac{3}{4}$ " COOLANT JACKET 10 PSI TEST
- REFLECTING SURFACES Ag OVER Ni OVER Cu R \approx .85
- CROSS SECTION \sim 6.5" SQUARE
- STEPPING MOTOR AND CIRCUITRY
- MINIMUM SHUTTER OPENING TIME = .015 SEC

4.3 SAMPLE CHAMBER

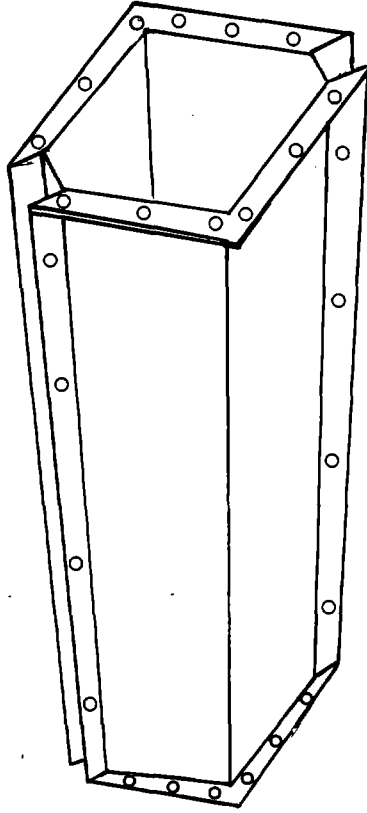
The sample chamber has been produced in two identical right angle sections using essentially the same fabrication techniques as were employed in the production of the beam shaper and the pulse shaping shutter. The two sections may be bolted together directly or may be separated by two spacers running the length of the tube. These spacers are designed to allow instrumentation access to the interior of the sample chamber. In order to reduce hot spots the spacers are made of solid copper since copper has a higher thermal conductivity than the rolled steel used in the rest of the construction. Furthermore, the copper has no noticeable grain structure which increases the overall reflectivity and should reduce heating due to reflective losses. Exhibit 12 schematically depicts the sample chamber.

4.4 TOA SHUTTER

The time of arrival (TOA) shutters (Exhibit 13) are designed to close and seal off sections of the sample chamber at times calculated to represent the arrival of the blast wave. Various ranges from the given nuclear detonation can be simulated by characterization of the thermal pulse shape through the operation of the pulse shaping shutter and heliostat control. Thus, for each pulse shape a number of runs will be performed with all the TOA shutters closing at later and later times to represent thermal layer development at longer and longer ground ranges while fewer heliostats provide flux in accordance with the inverse square relationship.

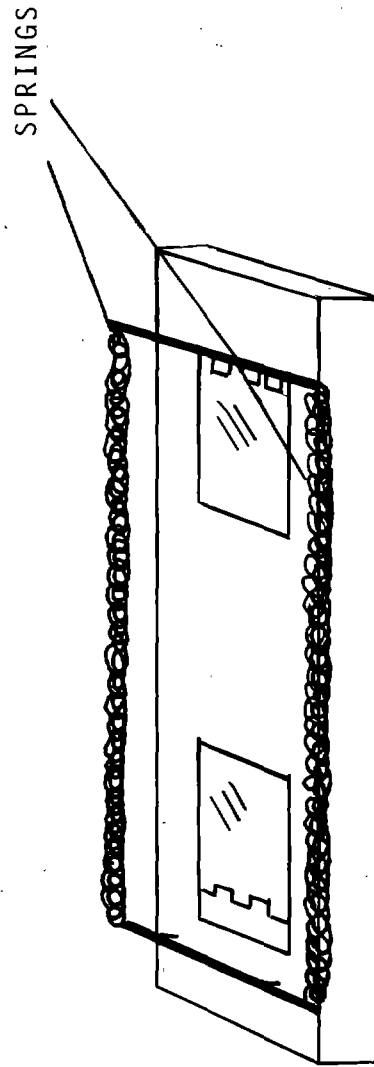
After operation of the TOA shutters, blow off within the sample chamber can be collected and analyzed. Since the apparatus is modular in design, sample chambers of various length can be bolted together and separated by TOA shutters to provide variable resolution of the thermal layer as a function of height. At present, only one 48" long sample chamber has been fabricated for the initial prototype.

SAMPLE CHAMBER



- 12 GAUGE WELDED STEEL
 - $\frac{3}{4}$ " DIAMETER COOLANT PORTS
 - 1" COOLANT JACKET 10 PSI
 - REFLECTING SURFACES Ag OVER Ni OVER Cu ($R \approx .85$)
 - CROSS SECTION \sim 6.5" SQUARE
 - LENGTH 48"
 - INSTRUMENTATION ACCESS THRU DIAGONALLY OPPOSING Cu STRIPS Ag OVER Ni
- EXHIBIT 12

TOA SHUTTER



- ELECTRICALLY RELEASED
- 14 GAUGE GALVANIZED STEEL GUIDES
- 16 GAUGE STAINLESS STEEL SHUTTERS
- 2 ~ 100 LB. SPRINGS
- MIN. CLOSING TIME ~ .015 SEC
- MIN. OPENING TIME ~ .015 SEC

EXHIBIT 13

5.0 INSTRUMENTATION

If all parameters could be measured in real time, then the number of runs for each soil sample and the number of TOA shutters could be reduced. (Runs at various peak fluxes could still be necessary to simulate range variations). Unfortunately, the environment in the sample chamber is expected to be quite severe.

The high flux levels alone put strong demands on probe survivability. Furthermore, measurement techniques which rely on ambient light will be hampered by the high and variable flux levels. Acoustic measurements may be confused by noise produced in the resonating sample chamber by soil during the blow off processes and by shutter action. Temperature measurements require assurance that the proper aspect of the thermal layer (gas temperature, large or small blow off particle temperature, etc.) is being unambiguously monitored and not affected by edge effects near the chamber walls.

Until the severity of the sample chamber environment has been measured under test conditions, it is difficult and impractical to make commitments to any particular type of instrumentation. Exhibit 14 lists some of the measurement techniques which have been examined so far and their probable applicability to TOA or real time measurements. Another system of interest, the Knollenberg spectrometer, was depicted in Exhibit 9. This system uses fiber optics and a laser source to determine particle size distributions by shadow size or forward scattering patterns. It is possible that, with a laser source, the ambient light levels will not be a problem. Probe cost and survivability may require that real time sampling of the blow off be done by "vacuuming" out samples from the column.

MEASUREMENT OF TOA CONDITIONS

	MEASUREMENT TAKEN		
	POST EXP	TOA	REAL TIME
● SMALL PARTICLE ARRIVAL BY LIGHT SCATTERING			
● MASS DISTRIBUTION BY IMPACT CASCADE			
● LARGE PARTICLE ARRIVAL FROM ACOUSTIC IMPACT			
● MASS DISTRIBUTION BY SIEVING			
● GAS TEMPERATURES BY ASPIRATED THERMOCOUPLES			
● INCIDENT ENERGY BY CALORIMETRY			
● SOUND VELOCITY BY ACOUSTIC RESONATOR			
● LOSS OF SOIL MASS BY WEIGHING			
● PARTICLE STATE BY MICROSCOPIC EXAMINATION			
● SOIL TEMPERATURE BY THERMOMETRIC PROBES			

EXHIBIT 14

6.0 TEST PLAN

There are three general phases to the present test plan as depicted in Exhibit 15. Laboratory tests will continue in the near future to make optical reflectivity and transmissivity measurements. These measurements will aid in predicting flux levels on the soil as a function of incident flux for geometries representative of the focal zones of candidate furnaces. Measurements of apparatus temperature variations as a function of coolant flow rate and incident flux for levels of these variables which can be generated in the lab will help to plan requirements for full scale testing.

Preliminary tests at solar furnaces will concentrate on characterizing flux variations in the apparatus as a function of heliostat operation, focal zone geometry etc., and survivability of components and subassemblies at moderate flux levels and generation of blow off and thermal layers for evaluation of sample chamber environment hazards to instrumentation.

After preliminary solar furnace tests more definite commitment to the various measurement techniques outlined in Section 5.0 can be made and a comprehensive test plan can be generated for full scale solar furnace operation.

At the present time it is envisioned that full scale tests will include both real soil samples and a parametric study of mock soil samples produced by mixing standard sand, clay, silt and organic matter as constituent components. Refinement of this test plan will be dependent upon results of preliminary testing.

TEST PLAN

LAB TESTS

- COOLANT FLOW
- HEAT LAMP/TEMPERATURE VARIATION
- TRANSMISSIVITY

PRELIMINARY FURNACE TESTS

- MODERATE FLUX COOLANT TESTS
- REFLECTIVITY DEGRADATION TESTS
- SURVIVABILITY TESTS
- INSTRUMENTATION TESTS
- PRELIMINARY SOIL TESTS

FULL SCALE FURNACE TESTS

- COOLANT TESTS
- SURVIVABILITY TESTS
- INSTRUMENTATION TESTS
- SOIL TESTS

7.0 SUMMARY

Past SAI experience has indicated that flux levels obtainable in solar furnaces are capable of causing blow off in a wide variety of soil samples. In order to experimentally examine thermal layer development it was realized that larger sample areas and, therefore, higher fluences would be a prime necessity. A second requirement appeared to be that the soil blow off be confined from expansion in the horizontal direction in order to increase the heating rate of the air above the soil as the hot particles were ejected.

These requirements lead to an evaluation of radiant heat sources and a conceptual design of an apparatus capable of interfacing with the most applicable source and providing the necessary containment. At the present time the French CNRS facility has been identified as being sufficient for the largest fraction of the required tests and a prototype apparatus fulfilling the basic test requirements has been designed and constructed.

Instrumentation sufficient to measure thermal layer conditions after the high flux environment has been terminated is being investigated and some real time measurements appear promising.

Department of Energy solar furnaces within the United States could be used for low flux level tests of the apparatus and for some soil tests if scheduling problems arise at the CNRS facility.

Principal conclusions are presented in Exhibit 16 while an outline of near term future plans appears in Exhibit 17.

CONCLUSIONS

- FLUXES PRODUCED BY CNRS SOLAR FURNACE ARE SUFFICIENT TO SIMULATE FLUXES WITHIN 75 TO 88% OF THE YIELD, HOB AND RANGE VARIATIONS OF INTEREST
- DESIGN AND FABRICATION OF PROTOTYPE TEST APPARATUS IS COMPLETE
- INSTRUMENTATION TO MEASURE TOA CONDITIONS APPEARS FEASIBLE AT PRESENT TIME
- REAL TIME MEASUREMENT TECHNIQUES ARE PROMISING BUT WILL DEPEND ON SAMPLE CHAMBER ENVIRONMENT AT HIGH FLUX
- PRELIMINARY TESTING CAN BE PERFORMED AT DOE FACILITIES

FUTURE PLANS

- LABORATORY TEST OF COOLANT/TEMPERATURE
- TOA INSTRUMENT INTEGRATION
- PRELIMINARY SOLAR FURNACE TESTS
- CONTINUED DEVELOPMENT OF REAL TIME MEASUREMENT APPARATUS
- SOIL PROPERTY MEASUREMENTS

EXHIBIT 17

SECTION I

INTRODUCTION

1. BACKGROUND

The close of the atmospheric nuclear testing era forced the development of nuclear weapon simulation techniques which could be used to examine both nuclear weapon effects and structural vulnerability to the effects. During 1976, a preliminary design for a large area high flux thermal radiation generator was conceived. The Defense Nuclear Agency (DNA) funded a small program during FY 77 to test the thermal radiation generator concept. The results of the initial tests indicated that a high flux (greater than 200 cal/cm²-sec) and large area thermal radiation generator could be developed. Subsequently DNA funded a full scale development program (DNA001-77-C-0200) to create a large area thermal radiation simulator. This paper describes the thermal radiation simulator development program.

SECTION II

THE THERMAL RADIATION SIMULATOR DEVELOPMENT PROGRAM

2. GENERAL

The purpose of the thermal radiation simulator (TRS) development program was to develop a TRS which could produce a high flux (~200 cal/cm²) and fluence (~200 cal/cm²) thermal radiation pulse over areas which could equal or exceed 100 square meters (1075 foot²). The TRS was to have an adjustable flux, fluence, and pulse duration. It was also to be self-consuming upon ignition and have as few structural parts as possible.

3. CREATION OF INTENSE THERMAL RADIATION FIELDS

3.1 Nuclear Weapons

The detonation of a nuclear weapon in the atmosphere produces an extremely intense thermal radiation field. A description of the thermal radiation generated by a nuclear weapon is found in Reference 1.

"Initially, radiation emitted during a nuclear explosion is in the soft X-ray region of the spectrum, but the X-rays are absorbed in the air, thereby, heating it to high temperatures. This heated air, which constitutes the fireball, in turn radiates in a spectral region roughly similar to that of sunlight received at the earth's surface

(6000°K Blackbody). It is the radiation (ultraviolet, visible, and infrared) from the fireball, traveling with the velocity of light, which is received at distances from the explosion and constitutes the thermal radiation produced by a nuclear weapon."

"For an air burst at altitudes below 50,000 feet, the thermal radiation is emitted in two pulses. The first, which is quite short, carries roughly 1 percent of the total radiant energy; the second pulse is the more significant and is of longer duration. The total length of the effective thermal pulse increases with the energy yield of the explosion. Thus, the duration of the effective pulse from a 10-megaton air burst is about 30 seconds, whereas from a 1-kiloton explosion it is roughly 0.3 second."

"In an ordinary air burst, roughly 30 to 40 percent of the total energy yield is emitted from the fireball as thermal radiation. This means that for every kiloton of energy released, one-third of a kiloton, i.e., 3.3×10^{11} calories, is in the form of thermal radiation. This is equivalent to nearly 400,000 kilowatt hours, and such a large amount of energy has important consequences."

To study these consequences in an era of prohibited atmospheric testing, a thermal radiation simulator must be built. Subsequent paragraphs describe techniques for generating thermal radiation fields with sufficient intensity to allow the study of thermal radiation effects on various targets and structures.

3.2 Electric and Solar Thermal Radiation Sources

3.2.1 General

Studies by Knasel (References 2, 3) have shown that solar and electric thermal radiation sources are available to study thermal radiation effects on small samples or targets. Table 1 (Reference 3) presents a list of solar and electric thermal radiation sources compiled by Knasel.

Table 1 Thermochemical, Solar, and Electric Thermal Radiation Sources

Location	Power (calorie) ($\times 10^3$)	Peak Flux (cal/cm ² -sec)	Sample Area (m ²)
Thermochemical Source (TRS)	500,000	200-350	200
Sandia Base Albuquerque	407	60	4
Odeillo-Font Romeu France	239	400	0.06
Georgia Tech Atlanta	95.7	90	0.1
Odeillo-Font Romeu France	23.9	125	0.01
White Sands Missile Range New Mexico	5.98	100	0.01
Flash lamps ^a	7.18	3000 to 4000	0.01

^aFlash lamps may be used at any location where sufficient power can be supplied.

3.2.2 Electric Thermal Radiation Sources

All electric thermal radiation sources are severely limited in size by their power consumption. Maximum practical power supplies to electric sources are about 30 KW. Power supplies and lines supplying larger electric thermal radiation simulators become unwieldy, immobile, and impractical. To produce a thermal radiation pulse with a fluence of only 12 cal/cm² over an area of approximately 50m², nearly 25 MW of power would be required. This power is approximately equal to the amount of power that a city with a population of 100,000 would use during the time that the thermal radiation pulse is produced. Therefore, though large area electric thermal radiation simulators are conceivable, the practical area limit of an electric thermal radiation simulator is approximately 0.1m².

3.2.3 Solar Thermal Radiation Sources

Extensive studies by Knasel (References 2 and 3) have shown that a number of solar furnace installations can be used to produce high intensity light for thermal radiation experiments. In addition, the spectral characteristics of the solar radiation are quite similar to those found in nuclear weapon thermal radiation.

The low intensity of sunlight reaching the earth and the physical size of existing solar furnaces limit the thermal radiation target area to less than 4m^2 for fluxes of $60\text{ cal/cm}^2\text{-sec}$ and 0.3m^2 for fluxes exceeding $100\text{ cal/cm}^2\text{-sec}$. These target areas, though sufficient for small sample irradiations, are too small for tests which require irradiations of full scale military equipment or examination of macroscopic material response to thermal radiation.

3.3 Thermochemical Thermal Radiation Sources

3.3.1 General

A thermochemical thermal radiation source releases energy as light during an exothermic chemical reaction. The type of reaction most commonly used to generate light is the oxidation of a metal. If the salt formed by the metallic oxidation reaction has a high melting point, little energy released by the reaction can be absorbed as translational energy in the salt's molecules. Some energy in the salt is absorbed as vibrational energy however most is released as light. If the energy release per gram of metallic salt is high ($>2000\text{ cal/gm}$), the majority of the reaction's energy will be released in the form of visible and near infrared light.

A TRS utilizing appropriate combinations of thermochemical light sources can be built to very large dimensions. In addition, a thermochemical TRS can produce flux levels as high as $375\text{ cal/cm}^2\text{-sec}$. Initial studies of large thermochemical systems demonstrated that a large area, high flux TRS could be built. Succeeding paragraphs explain the selection of pyrotechnic mixtures chosen by SAI to create a large area TRS.

3.3.2 Pyrotechnic Mixtures

Though many pyrotechnic mixtures that produce intense light are available, several criteria had to be met before a mixture for the TRS could be accepted. The criteria were:

- a. The mixtures must have a large energy release per unit weight of pyrotechnic mixture.
- b. The pyrotechnic mixture must be safe to handle and ship. Both reactants and products must be non-toxic.
- c. The mixture must have a low cost per unit weight.
- d. The material must be readily available in a convenient form.

Four metal oxidation reactions release large quantities of light, utilize non-toxic reactants, and produce non-toxic products. They are the reactions of aluminum, zirconium, magnesium, and titanium with oxygen. Table 2 presents the reactions, products and energy released during these metal oxidation reactions.

Table 2 Metal Oxidation Reactions

Metal	Reaction	Energy Release per Mole of Product (kcal/mole)	Energy Release per gram of Metal (kcal/gm _M)
Aluminum	$2Al + \frac{3}{2} O_2 \rightarrow Al_2O_3$	389	7.21
Magnesium	$Mg + \frac{1}{2} O_2 \rightarrow MgO$	146	6.00
Titanium	$Ti + O_2 \rightarrow TiO_2$	214	4.47
Zirconium	$Zr + O_2 \rightarrow ZrO_2$	179	1.96

To produce high intensity bursts of light with these metals, large quantities (>1.0Kg) of the metal must be ignited and burned in a relatively short time (<1 sec). To accomplish this type of burn, the metal must be finely divided and intimately mixed with oxygen. Magnesium and zirconium, in the finely divided state, are extremely flammable and present enormous handling, processing and shipping problems. In addition, titanium, magnesium, and zirconium powders are very expensive. Aluminum powder, in contrast, is a readily available, low cost, commercially produced product that is shipped as a non-hazardous substance. In addition, aluminum releases upon oxidation more energy per unit weight than any of the other metals studied.

Several tests were conducted to examine various techniques for mixing and igniting aluminum and oxygen. These tests, described in succeeding portions of this text, demonstrated that aluminum and oxygen could be readily mixed and ignited in large TRS systems. The results of these tests and the fact that aluminum and oxygen mixtures met the criteria established for TRS pyrotechnic mixtures determined the acceptance of aluminum and oxygen as the pyrotechnic mixture for future TRS work.

4. EARLY TRS RESEARCH

Initial work conducted during 1976 under contract DNA001-75-C-0209 proved that aluminum powder could be rapidly mixed with oxygen and burned to create high flux and fluence light pulses over large areas. Several techniques for mixing and igniting the Al and O₂ mixtures were examined during the tests. The most promising technique was one which mixed and ignited the reactants by use of a small quantity of explosive. Figure 1 illustrates the explosive mixed system used on early TRS tests.

These initial tests highlighted areas of research and problems which had to be pursued to develop a useful TRS. Particular problems and research areas uncovered in the early TRS work were:

- a. Early TRS systems produced excessive airblast during TRS ignition.
- b. Waveforms of early TRS systems were difficult to control.
- c. Scaling laws for flux and fluence generated by various yield TRS systems had to be developed.
- d. Techniques for varying pulse signatures had to be developed.
- e. Techniques for the control and calculation of TRS debris had to be developed.

5. LABORATORY EXPERIMENTS

5.1 General

As discussed previously, several problem areas were identified on the initial series of TRS tests. The most serious problem areas were the airblast output generated by TRS ignition and the lack of control over TRS radiation pulse shapes. The laboratory research program was developed to study these problem areas and to find mechanisms for their control.

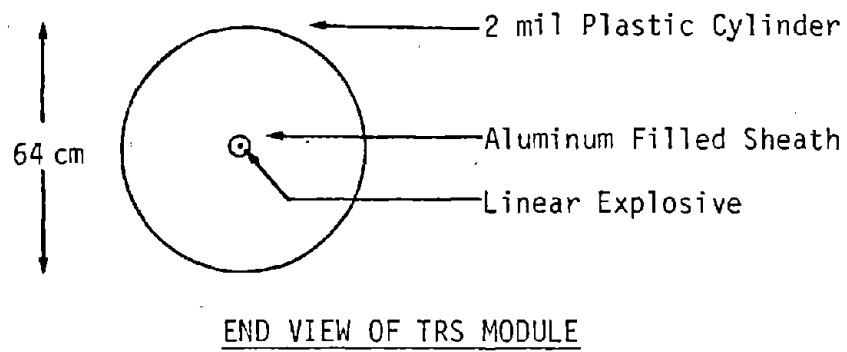
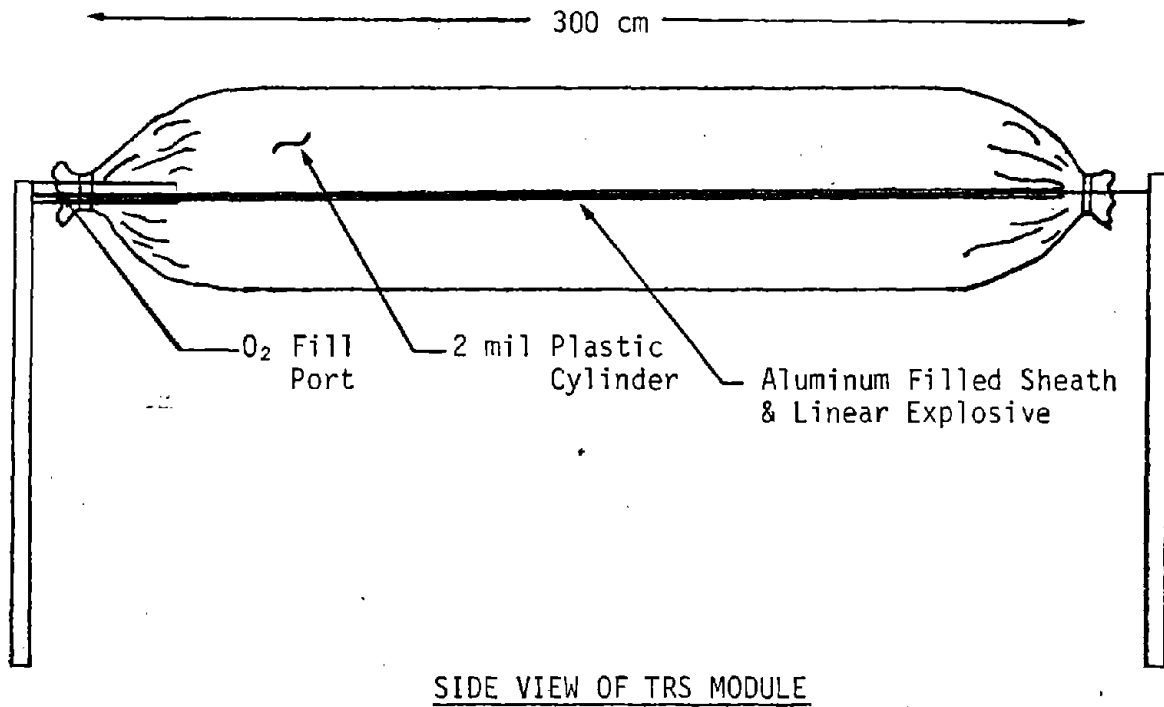


Figure 1 An Early E-System TRS Module

A series of small experiments indicated that the combustion rate of Al was responsible for the blast generated during a TRS burn. It was also apparent that control of the Al combustion rate could lead to control of the TRS pulse shape. Research indicated that variables which could effect the Al combustion rate were:

- a. The mixing rate of Al and O_2 in a TRS,
- b. The Al particle size, and
- c. The concentration of O_2 available to the Al- O_2 reaction.

A research program was conducted to examine these variables. In general the program was a 6 variable study in which a variety of parameters effecting thermal radiation and side effects (airblast and debris) output of the simulator were examined. The variables were:

- a. Mixing Technique. High explosive (HE) dispersal and high pressure gas dispersal of Al into an oxygen atmosphere were examined.
- b. Mixing Rate. The mixing rates (i.e. the HE to Al weight ratio or Al weight to driver gas pressure ratio) of Al and O_2 were varied.
- c. O_2 /Al Ratio. The weight ratios of Al to O_2 in the TRS were varied to examine reactant concentration effects on TRS output.
- d. Al Particle Size. The size of Al particles and particle size distribution in a mixture of Al powders were varied.
- e. Physical Size. The physical size of systems were varied to determine Al yield scaling effects on TRS output.
- f. Output Parameters. Flux, fluence, airblast, debris and convective heating (parameters effected by the other five variables) were measured.

The basic research approach was to hold 4 of the first 5 variables constant and change the other. Flux, fluence, and airblast, subsets of variable "f", were measured on each experiment. The effect of variables "a" through "e" on TRS output were recorded, analyzed, and used to design larger TRS systems. Subsequent sections describe the laboratory experiments in greater detail.

5.2 Laboratory TRS Design

Three small TRS designs were created for the laboratory research program. Figure 2 presents an illustration of the high-explosive mixed TRS (E-System) used in the laboratory experiments. Figures 3 and 4 present lab-scale high pressure gas mixed (C-System) and pre-mixed (K-System) TRS designs.

5.3 Laboratory TRS Flux Output

The laboratory experiments illustrated the expected trend in flux output of TRS systems. Rapidly mixed TRS systems which burned Al powder of small particle sizes produced the highest flux. Surprisingly, C-system TRS designs produced peak power outputs which exceeded those of many E-system TRS. E-system TRS designs which burned 6 μ Al powder and had low Al to HE ratios produced the greatest peak power outputs of all lab-scale TRS systems.

5.4 Laboratory TRS Fluence Output

The fluence output of TRS systems examined during the laboratory experiments illustrated two distinct trends.

For E-system TRS designs, a slow mixing rate (i.e. a high Al to He ratio) coupled with a high concentration of oxygen (i.e. a high O₂ to Al ratio) produced the greatest fluence. A new ratio combining these two variables for TRS designs with constant weight or scaled Al yields was developed: the O₂ to HE weight ratio. If energy or fluence outputs are scaled linearly with the Al yield, the energy release per gram of Al is determined. The product of the O₂/Al weight ratio and Al/HE weight ratio is the O₂/HE ratio. Figure 5 illustrates the interrelationship between scaled TRS fluence and the O₂/HE weight ratio of E-system TRS designs. Also illustrated in Figure 5 is the dependence of TRS fluence output on Al particle size. For E-systems TRS designs with constant O₂/HE weight ratios, fluence output is inversely proportional to the average particle diameter of Al powder burned in the TRS.

5.5 Summary of Laboratory Experiments

Variables which effected the combustion rate of Al and O₂ in the laboratory TRS designs were examined. The effect of combustion rate on flux, fluence, and airblast output of the small TRS designs were determined. Techniques for thermal radiation pulse shaping were also examined. The results of many TRS tests indicate that rapid rise time, high-peak power radiation pulses accompanied by intense airblast may be produced by systems which burn very fine Al powder at rapid combustion rates. High fluence pulses with lower peak power and small airblast signals may be created with TRS designs that mix Al slowly with O₂

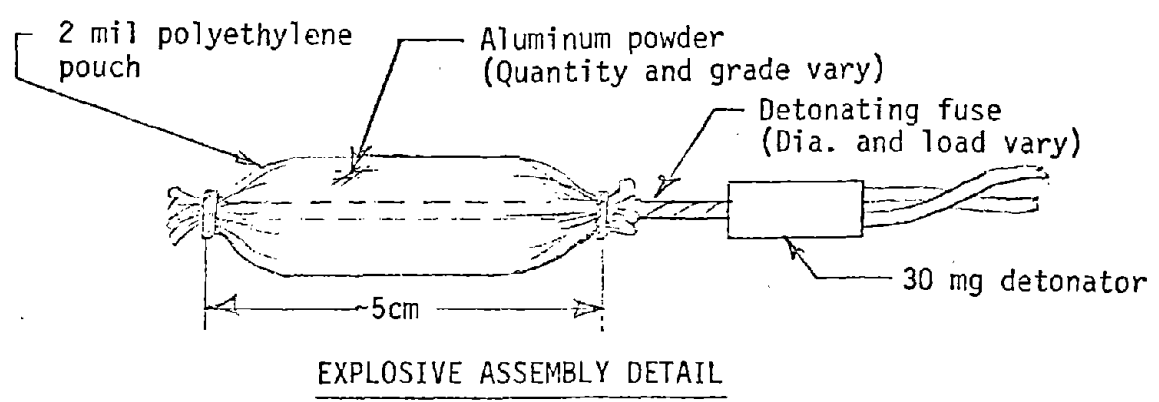
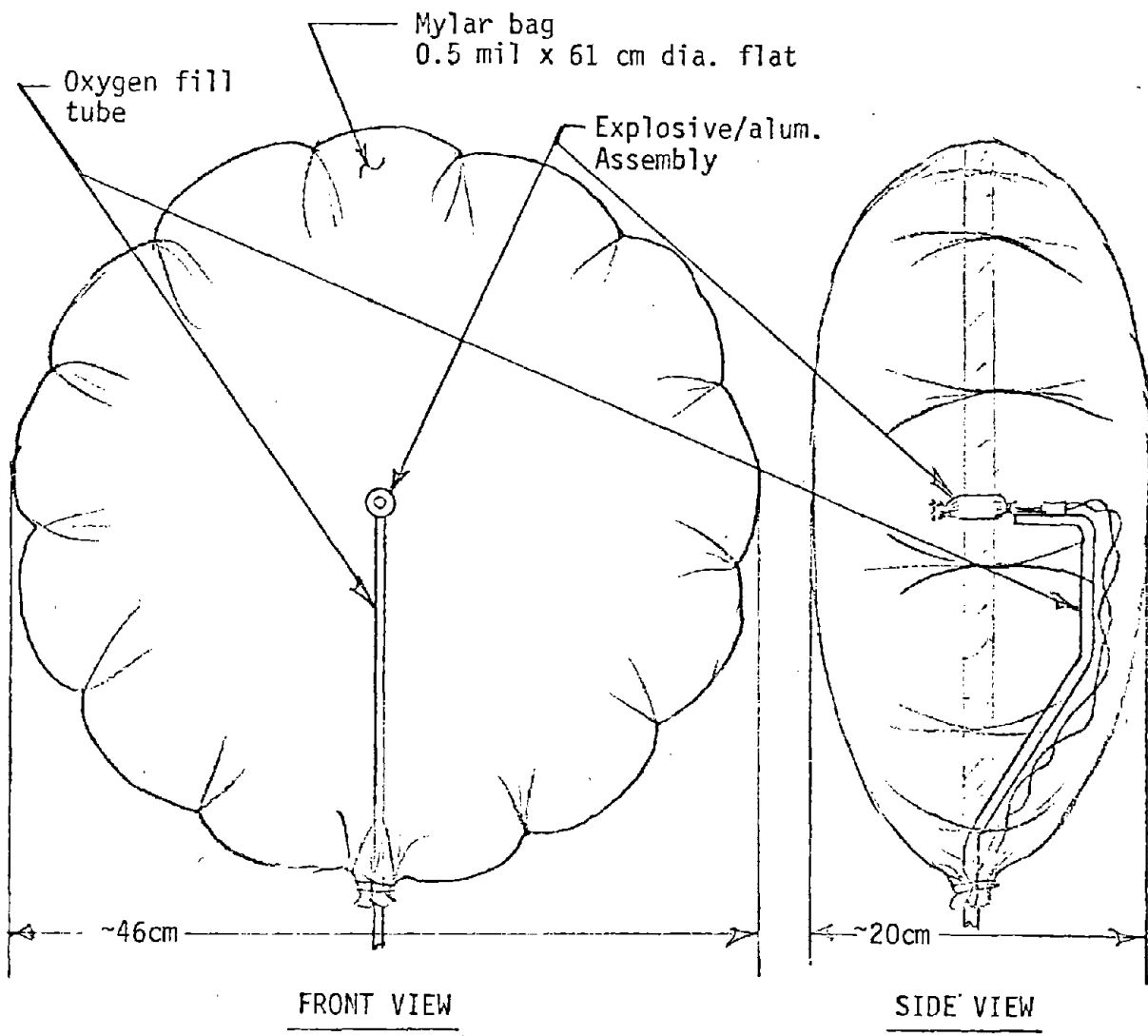


Figure 2 Laboratory E-System TRS.

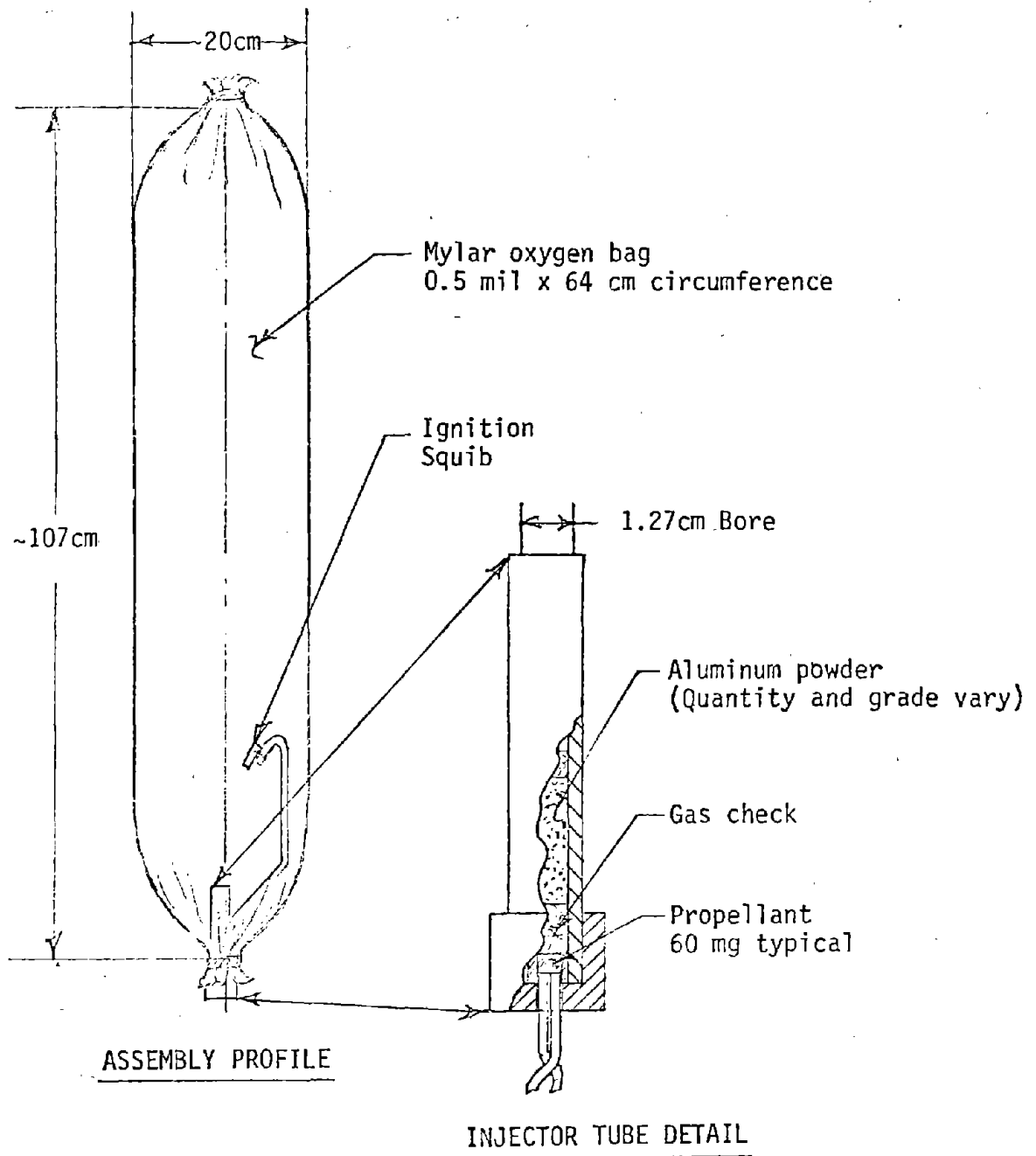


Figure 3 Laboratory C-System TRS

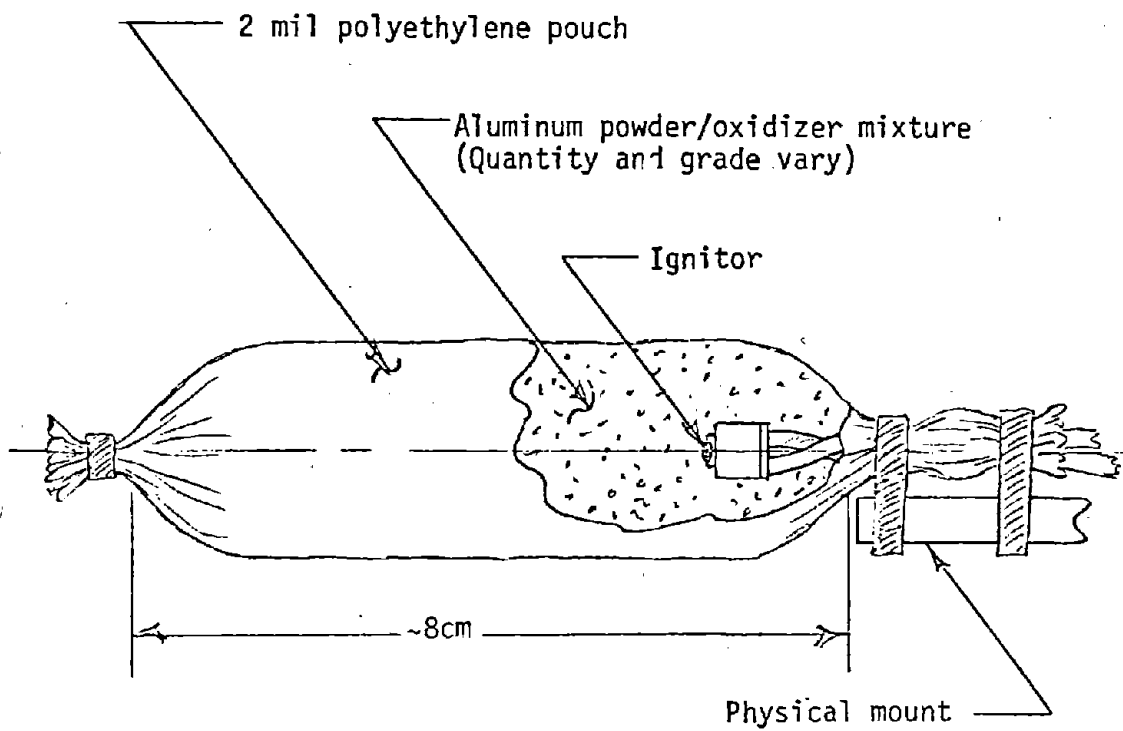


Figure 4 Laboratory K-System TRS

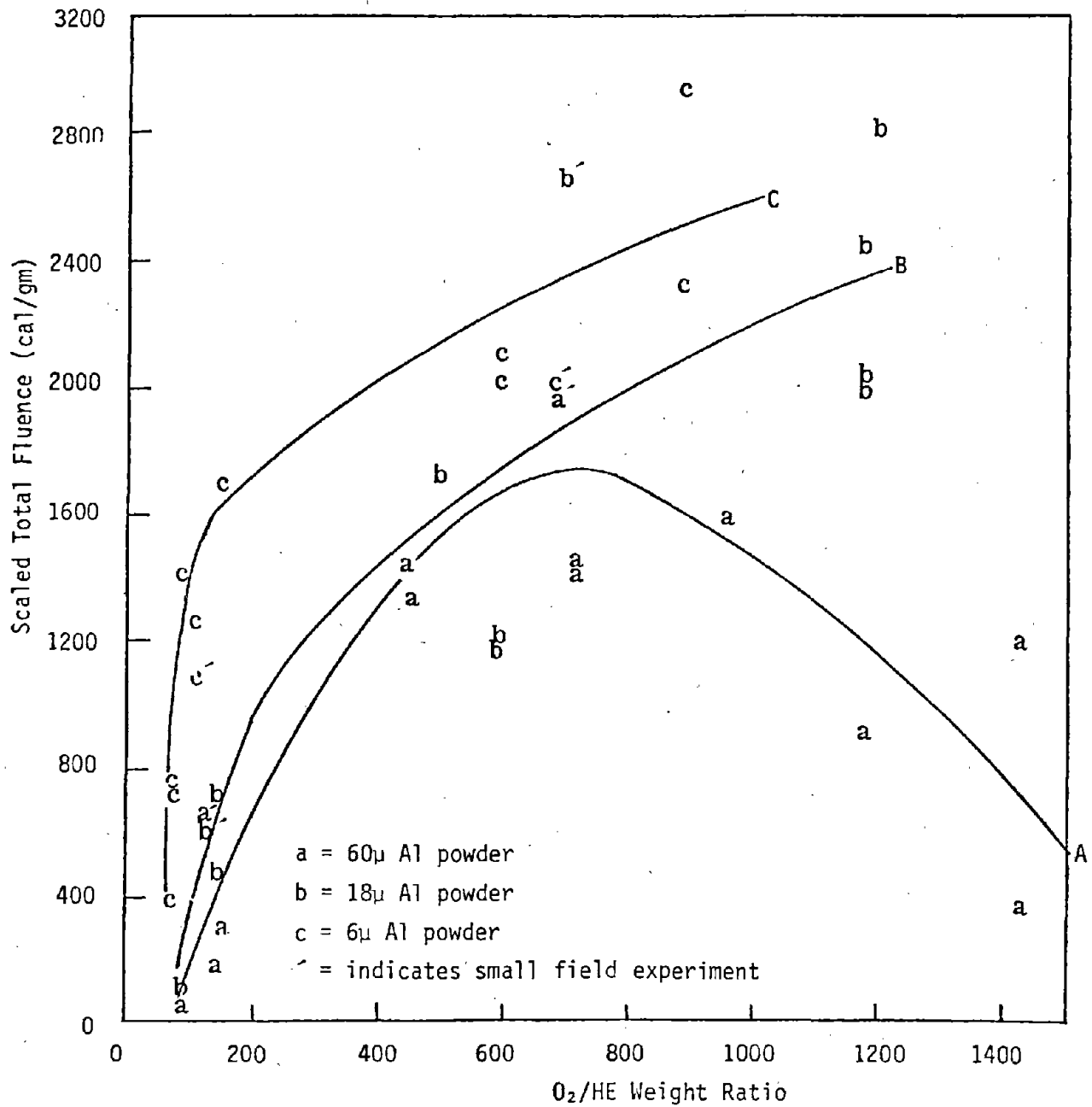


Figure 5 The Effect of the O₂/HE Weight Ratio on TRS Fluence of E-System TRS Modules.

6. SMALL FIELD EXPERIMENTS

6.1 General

TRS systems of various sizes may be required for future thermal radiation experiments. The concept of modularized TRS units was developed early in the research program. To create large or small TRS systems, TRS modules can be added or subtracted from a TRS design.

To determine dimensions for a module, a simple study of inflated plastic cylinders was conducted. The study indicated that TRS modules with length to diameter ratios of 5 and inflated to an over pressure of 0.1 PSI had sufficient structural strength to resist deformation by 35 mph winds.

A survey of common plastic materials indicated that "lay-flat" plastic tubing in 100 cm widths (One hundred centimeter lay-flat tubing can be inflated to form a cylinder with a diameter of 64 centimeters.) could be purchased in many cities. Because this material was readily available, it was chosen as the base for the TRS module. The dimensions of the TRS module became those of a cylinder with a diameter of 64 cm and a length of 300 cm.

The small field experiments were designed to create a controlled full-scale TRS module and to examine the effects of Al yield scaling in TRS systems. In addition, the dimensions of these tests allowed examination of TRS debris problems which could not be studied on smaller tests. Field experiments were conducted at the explosive test facility leased by SAI near Pleasanton, California. A series of 12 tests were conducted during this portion of the research program. TRS flux, fluence, and airblast output were measured on each test. Debris and TRS fireball characteristics of each experiment were recorded with high speed photography. Succeeding paragraphs address the small field experiments in greater detail.

6.2 Small Field Experiment Set-Up

The purpose of the small field tests was to utilize the results of the laboratory tests to create large TRS modules. The effects on TRS output due to increased simulator dimensions were examined. The weight ratios of Al to high explosive and O_2 to Al were held constant between lab and field experiments. Aluminum powder yields on these field scale experiments were increased by a factor of 20 over the lab tests. Figures 6 through 8 illustrate the TRS designs and experimental set up used on the tests. The FPT-100 photo-diode and CELESCO LC 71 airblast gauge, used on lab TRS experiments, were also used on these tests.

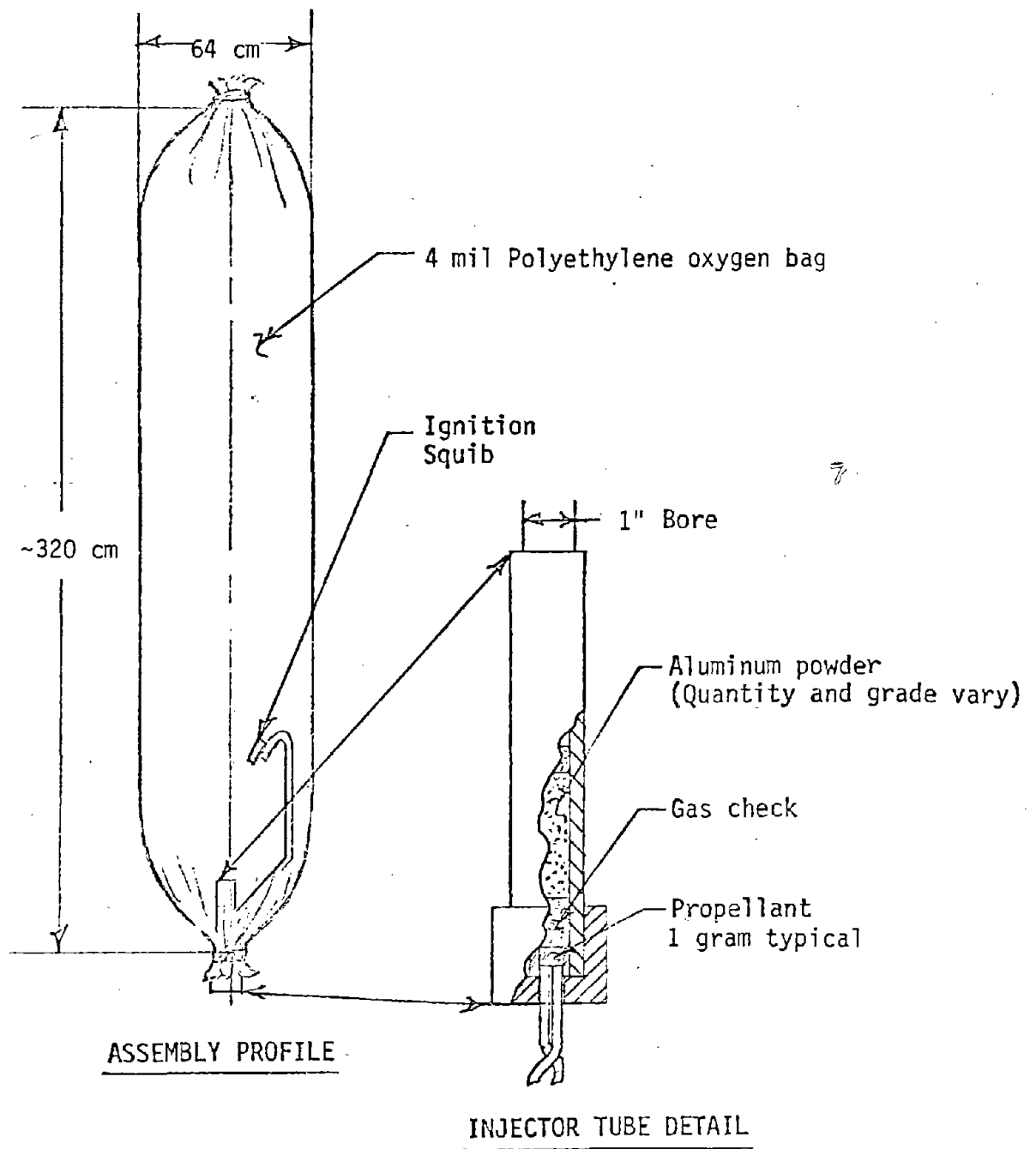
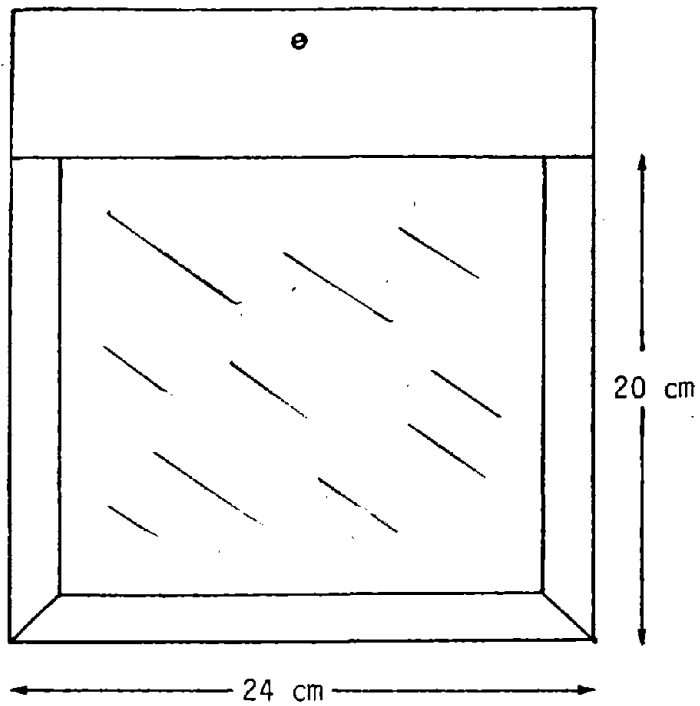


Figure 6 A C-System TRS Module Examined on the Small Field Experiments



PLAN VIEW OF TRS MODULE

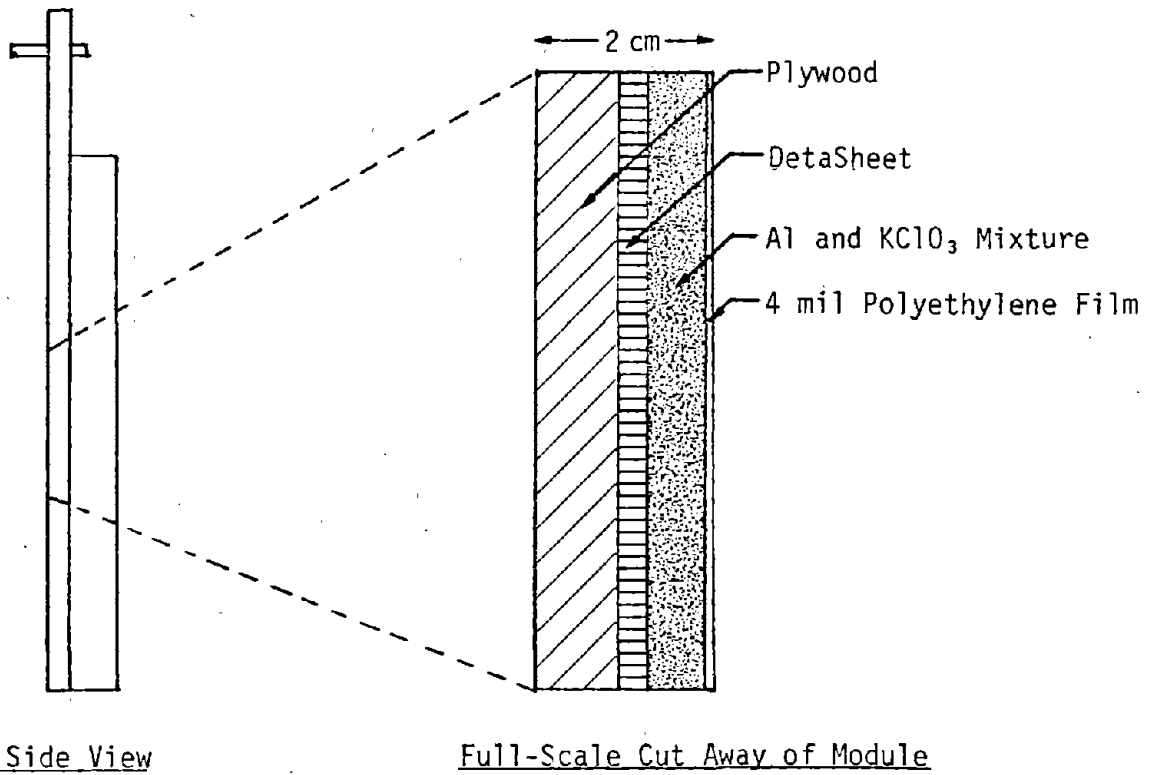
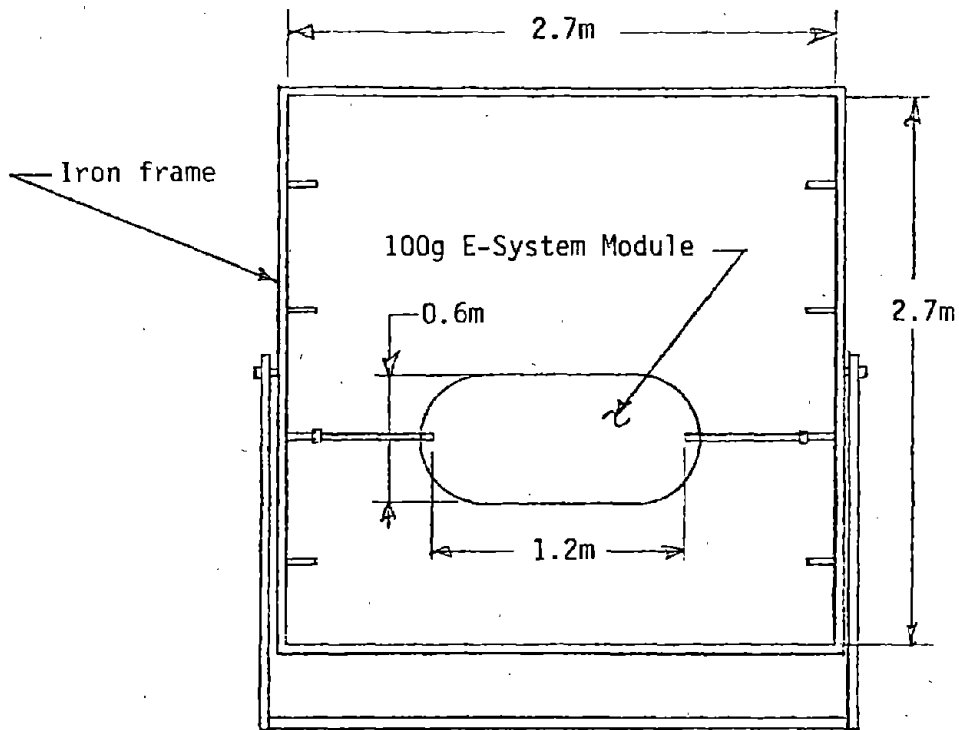
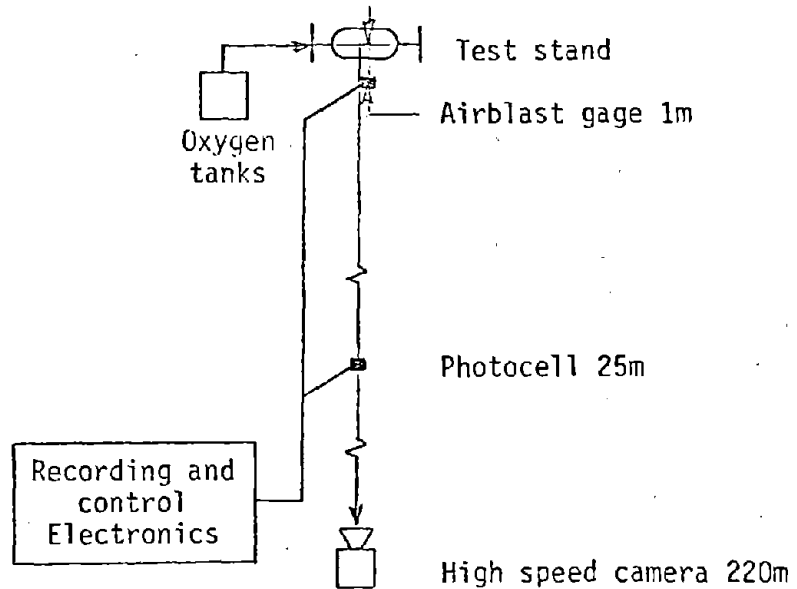


Figure 7 K-System TRS Module Used on Small Field Experiments



TEST STAND DETAIL



SITE LAYOUT

Figure 8 Set Up of Small Field Experiments and an E-System TRS Module:

6.3 C-System Aluminum Injectors

Observations of the first small field experiments indicated that large versions of the Al injector used on the lab experiments would not mix Al and O₂ effectively in a TRS. To combat this problem, an aluminum powder fluidizer was developed. The fluidizer mixes Al powder with nitrogen gas and sprays the Al at a metered rate into the oxygen filled bag of a TRS. All field size C-system TRS experiments utilized the Al fluidizer for Al powder injection. Figure 9 is an illustration of the Al fluidizer.

6.4 Variables Examined on the Small Field TRS Experiments

As stated previously, the small field experiments were extensions of lab experiments. The primary variable examined during this portion of the research program was the effect of increased TRS dimensions on TRS output. Twelve promising TRS designs were chosen from the 60 lab experiments. The Al powder yields of the lab experiments were increased by factors of 20 to 40. All other combustion related variables were held constant. In this manner, the effect of increased TRS dimensions could be examined. The scale of the experiments also allowed a more accurate determination of airblast overpressure and TRS debris characteristics.

6.5 Small Field TRS Flux Output

Figures 10a and 10b present the time dependent power output of lab and field TRS systems respectively. Power outputs of the two experiments have been scaled to equivalent Al powder yields. Variables effecting Al-O₂ combustion rates have been held constant between the two experiments.

6.6 Small Field TRS Fluence Output

Fluence outputs of the small field TRS systems followed trends that were in agreement with the lab experiments.

Field-scale E-system TRS designs, for given O₂/HE weight ratios, produced scaled total fluence outputs (cal/gm) which were identical to those produced by similar lab experiments. Field-scale C-system TRS designs which had mixing rates and reactant concentrations similar to those of given lab systems also produced scaled total fluence outputs that were equivalent to lab experiments.

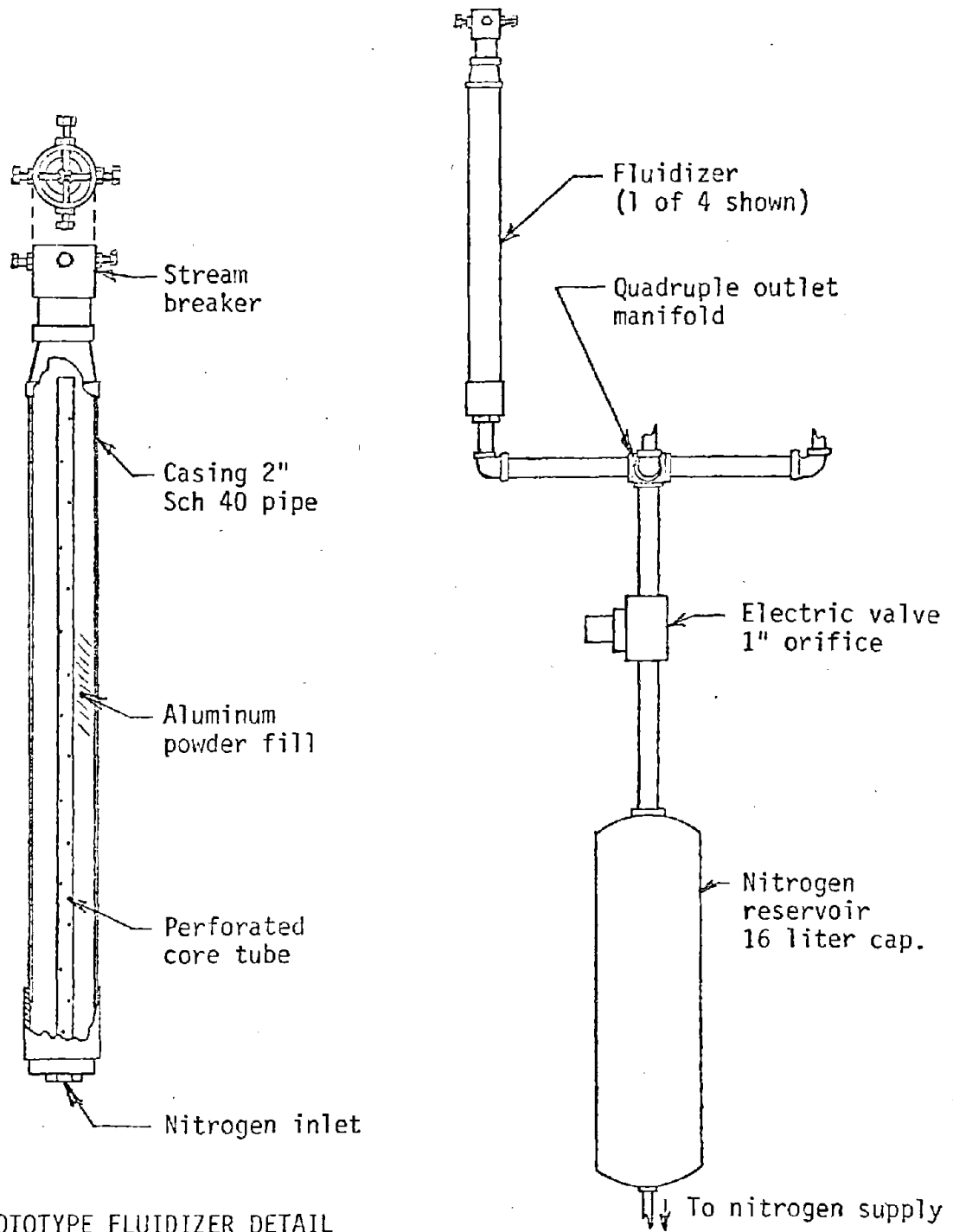


Figure 9 Aluminum Powder Fluidizer

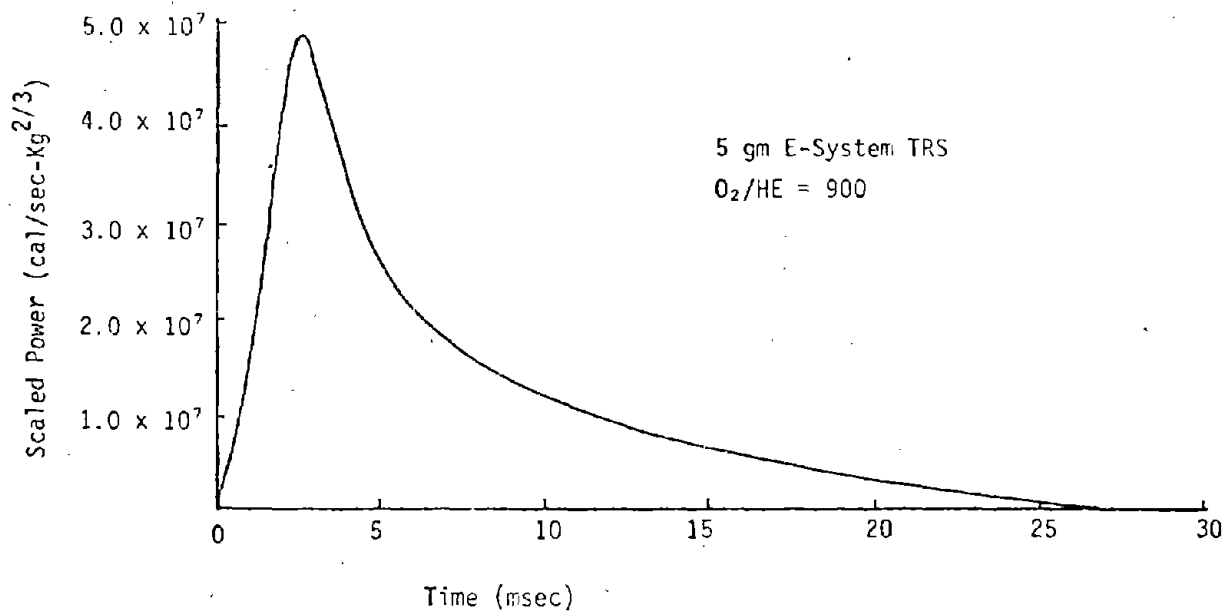


Figure 10a Lab-Scale E-System TRS

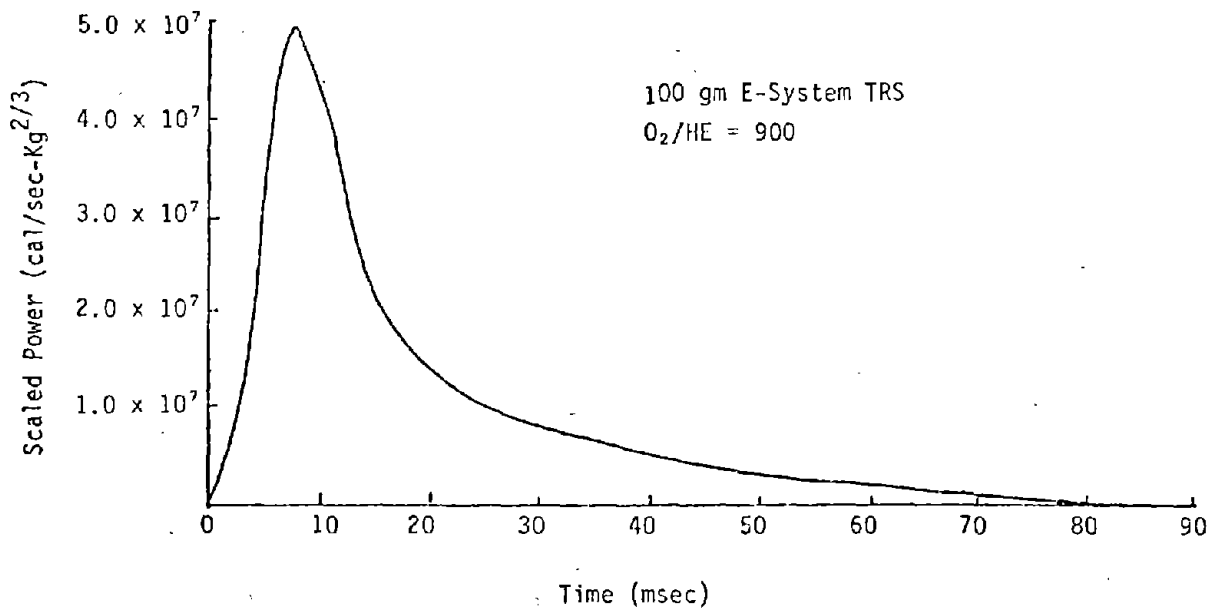


Figure 10b Small Field-Scale E-System TRS

Figure 10 Scaled Power Curves for two E-System TRS Designs.

7. LARGE FIELD EXPERIMENTS

7.1 General

The purpose of the large field experiments was to examine E and C system multiple module effects on TRS output. Fourteen large tests were completed during this phase of the research program. Five events conducted during 1976 were also used as data sources. With the completion of the large field experiments, sufficient data had been compiled to allow completion of the TRS development program. Subsequent paragraphs describe the results of the large field TRS experiments.

7.2 Experiment Set Up

Four different experimental set-ups were used to examine large TRS radiation output. The set-ups were:

- a. Vertical Single Module C-system TRS Designs. A vertical stand which held a single AI Fluidizer unit and a single, large oxygen bag was constructed. (Figure 11)
- b. Vertical Multi-Module C-system TRS Design. A vertical stand which held 4 AI fluidizer units and four oxygen bags was constructed. (Figure 12)
- c. Vertical Multi-Module E-system TRS Design. A vertical stand which held 12 E-system TRS modules was constructed. (Figure 13).
- d. Horizontal Multi-Module E-system TRS Design. A horizontal frame which held 8 E-system TRS modules and could be raised to a height of 6 meters was constructed (Figure 14)

Set-ups "a" through "c" were instrumented with FPT-100 photo-diodes; CELESCO LC 71, PCB, and TYCO HFG airblast gauges; Medtherm GT-1600 high speed calorimeters, SAI fluence calorimeters; and SAI aspirating thermocouples. Set up "d" was instrumented with the CELESCO LC 71 airblast gauge and a Medtherm GT-1600 highspeed calorimeter.

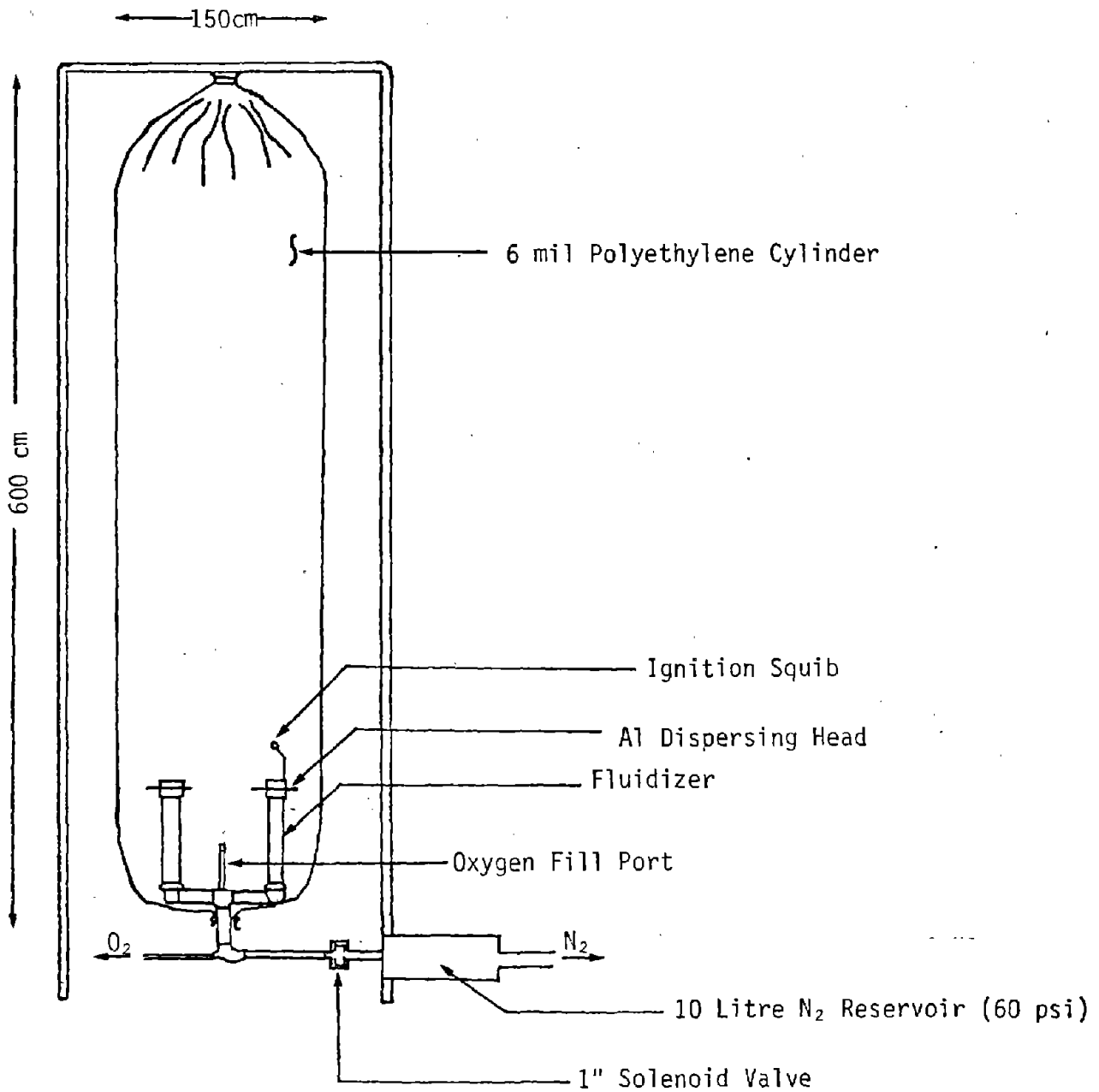


Figure 11 A Large C-System TRS Module

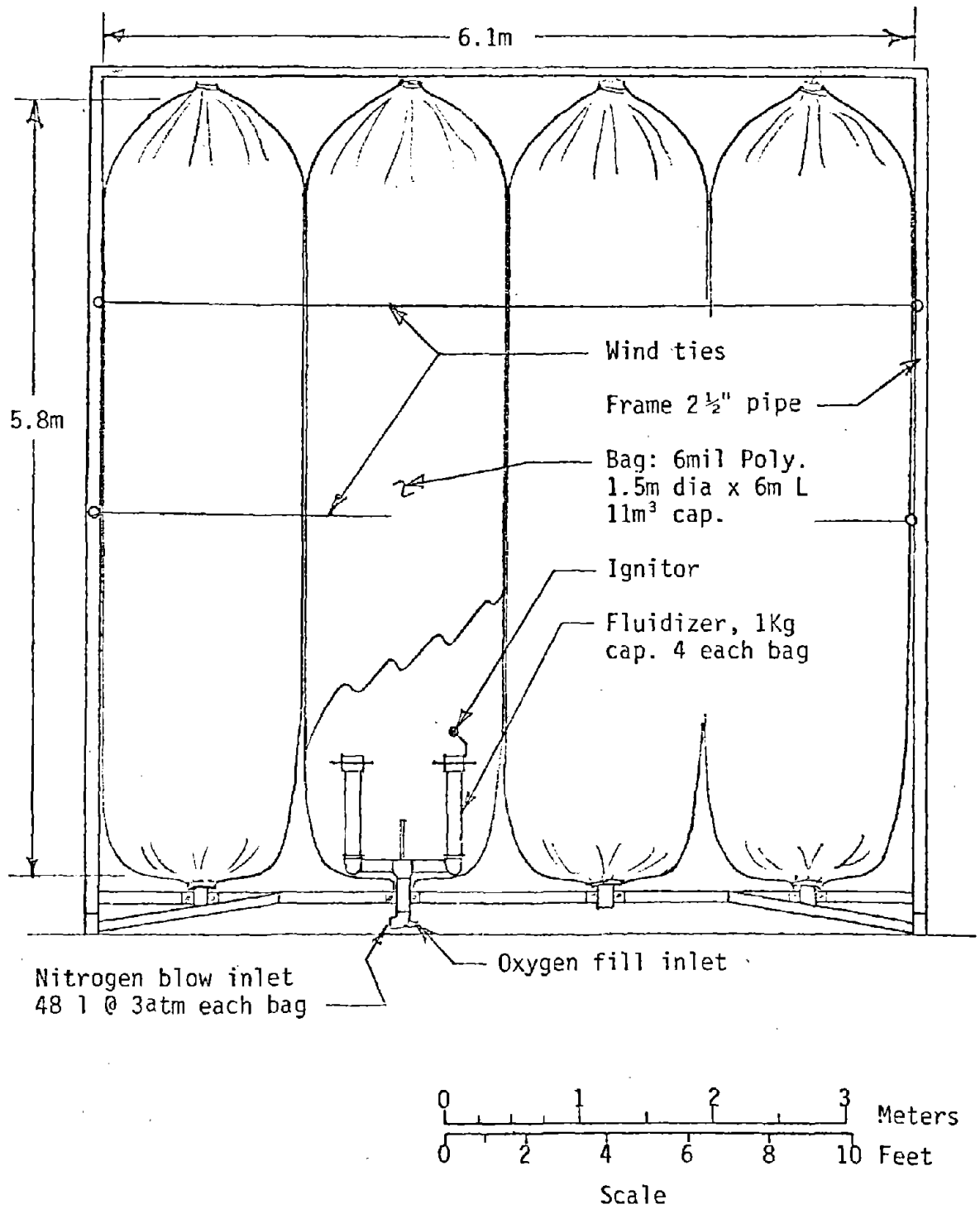


Figure 12 A 4 Module Vertical C-System TRS Array

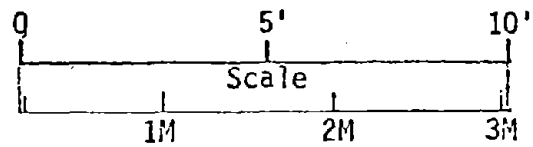
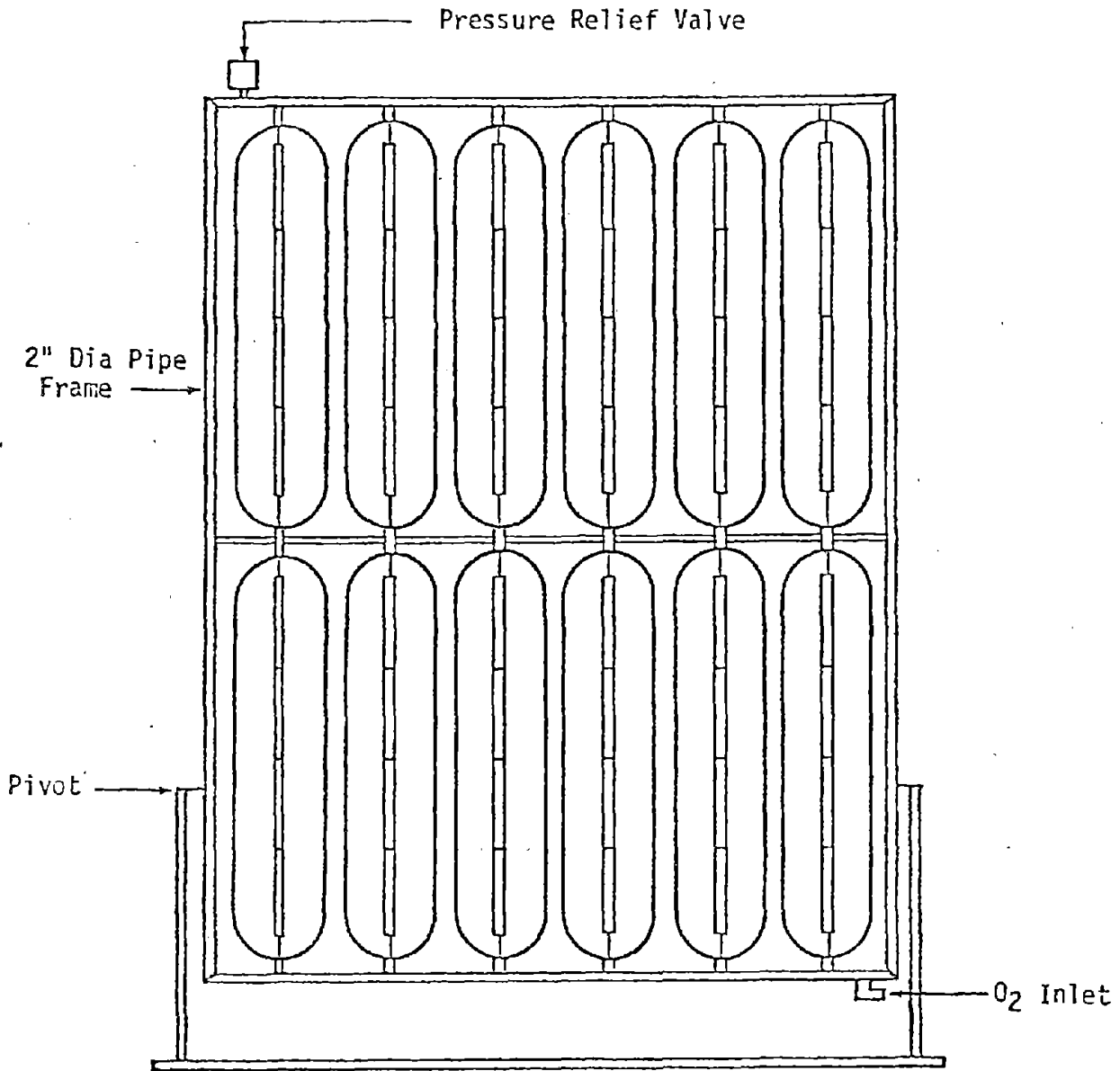
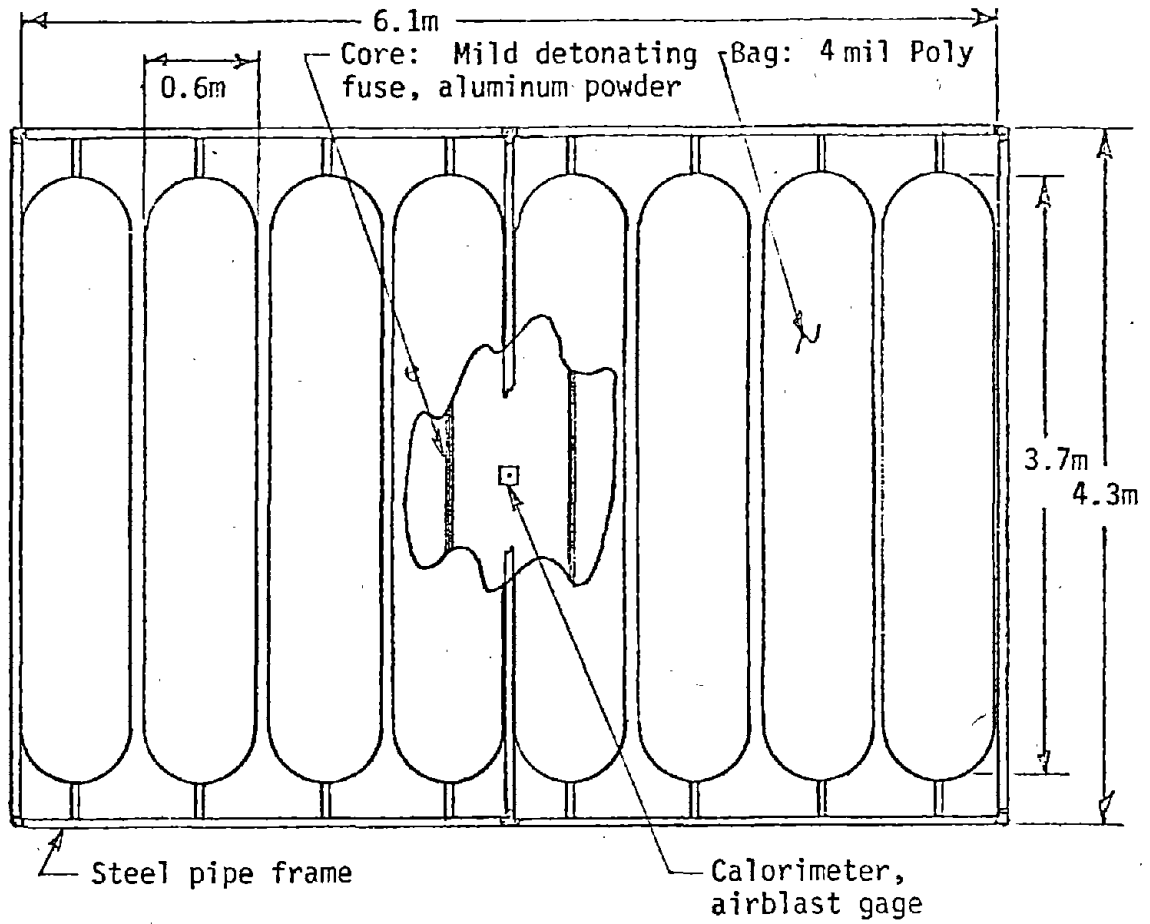
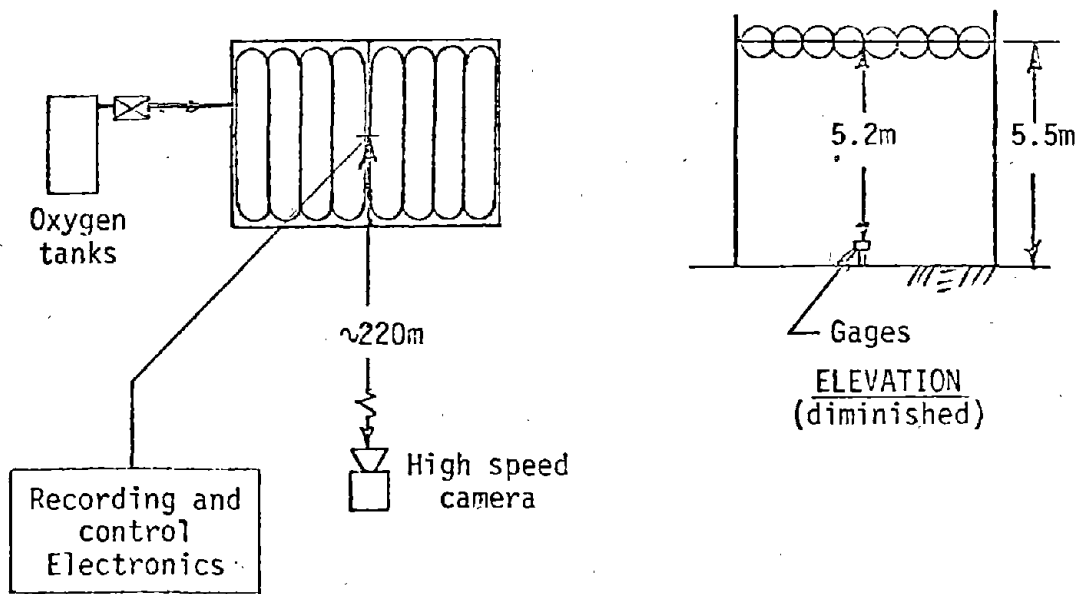


Figure 13 A 12 Module Vertical E-System TRS Array



PLAN VIEW



SITE LAYOUT

Figure 14 An 8 Module Horizontal E-System TRS Array

7.3 The C-System Single Module TRS

Experiments with the Al fluidizer and a cost analysis of hardware associated with it indicated that the fluidizer should inject 4 to 5 kg of Al powder into a single TRS module. Field experiments proved that the fluidizer could easily spray and mix Al over a vertical distance of 6 meters. To maintain structural integrity in the module, a plastic cylinder with an L/D ratio of 4 was chosen to contain the oxygen of the TRS. When inflated to an overpressure of 0.1 PSI, the C-system TRS module became a cylinder with a length of 6 meters and a diameter of 152 cm. This cylinder provided an Al/O₂ weight ratio in the TRS module of 3.5. Figure 11 illustrates the single C-system TRS module. Peak power outputs for the module vary from 1×10^7 cal/sec to 3.5×10^7 cal/sec. The total energy output of a module is approximately 9×10^6 calories.

7.4 Large Field TRS Flux Output

The peak power generated by each TRS studied in this portion of the research program was measured in a plane, perpendicular to the plane of the TRS. In general, the peak power generated by TRS systems with multiple modules of similar combustion properties (i.e. Al/O₂ and Al/HE weight ratios, mixing techniques, and Al yields), was a linear function of the number of modules composing the TRS. Figure 15 presents the normalized peak power outputs of several multi-module TRS systems.

The peak power output of the C-system module was studied on several experiments. In general, the C-system module can rise to peak power over controlled time periods which can be varied from 25 msec to 500 msec. The peak power output is dependent upon the TRS ignition system, fluidizer mixing rate, and Al particle size.

7.5 Large Field TRS Fluence Output

In general, two problems were addressed in the TRS fluence study. The first problem was the determination of the fluence output of a C-system TRS module. The second problem was the determination of multiple module effects on TRS fluence output.

TRS systems which burned 18 μ Al powder were more efficient than TRS systems which burned 6 μ Al powder. For given combustion conditions (i.e. Al/O₂ and HE/O₂ ratios, ignition conditions, and Al yield) the scaled fluence output of multi-module TRS systems was similar to the single module output. This indicates that the energy output from multi-moduled TRS systems increases linearly with the number of modules used in the TRS.

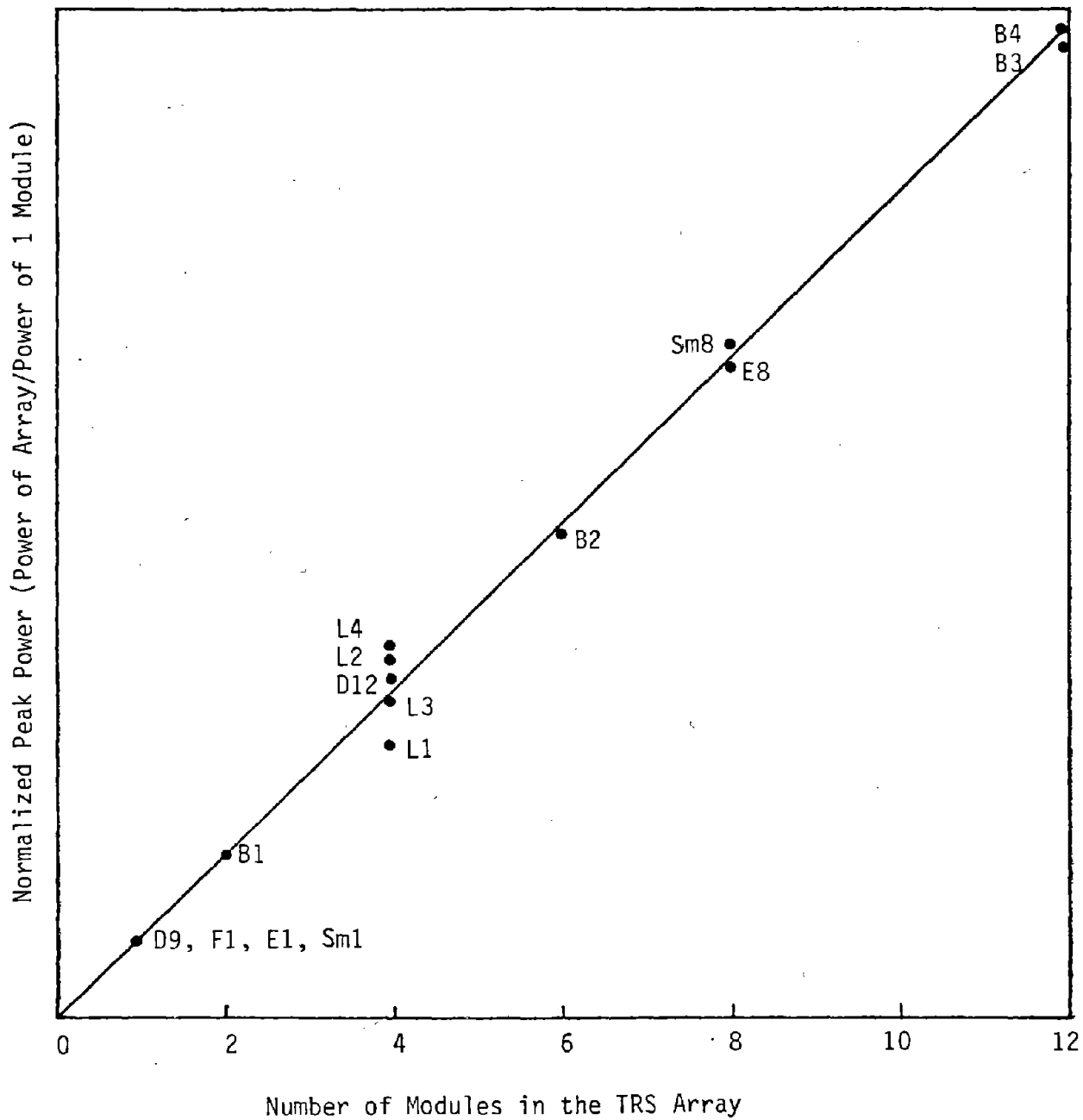


Figure 15 Normalized Power Outputs of Multiple Module TRS Arrays

8.

SUMMARY

With the completion of the large TRS testing program, a large high flux and fluence TRS had been developed. Fluxes of $200 \text{ cal/cm}^2\text{-sec}$ and fluences of 100 cal/cm^2 had been achieved. Since the completion of the research program the TRS has been used to successfully irradiate soils, aircraft, shelter, missiles, and tank components. Some problems concerning thermal pulse rise time, convective vs radiative heating, and pulse reproducibility have been encountered since the initial research project. These problems are currently being addressed under other DNA and Army (BRL) programs.

REFERENCES

1. Glasstone, Samuel The Effects of Nuclear Weapons, (Revised Edition), U.S. Department of Defense/U.S. Atomic Energy Commission, April 1962.
2. Knsel, T.M. Experimental Studies of Soil Thermal Irradiation, Volume I, Soil Blow-Off Data Analysis Science Applications, Inc., McLean, Virginia, April 1977.
3. Kansel, T.M. "A Briefing for DNA on Thermal Radiation Sources", Science Applications, Inc., McLean, Virginia, August 1977.

THERMAL/BLAST SIMULATION FACILITIES
AT THE U.S. ARMY BALLISTIC RESEARCH LABORATORY

Three thermal/blast test facilities are in the various stages of development, activation, and operation at the U.S. Army Ballistic Research Laboratory by the Target Loading and Response Branch of the Terminal Ballistics Division. The development of a thermal/blast test capability was initiated in September, 1976 when the need to test various items or components, of Army interest, to the synergistic effects of both thermal and blast environments from nuclear weapons became apparent. This requirement introduced the need to thermally expose a large target in conjunction with a blast simulator.

The BRL had at its disposal a unique blast test facility, the Dual Shock Tube Facility, that it was thought could be used as the basis for the desired thermal/blast testing. This facility, Figure 1, consists of two large diameter parallel shock tubes. The larger of the two shock tubes is 2.44 m in diameter and the smaller has a diameter of 1.68 m. Both of the shock tubes are capable of generating shock overpressures up to 140 kPa. While either shock tube could be used as a part of a thermal/blast facility, emphasis has been placed on the 2.44 m unit since it is capable of accommodating a larger target.

The first target to be exposed to a combined thermal/blast environment at the BRL was a UH-1 helicopter tail boom. This target was exposed outside the exit plane of the shock tube and the thermal environment was provided by burning sheet propellant as shown in Figure 2. The use of sheet propellant as a thermal source had been developed by the Naval Ordnance Laboratory who provided the BRL with source materials for this experiment. Several deficiencies were noted with the application of this technique and these are evident in the post test photograph of the target, Figure 3. Only a portion of the target could be heated by the thermal source and the heating pattern was uneven over the surface of the target. There was also a question as to how well the simulated thermal pulse compared with that generated by a nuclear detonation. The desired thermal pulse shape taken from "DNA EM-1, Capabilities of Nuclear Weapons" is shown in Figure 4.

A second attempt to perform a thermal/blast test of a UH-1 tail boom was done in December, 1976 and used a technique which had been recently developed by the Science Applications, Inc. The thermal source, Figure 5, consisted of large polyethylene bags filled with oxygen in which fine aluminum powder was explosively distributed and ignited. In this test, a fortuitous failure occurred when the shock tube failed to fire. The results of the test however, indicated that an excessive blast overpressure, capable of causing blast damage by itself, had been generated by the thermal source. Recordings of the thermal output of the source, Figure 6, were again quite different in nature from the desired nuclear environment. At this juncture the SAI undertook an additional development effort which resulted in the SAI "blast-less flash-bulb" technique which will be described in detail in another paper given to this symposium.

The SAI "flash-bulb" technique consists basically of burning powdered aluminum in an oxygen atmosphere. The basic differences between the original attempt to use this concept and the currently used procedure are that the aluminum is sprayed into the oxygen using pressurized nitrogen and the mixture is ignited by a flame rather than mixing and igniting explosively. Figure 7 shows this technique deployed outside the exit plane of the 2.44 m shock tube for a thermal/blast test of a LANCE missile. The thermal output of the "flash-bulb" source is shown in Figure 8.

One disadvantage to the type of test shown in Figure 7, is that the blast pressures which can be applied to the target outside the shock tube are only in the order of 15 kPa. Many of the targets, of interest to the Army, are small enough to be placed within the shock tube where the target can be exposed to shock overpressures compatible with the design or test criteria. In order to move the target into the shock tube another problem had to be addressed. Since both thermal and blast exposure would be on the same side of a target it would initially seem that the thermal source should be placed upstream (between the shock tube diaphragm and the target). This however means that the shock wave incident upon the target would have to pass through the thermal source residue and the presence of these combustion products will alter the shock wave characteristics. In order to overcome this problem a ground plane table and model rotator have been designed and

are currently being installed in the shock tube. Figure 9 is a sketch of this test station. The thermal source is contained by the shock tube with polyethylene membranes at either end. The target is mounted on the rotating platform and faced toward the thermal source. The target face is thermally irradiated and then turned 180° to face into the incident blast wave. The rotator is capable of turning a target weighing 250 kg through 180° in 1 second or less. The rotator and table are designed to support a model with a frontal area of 0.5 m² against the subjected blast loads. The 0.5 m² frontal area limitation was established since that is the largest target which could be placed in the shock tube without causing choked flow in the shock tube.

If one assumes a maximum model rotation time of 1 second, and combines this with the thermal pulse durations and shock wave arrival times from various nuclear weapon yields, Figure 10 can be generated which indicates the thermal/blast capabilities of this facility. The accepted total thermal pulse duration is $10 t_{\max}$, where t_{\max} is the time of maximum flux as shown in Figure 4. If a total thermal exposure of $10 t_{\max}$ is required the line labeled $t_t = 10 t_{\max}$ indicates the maximum unscaled capabilities of the facility. If however one can begin to rotate the model when a thermal pulse length of $5 t_{\max}$ has been delivered, the maximum unscaled capabilities are indicated by the upper curve. It should be noted that terminating the thermal exposure at $5 t_{\max}$ results in a thermal fluence delivered that is only 6% lower than the total $10 t_{\max}$ exposure. For many test objectives it may be desirable to accept the reduced fluence in order to extend the facility capabilities.

A recent series of thermal calibration tests within the 2.44 m shock tube failed to deliver thermal fluences as high as desired for this facility. Figure 11 is a typical result obtained from these tests. Fluences of the order of 60 cal/cm² had been desired as opposed to those in the order of 20 cal/cm² actually achieved. While a level of 20 cal/cm² is adequate to test many potential targets, particularly those where the man exposed criteria dictates the test levels, efforts are currently underway to extend the thermal capabilities of the facility.

The third thermal/blast test facility which is being assembled is intended to provide a capability to perform basic plate and panel response experiments. Figure 12 is a sketch of this facility. The thermal source chamber is mounted over the existing 0.6 m shock tube. A polyethylene membrane over the chamber end contains the oxygen and the test plate or panel is mounted in a framework in front of the thermal chamber. The test target is subjected to the thermal environment and then dropped in front of the shock tube for blast loading. Timing can be varied between thermal and blast exposure and thermal levels may be varied by moving the chamber longitudinally along the shock tube to produce different test conditions.

In all of the SAI "flash-bulb" sources the thermal pulse rise time (time to t_{max}) can be varied by changing aluminum particle size, nitrogen delivery rates, and ignition times. Fluence output from the source is varied by altering the quantity of aluminum supplied to the reaction and the flux is varied by changing the distance between source and target.

The BRL has currently at its disposal the facilities to perform a limited range of thermal/blast testing. Large targets can be exposed to thermal/blast environments outside the exit plane of the 2.44 m shock tube. Thermal fluence levels up to 60 cal/cm^2 have been demonstrated but the blast overpressure level is limited to the order of 15 kPa. Moderate sized targets can be exposed to thermal fluences up to approximately 20 cal/cm^2 and blast pressures of 70 kPa inside the 2.44 m shock tube. In the near future it is expected that the thermal fluence levels in the 2.44 m shock tube will be increased to the order of 60 cal/cm^2 . It is also expected that plates and panels may be tested up to thermal levels of 60 cal/cm^2 or greater and shock overpressure levels of 550 kPa.

While the current and near future capabilities represent a unique testing capability, the BRL expects to continue its effort to further expand and extend the capabilities of these facilities in an ongoing thermal/blast program.

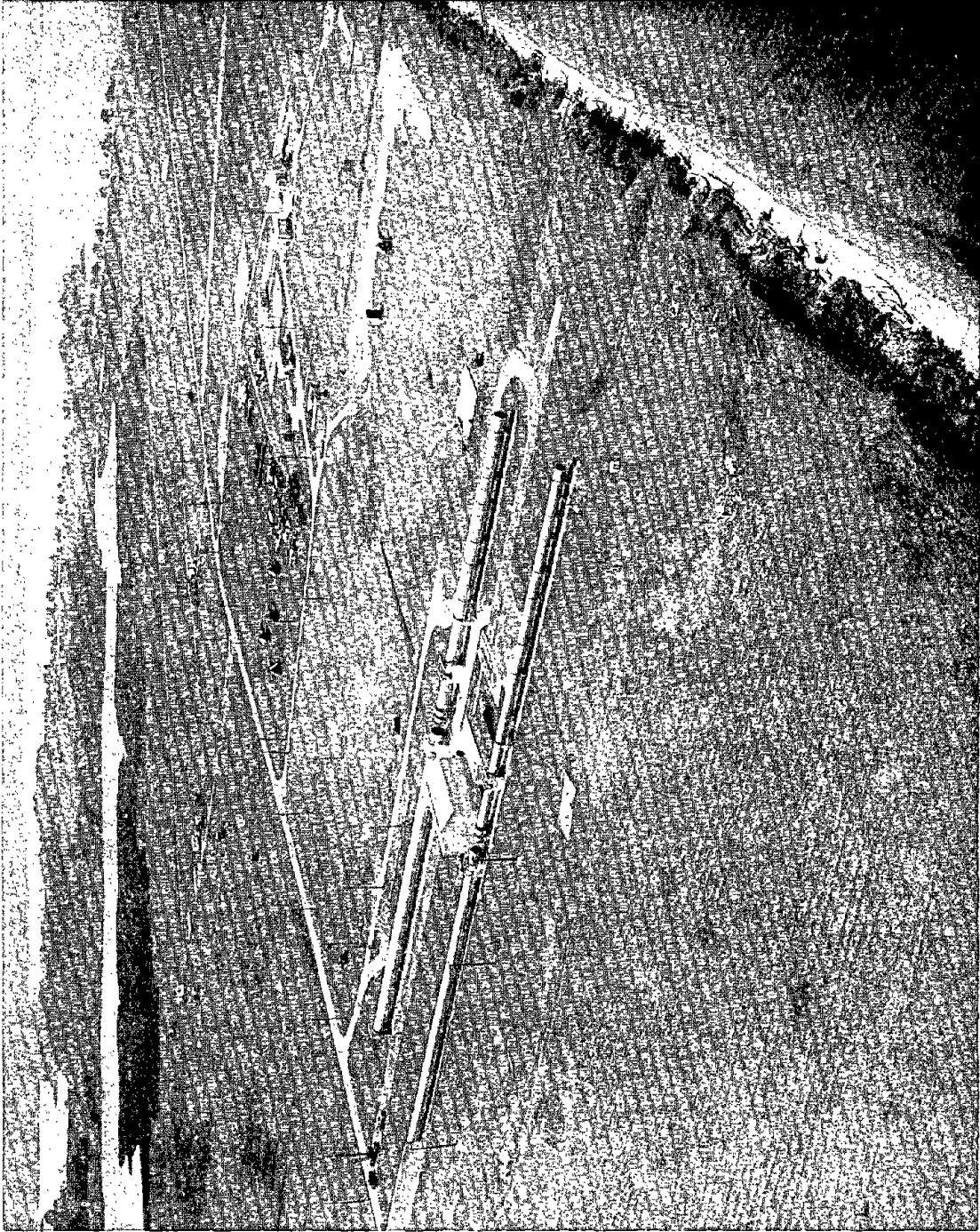


Figure 1. The BRL Dual Shock Tube Facility

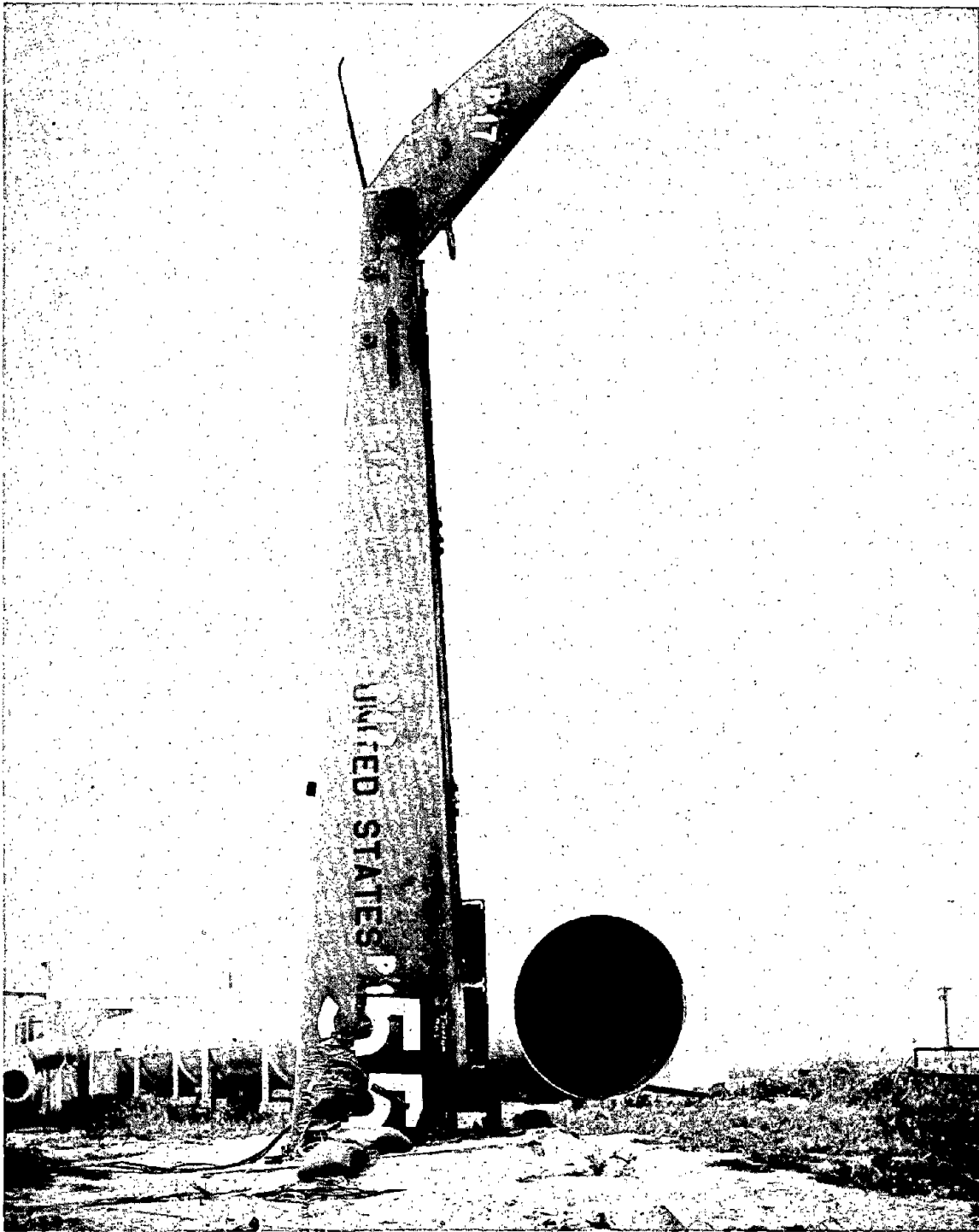


Figure 2. Set-Up of Thermal/Blast Test of UH-1 Tail Boom Using Shett Propellant.

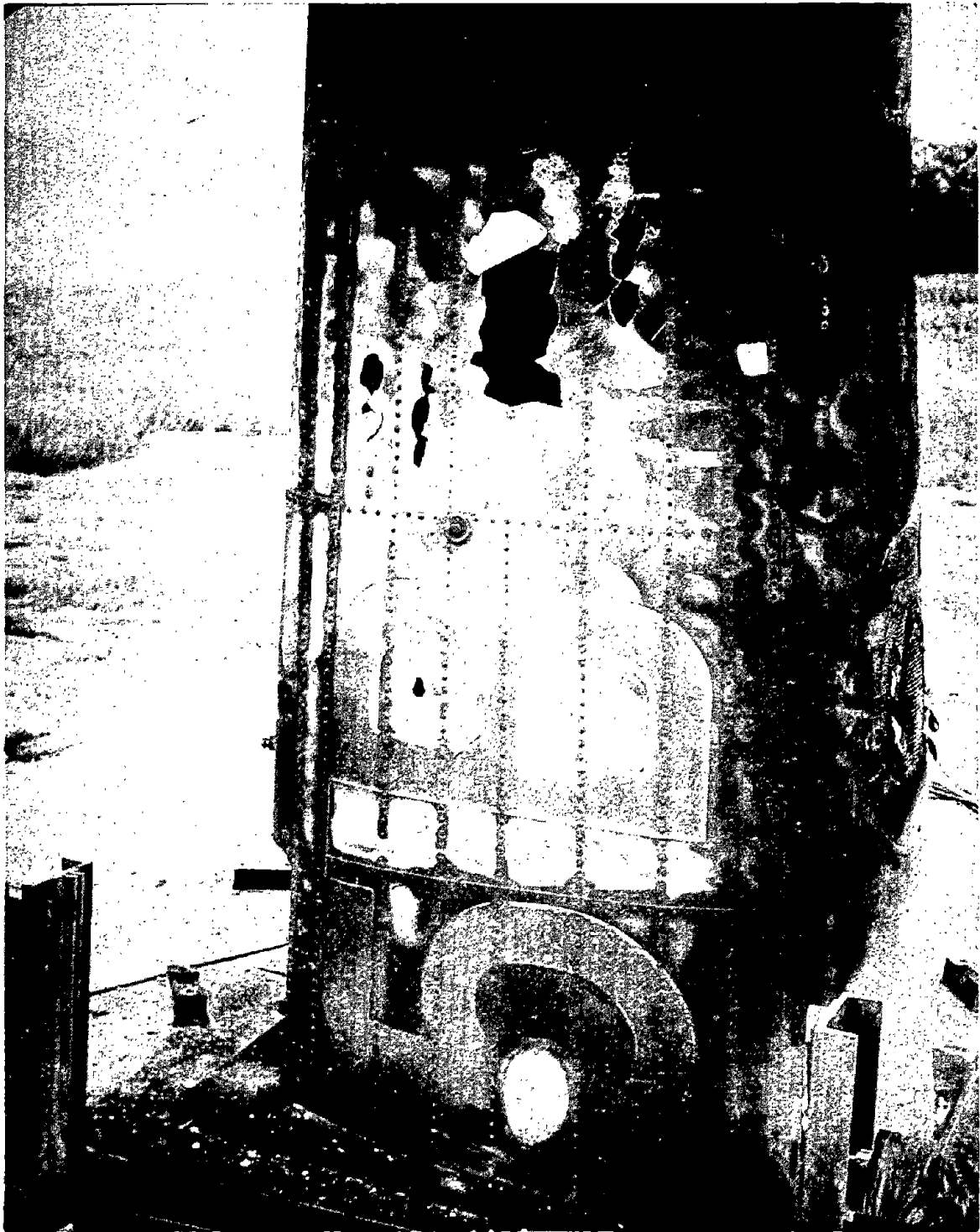


Figure 3. Post-Test Condition of UH-1 Tail Boom Following Exposure to Thermal/Blast.

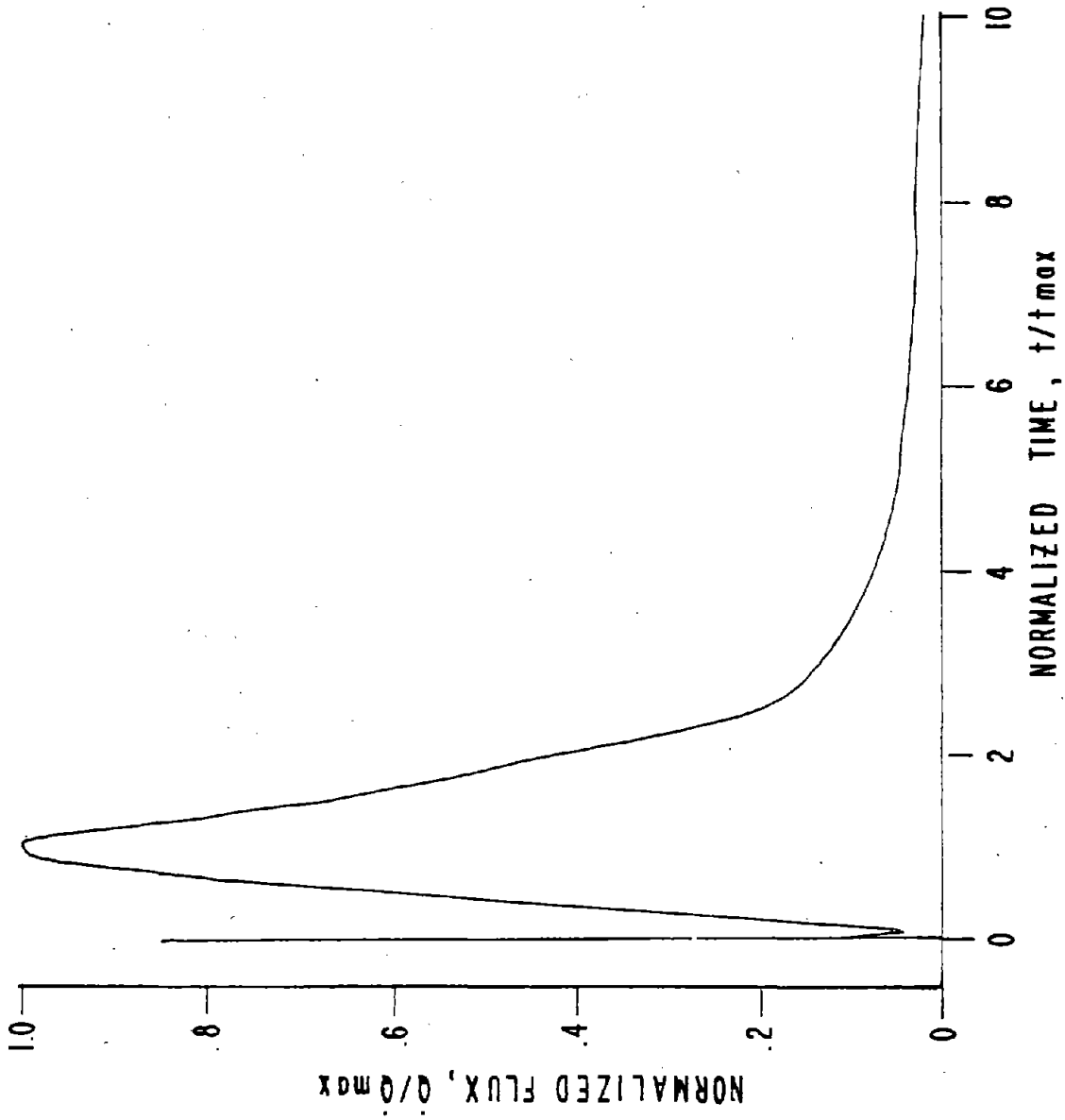


Figure 4. Thermal Pulse Shape from "DNA EM-1".

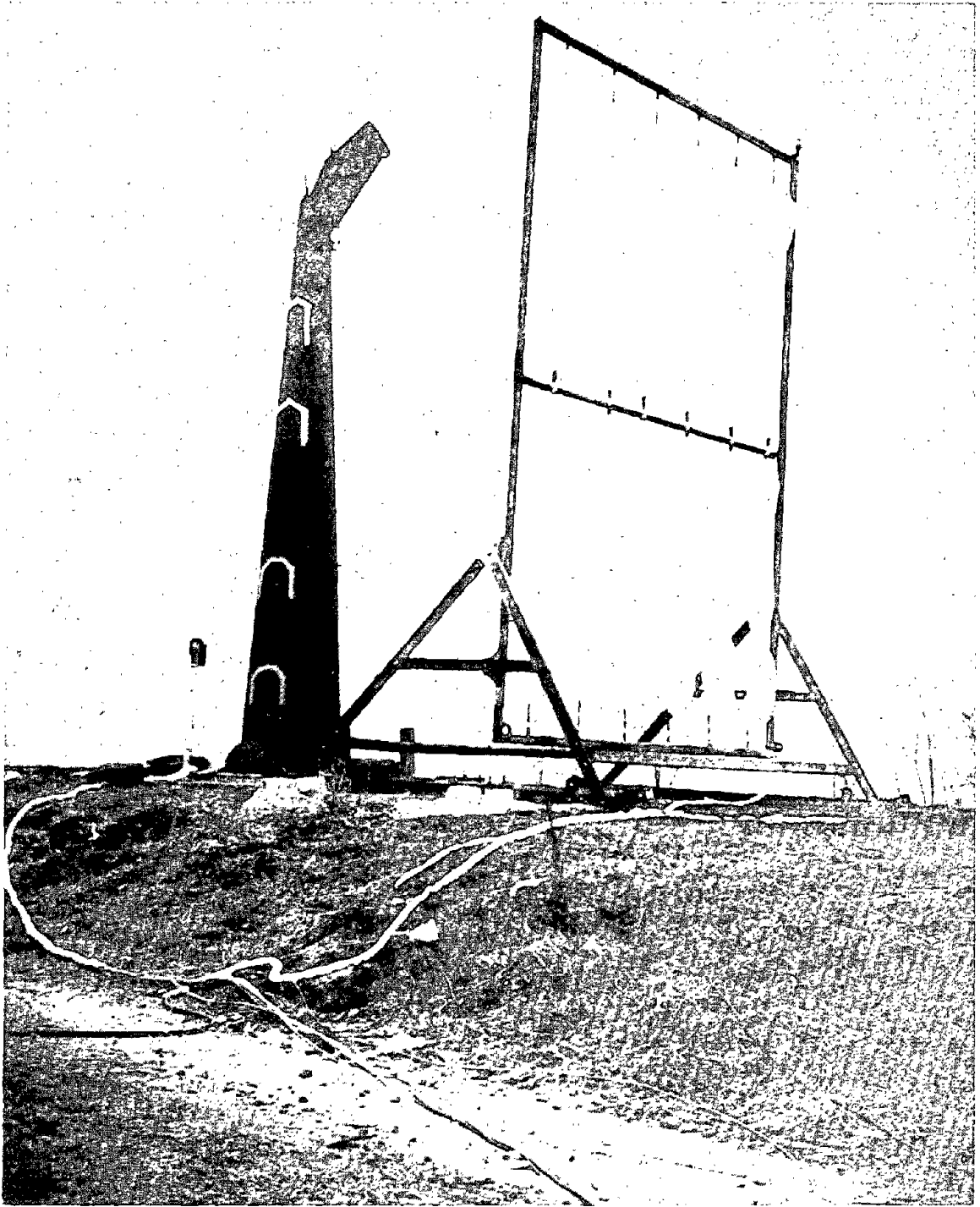


Figure 5. Set-Up of Thermal/Blast Test of UH-1 Tail Boom
Using SAI Explosively Driven Source.

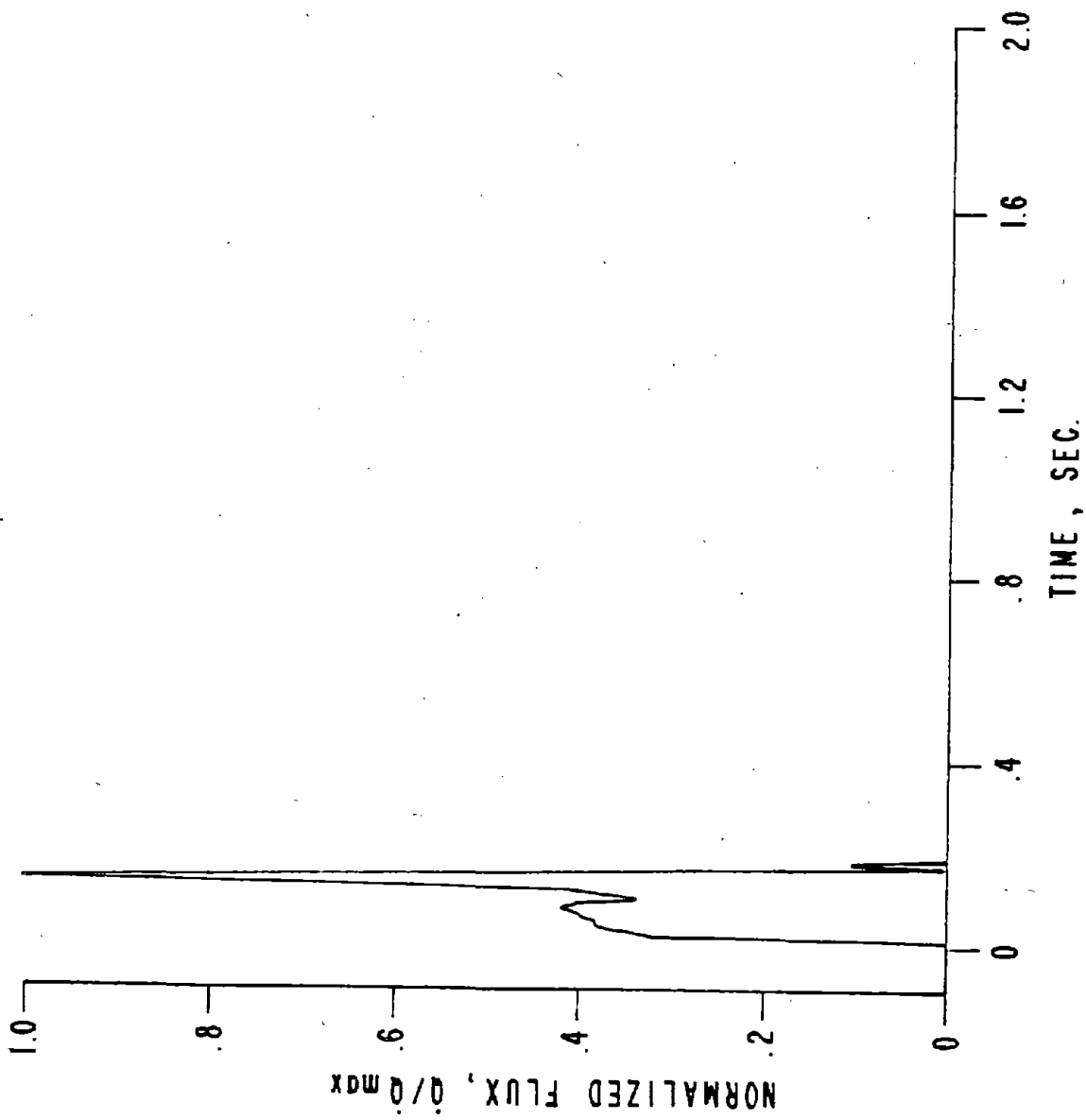


Figure 6. Thermal Pulse Shape from SAI Explosively Driven Source.

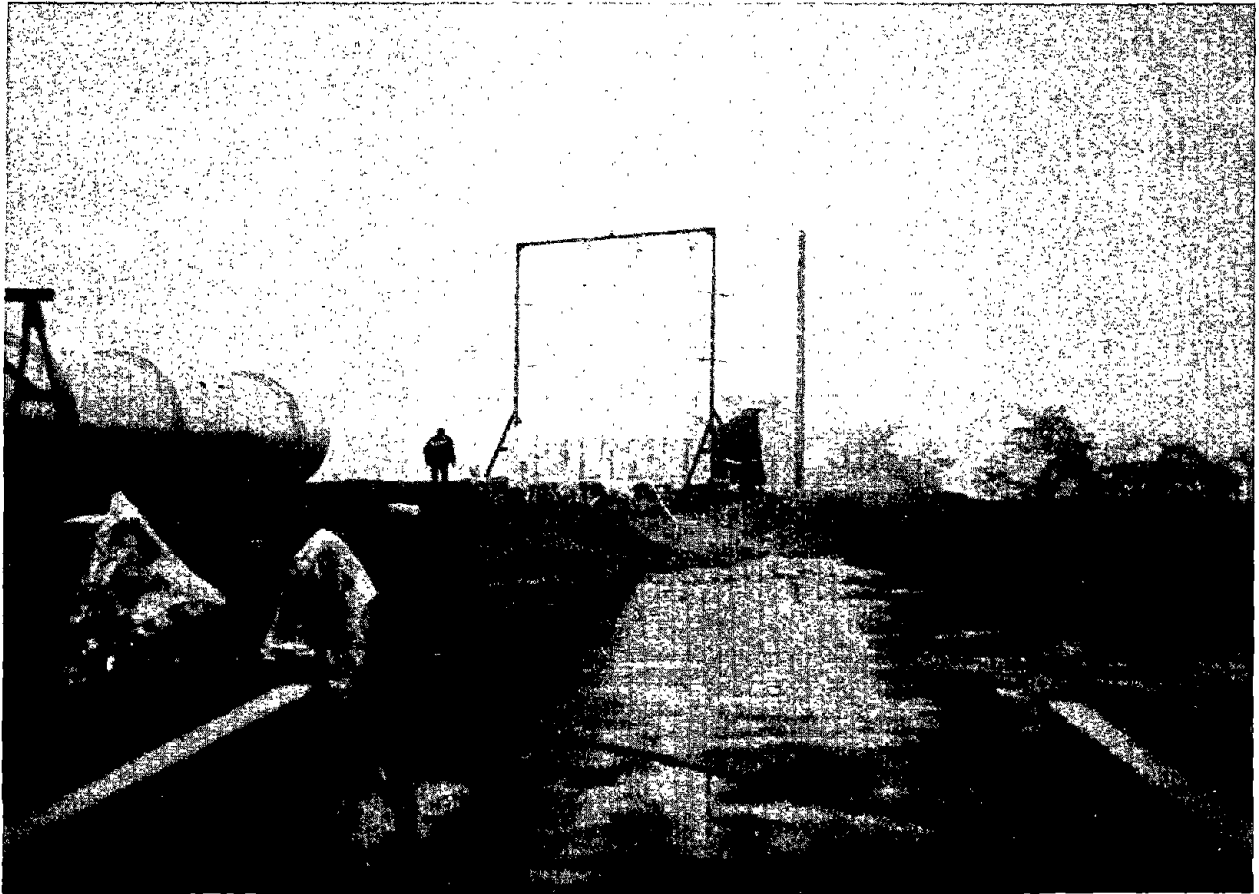


Figure 7. Set-Up of Thermal/Blast Test of LANCE Using SAI
"Blash-Bulb" Source.

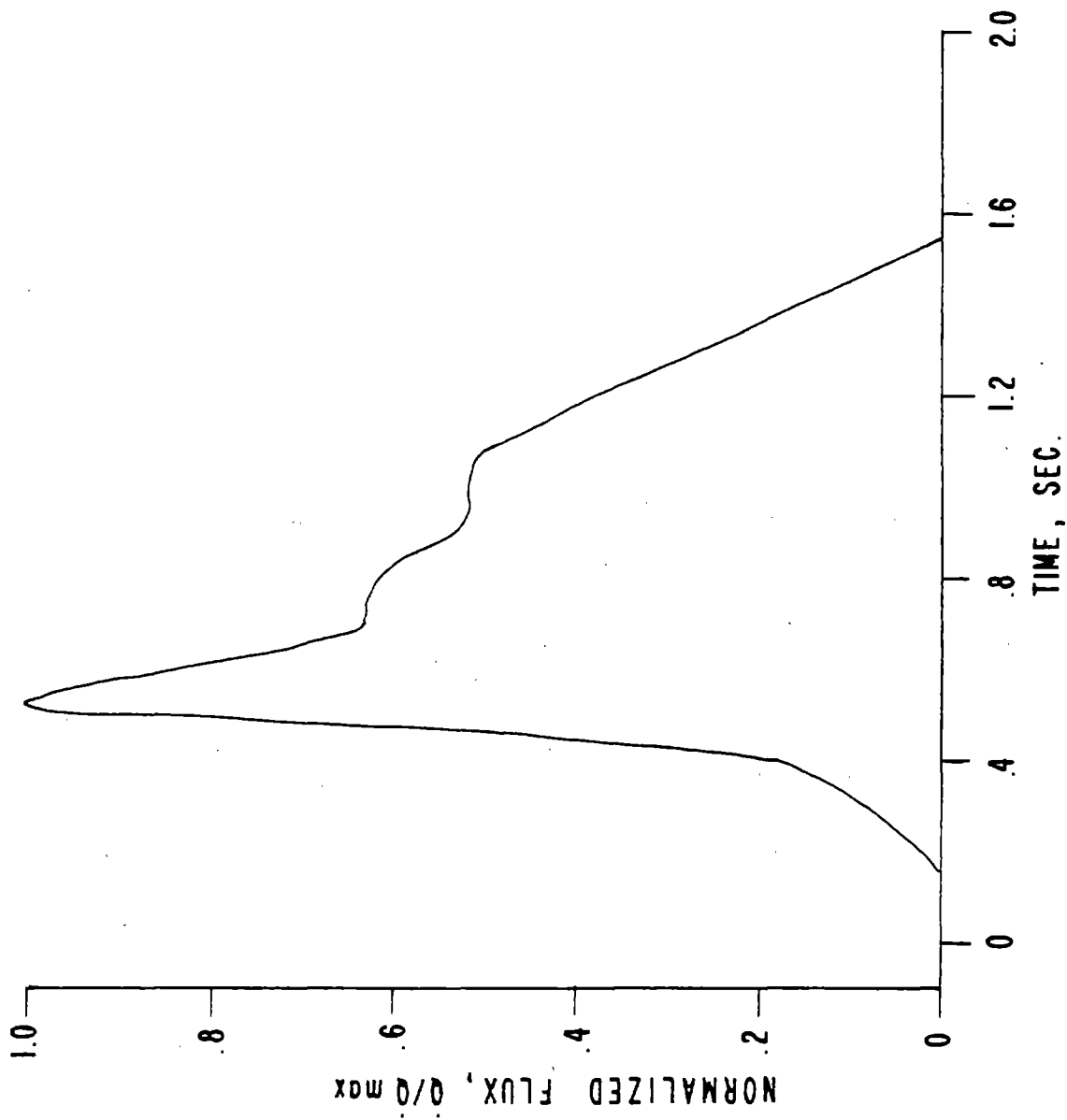
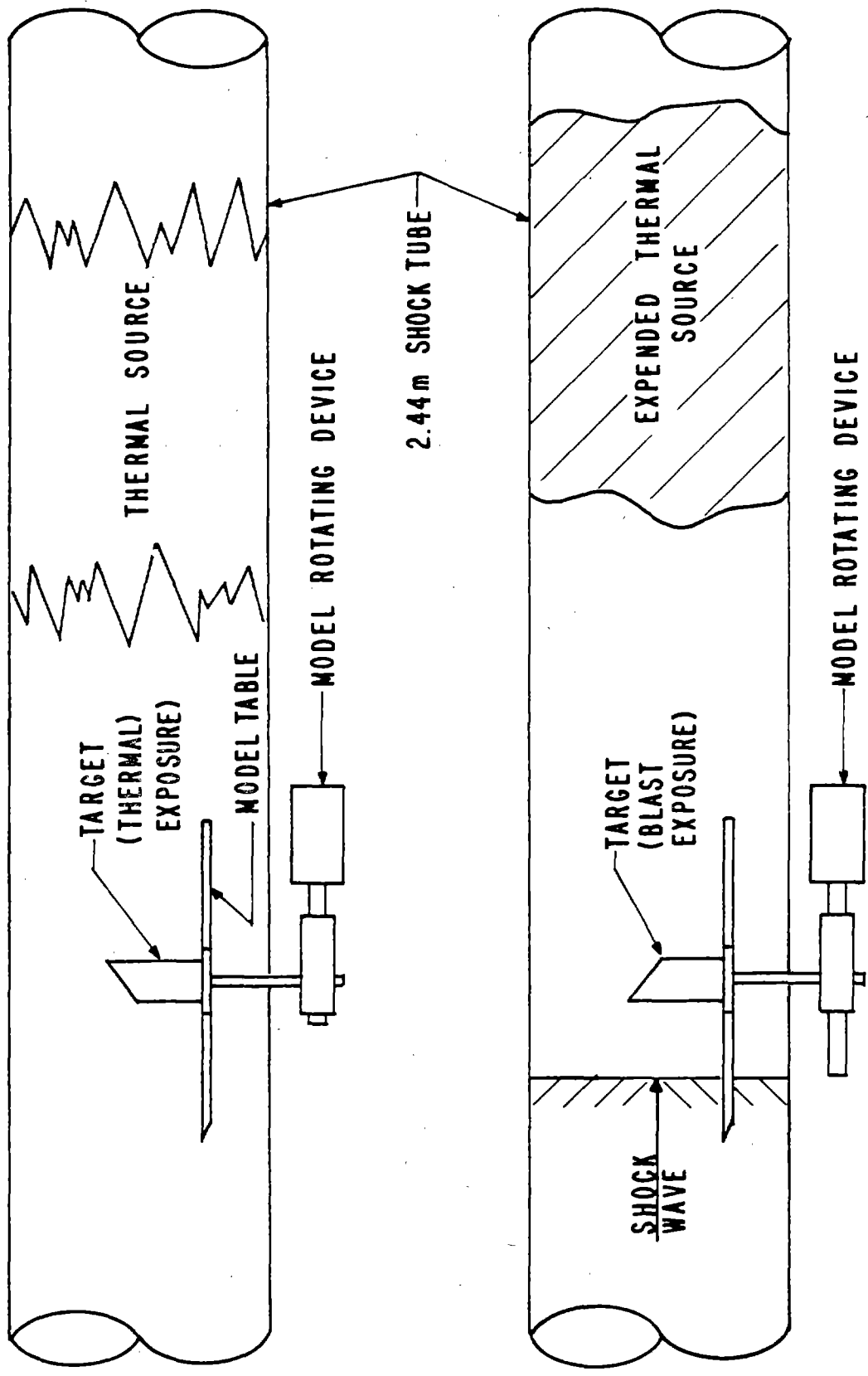


Figure 8. Thermal Pulse Shape from SAI "Flash-Bulb" Source.



**TARGET TO SOURCE SEPARATION & SOURCE VOLUME
WILL BE DETERMINED FROM DESIRED FLUX & FLUENCE LEVELS**

Figure 9. Thermal/Blast Test Station in BRL 2.44 m Shock Tube.

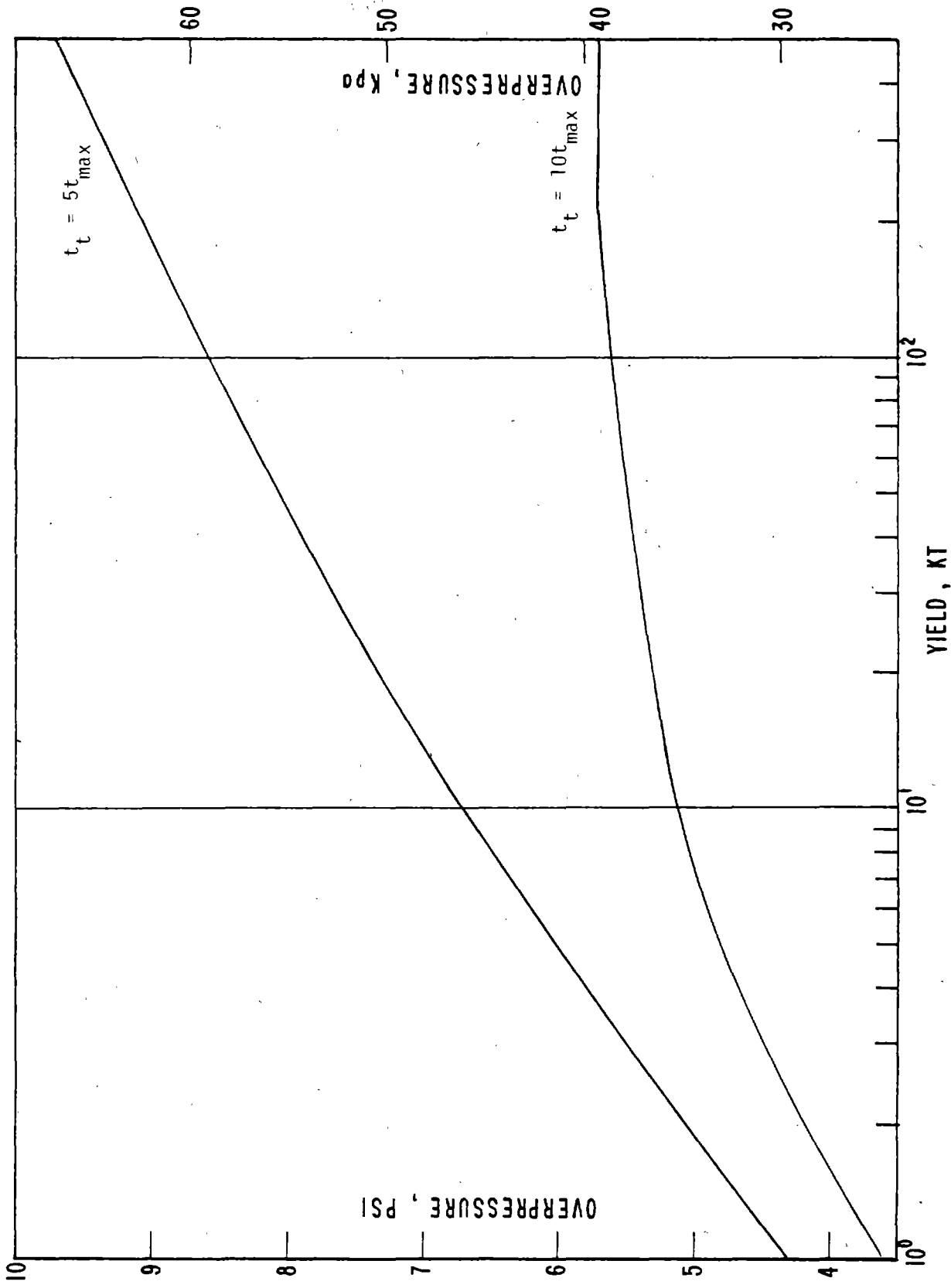


Figure 10. Capability of BRL 2.44 m Thermal/Blast Facility.

TEST-2.44M S.T. TS CAL
SHOT-15
STATION-1.51M (CM)

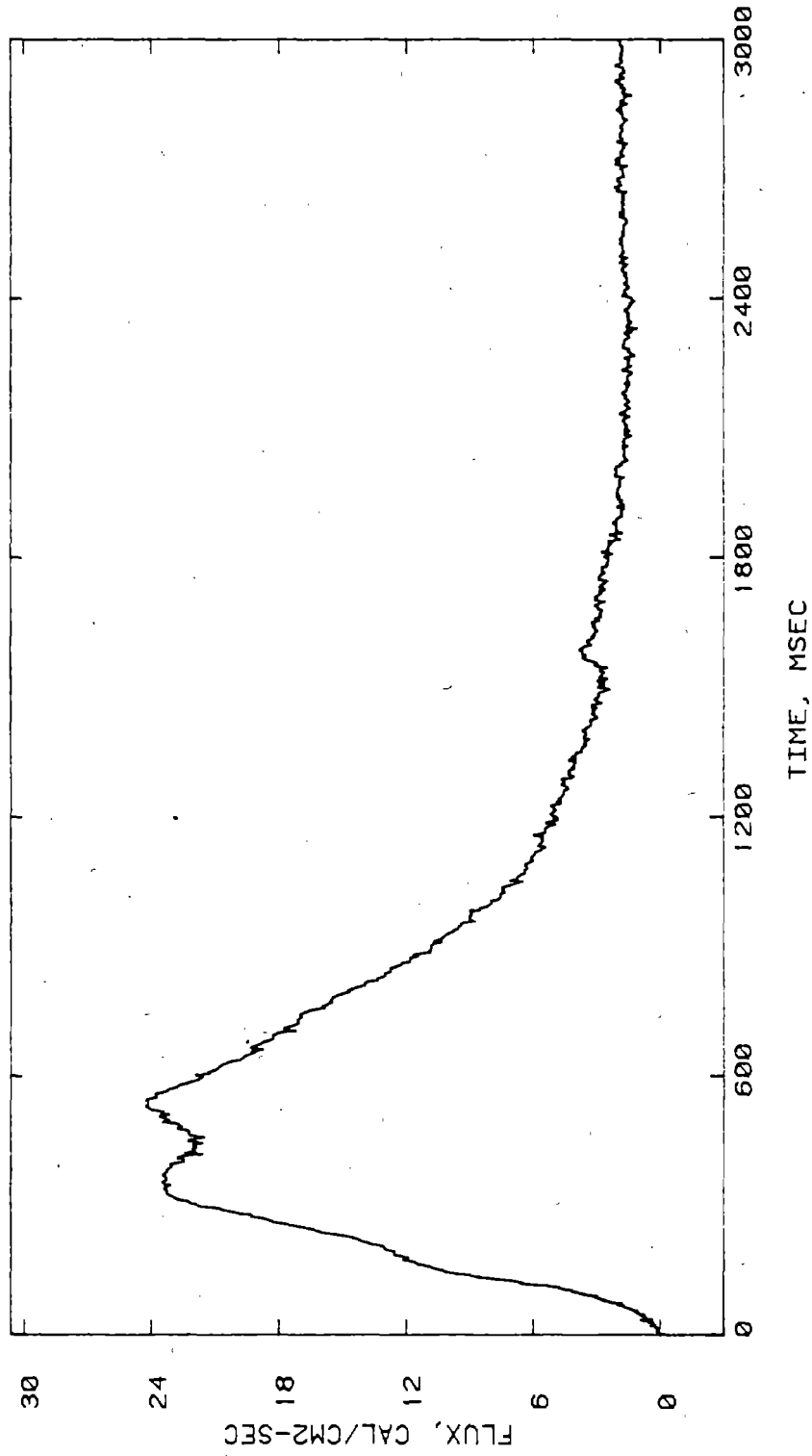


Figure 11. Thermal Pulse Shape in the 2.44 m Shock Tube.

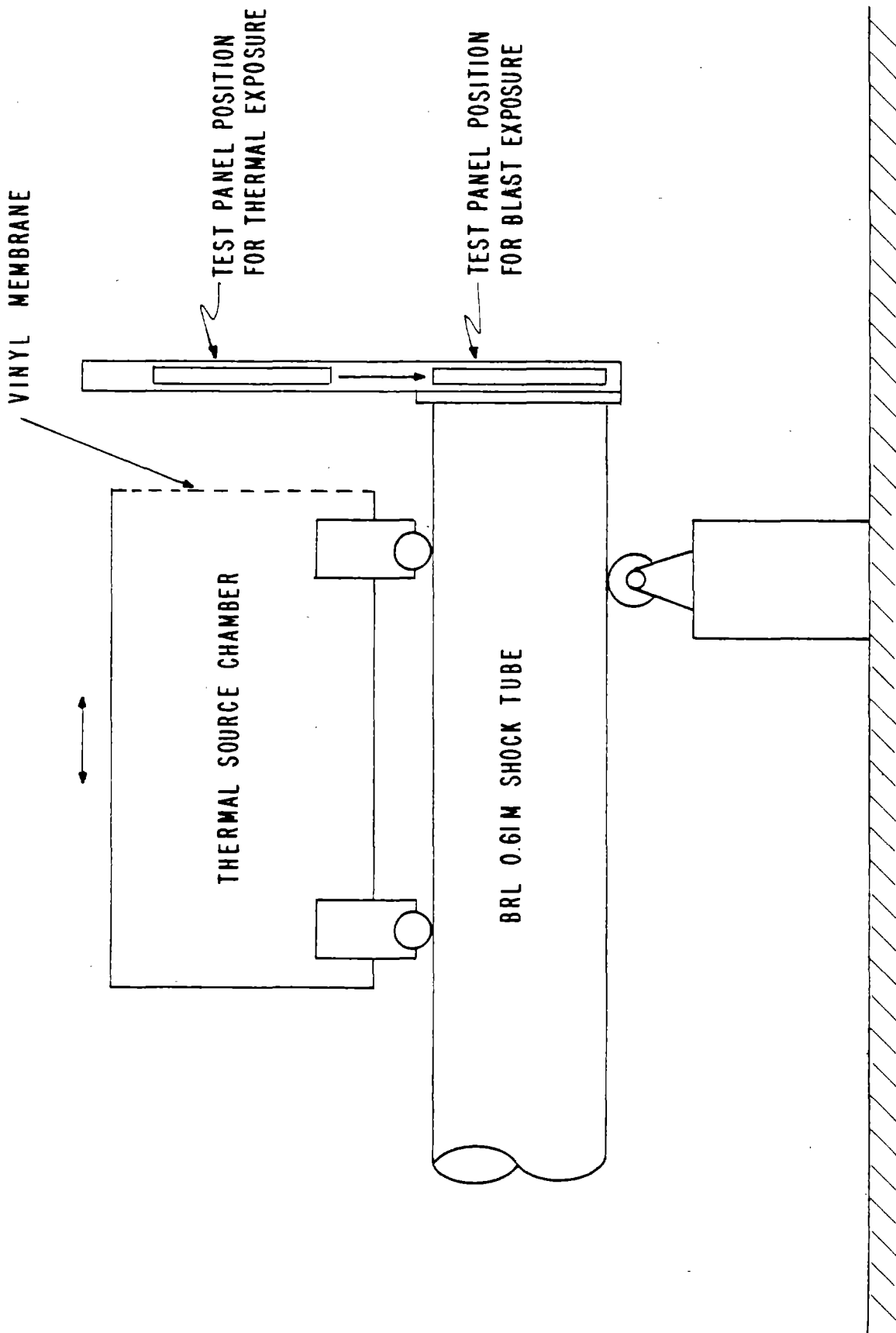


Figure 12. Thermal/Blast Test Station at the BRL 0.6 m Shock Tube.

ABSTRACT

The self-similar theory of intense explosions is used to compare the amounts of explosive required to produce transient surface loads for structural testing using spherical, cylindrical, and plane blast waves. To compare peak pressures at large standoff distances, the incident pressure ahead of the shock (neglected in the self-similar theory) is taken into account by using an approximation suggested by Korobeinikoff. The resulting shock pressures agree almost identically with compiled data from spherical charges out to overpressures of 0.04 atm, which is the lowest pressure reported. Comparison of blast waves in spherical and plane geometries shows that plane blast waves from flat sheet charges give a good simulation of spherical blast waves and require much less explosive. Sheet charges offer the further advantage of providing a continuous range of pulse durations from the submicrosecond pulses of charges in contact with the model to the millisecond pulses of flat charges in a shock tube. Surface pressure measurements on cylindrical models are given for lateral blast loads with exponential decay constants ranging from 20 to 1000 μ sec. Measured peak pressures compare well with theory.

LIST OF ILLUSTRATIONS

Figure

- 1 Peak Pressure-Impulse Ranges for Structural Response (6-inch diameter cylinders; hyperbolic curves are buckling thresholds for 6061-T6 aluminum shells with $L/D = 1$).
- 2 Pressure Behind Shock in Self-Similar Blast Waves.
- 3 Incident Pressure Pulses in Self-Similar Blast Waves.
- 4 Dynamic Pressure Pulses in Self-Similar Blast Waves.
- 5 Incident Shock Overpressure Ratio vs. $R = r_2/(E_o/p_1)^{1/\nu}$.
- 6 Reflected Shock Overpressure Ratio vs. $R = r_2/(E_o/p_1)^{1/\nu}$.
- 7 Similarity of Pressure Pulses from Plane and Spherical Blasts.
- 8 Sheet Charges for Free-Running Blast Waves.
- 9 Arrangement of Flat Charges in Shock Tube.
- 10 Pressure Pulses at $\theta = 0^\circ$ for Detasheet Charges at $x = 0.5$ Foot (sweep rate $20 \mu\text{sec/cm}$)
- 11 Shock Tube Pressure Pulses at Standoffs from 1 foot to 20 feet [all at charge density $w = 0.316$ psf, except $w = 0.52$ psf x 2 in (e)].
- 12 Pressure-Impulse Curves for Asymmetric Loads (6-inch-diameter models).
- 13 Comparison of Theoretical and Experimental Peak Pressures.

I INTRODUCTION

Direct simulation of nuclear airblast effects requires detonation of very large charges of chemical explosives. The largest simulation to date is a 1 KT nuclear equivalent yield. For targets in which the resulting loading pulses for the test yield have durations much longer than the characteristic response time of the target structure, results of the test can sometimes be interpreted as being the same as would occur for larger nuclear bursts. Testing with large explosive charges has the advantage of providing large test areas over a wide range of incident pressures; many targets, large and small, are placed along arcs at various ranges. The disadvantages are that the largest practical charges are still much smaller than many nuclear explosions of interest, and the shots are infrequent so that many targets of the same type are tested at once rather than sequentially. This gives little or no opportunity to improve a test on a particular target as a result information from a previous test.

These and other limitations of direct simulation are the motivation for the simulation techniques described at this conference. One class of simulation technique consists of testing with plane waves rather than spherical waves, so that only a column of the spherical wave is reproduced, usually by means of a shock tube. The target is placed in or near the mouth of the shock tube, usually only one target per test. The advantages are that each individual test is much less expensive, and a sequence of tests can be quickly performed with the full benefit of previous tests in planning the next. Also, tests can be performed with various shock tube lengths and charge weights to completely define target response over the range of pulse duration and peak pressure of importance to the target. With this information, response to nuclear explosions can be predicted for any yield or range. The disadvantages are that many more tests must be performed in order to characterize response of a group of targets, and the shock tube does not reproduce exactly the same blast wave as from a spherical explosion. Because of the advantages and disadvantages of each approach, both large spherical explosions and smaller explosions in shock tubes are in common use.

The ability to use plane blast waves to produce a range of peak pressures and pulse durations has been used to characterize target response to any weapon effect that produces damage by transient surface pressures. These effects include x-ray blowoff and loads from laser and plasma beams. The plane waves are generated by sheet explosive charges, placed in a shock tube for long pulse durations and detonated as a free-standing sheet close to the target for short pulse durations. In the limit of impulsive loads, the sheet is placed in direct contact with the target. Of course, as the explosive is placed closer to the target, the thickness to produce a given level of response becomes smaller, and vice versa. For long duration, high pressure pulses, the sheet is thick enough that in practice it consists of a gridwork of Primacord or a pad of explosive.

To characterize critical loads for target damage, it is convenient to describe the loading pulses in terms of the peak pressure and impulse intensity (area under the pressure-time history) that they produce on the target surface. This characterization is convenient because in the limits of long and short pulses, target response depends only on peak pressure or impulse, respectively. Figure 1 gives an example of this characterization scheme as applied to cylindrical targets under side-on blast waves. Critical curves for buckling of a thick and a thin aluminum shell are given as examples. Each curve is hyperbolic in shape and approaches asymptotes of constant peak pressure and constant impulse for the extremes of long and short pulses. Also indicated in the figure are the three methods of using sheet charges: in shock tubes, as a free-standing charge and in contact with the target. Loci of surface pulses from free-standing spheres are also shown for comparison. A more complete discussion of this critical load characterization is given in References 1 and 2.

The theory for blast waves from sheet charges is similar to that for blast waves from spherical charges. Both begin by considering a sudden release of energy from a small volume and follow the blast as it expands away from the energy source. In a useful range of pressures, the blast waves can be described by a self-similar theory in which the wave at any instant is similar to the wave at any other instant. The range of applicability

of this theory is from very high pressures but at ranges far enough from the explosion that the energy is almost entirely in the blast wave, down to much smaller pressures but still large compared with the ambient pressure ahead of the shock. At lower pressures the energy of the ambient air entering the blast wave is comparable to the initial energy release so that the wave is no longer self-similar and a more complete theory must be used.

The purpose of this paper is to use the self-similar theory to show the degree of simulation of spherical waves with plane waves, and to give formulas that can be used to specify the amount of explosive and standoff distances needed for specified peak pressures and impulses. The self-similar theory is extended to include the effect of the ambient pressure ahead of the shock so that peak pressures can be calculated down to overpressures well below the range of practical interest. For completeness, results are given for all three geometries: spherical, cylindrical, and plane. Examples are given to show the explosive weights and standoffs needed for representative targets. The paper concludes with surface pressure measurements on cylindrical targets as in Figure 1 and a comparison of these measurements with the theory.

II INTENSE EXPLOSIONS IN A PERFECT GAS

A. Characteristic Length and Self-Similarity

In the self-similar theory the explosion is idealized as a sudden release of a finite energy E_3 in a small volume of gas, giving in the limit an infinite energy density at a mathematical point for a spherical explosion. As the gas expands away from the point of energy release, it drives an intense spherical shock into the surrounding undisturbed gas. The average energy per unit volume within the expanding sphere decreases, eventually becoming comparable to the energy density in the undisturbed ambient gas,* initially at pressure p_1 and density ρ_1 .

In a perfect gas with specific heat ratio γ , the ambient gas has an internal energy (per unit volume) of

$$e = \frac{p_1}{(\gamma-1)}$$

The release energy per unit volume of the blast sphere at radius r is

$$e_b = \frac{E_3}{\frac{4}{3} \pi r^3}$$

These energy densities are equal at radius

$$r_e = \left[\frac{3(\gamma-1)E_3}{4\pi p_1} \right]^{1/3}$$

* Most of the gas and energy are contained in a thin layer immediately behind the shock, but the average energy decrease with increasing volume still gives a measure of the local energy density decrease. Also, the apparent release energy E_3 is related to the chemical energy release through a complex process not treated here. Brode³ showed that peak pressures from the self-similar theory are matched (in its range of validity) to numerical calculations for spherical explosions from TNT by taking E_3 equal to the explosive release energy. The same result is demonstrated here using compiled data from experimental pressure measurements.

For a cylindrical explosion from a release energy E_2 per unit length along the axis, $e_b = E_2/\pi r^2$ and the energy densities are equal at

$$r_e = \left[\frac{(\gamma-1)E_2}{\pi p_1} \right]^{1/2}$$

For a plane explosion from a release energy E_1 per unit area, $e_b = E_1/2r$ and the energy densities are equal at

$$r_e = \frac{(\gamma-1)E_1}{2p_1}$$

Thus, in each geometry a characteristic length r_o can be defined by

$$r_o = \left(\frac{E_o}{p_1} \right)^{1/\nu} \quad (1)$$

where $\nu = 1, 2,$ and 3 for plane, cylindrical, and spherical explosions, and it is understood that the release energy E_o has appropriate units in each case.* From the above examples we see that r_o is the distance (within a multiplicative constant) at which the release energy becomes comparable to the initial energy of the ambient gas enveloped by the blast. For a one-pound pentolite sphere in a standard atmosphere, $r_o = 10.0$ feet.

If we confine our attention to the early motion ($r \ll r_o$), the energy within the blast is so large compared to the ambient energy $p_1/(\gamma - 1)$ that the ambient energy can be neglected. Stated another way, near the explosion the shock pressure is so much greater than p_1 that p_1 can be neglected. Under these conditions the ambient gas is described by its density ρ_1 alone and there is no characteristic length. Consequently, with no length as a basis of comparison, the blast wave at any instant is identical to the blast wave

* The nomenclature E_o and r_o rather than E_ν and r_ν is conventional. In Section III when we make comparisons among geometries, the subscript ν must be used to avoid confusion.

at any other instant, except for scale changes as the sphere expands--the wave is self-similar. This self-similarity greatly simplifies the mathematical treatment because the flow can be described in terms of a single parameter ξ which is an appropriate combination of r and time t , rather than in terms of both r and t independently. At later times, as r approaches r_0 , this simplification is no longer appropriate and the pressure p_1 ahead of the shock must be considered. This will be done later. Also, the self-similar theory gives an infinite pressure as $r \rightarrow 0$ and is therefore inapplicable at small distances from a real explosion. For small r the mechanism of energy release and the properties of real gases must be considered. These effects have been treated by several authors, for example by Brode.^{3,4}

In the self-similar approximation there are five fundamental parameters:

$$E_0, \rho_1, \gamma, r, \text{ and } t$$

There are three fundamental units: force, distance, and time. The fundamental parameters can therefore be reduced to two dimensionless combinations. These are taken as

$$\gamma \text{ and } \xi = r \left(\frac{\rho_1}{E_0 t^2} \right)^{\frac{1}{\gamma+2}} \quad (2)$$

The specific heat ratio γ is a constant for any given problem so that ξ is the single independent variable, demonstrating the self-similar nature of the problem. The dependent variables of primary interest are the pressure p , density ρ , and particle velocity v .

B. Motion of the Shock Front

Before attempting to describe the complete flow within the blast sphere, let us examine the motion of the shock front and the values of p , ρ , and v just behind the shock. At each (and every) instant the pressure wave appears as shown in Fig. 2, in which both p and r have been normalized to their values p_2 and r_2 at the shock front. Since ξ is the only independent variable, each relative position behind the shock corresponds to a value of ξ and, in

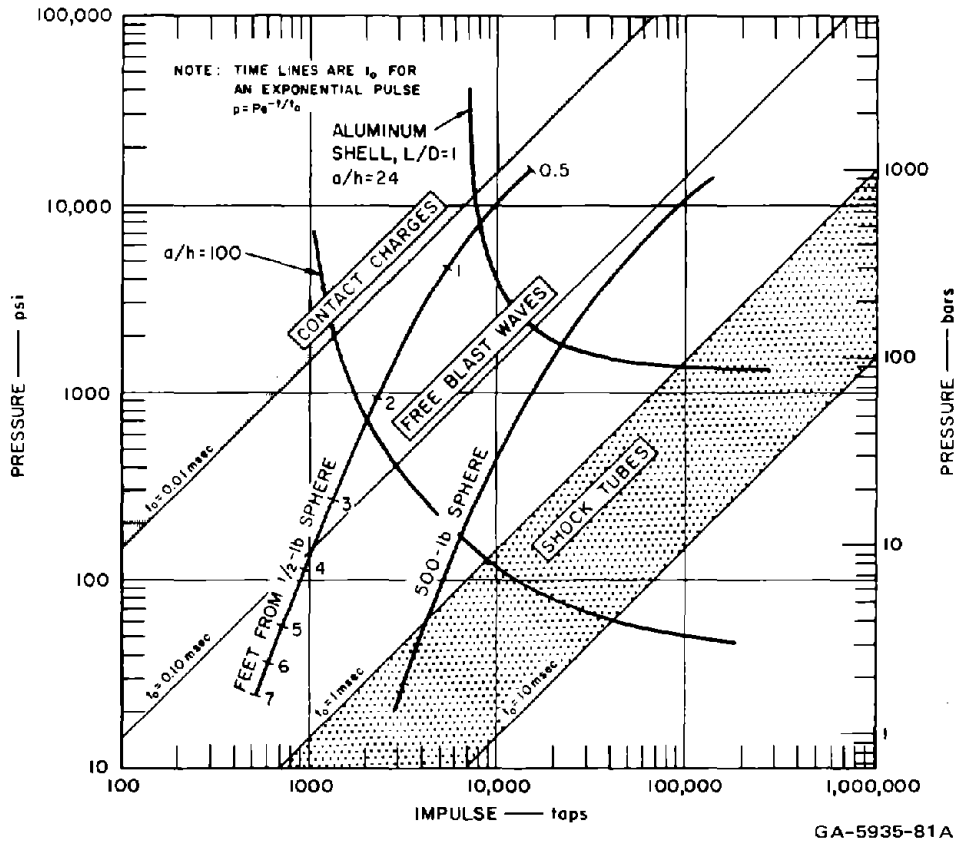


FIGURE 1 PEAK PRESSURE-IMPULSE RANGES FOR STRUCTURAL RESPONSE
 (6-inch diameter cylinders; hyperbolic curves are buckling thresholds for 6061-T6 aluminum shells with L/D = 1)

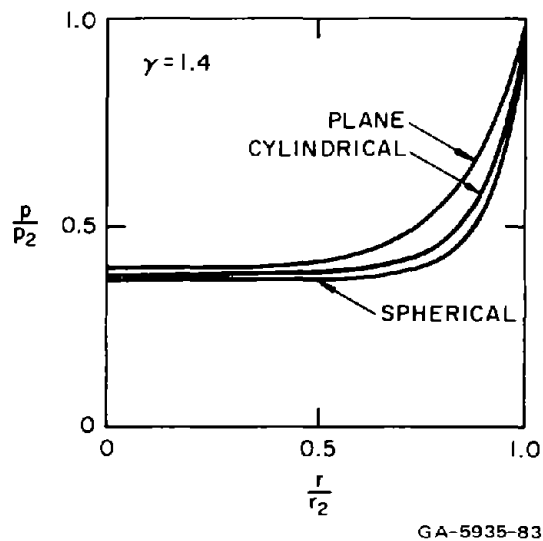


FIGURE 2 PRESSURE BEHIND SHOCK IN SELF-SIMILAR BLAST WAVES

particular, the position of the shock itself corresponds to a unique value ξ_0 . From Eq. (2) the position of the shock is then

$$r_2 = \xi_0 \left(\frac{E_0 t^2}{\rho_1} \right)^{\frac{1}{\nu+2}} \quad (3)$$

and the velocity of the shock is

$$U = \frac{dr_2}{dt} = \left(\frac{2}{\nu+2} \right) \frac{r_2}{t} = \frac{2\xi_0}{\nu+2} \left(\frac{E_0}{\rho_1} \right)^{1/2} r_2^{-\frac{\nu}{2}} \quad (4)$$

The variables at the shock front can then be calculated directly from the strong shock relations:

$$v_2 = \frac{2U}{\gamma+1}, \quad \rho_2 = \left(\frac{\gamma+1}{\gamma-1} \right) \rho_1, \quad p_2 = \frac{2\rho_1 U^2}{\gamma+1} \quad (5)$$

For example, the pressure behind the shock is

$$p_2 = \frac{8E_0 \xi_0^{\nu+2}}{(\nu+2)^2 (\gamma+1)} \cdot \frac{1}{r_2^\nu} \quad (6)$$

Thus, using only dimensional analysis, all of the quantities at the shock can be determined within an unknown constant which can be determined by a single experiment. The dimensional analysis also shows that if all the flow variables are measured as a function of time at a single radius from any single explosion, these data can be used to calculate the complete flow for any other combination of charge and radius, so long as the self-similar approximation is valid.

C. Pressure Pulses from the Self-Similar Solution

Solutions in terms of simple analytic functions for the complete flow behind the shock were found independently by Taylor,⁵ Sedov,⁶ and von Neumann.⁷

Curves and tables of p/p_2 , ρ/ρ_2 , and v/v_2 as functions of the distance $\lambda = r/r_2$ behind the shock are given by Sedov⁶ for all three geometries. For blast load calculations we need to find p , ρ , and v as functions of time at a fixed radius r_f . Here we will find the incident pressure pulse $p(t)$, and the dynamic pressure pulse $p_d(t)$. From Eqs. (6) and (3) the peak incident pressure is

$$p_f = \frac{8E_o}{\alpha(\nu+2)^2(\gamma+1)} \cdot \frac{1}{r_f^\nu} \quad (7)$$

at time

$$t_f = \left(\frac{\alpha \rho_1}{E_o} \right)^{1/2} r_f^{\frac{\nu+2}{2}} \quad (8)$$

where the parameter $\alpha = \xi_o^{-(\nu+2)}$ is given by Sedov as a function of γ in each geometry.* At a later time t the shock front r_2 has continued past $r = r_f$ and the pressure at r_f has decayed because both p/p_2 (see Fig. 2) and p_2/p_f decrease with time. We define a normalized pulse time τ after the shock has passed according to

$$\tau = \frac{t-t_f}{t_f} = \left(\frac{r_f}{r_2} \right)^{\frac{\nu+2}{2}} - 1 \quad (9)$$

in which Eq. (3) has again been used. The pressure at τ is

Equation 10

$$p(\tau) = p_f \left(\frac{p_2}{p_f} \right) \left(\frac{p}{p_2} \right) = p_f \left(\frac{r_f}{r_2} \right)^\nu \left(\frac{p}{p_2} \right) \quad (10)$$

Equations (9) and (10) are parametric equations for p and τ with r_f/r_2 as a parameter. We can now replace r_f by r without confusion so that these equations become

$$\tau = \lambda^{\frac{\nu+2}{2}} - 1, \quad \frac{p(\tau)}{p_f} = \lambda^\nu P_\nu(\lambda) \quad (11)$$

* $\alpha = 1.075, 1.00,$ and 0.85 for plane, cylindrical, and spherical waves, respectively, when $\gamma = 1.4$.

where $p_v(\lambda)$ is p/p_2 vs. $\lambda = r/r_2$ as tabulated by Sedov,⁶ pp. 222-223, and given here in Fig. 2.

Curves of $p(\tau)/p_f$ are given in Fig. 3 for $\nu = 1, 2,$ and 3 . The general shapes of the curves do not differ appreciably for small τ , but for large τ the pressure decays more slowly in cylindrical and plane geometry than in spherical geometry. (A better comparison between the plane and spherical pulses is given in Fig. 7, with the time scale for the plane wave compressed to give close agreement at early times.) For $\tau \gg 1$ the limiting forms of Eqs. (11), along with the observation that $p_v(\lambda = 0)$ are constants, yield

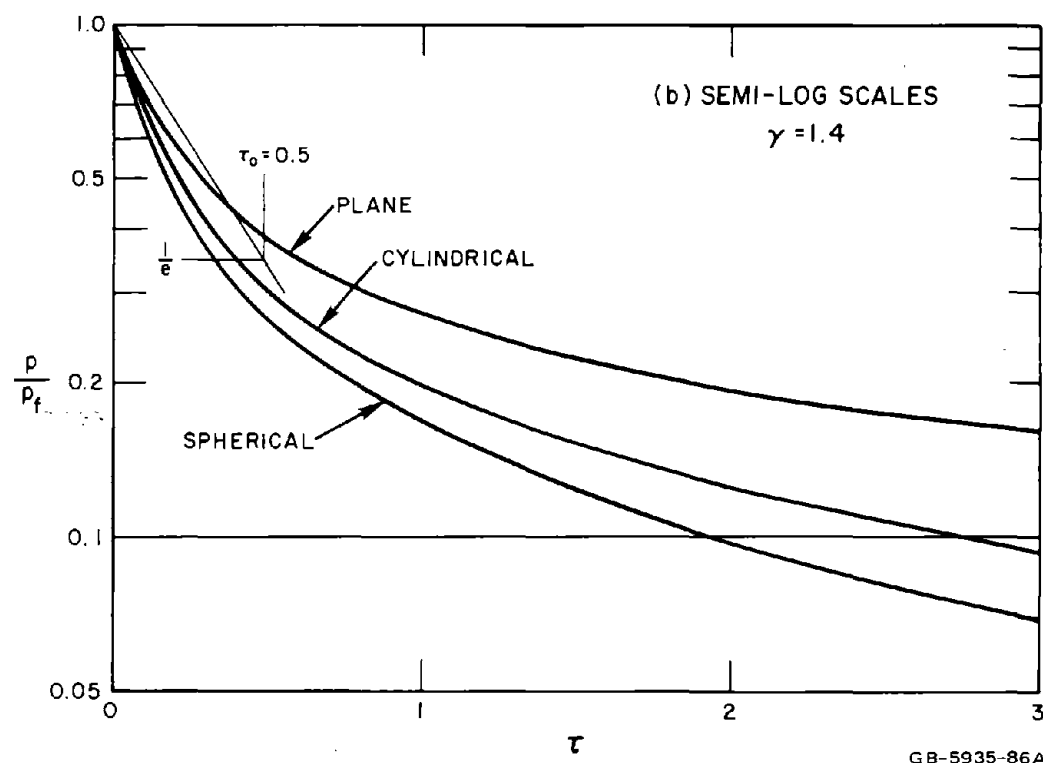
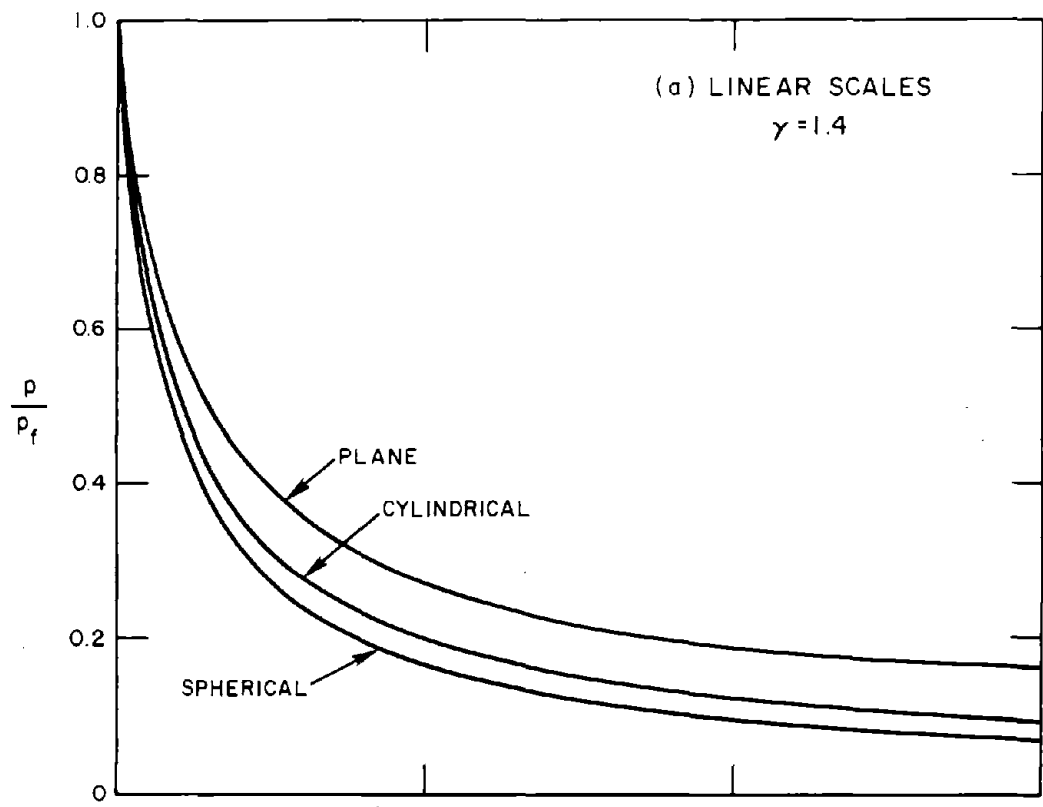
$$\frac{p(\tau)}{p_f} \rightarrow p_v(0) \tau^{-\frac{2\nu}{\nu+2}}$$

Thus, for large times the incident pressure decays as $t^{-2/3}$, t^{-1} , and $t^{-6/5}$ in plane, cylindrical, and spherical geometries.

By a similar procedure, the dynamic pressure pulse can be expressed by

$$p_d(\tau) = p_{df} \lambda^\nu g(\lambda) v^2(\lambda) \quad (12)$$

where $g(\lambda) = \rho/\rho_2$ and $v(\lambda) = v/v_2$ are the normalized density and particle velocity, also tabulated by Sedov. Semilog plots of $p_d(\tau)$ for plane and spherical waves are given in Fig. 4. These pulses are very nearly exponential (straight lines here) and decay more rapidly than the incident pressures in Fig. 3. The pulse can therefore be approximated by $p_d = p_{do} e^{-\tau/\tau_0}$. Although direct comparison is difficult because the incident pulse shapes differ widely from an exponential shape (see Fig. 3), comparison of the semi-log straight lines approximating the plane wave pulses at early times in Figs. 3 and 5 give a characteristic time τ_0 for the dynamic pressure which is about one-third of that for the incident pressure. Surface pressures (given in the next section) measured on cylindrical models are very nearly exponential in shape, with characteristic times near $\tau_0 = 0.5$ for explosions small enough that diffraction flow dominates. For very large explosions, in which the total blast duration is large compared to the duration of the diffraction



GB-5935-86A

FIGURE 3 INCIDENT PRESSURE PULSES IN SELF-SIMILAR BLAST WAVES

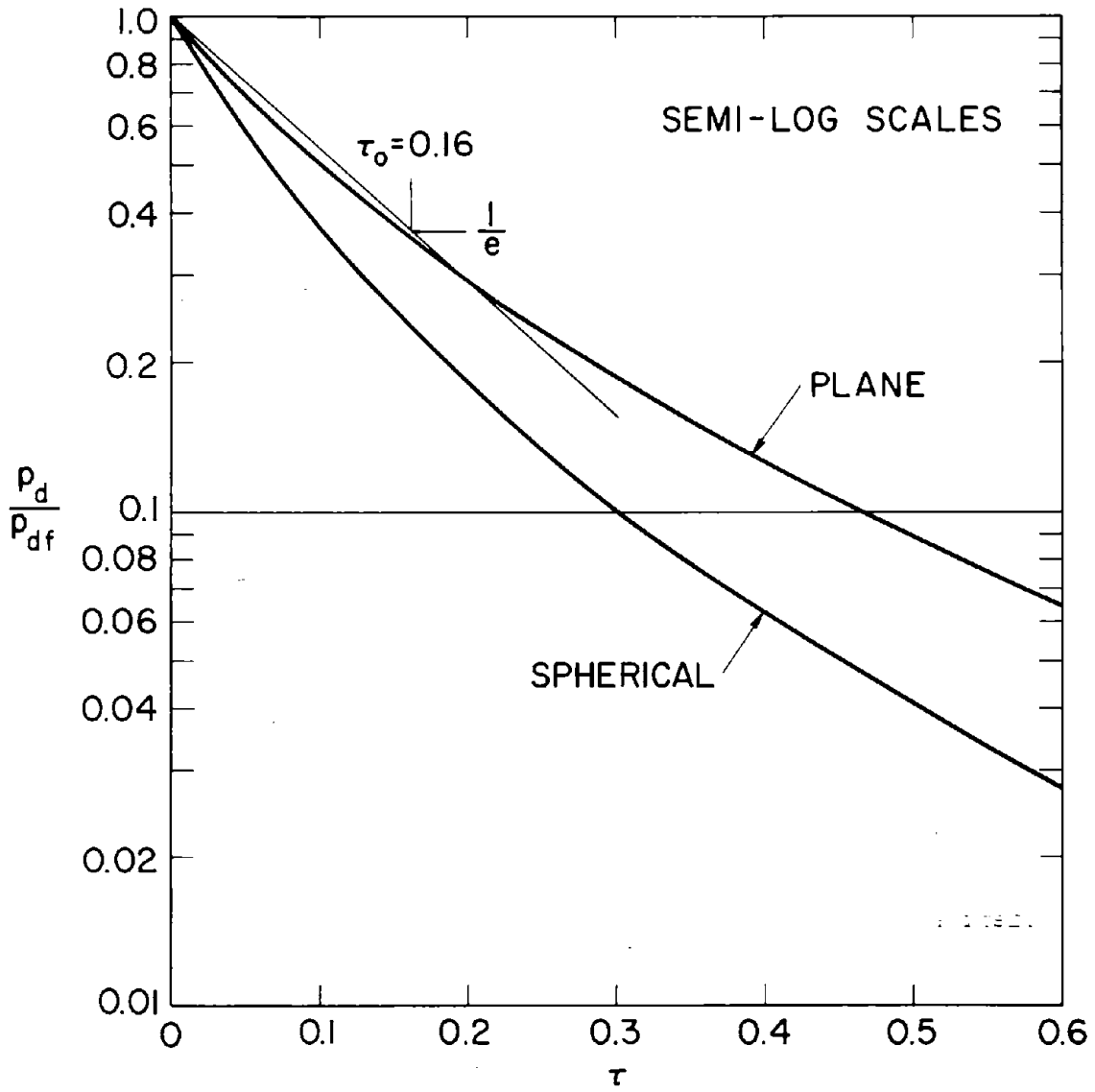


FIGURE 4 DYNAMIC PRESSURE PULSES IN SELF-SIMILAR BLAST WAVES

flow, the initial diffraction pressure spike can be neglected and only drag flow need be considered. For these pulses Fig. 5 suggests that the shape will again be exponential, but with $\tau_0 \approx 0.16$.

D. Shock Front Motion into an Initial Pressure

At large distances from the charge the shock pressure p_2 becomes comparable to the initial ambient pressure p_1 ahead of the shock and the self-similar theory no longer applies. When p_1 is taken into account, energy enters the blast sphere as it envelops the surrounding gas and the shock therefore decays less rapidly with distance than in the self-similar theory (in which the total energy is assumed constant). The complete flow can only be determined numerically,³ but a method for finding simple approximate expressions for the modified shock front motion and pressure is suggested by Korobeinikoff.⁷ He compared the dependence on r_2 of the particle velocity v_2 just behind the shock front as given by the self-similar theory (valid for small r_2) and by the asymptotic theory of Landau (Ref. 8, pp. 375-377, valid for large r_2) and observed that there was little change in this dependence. This is demonstrated in Table I. On the basis of this observation, he suggested that for intermediate values of r_2 the particle velocity can be taken from the self-similar theory and the shock velocity U can then be calculated from the particle velocity jump condition across the shock. Using this modified expression for U , the pressure p_2 and density ρ_2 can then be determined from the other two jump conditions.

Table I
DEPENDENCE OF PARTICLE VELOCITY v_2 ON SHOCK RADIUS r_2

Theory	Geometry		
	$v = 1$ plane	$v = 2$ cylindrical	$v = 3$ spherical
Self-similar	$r_2^{-1/2}$	r_2^{-1}	$r_2^{-3/2}$
Acoustic shock	$r_2^{-1/2}$	$r_2^{-3/4}$	$r_2^{-1} \log^{-1/2} \left(\frac{r_2}{r_0} \right)$

Conservation of mass, momentum, and energy across the shock give the following jump conditions for a perfect gas:

$$\frac{v_2}{c_1} = \frac{2}{\gamma+1} \left(\frac{M^2-1}{M} \right)$$

$$\frac{p_2}{p_1} - 1 = \frac{2\gamma}{\gamma+1} (M^2 - 1) \quad (13)$$

$$\frac{\rho_2}{\rho} = \frac{(\gamma+1)M^2}{2 + (\gamma-1)M^2}$$

expressed in terms of shock Mach number M , defined by

$$M = \frac{U}{c_1}, \quad c_1^2 = \frac{\gamma p_1}{\rho_1} \quad (14)$$

where c_1 is the sound speed in the ambient gas ahead of the shock. From Eqs. (4) and (5), the particle velocity from the self-similar solution is

$$v_2 = \frac{4}{(\nu+2)(\gamma+1)} \left(\frac{E_o}{\alpha \rho_1} \right)^{1/2} r_2^{-\nu/2} \quad (15)$$

in which we have used $\alpha = \xi_o^{-(\nu+2)}$. Since we now take account of p_1 , it is convenient to express r_2 in terms of the characteristic length $r_o = (E_o/p_1)^{1/\nu}$, giving a dimensionless shock radius R :

$$R = \frac{r_2}{r_o} \quad (16)$$

With this definition and c_1 from Eq. (14), the particle velocity is expressed by

$$\frac{v_2}{c_1} = \frac{4R^{-\nu/2}}{(\nu+2)(\gamma+1)(\alpha\gamma)^{1/2}} \quad (17)$$

By combining (17) with the first of Eqs. (13), the desired expression for shock velocity is found to be:

$$M = A + \sqrt{A^2 + 1} \quad (18)$$

in which

$$A^2 = \frac{R^{-\nu}}{\alpha\gamma(\nu+2)^2} \quad (19)$$

Substitution of Eq. (18) into Eqs. (13) gives the variation of v_2 , p_2 , and ρ_2 with distance. For example, the overpressure is

$$\frac{p_2}{p_1} - 1 = \frac{4\gamma}{\gamma+1} A^2 \left[1 + (1 + A^{-2})^{1/2} \right] \quad (20)$$

The limiting form for small radius R (large A) is

$$\frac{p_2}{p_1} - 1 = \frac{8\gamma}{\gamma+1} A^2 = \frac{8R^{-\nu}}{\alpha(\nu+2)^2(\gamma+1)} \quad (21)$$

In the limit as $p_1 \rightarrow 0$ (after multiplying by p_1), this is seen to coincide with the self-similar formula (6).

For large R the self-similar particle velocity (15) becomes a poor approximation for cylindrical and spherical waves (see Table I). In this range the small disturbance expressions in Table I can be used, matching the large and small R expressions at some intermediate value of R . For example, in the spherical case Korobeinikov matches them at $R = 2$ to obtain

$$\frac{v_2}{c_1} = \begin{cases} \frac{4R^{-3/2}}{5(\gamma+1)(\alpha\gamma)^{1/2}} & R \leq 2 \\ \frac{4R^{-1}[\log(R/2) + 1]^{-1/2}}{5(\gamma+1)(2\alpha\gamma)^{1/2}} & R \geq 2 \end{cases} \quad (22)$$

Similarly, for cylindrical blast waves we take

$$\frac{v_2}{c_1} = \begin{cases} \frac{R^{-1}}{(\gamma+1)(\alpha\gamma)^{1/2}} & R \leq 2 \\ \frac{R^{-3/4}}{2^{1/4}(\gamma+1)(\alpha\gamma)^{1/2}} & R \geq 2 \end{cases} \quad (23)$$

By using these expressions, the incident overpressure throughout the entire range of R is found to be given by Eq. (20) with the following expressions for A^{-2} :

$v = 1$ Plane waves

$$(\alpha = 1.075 \text{ for } \gamma = 1.4) \quad A^{-2} = 9\alpha\gamma R \quad \text{all } R$$

$v = 2$ Cylindrical waves

$$(\alpha = 1.00 \text{ for } \gamma = 1.4) \quad A^{-2} = \begin{cases} 16\alpha\gamma R^2 & R \leq 2 \\ 16\sqrt{2}\alpha\gamma R^{3/2} & R \geq 2 \end{cases} \quad (24)$$

$v = 3$ Spherical waves

$$(\alpha = 0.85 \text{ for } \gamma = 1.4) \quad A^{-2} = \begin{cases} 25\alpha\gamma R^3 & R \leq 2 \\ 50\alpha\gamma R^2 [\ln(R/2) + 1] & R \geq 2 \end{cases}$$

The reflected overpressure ratio is given by

$$\frac{p_r}{p_1} - 1 = \left[\frac{(2\mu+1)p_2/p_1 + 1}{\mu p_2/p_1 + 1} \right] \left(\frac{p_2}{p_1} - 1 \right) \quad (25)$$

where $\mu = (\gamma - 1)/(\gamma + 1)$.

Figures 5 and 6 give curves of incident and reflected overpressure ratios from these equations. Also shown are (dashed) curves from compiled data on spherical pentolite explosions, taken from Goodman.¹⁰

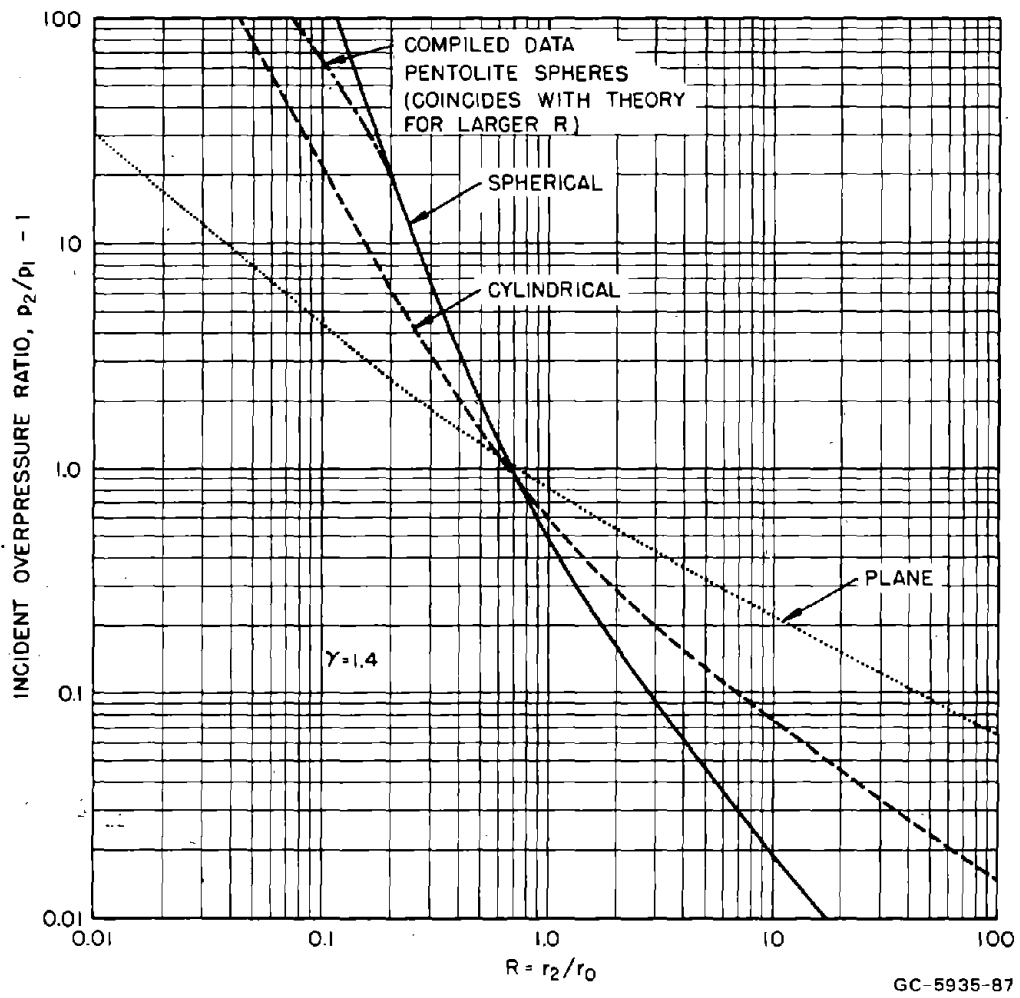


FIGURE 5 INCIDENT SHOCK OVERPRESSURE RATIO vs. $R = r_2/(E_0/\rho_1)^{1/2}$

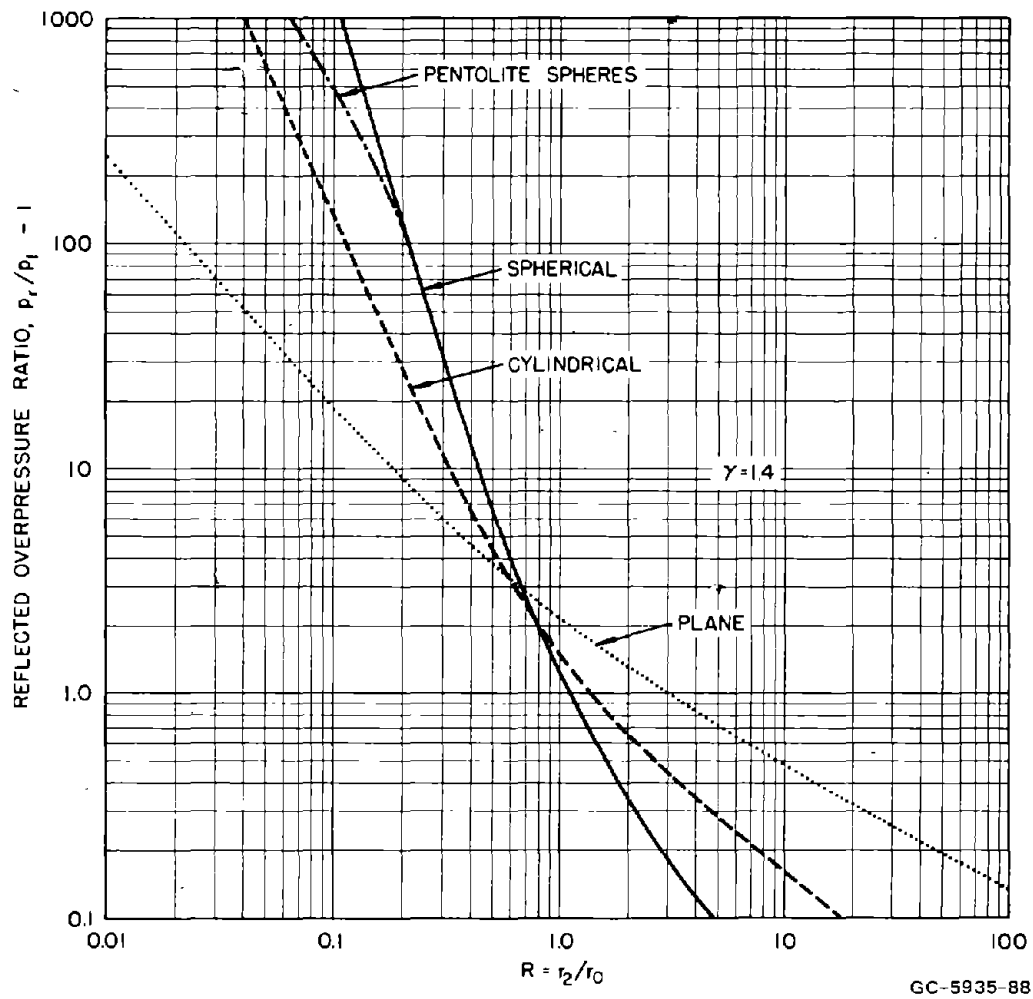


FIGURE 6 REFLECTED SHOCK OVERPRESSURE RATIO vs. $R = r_2/(E_0/p_1)^{1/2}$

The approximate theory matches identically with the experimental data for $R > 0.2$ if E_0 is calculated on the basis of 1430 cal/gm (pressures were measured only out to $R = 7$). At smaller radii real gas and explosive properties become important and the measured pressures are smaller than predicted by the self-similar theory. At larger radii other mechanisms of wave damping, such as viscosity, become important. However, the range of validity of the approximate theory is quite broad, giving reliable reflected overpressure ratios from about 0.1 to 100, a useful range for studying structural response. This excellent agreement for spherical explosions gives some confidence in using the approximate solutions for cylindrical and plane blast waves, for which few experimental data are available. Comparison of theory and experiment for plane waves is made in Section IV.

III APPLICATION OF THEORY TO LOAD SIMULATION

A. Comparison of Simulation with Spherical and Plane Waves

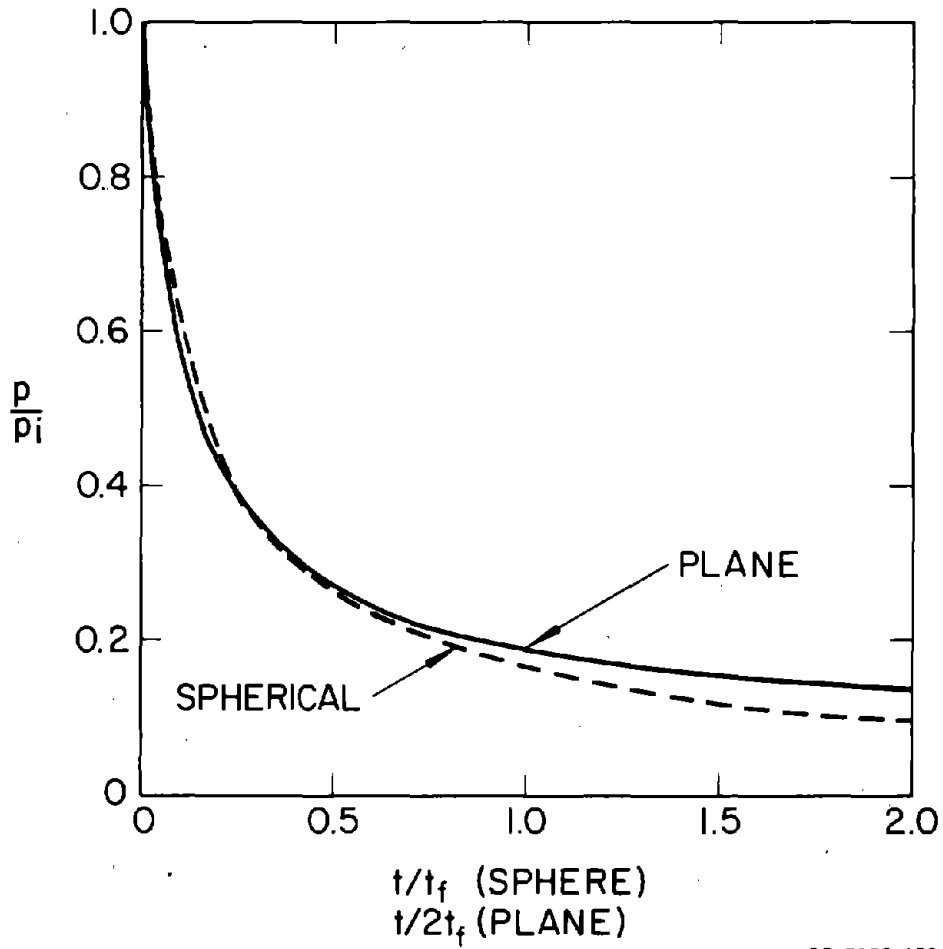
As an example of the application of the preceding theory, let us compare the spherical and sheet charges that produce (nearly) the same pressure pulses. Incident pressure pulse shapes are compared in Fig. 7, taken from Fig. 3 with the time scale for the plane wave compressed by a half to give close agreement at early times. With this modification the two pulses are nearly identical until p/p_1 falls below 0.2. At later times the pressure decays more slowly for the plane wave, but the difference is not great.* Pulse shapes for dynamic pressure are essentially identical, even at late times, as can be seen by applying a time compression of 0.65 to the plane wave pulse in Fig. 4.

Knowing that the pulse shapes are similar in the self-similar range, we can logically compare the charge weights and standoff distances for plane and spherical blast waves that give the same peak pressure and duration. To distinguish among variables from different geometries, in the following we attach a subscript v . The standoff distances are denoted by x_v , which in dimensionless form becomes

$$R_v = \frac{x_v}{s_v}, \quad s_v = \left(\frac{E_v}{p_1} \right)^{1/v} \quad (26)$$

where s_v are the characteristic lengths defined by Eq. (1), repeated above with the effective explosive release energies denoted by E_v (having units of energy per unit area in plane geometry, energy per unit length in cylindrical geometry, and total energy of the charge in spherical geometry). In these terms the incident pressure ratios and characteristic times in Eqs. (7) and (8) are given by

* A feature of spherical blast waves not included in the self-similar theory is the negative phase of pressure, giving a relative vacuum compared with the initial pressure p_1 (recall that p_1 was considered negligible compared with the blast pressures).



GP-5935-132

FIGURE 7 SIMILARITY OF INCIDENT PRESSURE PULSES FROM PLANE AND SPHERICAL BLASTS

$$\frac{p_i}{p_1} = \frac{8R_v^{-2}}{\alpha_v(2+v)^2(\gamma+1)} \quad (27)$$

$$t_{fv} = \left(\frac{\alpha_v \rho_1}{p_1} \right)^{1/2} s_v r_v^{(v+2)/2} \quad (28)$$

By equating peak pressures from Eq. (27) for plane and spherical blast waves we find

$$R_1 = \frac{25\alpha_3}{9\alpha_1} R_3^3 = 2.16R_3^3 \quad (29)$$

in which $\alpha_1 = 1.075$ and $\alpha_3 = 0.85$ have been taken for $\gamma = 1.4$ as noted earlier. From Fig. 7 the incident pressure durations are made comparable by taking $2t_{f1} = t_{f3}$. Use of this condition in Eq. (28) results in

$$2\alpha_1^{1/2} s_1 R_1^{3/2} = \alpha_3^{1/2} s_3 R_3^{5/2} \quad (30)$$

Equation (30) is combined with Eq. (29) to yield

$$s_1 = \frac{1}{2} \left(\frac{27}{125} \right) \frac{\alpha_1}{\alpha_3} s_3 R_3^{-2} = \frac{0.137}{x^2} s_3^3 \quad (31)$$

From the definition of s_v in Eq. (26), s_1 is proportional to the thickness of the sheet charge (weight per unit area) and s_3 is proportional to the radius of the spherical charge (s_3^3 is proportional to the total charge weight). In these terms Eq. (31) becomes

$$w_1 = \frac{0.137}{x_3^2} w_3, \quad \text{or} \quad w_3 = 81x_1^2 w_1 \quad (32)$$

where w_1 is weight per unit area of the sheet charge and w_3 is total weight of the spherical charge. Also, by combining Eqs. (29) and (31) with the definition of R_v from Eq. (26) the following additional relationship is obtained.

$$x_1 = \frac{3}{10} x_3 \quad (33)$$

Equations (32) and (33) are the desired relations between charge size and model-to-charge distances and are applicable for pressure pulses in the range of approximate validity of the self-similar theory. This range is rather narrow ($5 \lesssim p_1/p_1 - 1 \lesssim 50$), but the corresponding range in reflected pressure with $p_1 = 14.7$ psi is $300 \lesssim p_r \lesssim 5000$ psi, which happens to be the range in which many structural models of interest are damaged. Also, since Eqs. (32) and (33) are comparative, their range of validity is probably somewhat larger than the range of absolute accuracy of the self-similar theory. From Eq. (33) we see directly that the space required for a sheet charge experiment is inherently less than that required for a spherical charge, the standoff distance being only 30 percent of that for a spherical charge. From Eq. (32) we see, as expected, that at large distances (long durations) a great savings in weight can be achieved by using one-dimensional blast waves. For example, to simulate an incident overpressure ratio of 10 from a 1 kT nuclear surface burst would require only 40 pounds of pentolite in a 95-foot long, 6-foot-diameter shock tube. In a direct simulation, the target would have to be placed at 315 feet from a 500 ton pentolite charge. Examples relating to the use of one-dimensional blast waves to characterize target response over the entire range of importance to the target are given in the next subsection.

B. Estimates of Charge Weights and Standoffs for Target Response Characterization

As shown in Fig. 1, surface pressure characteristic times for which sheet charges appear attractive for investigating response of 6-inch-diameter model targets are in the range $10^{-5} < t_0 < 10^{-3}$ sec. With the self-similar theory, the range of sheet charge thickness and standoff distances required to give these characteristic times for the incident pressure pulses are easily estimated. We consider that we are simulating asymmetric loads from lateral blast waves and seek the charges

and standoffs that produce a peak surface pressure of, say, 3000 psi at each extreme in duration. Parameters for other pressures are found in a similar way.

As shown by experiments presented in the following section, the peak pressure produced on a model for moderately sized charges is the reflected pressure p_r corresponding to the incident pressure p_i . Thus, a model surface pressure of 3000 psi is obtained for a reflected overpressure ratio of about 200 which, from Fig. 6, requires that $R_1 = 0.012$. The explosive thickness to produce this pressure at various incident pressure durations can be calculated from Eq. (28). We first use definition (26) to obtain

$$s_1 = h \frac{Y}{p_1} \quad (34)$$

where h is the explosive thickness and Y is its effective release energy per unit volume. PETN has an energy release of about 1600 cal/gm which, at a 1.4 gm/cm^3 density, gives $Y \approx 10^{11} \text{ ergs/cm}^3$. Substituting Eq. (14) into Eq. (28) gives for the explosive thickness

$$h = \frac{p_1}{Y} \left(\frac{p_1}{\alpha_1 \rho_1} \right)^{1/2} \frac{1}{R_1^{3/2}} t_{f1} \quad (35)$$

As discussed previously, the initial portion of the incident pressure pulse can be approximated by an exponential with a characteristic time $t_o = 0.5t_{f1}$. Thus we can substitute $10^{-5} \approx 0.5t_{f1} \approx 10^{-3}$ into Eq. (35) with $p_1 = 10^6 \text{ dyne/cm}^2$, $\rho_1 = 1.293 \times 10^{-3} \text{ gm/cm}^3$, $Y = 10^{11} \text{ ergs/cm}^3$, and $R_1 = 0.012$ to obtain the range for h at this pressure:

$$0.0040 \bar{< h < 0.40 \text{ cm} \quad (36)$$

To obtain the corresponding standoff distances, we use Eqs. (26) and (34) to get

$$x_1 = R_1 h \frac{Y}{p_1}$$

which, with Eq. (36), yields

$$4.8 \lesssim x_1 \lesssim 480 \text{ cm}$$

(37)

Thus, the required standoff distances range from about 2 inches to 20 feet and explosive thicknesses range from about 2 mils to 0.2 inch. These ranges can be readily obtained experimentally. The lower limit of 2 mils for explosive thickness cannot be obtained in a continuous sheet, but thin extruded rods of explosive can be used to give an average thickness of 2 mils at a spacing small compared to the 2-inch standoff. Near the upper limit of standoff distance, $x = 20$ feet, a shock tube is required to maintain one-dimensional flow.

078 4 100

IV CYLINDRICAL TARGET SURFACE LOADS FROM SHEET CHARGES

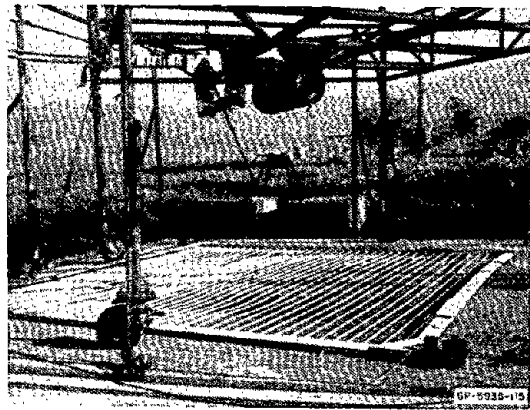
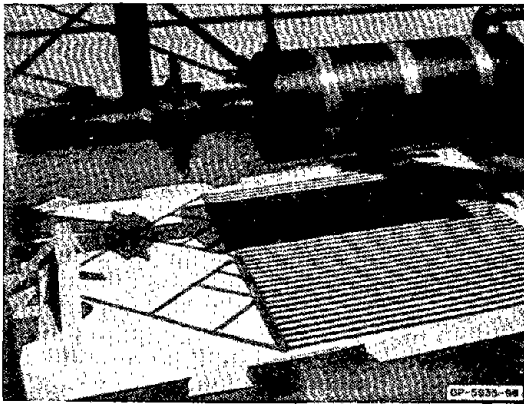
In the following we give a brief description of the experimental arrangements used for producing side-on loads from sheet charges and of the pressure measurements made on 6-inch-diameter targets. A more detailed description is given in Ref. 11.

A. Experimental Arrangements

Two basic experimental arrangements were used for simulating asymmetric loads. Free blast waves from flat charges on the ground, shown in Fig. 8, were used for short duration loads ($10 < t_0 < 100 \mu\text{sec}$), and shock tube blast waves from flat charges, as shown in Fig. 9, were used for longer duration loads ($100 < t_0 < 1000 \mu\text{sec}$). In both arrangements the charges were made from strands of Primacord because it is inexpensive and readily available in sizes from 25 to 400 grains of PETN per foot. Strand spacing was generally 1/16 of the standoff distance to the model, small enough to give a smooth load distribution.* For very small loads, strips or extruded rods of Detasheet D explosive were used in sizes as small as 4 grains/ft.

The essential difference between the free blast and shock tube blast arrangements is in the method of detonation. In the shock tube the charge was detonated simultaneously at many points in order to initiate a one-dimensional blast up the tube. With the 7-point initiation scheme in Fig. 9, this gave a satisfactorily uniform shock wave at standoff distances larger than about 2 feet. At 1 foot, however, the detonation time was too long compared to the pulse duration and pressures at the center of the model were as high as twice the pressure near the ends. The free blast wave arrangement circumvents this difficulty by allowing line detonation of the charge, initiated at a single point

* This spacing rule is justified in Ref. 11 using the intense explosion theory developed in Section II.



(a) DETASHEET CHARGE AT $X = 0.5$ FT.

(b) PRIMACORD CHARGE AT $X = 4$ FT.

FIGURE 8 SHEET CHARGES FOR FREE-RUNNING BLAST WAVES

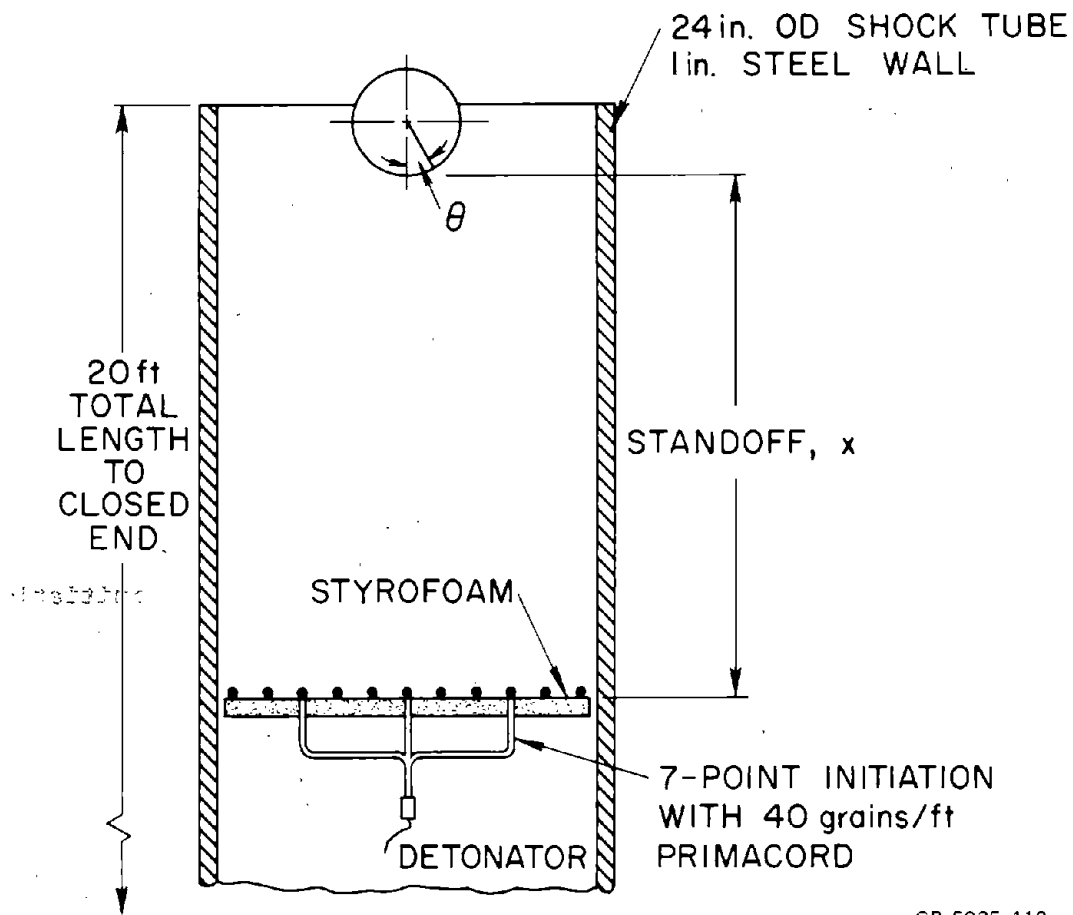


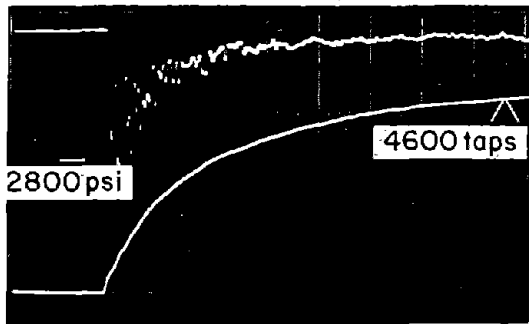
FIGURE 9 ARRANGEMENT OF FLAT CHARGES IN SHOCK TUBE

(e.g., at the apex of the lead-in triangle on the left in Fig. 8a). This produces a two-dimensional blast wave, inclined to the initial plane of the charge and to the model, but since there are no shock tube walls there is no difficulty with reverberation of this inclined wave. The model axis was oriented in line with the detonation direction to give the desired plane of symmetry in the pressure distribution. The blast sweeps along the model at the detonation velocity, fast enough to have a negligible effect on structural response. For average charge thicknesses small compared to the standoff, the shock angle at the model standoff is shallow enough that the one-dimensional theory can be used to estimate pressures. Pulse degradation because of lateral flow was made small by maintaining the lateral dimensions of the charge at least twice the standoff between charge and model.

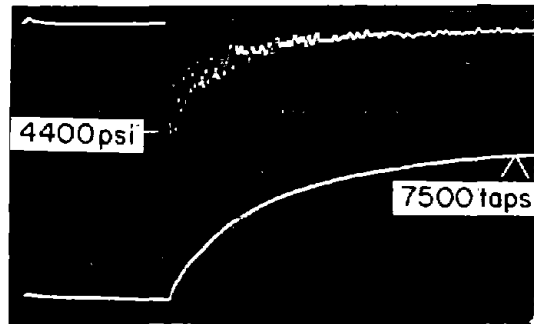
B. Pressure Measurements

Pressures were measured using Kistler Model 601H and 603H quartz gages on a rigid steel model 6 inches in diameter and 15 inches long. Gages were located at 22.5 degree intervals around the model at midspan, and at $\theta = 0^\circ$ (facing the blast) and $\theta = 90^\circ$ at 3 inches in from each end of the model. Pulse shape was very nearly uniform over the front half of the model, so only records from $\theta = 0^\circ$ are given here.

Figures 10 and 11 show that pulse shapes were generally exponential for free blast waves at a small standoff, $x = 0.5$ foot, and for shock tube blasts at standoffs from $x = 1$ foot to $x = 20$ feet, the full length of the tube. In the shock tube for $x < 20$ feet, the charges were freely suspended and the model received a second pulse, reflected from the bottom of the tube. However, even in the worst case, at $x = 10$ feet, this second pulse was small and could be neglected in structural testing. The characteristic times P/I (I is the time integral of the pressure, given by the lower traces in Figs. 10 and 11) of the pulses shown range from 20 μsec for $x = 0.5$ foot to 1000 μsec for $x = 20$ feet. At the longer durations the main body of the pulse is still a simple exponential decay, but this is preceded by a short (compared to the main pulse) pressure spike. The spike appears to be at the reflected pressure and the peak of the main body appears to be at the drag pressure.



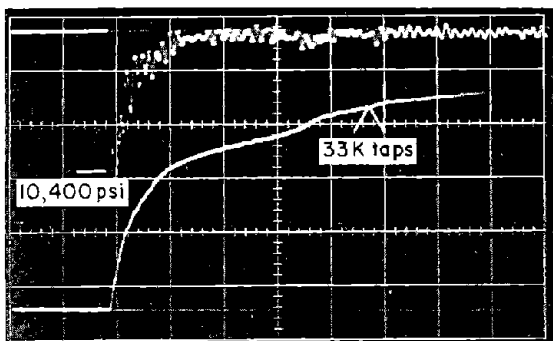
h = 4.4 mils



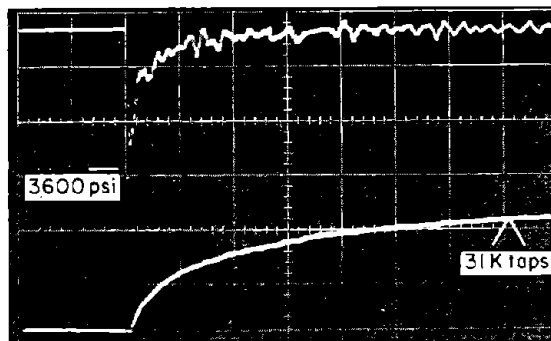
h = 8.8 mils

GP-5935-108

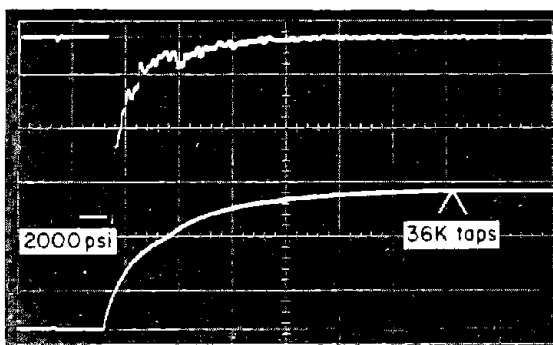
FIGURE 10 PRESSURE PULSES AT $\theta = 0^\circ$ FOR DATASHEET CHARGES AT $x = 0.5$ FOOT
(sweep rate $20 \mu\text{sec/cm}$)



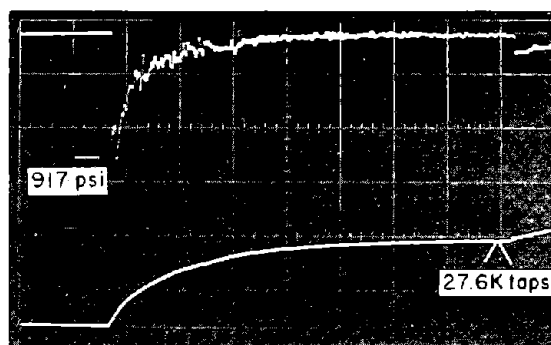
(a) $x = 1$ ft, SWEEP RATE = $50 \mu\text{sec/cm}$



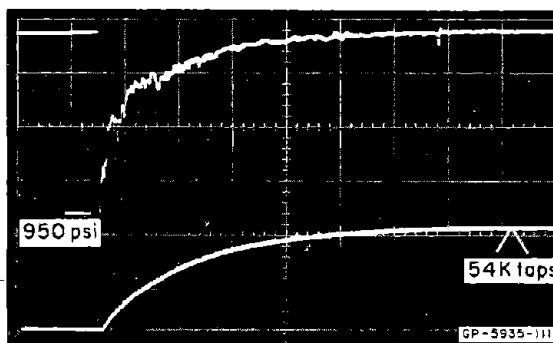
(b) $x = 2.5$ ft, SWEEP RATE = $200 \mu\text{sec/cm}$



(c) $x = 5$ ft, SWEEP RATE = $500 \mu\text{sec/cm}$



(d) $x = 10$ ft, SWEEP RATE = $500 \mu\text{sec/cm}$



(e) $x = 20$ ft, $w_{\text{eff}} = 0.52 \text{ psf} \times 2$,
SWEEP RATE = 1 msec/cm

FIGURE 11 SHOCK TUBE PRESSURE PULSES AT STANDOFFS FROM 1 FOOT TO 20 FEET
[all at charges density $w = 0.316 \text{ psf}$, except $w = 0.52 \text{ psf} \times 2$ in (e)]

The distribution of peak pressure around the front half of the model, facing the blast, was found to be given within ± 10 percent by

$$p = (p_r - p_i)\cos^2\theta + p_i, \quad -90^\circ < \theta < 90^\circ$$

where p_r and p_i are the reflected and incident overpressures. Few measurements were made on the back half of the model because the pressures were very low compared to the front face pressure and mechanical gage vibrations made accurate measurement difficult. These pressures were always less than p_i and, since $p_r \gg p_i$ for loads of interest, were considered to be of little importance for structural response.

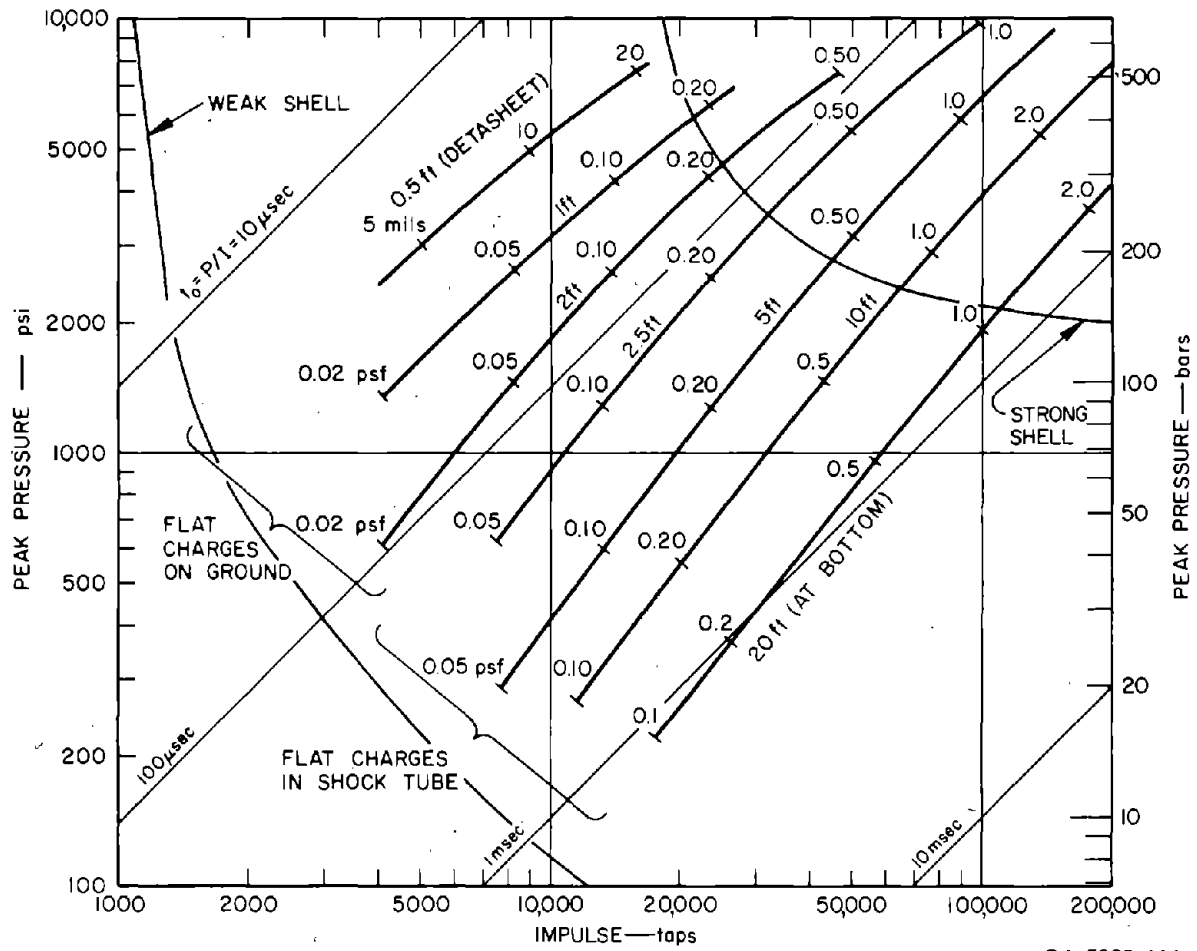
Peak pressures and impulses from these techniques are given in Fig. 12. The three uppermost curves are for charges on the ground at standoffs of 0.5, 1, and 2 feet, and the four lower curves are for charges in the shock tube at standoffs of 2.5, 5, 10, and 20 feet. The parameter varied along each curve is the density (or equivalent thickness) of the charge, in pounds per square foot (for Primacord) or in mils (for detasheet). Also shown are two hyperbolic critical load curves for damage to a typical weak shell and strong shell, to demonstrate that the loads here are in the region of interest for structural response.

C. Comparison of Theory and Experiment

To compare the pressures in Fig. 12 with the theory of plane expansion from an intense explosion, the explosive yield of Primacord is assumed to be 1570 calories/gm. This is at the lower extreme given for PETN (from 1570 to 2000 cal/gm) by Kinney¹² and is chosen because the PETN here is packed at a relatively low density. Furthermore, the Primacord plastic and braid sheath tend to reduce the effective yield by absorbing more chemical energy than they release. Assuming this yield, the energy release in ergs/cm^2 is

$$E_1 = \left[w_{\text{eff}} \text{ psf} \right] \left[\frac{454 \text{ gm}}{1 \text{ lb}} \right] \left[\frac{\text{ft}^2}{(30.5 \text{ cm})^2} \right] \left[4.19 \times 10^7 \frac{\text{ergs}}{\text{cal}} \right] \quad (39)$$

$$E_1 \left(\frac{\text{ergs}}{\text{cm}^2} \right) = 3.21 \times 10^{10} w_{\text{eff}} \text{ (psf)}$$



GA-5935-114

FIGURE 12 PRESSURE-IMPULSE CURVES FOR ASYMMETRIC LOADS
(6-inch-diameter models)

where w_{eff} is the effective charge density. For the charges on the ground and at the bottom of the shock tube, $w_{\text{eff}} = 2w$ because expansion is confined to one direction. From Eq. (26) the characteristic length is

$$s_1 = \frac{E_1}{p_1} = \frac{3.21 \times 10^{10} w_{\text{eff}} \frac{\text{ergs}}{\text{cm}^2}}{1.013 \times 10^6 \frac{\text{dynes}}{\text{cm}^2}} = 3.16 \times 10^4 w_{\text{eff}} \text{ cm}$$

or, dividing by 30.5 cm/ft,

$$s_1(\text{ft}) = 1040 w_{\text{eff}} (\text{psf}) \quad (40)$$

Using s_1 from Eq. (40), the pressures in Fig. 12 are replotted against $R = x/s_1$ in Fig. 13. Data for all three standoffs from charges on the ground fall on a single curve, demonstrating that the normalization to s_1 is appropriate. The curve is therefore simply labeled "running detonation" to emphasize that this is the most significant departure from a truly one-dimensional wave. At the low pressure end of the data (overpressure ratio about 20, or about 300 psi), the measured pressures are only a few percent smaller than the theoretical curve. Furthermore, the theoretical and experimental curves have the same slope. At higher pressures (above about 1500 psi) the measured pressures begin to fall away from the theoretical curve until at $R = 0.003$ the measured pressure is less than half the theoretical pressure. This difference is caused partly by the neglect of real gas and explosive behavior in the self-similar theory, and partly because the shock angle caused by the running detonation increases with decreasing R , thereby giving a larger difference from the normally reflected shock assumed in the theory. Pressures from shock tube loads, in which the shock is normally incident upon the model, are plotted as the solid curve in Fig. 13 and are in closer agreement with the theory.

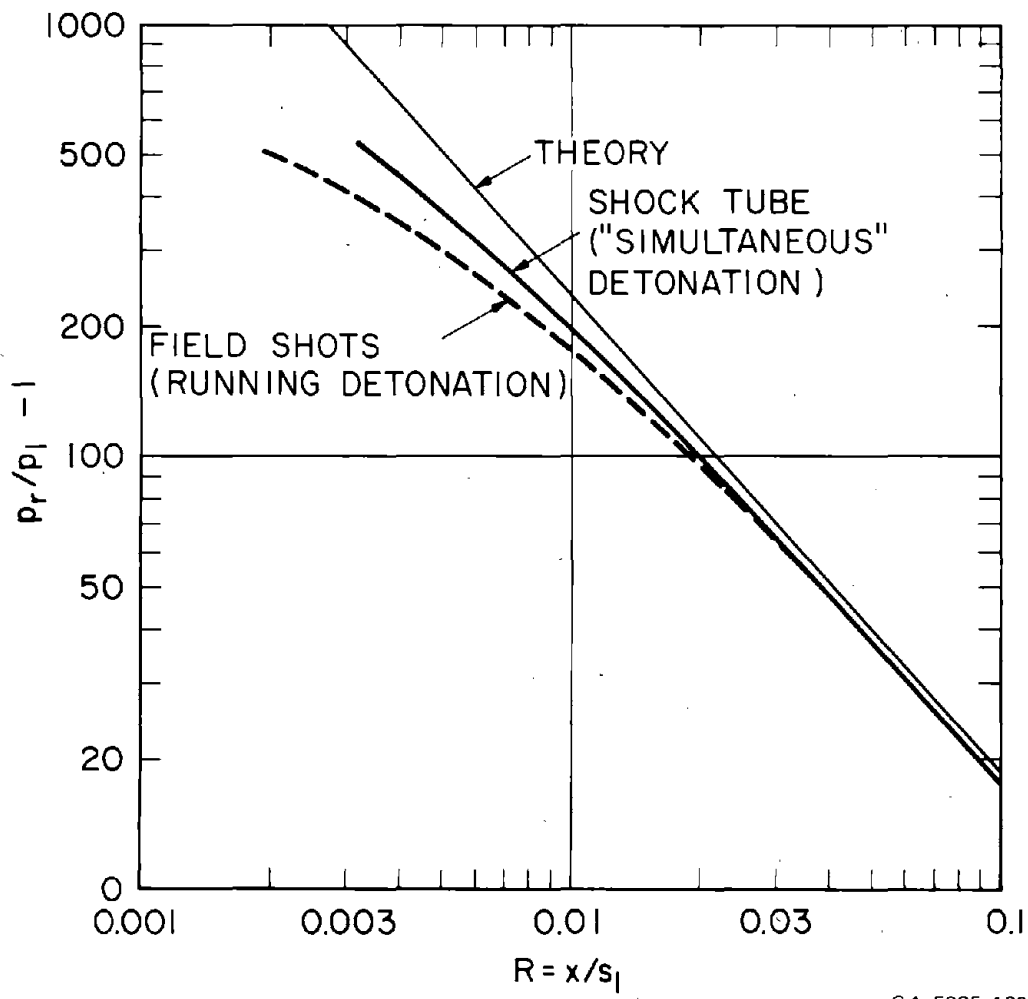


FIGURE 13 COMPARISON OF THEORETICAL AND EXPERIMENTAL PEAK PRESSURES

V CONCLUDING REMARKS

Use of the self-similar theory of intense explosions has shown that blast waves from spherical charges can be simulated to good accuracy with blast waves from sheet charges over a useful pressure range. An extension of the theory to include the effect of the ambient gas pressure ahead of the shock has given simple formulas that accurately predict peak pressures down to the lowest pressures of interest for target response testing and analysis. The theory and example pressure measurements have also shown that use of sheet charges is a convenient means to provide loads to characterize target response over the complete range of concern for the target. These data can then be used to determine response of the target to a wide range of weapon effects.

Although the theory does not give results as complete as those from numerical codes, the formulas show explicitly the relationships among charge weights and standoff distances for each geometry and give a means to quickly estimate values for various test options. After deciding how the tests will be performed, more detailed code calculations can be made to refine and extend the load characterization as needed.

REFERENCES

1. Abrahamson, G. R., and H. E. Lindberg, "Peak Load-Impulse Characterization of Critical Pulse Loads in Structural Dynamics," Dynamic Response of Structures, Proceedings, Symposium at Stanford University, Stanford, Calif. June 1971, Ed. G. Herrmann and N. Perrone, Pergamon Press Inc., New York, 1972, pp. 31-53.
2. Same article as Ref. 1, Nuclear Engineering and Design, 37, 1, pp. 35-46, 1976.
3. Brode, H. L., "Blast Wave from a Spherical Charge," Phys. Fluids, 2, 2, pp. 217-229, March-April 1959.
4. Brode, H. L., "Numerical Solutions of Spherical Blast Waves," J. Appl. Phys., 26, 6, pp. 766-775, June 1955.
5. Taylor, G. I., "The Formation of a Blast Wave from a Very Intense Explosion, I. Theoretical Discussion," Proc. Royal Soc., A, Vol. CCI (1959), pp. 159-174, and II, The Atomic Explosion of 1945," ibid. pp. 175-186.
6. Sedov, L. I., Similarity and Dimensional Methods in Mechanics, Academic Press, New York, N.Y., 1959, pp. 146-260.
7. Bethe, H. A., et al., "Blast Wave," LA-2000, Los Alamos Scientific Laboratory of the Univ. of California, written August 1947, distributed March 1958, Chapter 2, "The Point Source Solution," by John von Neumann, pp. 27-56.
8. Korobeinikov, V. P., "Approximate Formulas for Calculation of the Characteristics of a Shock Wave Front in the Case of a Point Explosion in a Gas," Dokl. Akad. Nauk SSSR, 3, 3, 1956, pp. 557-559, Translated Associated Tech. Services, Inc., Glen Ridge, N.J.
9. Landau, L. D. and E. M. Lifshitz, Fluid Mechanics, Vol. 6 of Course of Theoretical Physics, Addison-Wesley Publishing Co., Reading, Massachusetts, 1959, pp. 372-377, 392-396.
10. Goodman, H. J., "Compiled Free-Air Blast Data on Bare Spherical Pentolite," Ballistic Research Laboratories Report No. 1092, February 1960.
11. Lindberg, H. E., and R. D. Firth, "Simulation of Transient Surface Loads by Explosive Blast Waves," Stanford Research Institute Final Report, Contract AF 29(601)-7129, AFWL-TR-66-163, Vol. II, January 30, 1967.
12. Kinney, G. F., Explosive Shocks in Air, the Macmillan Co., New York, N.Y., 1962.

EFFECTS OF RIBS ON SHOCK WAVE PROPAGATION IN TUBES*

by

T. H. Schiffman[†] and H. F. Korman[‡]

ABSTRACT

Test data were derived on shock wave interaction with single ribs, two ribs, a smooth/ribbed interface entrance condition ranging from one to sixteen ribs, and an eighty-six continuous-rib array commencing at the shock tube diaphragm. Rib spacing variations were found to confirm that the MX rib spacing currently considered is expected to be nearly optimal for shock front attenuation. Furthermore, continuous ribs are essential for shock attenuation; and a shock forming in a continuous-rib zone that extends to the diaphragm decays only slightly less than the shock forming in a smooth zone and reflecting off the rib system. The data and their analysis and interpretation complement work previously reported on long continuous-rib portions following a smooth section.

* This paper reports work carried out at the Vulnerability and Hardness Laboratory, TRW Defense and Space Systems Group, Redondo Beach, California, under Air Force Contract Nos. F04704-76-C-0013 and F0474-77-C-0027, sponsored by the Department of Defense.

[†] Member of Technical Staff, TRW Defense and Space Systems Group, Redondo Beach, California.

[‡] Section Head, TRW Defense and Space Systems Group, Redondo Beach, California.

INTRODUCTION AND SUMMARY

In a previous report dealing with 250 tests on continuous protuberances, a detailed description of the shock tube, test configuration, and instrumentation was presented (Reference 1). The continuous protuberances extended to a length-to-diameter ratio (L/D) of 180 following a smooth section of L/D = 66. Results showed that protuberances are effective in attenuating shock front pressures, independent of spacing-to-diameter ratios between 1/2 and 2.

This paper complements the continuous-protuberance data with 82 tests on simplified rib configurations and continuous ribs starting at the diaphragm. Studied were (1) one rib and (2) two ribs at various spacings; (3) finite-rib data dealing with 1, 4, 8, and 16 ribs spaced one diameter apart and followed by a long smooth section; and (4) a series of 86 ribs, one diameter apart, starting two diameters from the diaphragm. This latter arrangement simulated shock formation in a trench with ribs upstream and downstream from the wave entrance. This avoids an interface between smooth and ribbed sections and, hence, the controversial shock reflection off the first few ribs that was suspected as being the major reason for the sharp initial decay when the shock first interacts with the ribbed section.

The data and their analysis from the one- and two-rib tests confirmed that the MX rib spacings under consideration are nearly optimal for shock attenuation. The finite rib data confirmed that the ribs have to be continuous to achieve a permanent decay; otherwise, the pressure in a long smooth section following a finite number of ribs approaches the smooth-walled value. Finally, a shock forming in a continuous-rib zone decays only slightly less than the shock forming in a smooth zone and reflecting off the first few ribs of a continuous-rib zone. Also, the pressure waveforms following well-formed shock fronts for $L/D \geq 17$ are similar to those formed in a ribbed zone after a smooth transition, i.e., they show the familiar pressure rise to a maximum pressure composed of a succession of steps created by the shock reflecting off the upstream and downstream protuberances.

SHOCK TUBE FACILITY AND TEST MATRIX

We present a brief description of the shock tube configuration in Figure 1, and its associated instrumentation in Figure 2 (taken from Reference 1). The test matrix for the portion of the shock tube program described in this memorandum is given in Tables 1 and 2.

The design of the shock tube facility was based on established techniques. A shock tube and a driver chamber are axially connected but are separated by two burst diaphragms (Figure 1). Systems are provided for controlling the gas and initial pressure in both the driver chamber and the driven chamber, and for recording the changing pressure at various stations along the shock tube when the burst diaphragms are broken. Distances along the tube axis are expressed in length-to-diameter ratios (L/D), starting with the diaphragm closest to the driven chamber. The pressure transducers are mounted in openings in the driven chamber at eight stations along its length.

The inside diameter of the driver chamber is 5 in. Although the driver length is 2.5 ft, provision has been made for reducing the length to 1.0 or 0.5 ft. (Some tests at lower pressures [Reference 1] were also conducted with another driver that was 8 ft long.)

The driven chamber of the shock tube has a nominal inside diameter of 3 in. and is made of multiple sections of pipe bolted together in various test configurations with lengths to about 60 ft ($L/D = 244$). In some of the tests of Reference 1, the shock tube was closed with a blind flange. For open-ended configurations used in the current test program, forty feet of smooth section preceded one or two protuberances of height $H = 0.173$ in. (area reduction 20%). These protuberances — or "chokes" as the one- and two-rib configurations are called — were spaced in fractions ($1/8$ to $1/2$) or simple multiples (1.0 to 10.0) of the nominal 3.068-in. diameter of the 3-in. schedule-40 pipe used for the spacers between the protuberances.

Configurations were also tested with 17 ft of smooth section followed by a ribbed section of up to 4 ft with rib spacing-to-diameter ratio (S/D) of one, to be followed again by a smooth section of 28 ft. Also tested was a ribbed section of 23 ft with S/D equal to one starting 0.5 ft from the

diaphragm, which was followed by a smooth section 26 ft long. High shock strengths P_2/P_1 were produced by evacuating the driven section and using helium (He) as the driver gas.

Figure 2 shows typical instrumentation and circuit connections used for recording pressure histories at various stations in the shock tube and for timing the difference in the shock front arrival times between various pairs of stations.

A summary test matrix is presented in Table 1, and a chronological test matrix comprising 82 shots is given in Table 2. The tests were conducted in the following order: (1) tests with a single 50% choke at $L/D = 155$ and its control with no choke; (2) tests with a new all-steel tube, a single 80% choke at $L/D = 156$ and two isolated chokes with midpoint at $L/D = 159$ and spacing ratios of 1, 3, 6, and 10, and no-choke control tests (for test layout see Figure 9); (3) finite rib entrance tests with 1, 4, 8, and 16 ribs spaced one diameter apart; (4) a single choke at $L/D = 154$, and double chokes, where the first choke is at $L/D = 154$ and the second choke is downstream at a spacing-to-diameter ratio of 1/8, 1/4, 1/2, 1, 1.5, 2, 3, and 10 (see Figure 9); and finally (5) protuberances spaced one diameter apart and ranging from $L/D = 2$ to 88, i.e., starting almost at the shock tube diaphragm.

ONE-RIB TESTS

Figure 3 presents a single-choke pressure attenuation as a function of orifice ratio, taken from pertinent literature (Reference 2). This figure presents both theoretical (for a flat-top wave) and experimental (for a particular peaked wave shape) features. It indicates that pressure attenuation is independent of shock strength (or overpressure, where the shock goes into a standard atmosphere), shape and size of pipe, shape of choke, and length-to-height ratio of choke. As seen from this figure, one would expect for MX only a 2% decay, and for the TRW shock tube tests a 3% decay. The continuous reapplication of protuberances after the shock has reformed could, however, lead to considerable attenuation (e.g., $0.98^{80} = 0.20$). Actually, one of the most important results to emerge from Reference 1 is that a length of pipe filled with protuberances would lead

to the same attenuation, regardless of spacing-to-diameter ratios between 1/2 and 2. The key parameters of protuberance height-to-diameter ratio and pipe length-to-diameter ratio are incorporated in a semiempirical prediction technique for shock front pressure attenuation analysis (Reference 1).

The purpose of the TRW single-choke tests was to verify specific area ratios with various shock strengths and peakedness factors beyond the experimental data range. Accordingly, single chokes were tested with shock strengths of 16 and 30 and a flow area ratio of 80%, and with shock strengths from 2 through 38 and a flow area ratio of 50%. Protuberance height-to-length ratio was 1:1 and 1:2, and peakedness factors of initial slope intercept of 0.003 to nearly flat-top waves were tested. These data, together with two-rib tests and finite rib entrance conditions, are useful in validating quasi-one-dimensional code calculations.

Figure 4 has superimposed on the data of Figure 3 the TRW test results, which are in excellent agreement at the 80% flow area and in fair agreement at the 50% flow area.

Figure 5 represents the pressure reflection from a single choke as computed in Reference 2; and Figure 6 represents the TRW results indicating that the theoretical calculations overestimate the strength of the reflected shock for all shock strengths at which the 50% choke was tested, and for the single shock strength in the 80% flow area.

Figure 7 illustrates the reflected shock waveform at station 147 from a single downstream choke for an 80% flow area, one for a 50% flow area, and one for a 0% flow area representing a blind flange test taken from Reference 1. As expected, and as shown in Figure 6, the largest reflection occurs for the 0% flow area and the smallest for the 80% flow area. It is this reflection that has been conjectured to be partially responsible for the decay in a continuous choke system. Hence, tests were also performed with the chokes near the diaphragm.

Figure 8 illustrates the transmitted shock across a 50% choke by comparing both choke and no-choke shock strength as a function of distance along the tube. The choke is evidently changing the slope of the attenuation-distance curves, and the indicated percentage of drop has been adjusted by normalizing at station 147 and comparing at station 167 with the choke being at station 155.

TWO-RIB TESTS

Figure 9 shows the two-rib layout, with a single choke indicated also, since it presents the limiting case for the spacing-to-diameter ratio $S/D = 0$ between ribs. This single choke case was further investigated by doubling the width of the choke and comparing it with the original rib. As previously reported in the literature, this has no effect on waveform, attenuation, or reflection. The most important aspect of the two-rib layout is that midway between the chokes the pressure shape can be studied for magnitude and potential pressure reverberations between chokes; these, incidentally, were not observed. As shown by shadowgraphs, previously observed and reproduced in Reference 1, the single-choke interaction is very complex and, hence, the double-choke interaction can be evaluated only with pressure sensors, as it would be nearly impossible to trace the various shock fronts and interfaces.

Figure 10 indicates the transmitted shock across a single and double choke with 80% flow area as a function of the spacing ratio for $S/D = 0, 1/8, 1/4, 1/2, 1, 1.5, 2, 3, 6,$ and 10 . The data show the largest attenuation near $S/D = 1$, i.e., the MX rib spacings under consideration are expected to be nearly optimal for shock attenuation. Equilibrium is obtained at or near $S/D = 3$, i.e., the pressure drop across two chokes does not change for $3 \leq S/D \leq 10$, but is more than twice the attenuation in this interval than it is for a single choke. Evidently, the largest drop occurs between $S/D = 1/2$ and $S/D = 1$, the values tested with continuous chokes (as well as $S/D = 2$) in Reference 1.

We see in Figure 11 the pressure waveforms at station 159, midway between two chokes with separation ratios of $S/D = 1, 3, 6,$ and 10 . As expected, the largest increase is for the closest spacing, and the smallest increase is for the largest spacing. No systematic, multiple-reflection pattern is discernible. The small oscillation shown for $S/D = 1$ is due to the vibration of the gauge mount at $L/D = 159$, which is in contact with the two chokes on each side. Figure 12 presents the peak pressure and the time-to-peak pressure after shock front arrival as a function of the separation distance for the data of Figure 11. The linear time variation is expected because the transmittal velocity behind the first choke and the

reflection velocity off the second choke are nearly constant. This reflection velocity for an incident pressure of 200 psi and an 80% choke is approximately 460 ft/s (compared with a transmittal velocity of 4000 ft/s).

FINITE-RIB ENTRANCE CONDITION

Figure 13 represents the shock front pressure attenuation for different numbers of ribs - 1, 4, 8, and 16 - starting at $L/D = 66$ and spaced $S/D = 1$ apart. Thus we have a smooth section, then a short-ribbed section, followed again by a long smooth section. From this figure, we can draw a main conclusion: the zero rib (smooth) case and the relatively few ribs (up to 16) are vastly different from the continuous-rib case. In fact, the continuous ribs are necessary to obtain the full shock attenuation with distance down the trench, otherwise the attenuation approaches asymptotically the smooth tube values. As far as the few ribs are concerned, there is initially greater attenuation with the larger ribbed section, as predicted by the semiempirical analysis technique. This is illustrated in Figure 14, which presents attenuation as a number of ribs at station 109, the first station where the effect of 1, 4, 8, and 16 ribs has been recorded. The drop in attenuation to 83% of its initial value occurs nonlinearly and indicates that had we used more ribs and taken the measurement also further downstream, we would have reached a similar asymptote. The effect of this rib system on reflection is indicated in Figure 15, which shows that the reflected shock at station 40 from various numbers of ribs is similar for 4, 8, 16, and 92 ribs. Only the reflection from a single rib is considerably smaller. Evidently the reflection takes place solely from the first few ribs; and to avoid such a reflection, the ribs must be started near the diaphragm, simulating a shock entering the MX nonhybrid trench where there is no smooth transition section.

RIBS-NEAR-DIAPHRAGM ENTRANCE CONDITION

Figure 16 presents the shock front decay in ribbed tubes $S/D = 1$, where the ribs start near the diaphragm $2 \leq L/D \leq 88$, and it compares the decay of ribs that follow a smooth transition section $66 \leq L/D \leq 159$ for $S/D = 1/2$, 1, and 2.

The solid curves for the smooth and ribbed sections where the ribs start at $L/D = 66$ present the results of a semiempirical prediction technique (Reference 1). This technique expands and extends the work of Reference 3, which was applicable to smooth and rough, but not ribbed, tubes.

We note that the shock forming in a continuous-rib zone decays only slightly less than the shock forming in a smooth zone and reflecting off the first few ribs of a subsequent continuous-rib zone. This is partially due to the failure of the rarefaction wave to catch up, and to the presence of initial dumping effects, giving a smooth tube constant pressure of shock strength 30 up to $L/D = 50$. This must, clearly, raise the ribbed tube pressure in this region compared with a region where the smooth tube pressure is dropping, as shown in Figure 16 for $L/D > 50$. However, as seen in Figure 17, the pressure waveforms following well-formed shock fronts for $L/D \geq 17$, although similar to the standard test configuration from Reference 1, in which protuberances start at $L/D = 66$, exhibit a steeper rise behind the shock front formation.

The data from Figure 16 suggest that the reflection off the first few ribs from an interface between smooth and ribbed tubes is not the only reason for the sharp initial pressure decay with distance that occurs when a shock first interacts with the ribs after travelling through a smooth transition section.

A measurement at 25 diameters beyond the last rib (station 113, Figure 17) indicates that the pressure has nearly the same value as that at the last observation station in the ribs ($L/D = 75$), confirming again the trend toward smooth-walled decay after the ribs stop. This behavior is significant for a hybrid nonventing trench.

CONCLUSIONS

The shock tube testing reported in this paper discussed the effects of variations in rib spacing, and the influence of a smooth section preceding the continuous-ribbed section. The results confirmed that the MX rib spacing currently studied is considered nearly optimal for shock front attenuation. In addition, it was demonstrated that continuous ribs are essential for shock attenuation and that a shock forming in a continuous-rib zone decays only slightly less than the shock forming in a smooth zone and reflecting off the rib system. From the latter, only the first few ribs contribute to the magnitude of the reflected shock. This reflection evidently is not the major reason for the sharp initial pressure decay, which is also predicted by the semiempirical analysis technique.

ACKNOWLEDGMENT

The authors are indebted to Messrs. Marvin W. Sweeney and Pat O'Neill. Mr. Sweeney suggested many portions of this study and gave freely of his expert advice. Mr. O'Neill supervised the shock tube tests and cleared up several pertinent points.

REFERENCES

1. Schiffman, T. H., Trench Blast Shock Tube Studies: High Pressure Shock Tube Testing of Multiple Protuberances, TRW Report 4731.5.78-036. TRW Defense and Space Systems Group, Redondo Beach, Calif., June 1978.
2. Ross, J. M., C. M. Nixon, and W. M. McMurty, "A Shock Tube Study of Attenuation of Air Flow Through Chokes," TN 152. Suffield Experimental Station, Ralston, Alberta, 1966.
3. Clark, R. O., A Study of Shock Wave Attenuation in Tunnels, BRL Report 1401. Ballistic Research Laboratories, Aberdeen Proving Ground, Md., 1962.

Table 1. Summary of Tests

I	<u>One- and Two-Rib Tests with Ribs of 80% Flow Area</u>
(a)	Ribs at $L/D = 159 \pm 0.5 S/D$; $S/D = 1, 3, 6, 10$
(b)	Ribs at $L/D = 154 + S/D$; $S/D = 0, 0.125, 0.25, 0.5, 1, 1.5, 2, 3, 10$
II	<u>One-Rib Test with Rib of 50% Flow Area at $L/D = 155$</u>
(a)	He 450 psia/air 14.7 psia, and $L_d = 2.5$ ft, 1 ft, 0.5 ft
(b)	He 4600 psia/air 14.7 psia, and $L_d = 1$ ft, 0.5 ft
(c)	He 4600 psia/air 5 psia, and $L_d = 0.5$ ft
(d)	He 4600 psia/air 2 psia, and $L_d = 0.5$ ft
III	<u>Entrance Conditions</u>
(a)	Finite rib test; ribs at $L/D = 66, 66-69, 66-73, 66-81$
(b)	Ribs starting near diaphragm; ribs at $L/D = 2-88$ (Also tested with He 600 psia/air 14.7 psia)
<u>NOTES</u>	
1.	All tests run with smooth tube as a control.
2.	Unless indicated otherwise, the following applies: Driver gas and pressure, $P_4 = 4600$ psia helium Driven gas and pressure, $P_1 = 14.7$ psia air Driver length, $L_d = 1$ ft Shock pressure, $P_2 = 450$ psia Shock strength, $P_2/P_1 = 30.6$ Spacing-to-diameter ratio, $S/D = 1$ Length-to-diameter ratio, $L/D = \text{variable}$

Table 2. Chronological Test Matrix

SHOT NUMBER	DRIVER			DRIVEN				NOTES
	GAS	LENGTH (ft)	P ₄ (psia)	GAS	P ₁ (psia)	S/D	END	
229, 230	He	1.0	450	Air	14.7	N/A	Open at L/D = 178	50% choke at L/D = 155
231	↓	1.0	4600	↓	↓	↓	↓	50% choke at L/D = 155
232	↓	1.0	450	↓	↓	↓	↓	No choke
233	↓	2.5	450	↓	↓	↓	↓	No choke
234, 235	↓	2.5	450	↓	↓	↓	↓	50% choke
236	↓	1.0	4600	↓	↓	↓	↓	No choke
237, 238	↓	0.5	4600	↓	↓	↓	↓	No choke
239	↓	↓	450	↓	14.7	↓	↓	No choke
240	↓	↓	4600	↓	5.0	↓	↓	No choke
241	↓	↓	4600	↓	2.0	↓	↓	50% choke
242	↓	↓	4600	↓	14.7	↓	↓	50% choke
243	↓	↓	450	↓	14.7	↓	↓	50% choke
244	He	0.5	4600	Air	2.0	N/A	Open at L/D = 178	No choke
245, 245A, 245B	He	1.0	4600	Air	14.7	N/A	Open at L/D = 174	All-steel tube with new 7 ft section.
246, 246A, 246B	↓	↓	↓	↓	↓	N/A	Open at a L/D = 190	No choke
247, 247A	↓	↓	↓	↓	↓	1.0	↓	80% chokes -- 2 L/D = 159 ± ¼
248, 248A	↓	↓	↓	↓	↓	N/A	↓	Choke at L/D = 156
249	↓	↓	↓	↓	↓	6.0	↓	80% chokes -- 2 at L/D = 159 ± 3
250	↓	↓	↓	↓	↓	3.0	↓	80% chokes -- 2 at L/D = 159 ± 1.5
251, 252	↓	↓	↓	↓	14.7	10.0	↓	80% chokes -- 2 at L/D = 159 ± 5
253, 253A	He	1.0	4600	Air	14.7	N/A	Open at a L/D = 190	No choke

Table 2. Chronological Test Matrix (Continued)

SHOT NUMBER	DRIVER			DRIVEN			NOTES	
	GAS	LENGTH (ft)	P ₄ (psia)	GAS	P ₁ (psia)	S/D		END
254, 254A	He	1.0	4600	Air	1.47	N/A	Open at L/D = 190	No ribs
255, 255A, 255B, 255C	↓	↓	↓	↓	↓	1.0	↓	Ribs - 4 L/D = 66 to 69 (80%)
256, 256A, 256B	↓	↓	↓	↓	↓	1.0	↓	Ribs - 16 L/D = 66 to 81'
257, 257A, 257B	↓	↓	↓	↓	↓	1.0	↓	Ribs - 8 L/D = 66 to 73
258, 258A	He	1.0	4600	Air	1.47	N/A	Open at L/D = 190	Rib, L/D = 66
258', 258A'	He	1.0	4600	Air	1.47	N/A	Open at L/D = 190	Begin 1, 2 - 80% choke tests. No choke
259, 259A	↓	↓	↓	↓	↓	10.0	↓	Chokes - 2 at L/D = 154, 164
260, 260A	↓	↓	↓	↓	↓	0	↓	Chokes - 2 at L/D = 154
261, 261A	↓	↓	↓	↓	↓	N/A	↓	Choke at L/D = 154
262, 262A	↓	↓	↓	↓	↓	1/8	↓	Chokes - 2 at L/D = 154, 154.125
263, 263A	↓	↓	↓	↓	↓	1/4	↓	Chokes - 2 at L/D = 154, 154.25
264, 264A	↓	↓	↓	↓	↓	1/2	↓	Chokes - 2 at L/D = 154, 154.5
265, 265A, 265B, 265C	↓	↓	↓	↓	↓	1.0	↓	Chokes - 2 L/D = 154, 155
266, 266A	↓	↓	↓	↓	↓	1.5	↓	Chokes - 2 L/D = 154, 155.5
267, 267A	↓	↓	↓	↓	↓	2.0	↓	Chokes - 2 L/D = 154, 156
268, 268A, 268B	↓	↓	↓	↓	↓	3.0	↓	Chokes - 2 L/D = 154, 157
269, 269A, 269B, 269C, 269D	He	1.0	4600	Air	14.7	N/A	Open at L/D = 190	No chokes
270	He	1.0	600	Air	14.7	1.0	Open at L/D = 190	Begin ribs-to-diaphragm tests: Ribs at 2 ≤ L/D ≤ 88
271, 272, 273, 274, 275	He	1.0	4600	Air	14.7	1.0	Open at L/D = 190	

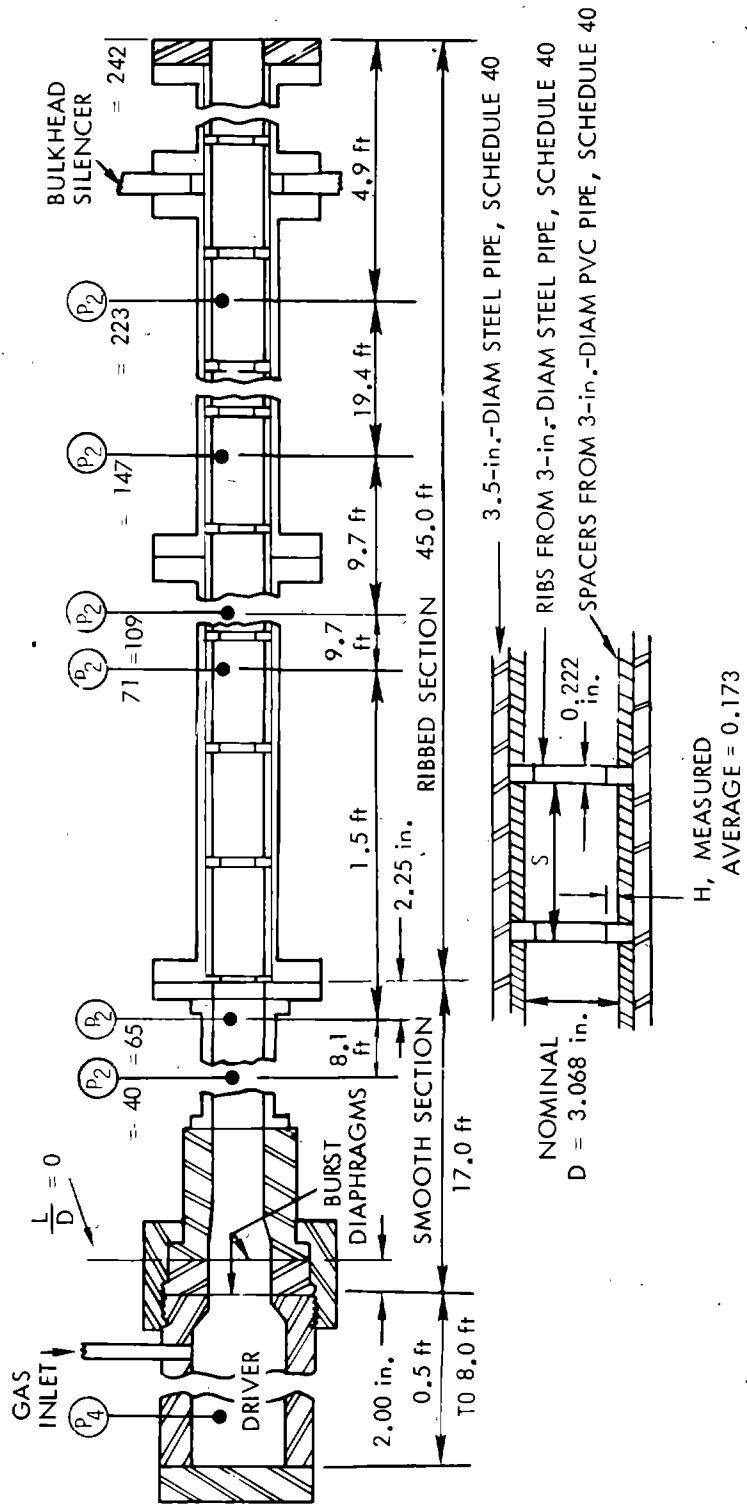
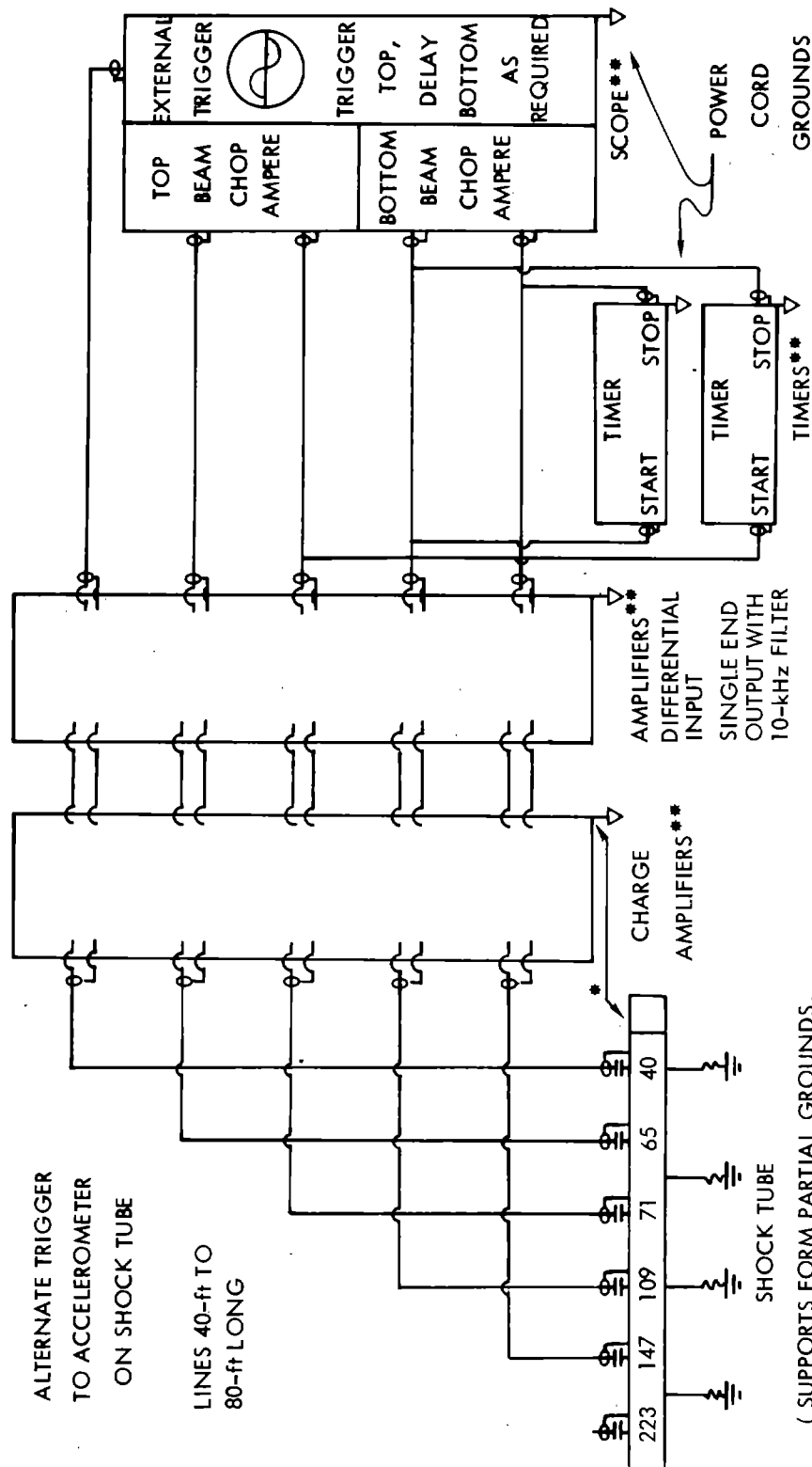


Figure 1. Shock Tube Configuration



(SUPPORTS FORM PARTIAL GROUNDS,
 PRESSURE STATION NUMBERS L/D
 FROM BURST DIAPHRAGM)

** TIE POINTS OF BONDING WIRE BETWEEN SHOCK TUBE AND EQUIPMENT
 SHIELDS SELECTED FOR MINIMUM NOISE

** TWO SCOPES AND ADDITIONAL COUNTERS AND AMPLIFIERS USED WHEN
 UP TO 8 CHANNELS RECORDED

Figure 2. Diagram of Equipment Connection

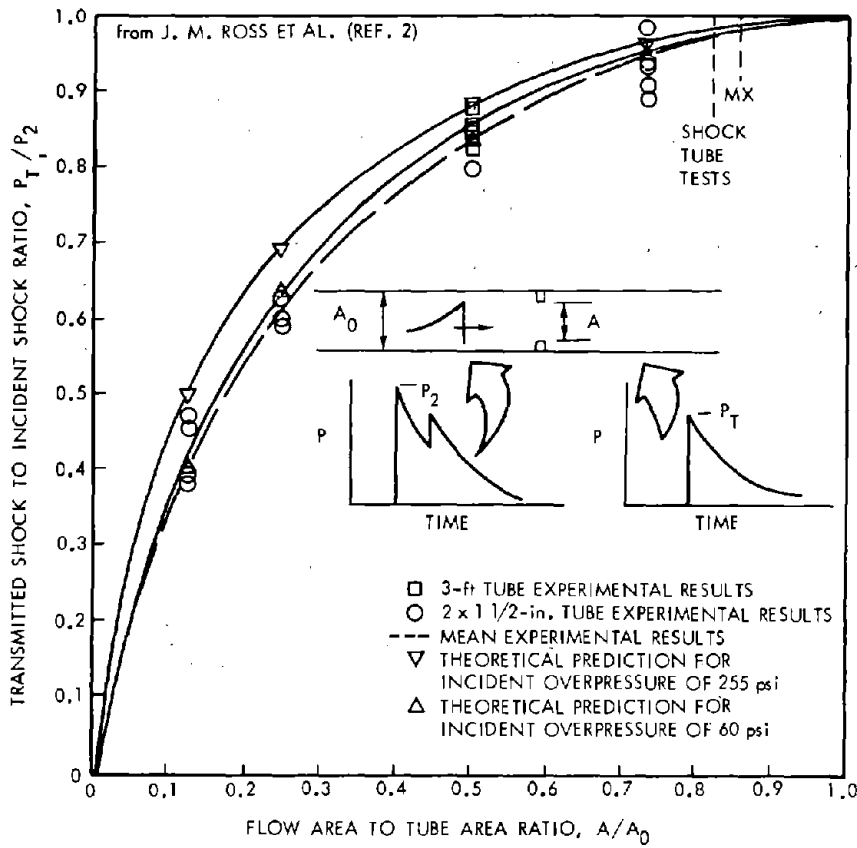


Figure 3. Single-Choke Pressure Attenuation

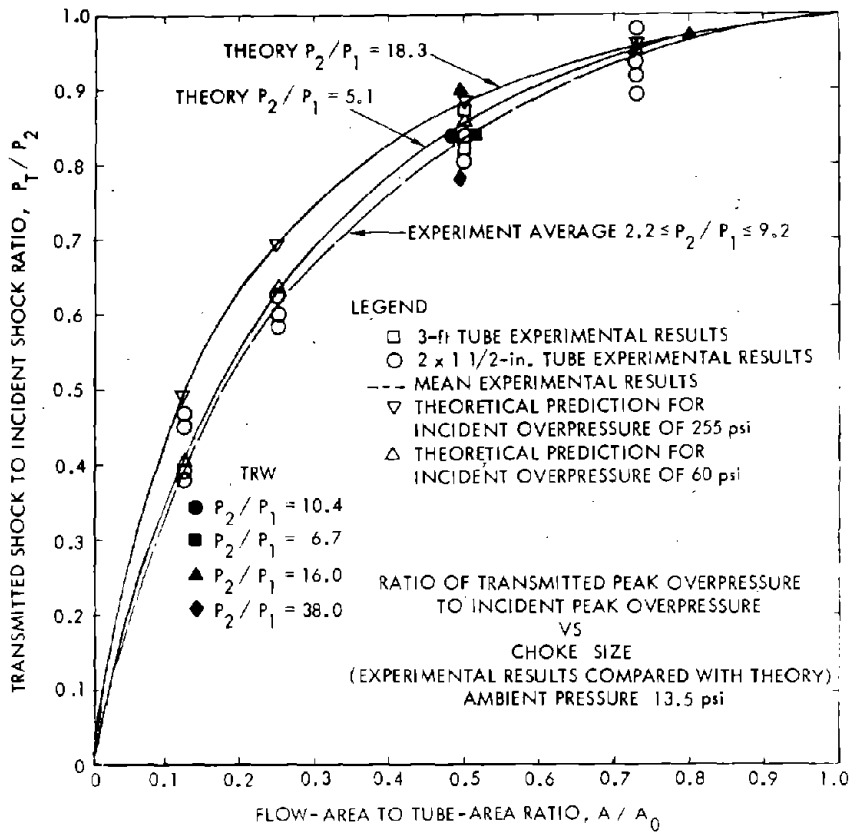


Figure 4. Comparison of TRW Data with Single-Choke Pressure

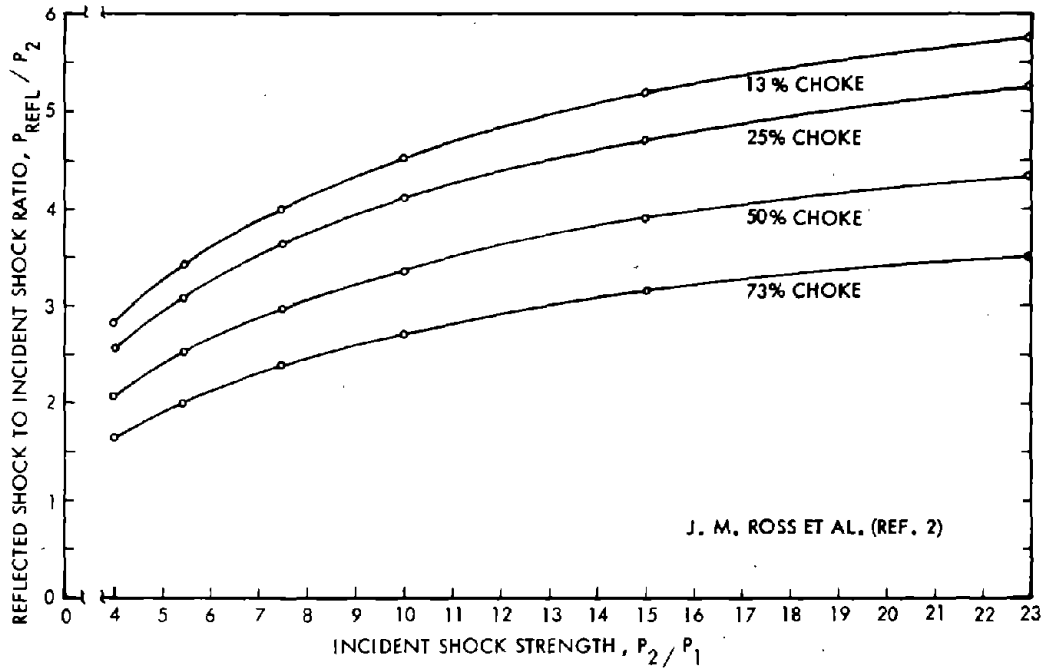


Figure 5. Pressure Reflection from Single Choke

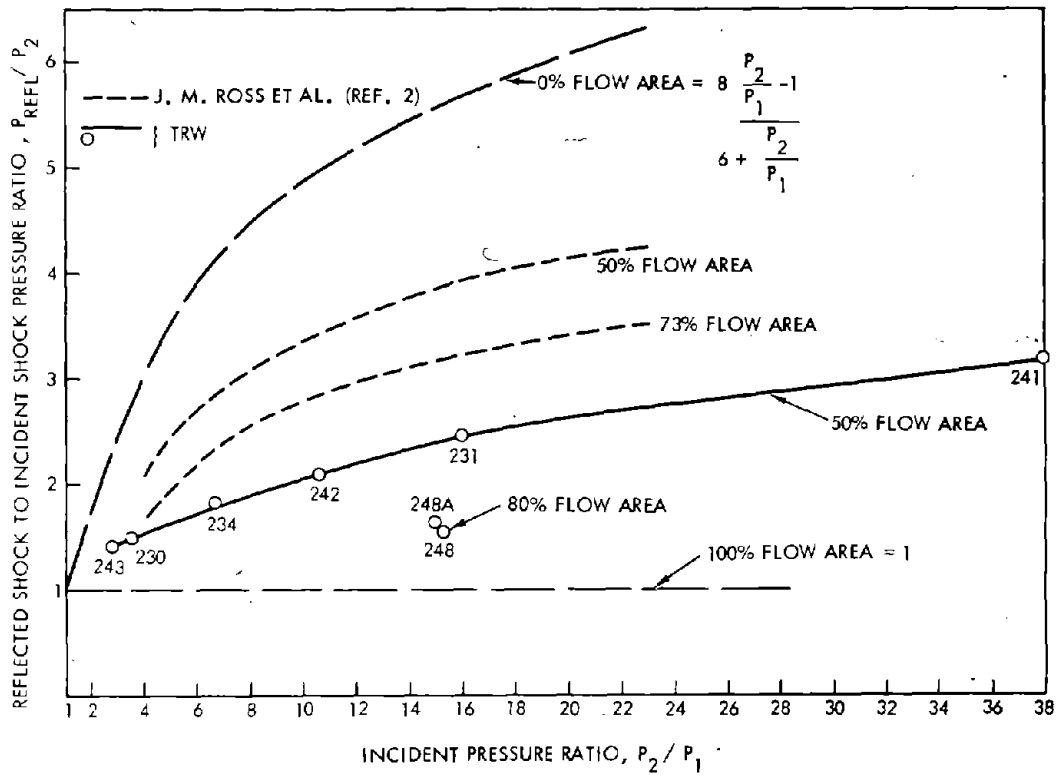


Figure 6. Comparison of TRW Data with Single-Choke Pressure Reflection

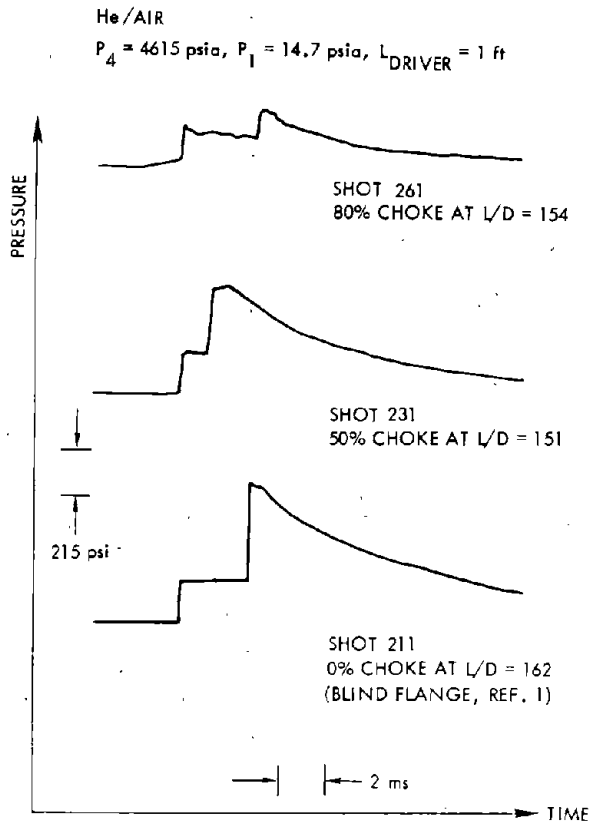


Figure 7. Reflected Shocks from Single Downstream Choke at Various Flow Area Ratios: Station 147

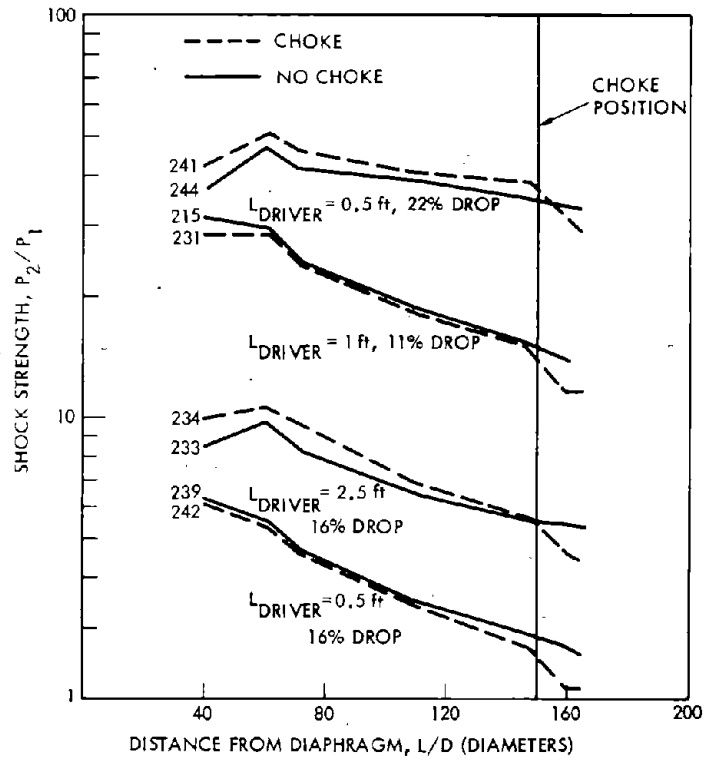


Figure 8. Transmitted Shock across 50% Choke

TWO 80% CHOKES $\left\{ \begin{array}{l} L/D = 159 \pm 0.5 S/D \\ S/D = 0 \\ = 1 \\ = 3 \\ = 6 \\ = 10 \end{array} \right.$ AND $\left\{ \begin{array}{l} L/D = 154 + S/D \\ S/D = 0 \text{ (SINGLE CHOKE)} \\ S/D = 1/8, 1/4, 1/2, 1, \\ 1.5, 2, 3, 10 \end{array} \right.$

SINGLE CHOKE, $L/D = 156$ FOR 50% CHOKE
 $= 156$ AND 66 FOR 80% CHOKE

PRESSURE STATIONS : $L/D = 40, 65, 71, 103, 147, 151, 159, 167, 171, \text{ AND } 175$

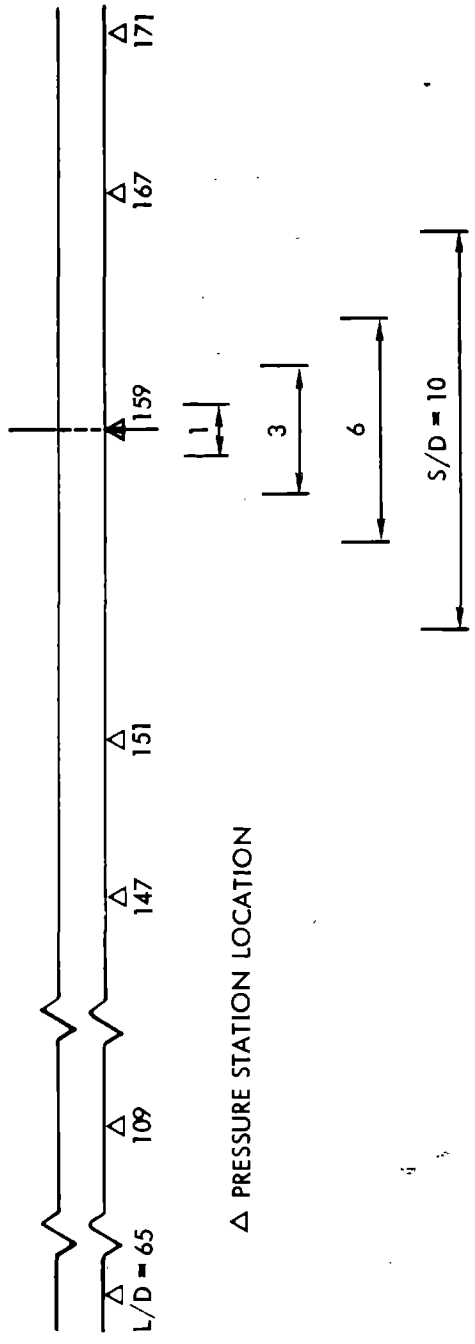


Figure 9. Two-Rib Layout

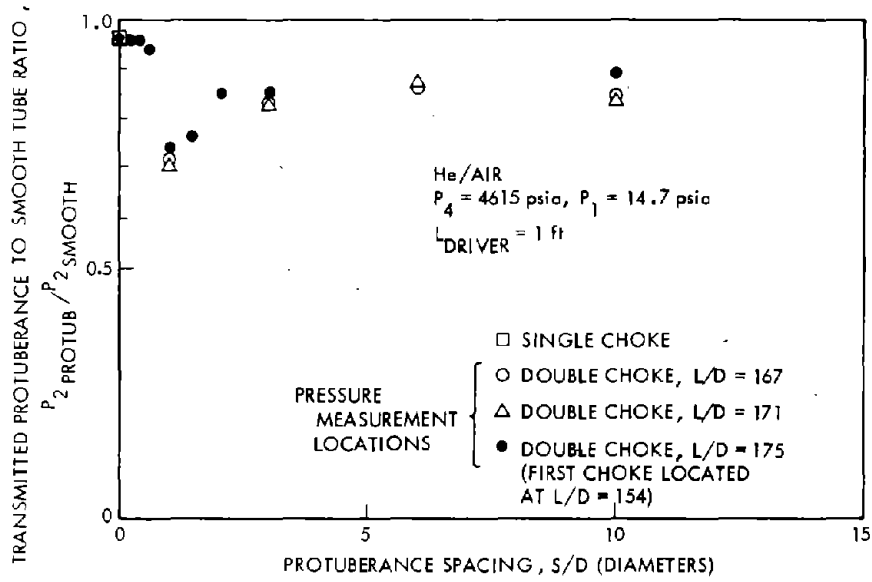


Figure 10. Transmitted Shock across Single and Double Choke with 80% Flow Area

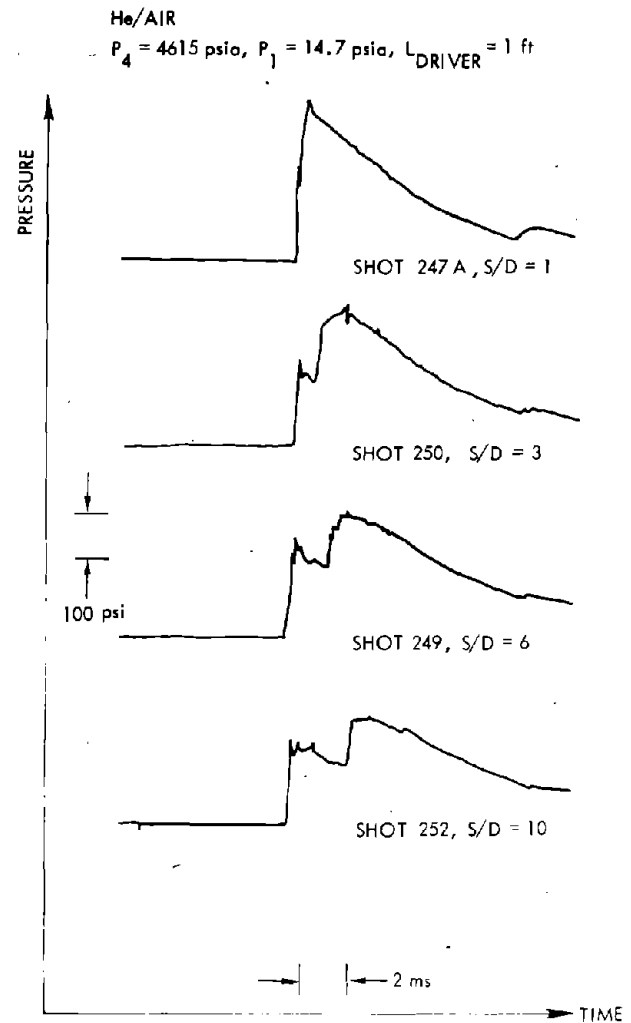


Figure 11. Pressure Waveforms at Midpoint between Two Isolated Chokes: Station 159

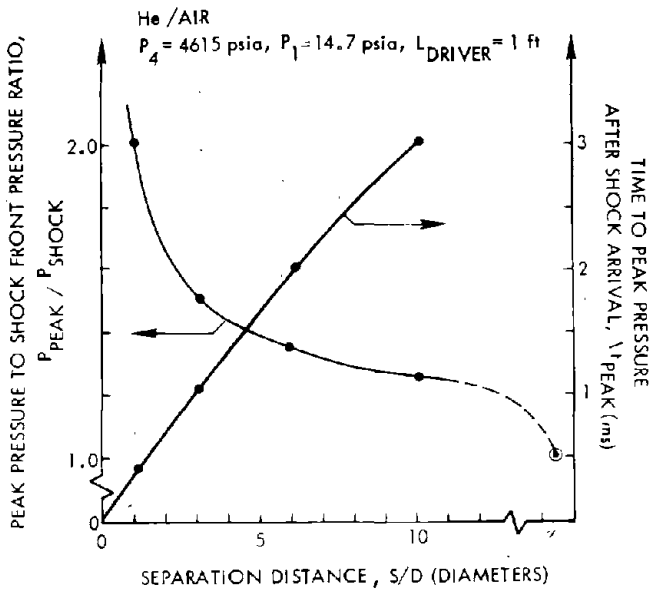


Figure 12. Peak Pressure and Time-to-Peak Pressure at Midpoint between Two Isolated Chokes: Station 159

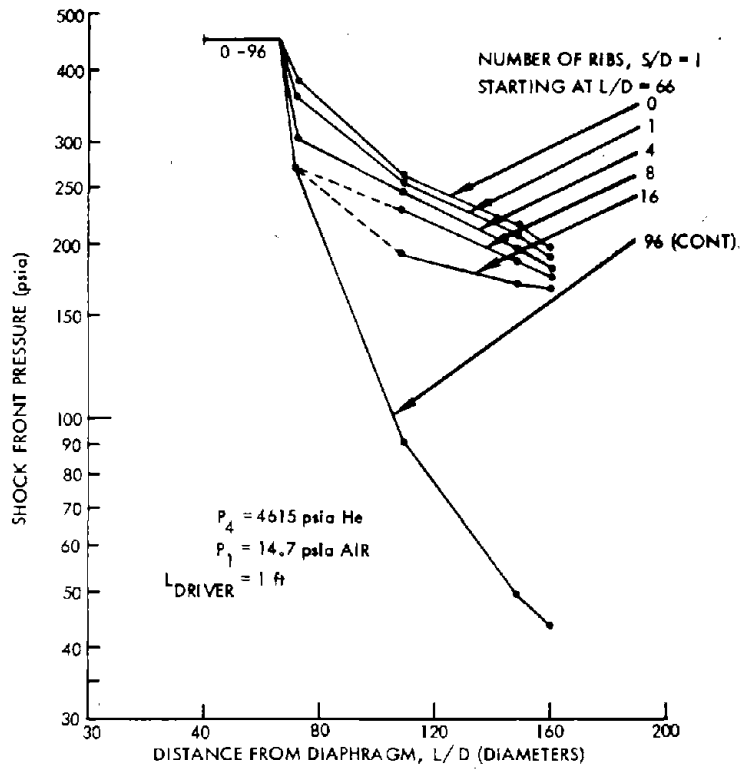


Figure 13. Shock Front Pressure Attenuation for Different Number of Rib Entrance Conditions

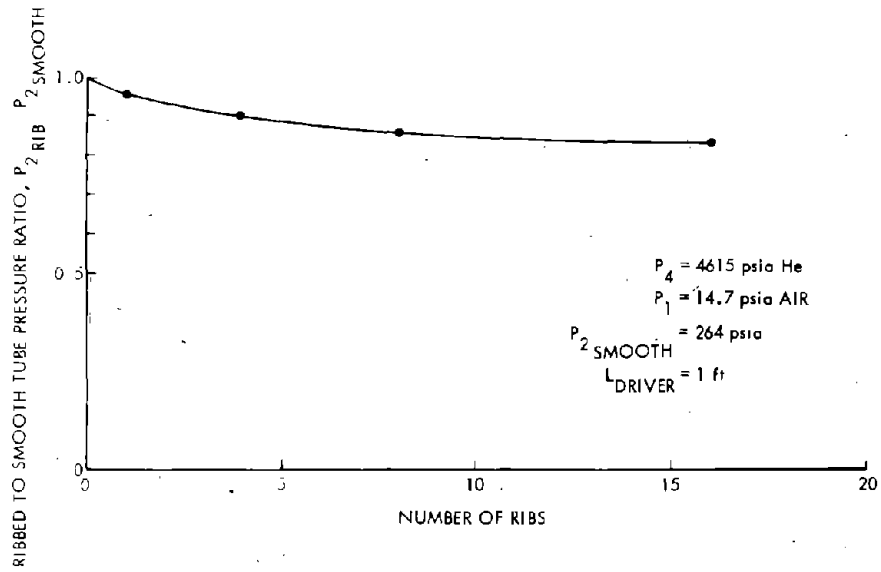


Figure 14. Pressure Drop at $L/D = 109$ vs Number of Ribs Spaced One Diameter Apart, Starting at $L/D = 66$

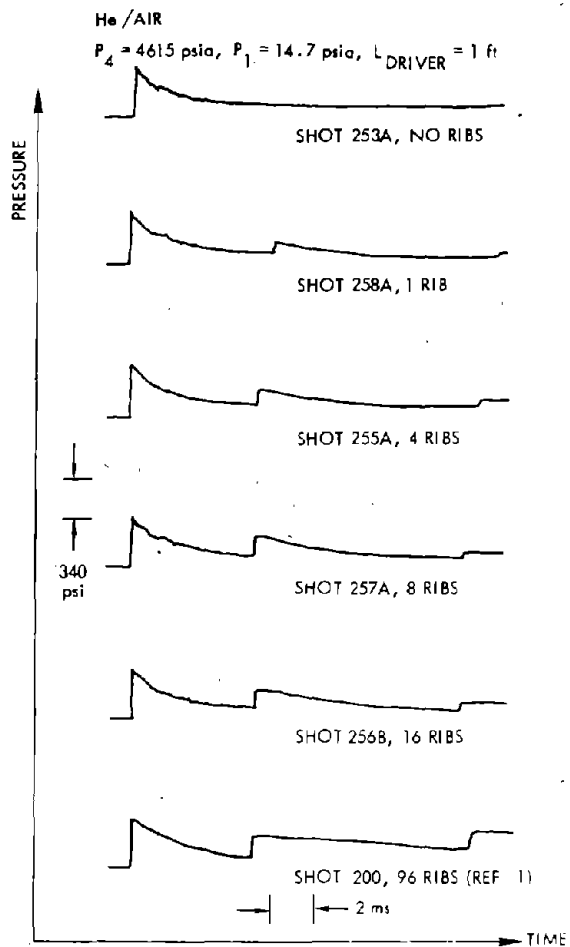


Figure 15. Reflected Shocks at Station 40 from Rib System Starting at Station 66

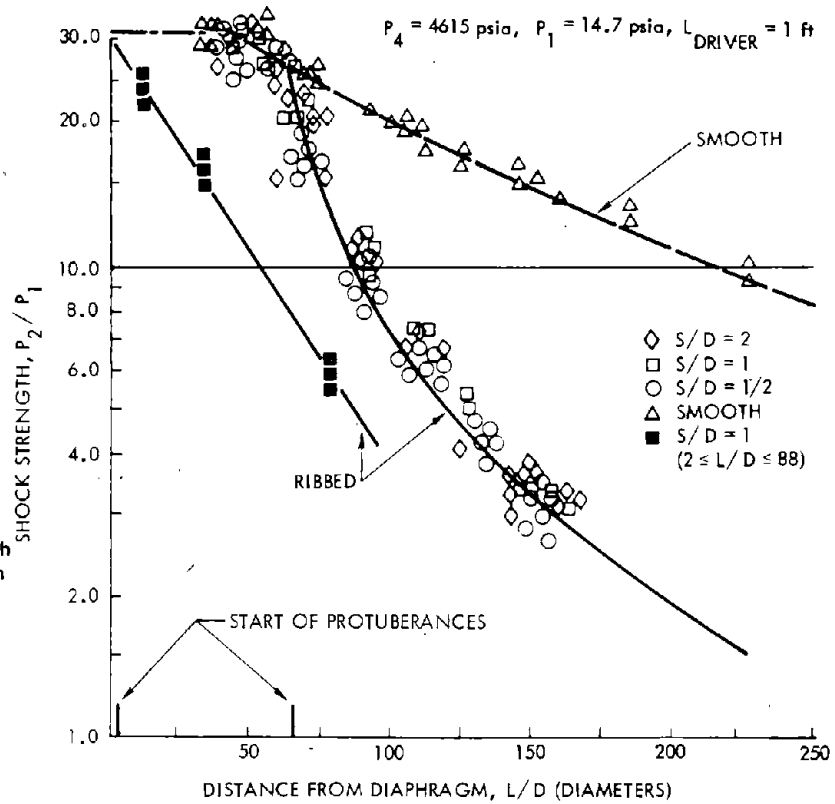
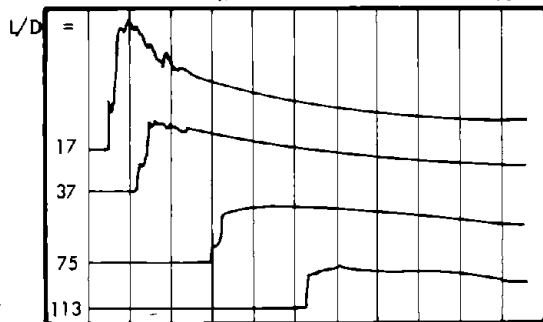


Figure 16. Shock Front Decay in Smooth Tubes and Ribbed Tubes with Ribs Starting at $L/D = 2$ and $L/D = 66$

He/AIR
 $P_4 = 4615 \text{ psia}$, $P_1 = 14.7 \text{ psia}$, 2 ms SWEEP, $L_{DRIVER} = 1 \text{ ft}$

(a) SHOT 274, PROTUBERANCES, $S/D = 1$
 FOR $2 \leq L/D \leq 88$, $P_{17} = 352 \text{ psia}$, $P_{75} = 85 \text{ psia}$, $P_{113} = 81 \text{ psia}$



(b) SHOT 89, PROTUBERANCES, $S/D = 0.5$
 FOR $L/D \geq 66$, $P_{40} = 428 \text{ psia}$, $P_{147} = 44 \text{ psia}$ (FROM REF. 1)

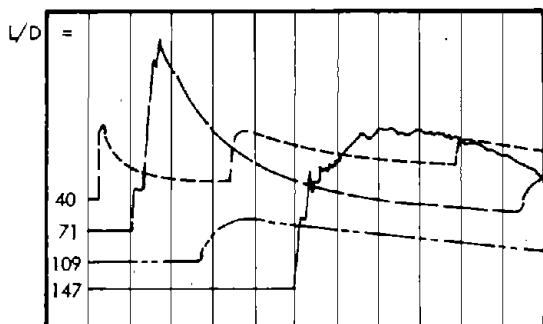


Figure 17. Waveform Comparison for Ribbed Tubes vs Smooth/Ribbed Tube Entrance Conditions

Abstract

A technique is described for generating a plane wave in water to simulate the pulse from an underwater nuclear explosion. The technique design consists of a vertical planar array of equally spaced point sources, each source consisting of a coil of Primacord explosive oriented with its axis horizontal. Pulses from single coil tests mathematically superpose to provide a satisfactory array pulse except for an excessive rise time. Analysis suggests that the array pulse rise time will be decreased if the linear density of the explosive strand forming the coil is decreased substantially over the final two-thirds of its length.*

Introduction

A technique has been under development for generating a plane wave in water to simulate the step-shaped pulse generated by an underwater nuclear explosion. The technique is being developed to improve the current method of loading submarine sections in which the energy source is concentrated as a large sphere or as a single line of explosive. The design consists of a vertical array of equally spaced point sources. Each source is a compact coil of Primacord explosive wound on a simple cylindrical mandrel; each coil is oriented with its axis horizontal and thus perpendicular to the array plane. The current design has 12-inch-diameter coils with the axes 24 inches apart. Simple small-scale exploratory experiments with a single 3-inch-diameter coil of mild detonating fuze (MDF) in a 6-inch-diameter water-filled steel pipe show that the coil source will probably be satisfactory in an array.

Free-field pressure pulses from a single coil of Primacord were measured by the Underwater Explosion Research Division (UERD). The on-axis pressure pulses were used to establish a mathematical formula describing propagation. This formula was used for superposition to predict the array pulse; thus off-axis pulse variations were not included. A pressure plateau was achieved but the pulse rise time was excessive.

* See 'Supplement' added after completion of the paper.

To aid development an approximate analysis was performed that resulted in a simple formula for the array pulse in terms of the source pulse. This formula shows that the array pulse rise time is comparable to the characteristic time of the source pulse. This characteristic time can be shortened by decreasing the linear density of the Primacord over a latter portion of the coil.

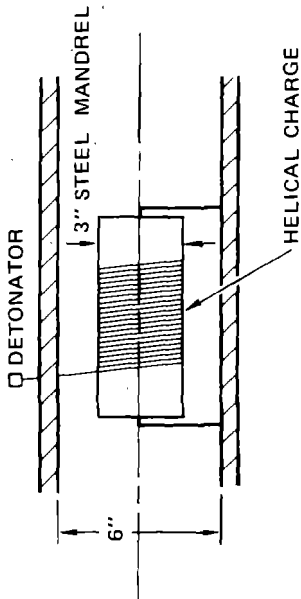
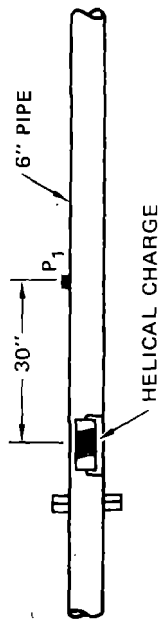
The main conclusion is that the coil shows promise as a practical source for an array.

Experiment and Theory

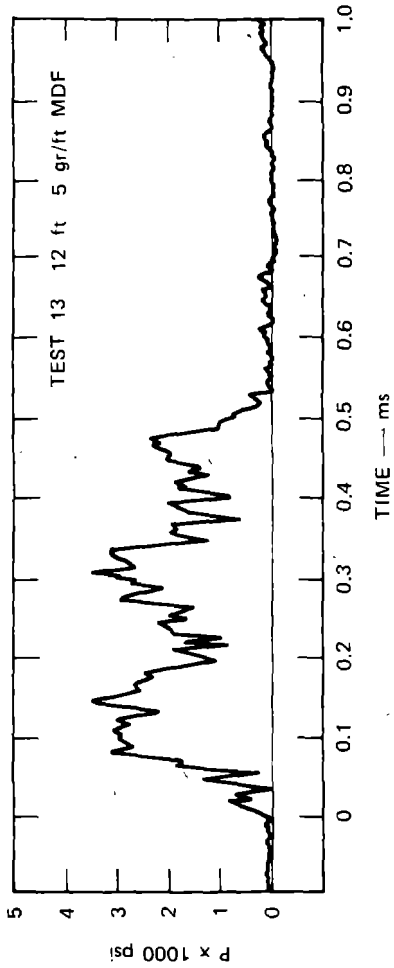
We conducted simple exploratory experiments with a single coil of mild detonating fuze (MDF) to ascertain suitability for an array. A coil of MDF wrapped on a grooved steel mandrel detonated in a water-filled steel pipe to represent an array produced a reasonably satisfactory pulse, as shown in Figure 1(a). Of practical significance is the result of a similar test with a cardboard mandrel. As shown in Figure 1(b), this test demonstrates that the pulse is not substantially influenced by the stiffness of the mandrel. A similar test with a coil of bare Detasheet showed that the pulse was not influenced by the lead sheath of the MDF. The pulses in Figure 1 should therefore be indicative of the array pulse from coils of Primacord on flexible mandrels.

A single coil of MDF was detonated in a large tank of water and the free-field pressure was monitored on the axis of the coil, as shown in Figure 2. A pressure pulse is shown in Figure 3(a). It compares favorably with the pulse in Figure 3(b), obtained in a UERD test³ using a coil of Primacord. The geometry of the MDF coil was a 1/8-scale version of the Primacord coil, but since no attempt was made to scale the explosive linear density, pressures are not equivalent.

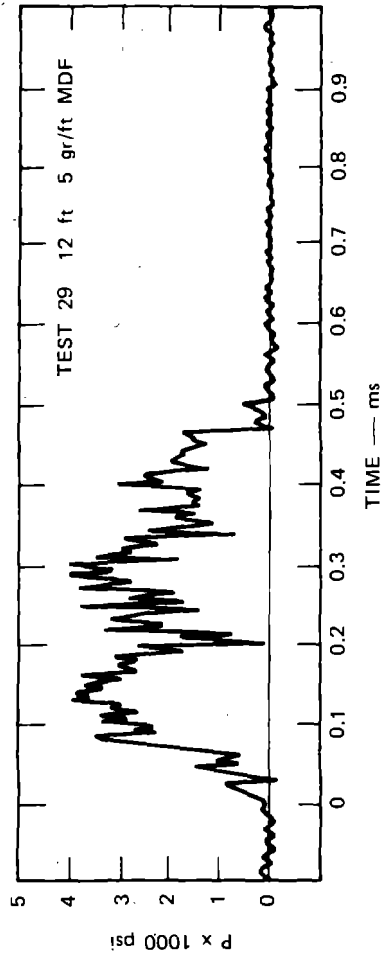
The UERD test³ was performed with the Primacord coil shown in Figure 4. The pressure transducers were located in the horizontal plane through the charge axis, as shown in Figure 5. The pressure pulses are shown in Figures 6 and 7. From the pulse arrival times and the transducer locations, the pulse wave velocity was calculated as 4800 ft/sec.



3-INCH HELICAL CHARGE IN AXIAL ORIENTATION

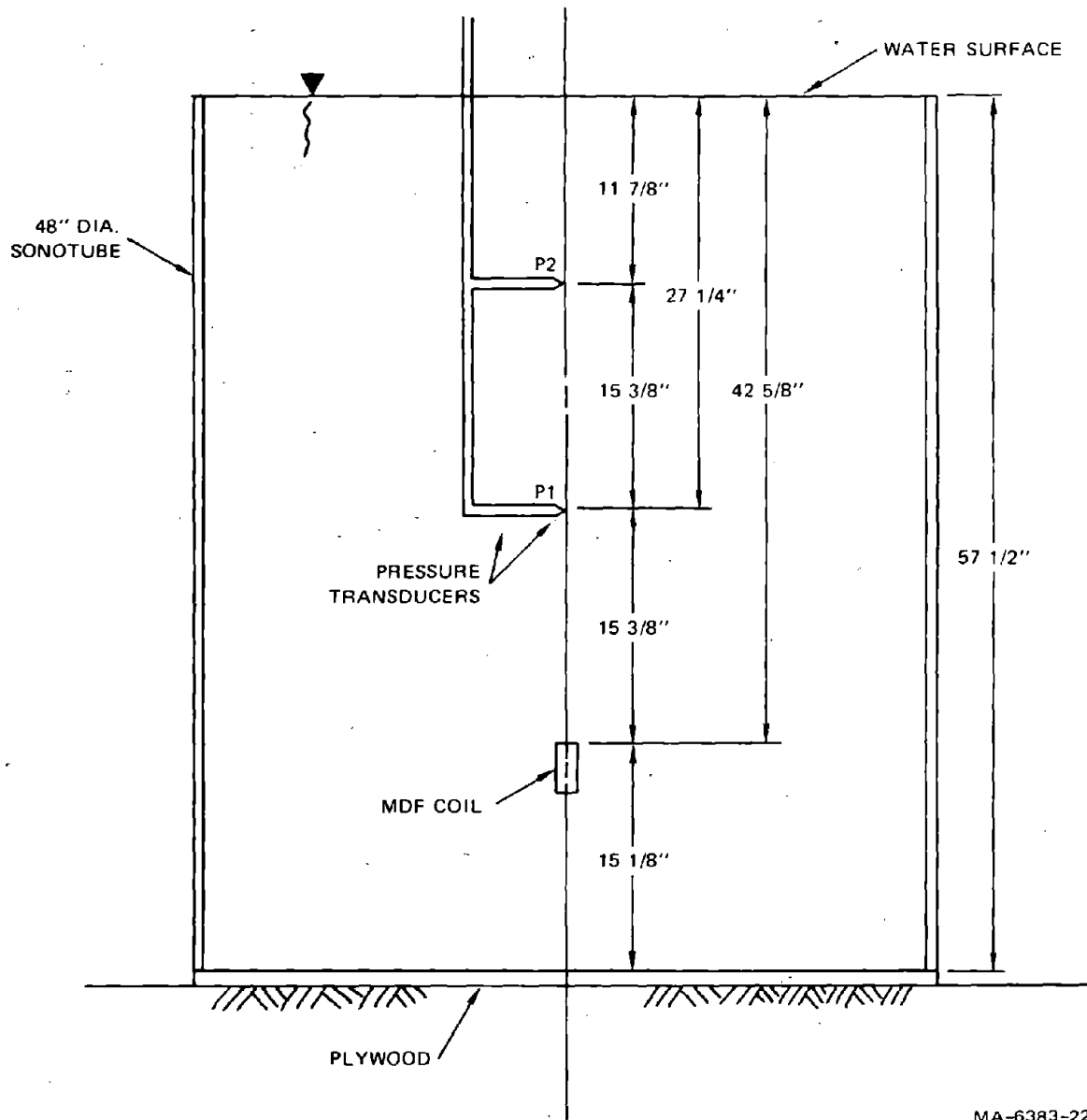


(a) 3-INCH-DIA. COIL ON SOLID STEEL MANDREL



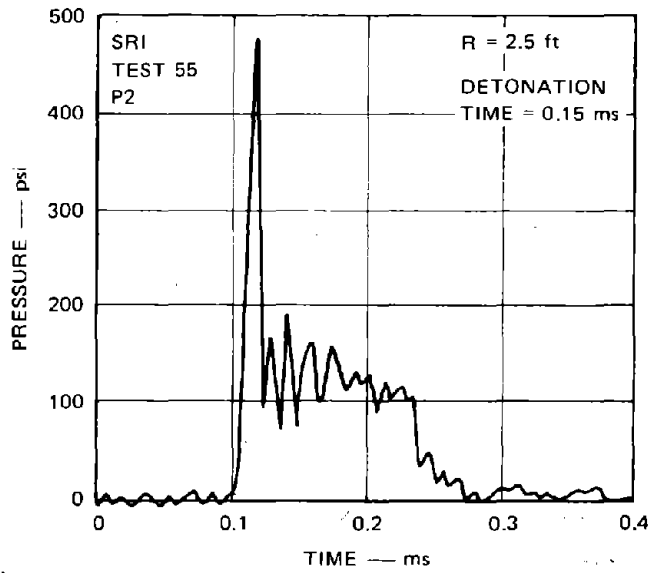
(b) 3-INCH-DIA. COIL ON CARDBOARD MANDREL

FIGURE 1 EFFECT OF MANDREL CONSTRUCTION ON PRESSURE PULSE

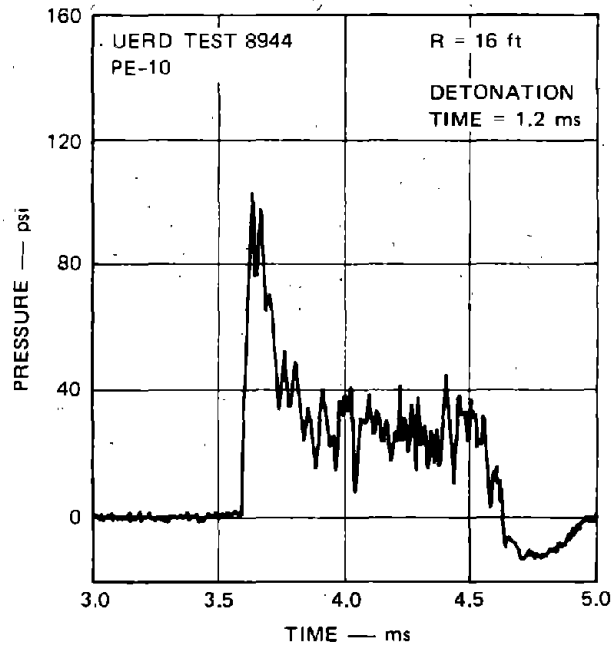


MA-6383-22

FIGURE 2 EXPERIMENT ARRANGEMENT FOR SCALED SINGLE SOURCE PULSE MEASUREMENTS



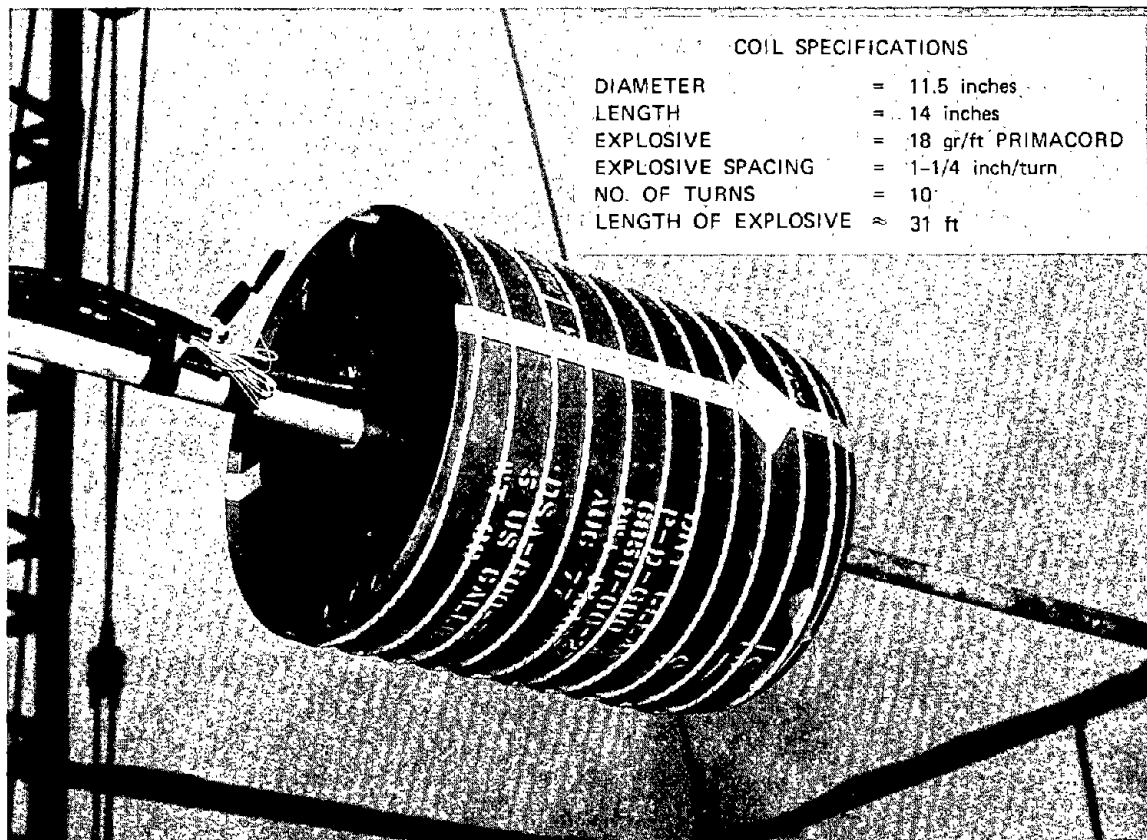
(a) PRESSURE FROM 1 1/2-INCH-DIA. COIL ($\approx 1/8$ SCALE)



(b) PRESSURE FROM 12-INCH-DIA. COIL

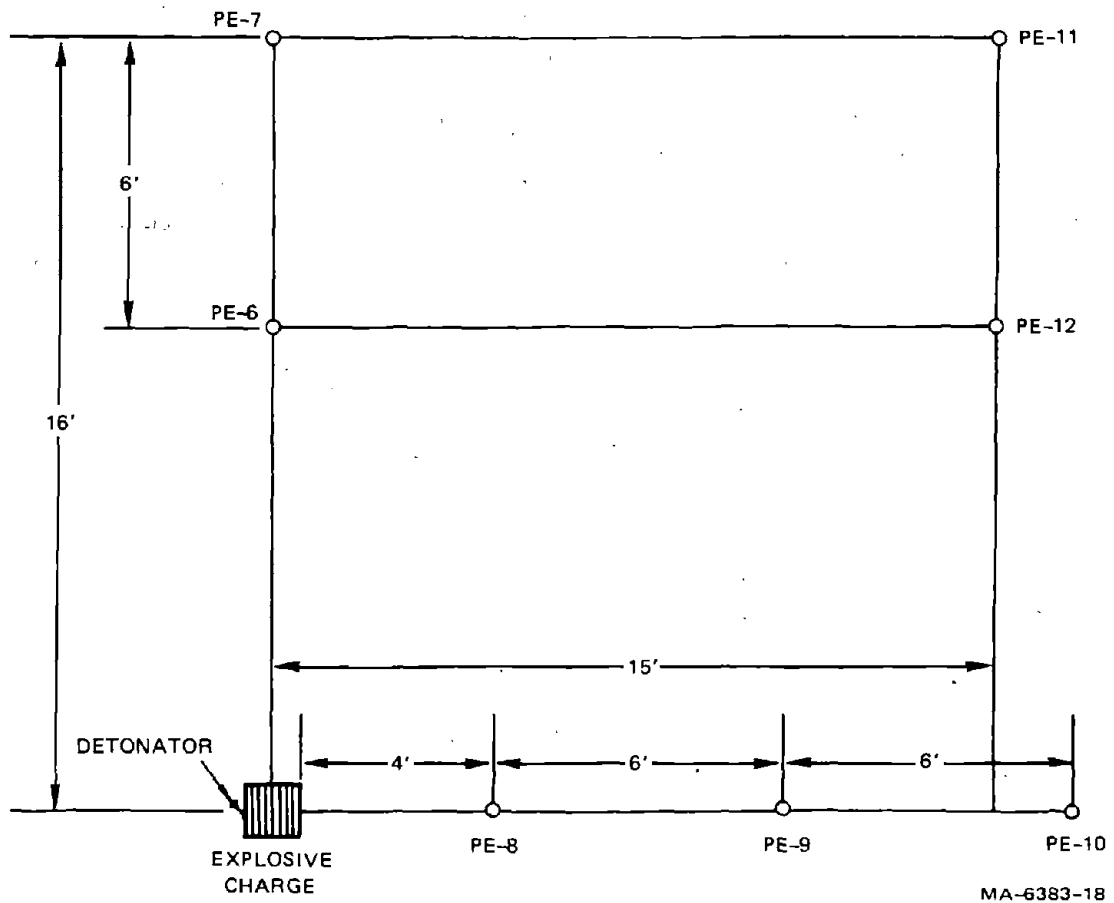
MA-6383-23

FIGURE 3 COMPARISON OF SINGLE-SOURCE SCALED PULSE WITH UERD PULSE



MP-6383-16

FIGURE 4 EXPLOSIVE COIL (UERD TEST 8944)



MA-6383-18

FIGURE 5 INSTRUMENTATION LAYOUT FOR UERD COIL EXPERIMENT 8944

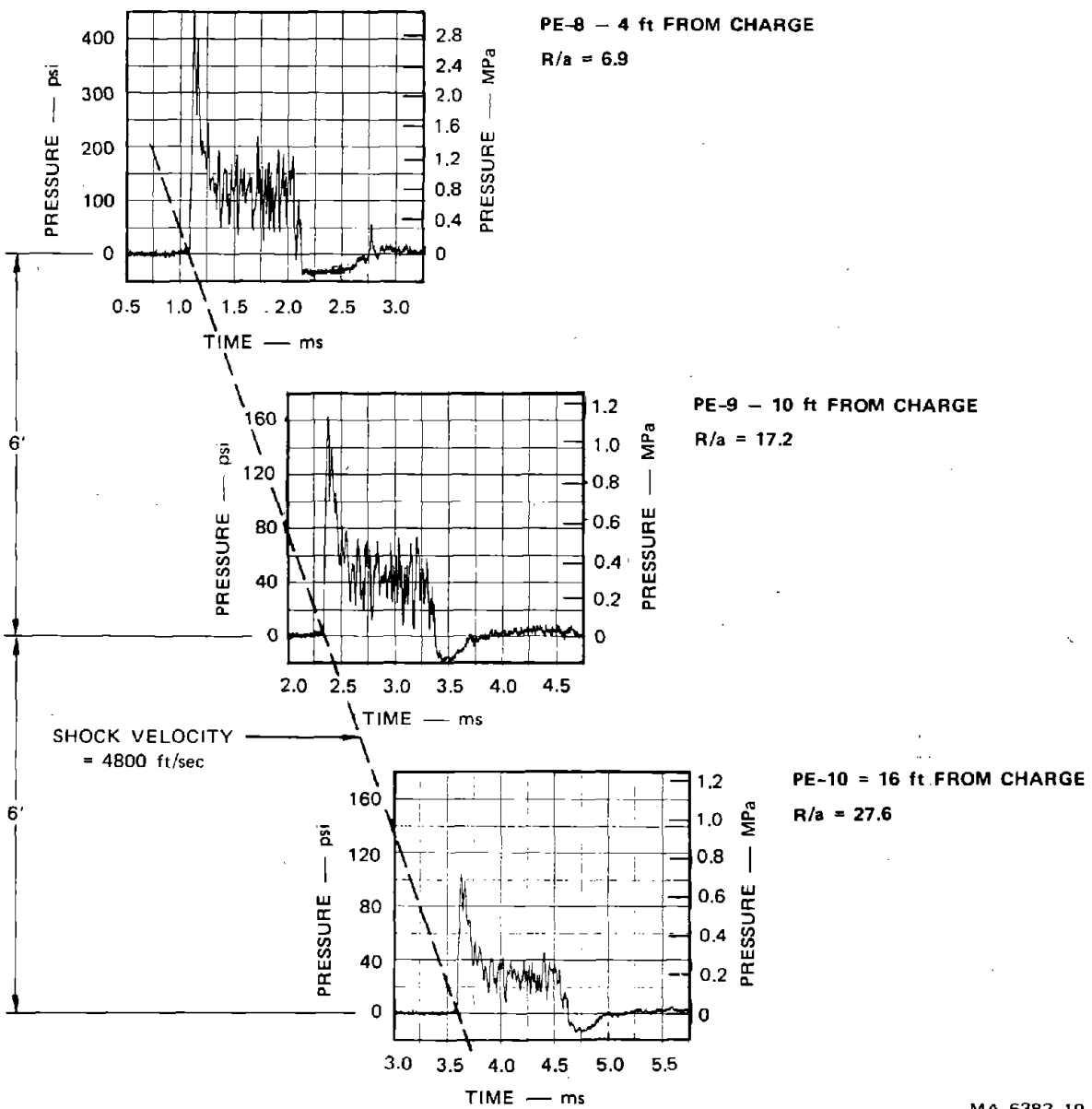
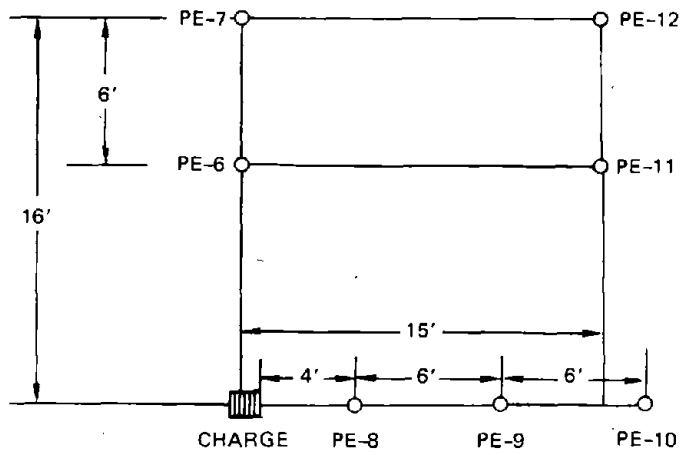
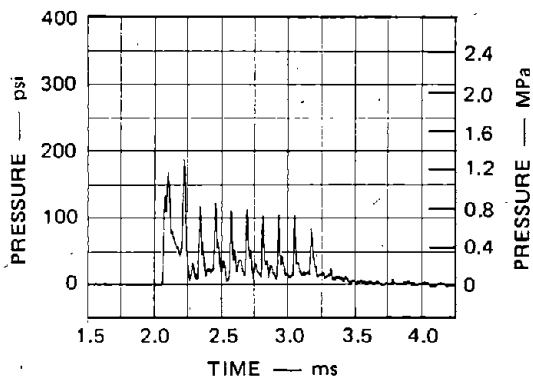
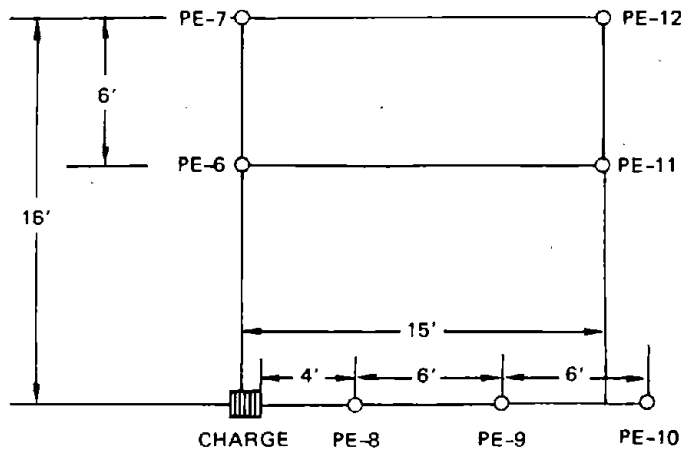
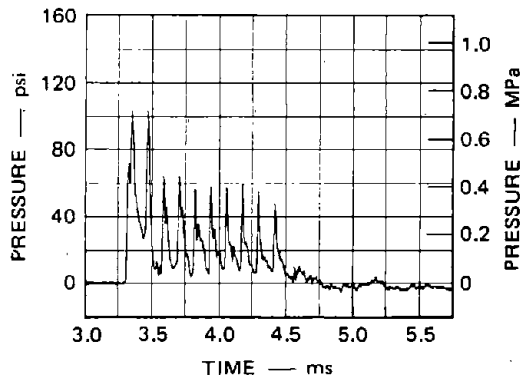


FIGURE 6 SINGLE-SOURCE PULSE SHAPES ON AXIS (UERD TEST 8944)

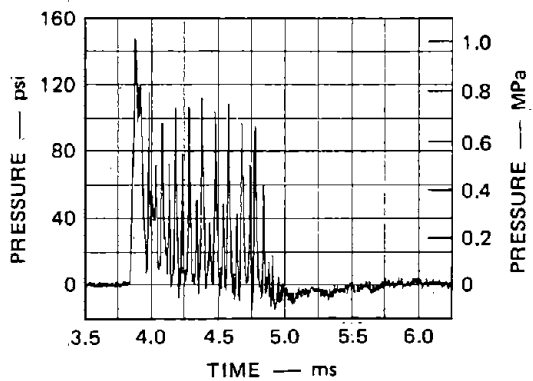
MA-6383-19



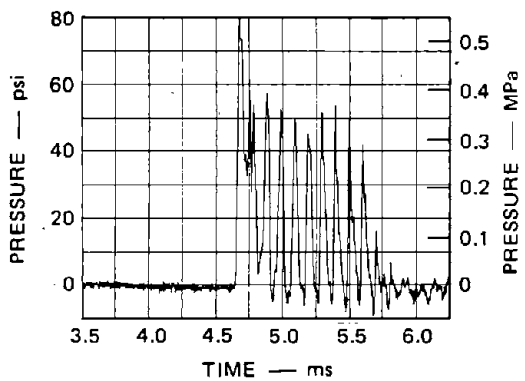
(a) PE-6 SIDE-ON TO CHARGE



(b) PE-7 SIDE-ON TO CHARGE



(c) PE-11 OBLIQUE TO CHARGE



(d) PE-12 OBLIQUE TO CHARGE

MA-6383-20

FIGURE 7 SINGLE-SOURCE PULSE SHAPES OFF AXIS (UERD TEST 8944)

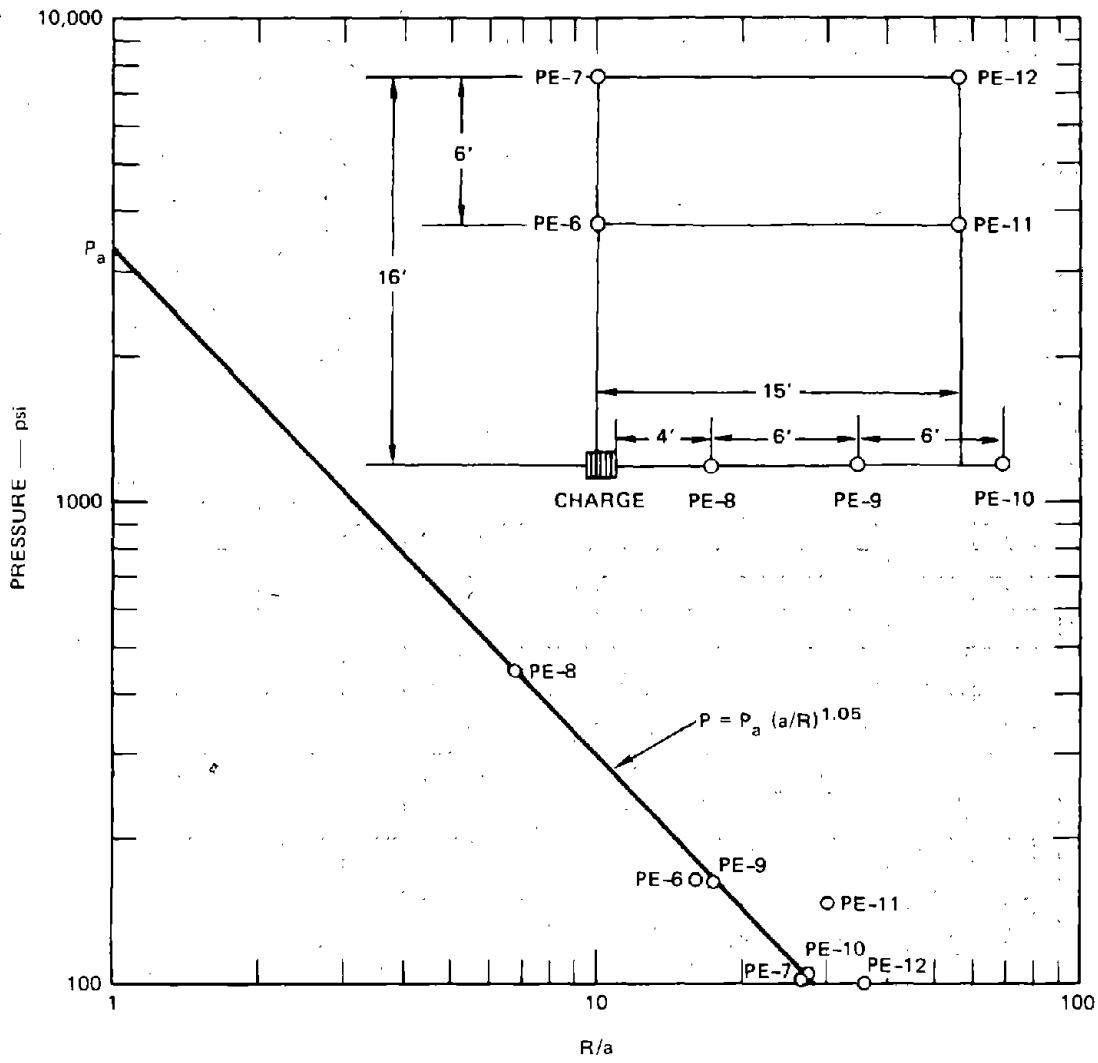
The pulse duration is 1.1 ms and almost equals the detonation time of the 31-foot-long strand of Primacord. Figure 6 shows the pulses obtained in the coil axis with shapes that resemble an exponential pulse superposed on a rectangular pulse. Figure 7 shows the pulses obtained off the coil axis with similar average shapes but with substantial oscillations attributed to the helical trajectory of the detonation front; the ten major oscillations represent the number of Primacord turns. The attenuation of the peak pressure approximately equals the geometrical attenuation of a spherical source ($R^{-1.05}$ as compared with R^{-1} , as shown in Figure 8).

We predicted the pulse from a square array of these Primacord coils at a uniform spacing of 2 feet. The prediction is based on the pulse of Figure 9(a) monitored by the on-axis transducer P-10 at a range of $R = 16$ feet. This prediction neglects dependence of pulse shape on angular departure from the coil axis and assumes that the peak pressure attenuation is that of spherical divergence. A smoothed version of the pulse, marked Pulse I in Figure 9(a) and shown separately in Figure 9(b), was provided as input to our superposition code. The resulting array pulse is shown in Figure 10(a) (the dashed curve marked 'theory' is discussed later). The pressure plateau is achieved but the rise time is too long.

We repeated the prediction process with Pulse II, shown in Figure 9(a) and 9(c), which represents a pulse with a pressure that decays to zero. The resulting array pulse, shown in Figure 10(b), appears to be satisfactory. It should be possible to bring Pulse I closer to Pulse II in an experiment by decreasing the linear density of the explosive after about 10 feet of the 31-foot-long coil.

The appendix describes a theory that provides a simple formula for the array pulse in terms of the source pulse, spacing, and standoff. Pulses $p(t)$ in spherical bubbles of radius a and spacing S provide an array pulse at station X (Figure A-2), a distance R from the array, equal to

$$p(R,t) = \frac{2\pi a^2}{S^2} \cdot \frac{1}{T} \cdot I(t-t_0) \quad (1)$$



MP-6383-16

FIGURE 8 SINGLE-SOURCE PEAK PRESSURE ATTENUATION (UERD TEST 8944)

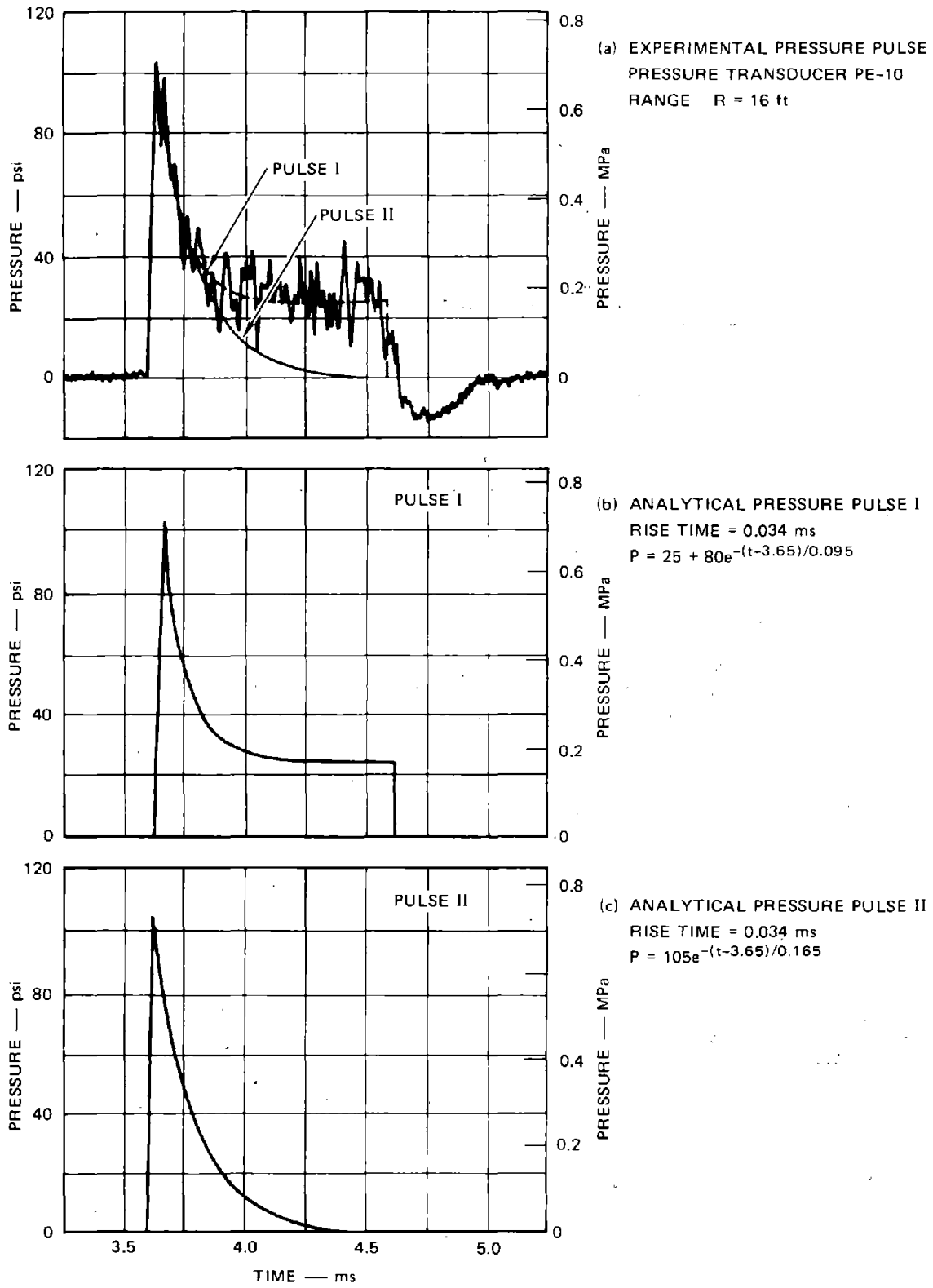
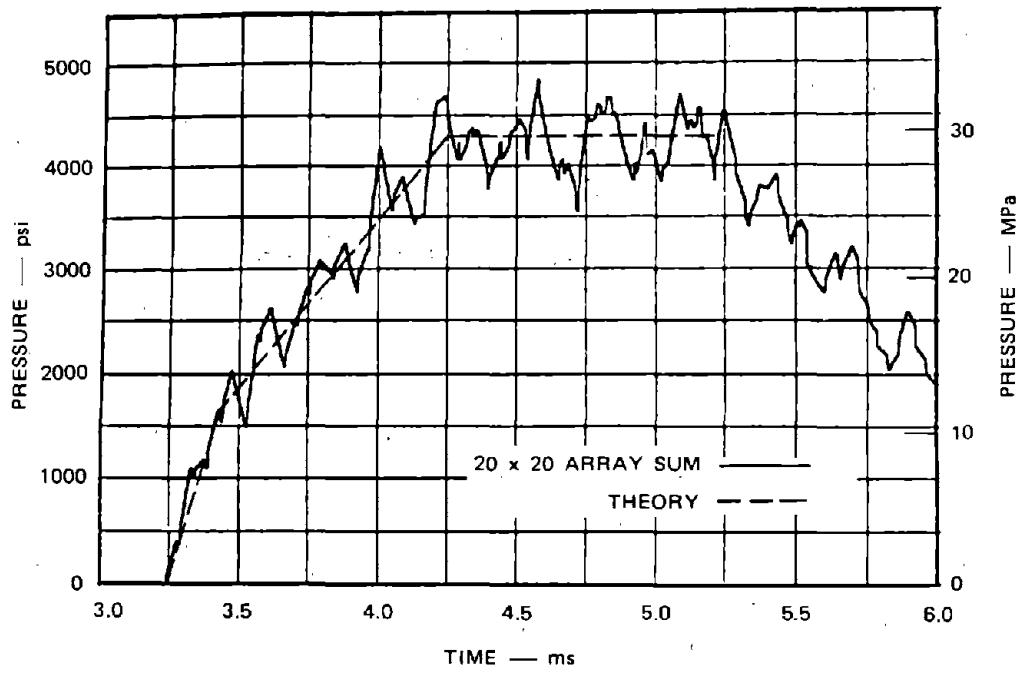
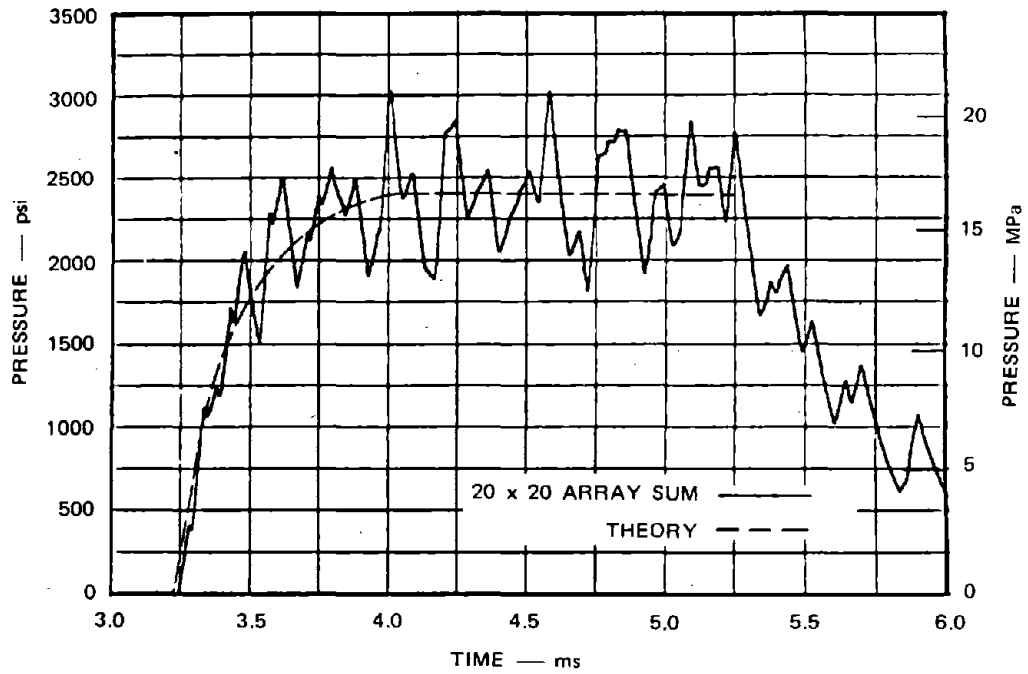


FIGURE 9 ANALYTICAL APPROXIMATIONS OF SINGLE-SOURCE PULSE (UERD TEST 8944)

MA-6383-24



(a) SUMMATION OF PULSE I AT R = 16 ft



(b) SUMMATION OF PULSE II AT R = 16 ft

MA-6383-21

FIGURE 10 SUMMATION OF SINGLE-SOURCE PULSES (UERD COIL TEST 8944)

where $T = a/c$ is a time characteristic of the source, c being the fluid acoustic velocity. In formula (1), $I(t-t_0)$ is the source impulse at time $t-t_0$, where t_0 is the time at which an acoustic signal first arrives at X , that is, $t_0 = R/c$. Thus

$$I(t-t_0) = \int_0^{t-t_0} p(\tau) d\tau \quad (2)$$

Each source delivers a constant impulse so that the array pressure pulse given by formula (1) will provide a constant pressure. Also, the rise time of the array pulse is approximately equal to the source pulse characteristic time (see Eq. A34).

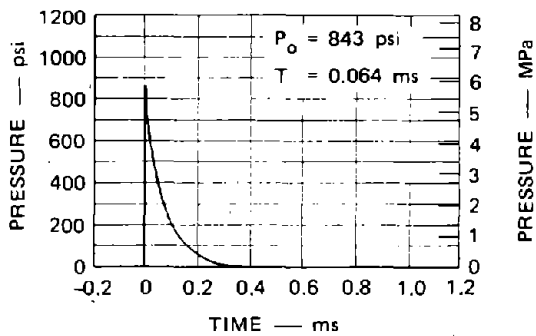
Figure 10 shows the array pulses obtained by the analysis, labeled 'theory,' for the source pulses I and II of Figure 9. Apart from the lack of oscillation, they show agreement with the array pulses obtained by the superposition code; oscillations are absent because of the assumption of continuous distribution of sources.

Figure 11 shows further similar comparison between the array pulses obtained by analysis and by the superposition codes. The main purpose of generating these pulses is to show the decrease of oscillation with range or stand-off. However, large target stand-offs require large arrays, resulting in less economical systems that require more explosive.

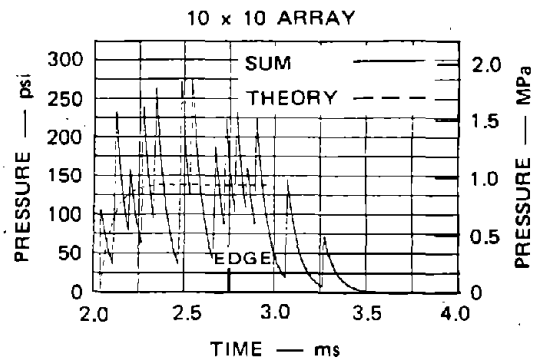
Figure 12 shows that the array pulse is the same at points opposite the edge and at the center of an array mesh.

Conclusions and Recommendations

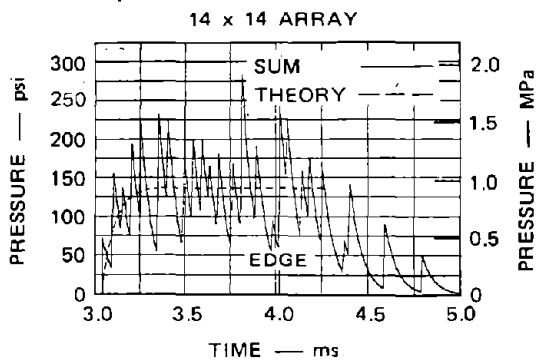
The main conclusion is that the experimental and theoretical results for the practical coil source are sufficiently encouraging to pursue development toward an array test. As shown in Figure 10, a pressure plateau is predicted for an array of Primacord coils. Figure 10(a) shows the array pulse from the current 31-foot-long strand coil design, which is



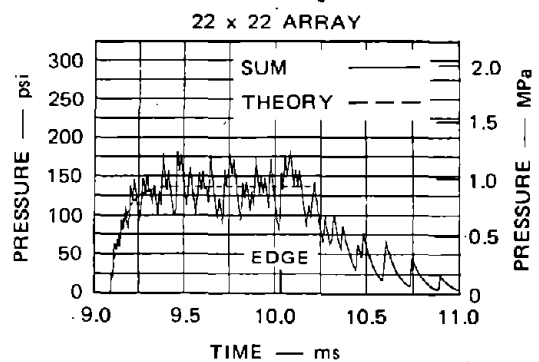
(a) SOURCE PRESSURE PULSE



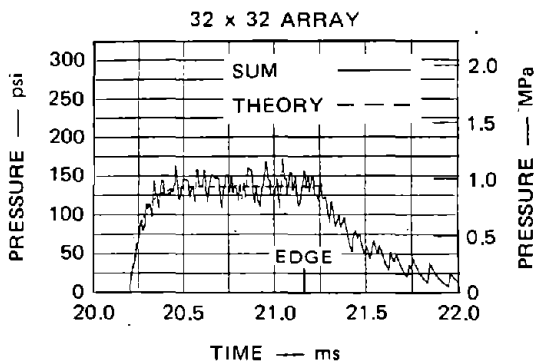
(b) ARRAY SUMMATION AT R = 10 ft



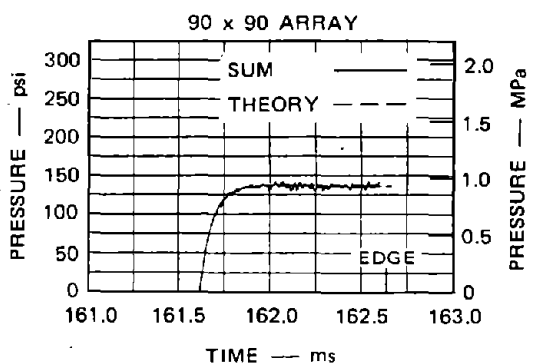
(c) ARRAY SUMMATION AT R = 15 ft



(d) ARRAY SUMMATION AT R = 45 ft



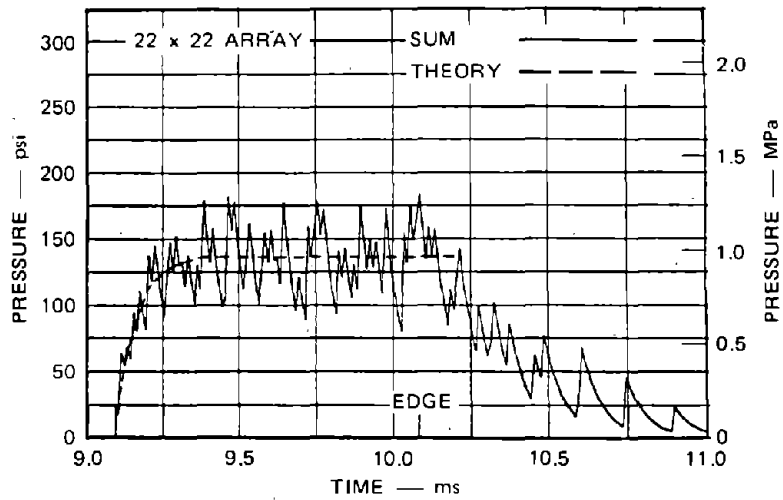
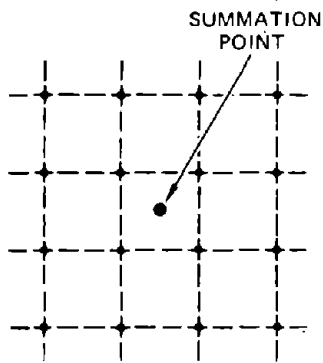
(e) ARRAY SUMMATION AT R = 100 ft



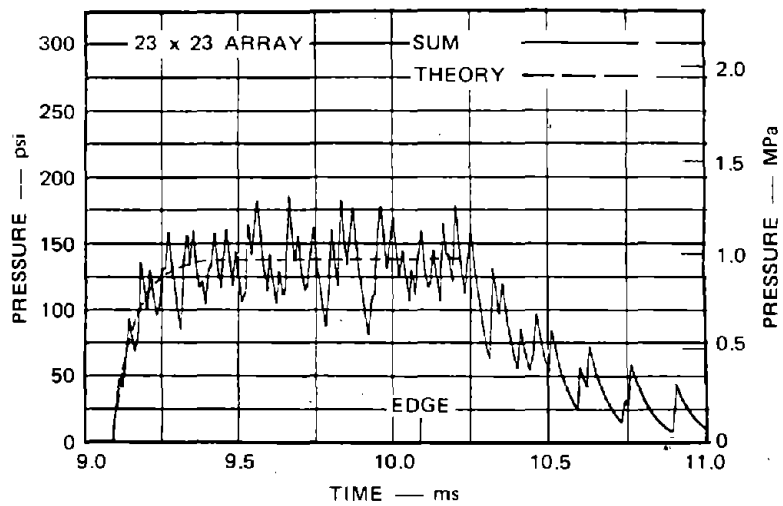
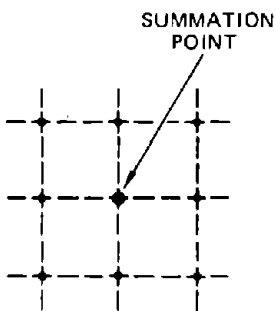
(f) ARRAY SUMMATION AT R = 800 ft

MA-6383-25

FIGURE 11 VARIATION OF ARRAY PULSE WITH STAND-OFF
(Source spacing 2 feet)



(a) EVEN NUMBER OF ARRAY SOURCES, R = 45 ft



(b) ODD NUMBER OF ARRAY SOURCES, R = 45 ft

MA-6383-26

FIGURE 12 COMPARISON OF ARRAY PULSES AT POINTS OPPOSITE EDGE AND AT CENTER OF AN ARRAY SQUARE

of uniform linear density. Figure 10(b) shows the trend of the array pulse if the linear density is reduced substantially after about 10 feet of strand. The pressure plateau for this two-stage coil is approaching the level of interest in testing of submarine sections. Also, this recommended design shortens the rise time from 1 ms to about 0.25 ms.

Supplement

This paper is essentially the same as reference 4 that reports on work carried out in late 1977 and early 1978. The results included observations that are not consistent. Specifically,

- The MDF coil charge generates a rectangular pulse with a short rise time and a duration equal to the detonation time when it is detonated in a water-filled pipe (Figure 1).
- Superposition of the free-field pulse from a coil charge predicts a flat pulse with a long rise time and a duration that depends on the arrival time of a disturbance from the edge of the array [Figure 10(a)]; an infinite array produces an infinitely long pulse.

These pulse shapes should be the same. Symmetry and energy arguments give credence to the results from a coil in a water-filled pipe. Examination of the superposition analysis in the Appendix revealed that it required extending so as to satisfy the bubble pressure conditions. The resulting extension of the theory provided the required agreement for the array pulses.

The conclusion remains that the helical coil of Primacord is probably satisfactory as a candidate source for the planar array, but without the need for a two-stage coil.

References

1. C. M. Romander and G. R. Abrahamson, "Simulation of Plane Underwater Shock Waves Using an Array of Point Volume Sources," SRI Final Report DNA 4418, Contract No. DNA001-73-C-0208 (September 1977).
2. A. L. Florence and C. M. Romander, "Evaluation of the Shock Block Technique for Generating Underwater Plane Waves," SRI Interim Report DNA4448Z, Contract No. DNA001-77-C-0210 (October 1977).
3. J. D. Gordon, UERD, private communication (February 1978).
4. A. L. Florence and C. M. Romander, "Source Development for an Array to Generate Underwater Rectangular Pulses," SRI Final Report DNA 4589F, Contract No. DNA001-77-C-0210 (April 1978).

Appendix

Theory of Step Plane Wave Generation in a Fluid by a Planar Array of Spherical Pistons

Introduction

The theory outlined here was carried out to assist in the design of an experimental technique for simulating underwater shock waves generated by submerged nuclear explosions. An idealization of the simulation technique consists of a vertical planar array of regularly spaced 'point' volume sources consisting of expanding gaseous spherical pistons. In the experiment the gas is generated by a coil of Primacrod explosive. The expansion rate is determined to provide a step pressure wave at points several source spacings away from the plane of the array upon superposition of the waves arriving from each source.

The theory is developed in three parts:

- (1) Determination of the expansion rate of the spherical piston
- (2) Analysis of the spherical wave produced by one expanding piston
- (3) Superposition of the spherical waves to determine the wave produced by a regular array of sources.

In the spherical piston idealization, the fluid pressures and particle velocities of interest are assumed to be small enough everywhere to allow the use of acoustic theory.

The principal result is that a regular array of sources produces a plane wave with the required constant pressure and particle velocity. The wave has a short rise time comparable with the characteristic pulse time of the individual source pulse.

Piston Expansion Rate

Figure A-1 represents a square tube of fluid associated with one expanding spherical piston in a regular array. Due to symmetry, the effect of the remaining pistons is to provide fixed side walls for the section of fluid. When the wave front is several source spacings away, the wave front is almost planar. At this time let the particle velocity just behind the wave front be V_{∞} and the piston radius be a . In a small increment of time Δt the particles at the wave front have moved a distance $V_{\infty}\Delta t$ and, for a square tube of side S , have swept a volume $V_{\infty}S^2\Delta t$. Meanwhile, the half-volume of the spherical source has increased by $2\pi a^2\Delta a$. If fluid compressibility is neglected, as an approximation these two incremental volumes are equal. Therefore

$$2\pi a^2 \cdot \Delta a = V_{\infty} S^2 \cdot \Delta t$$

which, in the limit, gives the piston radial velocity

$$V_a = \frac{S^2 V_{\infty}}{2\pi a^2} \quad (A1)$$

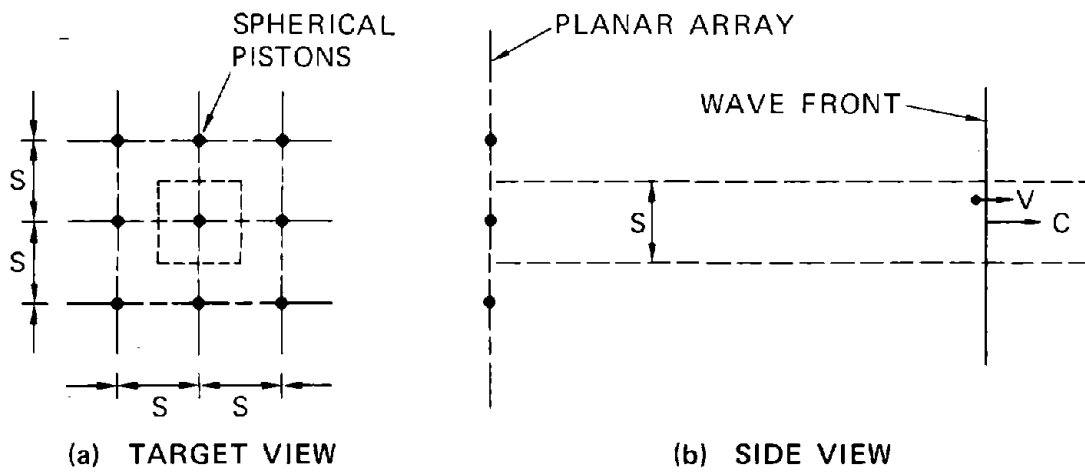
where $V_a = da/dt$. Because the step wave to be simulated has a constant particle velocity V_{∞} , the piston has a constant velocity determined by equation (A1). Acoustic theory allows the piston radius, a , to remain at its initial value.

Spherical Wave

The pressure p and particle velocity v for a fluid element at radius r from the center of the spherical source are related by the equation of motion

$$\frac{\partial p}{\partial r} = -\rho \frac{\partial v}{\partial t} \quad (A2)$$

where ρ is the fluid density.



MA-6383-27

FIGURE A-1 FLUID REGION ASSOCIATED WITH ONE PISTON

The temporal rate of change of the acoustic pressure-volume change relationship $p = -K\Delta$, where K is the constant modulus and Δ the dilatation, gives

$$\frac{\partial p}{\partial t} = -K \left(\frac{\partial v}{\partial r} + 2 \frac{v}{r} \right) \quad (\text{A3})$$

The velocity potential ϕ is defined by

$$v = \frac{\partial \phi}{\partial r} \quad (\text{A4})$$

and equation (A2) is satisfied if

$$p = -\rho \frac{\partial \phi}{\partial t} \quad (\text{A5})$$

Introducing the velocity potential in equation (A3) by means of (A4) and (A5) results in

$$\frac{\partial^2 \phi}{\partial r^2} + \frac{2}{r} \frac{\partial \phi}{\partial r} = \frac{1}{c^2} \frac{\partial^2 \phi}{\partial t^2} \quad (\text{A6})$$

where $c = (K/\rho)^{\frac{1}{2}}$ is the acoustic wave velocity.

The Laplace transform of the velocity potential is

$$\phi(r,s) = \int_0^{\infty} \phi(r,t) e^{-st} dt \quad (\text{A7})$$

so the transform of equation (A6) is

$$\frac{d^2 \bar{\phi}}{dr^2} + \frac{2}{r} \frac{d\bar{\phi}}{dr} - \left(\frac{s}{c} \right)^2 \bar{\phi} = 0 \quad (\text{A8})$$

when the initial conditions are

$$\phi(r,0) = 0 \quad \frac{\partial \phi}{\partial t}(r,0) = 0 \quad (\text{A9})$$

initial conditions (A9) describe an initial state of zero pressure and particle velocity.

The solution of equation (A8) that enables the velocity potential to satisfy the zero pressure and particle velocity conditions at infinity is

$$\bar{\phi}(r,s) = \frac{B(s)}{r} e^{-\frac{s}{c}r} \quad (\text{A10})$$

At the piston the particle velocity is

$$\frac{\partial \phi}{\partial r}(a,t) = V(a,t) = V_a H(t) \quad (\text{A11})$$

so that

$$\frac{d\bar{\phi}}{dr}(a,s) = \bar{V}(a,s) = \frac{V_a}{s} \quad (\text{A12})$$

Hence, equations (A10) and (A12) determine $B(s)$ and give

$$\bar{\phi}(r,s) = \frac{-acV_a}{rs \left(s + \frac{c}{a}\right)} e^{-\frac{s}{c}(r-a)}$$

The inverse of which is

$$\phi(r,t) = -\frac{acV_a}{r} \cdot \frac{1}{2\pi i} \int_{\gamma-i\infty}^{\gamma+i\infty} \frac{e^{\frac{s}{c}[ct-(r-a)]}}{s \left(s + \frac{c}{a}\right)} ds$$

where $\gamma > 0$. Simple poles exist at $s = 0$ and $s = -c/a$ so summation of the two residues leads to the results

$$\phi(r,t) = \frac{-V_a a^2}{r} \left[1 - e^{-\frac{1}{a} [ct - (r-a)]} \right] \quad r - a < ct \quad (A13)$$

$$\phi(r,t) = 0 \quad ct < r - a \quad (A14)$$

The zero result (A14) simply means that the wave front has not yet arrived at a certain radius if $ct < r - a$.

The pressure pulse from a single source, from (A5) and (A13), is

$$p(r,t) = \rho c V_a \frac{a}{r} e^{-\frac{1}{a} [ct - (r-a)]} \quad r - a < ct \quad (A15)$$

and the piston pressure is

$$p(a,t) = \rho c V_a e^{-\frac{c}{a} t} \quad (A16)$$

Pulse from an Array

The wave and piston pressures (A15) and (A16) at a distance r from a single source may be expressed in the form

$$p(\tilde{r},t) = P \frac{a}{\tilde{r}} e^{-(t-\tilde{t})/T} \quad (A17)$$

$$p(a,t) = P e^{-t/T} \quad (A18)$$

where the durations T and \tilde{t} defined by

$$T = a/c \quad \tilde{t} = (\tilde{r} - a)/c \quad (A19)$$

are the piston pulse characteristic time and the pulse transit time, and $P = \rho c V_a$.

Figure A-2 shows the plane of the array and the monitoring point X a distance R away. It is assumed that R is sufficiently larger than the array spacing S to permit the discrete source distribution to have the same effect as a continuous distribution. For sources in a square array of spacing S, the number of sources, $N = n^2$, within the circle of radius \tilde{h} (Figure A-2) is given approximately by equating the circular area to the area of a square of side nS , that is,

$$\pi \tilde{h}^2 = n^2 S^2$$

Hence the number of sources is

$$N = n^2 = \frac{\pi \tilde{h}^2}{S^2} \quad (\text{A20})$$

The number of sources within the annulus of width $d\tilde{h}$, according to (A20), is

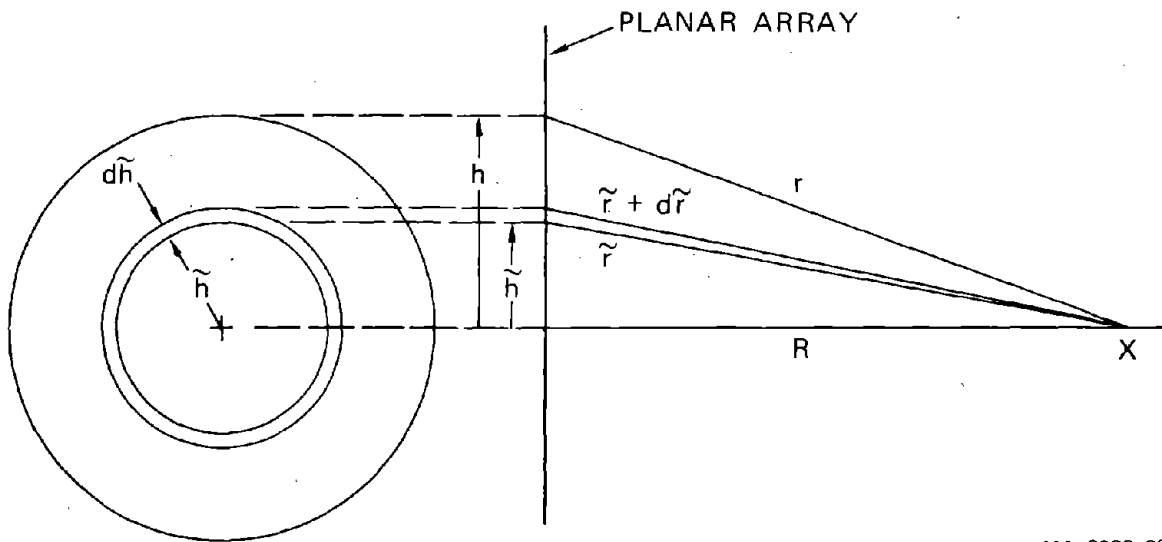
$$dN = \frac{2\pi \tilde{h} d\tilde{h}}{S^2} \quad (\text{A21})$$

and \tilde{h} is related to \tilde{r} by

$$\tilde{h}^2 = \tilde{r}^2 - R^2 \quad ; \quad d\tilde{h} = \frac{\tilde{r}}{(\tilde{r}^2 - R^2)^{1/2}} d\tilde{r} \quad (\text{A22})$$

In Figure A-2 let \tilde{r} be the distance from X of all sources that have pulses just arriving at X. The time is therefore $t = (\tilde{r} - a)/c$; also, the transit time from a source a distance \tilde{r} from X is $\tilde{t} = (\tilde{r} - a)/c$. Thus (A17), for a single source at a distance \tilde{r} from may be written in the form

$$p(\tilde{r}, t) = P \frac{a}{\tilde{r}} e^{-(\tilde{r}-\tilde{t})/a} \quad (\text{A23})$$



MA-6383-28

FIGURE A-2 GEOMETRICAL NOMENCLATURE

The contribution to the plane wave pulse at X from all sources in the annulus of width dh, by (A23), is

$$dp = P \frac{a}{r} e^{-(r-\tilde{r})/a} dN$$

which becomes

$$dp = P a \frac{2\pi}{S^2} e^{-(r-\tilde{r})/a} \tilde{r} dr \quad (\text{A24})$$

after using (A21) and (A22). Consequently, the plane wave pulse at X at time t by integration of (A24) is

$$p(R,t) = 2\pi \frac{Pa^2}{S^2} \left(1 - e^{-(r-R)/a} \right)$$

or in terms of time

$$P(R,t) = \frac{2\pi Pa^2}{S^2} \left(1 - e^{-(t-t_0)/T} \right) \quad (\text{A25})$$

where $t_0 = (R - a)/c$ is the time when the first source pulses arrive at X. For times, $t - t_0$, well in excess of the source pulse characteristic time T, formula (A25) gives

$$P(R,t) = \frac{2\pi a^2}{S^2} P \quad (\text{A26})$$

which is constant, as required. Inserting $P = \rho c V_a$ in (A26) and eliminating the area ratio (A1) gives $p_\infty = \rho c V_\infty$, as it should.

If time is calculated from the moment of arrival at the point X and the result (A26) is used, equation (A25) may be written in the form

$$p(t) = p_\infty \left(1 - e^{-t/T} \right) \quad (\text{A27})$$

From this expression, the pulse rise time, estimated as the time when the tangent at the origin intersects the plateau pressure, is simply $t_r = T$. At this time the radius of the circle containing all the sources that have contributed to the plane wave pulse is $h = (2aR)^{1/2}$, and the number of sources is found by substituting this radius for \tilde{h} in equation (A20).

Numerical Example

An array design is considered for producing a plane wave with a pressure of $p = 100$ bars (1450 psi)

Plane wave pressure	P_∞	100 bars
Fluid density	ρ	1 g/cm ³
Fluid sound speed	c	1500 m/s
Acoustic impedance	ρc	0.15 bar-s/cm
Plane wave particle velocity	$V_\infty = p_\infty / \rho c$	6.67 m/s
Source pulse characteristic time	T	0.1 ms
Source radius	$a = cT$	0.15 m (6 in.)
Source spacing	S	0.60 m (2 ft)
Source piston velocity	$V_a = \frac{S^2}{2\pi a^2} V_\infty$	16.99 m/sec
Initial source pressure	$P = \rho c V_a$	255 bars
Target stand-off	R	4.8 m (16 ft)
Plane wave arrival time	$t_o = (R - a)/c$	3.2 ms
Plane wave rise time	$\sim T$	~ 0.1 ms

General Formulation

The single-source constant-volume-rate-expansion pulse (Eq. A17) was used in a computer code that sums the pressures from an array of single sources. The code assumes that the pressure from each source attenuates according to spherical divergence. The relationship expressed by Equation (A25) for the sum of exponential pulses was verified by the code (see Figure 11). Other simple pulse shapes such as a step wave of duration T were also used in the code. These pulses, when summed by the code, also resulted in a constant pressure plane wave. When the formulation of the pulse from an array is examined, it becomes clear that any

pulse shape from a source that attenuates according to spherical divergence rules will result in a constant pressure plane wave when used in an array. The proof follows.

$$p(\tilde{r}, t) = P \frac{a}{\tilde{r}} f[(r - \tilde{r})/a] \quad (\text{A28})$$

where $f[(r - \tilde{r})/a]$ is a pulse shape function and P is the peak pressure at the bubble surface.

The contribution to the plane wave pulse at X from all sources in the annulus of width dh is, by (A28),

$$dp = P \frac{a}{\tilde{r}} f[(r - \tilde{r})/a] dN$$

and substituting (A21) and (A22)

$$dp = P \frac{a}{\tilde{r}} f[(r - \tilde{r})/a] \frac{2\pi\tilde{r}}{S^2} d\tilde{r} \quad (\text{A29})$$

Because of the spherical divergence assumed in our single source model, the dependence of dp on \tilde{r} in (A29) vanishes, leaving

$$dp = \frac{2\pi a}{S^2} P f[(r - \tilde{r})/a] d\tilde{r} \quad (\text{A30})$$

Changing variables from space to time and noting that $r = a + ct$, $\tilde{r} = a + c\tilde{t}$, and $d\tilde{r} = cd\tilde{t}$, we transform (A30) to

$$dp = \frac{2\pi ac}{S^2} P(t - \tilde{t}) d\tilde{t} \quad (\text{A31})$$

where $P(t)$ is the pulse shape of the single source.

Integration of (A31) gives the plane wave pressure at X .

$$p(R, t) = \frac{2\pi ac}{S} \int_{t_0}^t P(t - \tilde{t}) d\tilde{t} \quad (\text{A32})$$

$$= \frac{2\pi ac}{s^2} \int_0^{t-t_0} P(\tau) d\tau = \frac{2\pi ac}{s^2} I(t - t_0) \quad (A32)$$

where $t_0 = (R - a)/c$ is again the time when the first source pulses arrive at X. It is noted that (A32) is the product of a constant, $\frac{2\pi ac}{s^2}$, and the impulse of a single source. The pressure at X then is

$$\lim_{t \rightarrow \infty} p(R, t) = \frac{2\pi ac}{s^2} I_{\infty} \quad (A33)$$

where I_{∞} is the impulse of a single source. Since the impulse for a single source has a constant value, the pressure from an array of spherical sources with an arbitrary pulse shape will add up to a constant. The rise time of the summed pulse will depend on the impulse delivered by the single source as a function of time.

An approximation to the array pulse rise time may be obtained from the time at which the tangent of the pulse at the origin $t = t_0$ intersects the pressure plateau given by (A33). From equations (A32) and (A33), this time is

$$t_r = \frac{I_{\infty}}{P(0)} \quad (A34)$$

which is frequently defined as the source pulse characteristic time.

Summary

A line or tapered charge is often used to simulate the shock wave generated by an underwater nuclear burst. Because of the increasing utilization of shock-response analysis codes in conjunction with underwater shock tests, a more precise description of the pressure field generated by a line or tapered charge is required. It is found herein that, at distant field points nearly aligned with the axis of the charge, the virtually acoustic field is essentially spherical. This result admits an exceedingly simple, complete description of the incident-wave field.

LOCAL SPHERICITY OF THE ACOUSTIC FIELD

GENERATED BY A LINE CHARGE

Introduction

The simulation of underwater nuclear attack against submerged structures requires the generation of shock waves with roughly rectangular pressure profiles. In contrast to compact charges, line and tapered charges produce such shock waves at distant field points nearly aligned with the charge axis. But also in contrast to compact charges, data from a few pressure gauges are not sufficient to characterize thoroughly the incident-wave (essentially acoustic) field because of the gross departure from charge sphericity.

Thorough characterization of the incident-wave field seen by a shock-wave-excited, submerged structure has recently become an important requirement. This is due to the increasing utilization of finite-element shock-response codes for the treatment of underwater shock problems (see, e.g., [1]). Such codes generally require a complete specification of the (scalar) pressure and (vector) fluid-particle-velocity fields in the vicinity of the target under consideration.

Studies of the pressure field produced by a line charge date back many years (see, e.g., [2] and [3]). None known to the author, however, examine the fluid-particle-velocity field generated by such a charge. Hence the present study specifically examines the latter field on the basis of a line-charge model consisting of a linear array of acoustic sources. Although this model is not entirely satisfactory, it is sufficient, when supported by experimental data, to conclude that the virtually acoustic field at distant field points nearly aligned with the charge axis is essentially spherical.

Acoustic Analysis

In the limit of small disturbances, Figure 1 yields for the pressure and fluid-particle-velocity field increments appropriate to a line charge [4]

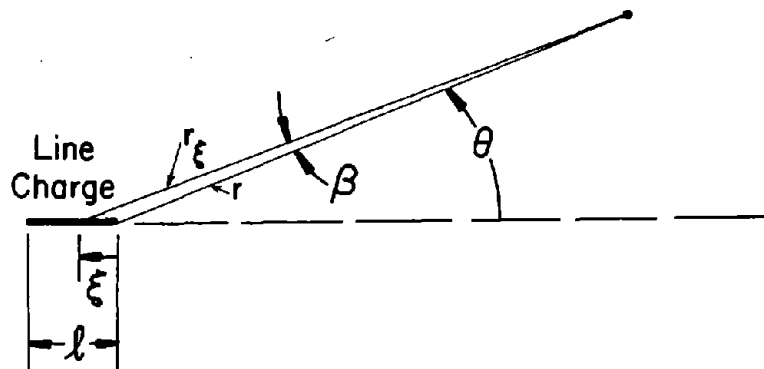


Figure 1. Geometry of the Line Charge Problem

$$dp_L(r, \theta, t) = \frac{w}{r} \int_0^{\xi} H(\xi) H(l - \xi) e^{-t\xi/\tau} H(t\xi) d\xi$$

$$du_{rL}(r, \theta, t) = \left[\frac{1}{\rho c} dp(r, \theta, t) + \frac{1}{\rho r} \int_0^{t\xi} dp(r, \theta, t') dt' \right] \cos \beta \quad (1)$$

$$du_{\theta L}(r, \theta, t) = -du_{rL}(r, \theta, t) \tan \beta$$

where each increment of the line charge is treated as a spherical source, and where

$$r_{\xi} = (r^2 + 2r\xi \cos \theta + \xi^2)^{\frac{1}{2}}$$

$$t_{\xi} = t - \xi/C - r_{\xi}/c \quad (2)$$

In the expressions above, w is the constant charge density, $H(z)$ is the Heaviside step-function, τ is a characteristic decay time, ρ and c are fluid density and sound velocity, respectively, and C is the detonation velocity for the line charge.

For $\theta^2 \ll 1$, $l^2 \ll r^2$, $u_{\theta L}$ can be neglected in comparison with u_{rL} , and (1) lead to

$$p_L(r, \theta, t) = \frac{w}{r} \int_0^x \left(1 - \frac{\xi}{r} \cos \theta\right) e^{-(t_r - \xi/c_e)/\tau} d\xi$$

$$u_{rL}(r, \theta, t) = \frac{1}{\rho c} p_L(r, \theta, t) \quad (3)$$

$$+ \frac{w\tau}{\rho r^2} \int_0^x \left(1 - e^{-(t_r - \xi/c_e)/\tau}\right) \left(1 - 2\frac{\xi}{r} \cos \theta\right) d\xi$$

where $t_r = t - r/c$ and

$$x = \begin{cases} c_e t_r, & t_r \leq l/c_e \\ l, & t_r > l/c_e \end{cases} \quad (4)$$

$$c_e = \frac{c C}{c + C \cos \theta}$$

Evaluation of the integrals in (3) yields, for $t_r \leq \ell/c_e$,

$$\begin{aligned}
 p_L(r, \theta, t) &= w \frac{c_e \tau}{r} \left[1 - e^{-t_r/\tau} + \frac{c_e \tau}{r} \left(1 - e^{-t_r/\tau} - t_r/\tau \right) \cos \theta \right] \\
 u_{rL}(r, \theta, t) &= \frac{w}{\rho c} \left(\frac{c_e \tau}{r} \right) \left\{ \left(1 - \frac{c\tau}{r} \right) \left(1 - e^{-t_r/\tau} \right) + \frac{ct_r}{r} \right. \\
 &\quad \left. + \frac{c_e \tau}{r} \left[\left(1 - 2\frac{c\tau}{r} \right) \left(1 - e^{-t_r/\tau} - t_r/\tau \right) - \left(\frac{ct_r}{r} \right) \frac{t_r}{\tau} \right] \cos \theta \right\} \quad (5)
 \end{aligned}$$

and, for $t_r > \ell/c_e$,

$$\begin{aligned}
 p_L(r, \theta, t) &= w \frac{c_e \tau}{r} \left\{ e^{\ell/c_e \tau} - 1 - \frac{c_e \tau}{r} \left[e^{\ell/c_e \tau} \left(\frac{\ell}{c_e \tau} - 1 \right) + 1 \right] \cos \theta \right\} e^{-t_r/\tau} \\
 u_{rL}(r, \theta, t) &= \frac{w}{\rho c} \left(\frac{c_e \tau}{r} \right) \left\{ \left(1 - \frac{c\tau}{r} \right) \left(e^{\ell/c_e \tau} - 1 \right) e^{-t_r/\tau} + \frac{c}{c_e} \left(\frac{\ell}{r} \right) \right. \\
 &\quad \left. - \frac{c_e \tau}{r} \left[\left(1 - 2\frac{c\tau}{r} \right) \left(e^{\ell/c_e \tau} \left[\frac{\ell}{c_e \tau} - 1 \right] + 1 \right) e^{-t_r/\tau} + \frac{c}{c_e} \left(\frac{\ell}{c_e \tau} \right) \frac{\ell}{r} \right] \cos \theta \right\} \quad (6)
 \end{aligned}$$

Representative pressure and fluid-particle-velocity profiles from (5) and (6) are shown in Figure 2 for $c\tau/\ell \approx c\tau/l \ll 1$.^{*} Under these conditions, as well as the original requirements that $\theta^2 \ll 1$ and $\ell^2 \ll r^2$, the terms underlined by dashed lines may be neglected.

Local representation of the field described by (5) and (6) in terms of a spherical wave in the region $r \approx R$, $\theta^2 \ll 1$ may be effected as

$$\begin{aligned}
 p_S(r, \theta, t) &= w \frac{c_e \tau}{r} \left[1 - e^{-t_r/\tau} + \frac{c_e \tau}{R} \left(1 - e^{-t_r/\tau} - t_r/\tau \right) \right] \\
 u_{rS}(r, \theta, t) &= \frac{w}{\rho c} \left(\frac{c_e \tau}{r} \right) \left\{ \left(1 - \frac{c\tau}{r} \right) \left(1 - e^{-t_r/\tau} \right) + \frac{ct_r}{r} \right. \\
 &\quad \left. + \frac{c_e \tau}{R} \left[\left(1 - \frac{c\tau}{r} \right) \left(1 - e^{-t_r/\tau} - t_r/\tau \right) - \frac{1}{2} \left(\frac{ct_r}{r} \right) \frac{t_r}{\tau} \right] \right\} \quad (7)
 \end{aligned}$$

^{*}The $O(\ell/r)$ late-time residual flow is due to a line-charge model whose pressure profile nowhere crosses into the negative pressure region.

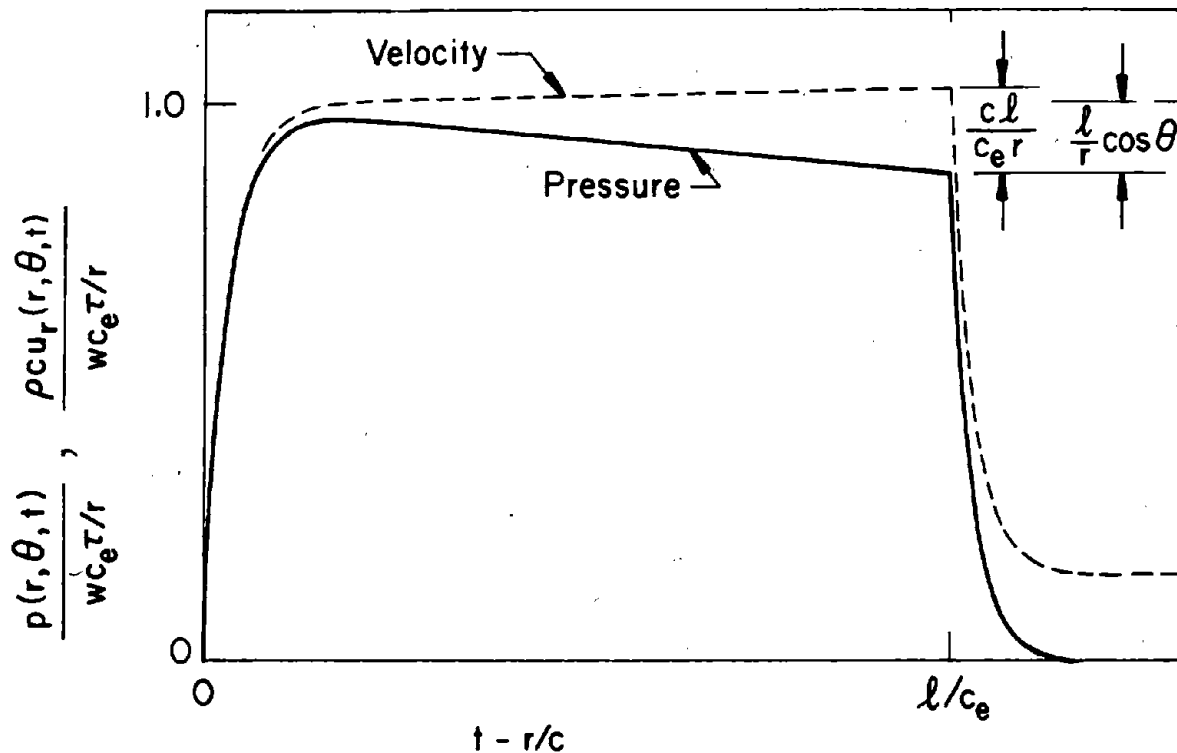


Figure 2. Analytical Pressure and Fluid-Particle-Velocity Histories for a Line Charge

for $t_r \leq l/c_e$, and as

$$\begin{aligned}
 p_s(r, \theta, t) &= w \frac{c_e \tau}{r} \left\{ e^{l/c_e \tau} - 1 - \frac{c_e \tau}{R} \left[e^{l/c_e \tau} \left(\frac{l}{c_e \tau} - 1 \right) + 1 \right] \right\} e^{-t_r/\tau} \\
 u_{rs}(r, \theta, t) &= \frac{w}{\rho c} \left(\frac{c_e \tau}{r} \right) \left\{ \left(1 - \frac{c \tau}{r} \right) \left(e^{l/c_e \tau} - 1 \right) e^{-t_r/\tau} + \frac{c}{c_e} \left(\frac{l}{r} \right) \right. \\
 &\quad \left. - \frac{c_e \tau}{R} \left[\left(1 - \frac{c \tau}{r} \right) \left(e^{l/c_e \tau} \left[\frac{l}{c_e \tau} - 1 \right] + 1 \right) e^{-t_r/\tau} + \frac{c}{2c_e} \left(\frac{l}{c_e \tau} \right) \frac{l}{r} \right] \right\} \quad (8)
 \end{aligned}$$

for $t > l/c_e$. Similarly, local representation in terms of a plane wave in the region may be effected as

$$p_p(r, \theta, t) = w \frac{c e^\tau}{R} \left[1 - e^{-t_r^*/\tau} + \frac{c e^\tau}{R} \left(1 - e^{-t_r^*/\tau} - \frac{t_r^*}{\tau} \right) \right] \quad (9)$$

$$u_{rP}(r, \theta, t) = \frac{1}{\rho c} p_p(r, \theta, t) \cos \theta$$

for $t \leq \ell/c_e$, and as

$$p_p(r, \theta, t) = w \frac{c e^\tau}{R} \left\{ e^{\ell/c_e \tau} - 1 - \frac{c e^\tau}{R} \left[e^{\ell/c_e \tau} \left(\frac{\ell}{c_e \tau} - 1 \right) + 1 \right] \right\} e^{-t_r^*/\tau} \quad (10)$$

$$u_{rP}(r, \theta, t) = \frac{1}{\rho c} p_p(r, \theta, t) \cos \theta$$

for $t > \ell/c$. In (9) and (10), $t_r^* = t - (r \cos \theta)/c$. A comparison of (7) and (8) with (5) and (6), respectively, shows that the local spherical wave model is quite accurate. A comparison of (9) and (10) with (5) and (6), respectively, shows that the local plane wave model becomes inaccurate as time proceeds because of its omission of the terms in (5) and (6) underlined by solid lines. This may readily be observed in Figure 2 as the discrepancy between the velocity and pressure curves. Hence, unless $\ell \ll r$, the local plane wave model does not satisfactorily describe the fluid-particle-velocity field.

Comparison with Experimental Results

Extensive experimental data from tapered charge tests conducted in the Chesapeake Bay are provided in [5]. Both pressure histories produced by piezoelectric pressure gauges and fluid-particle-velocity histories produced by waterproofed velocity meters are displayed. Figure 3 shows representative results from [5], as corrected in accordance with [6]. The pressure histories of Figures 2 and 3 demonstrate that the assignment of appropriate values for w and τ would produce an excellent acoustic representation of the experimental pressure history up to $t = \ell/c_e \approx (11.2 \text{ ft}) / (4.5 \text{ ft-msec}^{-1}) \approx 2.5 \text{ msec}$. The resulting acoustic model cannot then match the long tail between $t = 2.5 \text{ msec}$ and $t = 5.5 \text{ msec}$, however.

As indicated by the acoustic analysis, Figure 3 demonstrates that a local spherical wave representation calibrated to the incident-wave pressure history produces highly accurate results for radial fluid-particle velocity. In fact, the major discrepancy between the two fluid-particle-velocity histories in Figure 3 is caused by the approximately 0.1-msec delay in velocity-meter response associated with the time it takes the wave front of an acoustic wave to traverse the length of the four-inch-long meter [7].

Finally, Figure 3 shows that a plane-wave model, which would yield the $p/\rho c$ curve as a velocity history, is about 17% below the measured response at $t = 2.5 \text{ msec}$. This agrees almost perfectly with the acoustic-model prediction of $100 \cdot c \ell / c_e r$ % error at this time for $c = 5 \text{ ft/msec}$, $c_e = 4.5 \text{ ft/msec}$, $\ell = 11.2 \text{ ft}$ and $r = 72.75 \text{ ft}$.

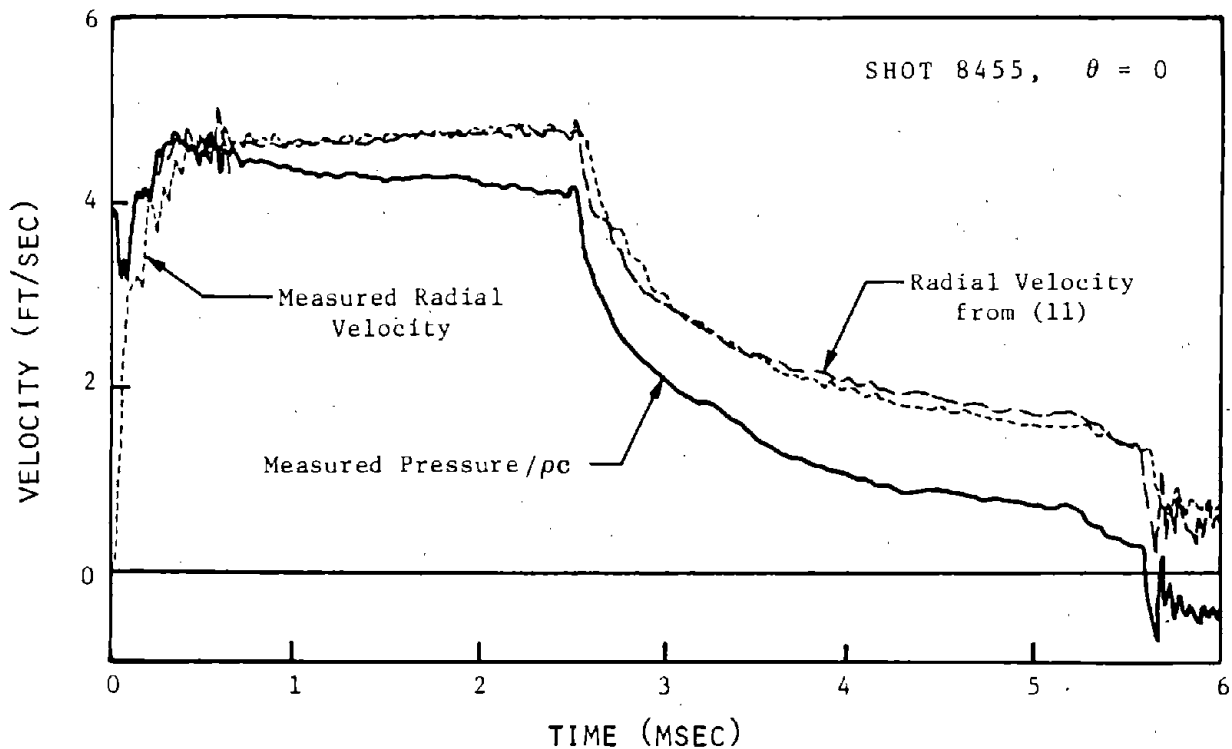


Figure 3. Measured and Calculated Histories for a Tapered Charge

Conclusion

This study has shown that the acoustic field generated at some distance from, and along the axis of, a line charge is accurately represented as

$$p_L(r, \theta, t) = \frac{R}{r} [p_1(t_r) + \frac{\lambda}{r} p_2(t_r)]$$

$$u_{\theta L}(r, \theta, t) = 0 \tag{11}$$

$$u_{rL}(r, \theta, t) = \frac{1}{\rho c} p_L(r, \theta, t) + \frac{1}{\rho r} \int_0^t p_L(r, \theta, t') dt'$$

where $p_1(t)$ and $p_2(t)$ may be experimentally determined. Furthermore, because $p_1(t)$ and $p_2(t)$ are comparable in magnitude, $p_L(r, \theta, t)$ is accurately represented in the region $r \approx R$ as a spherical wave:

$$p_L(r, \theta, t) \approx \frac{R}{r} [p_1(t_r) + \frac{\lambda}{R} p_2(t_r)] \tag{12}$$

which, along with the last of (11), constitutes an exceedingly simple result.

References

1. J. A. DeRuntz, T. L. Geers, C. A. Felippa, "The Underwater Shock Analysis (USA) Code, A Reference Manual," Final Report on Contract No. DNA001-76-C-0285, 1978
2. G. Charlesworth and A. R. Bryant, "An Approximate Calculation of the Pressures Produced by Detonating Line Charges Underwater," Underwater Explosion Research; Volume 1: The Shock Wave, Office of Naval Research, 1950
3. G. K. Hartman, "Kinematic Description of the Shock Wave Formed by the Detonation of an Underwater Line Charge," NAVORD Report 6692, U.S. Naval Ordnance Laboratory, White Oak, Maryland, 1959
4. R. H. Cole, Underwater Explosions, Princeton University Press, Princeton, New Jersey, 1948
5. J. D. Gordon, "Water Pressure and Velocity from the Shock Wave of a Tapered Charge Fired in the Chesapeake Bay During September 1973," Enclosure (1) to NSRDC letter, Ser. 177-125 of 17 October 1973
6. J. D. Gordon, "Recalibration of Pressure Gages Used in the Free Field and Side-On Model Tests," Enclosure (1) to NSRDC letter Ser. 177-23 of 29 March 1974
7. J. D. Gordon, "The Development of a Water Particle Velocity Meter," Shock and Vibration Bulletin, Vol. 45, Part 2, p. 151, June 1975

Acknowledgment

This study was sponsored by the Office of Naval Research under Contract N00014-72-C-0347.

DISTRIBUTION LIST

DEPARTMENT OF DEFENSE

Assistant to the Secretary of Defense
Atomic Energy
ATTN: Executive Assistant

Defense Advanced Rsch. Proj. Agency
ATTN: TIO

Defense Civil Preparedness Agency
ATTN: Hazard Eval. & Vul. Red. Div., G. Sisson

Defense Documentation Center
12 cy ATTN: DD

Defense Intelligence Agency
ATTN: DB-4C, E. O'Farrell
ATTN: DT-1C
ATTN: DT-2

Defense Nuclear Agency
ATTN: DDST
ATTN: SPTD
ATTN: STSP
ATTN: SPAS
4 cy ATTN: TITL
6 cy ATTN: SPSS

Department of Defense Explo. Safety Board
ATTN: Chairman

Field Command
Defense Nuclear Agency
ATTN: FCPR
ATTN: FCTMOF
ATTN: FCT
ATTN: FCTMO, R. Davis
ATTN: FCT, R. Delaar
ATTN: FCTMEI, N. Gantick
ATTN: FCTMEI, J. Holland
ATTN: FCTM, C. Keller
ATTN: FCTMES, D. Martens
ATTN: FCT, F. McMullan
ATTN: FCTMD, D. Shivell
ATTN: FCTMA, L. Stefani
ATTN: FCTMO, J. Strode
ATTN: FCTMO, J. Thomas
ATTN: FCTM, W. Tyler
ATTN: FCTMD, R. Bestgen
ATTN: FCPRK, M. Marlett

Field Command
Defense Nuclear Agency
ATTN: FCPRL
ATTN: FCPRL, W. Beyatte
ATTN: FCPRL, R. Gordon
ATTN: FCPRL, T. Mills

Field Command Test Directorate
Test Construction Division
Defense Nuclear Agency
ATTN: FCTC

NATO School (SHAPE)
ATTN: U.S. Documents Officer

DEPARTMENT OF DEFENSE (Continued)

Under Secy. of Def. for Rsch. & Engrg.
ATTN: Strategic & Space Systems (OS)

DEPARTMENT OF THE ARMY

Chief of Engineers
Department of the Army
ATTN: DAEN-RDM
ATTN: DAEN-MCE-D

Deputy Chief of Staff for Ops. & Plans
Department of the Army
ATTN: MOCA-ADL

Deputy Chief of Staff for Rsch. Dev. & Acq.
Department of the Army
ATTN: DAMA-CSM-N

Harry Diamond Laboratories
Department of the Army
ATTN: DELHO-N-P
ATTN: DELHO-I-TL

U.S. Army Armament Research & Development Command
ATTN: LCWSL, M. Ravotto
ATTN: LCWSL, D. Waxler

U.S. Army Ballistic Research Labs.
ATTN: DRDAR-BLT, W. Taylor
ATTN: DRDAR-BLE, J. Keefer
ATTN: Technical Library
ATTN: DRDAR-BLV
ATTN: DRDAR-BLT, B. Bertrand
ATTN: DRDAR-BLT, N. Ethridge
ATTN: DRDAR-BLT, N. Huffington
ATTN: DRDAR-BLT, C. Kitchens
ATTN: DRDAR-BLV, E. Quigley
ATTN: DRDAR-BLT, G. Teel

U.S. Army Engr. Waterways Exper. Station
ATTN: J. Strange
ATTN: G. Jackson
ATTN: Library
ATTN: W. Flathau

U.S. Army Material & Mechanics Rsch. Center
ATTN: Technical Library

U.S. Army Materiel Dev. & Readiness Cmd.
ATTN: DRXAM-TL

U.S. Army Missile R&D Command
ATTN: RSIC

U.S. Army Mobility Equip. R&D Cmd.
ATTN: DRDME-WC

U.S. Army Natick Rsch. & Dev. Command
ATTN: DRDNA-UST, W. Crenshaw

U.S. Army Nuclear & Chemical Agency
ATTN: Library
ATTN: G. McCall
ATTN: J. Sims

DEPARTMENT OF THE NAVY

David Taylor Naval Ship R & D Ctr.
ATTN: Code 1844
ATTN: Code L42-3
ATTN: Code 17
ATTN: Code 177, E. Palmer
ATTN: Code 1740.1
ATTN: Code 1770.1, V. Bloodgood
ATTN: Code 1740.1, W. Conley
ATTN: Code 1740.4, J. Gordon
ATTN: Code 1770.4, R. Walker
2 cy ATTN: Code 1740.5, B. Whang

Naval Construction Battalion Center
Civil Engineering Laboratory
ATTN: Code L51, R. Odello
ATTN: Code L08A
ATTN: Code L51, W. Armstrong

Naval Electronic Systems Command
ATTN: PME 117-21

Naval Facilities Engineering Command
ATTN: Code 03T
ATTN: Code 04B
ATTN: Code 09M22C

Naval Material Command
ATTN: MAT 08T-22

Naval Ocean Systems Center
ATTN: G. Meyer

Naval Research Laboratory
ATTN: Code 2627
ATTN: Code 8440, G. O'Hara
ATTN: Code 8404, H. Pusey

Naval Sea Systems Command
ATTN: SEA-09G53
ATTN: SEA-0351

Naval Ship Engineering Center
ATTN: Code 09G3
2 cy ATTN: SEC-6105D

Naval Surface Weapons Center
ATTN: Code R14, I. Blatstein
ATTN: Code F31
ATTN: Code R14, M. Giltrud
ATTN: Code R14, D. Nicholson
ATTN: Code R15, J. Petes
ATTN: Code R15, J. Pittman

Naval Surface Weapons Center
ATTN: Tech. Library & Info. Services Branch

Naval Weapons Evaluation Facility
ATTN: R. Friedberg
ATTN: R. Tillery

Office of Naval Research
ATTN: Code 474, N. Perrone
ATTN: Code 715

Office of the Chief of Naval Operations
ATTN: OP 03EG
ATTN: OP 981

DEPARTMENT OF THE NAVY (Continued)

Strategic Systems Project Office
Department of the Navy
ATTN: NSP-272
ATTN: NSP-43

DEPARTMENT OF THE AIR FORCE

Air Force Geophysics Laboratory
ATTN: LWV, K. Thompson

Air Force Institute of Technology
ATTN: Library

Air Force Systems Command
ATTN: DLW
ATTN: IG, J. Neal

Electronics Systems Division
ATTN: TOST, P. Zielie

Air Force Weapons Laboratory, AFSC
ATTN: SUL
ATTN: DE, M. Plamondon
ATTN: DES-C, R. Henny
ATTN: DEX
ATTN: DED, G. Lederman
ATTN: DED, R. Matalucci
ATTN: DED, D. Ray
ATTN: DEX, J. Renick
ATTN: DED, J. Williams

Assistant Chief of Staff
Intelligence
Department of the Air Force
ATTN: INT

Deputy Chief of Staff
Research, Development & Acq.
Department of the Air Force
ATTN: AFRDQSM

Space & Missile Systems Organization
Air Force Systems Command
ATTN: MNNH, T. Edwards
ATTN: MNNH, D. Gale

Strategic Air Command
Department of the Air Force
ATTN: NRI-STINFO Library

Vela Seismological Center
ATTN: G. Uirrich

DEPARTMENT OF ENERGY

Department of Energy
Albuquerque Operations Office
ATTN: CTID

Department of Energy
ATTN: Doc. Con. for Classified Library

Department of Energy
Nevada Operations Office
ATTN: Mail & Records for Technical Library

Office of Military Application
Department of Energy
ATTN: Doc. Con. for Res., Dev. & Test

DEPARTMENT OF ENERGY CONTRACTORS

Lawrence Livermore Laboratory
ATTN: L-96, L. Woodruff
ATTN: Technical Information Dept. Library
ATTN: P. Brown
ATTN: H. Glenn
ATTN: G. Kramer
ATTN: W. Nok

Los Alamos Scientific Laboratory
ATTN: MS 364
ATTN: B. Craig
ATTN: M. Sanford

Sandia Laboratories
ATTN: 3141

Sandia Laboratories
ATTN: Library & Security Classification Div.

DEPARTMENT OF DEFENSE CONTRACTORS

Acurex Corp. *
ATTN: J. Huntington
ATTN: C. Wolf
ATTN: K. Triebes

Aerospace Corp.
ATTN: Technical Information Services
ATTN: D. Holmes
ATTN: R. Mortensen

Agbabian Associates
ATTN: M. Balachandra
ATTN: J. Malthan
ATTN: F. Safford

Boeing Co.
ATTN: Aerospace Library
ATTN: R. Dyr Dahl
ATTN: K. Holsapple
ATTN: R. Schmidt

California Research & Technology, Inc.
ATTN: M. Rosenblatt
ATTN: S. Schuster

California Research & Technology, Inc.
ATTN: D. Orphal

Civil Systems, Inc.
ATTN: J. Bratton
ATTN: J. Phillips
ATTN: E. Bultmann
ATTN: L. Melzer

EG&G Washington Analytical Services Center, Inc.
ATTN: Library
ATTN: E. Jaramillo
ATTN: J. Mackey

Electro-Mechanical Systems of New Mexico, Inc.
ATTN: R. Shunk

General Electric Company-TEMPO
Center for Advanced Studies
ATTN: DASIAC
ATTN: R. Rowland
ATTN: J. Kelso

DEPARTMENT OF DEFENSE CONTRACTORS (Continued)

Eric H. Wang
Civil Engineering Rsch. Fac.
The University of New Mexico
ATTN: N. Baum
ATTN: H. Auld
ATTN: K. Bell
ATTN: D. Calhoun
ATTN: G. Leigh
ATTN: H. Wampler

General Electric Company
ATTN: L. Kennedy

Geocenters, Inc.
ATTN: E. Marram

Georgia Institute of Technology
Office of Contract Administration
ATTN: Rsch. Security Coordinator for
S. Hanagud

H-Tech. Labs, Inc.
ATTN: B. Hartenbaum

IIT Research Institute
ATTN: Documents Library

Institute for Defense Analyses
ATTN: Classified Library

Jaycor
ATTN: H. Linnerud

Jaycor
ATTN: P. Nakayama

Kaman Sciences Corp.
ATTN: Library
ATTN: D. Sachs

Lockheed Missiles & Space Co., Inc.
ATTN: TIC-Library

Lockheed Missiles and Space Co., Inc.
ATTN: T. Geers
ATTN: Technical Library

Lovelace Biomedical & Environmental Research
Institute, Inc.
ATTN: D. Richmond
ATTN: R. Fletcher

Martin Marietta Corp.
ATTN: C. Ernst
ATTN: R. Heyman

Merritt CASES, Inc.
ATTN: J. Merritt
ATTN: H. Davis

Pacifica Technology
ATTN: J. Kent
ATTN: R. Allen

Princeton Combustion Research Laboratories, Inc.
ATTN: M. Summerfield

DEPARTMENT OF DEFENSE CONTRACTORS (Continued)

Physics International Co.

ATTN: C. Vincent
ATTN: E. Moore
ATTN: Technical Library
ATTN: F. Sauer
ATTN: J. Thomsen

R & D Associates

ATTN: R. Port
ATTN: C. MacDonald
ATTN: Technical Information Center
ATTN: J. Lewis
ATTN: H. Brode
ATTN: H. Carpenter
ATTN: A. Kuhl
ATTN: J. Whitener

R & D Associates

ATTN: H. Cooper

Radkowski Associates

ATTN: P. Radkowski

Rand Corp.

ATTN: A. Laupa

Science Applications, Inc.

ATTN: Technical Library
ATTN: J. Craig
ATTN: H. Wilson
ATTN: M. McKay
ATTN: R. Schlaug

Science Applications, Inc.

ATTN: J. Dishon

Science Applications, Inc.

ATTN: M. Knasel
ATTN: M. McDonnell
ATTN: B. Chambers

Science Applications, Inc.

ATTN: D. Hove

DEPARTMENT OF DEFENSE CONTRACTORS (Continued)

Southwest Research Institute

ATTN: W. Baker
ATTN: A. Wenzel

SRI International

ATTN: B. Gasten
ATTN: G. Abrahamson
ATTN: A. Florence
ATTN: H. Lindberg
ATTN: P. Senseny

Systems, Science & Software, Inc.

ATTN: Library
ATTN: D. Grine
ATTN: J. Baker
ATTN: J. Barthel
ATTN: P. Coleman
ATTN: E. Demaris
ATTN: H. Kratz
ATTN: C. Peterson
ATTN: T. Pierce
ATTN: K. Pyatt
ATTN: R. Sedgewick

TRW Defense & Space Sys. Group

ATTN: D. Baer
ATTN: Technical Information Center
ATTN: J. Lai
2 cy ATTN: P. Dai

TRW Defense & Space Sys. Group

ATTN: E. Wong
ATTN: N. Lipner
ATTN: T. Schiffman
ATTN: G. Hulcher

Weidlinger Assoc., Consulting Engineers

ATTN: M. Baron
ATTN: D. Ranlet

Weidlinger Assoc., Consulting Engineers

ATTN: J. Isenberg